Diss. ETH No. 14'871

Initial phase of

landslide generated impulse waves

A dissertation submittet to the

Swiss Federal Institute of Technology Zürich

(ETH Zürich)

for the degree of

Doctor of Technical Sciences

presented by

Hermann M. Fritz

Dipl. Bau-Ing. ETH
born on May 20, 1972
citizen of Zürich (ZH)

accepted on the recommendation of

Prof. Dr.-Ing. H.-E. Minor, examiner
Prof. Dr. W.H. Hager, co-examiner
Prof. Dr. I. Grant, co-examiner

2002

Table of contents

Abstract

Large water waves in reservoirs, lakes, bays and oceans may be generated by landslides, shore instabilities, snow avalanches, glacier and rock falls. For Alpine lakes impulse waves are particularly significant, due to steep shores, narrow reservoir geometries, possible large slide masses and high impact velocities. The resulting impulse waves can cause disaster due to run-up along the shoreline and overtopping of dams. The complexity of the phenomena posed formidable challenges to physical model experiments that encompassed laboratory set-up, measurement techniques and data analysis. The verified scaling law was based on the generalized Froude similitude. The granular rockslide impact experiments were conducted in a rectangular prismatic water wave channel. The slide impact characteristics were controlled by means of a novel pneumatic landslide generator, which allowed exact reproduction and independent variation of single dynamic slide parameters within a broad spectrum. The following four relevant parameters governing the wave generation were analyzed: granular slide mass, slide impact velocity, stillwater depth and slide thickness. The slope angle $\alpha = 45°$, the slide granulate density $\rho_g = 2.64$ t$/$m^3 and the grain diameter were not altered. State-of-the-art laser measurement techniques such as digital particle image velocimetry (PIV) and laser distance sensors (LDS) were applied to the decisive initial phase. The wave generation was characterized by an extremely unsteady three phase flow consisting of the slide granulate, water and air entrained into the flow. PIV provided instantaneous velocity vector fields in a large area of interest and gave insight into the kinematics of the wave generation process. Differential estimates such as vorticity, divergence, elongational and shear strain were extracted from the velocity vector fields. The fundamental assumption of irrotational flow in the Laplace equation was confirmed experimentally. At high impact velocities flow separation occurred on the slide shoulder resulting in a hydrodynamic impact crater, whereas at low impact velocities no flow detachment was observed. The hydrodynamic impact craters may be distinguished into outward and backward collapsing impact craters. The maximum crater volume, which corresponds to the water displacement volume, exceeded the landslide volume by up to an order of magnitude. The water displacement caused by the landslide generated the first wave crest and the collapse of the air cavity followed by a run-up along the slide ramp issued the second wave crest. The extracted water displacement curves may replace the complex wave generation process in numerical models. The recorded wave profiles were extremely unsteady and non-linear. Four wave types were determined: weakly non-linear oscillatory wave, non-linear transition wave, solitary-like wave and dissipative transient bore. Most of the generated impulse waves were located in the intermediate water depth wave regime. Nevertheless the propagation velocity of the leading wave crest closely followed the theoretical approximations for a solitary wave. Between 5 and 50% of the kinetic slide impact energy propagated outward in the impulse wave train. The main wave characteristics were related to the landslide parameters driving the

whole wave generation process. The subaqueous slide run-out, the water displacement and the main wave characteristics were all described by multiple regressions of the following three dimensionless quantities: the slide Froude number, the relative slide volume and the relative slide thickness. The slide Froude number was identified as the dominant parameter. The obtained predictive equations allow a rapid assessment of the threats posed by a possible event. A detailed investigation, however, would require a full numerical simulation including the lake bathymetry and the surrounding topography. The physical model results were compared to the giant rockslide generated impulse wave which struck the shores of the Lituya Bay, Alaska, in 1958. The measurements obtained in the physical model were in agreement with the in-situ data.

Zusammenfassung

Impulswellen in Seen und Stauseen, Meeresbuchten und Ozeanen entstehen hauptsächlich als Folge von Erdrutschen und Uferinstabilitäten, Fels- und Bergstürzen sowie Gletscherabbrüchen und Schneelawinen. Für alpine Seen und Stauseen sind Impulswellen besonders relevant wegen den steilen Uferböschungen, geringen Seebreiten sowie möglichen grossen Rutschmassen und hohen Eintauchgeschwindigkeiten. Die auflaufenden Impulswellen können Uferbereiche verwüsten sowie an Talsperren überschwappen. Die Initialphase von Impulswellen mit dem Eintauchen der Rutschmasse und der Wellengenerierung sowie dem Nahbereich der Wellenausbreitung wurde in einem physikalischen Modell untersucht. Die Froude'sche Modellähnlichkeit wurde verifiziert und die Versuche in einem prismatischen Wellenkanal mit Rechteckquerschnitt durchgeführt. Die granularen Rutschmassen wurden mit einem eigens entwickelten pneumatischen Rutschgenerator auf die Eintauchgeschwindigkeit beschleunigt, womit eine nahezu exakte Reproduktion von Experimenten sowie eine unabhängige Variation einzelner Rutschparameter ermöglicht wurde. Untersucht wurde der Einfluss der folgenden vier Parameter: granulare Rutschmasse, Eintauchgeschwindigkeit des Rutsches, Ruhewassertiefe und Rutschmächtigkeit. Der Böschungs- und Eintauchwinkel $\alpha = 45°$, die Rutschgranulat-Dichte $\rho_g = 2.64 \text{ t/m}^3$ und der Korndurchmesser wurden nicht variiert. Die Impulswellengenerierung wird durch eine instationäre Dreiphasen-Strömung gekennzeichnet, bestehend aus dem Rutschgranulat und dem Wasser sowie eingetragener Luft. Particle image velocimetry (PIV) ermöglicht das grossflächige Erfassen von momentanen Strömungsfeldern im Eintauch- und Wellengenerierungs-Bereich. Rotations-, Divergenz- und Deformationsfelder wurden aus den momentanen Geschwindigkeitsfeldern berechnet. Die Strömung unter Impulswellen war weitgehend rotationsfrei und bestätigte experimentell diese grundlegende Annahme in der Laplace-Gleichung. Ein hydrodynamischer Eintauchkrater bildete sich bei hohen Eintauchgeschwindigkeiten als Folge der Strömungsablösung an der Schulter des Rutsches aus, während bei geringen Eintauchgeschwindigkeiten keine Strömungsablösung beobachtet wurde. Die hydrodynamischen Eintauchkrater können in nach innen und nach aussen kollabierende Krater unterteilt werden. Das maximale Kratervolumen, welches der Wasserverdrängung entspricht, überschritt das Rutschvolumen je Einheitsbreite um bis zu einer Grössenordnung. Der erste Wellenkamm wurde direkt durch den eintauchenden Rutsch erzeugt, während das wiederholte Auf- und Zurücklaufen von Wassermassen auf der Böschung der Sturzbahn die nachfolgenden Wellen erzeugte. Die ermittelten Wasserverdrängungs-Ganglinien könnten als Anfangsbedingung für numerische Simulationen dienen – ohne dabei auf die Details der komplexen Wellengenerierung einzugehen. Die Wellenaufzeichnungen waren extrem instationär und nichtlinear. Vier Wellentypen wurden bestimmt: leicht nicht-lineare oszillierende Welle, nicht-lineare Übergangswelle, Soliton-ähnliche Welle und dissipative transiente Bore.

Typischerweise liegen Impulswellen im Übergangsbereich zwischen den Flach- und Tiefwasser-Regimen. Trotzdem konnte die Wellenausbreitungs-Geschwindigkeit des ersten Wellenkamms mit der Solitärwellen-Theorie beschrieben werden. Zwischen 5 und 50% der kinetischen Rutschenergie wurde beim Eintauchen in Wellenenergie umgewandelt. Die subaquatische Rutschauslauflänge, die Wasserverdrängung und die Wellenparameter wurden als Funktion der relevanten Rutschparameter dargestellt. Die folgenden dimensionslosen Parameter wurden berücksichtigt: Froude-Zahl des Rutsches, relatives Rutschvolumen und relative Rutschmächtigkeit. Die Froude-Zahl des Rutsches war dabei die dominante Grösse. Die ermittelten Dimensionierungsgleichungen ermöglichen eine Vorhersage möglicher Bedrohungen. Eine exakte Untersuchung einzelner Ereignisse erfordert eine numerische Simulation oder eine spezifische Modelluntersuchung unter Berücksichtigung der lokalen Topographie. Die Resultate der systematischen Modelluntersuchung wurden mit der grössten je auf-gezeichneten Impulswelle in der Lituya Bucht in Alaska 1958 verglichen. Die physikalischen Modellmessungen und die in-situ Daten zeigen eine erfreuliche Übereinstimmung.

1 Introduction

1.1 Problem outline

In general impulse waves are gravity water waves, which may be generated by various dynamic water displacing events such as mass flows, volcanic eruptions, earthquakes, asteroid impacts or underwater explosions. The mass flows may be subdivided into high density rock and soil movements and low density glacier falls and snow avalanches. Herein only impulse waves generated by landslides are considered, whereas other causes are only used for comparisons. Among all mass flows landslides contributed to the most destructive impulse waves in recorded history.

The classification of the landslide and water body interaction is based on the initial position of the landslide relative to the still water surface. Three categories are commonly used: subaerial landslide impacts, partially submerged landslides and subaqueous or submarine landslides. The initial position of the landslide determines the physical characteristics of the process and in particular the role of the air as third phase. Subaqueous or submarine landslide may be treated as a two phase flow consisting of slide material and water interaction. For subaerial landslide impacts three phases become of importance: slide material, water, and air. There is a gradual transition from subaqueous to subaerial landslides with decreasing submergence. This classification is commonly used for observations and both physical and numerical models of landslide generated impulse waves. Only subaerial landslide impacts into water bodies are considered herein.

Impulse waves occur in almost all water bodies including reservoirs, lakes, bays and oceans. The water body has no triggering effect on subaerial landslides, whereas partially submerged and subaqueous landslides can be triggered by varying water levels in reservoirs or tides in oceans. For Alpine lakes impulse waves are particularly significant, due to steep shores, narrow reservoir geometries, possible large slide masses and high impact velocities. Impulse waves are commonly referred to tsunamis if they occur in oceans. Tsunami is a Japanese two character word with "tsu" meaning harbor and "nami" wave. The term tsunami does not indicate the wave generation mechanism in the terminology used in Japan and by the scientific community, whereas the general public sometimes refers only to seismic sea waves. In recent studies on tsunami generation mechanisms the importance of landslides and in particular submarine landslides has continuously increased, although the majority is generated by earthquakes now as before. Landslides account for roughly 10 % of tsunamis observed in oceans (Kajiura, 1990).

The impulse wave phenomenon may be subdivided into three main phases shown in Fig. 1.1. The first stage involves the whole wave generation process with the landslide impact and the run-out along the bed of the water body, the water displacement and the wave formation. The second stage embraces the propagation of the impulse wave train

over the water body including lateral spreading and dispersion. The third stage is characterized by the wave run-up along the shoreline and includes also the transformation of the waves with decreasing water depth. The transition between the different phases is fluent. In particular in narrow Alpine reservoirs or lakes the wave run-up can begin even before the landslide motion has terminated actually skipping the intermediate wave propagation stage. The focus of the present study is on the wave generation process and the near field wave propagation. Regarding the wave run-up it is referred to Müller (1995).
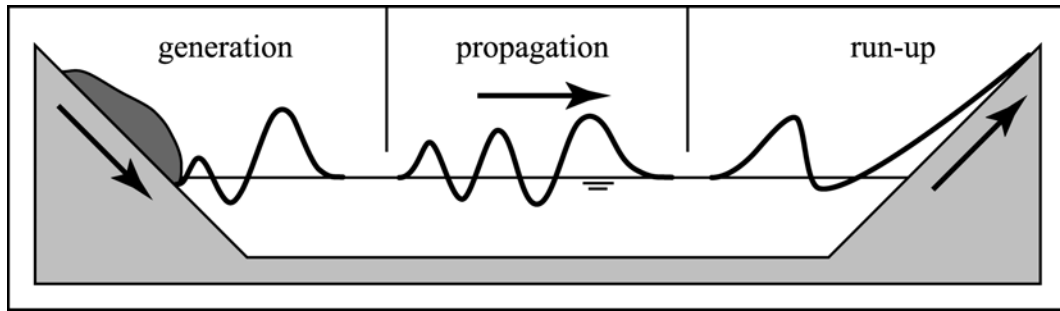
Figure 1.1 **Phases** of landslide generated impulse waves: wave generation by landslide impact, wave propagation over water body and wave run-up along the shoreline.

Impulse waves can cause disaster due to run-up along the shoreline and overtopping of dams. The wave run-up is the most threatening stage accounting for most of the fatalities. The worst catastrophe in the history of Alpine hydraulic construction was caused by a massive landslide impact into the Vajont reservoir in northern Italy in 1963. The resulting impulse wave ran up 270 m in the prolongation of the slide axis and overtopped the dam by over 100 m. The subsequent dam break like flood wave down the Piave valley erased several villages resulting in 2000 casualties. Even for ships the wave propagation in relatively deep water does usually not cause damage due to the long wave length and relatively small wave steepness. The largest water wave in recorded history was generated by a landslide impact into the Lituya bay on the south shore of Alaska in 1958. The wave exceeded 100 m in wave height and chopped trees up to 500 m above the mean sea level. Nevertheless the shipping boat in the middle of the bay was able to ride the wave, whereas the boats near the shore were smashed against the shore. This characteristic behavior explains the origins of the word tsunami as harbour wave. Further tsunamis are often difficult to observe on the open ocean due to the long wave length. Landslide generated impulse waves tend to be shorter in wave length than earthquake generate impulse waves. Earthquake generated impulse waves are shallow water waves whereas landslide generated impulse waves often fall into the intermediate water depth regime.

In most cases it is difficult to prevent a landslide from occurring. In some cases it was possible to stop the creeping of active landslides with massive remedial methods. The key and also most costly example is the Clyde dam in New Zealand. The creeping of several active slides was stopped by a combination of drainage works to lower the groundwater level and large scale mass displacements unloading the head of active frontal lobes and buttressing the toe of the lobes (Jennings et al. 1991; Macfarlane and Gillon, 1996; Mac-

farlane and Jenks, 1996; Gillon and Saul, 1996). Small rock masses can be released artificially by blasting after securing the perimeter (Müller, 1992). Blasting is limited to small masses up to roughly $100'000\text{m}^3$. In most other cases continuous monitoring of potential slide masses is the sole remaining option. In particular landslides above reservoirs are continuously monitored. In the case of increased threat a controlled reservoir draw-down is the final measure. In the case of a potential landslide into an unregulated natural water body evacuation of threatened shorelines may be inevitable. A real time monitoring of incident waves parallel to the evacuation of threatened shorelines is only possible in oceans due to the sometimes large propagation distance. Both the reservoir draw-down and the evacuation require precise predictions of the wave characteristics in order to be effective.

1.2 Previous studies at VAW

The Laboratory of Hydraulics, Hydrology and Glaciology (VAW) of the Swiss Federal Institute of Technology (ETH) has investigated landslide generated impulse waves over the last three decades. Three main research studies and numerous consulting reports were presented. The majority of the consulting work was conducted by long time VAW senior researcher Dr. Andreas Huber. The three previous research studies are:

- Huber, A. (1980). Schwallwellen in Seen als Folge von Felstürzen (in German).
- Sander, J. (1990). Weakly nonlinear unidirectional shallow water waves generated by a moving boundary.
- Müller, D. (1995). Auflaufen und Überschwappen von Impulswellen an Talsperren (in German).

The present study is the fourth conducted on landslide generated impulse waves at VAW. Each of the four studies had a different focus. Huber conducted physical model experiments on granular landslide impacts into a two dimensional wave channel and a three dimensional wave basin covering all phases from the wave generation and propagation to the wave run-up. The wave generation process was treated as input-output model or "black box". Sander conducted both physical model experiments and numerical simulations on a piston type wave maker. Müller investigated the run-up along shorelines and the overtopping of dams by landslide generated impulse waves in a physical laboratory model.

1.3 Purpose of present research

The outlined impulse wave complex with the wave generation and propagation as well as the wave run-up is far to broad to be treated in a single Ph.D. study. The wave propagation and run-up are basic research topics in coastal and ocean engineering. Numerous design

guidelines based on experimental studies as well as analytical and numerical solutions are available. Hence the wave run-up is not considered at all herein and the wave propagation only regarding the near field. The focus of the present study on landslide generated impulse waves is set on the initial phase with the landslide impact and the wave generation. The wave generation by submarine and partially submerged landslides received strong attention over the last decade. Combined experimental and numerical models were presented yielding promising results. The wave generation by high speed subaerial landslide impacts was seldom considered over the last decade. Further numerical models which produce reasonable results were not available at the beginning of the present study, but significant progress has been made in this regard during the last few years. Therefore only subaerial landslide impacts are considered in this physical model study.

Although research on landslide generated impulse waves has been conducted over three decades at VAW various fundamental aspects remain unclarified. The current design approach for the wave height based on the study of Huber (1980) does not include any dynamic slide parameter such as the slide Froude number, whereas all other experimental studies on landslide generated impulse waves exhibited the importance of the slide Froude number. The discrepancy may not be resolved with the available experimental physical model studies due to the different modeling of the landslide. Huber's study is the only available systematic analysis of subaerial landslide impacts conducted with granular landslides. All other systematic experiments on subaerial landslide impacts were based on block models or pistons with a forced motion. The landslide and water wave interaction was treated as "black box" or input-output model in previous studies without investigating the complex processes involved. Therefore the present study aims to understand the initial phase of impulse waves generated by subaerial landslide impacts.

The purpose of the present study was based on hydrodynamic similarity, and the experiments in a two-dimensional physical model may be summarized as follows:

- Understand the mechanism of wave generation and the involved processes.
- Acquire instantaneous flow fields in the slide impact and wave generation area with particle image velocimetry (PIV) to analyze the landslide and water body interaction.
- Determine the subaqueous slide motion including the slide run-out, the duration of the slide motion and the velocity decay.
- Estimate the role of the three phases: water, slide granulate and entrained air.
- Determine the water displacement curve and the maximum water displacement.
- Provide a full description of the macro structure of the flow in the slide impact and wave generation area.
- Determine the water particle velocities in the slide impact and wave generation area.
- Ascertain the role of the different components of the deformation tensor including the vorticity, the divergence and the elongational and shear strains.
- Determine the wave types and the governing wave features.

- Quantify the effects of the slide impact velocity, the slide mass, the slide shape and the water depth.

- Provide predictive equations for the key wave parameters such as wave amplitude, wave period, wave length and propagation velocity.

- Compare the predictive equations with field observations of real events.

- Quantify the slide impact energy to wave energy conversion.

1.4 Thesis overview

The thesis starts with an overview on field observations of landslide generated impulse waves in Chapter 2. The synthesis of real events illustrates the diversity, complexity and the importance of this rare but sometimes very destructive natural hazard. The relevant range of the experimental parameters is verified. In Chapter 2 previous research studies on landslide generated impulse waves are presented in order to define the state-of-the-art. Further a brief overview on the most relevant analytical wave theories and in particular their validity ranges is given. In Chapter 3 the experimental setup with the novel pneumatic landslide generator is introduced. The properties of the artificial landslide granulate are determined. Possible scale effects are discussed. The implementation and combination of the three measurement systems is outlined. The particularities of particle image velocimetry (PIV) applied to an unsteady, three phase flow at large scale are emphasized. The measurement accuracies are estimated. In Chapter 4 the results of this physical model study are presented and compared with both previous similar studies and field observations. The open questions were discussed previously in [para 1.3]. A summary of the main results and an outlook concludes the thesis in Chapter 6.

2   Literature review

2.1 Introduction

At the beginning of any research on landslide generated impulse waves stands the rare natural phenomenon under investigation. Only few events of relevance regarding threats to human lives were reported in recorded history, but some of them rank among the most destructive natural disasters known. The literature on observations of landslide generated impulse waves is disperse, with original reports often difficult to obtain. A synthesis of subaerial landslide impacts and landslides with partial initial submergence is given in Appendix B. These cases may be used for comparison of both physical and numerical models with real world events. Herein only the classification of events and the conclusions drawn from the observed cased are presented. The modeling efforts regarding landslide generated impulse waves and related processes are reviewed. The landslide models are grouped into 3 main categories: sliding blocks, pistons and granular slides. Physical and numerical models are presented jointly. The research gaps are identified and the focus of the present study is outlined.

2.2 Observations of landslide generated impulse waves

2.2.1 Gravity water waves

In general impulse waves are gravity water waves generated by an impulsive disturbance of the water body. Herein only impulse waves generated by subaerial landslide impacts are considered. A short overview on the most relevant gravity water wave theories and in particular their validity ranges is presented in Appendix C. For further details and equations it is referred to the broad literature on water waves. Several books on surface gravity waves were presented during the past decades which may be grouped in two broad categories. The first group contains chapters on wave mechanics mainly as a prelude to coastal and oceanographical engineering. Included in this group are Sorensen (1993), Dean and Dalrymple (1991), Tucker (1991), Herbich (1990), Mei (1989), Sarpkaya and Isaacson (1981), Blevins (1979), Horikawa (1978, 1988), LeBlond and Mysak (1978), LeMéhauté (1976), Silvester (1974), Ippen (1966), Wiegel (1964), Wehausen and Laitone (1960), Stocker (1953), Lamb (1932). The second group focuses on the mechanics of water waves and waves in physics. These are mainly analytical contributions and cover also modern mathematical methods in nonlinear physics. Included in this group are Infeld and Rowlands (2000), Remoissenet (1999), Johnson (1997), Kneubühl (1997), Korsunsky (1997), Nettel (1995), Rahman (1995), Debnath (1994), Mader (1988), Lighthill (1978), Whitham (1974).

The parameters to describe impulse waves are shown in Fig. 2.1. The main slide parameters are the slide thickness s, the slide length l_s, the slide centroid velocity v_s at impact and the slide density ρ_s. The water body topography is characterized by the still water depth h and the hill slope angle α. The origin of the coordinate system is at the intersection of the still water surface with the hill slope.
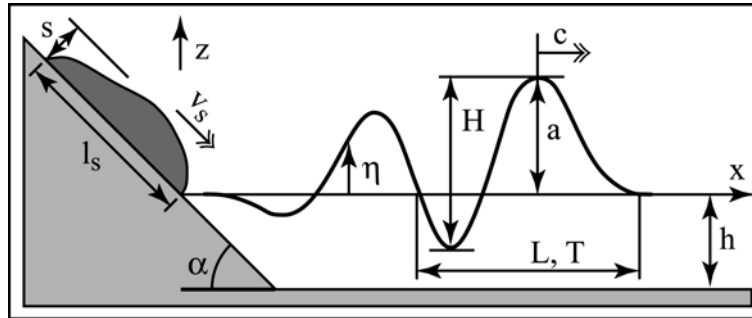
Figure 2.1   **Definitions** of the main slide, water body and impulse wave parameters.

The wave characteristics are described by the wave length L and the wave height H or the amplitude a. All other parameters, such as wave propagation velocity c and wave period T can be determined theoretically from these quantities. In the special case of the linear wave theory the wave height equals twice the wave amplitude. Impulse waves in the near field typically yield different crest and trough amplitudes. The wave length may be defined from crest to crest, trough to trough, surface upcrossing to upcrossing or down-crossing to downcrossing – they are all the same in the special case of the linear wave theory but different for the impulse waves in the near field. Most authors defined the wave length from surface upcrossing to upcrossing in order to account for the transient nature of impulse waves. The wave gauge recordings at location x in function of the time after impact t are commonly denoted by η.

2.2.2 Classification of events

The term landslide is widely used as an all inclusive term for almost all varieties of slope movements, including some that involve little or no true sliding. Regarding the landslide dynamics it is referred to [para A.2]. Slope movements have been classified in many ways. For the most common classification in the English literature after Varnes (1978) it is referred to [para A.1]. The cases of landslide and water body interactions are commonly grouped into the three categories shown in Fig. 2.2: subaerial landslide impacts, partially submerged landslides and subaqueous or submarine landslides. The initial position of the landslide determines the physical characteristics of the process and in particular the role of the air as third phase. Subaqueous or submarine landslide may be treated as a two-phase flow consisting of slide material and water interaction. For subaerial landslide impacts three phases become of importance: slide material, water, and air. There is a gradual transition from subaqueous to subaerial landslides with decreasing submergence. This classi-

fication is commonly used for observations and both physical and numerical models of landslide generated impulse waves. A synthesis of subaerial landslide impacts and landslides with partial initial submergence is given in [para B.1] and [para B.2], respectively.
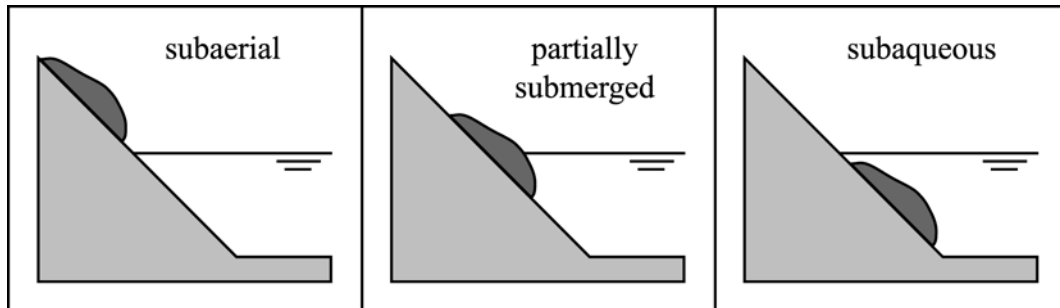
Figure 2.2 **Landslide classification regarding impulse wave generation** depends primarily on the initial position of the landslide: subaerial, partially submerged and subaqueous.

Submarine landslides are not considered in the present study. Although submarine landslides are being given increasing attention as a cause of tsunamis, which can ravage coastal areas (Moore and Moore, 1984, 1988; von Huerte et al., 1989; Harbitz, 1992; Jiang and Le Blond, 1992; Johnson and Mader, 1994). Submarine landslides account for roughly 10 % of tsunamis observed in oceans (Kajiura, 1990). They are often not detectable by seismicity based tsunami warning systems as exemplified by the wave that devastated New Guinea's north coast in 1998 (Tappin, et al., 1999).

2.2.3 Conclusions from observations

The following conclusions are drawn from the observations of landslide generated impulse waves presented in Appendix B:

• Information available from real events is limited to landslide scars and deposits, trimlines caused by wave run-ups, and distant tide gauge records.

• The largest wave run-up of 524 m in recorded history was caused by a high speed landslide impact.

• Simple back calculations from recorded wave run-up heights confirm that the major run-ups were produced by strongly nonlinear waves.

• Observed wave run-up heights along shorelines varied significantly. The first wave run-up depends mainly upon wave propagation direction relative to slide axis and bathymetry, whereas afterwards wave ray paths and interference by multiple reflections become more significant.

• The largest run-up heights usually occurred in direct prolongation of the slide axis.

• The first wave was not always the highest.

- The equivalent coefficient of friction f generally reduces with the volume of the mass movement and hence the velocity and the run-out distance increases with the landslide volume.

- For subaqueous landslides the equivalent coefficients of friction can be orders of magnitude smaller than for subaerial landslides and hence subaqueous run-out distances can be much larger than subaerial run-out distances.

- Submarine landslides run-out distances beyond 200km were estimated.

- Landslide velocities v_s up to 150 m/s were estimated.

- Impact landslide Froude numbers up to $\mathbf{F} = v_s / \sqrt{gh} = 5$ may be estimated.

- Events with landslide impact velocities below the m/s range usually do not generate relevant impulse waves.

- Landslides with submarine run-outs reached volumes V_s up to 5000 km^3.

- The landslide volume can exceed the volume of the water body.

- Events with volumes below 10'000 m^3 usually do not pose a threat due to landslide generated impulse waves and waves generated by events with volumes below 100'000 m^3 threaten mostly limited areas and small water bodies.

- The density of many common landslide materials are around 2.6 to 2.7 t/m^3.

- The mean porosity of debris avalanche deposits varies typically between 30 and 40 %.

- Hillslope angles α from near 0° to 90° are possible, but typical landslide volumes significantly decrease by orders of magnitude with increasing slope angle. Often reductions in slope angle occur near the water surface.

- One key triggering effect of submerged or subaqueous landslides is a change in pore water pressure, for example due to reservoir filling or drawdown and low tides.

- Major events are often preceded by several warning signals.

- The overall death toll over the last two centuries may be estimated to 60'000.

- There is a need for better prediction of both landslides and landslide generated impulse waves.

2.3 Modeling landslide generated impulse waves

2.3.1 Block models

The simplest of all block models used for impulse wave generation consisted of a heavy box sinking vertically into a water channel at one end. The bottom of the box was positioned on the water surface before initiating the experiment. The classic plunger configuration is due to Russell (1837 and 1844). Since the discovery of the solitary wave, the primary focus has been on the wave in the far field rather than the generator. Russel found that the volume of water displaced was the volume of water in the wave and that the wave moved at a constant celerity c according to $c = \sqrt{g(h + a)}$ given by Eq. C.8.

Monaghan and Kos (2000) used a combination of computer simulations and experiments to clarify the details of the wave formation and the dynamics of a box sinking from the water surface into a wave tank at one end. Both the experiments and the numerical simulations are two dimensional. The experiments in a 0.4 m wide wave tank showed that the jet from below the box forced the water in the tank upwards to form a reverse plunging wave and the solitary wave. A streak image shown in Fig. 2.3a), covering the area just in front of the falling block, visualizes the vortex formation during a preliminary experiment conducted by the author at VAW-laboratory. The reverse wave collapsed down the side of the block producing a vortex which followed the solitary wave down the tank. The vortex generation, shape and propagation downstream are similar to PIV velocity vector fields from an infinitesimal segment of a vortex ring formed by an impulsively started jet (Gharib et al., 1998, and Shusser and Gharib, 2000).
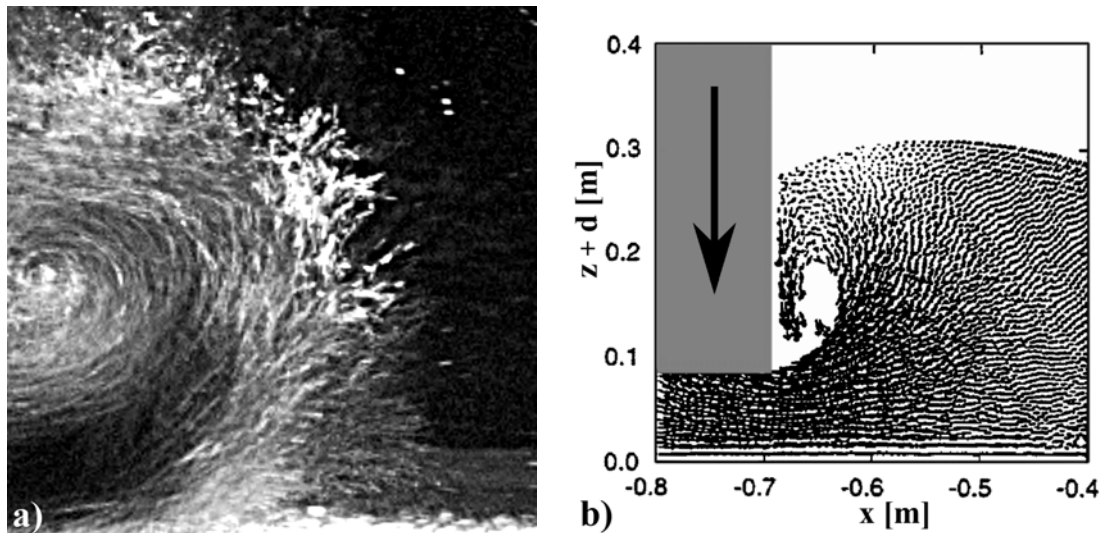
Figure 2.3   **Vertical block drop model: a) Flow visualization** of the vortex formation in front of the sinking block during preliminary experiments conducted at VAW-laboratory (area of view: 0.25×0.25 m); **b) SPH-simulation** of the flow field including cavity formation and collapse with accompanying air entrainment (Monaghan and Kos, 2000).

Monaghan and Kos (2000) successfully simulated both the dynamics of the box and the wave formation – including wave breaking and air entrainment during cavity collapse – with the Lagrangian particle method smoothed particle hydrodynamics (SPH) described in detail by Monaghan (1992). The numerical results overshot their experiments typically by 3 to 18 %. Most of the difference between the simulations and the experiments was due to the flow in the gaps between tank walls and block, which tends to reduce the wave height in the experiments by roughly the same amount as the difference observed between experiments and simulations. Monaghan et al. (1999) also simulated gravity currents descending a ramp in a stratified tank with the SPH method. Further SPH simulations by Monaghan and Kos (1999) accurately reproduced experiments on the run-up of a solitary wave on a beach of varying slope and in particular the breaking process during run-down

including bore formation. According to Monaghan simulations to predict impulse waves generated by the impact of a rock avalanche are in progress. From scaling theory Monaghan and Kos (2000) determined the leading wave crest amplitude a_{c1} to

$$a_{c1} = 3h\left(\frac{m_s}{40\rho_w shb}\right)^{2/3}\left(\frac{s}{h}\right)^{2/3}$$ (2.1)

if the drop height of the box is equal to the water depth h and with box mass m_s, water density ρ_w, box thickness s and width b. The amount of box energy converged into wave energy was estimated from simulations to 10 %.

Wiegel (1955) established wave profiles for initially submerged rigid bodies falling vertically and sliding down ramps in tanks, but he did not give details of motion near the sinking block. Denser solid blocks generated larger wave amplitudes. Significant was the dispersive character of the waves. Underwater landslide to wave energy conversions of 1 to 2 % were estimated. The rest of the total underwater landslide energy was dissipated by friction and turbulence.

Noda (1970) used linear theory to predict the form of the wave motion produced by a body falling vertically into a tank. The calculations are not self-consistent because they assume the motion of the block is known and further the assumption of linear motion breaks down near the falling box. The solution only produced reasonable agreement with experimental data for thin blocks with initial submergence. Even for initially submerged blocks the theoretical solutions increasingly depart from experimental data with increasing relative block thickness s/h and thereby increasing wave amplitude. The regions of wave types defined by a synthesis of the theoretical solution (Noda, 1970) and experimental results (Wiegel et al., 1970) is shown in Fig. 2.4. The wave type was determined by the slide Froude number $\mathbf{F} = v_s/\sqrt{gh}$ and the relative slide thickness $S = s/h$. Four main wave types were distinguished: oscillatory wave, transition wave, solitary wave, and bore.
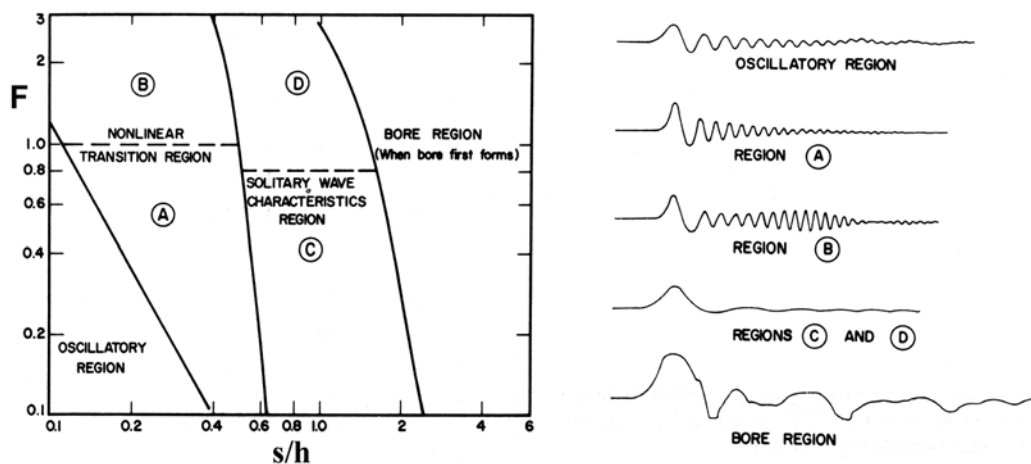
Figure 2.4 **Wave types** with typical wave profiles for a vertically falling solid block model depending on slide Froude number $\mathbf{F} = v_s/\sqrt{gh}$ and relative slide thickness $S = s/h$ as defined by Noda (1970) with experiments at $h = 0.45$, 0.6 and 0.75 m.

The author conducted preliminary experiments with vertically falling concrete blocks and a weighted wedge as shown in Fig. 2.3a) and Fig. 2.5, respectively. The wedge was on rollers to reduce friction and allow motion on a ramp with a hill slope angle $\alpha = 10°$. Regarding the potential collapse of the Cumbre Vieja volcano at La Palma and the possible tsunami generation reference is made to Day et al. (1999), Urgeles et al. (1999) and Ward and Day (2001), respectively.
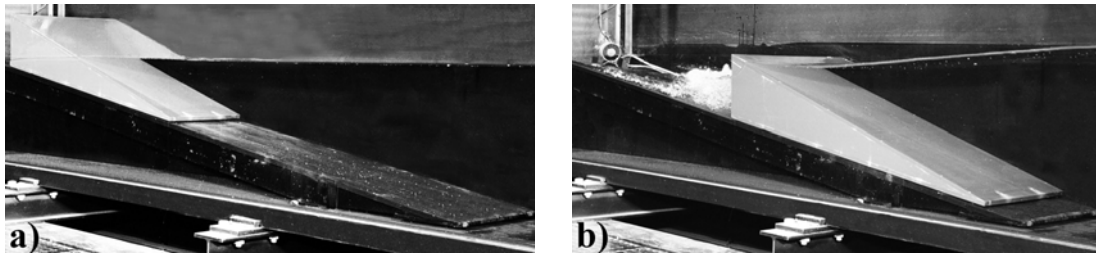
Figure 2.5 **Sliding block model** on rollers to reduce friction and enable wedge motion on a ramp with a hill slope angle of only 10° in the VAW-laboratory.

The fluid motion near the body in the wedge experiments differed significantly from the vertically falling block experiments because no water jet was driven from beneath the body and therefore no vortex formed in front of the block. In all block models reviewed here the block was abruptly stopped at the bottom of the incline by a stopper or simply rammed into the channel bottom. A large amount of the kinetic energy of the block was neither converted into wave energy nor dissipated by friction, drag or turbulence but simply taken out of the system by hitting the channel bottom or some sort of stopper. Further the amount of energy taken out of the system by hitting the channel bottom relative to the potential energy of the box increases with increasing slide Froude number. Therefore care has to be applied when interpreting small energy conversion coefficients computed by several authors from the potential energy of the block and the wave energy. Block models do not reproduce the long subaqueous landslide run-out lengths observed in nature and described in Chapter 2.

Kamphuis and Bowering (1970) conducted an experimental study in which a weighted tray was emplaced by a roller ramp – essentially frictionless sliding – into a flume 45 m long, 1 m wide, and of still water depth $h = 0.23$ and 0.46 m. The hill slope angle α was varied from 20° to 90°. The resulting wave heights decayed with increasing slope angle, but the effect was minor between 20° and 60°. The dependency of the relative wave height H/h in the far field on the slide Froude number $\mathbf{F} = v_s / \sqrt{gh}$ and the relative slide thickness $S = s/h$ are shown in Figs. 2.6a) and b), respectively. For relatively thick slides with $s/h \geq 0.5$ the far field wave height at location $x/h = 37$ was approximated by

$$\frac{H(x = 37h)}{h} = \mathbf{F}^{0.7} (0.31 + 0.2 \log q) \qquad \textbf{(2.2)}$$

where the dimensionless volume per unit width q is defined as

$$q = \frac{l_s}{h}\frac{s}{h} \qquad (2.3)$$

with slide thickness s and slide length l_s. The wave height decreased exponentially with distance from the source according to

$$\frac{H}{h} = \frac{H(x = 37h)}{h} + 0.35\,\mathrm{e}^{-0.08(x/h)} \qquad (2.4)$$

for $0.1 < q < 1$ and $10 \le x/h \le 48$. The wave period increased linearly with x/h, and seemed independent of other variables. Although wave height and velocity appeared to reach a stable value, wave period and wave length did not. Energy conversion from land-slide to water wave varied between 10 to 50 %.
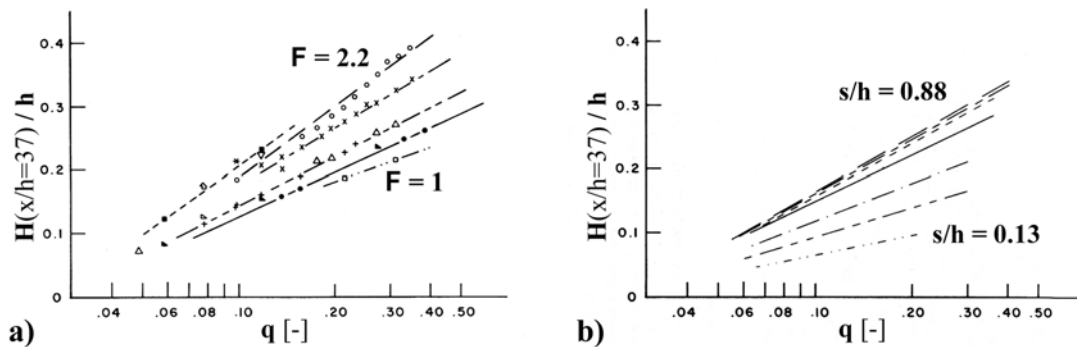
Figure 2.5 Dependency of relative wave height on: **a) slide Froude number** $\mathbf{F} = v_s/\sqrt{gh}$ and **b) relative slide thickness** $S = s/h$ (after Kamphuis and Bowering, 1970).

Law and Brebner (1968) previously undertook a similar experimental study involving a roller-bearing mounted tray which ran down a ramp. The hillslope angle α was varied from 18° to 25°. The attenuation with distance followed the relationship: $H \propto x^{-0.5}$. The Kamphuis and Bowering study produced better and more useful correlations – according to Brebner in Slingerland and Voight (1979).

Heinrich (1992), modeling landslides, made experimental and numerical studies of a rigid body with triangular cross section sliding down a ramp. The Nasa-Vof2D program is a nonlinear Eulerian code, which solves the complete Navier-Stokes equations by a finite difference method. The code extension allows movement of the fluid domain boundaries to simulate landslides. The code was applied to subaerial and submarine land-slides as well as to bottom movement. Exceptional agreement between experimental wave records and numerical simulations was obtained for submarine landslides and bottom motions. Velocity vector fields of the wave generation area computed for a subaerial land-slide impact are shown in Fig. 2.6a). A comparison of wave records with simulated wave profiles is shown in Fig. 2.6b). The comparison showed a good agreement for the first wave crest and trough, whereas in the dispersive trailing waves a phase shift and discrep-ancies in amplitude were observed. The numerical model is capable of simulating wedge

shaped solid block landslides. Further a three dimensional code version, Nasa-Vof3D, was developed (Heinrich, 1992).
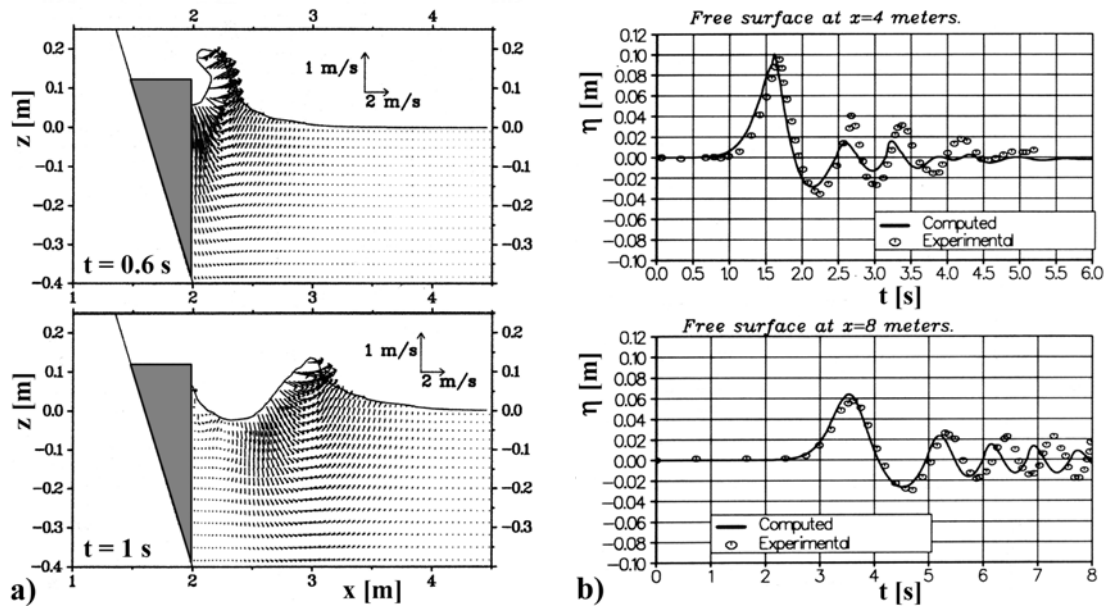
Figure 2.6 **Subaerial wedge impact generated waves: a) Nasa-Vof2D computed velocity vector fields** and wave profiles at $t = 0.6\,\text{s}$ and $1\,\text{s}$ after impact; **b) Comparison** between numerical and experimental wave profiles at locations $x = 4\,\text{m}$ and $8\,\text{m}$ (Heinrich, 1992).

Watts (1997, 1998, and 2000) physically modeled underwater landslides with blocks triangular in cross-section sliding down a ramp with a slope angle $\alpha = 45°$. The right triangle cross-section resulted in a separation of wave maker physics: the downward motion of the horizontal top face of the triangular block created the large trough above the block while the motion of the vertical front face created a crest ahead of the block (Watts, 1998). The Hammack number $Ha = t_{sd}\sqrt{gh}/(l_s \cos \alpha)$ was identified as the non-dimensional wave maker time. The Hammack number relates the time scale of wave generation, which depends on the time of slide water interaction t_{sd} and the horizontal projection of the slide length l_s, to the duration of linear long wave propagation out of the generation region (Hammack, 1973). Watts (2000) used the Ursell number to classify water waves propagating in constant depth. Most solid block experiments converted between 3 and 7 % of the maximum block kinetic energy into a characteristic wave energy. The energy conversion increased with decreasing initial submergence.

Watts et al. (2000) compared experiments and numerical simulations for water waves generated by an underwater landslide of semi-elliptical cross-section and concluded that depth-averaged nonlinear shallow water wave equations appear to underestimate the wave amplitudes. Depth-averaged nonlinear shallow water wave equations, in combination with different landslide models, were applied to landslide generated impulse waves by Raney and Butler (1975), Chiang et al. (1981), Chaudhry et al. (1983), Townson and Kaya (1988), Mader (1988, and 1999), Harbitz (1992), Jiang and Le Blond (1992, 1993,

and 1994), Johnson and Mader (1994), Imamura and Gica (1996), and Tinti and Bortolucci (2000). However, neglecting vertical accelerations is definitely inaccurate in the wave generation zone confirmed by the velocity vector fields shown in Fig. 2.6a), and on the shore, where run-up and wave breaking occur. The observations of real events (Chapter 2) showed that landslide generated impulse waves are mainly in intermediate water depth regime and therefore subjected to dispersion, which is not included in nonlinear shallow water wave equations.

2.3.2 Piston models

In some cases of landslide water body interaction the slide motion may be approximated by a vertical wall penetrating horizontally into the water body. This applies in particular to cases where the landslide volume exceeds the volume of the water body. Such examples are Vajont dam [para B.2.1] and Spirit Lake [para B.1.7]. The piston wave maker was applied by Miller (1970) in an experimental study on coastal landslides and by Hammack (1973) to study tsunami generation. The main disadvantage is of course that an assumption for the forced piston motion has to be made besides the fixed boundary condition given by the piston plate. For the plane wave maker theory and wave height to stroke ratios versus relative depths it is referred to Synolakis (1991), Madsen (1971), Hughes (1993), and Dean and Dalrymple (1991). Galvin (1964) reasoned that in shallow water the water displaced by the lavender should be equal to the crest volume of the propagating wave. The classic study of Ursell et al. (1960) is only applicable when the plate motions remain small.

Noda (1970) obtained a theoretical solution for the case of a wall moving horizontally into a body of water. A linearizing assumption was made that the wall displacement was much less than water depth. Maximum water surface elevation a occurred at $x/h \approx 2$ (not at x = 0) and was predicted by

$$\frac{a}{h} = 1.32 \frac{v_s}{\sqrt{gh}} \tag{2.5}$$

for a displacement at constant horizontal velocity v_s. The linear solution is compared to the nonlinear experimental data of Miller and White (1966) in Fig. 2.7. The linear solution gives conservative assumptions. The data from Das and Wiegel (1972) also confirmed the theoretical solution of Noda (1970). Noda (1971) attempted a Fourier analysis of the transient wave systems for approximations of the wave systems downstream from a probe. But the transient wave systems did not behave as if it were a series of steady sinusoidal waves and the discrepancies became larger with distance from the probe and increasing wave frequency.
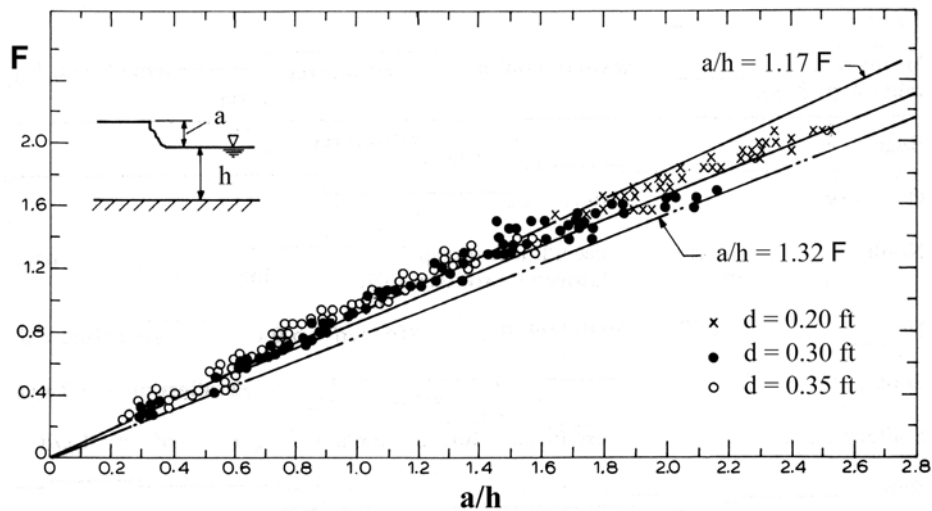
Figure 2.7 **Vertical wall penetrating horizontally** into a water body: comparison of the theoretical solution from Noda (1970) with the experimental data from Miller and White (1966).

Gozali and Hunt (1989) applied the method of characteristics to compute numerical solutions for water waves generated by a close landslides modelled with vertical wall moving horizontally into a reservoir. The nonlinear, non dispersive long waves approximation was applied. Hunt (1988) presented an analytical solution for water waves generated by distant landslides modeled by injecting a volume of fluid at a point source through the bottom of a reservoir.

Sander (1990) investigated unidirectional shallow water waves generated by a moving boundary as may be produced by a partially submerged landslide penetrating slowly – relative to wave propagation velocity – into a water body. A classical piston type wave maker with forced motion shown in Fig. 2.8 was used to produce waves within the following range: Froude number $\mathbf{F} = v_s \big/ \sqrt{gh}$ from 0.01 to 0.4, amplitude to water depth ratios from $a/h = 0.01$ to 0.4, and water depth from $h = 0.05$ to 0.15m.
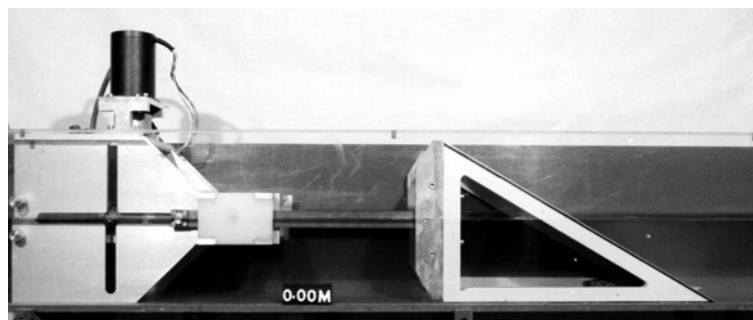
Figure 2.8 **Piston wave generator** with wedge and cross-like slot guided gearing in the VAW-laboratory (Sander, 1990).

Most of the generated waves were only weakly nonlinear. The type of boundary motion may have been similar to the Vajont landslide [para B.2.1] but relatively slower. At Vajont rough Froude number estimates ranged from $\mathbf{F} = 0.6$ to 1. The experiments

showed that for a wedge type piston wave generator both wave height and length are related to the piston or slide Froude number. Small Froude numbers produced smaller wave crests but deeper troughs whereas higher Froude numbers resulted in larger wave crests and smaller troughs. A numerical solution of Boussinesq type equations, presented by Wu (1981) and Villeneuve and Savage (1993), sufficiently well reproduced the weakly nonlinear shallow water waves recorded in the VAW-laboratory.

2.3.3 Granular slide models

Slingerland and Voight (1982) presented an empirical regression for the prediction of the dimensionless first wave amplitudes from the dimensionless slide kinetic energy. The maximum wave amplitude a of the semi-circular wave measured in prolongation of slide axis at a distance $x/h = 4$ was given by

$$\log\left(\frac{a}{h}\right) = -1.25 + 0.71 \log E_{sk} \tag{2.6}$$

with the dimensionless slide kinetic energy E_{sk} and still water depth h. The dimensionless slide kinetic energy was defined as

$$E_{sk} = \frac{1}{2} \cdot \frac{\rho_s}{\rho_w} \cdot \frac{V_s}{h^3} \cdot \frac{v_s^2}{gh} \tag{2.7}$$

with slide and water density ρ_s and ρ_w, respectively, slide impact velocity v_s and gravity g. The slide impact velocity may be estimated with Eq. 2.2. The data were derived from two 3-dimensional, site-specific physical model studies conducted at scales of 1:120 and 1:300 by Davidson and Whalin (1974), Davidson and McCartney (1975), and Ball (1970). In these studies, the slides were positioned initially with toes above the water level. The slides were either tabular or triangular in shape and consisted of gravel, iron or lead bags. A slide arrangement on hill slope is shown in Fig. 2.9a) and a characteristic radial wave pattern in Fig. 2.9b). The data comprised 20 experiments from 3 different slides with three water levels. The slide thickness s to water depth h ratio was within $0.37 < s/h < 0.8$, the slide volume V_s ranged from 0.7 to 39×10^6 m^3 in prototype scale and the slide Froude number $\mathbf{F} = v_s/\sqrt{gh}$ roughly from 0.5 to 5.
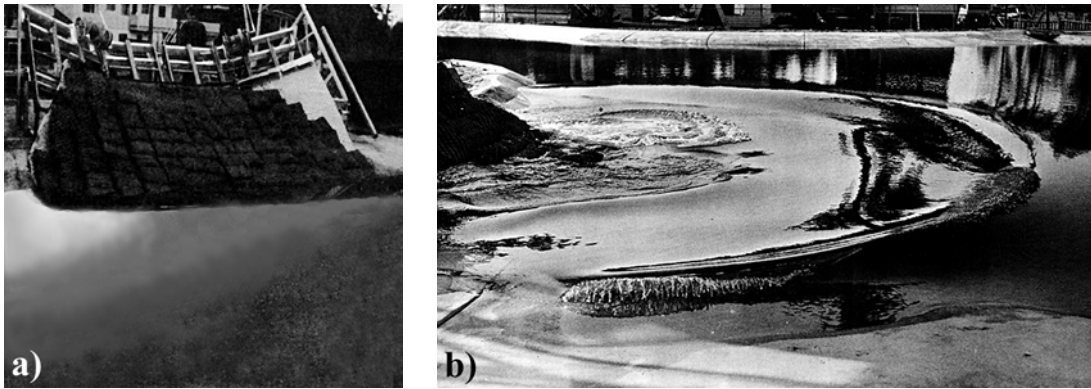
Figure 2.9   **Mica dam 3D-model** at a 1:300 scale: **a) Gravel bag** model of the Little Chief
Ridge slide with a volume $V_s = 1.5$ m^3 at laboratory scale; **b) radial impulse wave propagation**
in the roughly 60×30 m reservoir model (Photos: courtesy of Western Canada Hydraulics Ltd.).

Huber (1980) conducted the broadest experimental investigation of impulse waves
generated by granular rock avalanches. The study comprised over 1000 runs and included
both 2D and 3D experiments. In the 2D experiments the governing parameters were
varied as follows: slide mass $m_s = 5$ to 50 kg, impact slide front velocity $v_s = 1$ to 4 m/s,
water depth $h = 0.12$ to 0.36 m, and slope angle $\alpha = 28°$ to $60°$. The slide material con-
sisted of rounded river gravel with a continuous grain diameter distribution from 8 to
30 mm and a mean diameter of roughly $d_g = 20$ mm. The slide mass was positioned in tri-
angular shape behind a vertical flap gate on an inclined ramp. The granulate was released
from rest by sudden flap opening. In order to achieve different velocities the initial posi-
tion of the slide mass was moved along the ramp. A photo sequence of the finite mass of
gravel moving down an inclined ramp is shown in Fig. 2.10b).

Savage and Hutter (1989) reanalyzed the granular flow on the inclined plane and pre-
sented two numerical finite difference models, one of Lagrangian and the other of Eule-
rian type. The slide profiles computed at six different, dimensionless times using the
Lagrangian scheme are shown in Fig. 2.10a). The gravel masses spread quickly and
approached a long and thin layer with a depth of one to two particles in the laboratory
experiments and the mathematical models. Savage and Hutter (1989) concluded that the
granular flow for $t > 1$ s could no longer be treated as a continuum. Comparison of the
numerical solutions with laboratory experiments agreed regarding the motion of the front
and rear margins of the slide as well as the evolution of slide shape and thickness. For
modern concepts in modeling granular flows down an inclined plane or chute it is referred
to Mangeney et al. (2000), Wieland et al. (1999) and Pouliquen (1999a,b). Huber (1980)
remarked that the slide impact shape changed inherently with variations of both slide
impact velocity and slope angle. The changes in slide impact shape need to be considered
when interpreting the experimental data.
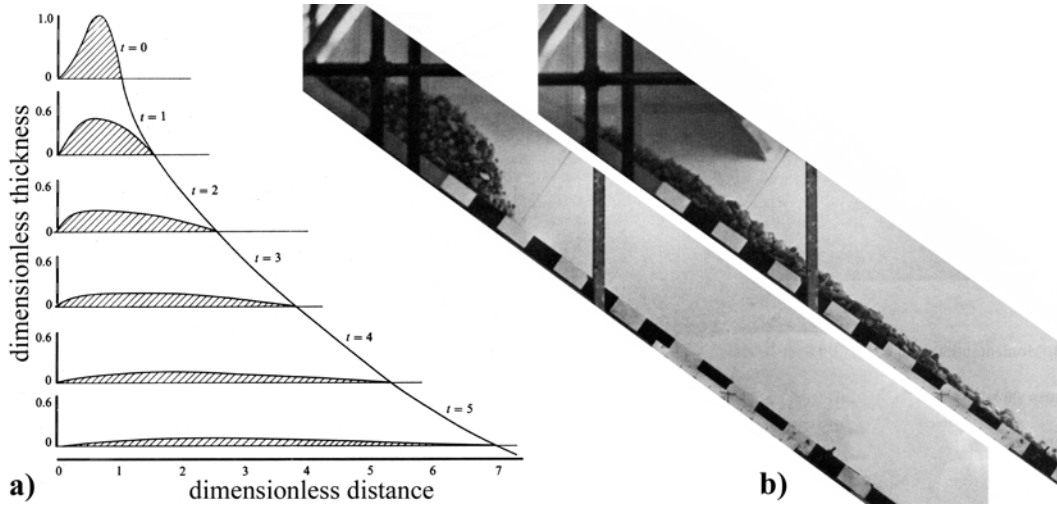
Figure 2.10 **Granular slide: a) Lagrangian computation** of rock avalanche profiles on a ramp with a slope angle $\alpha = 32°$ at six dimensionless times (Savage and Hutter, 1989); **b) Laboratory granular flow** on a plane with inclination angle $\alpha = 32°$ and slide mass $m = 30\,\text{kg}$ at $t = 0.1\,\text{s}$ and $0.6\,\text{s}$ after flap opening (experiment No. 106b, Huber, 1980).

The main experimental results of Huber (1980) were summarized in Huber and Hager (1997) as well as Vischer and Hager (1998). The wave height H for two dimensional (2D) impulse wave prediction was given by

$$H = 0.88 \sin\alpha \left(\frac{\rho_s}{\rho_w} \right)^{1/4} \left(\frac{V_s}{b} \right)^{1/2} \left(\frac{h}{x} \right)^{1/4} \tag{2.8}$$

with slope angle α, slide density ρ_s, water density ρ_w, slide volume V_s, slide width b, still-water depth h and location x. Slide induced waves in a water body propagate radially over the water surface until the first wave crest runs up along the shoreline. Thereafter complex wave patterns evolve and the effects of bathymetry, topography, wave reflection, refraction, diffraction and interference become more important than simple decay in wave height due to radial spreading as shown in Chapter 2. Huber (1980) conducted roughly 150 3D experiments in a wave basin. The radial spread was characterized by a strong dependency of wave height on the propagation direction γ and the radial travel distance r. By far the highest waves left the shore in the slide and momentum direction ($\gamma = 0$) as observed in Chapter 2. In contrast, lateral waves were significantly smaller. The strong directional component in radial wave propagation is shown in Fig. 2.11. The relative wave heights H/h in a 3D water body may be predicted by

$$\frac{H}{h} = 2 \cdot 0.88 \sin\alpha \cos^2\left(\frac{2\gamma}{3}\right) \left(\frac{\rho_s}{\rho_w} \right)^{1/4} \left(\frac{V_s}{bh^2} \right)^{1/2} \left(\frac{r}{h} \right)^{-2/3} \tag{2.9}$$

The decay in wave height with the relative propagation direction increased for 3D wave propagation compared to 2D wave propagation.
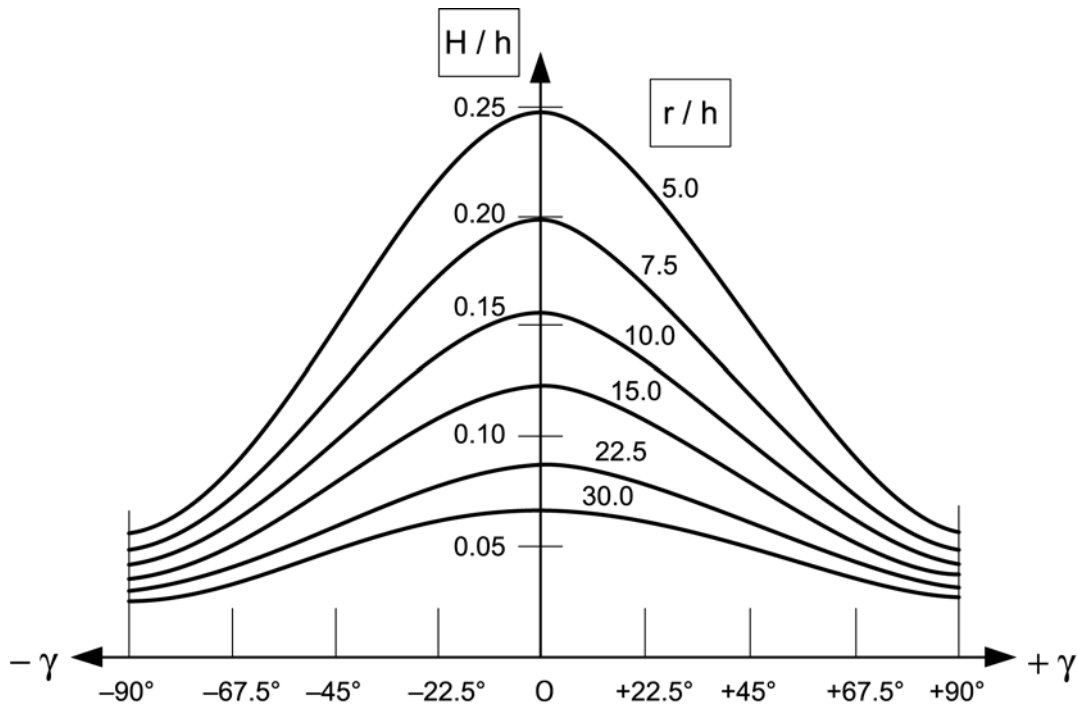
Figure 2.11 **3D radial impulse wave propagation:** relative wave heights *H/h* as a function of relative propagation distance *r/h* and lateral wave propagation direction γ where $\gamma = 0$ corresponds to slide axis (Huber and Hager, 1997).

Huber and Hager predicted a wave attenuation according to $(r/h)^{-2/3}$. Landslide generated impulse waves are strongly directional and vary with the propagation direction. The largest wave heights were always observed in prolongation of the slide axis. The analytical solution of Kranzer and Keller (1959) suggests a cylindrical divergence resulting in amplitudes diminishing as $1/r$. Van Dorn's (1961) studies of the four Redwing nuclear blasts at the Bikini Islands showed that the radial divergence follows $r^{-5/6}$ rather closely, as does a tsunami he was able to record, although he noted that experimental uncertainties encompass a $1/r$ spreading law. The dependency of the wave height on the propagation direction is a fundamental difference between landslide generated impulse waves and explosion generated waves. Further in real events multiple reflections, spectral superposition and interference may result in local large variations of wave heights.

Rzadkiewicz et al. (1997) conducted an experimental and numerical study on granular submarine landslides. In a 2D Navier-Stokes model (Nasa-Vof2D) the reology from fully solid to Newtonian fluid was included by a 2D diffusion model describing the mechanical behavior of sediments by a Bingham law. The numerical parameters, i.e. the plastic viscosity, the Bingham yield stress, the friction and diffusion coefficients were calibrated on the results from the laboratory experiments. A direct comparison between the laboratory and the numerical model is shown in Fig. 2.12. The simulations showed that the Bingham model associated with diffusion is not the most appropriate model for the

study of granular flows. Nevertheless the experimentally recorded wave profiles were reproduced with an acceptable accuracy.
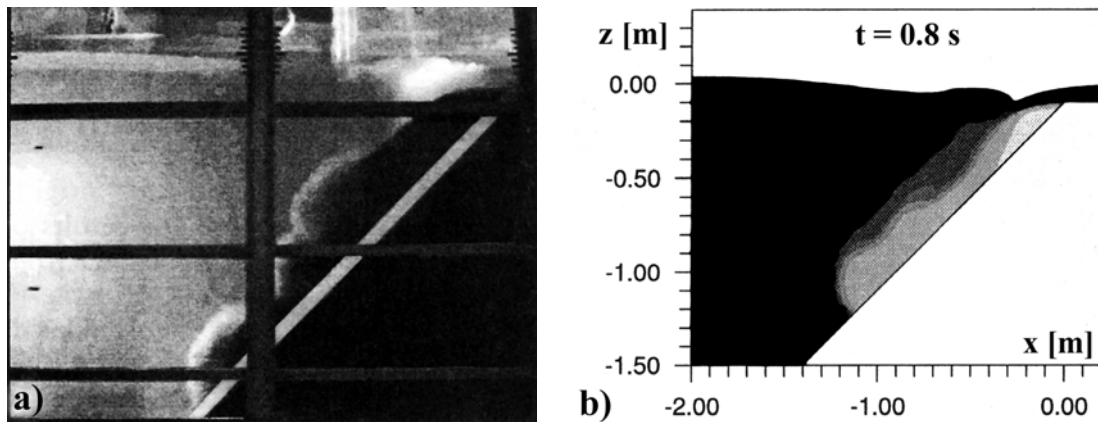
Figure 2.12 **Submarine landslide: a) photo from an experiment** with coarse sand sliding down a ramp with a slope angle $\alpha = 45°$ at $t = 0.8\,s$ (area of view: roughly $2 \times 2\,m$); **b) computed density map** at $t = 0.8\,s$ (Rzadkiewicz et al., 1997).

Watts (1997) conducted a laboratory study on submarine landslides with different granular media and blocks. Fine granular components were not included in the physical model leading to a relatively large slide porosity. In laboratory scale models of submarine landslides at low Reynolds numbers a flow through the granular media occurred and did not allow a realistic pressure distribution to form near the surface of the slide. For high speed subaerial landslide impacts into a water body the Reynolds numbers are orders of magnitude larger and the problem of flow through the granular media may be considered specific for submarine landslides (personal communication: Philip Watts, 1998).

2.3.4 Related models

Prins (1958) modeled impulse waves with an initial dam-up or lowering of the water surface over a finite length in a two dimensional water channel. The amount and length of the initial rise or lowering of the water level relative to the water depth determined the generated wave types. Prins differentiated four wave types: oscillatory waves, leading solitary waves followed by dispersive trailing waves, solitary waves separated from the trailing waves, and multiple solitary waves. The physical model data were compared with the theories of Unoki and Nakano (1953) and Kranzer and Keller (1955), but the wave heights could not be predicted satisfactorily.

Storr and Behina (1999) conducted an experimental study on large diameter gravity driven liquid jets impacting into a pool with variable water depth. A finite volume of liquid was released well above the water surface from a cylinder with variable diameter. The fluid properties of the jet were varied within the following ranges: density from 1 to 1.58 t/m^3, surface tension σ from 0.014 to 0.076 N/m, and dynamic viscosity μ from

0.0006 to 2 Ns/m^2. The viscosity of the liquid jet had a significant effect on the deformation of the jet during water penetration and both shape and size of the air cavity formation. The cavity formed by an organic liquid jet with a density of 1.58 t/m^3 impacting into the water pool is shown in Fig. 2.13a).

Crawford and Mader (1998) numerically modeled the interaction of typical stony asteroids with the atmosphere, and a 5 km deep ocean with a basalt bottom. The asteroid impact and air cavity formation was modeled with the CTH code for multi-dimensional, multi-material, large deformation and strong shock wave physics (McGlaun et al., 1990). The CTH code successfully modeled the impact of comet Shoemaker-Levy 9 on Jupiter (Crawford et al., 1994). The asteroids of variable diameter had a density of 3.32 t/m^3 and an impact velocity of 20 km/s. The maximum cavity at $t = 21$ s formed by a 500 m diameter asteroid is shown in Fig. 2.13b). The collapse of the cavities, the resulting impulse waves and the circular propagation was modeled with the ZUNI code which solves the incompressible Navier-Stokes equations (Mader, 1988). The generated impulse waves typically had wave periods of about 3 minutes and wave lengths of about 30 km. In deep ocean asteroid generated impulse waves – in analogy to landslide generated impulse waves – are not shallow water waves but intermediate depth water waves subjected to dispersion. Hills and Goda (2001) numerically simulated asteroid impacts into oceans with cavity formation and impulse wave generation using an SPH code. Several laboratory investigations focusing on cavity dynamics produced by rigid projectiles impacting with velocities up to 2 km/s into a water tank were presented (Lee et al., 1997; Shi and Takami, 2001; Hrubes, 2001).
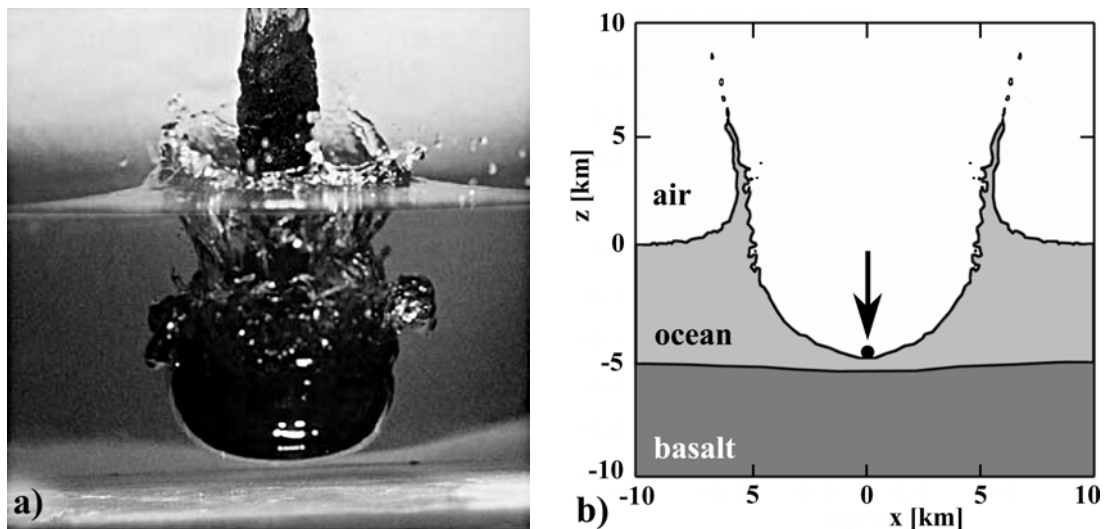
Figure 2.13   **Related impact models: a) Liquid jet impact into water pool:** photo from an experiment with a gravity driven organic jet of finite volume and density 1.58 t/m^3 (Storr and Behina, 1999); **b) Asteroid impact into ocean:** CTH code computation of cavity formation and impulse wave generation for an asteroid with a 500 m diameter and a density of 3.32 t/m^3 impacting with 20 km/s (Crawford and Mader, 1998).

LeMéhauté and Wang (1995) summarized the broad and previously classified literature on impulse wave generation by underwater explosions. In shallow water, where the explosion generated cavity reached the bottom, at most only 5 % of the explosion energy was transmitted in the form of water waves. In deeper water efficiency increased rapidly. Analogies to landslide generated impulse waves regarding wave characteristics and air cavity collapse were proposed. Johnson and Bermel (1949) and Jordaan (1969) conducted laboratory experiments on underwater explosions using falling weights as replacement for the explosion. Modern concepts regarding numerical modelling of explosion or cavity collapse generated impulse waves are given by Mader (1997).

2.4 Conclusions

2.4.1 Summary of previous studies

The following conclusions are drawn from the literature review on gravity water wave theories and both physical and numerical approaches on landslide generated impulse waves:

- Analytical solutions are somewhat deficient in accurately describing wave characteristics in the nonlinear range.

- Higher order analytical solutions are not necessarily better than their lower order counterparts.

- Landslide generated impulse waves are typically in the intermediate water depth regime.

- In solid block landslide models a large amount of the kinetic block energy is taken out of the system by hitting the channel bottom or some sort of stopper, which explains extremely low energy conversion coefficients.

- Solid block models do not reproduce the long subaqueous landslide run-out lengths observed in nature.

- Solid block models in most cases do not accurately simulate the slide deformation, porosity and time history of emplacement.

- The sole reason for conducting solid block landslide experiments is to provide high precision data sets – preferably obtained with laser measurement techniques – as reference data for numerical simulations.

- The following governing parameters regarding wave generation were identified: slide volume V_s, slide density ρ_s combining granulate density ρ_g and slide porosity n, slide impact velocity v_s, slide impact thickness s, slide width b, hillslope angle α, stillwater depth h.

- Huber (1980) did not include a slide thickness parameter into the predictive equation. The impact shapes of Huber's granular rock avalanches were inherently dependent on impact slide velocity, which needs to be considered when comparing results to solid block or other fixed shape models.

- All sliding block and granular bag experiments showed a strong dependency of generated wave heights on block slide impact shapes

- All sliding block and granular bag experiments showed a strong dependency of generated wave heights on slide Froude number, whereas Huber (1980) did not include a slide impact velocity parameter into the predictive equation.

- The effect of the hill slope angle on the wave height was relatively weak. All sliding block and granular bag experiments showed a decrease in generated wave heights with increasing slope angles for the same impact energy, whereas Huber (1980) showed a slight increase in generated wave heights with increasing slope angle.

- Available data sets from physical models are limited to wave gauge records at certain distances from the impact site.

- Numerical modelers need precision measurements of the slide impact and wave generation area as reference data sets.

- Any predictive equation obtained from 2D or 3D physical models is limited to the nearfield and may not be applied to the far field due to dispersion effects.

- Care is necessary when applying wave height predictive equations from rectangular 2D wave channel or 3D wave tank models to site specific situations due to the importance of bathymetry, topography and multiple wave reflections.

- Even site specific physical models have difficulties with reflection coefficients of multiple wave run-ups and are truncated once the first outward propagating wave crest ran up somewhere along the shore line.

- Complex wave patterns with interfering multiple wave reflections may be treated numerically.

- For landslide impacts with low Froude numbers $F < 1$ full numerical models of the whole process provide promising results and are better applicable to site specific situations. Physical modeling is limited due to scale effects such as water flow through the granular medium at low slide velocities.

2.4.2 Identified research gaps

The following research gaps are identified from previous physical and numerical approaches on landslide generated impulse waves:

- No numerical models are available to simulate subaerial landslide impacts into water bodies with impact Froude numbers $F > 1$, which is typical for Alpine events.

- The effect of the slide impact velocity and the slide Froude number on the main wave characteristics were not determined for granular slide models.

- The effect of the slide impact shape on the main wave characteristics was not investigated for granular slide models.

- Block and granular slide models provide controversial results regarding the effect of the hill slope angle.

- The temporal evolution of the water displacement and the maximum water displacement volume induced by the landslide impact in the wave generation area were not investigated.

- The temporal evolution of the subaqueous slide motion was not determined for granular slide impacts.

- The effect of the landslide deformability on the main wave characteristics is not quantified for granular slide experiments.

- No information was provided on the water particle velocities in the wave generation area.

2.4.3 Focus of the present research study

Obviously not all identified research gaps can be investigated in a single research study. The focus of the present study was set on subaerial landslide impacts with Froude numbers $F > 1$, which are of particular relevance for Alpine lakes and reservoirs. Physical model experiments were conducted, because no numerical models which produce promising results were available at the beginning of the present study. A granular landslide model was chosen since block models were analyzed previously and the identified gaps concerned primarily deformable landslides. A two dimensional model was selected because the radial wave propagation was analyzed by Huber (1980). The following issues were investigated in the present study:

- The effects of the slide impact velocity, the slide mass, the slide shape and the water depth were quantified.

- The water displacement curve and the maximum water displacement were determined.

- The subaqueous slide motion including the slide run-out, the duration of the slide motion and the velocity decay were investigated for granular slide impacts.

- Instantaneous flow fields in the slide impact and wave generation area were acquired with particle image velocimetry (PIV) to analyze the landslide and water body interaction.

- A full description of the macro structure of the flow in the slide impact and wave generation area was presented.

- The water particle velocities in the slide impact and wave generation area are determined.

- The role of the different components of the deformation tensor including the vorticity, the divergence and the elongational and shear strains was ascertained.

- The wave types and the governing wave features were ascertained.

- Predictive equations for the key wave parameters such as wave amplitude, wave period, wave length and propagation velocity were provided.

- The slide impact energy to wave energy conversion was quantified.

Not considered were the following gaps which remain to be ascertained in future research studies:

- The hill slope angle was constant at 45°. The effect of the hill slope angle was not investigated due to the weaker effect on the main wave characteristics compared to other parameters. The controversy between the block and granular slide models in this regard remains unresolved.

- The slide to water density ratio was not altered. Only the typical slide density given by natural rock formations was investigated. Lower densities of importance to avalanches and glacier break downs were not considered.

- The effect of the landslide deformability and the grain size distribution on the main wave characteristics is not quantified for granular slide experiments.

3   Physical model

3.1 Introduction

The initial phase of landslide generated impulse waves was investigated with a physical model. The governing similarity laws were identified beforehand. Possible scale effects were minimized by the dimensions of the experimental set-up selected. The two-dimensional wave channel and the novel pneumatic landslide generator are presented. The characteristics of the landslide granulate were determined. Three different measurement techniques were applied to the physical model: laser distance sensors (LDS), particle image velocimetry (PIV) and capacitance wave gages (CWG). An overview on the implementation and combination of the various systems is presented.

3.2 Similitude

3.2.1 Dimensional analysis

The rules of dimensional analysis may be found in any standard basic fluid mechanics text and will not be repeated here. Detailed discussions on dimensional analysis of fluid flow may be found in Hughes (1993), Spurk (1992), Zierep (1991), Dalrymple (1985), Yalin (1971), Sedov (1959), among others. Langhaar (1957) remarked that a complete solution cannot be obtained, nor can the inner mechanism of the phenomenon be revealed by dimensional analysis alone. It is recalled that the establishment of dimensionless numbers is arbitrary as soon as the number of parameters exceeds six, which leads to an arbitrariness in the determination of the conditions of similitude (Birkhoff, 1950). Dimensional analysis alone does not yield any indication whether some of the dimensionless numbers are less important than others or could even be neglected. It is anticipated that Froude similarity is assumed as in all previous studies on the topic [para 2.3]. This assumption is discussed below. The arbitrariness in the choice of dimensionless numbers for a complex phenomenon, even once Froude similarity is assumed, was confirmed by the literature review on modeling attempts of landslide generated impulse waves [para 2.3]. In such complex cases inspectional analysis of the physical process and the governing equations in combination with the scale model itself are supposed to provide the solution (Housen and Schmidt, 1983; Le Méhauté, 1990; Le Méhauté and Wang, 1995).

The governing parameters for the wave generation are:

b	[L]	slide and channel width
l_s	[L]	slide length
s	[L]	slide thickness

V_s	[L^3]	slide volume
α	[-]	hill slope angle
h	[L]	stillwater depth
x	[L]	wave propagation distance
g	[LT^{-2}]	gravitational acceleration
v_s	[LT^{-1}]	slide impact velocity
ρ_s	[ML^{-3}]	slide density
ρ_w	[ML^{-3}]	water density

The gravitational acceleration g and the water density ρ_w are constant. The slide width b corresponds to the width of the wave tank and remains constant in the chosen two-dimensional model. The slide volume V_s is not determined by the product of the slide thickness s, length l_s and width b for both the granular slides of the present experimental study and the natural landslides due to the variation in slide shape. Hence the slide volume V_s was considered. The slide length l_s before impact was difficult measure in the present study, whereas the slide thickness s and the slide volume V_s were determined accurately. The variations in the shapes of the slide profiles in the present study were minor, which makes the slide length l_s redundant. The slide geometries in the present study were described by the slide volume V_s, thickness s and width b. The slide density ρ_s is defined as

$$\rho_s = (1 - n)\rho_g \tag{3.1}$$

and comprises the granulate density ρ_g and the slide porosity n. The slide porosity n includes effects of the grain shape, the grain diameter d_g for uniform grain diameter granulates and the grain size distribution for heterogenic granulates. The assumption of Froude similarity implies Reynolds, Weber and Cauchy non-similarity, which requires that effects of the dynamic viscosity μ, the surface tension σ and fluid compressibility are negligible. Scale effects are discussed below.

An implicit parameter in the granular slide model is the slide deformability, which depends on the Coulomb friction, the grain shape, the grain size distribution, the saturation and the inter-granular collisions in granular flows. The slide deformability is of importance regarding the impulse wave generation due to changes in slide shape and energy dissipation due to internal friction at slope changes. The governing constitutive relations are not identified here. Possible constitutive relations which need to be treated numerically may be found in the broad literature on granular and debris flows. It is referred to Mangeney et al. (2000), Tognacca (1999), Iverson (1997), Hutter et al. (1996), Hunt (1994), Takahashi (1991), Campbell (1990) and Bagnold (1954), among others.

The remaining parameters can be reduced to six dimensionless parameters in a 2D model. According to the Π-Theorem of Buckingham (1914) the following dimensionless quantities were obtained:

$\Pi_1 = \mathbf{F} = v_s / \sqrt{gh}$ slide impact velocity relative to shallow water wave propagation velocity

$\Pi_2 = S = s / h$ dimensionless slide thickness or slide shape parameter

$\Pi_3 \ = \ V \ = \ V_s / (bh^2)$ dimensionless displacement volume

$\Pi_4 \ = \ x / h$ dimensionless wave propagation distance

$\Pi_5 \ = \ \rho_s / \rho_w$ dimensionless slide density

$\Pi_6 \ = \ \alpha$ hill slope angle

All variables characterizing the impulse waves depend upon the above quantities. The dimensionless side density and the hill slope angle were constant herein.

In the present research study all predictive equations were determined by multiple regressions of the measured values. The slide Froude number $\mathbf{F} = v_s / \sqrt{gh}$, the dimensionless slide volume $V = V_s / (bh^2)$ and the dimensionless slide thickness $S = s / h$ were introduced into the multiple regressions (Ratkowsky, 1990). The importance of the dimensionless quantities varied from case to case. The predictive equations were simplified by dumping dimensionless quantities with minor effects if possible. The ratio $V / S = V_s / (bhs)$ was introduced if the dimensionless slide volume V and thickness S yielded the same exponents with different signs. The quantity ratio V / S resulted in a dimensionless slide length. All parameter combinations were considered for each case but only the most significant is presented.

3.2.2 Generalized Froude model

An equality of Froude, Reynolds and Weber numbers is possible only at scale unity. Hence, Froude similitude governs under two conditions: where viscous forces and surface tension are negligibly small, as in non-breaking gravity waves or where the flow is very turbulent and the flow pattern to be reproduced in a scale model is short, as in a hydraulic jump, a propagating bore or a breaking wave. Indeed, in the latter case, the energy dissipation is mostly due to turbulent fluctuations and is not due to laminar viscous effects. While these viscous effects are linearly related to the velocity, the turbulent fluctuations are quadratic, i.e. proportional to the square of the average velocity, as are the inertial forces. Thus, the ratio of dissipative forces to gravity forces in a very turbulent flow is also a Froude number. This situation is of utter importance for free surface hydraulic models in general, since otherwise not even a transition from super- to sub-critical flow in an open channel or a stilling basin could be physically modeled. For example the depth at which air bubbles penetrate in a breaking wave differs from nature in the physical model, since the bubble size is determined by surface tension effects. Even though the fine structure of the flow may be different, the total amount of energy dissipated is in similitude. This is evidenced for the shear stress τ, since the viscous term becomes small if the Prandtl mixing length is in accordance with Froude similitude (Hinze, 1975). This condition is fulfilled in the case of fully turbulent flow occurring over a short distance and presenting a large velocity gradient. The same assumption – common for hydraulic jumps, bores and breaking waves – is made for the landslide impact process itself. Therefore the whole process including granular slide motion, slide impact, energy dissipation, wave generation, wave propagation and wave breaking should primarily obey the generalized Froude simil-

itude after LeMéhauté (1976, 1990). Given the assumption of Froude similarity, possible scale effects regarding each distinctive process are discussed below. The utter scale difference between prototype and model is characterized by the extreme magnitude of prototype to model length scale ratios $N_L = 50$ to 1'000 of relevance to Alpine lakes and reservoirs or even up to 10'000 if lateral collapses of volcanic islands in deep ocean are considered. and requires an in depth analysis of possible scale effects. It is recalled that in all practical cases of Froude scaling the gravitational scale and the mass density scale are $N_g = N_\rho = 1$, which allows to compute all other scale ratios and for example defines the time and velocity scales to $N_T = N_v = \sqrt{N_L}$.

3.2.3 Viscous effects

The criterion for satisfying both Froude and Reynolds similarity simultaneously is found by equating the two criteria

$$N_F = \frac{N_v}{\sqrt{N_g N_L}} = \frac{N_v N_L}{N_\nu} = N_R \qquad (3.2)$$

and resolving after the scale ratio of the kinematic viscosity defined as $N_\nu = N_\mu / N_\rho$ yields

$$N_\nu = N_L^{3/2} . \qquad (3.3)$$

With the relevant model length scale ratios $N_L = 50$ to 10'000 the kinematic viscosity scale ratios range from $N_\nu = 1/350$ to $1/10^6$. It is not possible to satisfy this criterion. Possible scale effects are not assessable by common laboratory techniques, since variations of kinematic viscosity by laboratory scale series, temperature variations or altering fluids are limited to roughly an order of magnitude.

Landslides are subjected to drag forces during impact and run-out. Similar to the drag on a ship's hull, the total drag force is considered as a combination of form and skin friction drag (Hughes, 1993). The form drag due to pressure differences around the solid body depends on the Froude number and hence is in similitude. The skin friction drag due to viscous shear stresses between the fluid and the granulate is a function of the grain size Reynolds number $R_* = v_* d_g / \nu$. Maximum values of $R_* = 3 \times 10^4$ were reached during slide impacts in experiments with $v_* = 8$ m/s, $d_g = 4$ mm and $\nu = 10^{-6}$ m^2/s. The densimetric Froude number $F_* = v_* / \sqrt{g d_g (\rho_g - \rho_w)/\rho_w}$ reached values up to 30. These values are beyond the ranges covered in the Shields diagram for sediment transport (Shields, 1936) and hence sheet flow was expected to occur (Pugh and Wilson, 1999). R_* and F_* rapidly decayed to zero during the slide run-out. Sediment transport on the slide surface was observed in the experiments. Sheet flow was visualized during the slide impact and cavity formation. The amount of slide granulate sheared off in the sheet flow is negligible.

A comparison of submarine landslide run-out distances with experimental run-out distances shows increasing differences with increasing scale ratios (Hampton et al.,

1996). The largest submarine landslide run-out distances were up to 10 times larger than granular model run-outs up-scaled by factors up to 10'000. During most of the run-out distance the landslide velocity lags the wave propagation velocity and therefore primarily affects the trailing waves (Ward, 2001). In narrow Alpine lakes or reservoirs the landslide run-out distance is strongly affected by the lake bathymetry and the slide usually rams into the opposite flank after a short travel distance. In super critical landslide impacts with **F** > 1 the initial impulse transfer forming the first wave crest is most important and trailing waves generated during landslide run-out are usually much smaller. Hence the influence of the not scaleable landslide run-out is not of relevance regarding high speed landslide impacts into Alpine lakes and reservoirs.

Model gravity waves attenuate stronger than in the prototype by internal friction and by bottom and side wall boundary layer friction arising from water viscosity. The wave attenuations due to internal friction and boundary layer developments are determined separately. The wave attenuation due to internal friction may be assessed with the analytical solution proposed by Keulegan (1950)

$$\frac{H(t)}{H(t = 0)} = e^{-(8\pi^2 \nu t / L^2)} \tag{3.4}$$

where $H(t)$ is the attenuated wave height at time t. In order to damp the wave height by 1 % due to internal friction Eq. 3.4 yields a propagation time $t = 127\,\mathrm{s}$ for a wave length $L = 1\,\mathrm{m}$. All impulse waves measured in the experiments had wave lengths of several meters with a typical propagation time $t = 5\,\mathrm{s}$ over the short measuring distance. Therefore internal friction is negligible and viscous dissipative effects in non-breaking waves are limited to the thin boundary layers. Viscous damping due to boundary layers is larger for shallow water waves than deep water waves, since no motion between water particles and bottom occurs for the latter (Biesel, 1949; Huber, 1976). Viscous damping due to boundary layers under a transient oscillatory flow with flow reversal is far more complicated than in simple pipe or open channel flow (Fredsøe and Deigaard, 1992; Nielsen, 1992; Raudkivi, 1990). The present physical model had a glass bottom outside the impact area and a glass and a steel side wall. The equivalent sand roughness coefficients may be estimated to 0 - 0.003 mm for glass and 0.03 - 0.06 mm for steel plates (Bollrich, 1989). During the passing of a transient impulse wave train several transitions between the laminar and the turbulent transition regimes may occur in the model. An experimental study in an oscillating water tunnel was conducted by Kamphuis (1975) and LDA-measurements in oscillatory boundary layers were presented by Cox et al. (1996), Cox and Kobayashi (2000), among others. Theoretical studies of the boundary resistance coefficient under waves were done mainly for laminar flows. Keulegan (1948) solved the linearized boundary layer equations for the damping of a solitary wave and presented the following relation

$$1 - \frac{a(x)}{a(x = 0)} = -\frac{h}{a(x = 0)} \left(\frac{x}{12h} \left(1 + \frac{2h}{b} \right) \sqrt{\frac{\nu}{g^{1/2} h^{3/2}}} \right)^{-4} \tag{3.5}$$

where $a(x)$ is the attenuated maximum positive amplitude at travel distance x. For the solitary wave the maximum positive amplitude a corresponds to the wave height H. The effects of wave amplitude a and wave channel width b in dependency of still water depth h on the wave attenuation given by Eq. 3.5 over a travel distance $x = 10\,\text{m}$ are shown in Figs. 3.1a) and 3.1b), respectively. All curves show a strong dependency on still water depth h and in particular a strong increase in wave damping for $h < 0.3\,\text{m}$. The maximum viscous wave attenuation due to boundary layers is estimated to less than 3 % over the measurement distance of roughly 7.5 m for $h \geq 0.3\,\text{m}$. No corrections were applied to measured wave profiles and the viscous effects were neglected. In general corrections of wave attenuation are difficult to apply, since the wave attenuation depends not only on water depth h and wave amplitude a but also strongly on the wave type (Hughes, 1993).
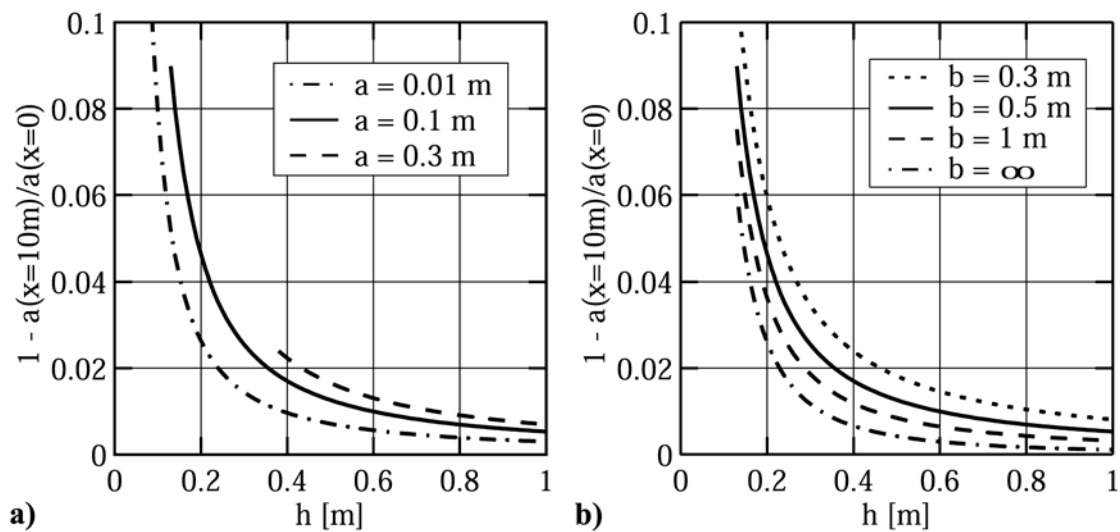
Figure 3.1 **Viscous boundary layer wave attenuation** $1 - a(x = 10)/a(x = 0)$ as a function of still water depth h given by Eq. 3.5 for: **a)** several positive wave amplitudes a and a given channel width $b = 0.5\,\text{m}$, **b)** several channel widths b and a given wave amplitude $a = 0.1\,\text{m}$.

The analytical solution of Keulegan (1948) compared well with experiments on the attenuation of a solitary wave along a rectangular channel conducted by Naheer (1978b). The Keulegan theory could even be extended to strongly nonlinear waves. Further experiments on the damping of solitary waves were conducted by Ippen et al. (1955), and Ippen and Kulin (1957). Kit and Shemer (1989) presented an alternative approach to determine the complex dissipation coefficients at the solid boundaries of a wave tank for nonlinear waves. The viscous damping may be neglected for the short measurement distance of the present physical model.

3.2.4 Surface tension effects

Surface tension effects are seldom encountered in gravity water wave problems in nature. Surface tension becomes important when water waves are very short or water depth is very shallow. The relative influence of surface tension is given by the ratio of inertial to surface tension forces known as the Weber number

$$\mathbf{W} = \frac{\rho_w c^2 L}{\sigma_w} \tag{3.6}$$

where σ_w is the surface tension of the water. The relative magnitude of surface tension forces may be evaluated using the linear wave theory expression for wave celerity

$$c^2 = \underbrace{\frac{gL}{2\pi}\tanh\left(\frac{2\pi h}{L}\right)}_{gravity} + \underbrace{\frac{2\pi\sigma_w}{\rho_w}\tanh\left(\frac{2\pi h}{L}\right)}_{surface\ tension} \tag{3.7}$$

where the surface tension term is included and not dumped as common for engineering applications. The relative contribution of the surface tension term can be expressed as a fraction by dividing the surface tension term by the gravity term. The surface tension term equals the gravity term for the wavelength $L = 0.0173$ m and the wave period $T = 0.074$ s, which marks the transition from gravity to capillary waves (Hughes, 1993). Surface tension effects contribute 1 % for the wavelength $L = 0.173$ m or solving by substitution for wave period and water depth yields $T = 0.33$ s and $h = 0.028$ m. This corresponds roughly to the rules of thumb $h > 0.02$ m and $T > 0.35$ s suggested by Le Méhauté (1976) in order to neglect surface tension effects in gravity wave propagation. All relevant parameters were well above these limits in all present experiments. Hence surface tension effects were irrelevant regarding impulse wave propagation below the wave breaking limit.

More difficult to determine is the role of surface tension in breaking waves. Entrained air bubbles in breaking waves are larger in the model because their size is determined by surface tension. Further the depth of air entrainment is greater in typical physical models (Hughes, 1993). Le Méhauté (1976, 1990) argued by virtue of the generalized Froude similitude that the process of energy dissipation during wave breaking is in similitude, even if the fine details of the flow process are different. Miller (1972) investigated the effect of surface tension on different breaking wave parameters by adding detergents. For a given piston Froude number, normal surface tension waves remained stable for a greater distance down the channel. For reduced surface tension wave breaking was observed for lower Froude numbers. Remarkable were significantly lower breaker heights for surface tension reduced solitary waves on steep slopes. Miller concluded that fluid surface tension played an important role and that it should be included in any theoretical treatment of the breaking process. Stive (1985) demonstrated with an experimental scale series of breaking waves on a beach that there are no significant deviations from Froude scaling, in a wave height range of approximately 0.1 m to 1.5 m. This result implied that the observed

difference in air entrainment had no significant influence on the wave dynamics. Nevertheless minor scale effects due to surface tension were observed by Stive at the lower end of his experimental range. The impulse waves of the present experimental study need to be upscaled in the other direction towards waves orders of magnitude larger, such as the 160m wave in Lituya Bay (Fritz et al., 2001). No surface tension effects are expected for impulse waves at prototype scale. In the experiments a minimal still water depth $h = 0.3$ m was chosen, which results in breaker heights $H_b = 0.78\,h = 0.23$ m. Hence surface tension effects are negligible for the present experimental research study.

3.2.5 Compressibility effects

Decisive regarding compressibility effects are not small scale physical models but the natural phenomena itself. The conditions for incompressible flow are $Ca \ll 1$ (Hughes, 1993) or $Ma < 0.2$ (Tritton, 1988). The Mach number Ma is related to the Cauchy number Ca by $Ma = \sqrt{Ca}$ and the Mach number is defined as $Ma = v_s / v_{sound}$. Maximum landslide velocities were estimated to $v_s = 150$ m/s by Körner (1976). In air under atmospheric conditions this yields Mach numbers $Ma \leq 0.5$. Melosh (1979, 1987) proposed that compressibility effects are of importance in the mechanics of high speed subaerial debris avalanches regarding fluidization and friction reduction, as discussed in Appendix A.2.

In pure water compressibility effects are irrelevant for landslide generated impulse waves, since $Ma \leq 0.1$ with maximum slide impact velocity $v_s = 150$ m/s and the sound velocity of 1480 m/s in water of 20° (Wagner and Kruse, 1998).

Skaldnev and Popov (1969) showed with an experimental scale series that breaker wave heights must exceed 0.5 m to prevent significant scale effects, when investigating wave induced pressure forces on dams. Scale effects on pressure forces resulting from compression in water and air mixtures can be significant, but wave induced pressure forces on structures were not investigated in the present study.

More difficult to assess is the role of compressibility effects in the wave generation area where massive phase mixing occurs due to air cavity collapse and slide detrainment during landslide run-out. Extensive work on cavity dynamics was conducted for both conventional and nuclear explosions under water spanning more than 12 orders of magnitude in yield up to mega tons of TNT equivalent (LeMéhauté and Wang, 1995). Of course in the intial phase of cavity formation both the air and water flow were compressible, but the subsequent cavity collapse and bore formation behaved incompressible. Explosion generated water waves could be scaled from the model to the prototype in very shallow water but not in intermediate or deep water. In deep water a small cavity is a vertically distorted model of a large cavity. Distortion is not allowed by the dispersion relationship in wave theory and hence the complete wave characteristics could not be scaled. The un-scaled atmospheric pressure caused the distortion of explosion generated air cavities in scale models. In scale models the atmospheric pressure would have to be reduced – similar to cavitation studies – in order to obtain undistorted air cavities (LeMéhauté and Wang,

1995). The cavity formation process of explosions is not of relevance for landslide impacts. The analogy to landslide generated impulse waves regarding cavity collapse and bore formation proposed by LeMéhauté and Wang (1995) suggests that the whole process of impulse wave generation by landslide impacts may be treated incompressible.

The air pressure inside the impact crater can be reduced. Abelson (1970) measured actual air under pressures inside impact craters formed by solid objects penetrating into a water pool. Those experiments covered a most interesting impact velocity range $10\,\mathrm{m/s} < v_s < 80\,\mathrm{m/s}$. For comparison landslides may impact into water bodies at velocities $v_s \le 150\mathrm{m/s}$. The measured air pressures inside impact craters formed by vertical and oblique entries are shown in Figs. 3.2a) and b), respectively.
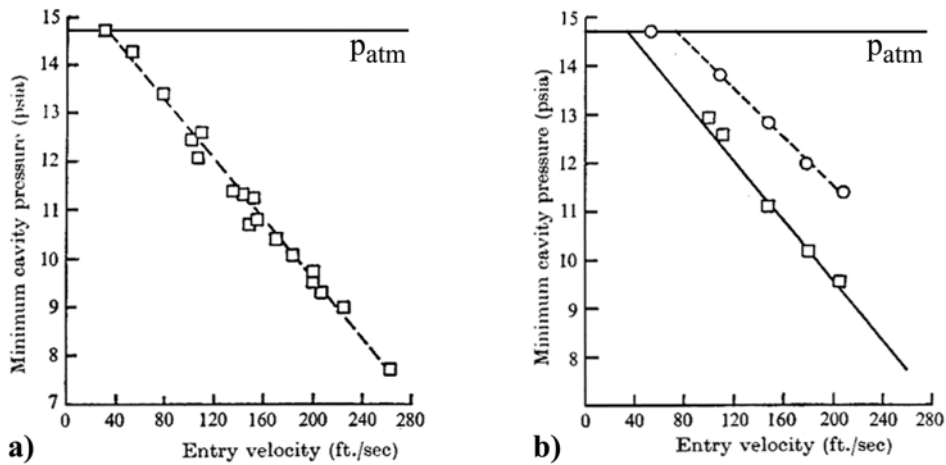
Figure 3.2 **Minimum air pressures** inside the impact crater before closure: **a) vertical entry** at 90°; **b) oblique entries** at (q) 60° and (m) 45° (Abelson, 1970).

Up to an impact velocity of $12\,\mathrm{m/s}$ the air pressure inside the crater matched the atmospheric pressure, thereafter the pressure decreased rapidly with increasing impact velocity to half the atmospheric pressure at $80\,\mathrm{m/s}$. Interestingly $v_s = 80\,\mathrm{m/s}$ corresponds to the maximum landslide velocity observed in the famous 1881 Elm landslide in Switzerland (Heim, 1932). Hence the air pressure inside the craters generated by impact velocities $v_s \le 8\mathrm{m/s}$ in the present experimental study did not depart from the surrounding atmospheric pressure. A laboratory scale series with impact velocities $v_s \le 10\mathrm{m/s}$ would not allow to investigate the unscaled air pressure. At even larger impact velocities the cavity pressures drop to roughly zero or close to the value for water vapor pressure (Lee et al., 1997). Froude scaling is definitely not sufficient for ultra high speed impacts $v_s > 150\,\mathrm{m/s}$.

Hyper velocity impact experiments of projectiles into water pools were conducted by Gault and Sonett (1982). The spherical projectiles with a diameter of 1 inch impacted with velocities from 1.25 to $6\,\mathrm{km/s}$ into a water tank with a stillwater depth $h = 0.3$ to $0.75\mathrm{m}$ resulting in Froude numbers from $\mathbf{F} = 460$ to 11000. The ambient air pressure was progressively varied from 0.008 atm to 1 atm. Variation of the background atmospheric pressure was found to be an important parameter. The cratering processes including the size

and shape of the transient cavities as well as their collapse at atmospheric pressure were grossly different from those in a low-pressure environment. However the radiating surface wave patterns were similar at all pressures. Disturbing was a small decay of the wave crest amplitudes with increasing ambient air pressure. This effect is expected to be negligible at the much lower impact velocities of landslide generated impulse waves. The hypersonic velocities of these experiments corresponded to Mach numbers $4 < Ma < 19$, whereas large body impacts on earth at $25 \, \text{km/s}$ would reach $Ma \sim 75$ with the speed of sound at sea level 347 m/s. Further hydrodynamic impact cratering experiments were conducted at up to $600 \, g$ in a centrifuge (Schmitt and Holsapple, 1980).

Most recent numerical simulations of the whole process from the landslide impact to the wave generation and propagation with an advanced compressible Navier-Stokes code allowed to alter the atmospheric pressure numerically (pers. com.: Charles L. Mader, LANL). The comparison of numerical results computed with different atmospheric pressures revealed changes to the collapse of the air cavity and the jet or rebound formation.

Hence it may be concluded after discussing all possible scale effects that the whole process including granular slide motion, slide impact, energy dissipation, wave generation, wave propagation and breaking primarily obey the generalized Froude similitude at the scale of the present experimental series.

3.3 Experimental set-up

3.3.1 Wave channel

The whole experimental set-up including the wave tank was designed by the author from scratch to meet the specific requirements posed by the physical modeling of high speed granular landslide impacts and the implementation of non-intrusive measurement techniques. The wave tank was manufactured by Schneider AG (Jona, CH). All experiments were conducted in the newly built water wave channel shown in Fig. 3.3. The rectangular prismatic wave tank was 11 m long, 0.5 m wide and 1 m deep. The cross-sectional dimensions were determined as such to avoid scale effects and the length was given by the available laboratory space. The massive steel main frame was designed to cope with the static and dynamic loadings. The continuous beam structure resting on three supports was statically indeterminate, which strongly damped vibrations. The construction had an accuracy of ± 1 mm. Deformations due to static and dynamic loadings were $< \pm 1$ mm. The front sidewall consisted of three 25 mm thick glass windows spanning 3.67 m each, whereas the back sidewall was made of a continuous, seamless steel plate. The bottom was made of steel plates in the slide impact area and glassed over the remaining two thirds of the channel length. This allowed optical access on two orthogonal axes. All glasses were monolithic fused silica to minimize transmission losses and avoid thermal destruction by the high energy density of the laser beam.
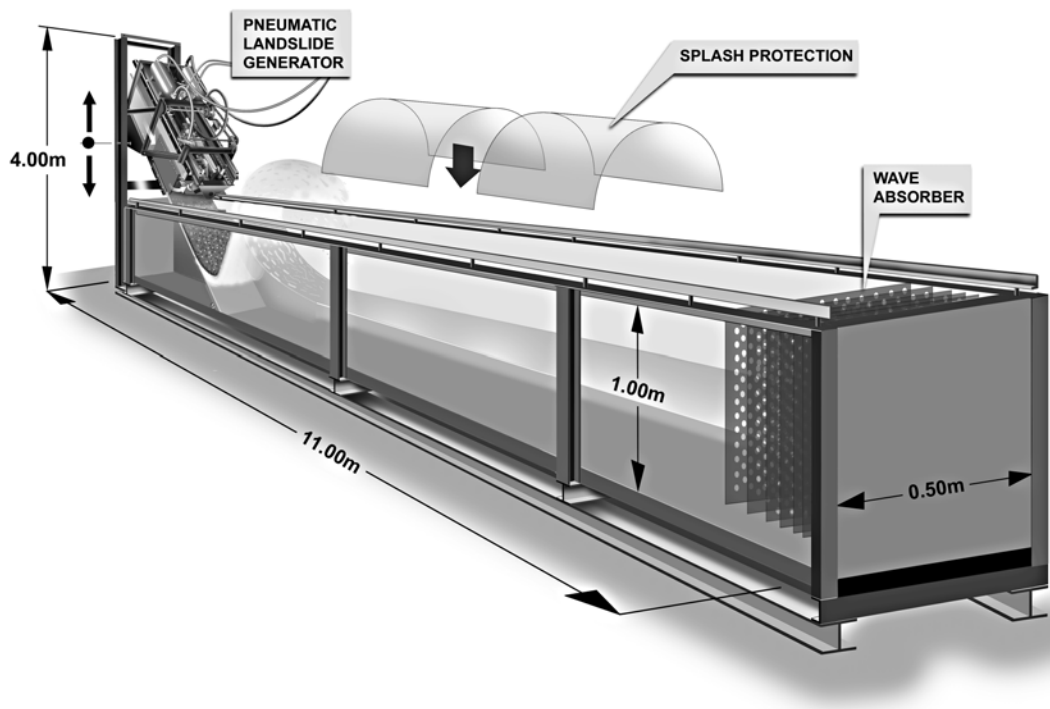
Figure 3.3   **Wave channel** with main dimensions, pneumatic landslide generator, splash protection and wave absorber.

At the front end of the channel a 3 m long hill slope ramp was built into the channel. The hill slope angle α was variable from 30° to 90°, but only the angle $\alpha = 45°$ was considered in this study. A framework was built onto the ramp as supporting structure for the novel pneumatic landslide generator described in [para 3.3.3].

The splash created by a high speed landslide impact would have reached up to the ceiling of the laboratory in some cases. Semi-cylindric splash protection elements covered the channel over roughly half its length in order to avoid short circuits and protect the sensitive electronics, laser and computer systems.

A progressive wave absorber (LeMéhauté, 1972) was built into the channel at the back end. The wave absorber reduced the reflected wave heights to prevent channel overtopping by superposed incident and reflected waves. The upright wave absorber was designed after Jamieson and Mansard (1987). The length of the wave absorber was reduced to 0.65 m compared to the design guidelines. The absorber still sufficiently damped the reflected waves without significantly affecting the length usable for wave propagation measurements. The absorber consisted of 6 perforated steel sheets positioned upright with progressively reduced spacing. The first 3 had a porosity of 50 % and the next 3 a porosity of 24 %. Reflection coefficients of upright porous wave absorbers may be found in Lee and Chwang (2000), Huang and Chao (1992), Fugazza and Natale (1992), Ouellet and Datta (1986), Madsen (1983) and Lean (1967). Pneumatic breakwaters (Skerrett, 1921; Bachus, 1955; Brevik, 1976) proved ineffective in wave damping during preliminary experiments even when injecting large amounts of compressed air.

3.3.2 Landslide material

3.3.2.1 Granulate

The Landslides were modeled with an artificial granular material (SD 104-C, Polycompound AG, Sissach, Switzerland). An artificial granulate had to be selected after preliminary tests with conventional sediments failed. The granular material had to be weaker than the glass of the channel sidewall in order to avoid scratching and maintain optical access. Grains of weak natural rocks such as limestone or marble disintegrated after a few experiments altering the grain size distribution. The artificial granular material consisted of 87 % barium-sulfate compounded with 13 % polypropylene (figures in weight percentage). The extrusive fabrication process with subsequent chopping created roughly cylindric grains with a mono-disperse grain diameter $d_g = 4$ mm. The granulate is shown in Fig. 3.4a).
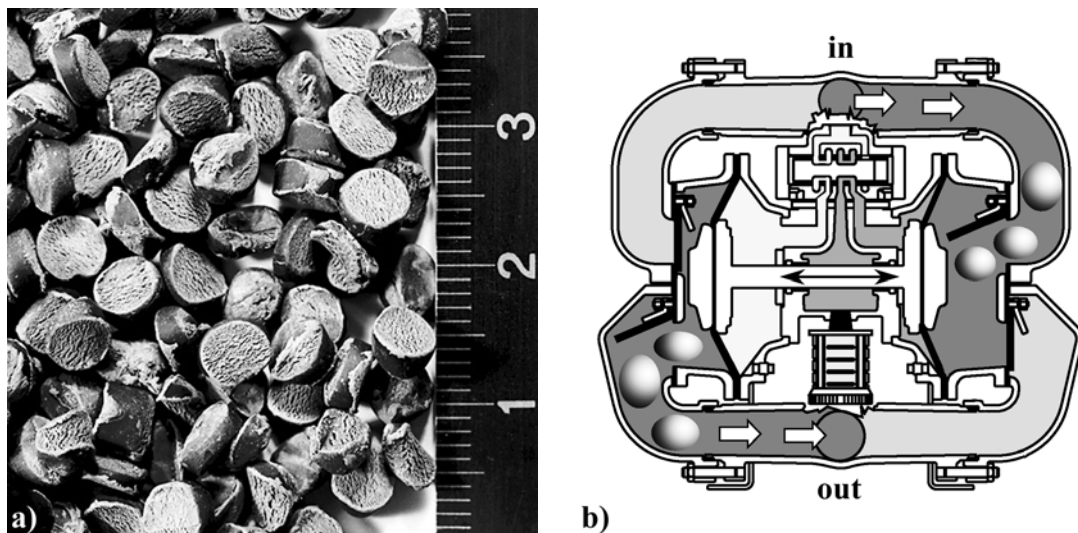
Figure 3.4   **a) Landslide material**: PP-BaSO$_4$ granulate with grain diameter $d_g = 4$ mm, grain density $\rho_g = 2.64$ t/m^3, porosity $n = 39$ % and slide density $\rho_s = 1.62$ t/m^3; **b) suction pump** during a cycle with left chamber on discharge stroke and right chamber on suction stroke.

Polypropylene ($\rho = 0.91$ t/m^3) was compounded with barium sulfate ($\rho = 4.5$ t/m^3) to reach the grain density $\rho_g = 2.64$ t/m^3. The granulate density perfectly matches common natural rock formations such as granite, limestone, sandstone and basalt. Natural rock densities vary roughly within 2 - 3.1 t/m^3 with a concentration around 2.6 - 2.7 t/m^3 (De Quervain, 1980; Kündig et al., 1997). As a bulk granular medium the density is reduced to the slide density $\rho_s = 1.62$ t/m^3 due to the porosity $n = 39$ % according to Eq. 3.1. The estimated values for the slide density and porosity correspond to the granulate packing in the slide box. The granulate was slightly compacted during the filling of the slide box. The granulate packing in the slide box is random and may be somewhere in between the densest and the loosest packing. The assumed porosity corresponds to data from Alpine debris flows (Tognacca, 1999) and the disturbed debris deposits at Mount St. Helens (Glicken,

1996). The permeability may be computed to 0.16 m/s according to the Hazen formula which yields that the permeability roughly equals $100\,d_g^2$ (Lang and Huder, 1990).

The underwater landslide deposit was pumped out of the wave tank with a 25 mm suction pump after an experiment (Sandpiper SA2-A, Warren Rupp Inc., Mansfield, Ohio). A cycle scheme of the compressed air driven double diaphragm pump with flap valves is shown in Fig. 3.4b).

3.3.2.2 Internal friction angle

The brake-up of landslides and their transformation into a debris slide or avalanche strongly depend on slide formation, drop height relative to slide volume, topography and in particular slope changes (Heim, 1932; Hsü, 1989). Slide transformations during slide motion are extremely difficult to predict. Common to granular flow is the importance of both the dynamic bed friction angle δ and the effective internal friction angle ϕ' regarding the type of motion. The effective internal friction angle ϕ' is further of relevance regarding the slide deformation during slide penetration into the water body and slide run-out along the channel bottom. The internal friction angle ϕ' was determined in triaxial shear tests conducted at IGT-ETH (courtesy of Dr. Tom Ramholt, chair of Prof. Dr. S. Springman). The triax shear tests are described in Appendix D. The effective internal friction angle of the PP-BaSO$_4$ granulate was determined to $\phi' = 43°$.

The triax shear tests on the artificial granulate exhibited an exemplary behavior of a coarse granulate. Hence the artificial material ideally substituted natural granulates such as gravel often used in laboratory studies of landslides. The results obtained with the artificial granulate are therefore unconditionally comparable to results obtained in experiments with natural gravels. The type of granular motion down an inclined chute is determined to some extent by ratio of the dynamic bed friction angle δ and the effective internal friction angle ϕ'. The friction ratio may be defined as $\tan\phi'/\tan\delta$. The dynamic bed friction angle was determined to $\delta = 24°$ [para 4.3.1]. The friction ratio of the present study was 2.1. Hence the slip between the bed and the granular mass was dominant resulting in slug-type flow (Savage, 1979). For comparison the rounded river gravels used in the study of Savage and Hutter (1989) had a bed friction angle $\delta = 22°$ and an angle of internal friction $\phi' = 29°$, whereas Huber (1980) only determined the pile angle to $32°$ which roughly corresponds to ϕ'. The friction ratio of the Savage and Hutter study was 1.4 and relatively smaller than in the present study. The smaller the friction ratio the more the slide mass deforms during granular flow.

3.3.3 Pneumatic landslide generator

3.3.3.1 General considerations

Two main drawbacks of granular landslide models were ascertained in the previous chapters. Laboratory granular flows may be scaled roughly to events with landslide volumes

$V_s < 10^5 \, \text{m}^3$, whereas for larger landslide volumes friction reduction needs to be considered. All events with relevant impulse waves described in Appendix B involved mass movements with $V_s \geq 10^5 \, \text{m}^3$. Previous granular landslide models involved a granular mass released from rest on a ramp by flap opening. Different slide impact velocities were achieved by positioning the flap up or down along the ramp, which led to an inherent dependency of slide impact shape on both slide velocity and granulate composition. Hence experimental runs with different slide impact velocities or granulates often had significantly differing slide impact shapes. Further granular flows down a channel are strongly affected by the lateral boundaries, which are known to dramatically change the flow structure (Savage, 1979). In many cases a granular flow after few meters down an inclined channel may not be considered as two-dimensional any more due to the development of the pronounced tongue shape of the slide front. Consequently a novel landslide generation apparatus was conceived.

3.3.3.2 Pneumatic acceleration mechanism

The pneumatic acceleration mechanism was developed in close collaboration with Festo Inc. (Dietikon, CH). Intensive prototype testing and several modifications of the custom built pneumatic system were necessary regarding both hard- and software components, because translation velocities in industrial applications usually are $< 1 \, \text{m/s}$. For details regarding the pneumatic system it is referred to Fritz and Moser (2002). The pneumatic landslide generator allowed to control the slide impact characteristics, thus allowing exact reproduction and independent variation of single dynamic slide parameters. In particular different slide impact shapes were produced for the same slide velocity and mass. Further lateral boundary effects were limited to the reduced granular flow distance after slide release.

The pneumatic acceleration mechanism is shown in Fig. 3.5 prior to the installation into the framework on the hill slope ramp. The landslide material was filled into the box from behind. The box opening mechanism for controlled landslide release consisted of a pneumatic cylinder driven flap. The box was mounted onto the linear guides with ball bearing units designed for high speed motion (INA Inc., Herzogenaurach, D). The acceleration mechanism consisted of two double acting pneumatic linear drives. The rodless pistons had a diameter of 80 mm, which gave a total driving force of 8 kN at the maximum operating pressure of 8 bar. The longitudinally slotted cylinder design allowed a stroke of 1.25 m on a fixed total length of 1.77 m.
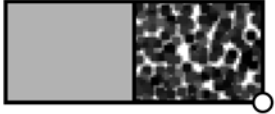
Figure 3.5   **Pneumatic slide acceleration mechanism** with the two double acting pneumatic linear drives, the plain bearing guides, the slide box and the pneumatic cylinder driven flap opening mechanism, prior to installation into the framework on the hill slope ramp.

The pneumatic landslide generator was built into the framework on the hill slope ramp shown in Fig. 3.6. The whole landslide generator was positionable roughly 1 m along the ramp with a gear drive. This mechanism allowed to adapt the position of the pneumatic landslide generator to varying water depths h and hillslope angles α prior to the experiment. The slide box end position was always located at a distance of 0.7 m from the still-water surface measured along the ramp (Fig. 3.14a).

3.3.3.3 Slide box

The slide box had a maximum inner volume of 0.0668 m^3. The inner box width was fixed to 0.472 m corresponding to 95 % of the channel width. The slide covered the whole channel width at impact on the water body due to the lateral spreading after the release of the slide from the box. The inner box length was reducible from 0.6 m to 0.3 m and 0.15 m with a positionable back plate. The inner box height s_{box} was reducible from 0.236 m to 0.118 m and 0.059 m with a positionable top plate. The considered combinations of slide masses and initial slide shapes are shown in Table 3.1. Prior to box filling the slide mass m_s was measured to an accuracy of ±0.01 kg with a precision balance (KB60.2, Mettler-Toledo, Nänikon, CH). The slide mass accuracy after box filling may be estimated to ±0.05 kg.

Table 3.1   **Initial slide masses and shapes** filled into the variable volume of the slide box confined with positionable top and back plates; (◐) slide front on the ramp.

s_{box} \ m_s	27.03 kg	54.06 kg	108.12 kg
0.236 m			
0.118 m			
0.059 m			

The slide shape in the box does not correspond to the slide impact shape. The slide impact shape strongly depends on the slide release velocity and the point of slide release. Preliminary experiments with calcite as slide material showed that the slide impact shape further depends on the slide material and granulate composition. Slide masses $m_s < 27$ kg were not considered. Preliminary experiments with $m_s = 13.5$ kg revealed granular flow instabilities. In particular the air cavities generated by the slide impact into the water body began to collapse laterally leading to a flow of water between the channel side walls and the slide, hence violating the two-dimensional model assumption. Similar instabilities were observed in laboratory gravity currents (Simpson, 1997).

3.3.3.4 Operation principle

The basic operation principle of the pneumatic landslide generator is shown in Fig. 3.6. The pneumatic drives pushed the slide box down the ramp with an acceleration $> g$. The flap opened during box acceleration. The flap opening was programmed to begin as late as possible but still to get the flap open before box deceleration. The slide was released by the box deceleration. The box was decelerated with pneumatic pressure reversal – injecting bursts of compressed air at the lower end and exhausting at the upper end of the cylinders. The remaining energy was absorbed by a custom built progressive shock absorber (Enidine Inc., Bad Bellingen, D).
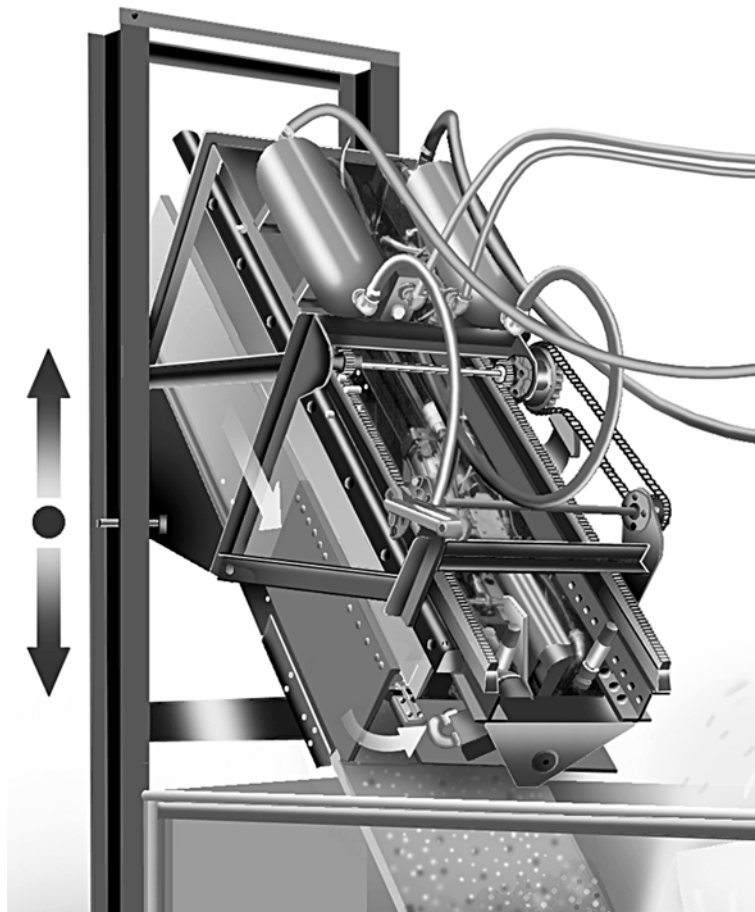
Figure 3.6 **Pneumatic landslide generator** operation scheme with flap opening during slide
box acceleration and slide release by box deceleration.

Real time problems posed a major challenge to the operation of the pneumatic system.
It was not possible to control the crucial flap opening and box deceleration with proximity
switches due to the response time of the solenoid valves. The box and the flap had a
response time of roughly 40 ms, which corresponds to a box travel distance of 0.32 m at
the maximum empty box velocity of 8 m/s. Therefore the pneumatic system was con-
trolled with preset trigger signals. Prior to each experiment the trigger settings had to be
determined and programmed to the control unit in LabVIEW. The pneumatic system is
shown in Fig. 3.7 during a slide impact experiment. The slide box is in the end position,
the flap open and the slide released.

Figure 3.7 **Slide impact experiment** at $\mathsf{F} = 2.0$, $m = 108$ kg, $h = 0.45$ m and $\alpha = 45°$ after slide release with the slide box in the end position.

3.3.3.5 Landslide generator performance

The box position was measured with a cable actuated transducer and a conductive plastic potentiometer (SGG-5000, Pewatron AG, Wallisellen, CH). The cable extension sensor had a high frequency response and a low torque which allowed to cope with accelerations up to 6 g and decelerations down to –12 g. The accuracy of the sensor was ±0.5 mm. The box position records of all experiments are shown in Fig. 3.8a). The flap opening was measured with a laser distance sensor (OADM, Baumer Electric AG, Frauenfeld, CH). The flap opening angle computed from a secant is shown in Fig. 3.8b). The flap had to be open at the maximum box velocity v_B reached during an experiment, but as late as possible. The flap trigger signal was set according to the value determined before each experiment. The 40 ms response times of the pneumatic box and flap to trigger signals are shown Fig. 3.8.
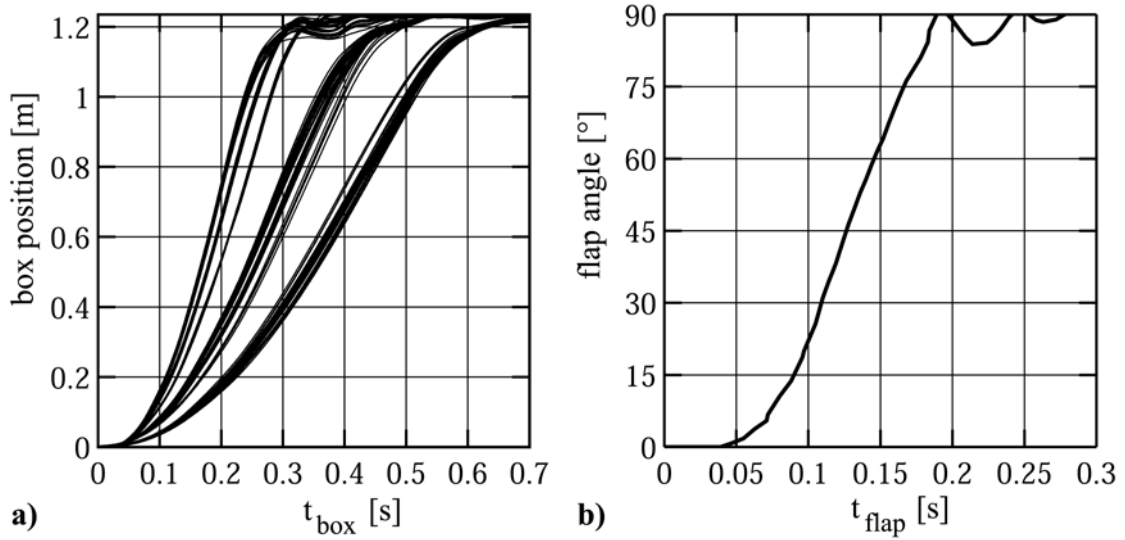
Figure 3.8 **a) Slide box position records** of all experimental runs, $t_{box} = 0$ corresponds to the start trigger; **b) Flap opening record**, $t_{flap} = 0$ corresponds to the flap opening trigger.

The box velocities v_{box} were derived from the box position records. The high frequency noise was removed from the raw position records prior to first and second derivation. The original signal was denoised with a Daubechies-wavelet transform (Daubechies, 1992; Strang and Nguyen, 1997). Correctly applied wavelet filters do not affect the transient signal whereas conventional filters would weaken the underlying peaks in the signal. The derived box velocity records are shown in Fig. 3.9.
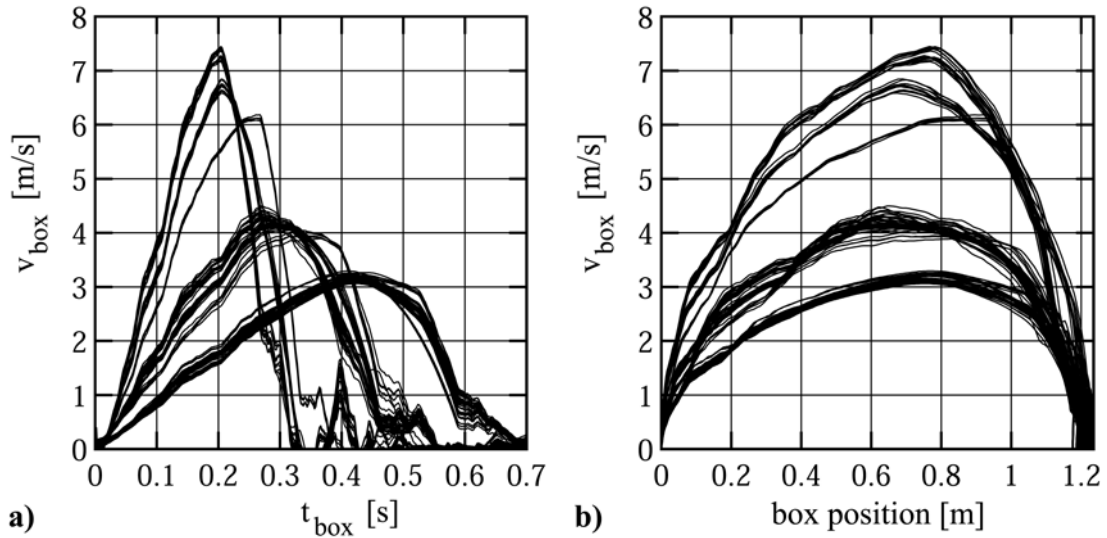
Figure 3.9 **Slide box velocity records**: **a)** versus time t_{box} after start trigger and **b)** versus box position along linear drives.

The slide release velocities corresponding to the box velocity peaks v_B are shown in Fig. 3.10. For each slide mass four different slide release velocities were considered. The

performance of the pneumatic system strongly depended on the accelerated mass, the propulsion pressure and the slope angle. The accelerated parts had a dead weight of 67 kg including the empty slide box. A maximum empty box velocity $v_B = 8$ m/s was reached at the maximum operating pressure of 8 bar and $\alpha = 45°$. The maximum box velocity decayed to $v_B = 6.13$ m/s for the maximum slide mass $m = 108.12$ kg. The pneumatic system could only be operated for slide release velocities $v_B > 3$ m/s. The minimal operatable slide release velocity $v_B = 3$ m/s roughly corresponds to the free fall velocity reachable over the acceleration distance of 0.8 m at $\alpha = 45°$. The bandwidth of generatable landslide shapes rapidly increased with increasing v_B. Preliminary experiments with throttle-valves showed that at $v_{box} < 3$ m/s no significant variation of the slide impact shape resulted with the pneumatic landslide generator. Hence lower velocities were generated by simple flap opening without box acceleration resulting in $v_B = 0$ m/s.
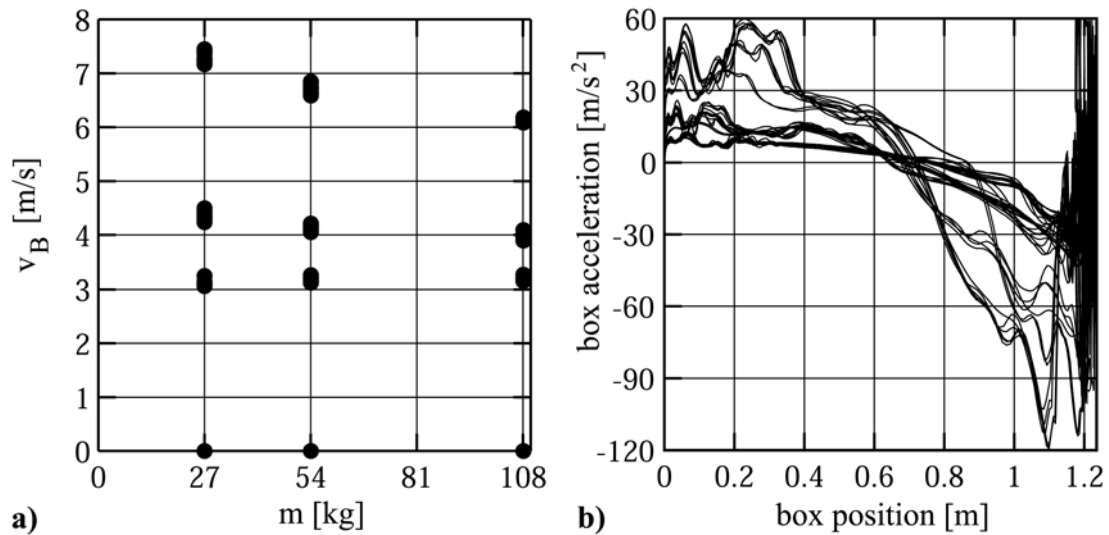
Figure 3.10 **a) Slide release velocities** corresponding to box peak velocities v_B; **b) Slide box acceleration** along the linear guides.

The slide box accelerations were computed as second derivative from the box position records. The box acceleration records along the linear drives are shown in Fig. 3.10b). At the maximum propulsion pressure of 8 bar the box accelerations were strongly dependent on the slide mass. For $m = 27$ kg acceleration peaks of 6 g were recorded, whereas for $m = 108$ kg the acceleration peaks decayed to 4 g. The characteristic oscillation (peak-trough-double peak) of the acceleration curves was observed at all operating pressures and for all pay loads. Box deceleration peaks of -12 g were reached at impact on the shock absorber at box position 1.085 m. Higher decelerations at best caused damage to the shock absorber as experienced by the author. The shock absorber and the pneumatic deceleration triggers, pressure and duration of the pressure reversal were adjusted prior to each experiment to avoid higher decelerations.

The slide release velocity v_B was one of the most important parameters, because v_B together with the point of slide release above the still water level determined the slide impact velocity v_s. Further v_B significantly influenced the generatable variation in slide impact shape. A statistical analysis of all slide release velocities is shown in Table 3.2. Each case comprised at least 5 runs.

Table 3.2   **Statistical analysis** of the slide release velocities v_B.

m_s	$\overline{v}_B$	$v_{B_{min}}$	$v_{B_{max}}$	$\Delta v_{B_{min}}$	$\Delta v_{B_{max}}$	σ_{v_B}	$\sigma_{\overline{v}_B}$
[kg]	[m/s]	[m/s]	[m/s]	[%]	[%]	[m/s]	[m/s]
	0	0	0	0	0	0	0
27.03	3.12	3.06	3.25	-2.0	4.2	0.055	0.014
	4.33	4.24	4.50	-2.1	3.9	0.077	0.019
	7.31	7.17	7.45	-1.9	1.9	0.100	0.029
	0	0	0	0	0	0	0
54.06	3.17	3.12	3.25	-1.7	2.5	0.046	0.014
	4.14	4.05	4.21	-2.3	1.6	0.042	0.012
	6.72	6.59	6.85	-2.0	1.9	0.085	0.027
	0	0	0	0	0	0	0
108.12	3.21	3.16	3.26	-1.6	1.8	0.035	0.014
	3.98	3.89	4.09	-2.1	2.8	0.075	0.034
	6.13	6.08	6.18	-0.8	0.8	0.038	0.017

The statistical properties were defined according to Coleman and Steele (1999), with mean $\overline{v}_B$, minimum $v_{B_{min}}$ and maximum $v_{B_{max}}$. The deviations of the minimum and the maximum from the mean were defined as $\Delta v_{B_{min}} = v_{B_{min}} - \overline{v}_B$ and $\Delta v_{B_{max}} = v_{B_{max}} - \overline{v}_B$, respectively. The standard deviation of the samples n was defined as

$$\sigma_{v_B} = \sqrt{\frac{1}{n-1} \sum_{i=1}^{n} (v_{B_i} - \overline{v}_B)^2} \tag{3.8}$$

and the standard deviation of the mean as

$$\sigma_{\overline{v}_B} = \frac{\sigma_{v_B}}{\sqrt{n}}. \tag{3.9}$$

The statistical analysis gives insight into the reproducibility of individual experiments. The largest deviations in slide release velocity v_B were within ±5 %. The scattering tends to decrease slightly for increasing box velocity. This behavior may be explained by the

larger driving pressures, which tends to reduce hysteresis effects in the pneumatic pressure control.

3.4 Measurement techniques

3.4.1 Instrumentation

Three different measurement techniques were built into the physical model: laser distance sensors (LDS), particle image velocimetry (PIV) and capacitance wave gages (CWG). An overview on the implementation and combination of the various systems is shown in Fig. 3.11. The pneumatics control unit served as trigger master. It controlled the pneumatic valves, pressure and position sensors and synchronized the start of landslide acceleration with the data acquisition of the two measurement PCs. The two PCs served as submasters. Real time problems were avoided by means of TTL hardware triggering pulses.
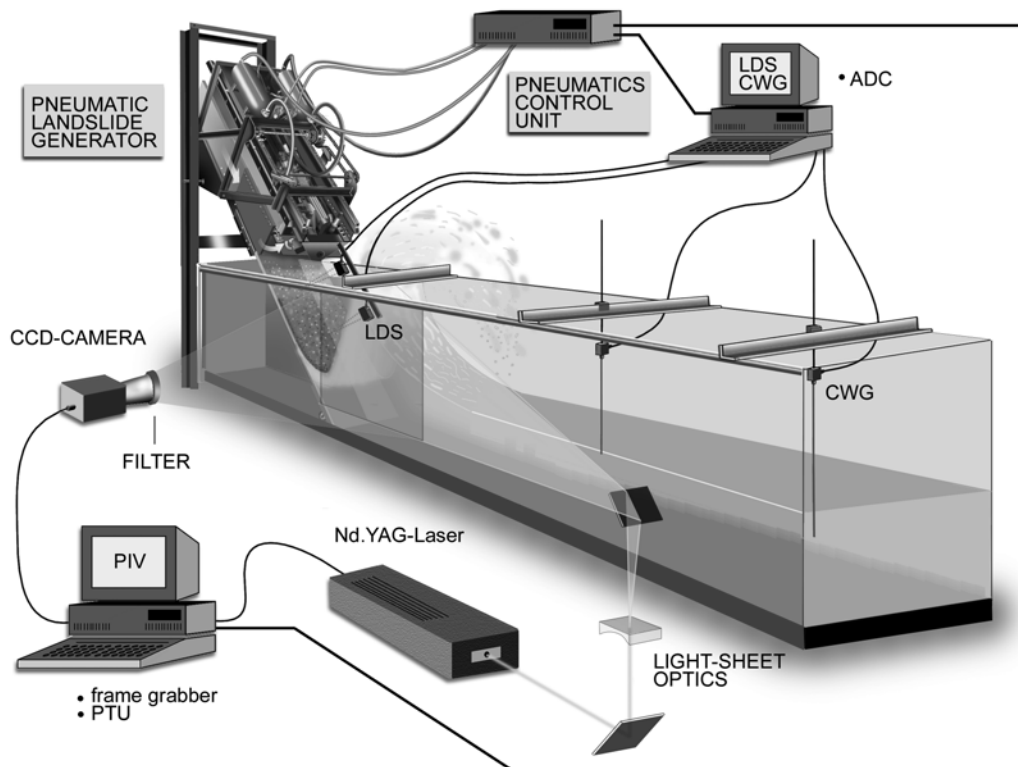
Figure 3.11 **Measurement setup** with pneumatic installation and the three measurement systems: laser distance sensors (LDS), capacitance wave gages (CWG) and particle image velocimetry (PIV). PIV-System with CCD-camera twin Nd.YAG-laser, simplified light-sheet and beam guiding optics.

The LDS-PC acquired the data from LDSs, CWGs, position and pressure sensors of the pneumatic landslide generator and made the analog-digital conversion after receiving the external TTL-start-trigger from the pneumatics control unit. Sensor calibration and

data acquisition programs were written in LabVIEW. The settings of the A/D-converter and the pneumatic control unit were adjusted from specific programmes written in Lab-VIEW. The remote control stand in front of the laboratory wave channel is shown in Fig. 3.12.
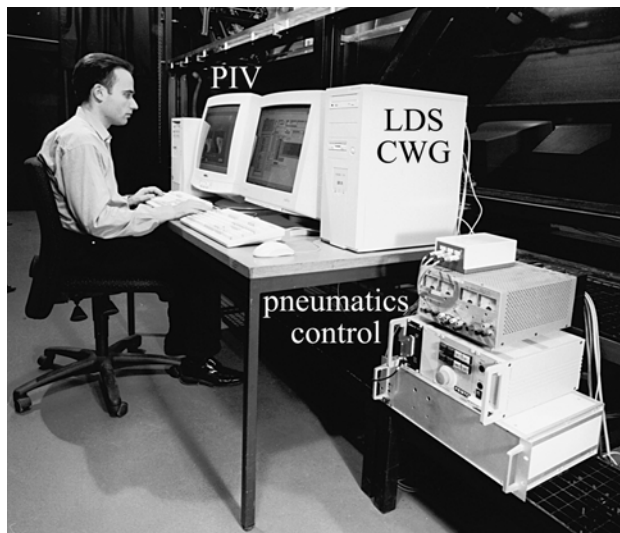
Figure 3.12   **Remote control stand** with the two PCs and the pneumatics control unit.

The programmable timing unit (PTU) in the PIV-PC was the key element for the timing of the whole PIV-system. The PTU-board received the external TTL-start-trigger from the pneumatics control unit, controlled the CCD-camera exposure and synchronization with the laser pulses. The frame grabber board (ITI IC-P) in the PIV-PC acquired the images from the CCD-camera at a data rate of roughly 30 MB/s. The images were captured in the RAM of the PIV-PC in real time and stored on the hard disks after the experiment.

3.4.2 Laser distance sensors (LDS)

The granular slide profiles were scanned in the channel axis before impact with two laser distance sensors (OADM, Baumer Electric AG, Frauenfeld, CH). A laser distance sensor and the measuring principle are shown in Figs. 3.13a) and b), respectively. The optical principle was based on triangulation. A pulsed red laser diode emitted pulses at a wavelength $\lambda = 675$ nm and a frequency of 100 Hz. The InGaP-laser illuminated a small bright spot on the granular slide surface. The laser beam had a diameter of 2 mm. An off-axis positioned linear photo diode array recorded the scattering of the laser pulse on the granular surface. The position detected on the photoelectric array allowed distance calculation with an accuracy of ± 0.5 mm for the measuring range of 400 mm. The laser distance sensor required a rough scattering surface on the target object and failed on smooth reflective surfaces.
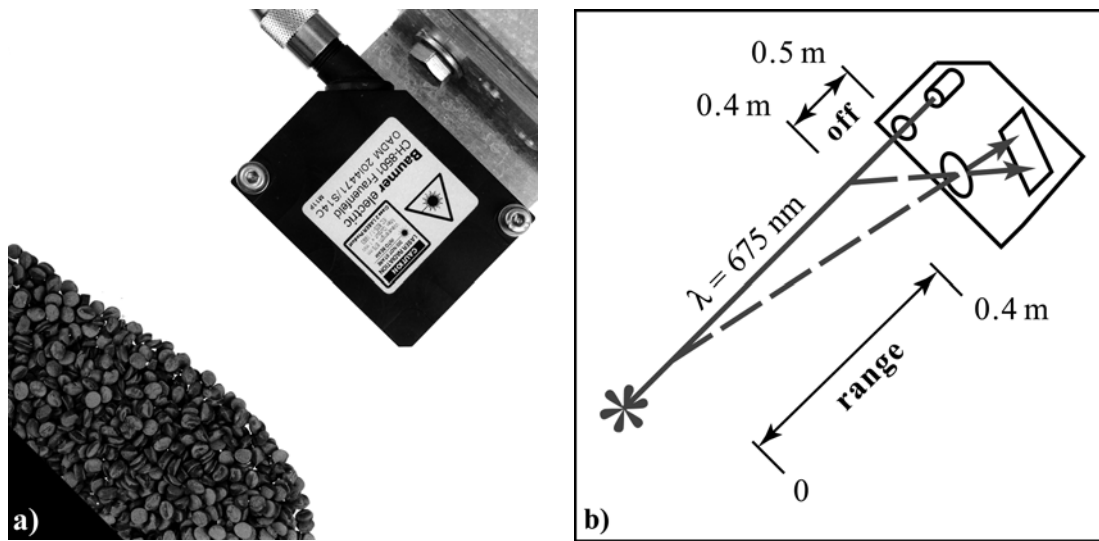
Figure 3.13 **a) Laser distance sensor** (LDS); **b) Measuring principle** based on triangulation.

Two laser distance sensors were positioned orthogonally to the ramp axis – one just in front of the flap end position and the other above the still water surface – as shown in Fig. 3.14a). The laser distance sensors had a response time of 10 ms. The sampling frequency was set to 0.5 kHz satisfying Nyquist's criterion. Two raw signals after analog-digital conversion are shown in Fig. 3.14b) together with the signals after applying a step response filter (Proakis and Manolakis, 1996).
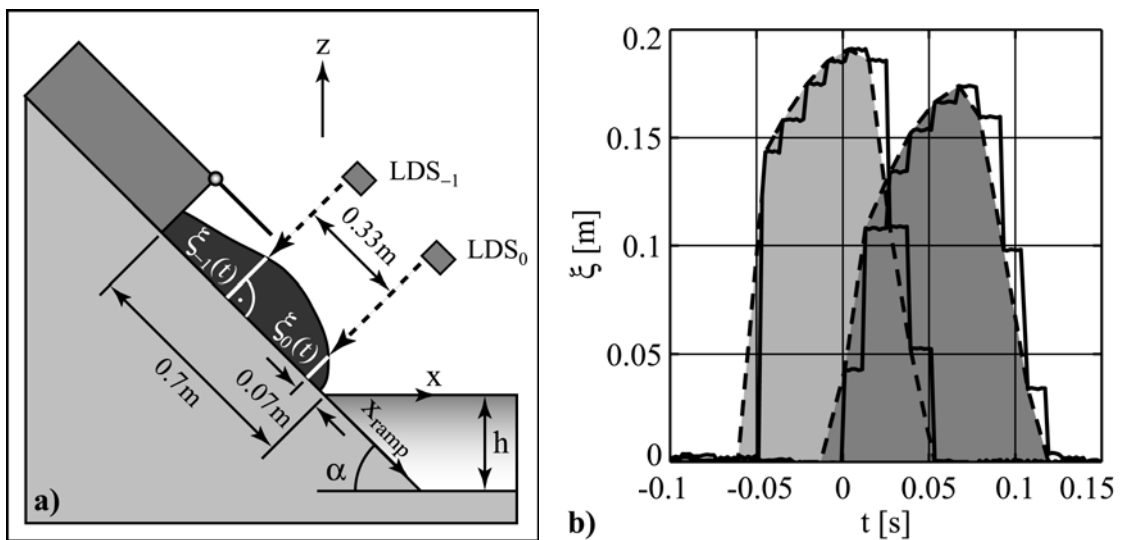
Figure 3.14 **a) Positioning** of the two laser distance sensors (LDS) relative to the still water surface; **b) Slide profiles** $\xi(t)$ at locations $x_{ramp} = (\blacksquare)$ –0.4 m and $(\blacksquare)$ –0.07 m, (—) raw signals after A/D-conversion, (– –) interpolated profiles of a run with $\alpha = 45°$, $m = 54$ kg, $s = 0.174$ m, $v_s = 5.53$ m/s.

The steps in the raw signal are due to the oversampling since the last value remains in an A/D-converter until a new value is collected. Time resolution is an issue at high slide

impact velocities. The response time of the laser distance sensors increased when the sensor internal electronics had to adjust the gain on the photoelectric array due to varying light scattering intensities. Intermittent signal drop outs due to the splash of the impact were present at certain slide impact characteristics. A sensor with a higher measuring frequency might reduce some of the problems.

3.4.3 Capacitance wave gages (CWG)

The wave features in the propagation area were determined with capacitance wave gages (CWG). Seven CWGs were positioned along the channel axis with a meter spacing as shown in Fig. 3.15. The position of the first wave gage was given by the landslide run-out distance and the deposit thickness. The wave gage locations along channel axis were not altered for different still water depths due to the difficult splash sealing – only the vertical positions were adjusted.
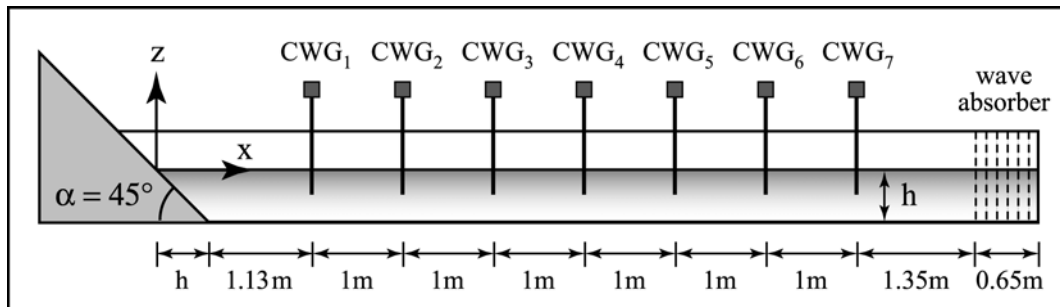
Figure 3.15 **Positioning** of the seven capacitance wave gages (CWG) along the channel axis.

Two capacitance wave gages and electronic instruments are shown in Fig. 3.16a). The electronic oscillators with a 4 to 20 mA signal output were manufactured by VEGA Inc. (Schiltach, D), whereas the probes were self-made. Probes with a measurement range of 0.6 m were used in the wave propagation area. Longer probes with a measurement range of 1.5 m were used in the Lituya Bay case study (Fritz et al., 2001) to measure the wave run-up. A sensor consisted of a stainless steel rod with a 3 mm diameter inserted into a PTFE-tube (Polytetrafluoroethylene, Teflon-PTFE, Du Pont Inc.). The PTFE-tubes with an outer diameter of 4 mm were 0.5 mm thick and sealed at the lower end by welding with PFA (Perfluoroalkoxy, Teflon-PFA, Du Pont Inc.).
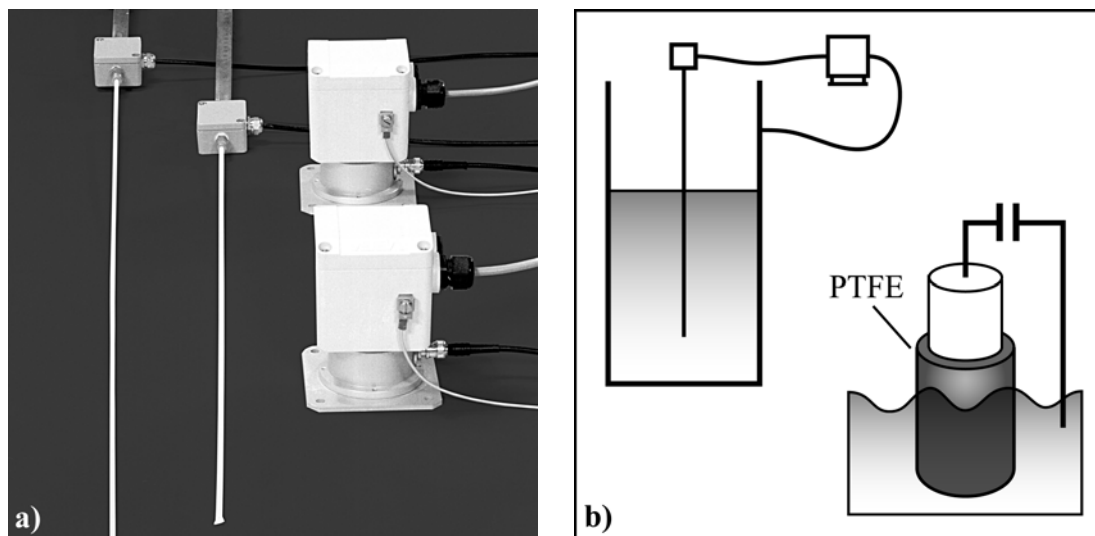
Figure 3.16 **a) Capacitance wave gages** (CWG) with measuring ranges of 0.6 m and 1.5 m and electronic instruments; **b) Measuring principle** with capacitor formation.

The measuring principle is shown in Fig. 3.16b). An electrical capacitor was formed between the electrode (steel rod) and the steel back wall of the wave channel. The PTFE-insulation had an electrical resistivity of 10^{16} Ωm, which is orders of magnitude larger than the electrical resistivity of water determined to $2.8 \cdot 10^5$ Ωm. The measured electrical resistivity variations of the channel water were < 1 %. For comparison air has an electrical resistivity of $4 \cdot 10^{13}$ Ωm (Denny, 1993). The water temperature and electrical resistivity were monitored with a conductivity meter (LF330, WTW GmbH, Weilheim, D). The water temperature was constant at $21 \pm 1°C$. A long-lasting algicide was added to the water (Desalgin Jet K, Bayrol GmbH, Planegg, D). The quarternay ammonium compound did not affect physical water properties such as surface tension or electrical conductivity and was pH-neutral, non foaming and biologically decomposable. Hence the capacitance was independent of the water properties and only depended on the sensor area in water contact and the thickness of the PTFE-insulator. The capacitance varied linearly with changes in water surface elevation. Deviations from the linear response were $< \pm 0.5$ mm. The probes were calibrated statically by varying the still water depth. The accuracy of the wave gages in a dynamic wave field below breaking limit may be given to ± 1.5 mm. The sensors had an excellent response time of a few hundred µs. The oscillators operated at a frequency of 300 kHz whereas the sampling frequency was set to 0.5 kHz.

Several other sensors failed during preliminary testing. Ultrasonic sensors – successfully applied in debris flow studies (Tognacca, 1999) – were not capable to cope with the high wave dynamics and dropped out completely for steep waves. Twin wire resistance wave gages (Huber, 1980; Sander, 1990; Müller, 1995) failed for several reasons: too small measuring range, too small linear range, signal drift, strong dependency on physical water properties, mechanical stability, splash and dirt sensitivity. The maximum wave

heights in the studies of Huber (1980), Sander (1990) and Müller (1995) were factors 3 to 10 smaller than in the present study.

3.4.4 Particle image velocimetry (PIV)

Particle image velocimetry (PIV) is a measurement technique which uses multiple images of flow tracing particles in a light sheet to measure the two in-plane velocity components of the host fluid simultaneously throughout the area of interest. The velocity vector fields were computed by the cross-correlation based PIV image analysis. Regarding the implementation of particle image velocimetry to the wave generation area of landslide generated impulse waves and the applied interrogation schemes it is referred to Appendix E. During each of the 137 experiments 50 double frames were acquired at 15 Hz covering a time span of $3\frac{1}{3}$ s. Each double frame allowed the computation of one velocity vector field. The data comprise experiments with the 72 different parameter combinations. In 49 cases, including all investigated parameter combinations at the still water depths $h = 0.3$ m and $h = 0.45$ m, juxtaposed areas of view were acquired in replicas. The camera positioning in two subsequent runs with the same experimental parameters is shown in Fig. 3.17.
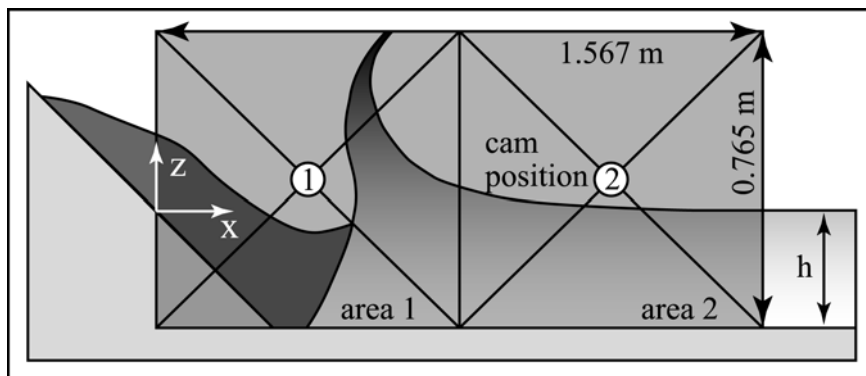
Figure 3.17   **CCD-camera areas of interest** acquired in two repeated runs with the same experimental parameters.

In 23 cases at $h = 0.675$ m only the first area of interest was acquired. Only fractions of the whole wave generation process could be acquired with a single area of view. Hence recordings of only one area of view were considered of limited value regarding the macro structure of the flow. Local details may be analyzed in individual areas of view. The primary interest of the present study was in the macro structure of the flow. Regarding the determined flow field quantities it is referred to Appendix F. Each data set includes the original PIV-images, the velocity vector field, the streamline plot, scalar fields of the velocity components and contour plots of the computed components of the deformation tensor.

4   Experimental Results

4.1   Introduction

Subaerial rockslide impacts into water bodies with the subsequent wave generation and propagation were considered in a geometrically undistorted Froude similarity model. A total of 137 experimental runs were conducted in the two dimensional physical model. A novel pneumatic landslide generator was used to generate a high-speed granular slide with controlled impact characteristics. The slide mass m, the slide velocity v_s and the slide thickness s were varied with the pneumatic landslide generator. The combination of several values of these three parameters produced 24 different slides. Further three water depths h were investigated resulting in 72 independent parameter combinations. Several runs were duplicated and some repeated few times. The slide impact angle was kept constant at $\alpha = 45°$. State-of-the-art laser measurement techniques such as particle image velocimetry (PIV) and laser distance sensors (LDS) were applied to the decisive initial phase with rockslide impact and wave generation. The 2 laser distance sensors scanned slide profiles before impact. PIV provided instantaneous velocity vector fields in a large area of interest and gave insight into kinematics of wave generation. Two thirds of the experiments were repeated to acquire adjacent areas of view with the PIV system. The wave profiles were recorded with 7 capacitance wave gages (CWG) positioned longitudinally along the channel using 1 m spacing. The wave characteristics such as wave height were related to the slide characteristics by dimensionless quantities resulting in hydraulic engineering solutions. The instantaneous velocity vector fields of the slide impact and wave generation area obtained by means of PIV may serve as reference data for numerical simulations.

4.2   Process overview

The pneumatic landslide generator allowed to significantly reduce the distance of granular sliding on the ramp. The granular slide motion before impact is only treated to the extent necessary for the determination of the slide impact characteristics. The pneumatic landslide generator and the subsequent granular motion down the inclined ramp governed the initial conditions at impact. The high-speed rockslide impact initiates an extremely unsteady energy conversion process with rapidly evolving flow fields, inter-phases and phase mixing which pose a major challenge to any measurement system. The complex phenomena that occur even on macro-scale during this extremely unsteady process with high-speed rockslide impact, air cavity formation, impulse wave generation, propagation and run-up are shown in the photo sequence of Figs. 4.1.
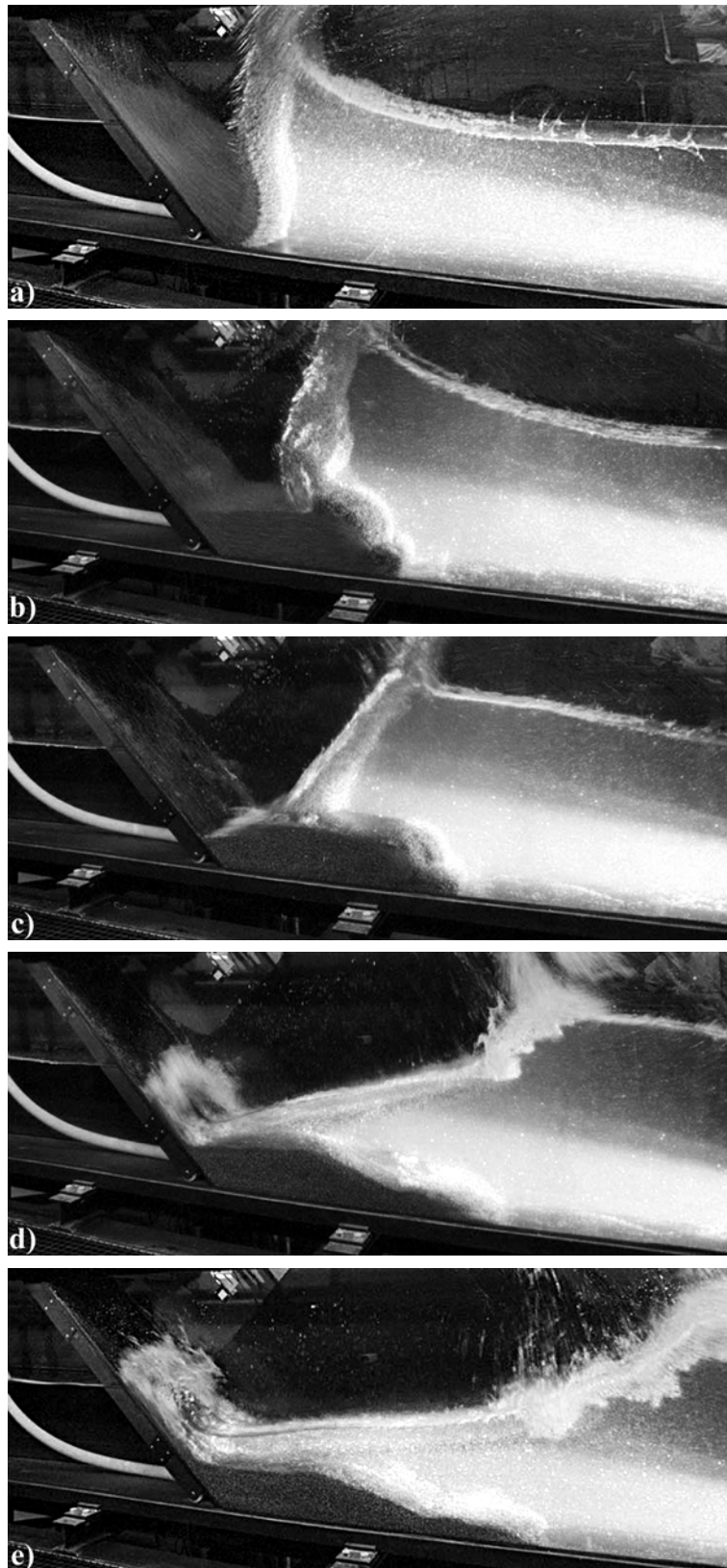
Figure 4.1 **Photo-sequence** of a granular slide impact at **F** = 3.3, *m* =108 kg, *h* = 0.45 m, *a* = 45°, area of view *x* = [-1 m, 2.5 m], *z* = [-0.45 m, 0.45 m], time increment of 0.2 s and first image roughly at *t* = 0.2 s.

The whole process of a high speed granular slide impact may be subdivided into two main stages: a) Rockslide impact and penetration with flow separation, impact crater formation and wave generation, and b) impact crater collapse with rockslide run-out and debris detrainment causing massive phase mixing. Impact stages overlap and their transition from wave generation to propagation and run-up is fluent. Slide bulking is caused by impact on the water surface and slide deflection at the channel bottom (Figs. 4.1a,b). Flow separation on the rockslide shoulder due to fast slide penetration into the water body creates a large air cavity on the back of the granular slide. During this separation stage three phases with sharp borderlines may be distinguished: water, granular material and air. The V-shaped impact crater in its maximum expansion by far exceeds the landslide volume. At the same time the splash reaches up to the splash protection shown in Fig. 3.7. The splash protection was located roughly 1.5 m above the still water surface or more than 3 water depths. In a large scale event the splash would break up and is expected to reach less high. The subsequent impact crater collapse during slide run-out along the channel bottom causes massive mixing of air and water (Figs. 4.1c,d). Typical for a high-speed slide impact the V-shape opens outward during collapse resulting in the first wave crest and a backward flow over the slide surface. Air is entrained into the water mainly due to air inclusion by flow reattachment during impact crater collapse and detrainment of the granular material during rockslide run-out along the channel bottom. Phase mixing had little effect on the leading wave because the main wave had propagated out of the impact area before air detrainment occurred. As the large nonlinear wave propagates outward the splash hits the wave crest from behind causing sort of a white-capping (Figs. 4.1d,e). Simultaneously the backward flow runs up the slide ramp. Thereafter the run-down generated a second outward travelling wave.

4.3   Subaerial slide motion

4.3.1 Slide impact velocity

A direct measurement of the slide centroid velocity during a slide impact experiment was difficult for several reasons. In granular flows the violation of the continuum assumption at slide fronts, density variations due to dilatation and velocity gradients within a slide pose a major challenge to any accurate velocity measurement (Savage, 1984). Except for the shortest slide, the slide front impacted the water surface before the rear end had left the slide box. Hence optical recording of images featuring the whole slide length was not possible. Therefore the following procedure to determine the slide impact velocity v_s was applied: first the dynamic bed-friction coefficient was determined in a preliminary series and then the slide impact velocity was extrapolated from the measured slide box velocity v_B along the centroid path determined from the measured slide profiles.

The concept of describing the motion of a deforming rockslide with the centroid position and the centroid velocity v_{sc} at incremental steps in time was introduced by Körner

(1976, 1983). The granular mass is treated as a frictional Coulomb continuum with a Coulomb basal friction law. The dynamic bed friction coefficient was determined to $\tan \delta = 0.44 \pm 0.02$ by minimizing the difference between computed and measured times of the centroid passings at the two laser distance sensors in preliminary experiments. The preliminary series of 7 experimental runs was initiated by simple flap opening without pneumatic acceleration resulting in a sliding velocity of roughly 3 m/s at the two laser distance sensors. Further no water was in the channel and the slide profiles where thus unaffected by the impact on the water surface. At higher impact velocities this approach was not applicable due to the limited time resolution of the laser distance sensors and the increasing number of drop out samples in the recorded slide profiles. The slide velocity extrapolation assumes a shear rate independence of shear stress. The assumption of shear rate independence of shear stress was confirmed by Hungr and Morgenstern (1984a,b). The high velocity ring shear tests demonstrated little rate-dependence although the rotation rate was varied by three orders of magnitude. Savage and Hutter (1989) also made the assumption of rate-independence, whereas Pouliquen (1999b) assumed $\delta(v_{sc}, s)$ a function of the slide thickness s and the slide centroid velocity v_{sc}. Fortunately the effect of the bed friction angle δ on the slide impact velocity decreases with increasing slide release velocity due to the short distance from slide release to impact. At a release velocity of 7 m/s an impact velocity of 8 m/s was reached corresponding to an increase in slide velocity of only 15%. Hence an error of a few percents in the bed friction angle does not have a relevant influence on the slide impact velocity at a high slide release velocity.

The equation for the slide centroid velocity v_{sc} may be deduced directly from the equation of Bernoulli and Newtons' second law of motion to

$$v_{sc} = \sqrt{v_B^2 + 2\,g\,\Delta z_{sc}(1 - \tan\delta \cot\alpha_{sc})} \qquad \textbf{(4.1)}$$

with the slide release velocity v_B, the dynamic bed friction angle δ, the angle from the horizontal to the centroid path α_{sc} and the centroid drop height Δz_{sc}. The parameter definition is shown in Fig. 4.2.
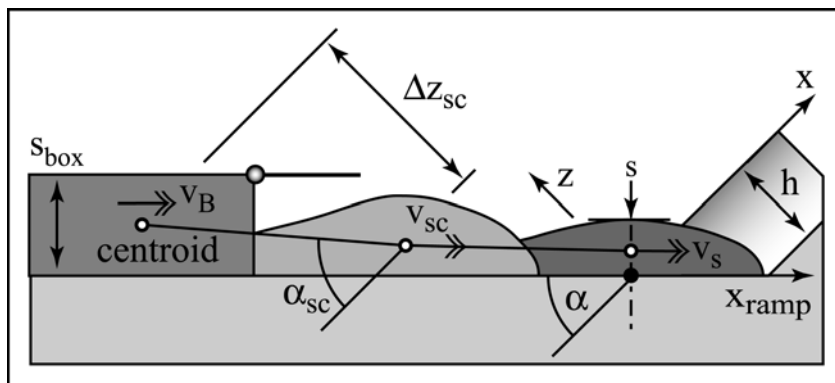
Figure 4.2   **Notation** for slide centroid velocity v_{sc} extrapolation from slide release velocity v_B and slide release position to slide impact velocity v_s.

The evolution of the slide centroid velocities v_{sc} extrapolated from the slide release velocities v_B with Eq. 4.1 are shown in Fig. 4.3. The positions and the velocities of slide release were averaged over slides with corresponding parameters before extrapolation. The slide centroid velocity v_{sc} was computed at the locations of the laser distance sensors with measured slide centroid coordinates s_{sc} and extrapolated to the slide impact velocity v_s. The positioning of the laser distance sensors is shown in Fig. 4.4. The slide impact velocity v_s corresponds to the slide centroid velocity v_{sc} at the location $x_{ramp} = 0$.
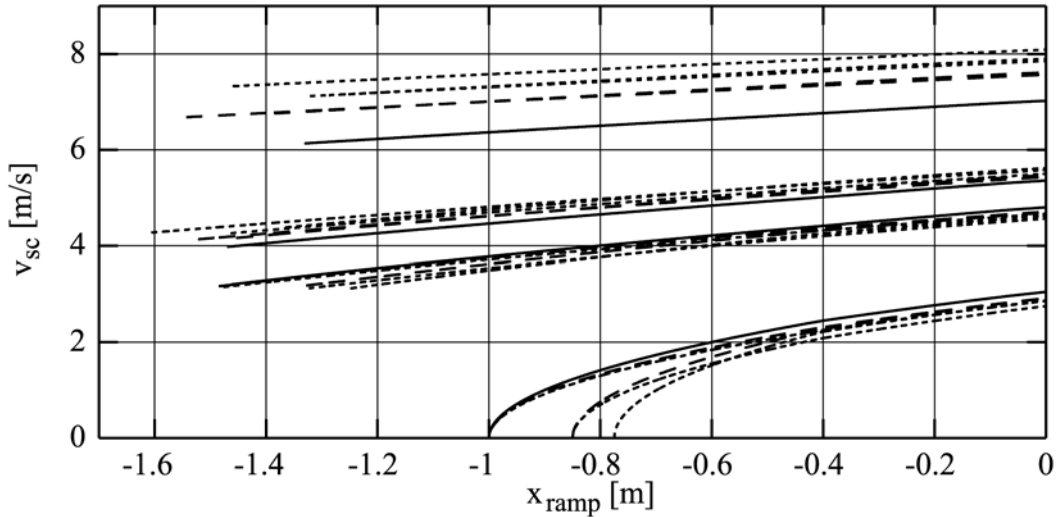
Figure 4.3   **Slide centroid velocity** extrapolations from release velocity v_B and location x_{ramp} with Eq. 4.1: (——) $m = 108$ kg, (— —) $m = 54$ kg, (••••) $m = 27$ kg.

The slide impact velocity v_s was varied from 2.7 m/s to 8.2 m/s or by a factor of 3. The corresponding drop heights may be calculated from the slide impact velocities v_s with Eq. 4.1. In order to achieve the same slide impact velocities without the pneumatic landslide generator the drop height would have to be varied from 0.7 m to 6 m above the still water surface. The investigated slide impact velocity range corresponds to a variation in slide drop height by a factor of 9. The investigated slide velocities were mass dependent. A maximum impact velocity $v_s = 8.2$ m/s was reached at $m = 27$ kg, whereas the maximum impact velocity decayed to $v_s = 7$ m/s for the maximum slide mass $m = 108$ kg. Further the impact velocity depended slightly on the distance of the slide centroid perpendicular to the pneumatic piston axis corresponding to the eccentricity – the closer the centroid to the piston axis the higher the slide release velocity. At the lowest slide velocities, which were generated by simple flap opening, a slight influence of the slide release shape due to the small differences in centroid drop heights was observed. The accuracy of the slide impact velocity v_s may be given to ±5 %.

4.3.2 Slide impact shapes

Different slide impact shapes were produced for the same slide velocity and mass. The slide profiles before impact were scanned with two laser distance sensors. The two laser distance sensors were positioned orthogonally to the ramp – one just in front of the flap end position and the other as close to the still water surface as possible avoiding drop outs – as shown in Fig. 4.4a). The notation used in the description of the subaerial granular flow and for the slide impact characteristics is shown in Fig. 4.4b).
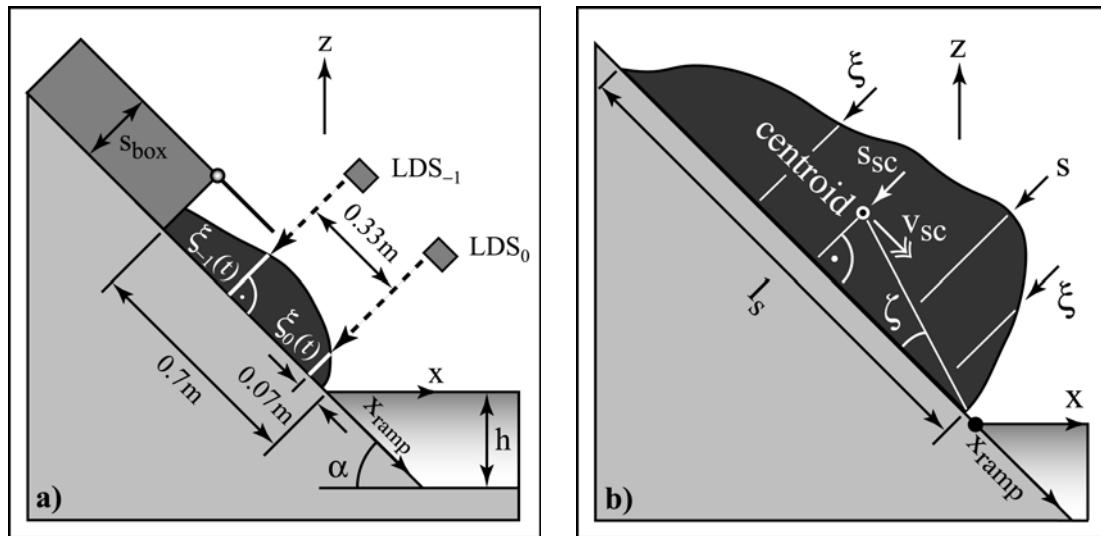
Figure 4.4   **a) Positioning** of the two laser distance sensors (LDS) relative to the still water surface; **b) Notation** for rockslide subaerial slide motion and impact characteristics.

Six different slides were generated for 4 different slide velocities resulting in a total of 24 slides. 3 different slide thicknesses were investigated for the slide mass $m = 27$ kg and 2 for $m = 54$ kg, whereas no variation was possible for $m = 108$ kg. The slide profiles $\xi(t)$ of slides with corresponding slide velocities are shown in Fig. 4.5 to 4.8, respectively. The pneumatic acceleration mechanism was positioned at the same distance from the still water surface. Hence the subaerial slide motion and the impact characteristics of runs with different still water depths h represent replicas. Therefore each slide was reproduced at least five times. Mean slide profiles were computed by averaging over the profiles of slides with corresponding parameters. The slide centroids at $x_{ramp} = -0.4$ m were matched on the time axis to the sample or ± 1 ms before computing the mean profiles. Averaging of slide profiles allowed to smoothen profiles and dampen random effects inevitable in granular flow measurements. Hence mean slide profiles are likely to give a better representation of the slide shape than individual profiles. At slow slide velocities (Fig. 4.5) the time resolution of the laser distance sensors is sufficient whereas at high velocities (Fig. 4.8) a higher time resolution would be desirable. The averaged profiles tend to represent slightly longer slide lengths than individual recordings because they start when the first profile rises and end when the last profile decays back to zero.
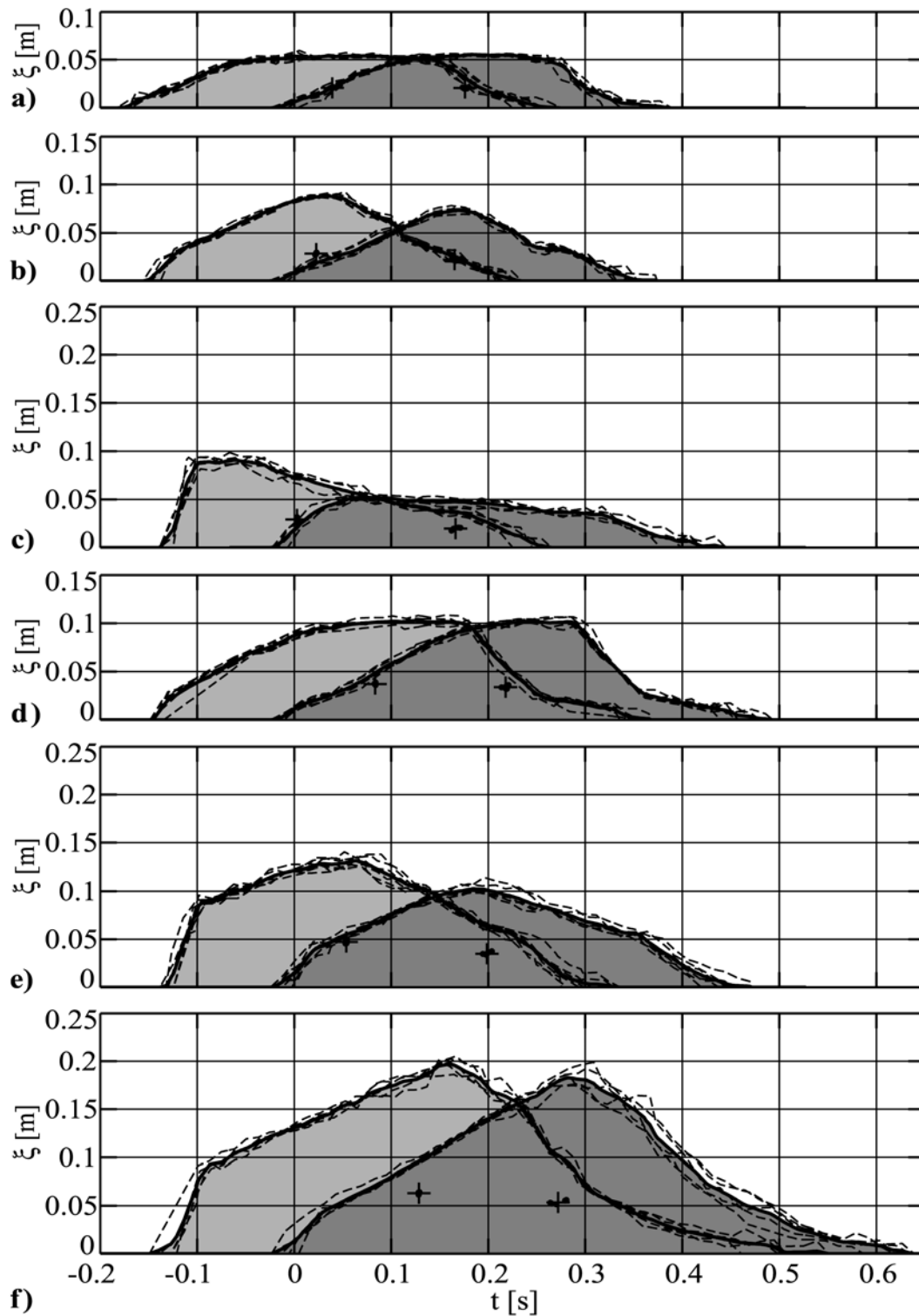
Figure 4.5 **Slide profiles** $\xi(t)$ at locations $x_{ramp} = ($ ⬜ $)$ –0.4 m and $($ ⬛ $)$ –0.07 m, (—) mean profiles, (– –) individual profiles, (+) mean centroids, (•) individual centroids, $\alpha = 45°$: **a)** $m = 27$ kg, $s = 0.055$ m ($s_{box} = 0.059$ m), $v_s = 2.87$ m/s, **b)** $m = 27$ kg, $s = 0.074$ m (0.118 m), $v_s = 2.77$ m/s, **c)** $m = 27$ kg, $s = 0.053$ m (0.236 m), $v_s = 2.88$ m/s, **d)** $m = 54$ kg, $s = 0.102$ m (0.118 m), $v_s = 2.94$ m/s, **e)** $m = 54$ kg, $s = 0.103$ m (0.236 m), $v_s = 2.94$ m/s, **f)** $m = 108$ kg, $s = 0.183$ m (0.236 m), $v_s = 3.08$ m/s.
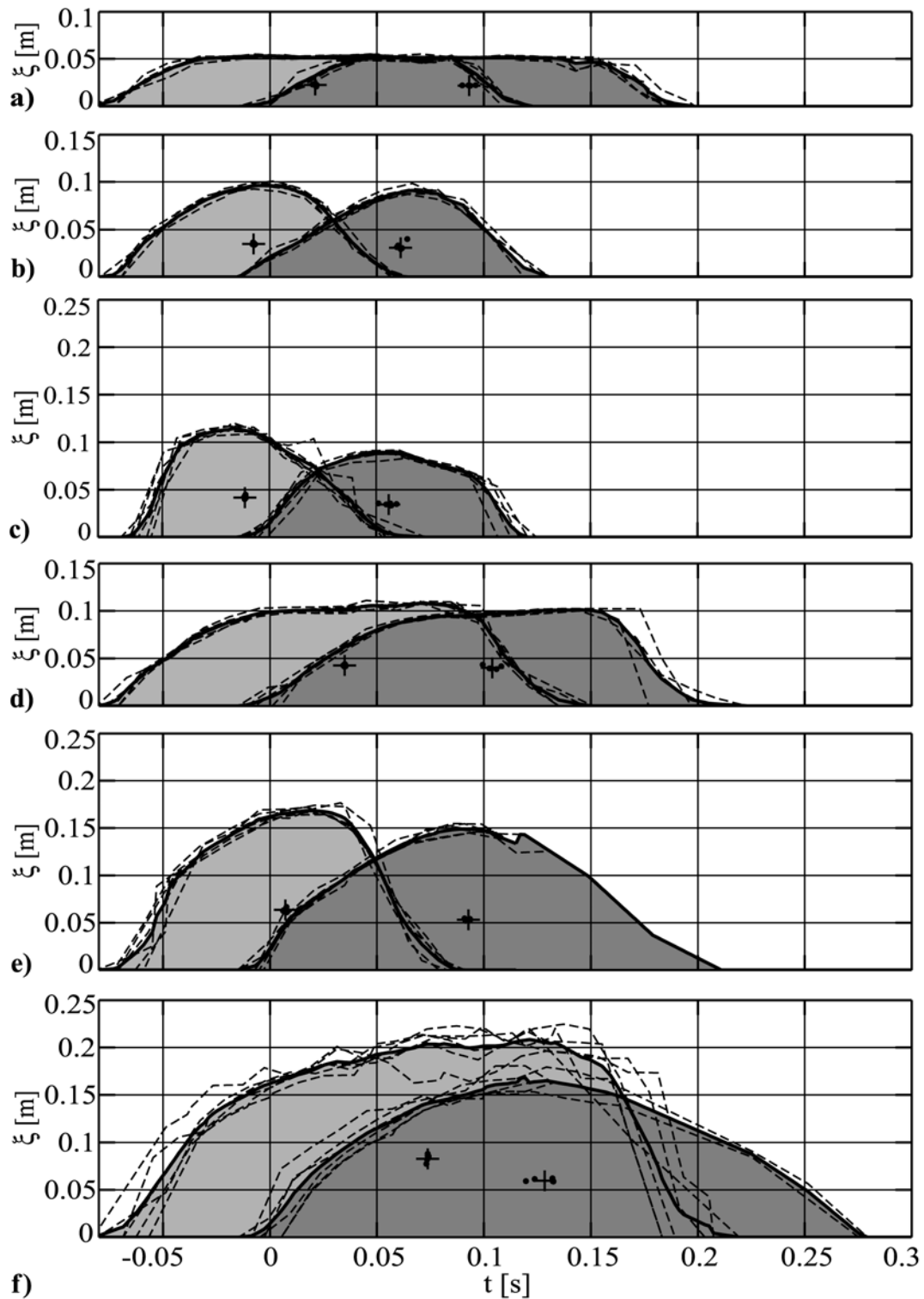
Figure 4.6 **Slide profiles** $\xi(t)$ at locations x_{ramp} = (▢) –0.4 m and (▣) –0.07 m, (—) mean slide profiles, (– –) individual slide profiles, (+) mean centroids, (•) individual centroids, $\alpha = 45°$: **a)** $m = 27$ kg, $s = 0.052$ m ($s_{box} = 0.059$ m), $v_s = 4.68$ m/s, **b)** $m = 27$ kg, $s = 0.091$ m (0.118 m), $v_s = 4.58$ m/s, **c)** $m = 27$ kg, $s = 0.088$ m (0.236 m), $v_s = 4.63$ m/s, **d)** $m = 54$ kg, $s = 0.101$ m (0.118 m), $v_s = 4.72$ m/s, **e)** $m = 54$ kg, $s = 0.149$ m (0.236 m), $v_s = 4.71$ m/s, **f)** $m = 108$ kg, $s = 0.168$ m (0.236 m), $v_s = 4.82$ m/s.
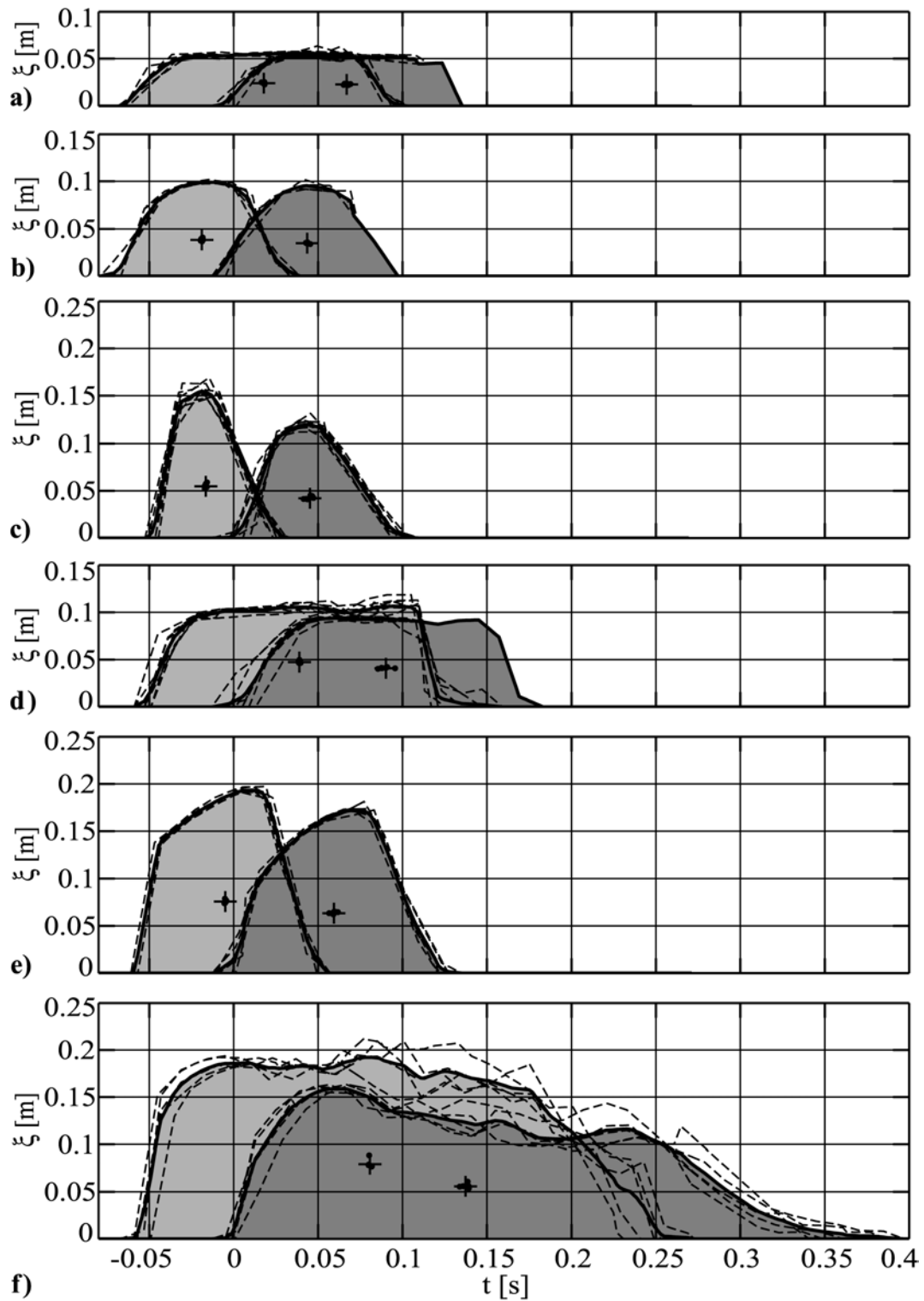
Figure 4.7 **Slide profiles** $\xi(t)$ at locations $x_{ramp} =$ (⬜) –0.4 m and (⬛) –0.07 m, (—) mean slide profiles, (– –) individual slide profiles, (+) mean centroids, (•) individual centroids, $\alpha = 45°$: **a)** $m = 27$ kg, $s = 0.052$ m ($s_{box} = 0.059$ m), $v_s = 5.58$ m/s, **b)** $m = 27$ kg, $s = 0.095$ m (0.118 m), $v_s = 5.51$ m/s, **c)** $m = 27$ kg, $s = 0.12$ m (0.236 m), $v_s = 5.63$ m/s, **d)** $m = 54$ kg, $s = 0.094$ m (0.118 m), $v_s = 5.44$ m/s, **e)** $m = 54$ kg, $s = 0.172$ m (0.236 m), $v_s = 5.49$ m/s, **f)** $m = 108$ kg, $s = 0.159$ m (0.236 m), $v_s = 5.38$ m/s.
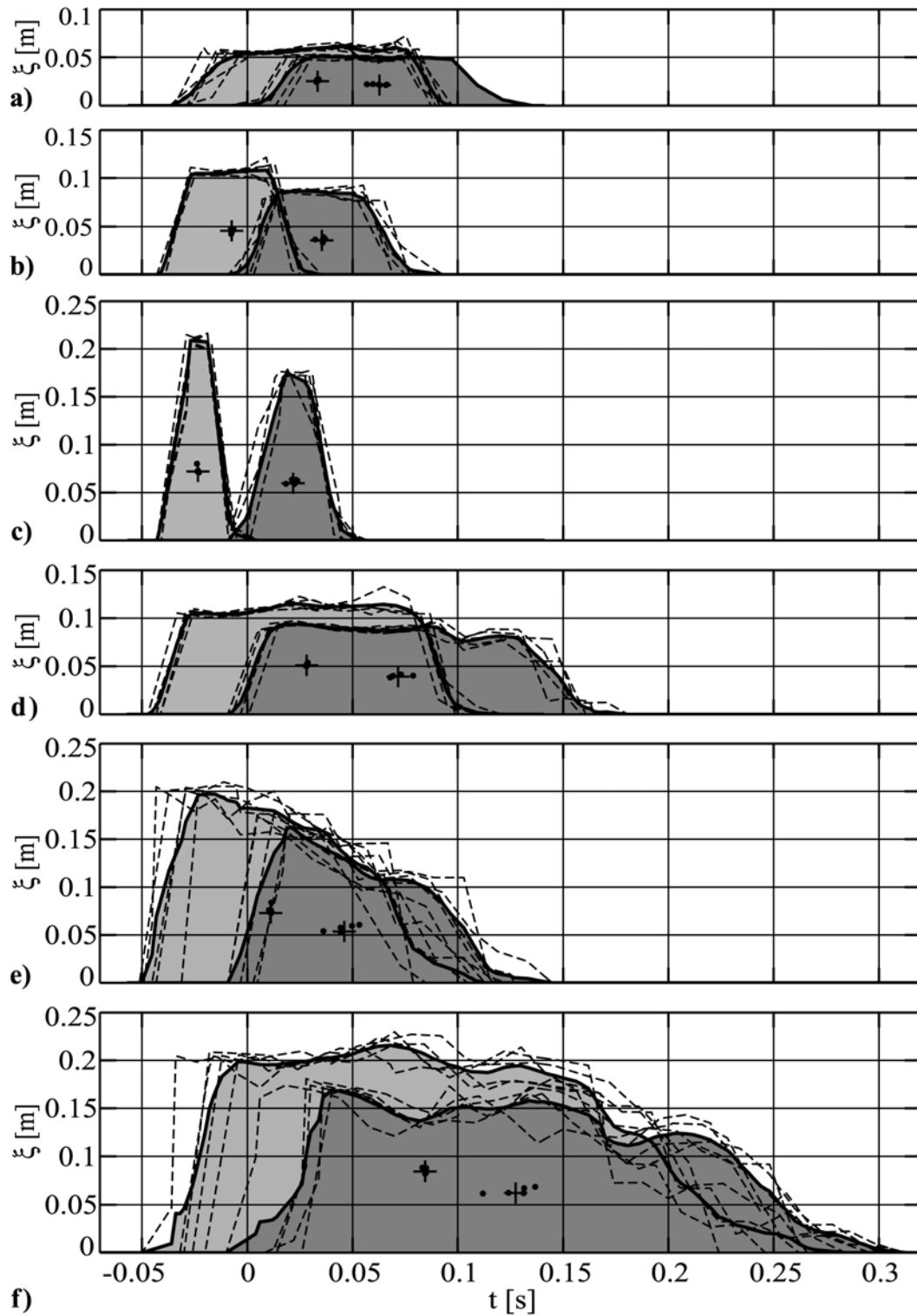
Figure 4.8 **Slide profiles** $\xi(t)$ at locations x_{ramp} = (⬜) –0.4 m and (⬛) –0.07 m, (—) mean slide profiles, (– –) individual slide profiles, (+) mean centroids, (•) individual centroids, α = 45°: **a)** m = 27 kg, s = 0.051 m (s_{box} = 0.059 m), v_s = 8.09 m/s, **b)** m = 27 kg, s = 0.086 m (0.118 m), v_s = 7.86 m/s, **c)** m = 27 kg, s = 0.175 m (0.236 m), v_s = 7.91 m/s, **d)** m = 54 kg, s = 0.094 m (0.118 m), v_s = 7.58 m/s, **e)** m = 54 kg, s = 0.163 m (0.236 m), v_s = 7.63 m/s, **f)** m = 108 kg, s = 0.169 m (0.236 m), v_s = 7.04 m/s.

The limited time resolution and many drop-outs at the slide front make it difficult to extract a front velocity with a reasonable accuracy from the slide profiles. Nevertheless a good representation of the slide thickness is given at all slide velocities. The slide impact shape strongly depends on the slide release velocity and the point of slide release. The bandwidth of generated landslide shapes rapidly increased with increasing slide velocity v_s. Further v_s significantly influenced the generated variation in slide impact shape. The slide impact thickness s approached the slide box thickness s_{box} with increasing slide velocity. At the lowest slide impact velocity the different slide release shapes resulted only in slightly different impact shapes whereas at the highest impact velocity a significant variation in slide thickness was achieved. The changes in slide profile over the short distance of 0.33 m separating the laser distance sensors are particularly significant at low slide velocities.

Integration over the slide profiles and multiplication with the slide centroid velocity show a mean increase in slide volume of roughly 10 % compared to the slide box volume. The slide mass was slightly compacted in the slide box. This increase in slide volume due to dilatation during slide deformation was matched by the increase in probe volumes observed in triax shear tests conducted at the lowest lateral tensions [para 3.3.2.2]. Dilatation inherent to granular flows typically leads to an increase in slide volume by up to 20 % after short flow distances (Savage, 1984). Lateral boundary effects were limited to the reduced sliding distance after slide release. Granular flows down chutes tend towards pronounced tongue shapes and a mass concentration along the axis.

Four parameters were extracted from the slide profiles to describe the slide characteristics during granular motion on the ramp: slide thickness s, centroid coordinate s_{sc} measured as orthogonal distance of slide centroid above the ramp, impact slide length l_s and the centroid angle ζ defined as angle between ramp and centroid as shown in Fig. 4.4b). The slide profiles $\xi(t)$ give a representation in time. Hence the slide thickness s is the only parameter directly measured. For the other three parameters the assumption of homogenous density and slide velocity distributions were made. The evolution of the slide thickness s, the centroid coordinate s_{sc} and the centroid angle ζ from the release point to the the water surface ($x_{ramp} = 0$) are shown in Figs. 4.9a,b,c), respectively. The slide shape was known at the slide release position and measured at $x_{ramp} = -0.4$ m and -0.07 m, respectively. The quantities were averaged over slides with corresponding parameters. Each curve represents the mean of at least five experimental runs. All three parameters decrease from the slide release point to the impact location. Particularly significant is the decay for slow slides with a large slide release thickness s_{box}.
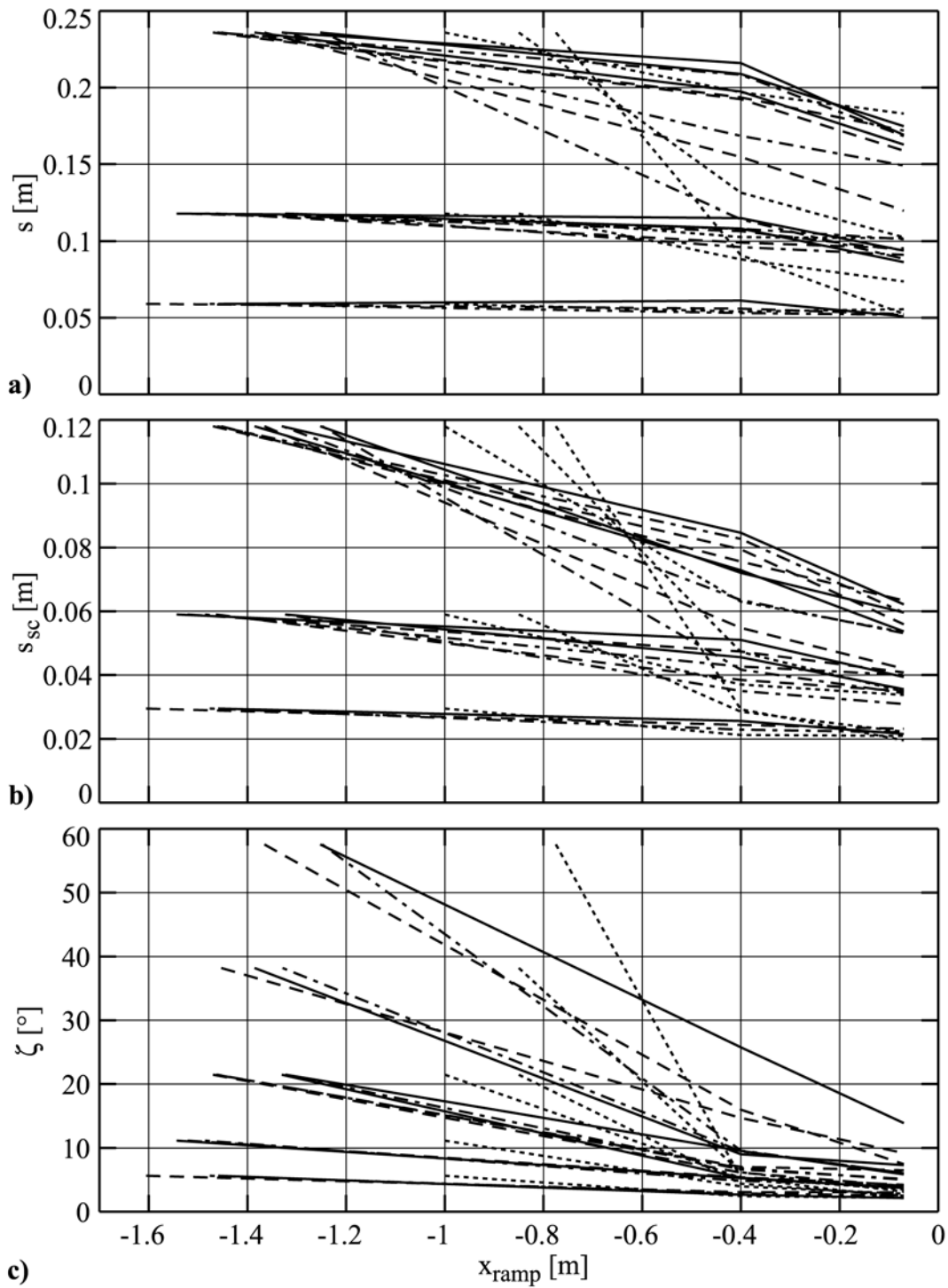
Figure 4.9 **Subaerial granular flow** along ramp after slide release: **a) slide thickness** *s*, **b) slide centroid distance** s_{sc} above ramp, **c) front-centroid angel** ζ and with (——) $v_s = 7$ to 8.1 m/s, (— —) $v_s = 5.2$ to 5.6 m/s, (– — ·) $v_s = 4.6$ to 4.8 m/s, (····) $v_s = 2.8$ to 3.1 m/s.

The orthogonal distance s_{sc} between slide centroid and ramp decays stronger than the slide thickness *s*. At slide release *s* corresponds to s_{sc} and s_{sc} to $s_{box}/2$. The corresponding values at impact are shown in Fig. 4.10a). A linear regression yields

$$s = 3s_{sc} \qquad\qquad (4.2)$$

with a correlation coefficient $r^2 = 0.97$. Hence the ratio between centroid coordinate s_{sc} and slide thickness s at impact was roughly constant for all slides investigated. Therefore in the present study one may choose either s or s_{sc} to form the relative slide thickness parameter. In this study the relative slide thickness was defined as $S = s/h$. This relationship is only valid for this particular experimental study and is only used here to describe the slide impact shapes.

The dependency of the slide centroid coordinate s_{sc} the slide impact velocity v_s is shown in Fig. 4.10b). The decay in the slide centroid coordinate s_{sc} from the point of release to the impact remained roughly constant for slides with a thin and elongated release shape. The impact shapes of slides with a short and thick release shape strongly depended on the slide impact velocity v_s. Hence the bandwidth of investigated slide thicknesses s at a given mass m and velocity v_s broadened significantly with increasing slide impact velocity v_s. At low slide impact velocities v_s the slide thickness s primarily depends on the slide mass m and the distance of granular motion along the ramp. The shape of these slides could not be altered by changing the release point without affecting the slide impact velocity v_s, because these cases were generated by means of simple flap opening. Therefore it was not possible to investigate the effects of the slide thickness on wave generation at low slide impact velocities v_s. In runs without pneumatic acceleration the slide impact shape was inherently dependent on slide mass m and slide impact velocity v_s similar as in the experimental investigation conducted by Huber (1980). In these cases different slide shapes at a given mass m, slide velocity v_s and impact angle α may be achieved by altering the internal friction angle ϕ or the bed friction angle δ.
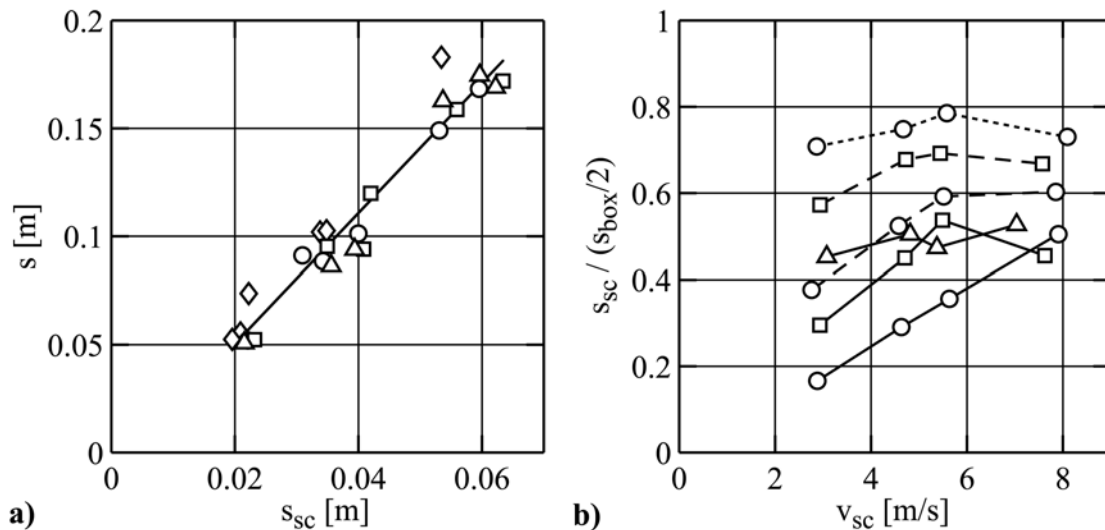
Figure 4.10 **Slide impact shape parameters: a) slide impact thickness** s with ($\Diamond$) $v_s = 2.8$ to 3.1 m/s, ($\bigcirc$) $v_s = 4.6$ to 4.8 m/s, ($\square$) $v_s = 5.2$ to 5.6 m/s, ($\triangle$) $v_s = 7$ to 8.1 m/s, (—) Eq. 4.2; **b) slide centroid coordinate** s_{sc} versus slide impact velocity v_s with ($\bigcirc$) $m = 27$ kg, ($\square$) $m = 54$ kg, ($\triangle$) $m = 108$ kg, (—) $s_{box} = 0.236$ m, (– –) $s_{box} = 0.118$ m, (---) $s_{box} = 0.059$ m.

The slide impact duration t_{si} was defined as the time difference between the passing of the slide front and the slide back as given by the slide profiles at location $x_{ramp} = -0.07$ m. The slide impact duration t_{si} corresponds to the duration from the slide impact until the rear end of the slide has passed the imaginary still water surface. The slide length at impact was then computed as $l_s = t_{si} v_s$ assuming a homogenous velocity distribution over the slide length. The slide length computed hereby may differ to some extent from a slide length measured from a photograph due to inevitable velocity gradients in granular flow. The slide lengths l_s computed from the extracted impact durations t_{si} are shown in Fig. 4.11a). The impact duration t_{si} at model scale varied roughly within 0.07 to 0.7 s and the slide length within 0.5 to 2.3 m. The measured ranges of slide thickness s and slide length l_s are shown in Fig. 4.11b). The experimental range is specific to this pneumatic landslide generator. Landslides with different slide thickness and length may occur in nature.
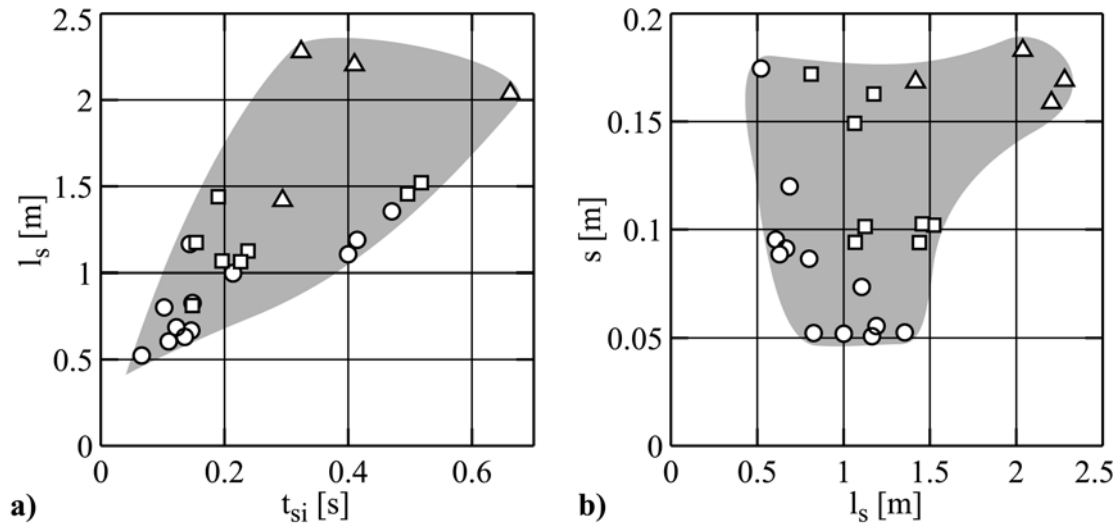
Figure 4.11 **a)** slide length l_s with ($\bigcirc$) $m = 27$ kg, ($\square$) $m = 54$ kg, ($\triangle$) $m = 108$ kg, ($\blacksquare$) range of experiments; **b)** slide length l_s versus slide thickness s with symbols as in a).

The ratio s/l_s is shown in Fig. 4.12a). The ratio s/l_s depended on the slide impact velocity v_s, the slide mass m and the slide release thickness s_{box}. The experiments cover a range of s/l_s from 0.03 to 0.33, or the slide length l_s varies from 3 to 30 times the slide thickness s. In nature also other values of s/l_s may be encountered. The ratio s/l_s versus the similar ratio $\tan(\zeta)$ is shown in Fig. 4.12b). The s/l_s ratio does not give an indication on the location of the slide centroid within the slide whereas the centroid angle ζ does. A linear regression yields

$$\frac{s}{l_s} = 1.35 \tan\zeta \qquad (4.3)$$

with a correlation coefficient $r^2 = 0.96$. The good correlation between the two ratios means that the slide centroid was located roughly at the same position within the slide at a given s/l_s. The empirical relationship of Eq. 4.2 together with Eq. 4.3 demonstrate that

the slide thickness to water depth ratio $S = s/h$ is sufficient to describe the shapes of the these experimental slides.
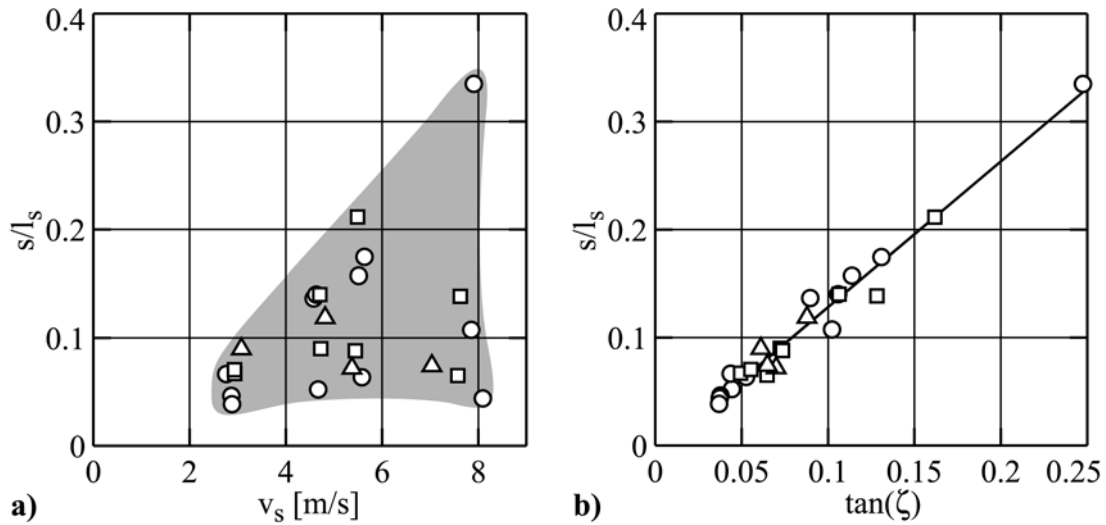
Figure 4.12 **Slide thickness to length ratio: a) dependency on v_s** with ($\bigcirc$) $m = 27$ kg, ($\square$) $m = 54$ kg, ($\triangle$) $m = 108$ kg, ($\blacksquare$) range of experiments; **b) correlation with centroid angle** ζ with (——) Eq. 4.3 and symbols as in a).

A front angle is not considered useful in this study due to the strong deformation and compaction of the slide front at impact on the water surface. A front angle was introduced by Kamphuis and Bowering (1970) in their impulse wave investigation with solid blocks. The wave characteristics were affected to some extent by the variable front angles of the blocks but the effect was much smaller than the one caused by S.

4.3.3 Range of experimental parameters

The dimensional analysis discussed in [para 3.2.1] resulted in six independent and dimensionless quantities. The dimensionless slide density ρ_s/ρ_w and the slide impact angle α were not altered and hence not included in the analysis. The dimensionless wave propagation distance x/h concerns only the wave characteristics. The observed relative wave propagation distance x/h decreased with increasing water depth due to the fixed length of the wave channel in the experiments. The remaining three dimensionless quantities were used to relate the wave parameters to the slide characteristics. The slide Froude number was defined as $\mathbf{F} = v_s/(gh)^{0.5}$ and forms the ratio between the slide impact velocity v_s and the shallow water wave propagation velocity $(gh)^{0.5}$. The slide Froude number only depends on the slide impact velocity v_s and the still water depth h. The slide Froude number does not account for nonlinear effects in wave propagation velocity. The bandwidth of investigated slide impact velocities v_s, still water depth h and corresponding slide Froude numbers is shown in Fig. 4.13a). By definition the effect of changes in water depth h on Froude number is relatively weaker than altering the slide impact velocity v_s. Chang-

ing the slide impact velocity does not affect the other dimensionless parameters, whereas by altering the water depth both the relative slide thickness $S = s/h$ and the relative displacement volume $V = V_s/(bh^2)$ are changed as well. The Froude number **F** range covered by the experiments spans roughly from 1 to 4.8. Froude values of 5 may be difficult to encounter in nature since in a typical Alpine lake with a water depth of 100 m an impact velocity of 160 m/s would be required. Even the Huascarán rockslide in Peru with a drop height of 4000 m did not reach velocities beyond 150 m/s (Körner, 1983). The Lituya Bay event had a Froude number **F** = 3.2 determined with a water depth $h = 122$ m and a slide impact velocity $v_s = 110$ m/s (Fritz et al. 2001).
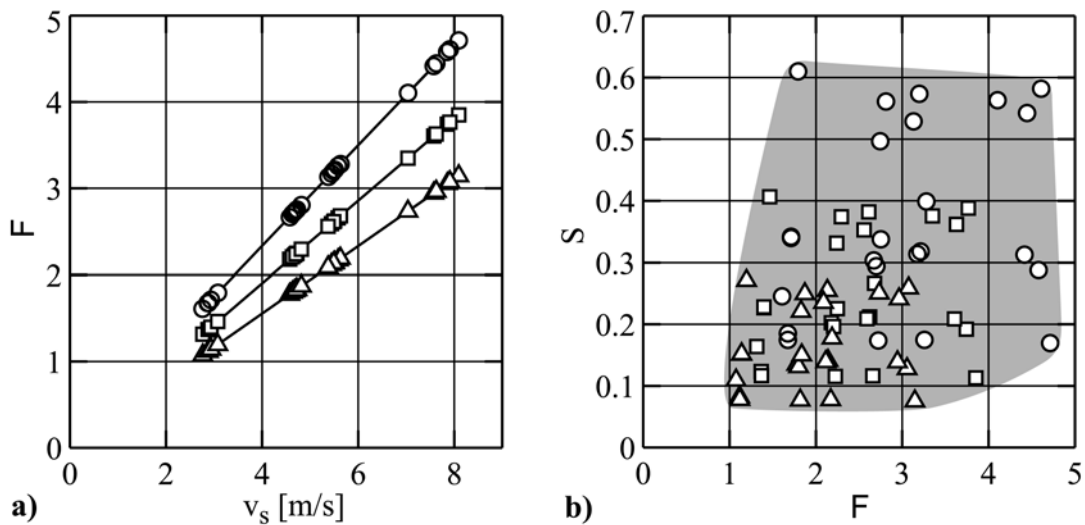
Figure 4.13 **Range of dimensionless quantities in experiments: a) Slide Froude-number** **F** $= v_s/(gh)^{0.5}$ dependency on v_s and h with (○) $h = 0.3$ m, (□) $h = 0.45$ m, (△) $h = 0.675$ m, (——) linear interpolations; **b) relative slide thickness** $S = s/h$ versus **F** with (▨) range of experiments and symbols as in a).

The relative slide thickness $S = s/h$ versus the Froude number is shown in Fig. 4.13b). At first sight a variation in S is simpler to achieve by varying h, but only a variation of the slide thickness s leaves the other dimensionless quantities unchanged. The pneumatic landslide generator enabled a variation in slide thickness at medium to high impact velocities v_s without affecting other slide parameters, whereas in granular flows of a finite mass down an inclined chute there is an inherent dependency of slide shape on drop height and granulate characteristics (Savage, 1979). The bandwidth of investigated relative slide thickness S spans roughly from 0.07 to 0.6. Larger S values may be achieved only by lowering the water depth below 0.3 m with the slide box thickness given by the pneumatic landslide generator and taking into account possible scale effects. In the Lituya Bay case study $S = 1$ was reached with a water depth $h = 0.18$ m at laboratory scale (Fritz et al., 2001). The effect of the relative slide thickness on the wave characteristics is expected to weaken for $S > 0.6$ according to the block study of Kamphuis and Bowering (1970).

Froude number and relative slide thickness versus the relative displacement volume $V = V_s/(bh^2)$ are shown in Figs. 4.14a) and b), respectively. The investigated relative slide volumes ranged from 0.07 to 1.6. Again due to the given slide box volume of the pneumatic landslide generator larger V values may only be achieved by lowering the water depth h. The Lituya Bay event with $V = 4.2$ was physically modeled with $h = 0.18\,\text{m}$ (Fritz et al., 2001).
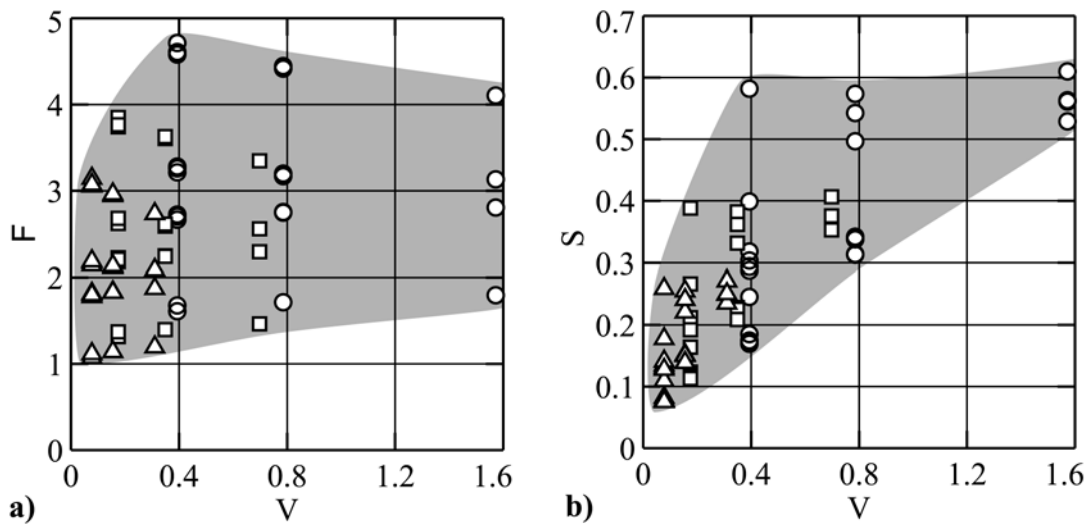
Figure 4.14 **Range of dimensionless quantities in experiments: a) Slide Froude-number** $\mathbf{F} = v_s/(gh)^{0.5}$ versus relative displacement Volume $V = V_s/(bh^2)$ with (◯) $h = 0.3\,\text{m}$, (☐) $h = 0.45\,\text{m}$, (△) $h = 0.675\,\text{m}$, (▨) range of experiments; **b) relative slide thickness** $S = s/h$ versus V and symbols as in a).

The investigated Froude number range was almost independent of the relative displacement volume V, whereas the relative slide thickness S range was depending on V.

4.4   Subaqueous slide motion

4.4.1 Slide impact and deformation

The penetration of the slide front was monitored by means of digital PIV-recordings and an additional analog VHS-camera. Four series of subsequent image recordings are shown in Figs. 4.15. All runs were conducted at $h = 0.675\,\text{m}$ and had exactly the same slide volume $V = 0.078$ and roughly the same slide thickness $S \approx 0.08$ but an increasing slide impact velocity v_s. The four experiments had increasing Froude numbers $\mathbf{F} = 1.1, 1.8, 2.2$ and 3.1, respectively. All experiments were recorded with the same image acquisition frequency. Therefore the difference in penetration velocity is reflected in the number of image recordings from the slide impact on the water surface until reaching the channel bottom. The image sequences exhibit the effect of the slide Froude number on the whole slide penetration and water displacement process. In the low Froude number experiment

at $\mathbf{F} = 1.1$, shown in Fig. 4.15a), the slide penetrated into the water body and the water flows around the shoulder and back of the slide without any flow separation. At higher Froude number experiments, shown in Figs. 4.15b,c,d), flow separation occurred on the slide shoulder forming a veritable hydrodynamic impact crater. The impact crater volume increased with increasing Froude number. The impact cratering and water displacement is discussed later in the context of the impulse wave generation.

The slide impact and penetration down the inclined ramp and along the channel bottom are complex processes involving slide compaction and deformation. In the experimental runs shown in Figs. 4.15 the slides had an initial slide thickness $s_{box}/h = 0.087$ and slide length $l_{box}/h = 0.89$ in the slide box. The corresponding slide profiles scanned before impact are shown in Figs. 4.5a) to 4.8a). The slides stretched out after slide release during the gravity driven subaerial motion before impact on the water surface. The relative slide thicknesses at impact were $S \approx 0.08$ and the relative slide lengths at impact $l_s/h = 1.25 \div 1.75$. The relative slide lengths before impact were not directly measured but extracted from the slide profiles assuming a constant velocity distribution over the whole slide and may further be somewhat affected by the impact on the water surface. At impact on the water surface and during the subaqueous slide motion down the inclined ramp massive slide compaction and deformation occurred. Measuring the slide thickness in image recordings is a difficult task, in particular when defining the location of the maximum slide thickness. In Fig. 4.15a) bulking occurred on the back of the slide due to the slide compaction and possibly the air detrainment of the slide. The air detrainment in the back of the slide indicates also the presence of a certain water flow through the granular media in order to fill the pore volume. In Fig. 4.15a) the slide thickness increased to $s/h = 0.28$ in front of the slide bulking on the back of the slide whereas the slide length reduced to $l_s/h = 0.75$. In this case the slide thickness increased by a factor of 3.5 whereas the slide length was halved before slide deflection at the channel bottom. Further mixing of the three phases water, air and granulate dominated in the wake of the slide. The situation gets even more complicated at higher Froude numbers due to difficulties in detecting the back of the slide behind the flow separation. The slide backs shown in Figs. 4.15b,c,d) were recovered from the lower bits with digital image enhancement techniques (Jähne, 1997). In Figs. 4.15b,c) a possible position of the maximum slide thickness may still be detected with a tangent parallel to the inclined plane, whereas this approach would not hold in Fig. 4.15d). In Figs. 4.15b,c) maximum slide thicknesses $s/h \approx 0.45$ may be measured corresponding to an increase in slide thickness by a factor of 5.5. This approach overestimates the representative slide thickness due to the convex shape of the slide surface. Further the point detected with a tangent to the slide surface parallel to the inclined ramp does not correspond to the point of flow separation. The tongue shaped slide front hides the point of flow separation in the channel axis below the lateral interface. In the Figs. 4.15b,c,d) the back of the slide completely crushes into the front. Thereby the slide lengths were reduced down to $l_s/h = 0.38 \div 0.58$ before slide deflection at the channel bottom. This corresponds to a reduction by a factor of 2 to 4 compared to the pre-impact slide lengths.
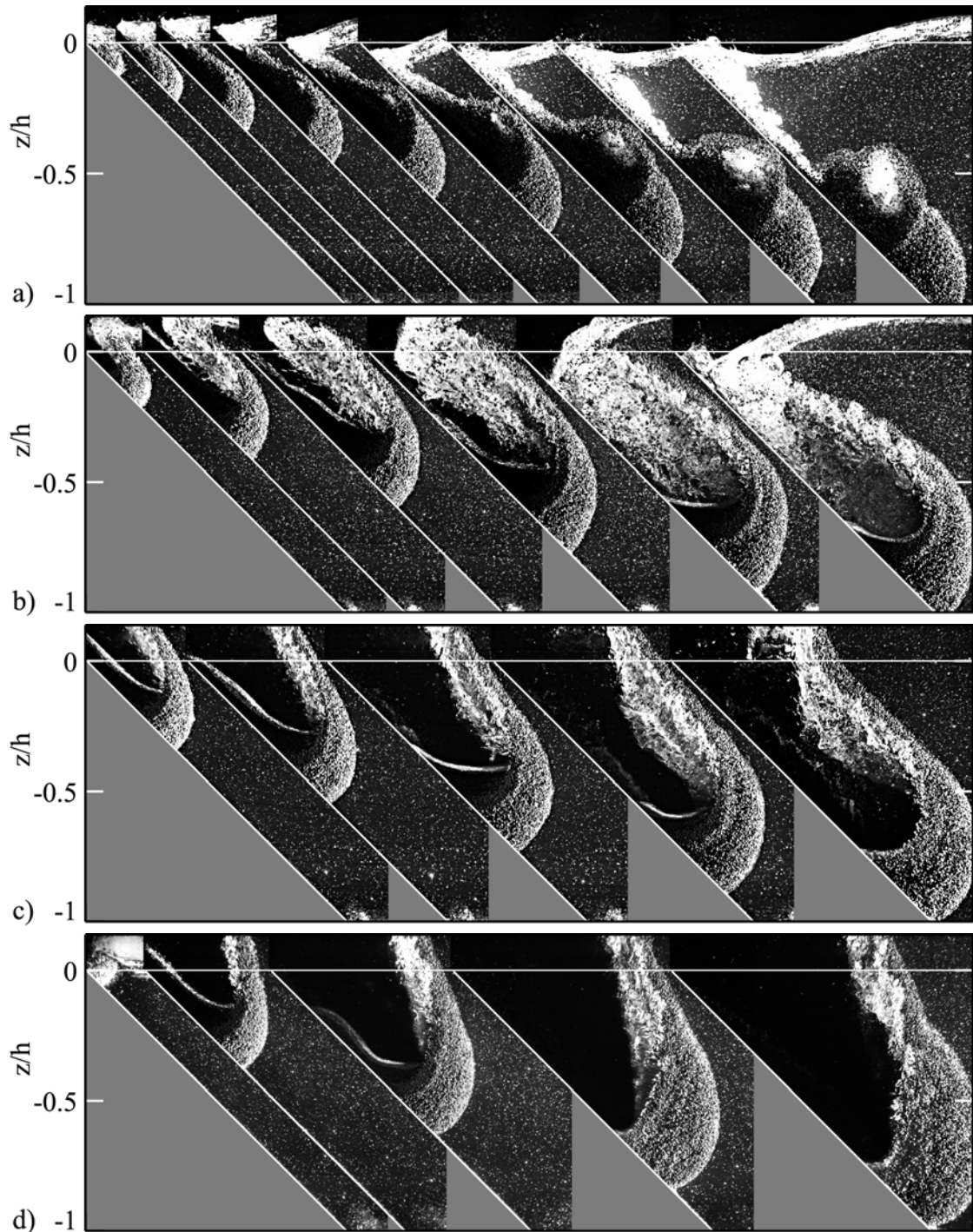
Figure 4.15 **Slide shape transformation** during penetration into the water body in a series of experiments with $V = 0.078$ at $h = 0.675\,\text{m}$ recorded with a time increment $\Delta t \sqrt{g/h} = 0.25$: **a) F** $= 1.12$, $S = 0.082$, first image at $t\sqrt{g/h} = 0.17$, **b) F** $= 1.82$, $S = 0.077$, first image at $t\sqrt{g/h} = 0.16$, **c) F** $= 2.17$, $S = 0.078$, first image at $t\sqrt{g/h} = 0.22$, **d) F** $= 3.14$, $S = 0.075$, first image at $t\sqrt{g/h} = 0.03$.

In Figs. 4.15b,c,d) massive landslide surface shearing occurred. Slide material was continuously sheared off at the interface between landslide and water resulting in sort of

an inverse sheet flow – the sheared off material remained behind roughly taking over the water velocity whereas the rest of the slide material penetrated farther. The amount of slide granulate sheared off is negligible.

Crack detection filters and interpolation schemes allowed to extract slide and wave profiles digitally from some PIV recordings (Jähne, 1997; Roth et al., 1999). In other cases the task may have to be done visually on the computer. An example without flow separation at $\mathbf{F} = 1.67$ is shown in Fig. 4.16.
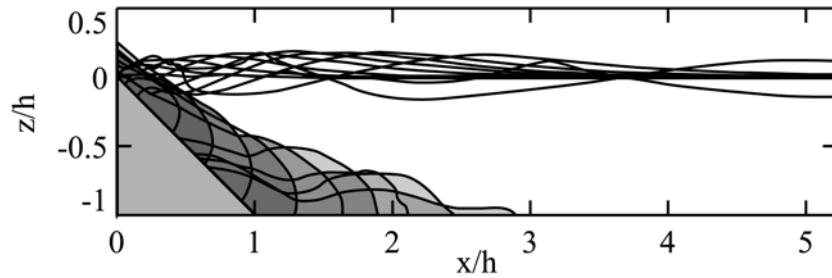
Figure 4.16 **Slide and free surface profiles** during slide penetration into the water body extracted from PIV-recordings at $V = 0.39$, $\mathbf{F} = 1.67$, $S = 0.185$, $h = 0.3\,\text{m}$, first profile at $t\sqrt{g/h} = 0.17$, trailing 6 profiles with a time increment $\Delta t\sqrt{g/h} = 0.38$, 8th profile at $t\sqrt{g/h} = 3.21$ and 9th profile at $t\sqrt{g/h} = 5.87$.

The slide profiles show an increase in slide thickness followed by a decay. The slide thickness reached a maximum after slide deflection on the channel bottom 2.7 times larger than at impact. All slides had a convex front and a concave back. The massive slide deformation is impressive when considering the high internal friction angle of $\phi' = 43°$ and reveals the consequences of the impact.

4.4.2 Slide front penetration

In a first stage the slide motion is considered solely without locking at the wave generation process. Hereby the focus was set on the temporal evolution of slide motion, the slide front displacement and velocity after impact. The PIV-image recordings were analyzed in a Lagrangian manner: extracting time and location of the slide front down the inclined plane and along the channel bottom. The parameter definitions are shown in Fig. 4.17. A special axial coordinate $\underset{\sim}{x}$ was introduced to describe the slide displacement, following the slide path from the stillwater surface initially down the inclined ramp and then along the channel bottom. The subaqueous slide front travel distance $\underset{\sim}{x}_{sf}(t)$ localizes the slide front along the ramp and channel bottom as a function of time after impact. The slide runout distance $\underset{\sim}{x}_{sd}$ measures the total slide travel distance from impact down the ramp and along the channel bottom to the front of the slide deposit. The slide front velocity v_{sf} was computed as the first derivation of the slide travel distance $\underset{\sim}{x}_{sf}(t)$.
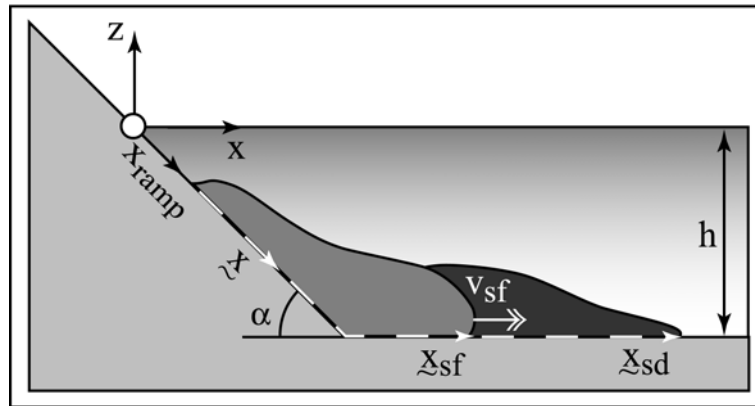
Figure 4.17 **Notation** regarding subaqueous slide penetration and run-out.

The temporal evolutions of the normalized slide front travel distance x_{sf}/h and the normalized slide front velocity $v_{sf}/\sqrt{gh}$ are shown in Figs. 4.18a,b), respectively. The data comprise experiments of all 72 different parameter combinations. In all cases the first part of the motion was measured from digital PIV image recordings. In 49 cases, including all parameter combinations at $h = 0.3\,$m and $h = 0.45\,$m, juxtaposed areas of view were acquired allowing to extract the whole slide front motion from impact to deposit. In 23 cases at $h = 0.675\,$m only the first part of the slide motion roughly from impact to the channel bottom was recorded digitally. In these cases the duration of slide motion t_{sd} and the slide run-out was extracted frame by frame from the additional analog VHS-video recordings. Hence the duration of slide motion t_{sd} from impact to deposit and the slide run-out x_{sd} were measured for all experiments. Both the displacement and slide front velocity curves show a continuous decay from impact to deposit. The slide front displacement curves are much smoother since they were actually measured whereas the slide front velocity curves were computed as first derivation of the displacement curves. Remarkable is the rapid decay of the slide front velocity. The slide front velocity decayed below the shallow water velocity $v_{sf}/\sqrt{gh} \leq 1$ at $t\sqrt{g/h} = 2$ even for extremely high impact velocity experiments at $\mathbf{F} = 4.7$. The duration of the subaqueous slide motion with $\mathbf{F} \geq 1$ was always shorter than the travel time with $\mathbf{F} < 1$. Therefore the total duration of slide motion t_{sd} may not be the key time scaling parameter regarding wave generation and in particular frequency of individual waves.
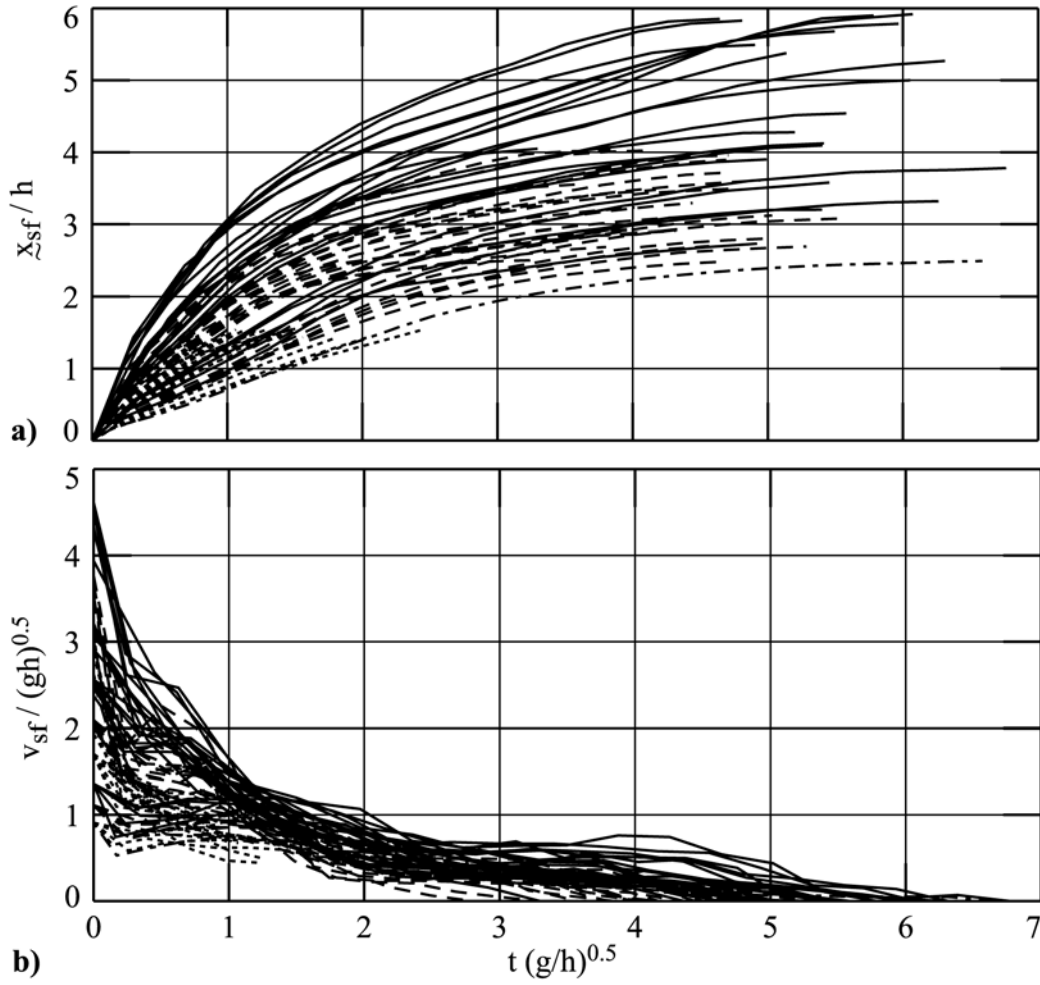
Figure 4.18 **Slide penetration: a) slide front displacement** with (——) $h = 0.3$ m, (— —) $h = 0.45$ m, (· — ·) $h = 0.675$ m, (····) $h = 0.675$ m with slide front not recorded until deposit; **b) slide front velocity** decrease from impact to deposit with symbols as in a).

Rescaling the time after impact by the duration of slide motion t_{sd} and the slide displacement by the slide run-out $\underset{\sim}{x}_{sd}$ allowed to collapse all displacement curves. The rescaled slide front travel distance $\underset{\sim}{x}_{sf}/\underset{\sim}{x}_{sd}$ and the slide front velocity $v_{sf}/v_{sf}(t = 0)$ are shown in Figs. 4.19a,b), respectively. The mostly continuous decay in slide displacement may be approximated with the empirical relationship

$$\frac{\underset{\sim}{x}_{sf}}{\underset{\sim}{x}_{sd}} = \frac{\mathrm{e} - \mathrm{e}^{\left(1 - \frac{t}{t_{sd}}\right)^{7/4}}}{\mathrm{e} - 1}. \tag{4.4}$$

The temporal evolution of the slide front velocity v_{sf} is noisier and somewhat more complicated. The slide and in particular the slide front strongly deformed and loosened up during the gravity driven motion down the inclined ramp after the slide was released from the slide box. At impact on the water surface the slide front was strongly compacted resulting in an additional local decay of the slide front velocity. All slides showed an ini-

tial decay in slide front velocity. Only a few slide fronts of relatively slow slides with $\mathbf{F} < 2$ managed to accelerate again slightly during the subaqueous motion down the inclined ramp. None of the slides significantly exceeded the impact velocity after impact confirming the definition of the slide Froude number with the centroid velocity at impact. Only in experimental studies of submarine slides the slide Froude number was defined with the maximum slide velocity reached during the subaqueous slide motion (Watts, 1997). In this context it is recalled that the slide front velocity does not correspond to the slide centroid velocity. The massive slide deformations shown in Fig. 4.15 resulted in shorter and thicker slides. These deformations require the slide centroid velocity to exceed the slide front velocity. Interestingly the deflection of the slides at the channel bottom did not cause a discontinuity in the evolution of the slide front velocities. The decrease of the slide front velocity may be expressed by the empirical relationship

$$\frac{v_{sf}}{v_{sf}\,(t=0)} \;=\; 1 - \left(\frac{t}{t_{sd}}\right)^{\frac{3}{4}} e^{\left(1 - \frac{t}{t_{sd}}\right)^{7/4}} \tag{4.5}$$

if low velocity slide impacts with minor accelerations after the initial front velocity decay are neglected.
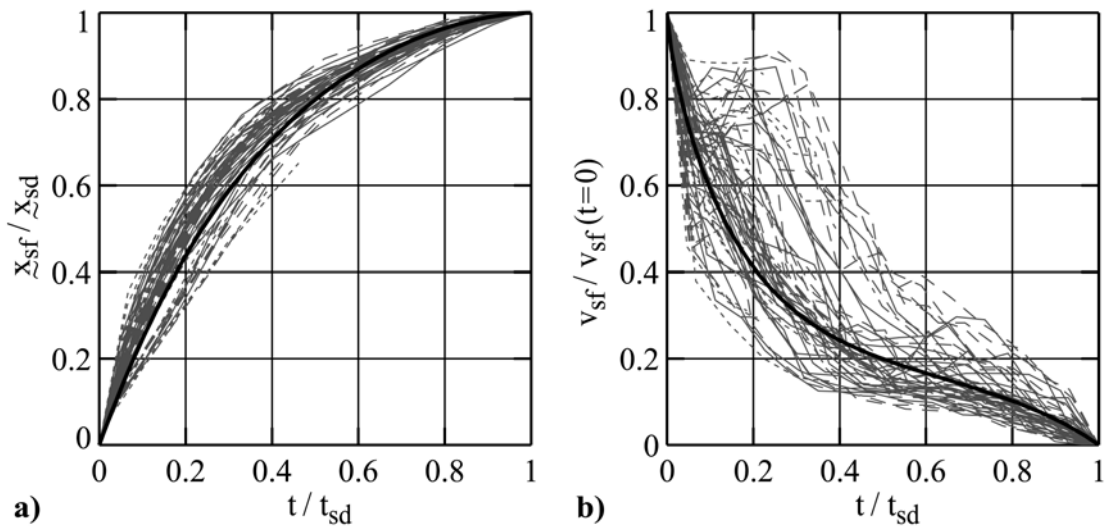
Figure 4.19 **Normalized slide penetration: a) slide front displacement** with (——) Eq. 4.4, runs with (——) $h = 0.3\,\mathrm{m}$, (— —) $h = 0.45\,\mathrm{m}$, (- — -) $h = 0.675\,\mathrm{m}$, (----) $h = 0.675\,\mathrm{m}$ with slide front not recorded until deposit; **b) slide front velocity** decrease from impact to deposit with (——) Eq. 4.5 and symbols as in a).

4.4.3 Slide run-out

In most cases the duration of slide motion t_{sd} from impact to deposit and the slide run-out x_{sd} were measured from the digital PIV-images, whereas in some cases the values had to

be extracted from the additional analog VHS-video recordings. The time of slide impact had to be interpolated manually for the analog recordings. A comparison of several redundant digital and analog recordings revealed no relevant differences regarding the duration of slide motion t_{sd} and the slide run-out $\underset{\sim}{x}_{sd}$. The the slide run-out $\underset{\sim}{x}_{sd}$ versus the duration of slide motion t_{sd} from impact to deposit is shown after normalization with the stillwater depth h in Fig. 4.20a). The normalized duration of slide motion spanned a range $2.8 < t_{sd}\sqrt{g/h} < 6.8$ and the normalized slide run-out $1.8 < \underset{\sim}{x}_{sd}/h < 6$. Only a weak trend towards larger slide run-outs with increasing time of slide motion may be identified visually. An exponential regression yielded an extremely poor correlation coefficient $r^2 = 0.19$. Hence a simple back-calculation of the duration of the slide and water interaction from the landslide run-out length is not possible. This would be of interest regarding pre-historic real events, where often only the landslide run-out length is given by the landslide deposit. Both the landslide run-out length $\underset{\sim}{x}_{sd}$ and the duration of slide motion t_{sd} will be determined later by multiple regressions with the governing dimensionless quantities [para 4.4.4].

The duration of slide motion t_{sd} versus the slide impact duration t_{si} is shown after normalization in Fig. 4.20b). It is recalled that the slide impact duration t_{si} corresponds to the timespan from impact until the back of the slide penetrated below the imaginary water still water surface.
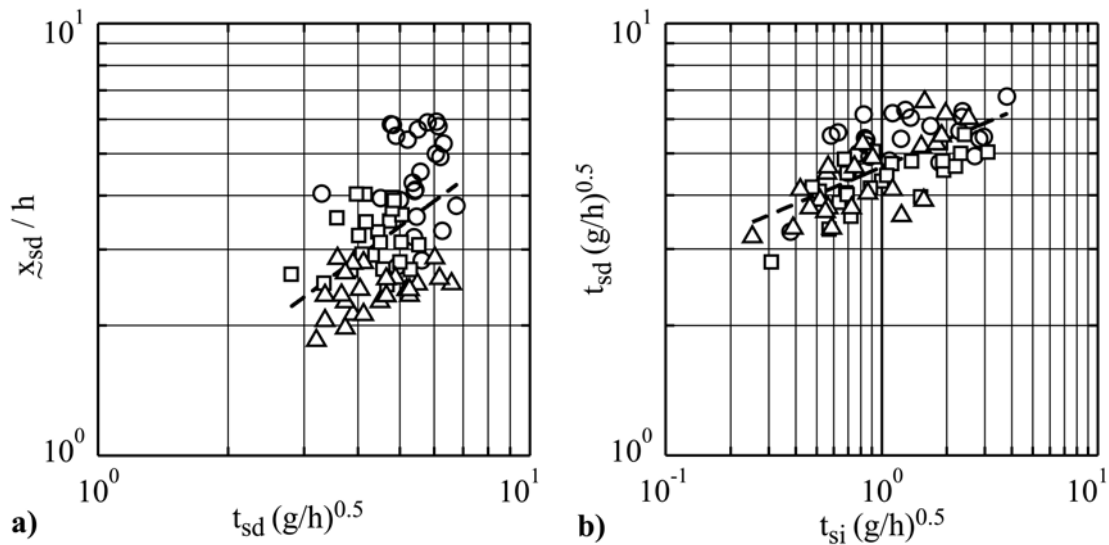
Figure 4.20 **a) Slide run-out** $\underset{\sim}{x}_{sd}/h$ versus duration of subaqueous slide motion $t_{sd}\sqrt{g/h}$ with ($\bigcirc$) $h = 0.3$ m, ($\square$) $h = 0.45$ m, ($\triangle$) $h = 0.675$ m and (– –) regression; **b) duration of slide motion** $t_{sd}\sqrt{g/h}$ versus duration of slide impact $t_{si}\sqrt{g/h}$ with symbols as in a).

All the slide material had always penetrated below the stillwater surface before the slide front settled down. Hence the duration of slide motion t_{sd} was always larger than the slide impact duration t_{si}. There is a slight trend towards a larger duration of slide motion with increasing slide impact duration. An exponential regression yields a poor correlation coefficient $r^2 = 0.43$. The slide impact duration inherently depends on the slide impact veloc-

ity, the slide volume and the slide thickness. Therefore a certain effect of the slide impact duration t_{si} on the duration of slide motion t_{sd} is not surprising. Nevertheless the slide impact duration t_{si} does not replace the slide impact velocity, the slide volume and the slide thickness. Different combinations of the slide impact velocity, the slide volume and the slide thickness may result in the same impact duration t_{si}.

Neither Huber (1980) nor Kamphuis and Bowering (1970) did actually measure the duration of slide motion t_{sd}. In a block slide study conducted by Walder et al. (2002) on landslide generated impulse waves the measured durations of side motion were within $3.4 < t_{sd}\sqrt{g/h} < 11$. Walder tried to compute the duration of slide motion t_{sd} from the slide run-out x_{sd} for Huber's and Kamphuis and Bowering's experiments. The duration of slide motion t_{sd} estimates for Huber's and Kamphuis and Bowering's experiments were in the ranges $3.5 < t_{sd}\sqrt{g/h} < 17$ and $0.9 < t_{sd}\sqrt{g/h} < 3.1$, respectively. However the present study demonstrated that their is no simple function relating the duration of slide motion and the slide run-out. Therefore these computations need to be considered carefully. Nevertheless the present experimental study with a measured duration of slide motion range $2.8 < t_{sd}\sqrt{g/h} < 6.8$ nicely overlaps with these earlier studies.

4.4.4 Prediction of slide run-out

The predictive equations for both the subaqueous slide run-out length x_{sd}/h and the duration of slide motion $t_{sd}/\sqrt{gh}$ were determined by multiple regressions of the measured values. The dimensionless quantities were obtained previously [para 3.2.1]. The slide Froude number $\mathbf{F} = v_s/\sqrt{gh}$, the dimensionless slide volume $V = V_s/(bh^2)$ and the dimensionless slide thickness $S = s/h$ were introduced into the multiple regressions (Ratkowsky, 1990). The multiple regression solves for the unknown coefficients by performing a least squares fit. The multiple regression for the subaqueous slide run-out yields

$$\frac{x_{sd}}{h} = 3.7\left(\frac{v_s}{\sqrt{gh}}\right)^{0.3}\left(\frac{V_s}{bh^2}\right)^{0.3}$$

(4.6)

with a good correlation coefficient $r^2 = 0.84$. The slide Froude number $\mathbf{F} = v_s/\sqrt{gh}$ and the dimensionless slide volume $V = V_s/(bh^2)$ are the dominant parameters. An increase in slide Froude number or slide volume causes a larger subaqueous slide run-out. An increase in slide thickness $S = s/h$ produces a shorter slide run-out but the effect was weak. Hence the influence of the dimensionless slide thickness S was neglected. Slim, fast and large volume slides travel farther than thick, slow and small slides.

The multiple regression for the duration of subaqueous slide motion t_{sd} yielded exponents of 0.3 and –0.3 for the slide volume $V = V_s/(bh^2)$ and the slide thickness $S = s/h$, respectively. Hence the parameters were reduced by introducing a new parameter defined as V/S, which may be interpreted as a dimensionless slide length. The multiple regression with the slide Froude number $\mathbf{F}$ and the combined volume to thickness parameter V/S yields

$$t_{sd}\sqrt{\frac{g}{h}} = 5.2\left(\frac{v_s}{\sqrt{gh}}\right)^{-0.2}\left(\frac{V_s}{bhs}\right)^{0.3} \tag{4.7}$$

with a correlation coefficient $r^2 = 0.55$. An increase in slide volume increases the duration of slide motion, whereas an increase in slide thickness decreases the duration of slide motion. Hence duration of subaqueous slide motion is longer for thin and elongated slides than for short and thick slides. It is not surprising that the multiple regression of the duration of slide motion t_{sd} resulted in a smaller correlation coefficient than the previous regression for the slide run-out $\underset{\sim}{x}_{sd}$. The last part of the slide motion involved primarily local deformation at the slide front, whereas the bulk of the slide mass had already settled. The final settling down of the slide front was a slow process which may have introduced a certain scattering into the duration of the slide motion. Comparisons between the measured values and prediction computed with Eqs. 4.6 and 4.7 are shown in Figs. 4.21a,b), respectively. The largest deviations between the measured and the computed values of both the slide run-out $\underset{\sim}{x}_{sd}$ and duration of subaqueous slide motion t_{sd} are $< 33\%$.
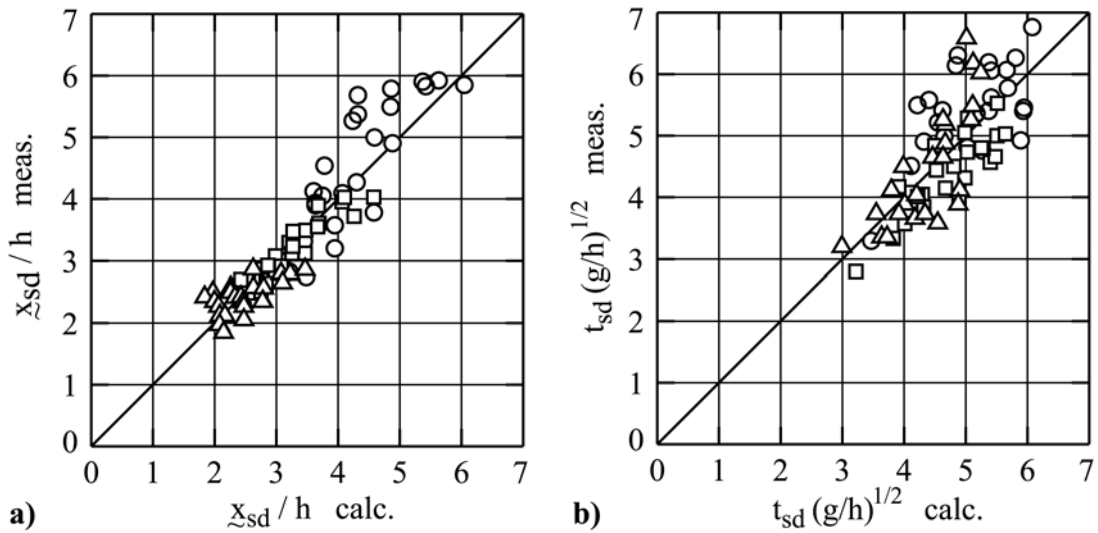
Figure 4.21 **Comparison between measured and computed values: a) slide run-out** $\underset{\sim}{x}_{sd}/h$ measured versus $\underset{\sim}{x}_{sd}/h$ computed with Eq. 4.6 and symbols (○) $h = 0.3$ m, (□) $h = 0.45$ m, (△) $h = 0.675$ m; **b) duration of subaqueous slide motion** $t_{sd}\sqrt{g/h}$ measured versus $t_{sd}\sqrt{g/h}$ computed with Eq. 4.7 and symbols as in a).

4.4.5 Slide deposit

Juxtaposed digital PIV-images recorded at two experiments with the same parameters are available for all experiments at $h = 0.3$ and 0.45 m, whereas at $h = 0.675$ m only one area of view was acquired. The mounted, last PIV-images of each sequence for all experimental parameters at $h = 0.3$ m are shown in Figs. 4.22.
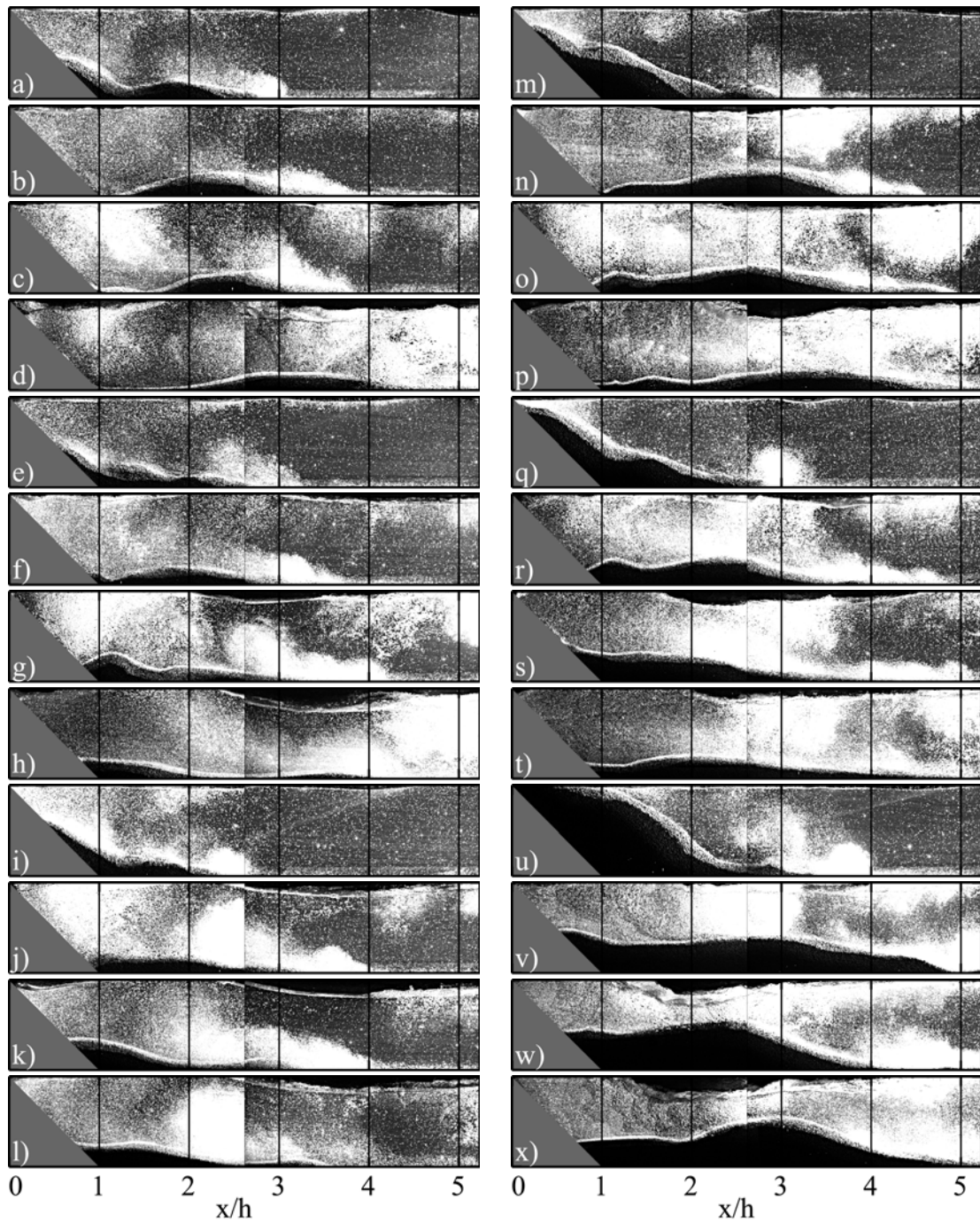
Figure 4.22 **Slide deposits** of a series of experiments at $h = 0.3\,\text{m}$, all images recorded at $t\sqrt{g/h} = 15$, **a)** to **l)** $V = 0.39$, **m)** to **t)** $V = 0.78$, **u)** to **x)** $V = 1.57$: **a)** $F = 1.67$, $S = 0.18$; **b)** $F = 2.73$, $S = 0.17$; **c)** $F = 3.26$, $S = 0.17$; **d)** $F = 4.72$, $S = 0.17$; **e)** $F = 1.61$, $S = 0.25$; **f)** $F = 2.67$, $S = 0.3$; **g)** $F = 3.21$, $S = 0.32$; **h)** $F = 4.58$, $S = 0.29$; **i)** $F = 1.68$, $S = 0.18$; **j)** $F = 2.7$, $S = 0.3$; **k)** $F = 3.28$, $S = 0.4$; **l)** $F = 4.61$, $S = 0.58$; **m)** $F = 1.71$, $S = 0.34$; **n)** $F = 2.75$, $S = 0.34$; **o)** $F = 3.17$, $S = 0.31$; **p)** $F = 4.42$, $S = 0.31$; **q)** $F = 1.71$, $S = 0.34$; **r)** $F = 2.74$, $S = 0.5$; **s)** $F = 3.2$, $S = 0.57$; **t)** $F = 4.45$, $S = 0.54$; **u)** $F = 1.79$, $S = 0.61$; **v)** $F = 2.81$, $S = 0.56$; **w)** $F = 3.13$, $S = 0.53$; **x)** $F = 4.1$, $S = 0.56$; image heights correspond to the stillwater depth h.

At the time of the image recordings the two principal waves had propagated outwards, whereas the reflections from the channel head wall had not arrived yet. This is of importance because back and forth travelling waves induced some sediment transport on the slide surface after the actual experiment. The PIV-images give a good impression of the slide deposits. The deposits were always symmetric about the channel axis but with some three dimensional structure on the surface of the deposits. The apparent slide volume and centroid position extractable from the PIV-images may therefore be somewhat biased. All slide deposits were fully submerged. The largest slide at the lowest water depth with the slowest impact velocity shown in Fig. 4.22u) is at the transition to partial submergence. A further reduction of the water depth would lead to partial submergence of the slide deposits as shown by Huber (1980). The slide deposits of the present study visually correspond to Huber's slide deposits regarding the slide run-out and the shape of the deposit. The deposits confirmed that larger and faster slides travel farther. Further thin slides reached farther than thick slides at the same impact velocity and with the same slide volume. For example the slides shown in Figs. 4.22d,l) primarily differed in the slide thickness $S = s/h$. The slide for $S = 0.17$ travelled well beyond the transition from the slide ramp to channel bottom, whereas the deposit centroid of the slide at $S = 0.58$ remained close to the foot of the incline. The effect of the slide thickness is significantly weaker when only the slide run-out is considered, which is determined by the front of the slide deposit.

4.4.6 Equivalent coefficient of friction

The ratio of the drop height of the highest point on the breakaway rim and the horizontal projection of the distance from this point to the tip of the landslide deposit was called "Fahrböschung" by Heim (1932). This ratio was considered an equivalent coefficient of friction by Shreve (1968). The definition of the equivalent coefficient of friction $f = \Delta x / \Delta z$ is shown in Fig. 4.23. The concept of the equivalent coefficient of friction was previously only applied to either subaerial or subaqueous landslides and not to landslide impacts into water bodies.
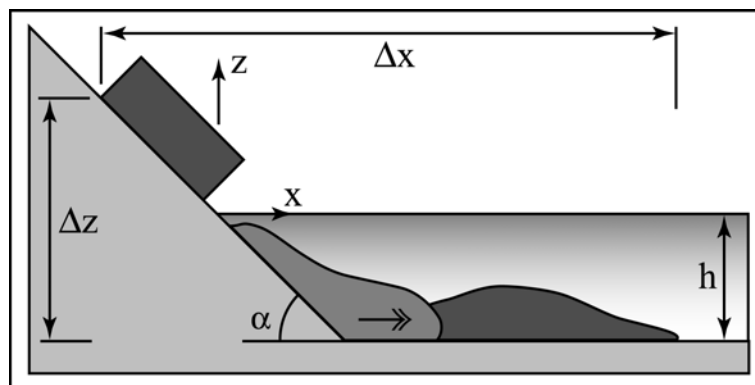
Figure 4.23 Definition of the equivalent coefficient of friction $f = \Delta x / \Delta z$.

From a physical point of view it would be more appropriate to measure the ratio of the drop height to the horizontal projection of travel distance for the slide centroid before and after the movement, but this is often difficult to determine for observations of real events. Therefore most authors determined the equivalent coefficient of friction $f = \Delta x / \Delta z$ as shown in Fig. 4.23 from the top of the landslide scarp to the margin of the landslide deposit.

The equivalent coefficient of friction was determined for all slides of the present physical model study in order to set the stage for a comparison between the observations and the experimental model results. The issue was complicated by the fact that the sub-aerial slide motion was cut short by the pneumatic landslide generator in the physical model [para 3.3.3]. The part of the drop height Δz_{0B} which was cut short by the pneumatic landslide generator was computed by

$$\Delta z_{0B} = \frac{v_B}{2g(1 - \tan\delta \cot\alpha)} \tag{4.8}$$

with the slide box velocity v_B, the gravity g, the bed friction angle $\delta = 24°$ and the slope angle $\alpha = 45°$. An analogue relationship allowed to determine the part of the horizontal travel distance Δx_{0B} which was cut short by the pneumatic landslide generator. Hereby any deformation of the slide mass to the point of slide release from the slide box was neglected. The remaining parts of the drop height and the horizontal travel distance were determined by the point of slide release from the slide box and the slide deposit on the channel bottom. The total drop height divided by the total horizontal travel distance resulted in an equivalent coefficient for each experiment.

The multiple regression for the equivalent coefficient of friction f yields

$$f = 0.54\left(\frac{v_s}{\sqrt{gh}}\right)^{1/4}\left(\frac{V_s}{bh^2}\right)^{-0.1} \tag{4.9}$$

with a correlation coefficient $r^2 = 0.88$. The dominant parameters were the slide Froude number $\mathbf{F} = v_s/\sqrt{gh}$ and the dimensionless slide volume $V = V_s/(bh^2)$. The dimensionless slide thickness $S = s/h$ had almost no effect on the correlation. The comparison between the measured values and predictions computed with Eq. 4.9 is shown in Fig. 4.24a). The largest deviations between the measured and the computed values of f are within $\pm 10\,\%$. The dominant influence of the slide Froude number $\mathbf{F} = v_s/\sqrt{gh}$ on the equivalent coefficient of friction f is shown in Fig. 4.24b).

Unlike the coefficient of friction, which is a material constant and whose value is independent of the size of a sliding block, the value of the equivalent coefficient of friction is a function of the total landslide volume. This fundamental observation from the analysis of real events is confirmed at laboratory scale. An increase in slide volume leads to a reduction in the effective coefficient of friction f. An augmentation of the slide impact velocity caused an increase in the equivalent coefficient of friction f. This may be related primarily to an over proportional effect of the water on the landslide motion at high impact

velocities, whereas the bed friction angle was independent of any shear rates. The slide is affected by both the form or pressure drag and the skin friction drag after impact.
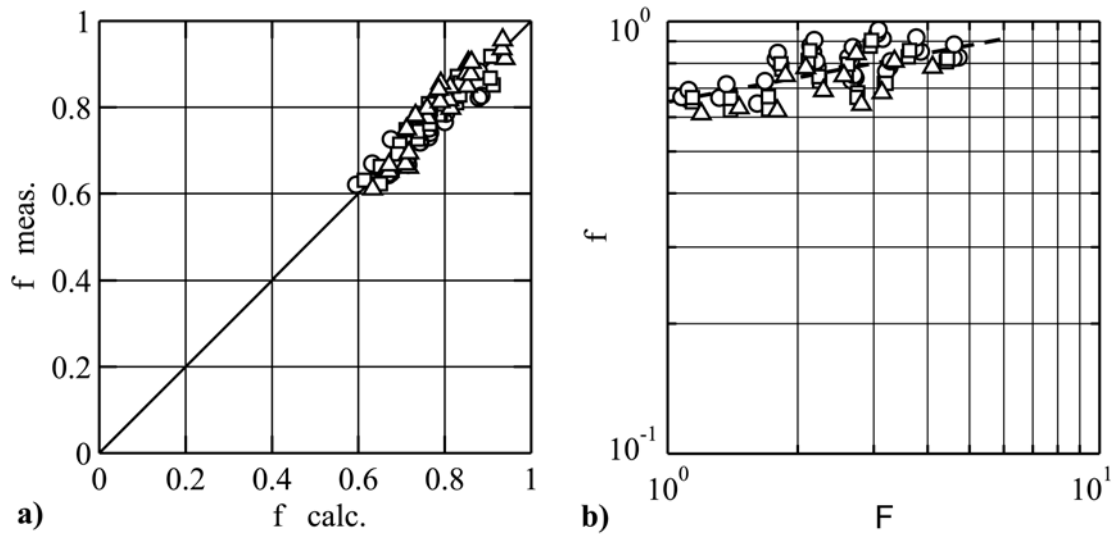
Figure 4.24 **Equivalent coefficient of friction: a)** f measured versus f computed with Eq. 4.9 and ($\bigcirc$) $h = 0.3\,\mathrm{m}$, ($\square$) $h = 0.45\,\mathrm{m}$, ($\triangle$) $h = 0.675\,\mathrm{m}$; **b)** f versus $\mathbf{F} = v_s / \sqrt{gh}$ with ($\mathbf{-\ -}$) regression ($r^2 = 0.39$) and symbols as in a).

4.5 Wave generation

4.5.1 Wave generator

Impulse waves are formed by a rapid or impulsive transfer of momentum from a mass flow to a water body. The wave generator is the landslide. The landslide may be considered as a moving object causing a disturbance of the water body. The duration and the extent of the disturbance are described in the previous chapter on the subaqueous landslide motion. The driving force of the landslide is simply gravity. The force exerted by the landslide on the water may consist of three components, one due to the displacement of the water, the pressure drag and the viscous drag. Not all of the landslide energy is transferred onto the water body. Frictional losses are due to the bed friction between the landslide and the bedrock corresponding to the inclined ramp and the channel bottom in the experiments. Further the landslide impacts on the channel bottom at the inclination change. Therefore part of the landslide energy is taken out of the system or lost in internal deformation of the slide. The water displacement resulting in an uplift or hump at the free surface forms the potential energy, whereas the velocity distribution in the water body determines the kinetic energy passed onto the water body by the landslide.

A direct measurement of the individual landslide forces acting on the water body is difficult even with the advanced PIV data available. The pressure distribution on the land-

slide surface would be of interest to numerical modelers (pers. com.: Dr. Charles L. Mader, LANL). If the flow field under investigation were nearly two dimensional, steady as well as incompressible the pressure field could be estimated through the numerical integration of the steady Navier-Stokes equations in two-dimensional form (Imaichi and Ohmi, 1983; Hudson et al., 1995). The task may be difficult in the present unsteady flow and the necessary gradients of the particle velocity v_p were affected by the spatial windowing resolution. Further the temporal evolution of both the potential and kinetic energy of the flow field in the wave generation area would be of interest to numerical modelers (pers. com.: Dr. Steven Ward, UCSC). Basically, PIV could provide all the necessary data with the water and slide surfaces as well as the velocity vector fields, but the task would require extremely large measurement areas. Even two adjacent areas of view mounted together were not sufficient in most cases, although covering an instantaneous measurement area of roughly $0.8 \times 1.6\,\mathrm{m}$.

Since a direct measurement of the individual forces exerted by the landslide onto the water body was not possible, the focus was set on their effects. The water displacement and the displacement rate may be extracted from the PIV recordings. A total of 49 sets of PIV recordings consisting of two juxtaposed areas of view were analyzed in this regard. The area of view covered in a single recording was not sufficient in most cases. The coupling between the mass flow and the water displacement is of crucial importance to numerical modelers (Heinrich, 1992; Jiang and LeBlond, 1992 and 1993; Rzadkiewicz et al., 1996; Mader, 1999; Ward, 2001).

4.5.2 Flow separation

A relative motion between an object and a fluid is a common occurrence. In the flow under investigation the landslide obviously was the moving object and the water the surrounding fluid. The broad literature on flow separation generally assumes all the boundaries of the fluid so far away that they do not have any effect (Simpson, 1989). The present situation is complicated by the interference of the ambient air as third phase. Several definitions and criteria for flow separation were introduced. Flow separation occurs if firstly the flow develops a region of adverse pressure gradients and secondly this is large enough. The pressure differences are proportional to the square of the impact velocity in analogy to the drag exerted on the landslide. Separation necessarily involves the existence of a region in which the vorticity has an opposite sign from that associated with the flow as a whole. The key to understanding when separation may occur is to understand how this reversed vorticity is introduced into the flow (Tritton, 1988).

In the present unsteady flow pressure differences could not be extract from the velocity vector fields. Further the reversed vorticity approach was not applicable, because the flow fields within the slide granulate and the air were not acquired. Therefore the flow separation was defined by the occurrence of a water body detachment on the back of the slide. This definition allowed to classify all experiments conducted into separated and

unseparated flows. Characteristic examples of an unseparated and a separated flow around penetrating landslides are shown in Figs. 4.25a) and b), respectively. The separation point accompanied by a detachment of the water body was typically located on the slide shoulder as shown in Fig. 4.25b).
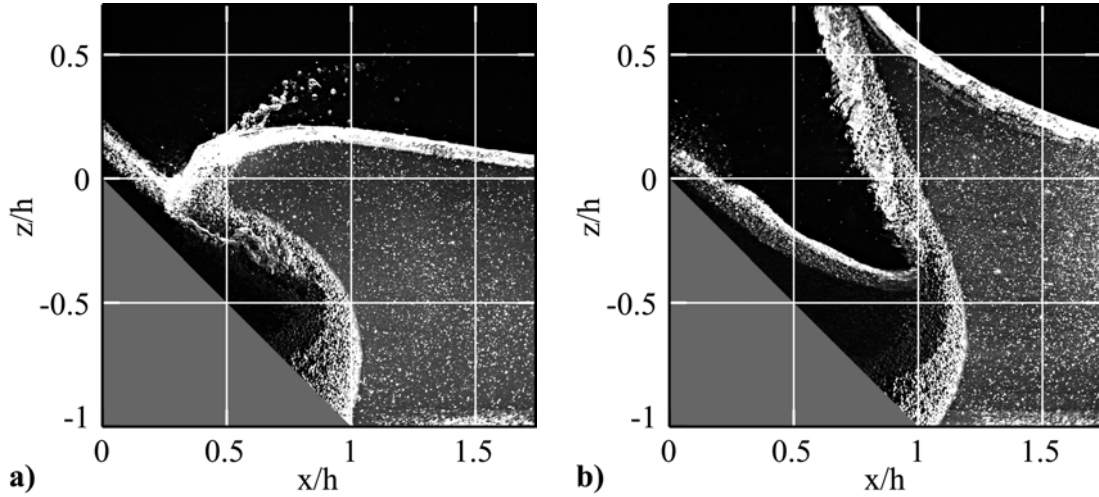
Figure 4.25 **Flow separation** on the slide shoulder at $h = 0.45$ m: **a) unseparated flow** at $\mathbf{F} = 1.4$, $V = 0.35$, $S = 0.23$ and $t\sqrt{g/h} = 1.13$; **b) separated flow** at $\mathbf{F} = 2.6$, $V = 0.35$, $S = 0.21$ and $t\sqrt{g/h} = 0.79$.

The examples shown in Figs. 4.25 demonstrate a strong influence of the flow separation on the displaced water volume. The only significant difference between the two experiments was the impact Froude number. The water displacement at very low slide impact velocities $\mathbf{F} \ll 1$ may approach the asymptotic water displacement volume given by the slide volume added to the water body. The water displacement was similar to the landslide volume at $\mathbf{F} = 1.4$ shown in Fig. 4.25a). Only a minor addition was due to the trough formed on the back and in the wake of the slide. Interestingly no flow separation occurred at $\mathbf{F} = 1.4$, which corresponds to $\mathbf{F} \sin \alpha = v_s \sin \alpha / \sqrt{gh} = 1$. The detachment of the water body on the slide shoulder at $\mathbf{F} = 2.6$ shown in Fig. 4.25b) caused a hydrodynamic impact crater. The displaced water volume obviously exceeded the landslide volume significantly.

The flow separation always initiated on the inclined ramp with locally reduced water depths and accordingly lower shallow water wave propagation velocities. Nevertheless the slide Froude number lent itself as primary classification parameter, which was defined using the stillwater depth of the wave tank. Flow separation was always observed if the slide Froude number $\mathbf{F} = v_s / \sqrt{gh}$ fulfilled the empirical relationship given by

$$\mathbf{F} > \left(\frac{5}{3} + \frac{1}{2}S \right) \tag{4.10}$$

with the relative slide thickness $S = s/h$. The water depth at the actual point of separation on the ramp was smaller and therefore also the water displacement under the wave crest would be reduced. Noteworthy is the analogy of the first term in the separation criterion

given by Eq. 4.10 to the formation of roll waves determined by the Vedernikov number (Liggett, 1994). The graphical representation of Eq. 4.10 is shown in Fig. 4.26.
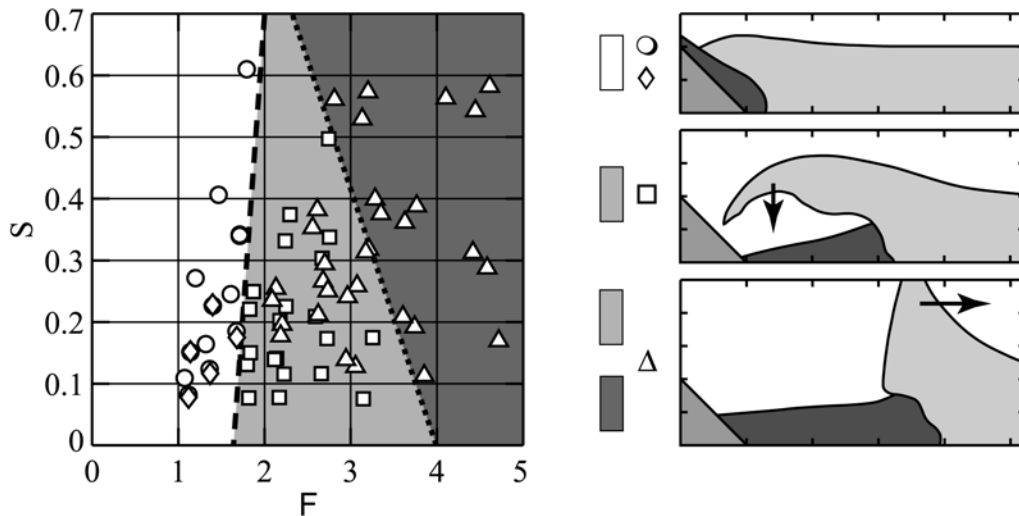
Figure 4.26 **Flow separation and crater type formation:** slide thickness $S = s/h$ versus slide Froude number $\mathbf{F} = v_s/\sqrt{gh}$ with ($\bigcirc$) no flow separation, ($\diamondsuit$) local flow separation, ($\square$) backward collapsing impact craters, ($\triangle$) outward collapsing impact craters, (— —) Eq. 4.10, (••••) Eq. 4.12, (▨) complex transition region with backward and outward collapsing craters, (▨) only outward collapsing craters.

The separation criterion defined in Eq. 4.10 indicates a slight increase in the Froude number at which separation occurred with the relative slide thickness $S = s/h$. A thick slide continuously built up its thickness from the front to the maximum slide thickness, whereas thin slides quickly reached a plateau in slide thickness. Hence the inflow of slide material continuously increased in the case of a thick slide until the maximum thickness was reached. Thick slides therefore may have deformed into or filled a possible small separation area with a small impact crater. Local flow separations at impact with immediate reattachment of the flow on the back of the slide occurred in some cases below the limit defined in Eq. 4.10. Local flow separations neither resulted in a significant impact crater nor did the overall water displacement volume exceed the landslide volume during the separation. Hence their effect on the wave generation process is secondary. The landslide may be considered as a moving wall if the slide thickness significantly exceeds the water depth. No flow over the back of the landslide and therefore no flow separation would occur if $S \gg 1$. The maximum dimensionless discharge per unit width equals $\mathbf{F} \cdot S$, but did not result in an improved classification.

4.5.3 Hydrodynamic impact crater types

Localized impulsive disturbances of the free surface of a liquid is a phenomenon which is encountered in a multiplicity of physical and man-made or natural phenomena. In general

the fall of objects, from small droplets to large hypothetical meteorites in the ocean, or man-made underwater explosions are phenomena causing impact craters or cavities which ultimately collapse and form a rebound as a vertical spike or dome reaching considerable height above the still water surface (Holst, 1977). A hydrodynamic impact crater may only form if flow separation on the slide shoulder occurs. Hence hydrodynamic impact cratering is of importance if the slide Froude number is within the separated flow region defined by Eq. 4.10. The dominant mechanism governing the formation of the hydrodynamic impact crater is the transfer of the kinetic energy from the mass flow to the fluid. This energy transfer is driven by the dissipative processes associated with drag on the landslide. An analytical model specified the energy transfer for cavity production as equivalent to the energy dissipated by velocity-dependent drag on the water entering object (Lee et al., 1997). The impact velocity and the shape of the landslide are critical parameters. As a landslide penetrates the free surface, the impact crater expands until the difference between the pressure in the surrounding fluid and that in the crater balances the induced inertial effects and drives the fluid back towards its undisturbed state. The ensuing crater collapse can lead to a closure resulting in the formation of an instantaneous cavity. In the literature it is generally distinguished between a surface and a deep closure (Birkhoff and Zarantonello, 1957).

In the present study on landslide generated impulse the distinction between a deep and a surface closure was not considered. The occurrence of a closure allowed to distinguish between a backward and an outward collapse of the water craters shown in Figs. 4.27a) and b), respectively. In both cases the water was initially expelled upwards and outward by the entry of the landslide forming a water crater. The uplift later evolved into a leading wave. The water crater exposed the soil and the back of the landslide to the atmosphere. As the process of crater growth has terminated outward bulk motion of water was still present as a residuum. Although impact cratering is a dynamic event of great complexity, the experiments showed that the collapse proceeded in an orderly fashion and the crater wall mediated the outward flow field. The backward collapsing impact crater at $\mathbf{F} = 2.75$ shown in Fig. 4.27a) was governed by a surface closure resulting in the inclusion of air pockets in the form of a cavity.

The outward collapsing impact crater formed by a high speed landslide impact at $\mathbf{F} = 4.1$ is shown in Fig. 4.27b). In contrast to the backward collapse no closure occurred in this case. The collapse occurred after the water crater reached its maximum size and the water rushed inwardly on the back of the slide under the influence of gravity. The outward collapsing cavity resulted in a main positive leading wave and negative base surge. The inrush of water tending to fill the crater from downstream can qualitatively be viewed as an example of the classical dam break problem (Stoker, 1957; Lauber, 1997). The backward motion was initiated at the bottom of the crater wall were the hydrostatic pressure was the largest. Nevertheless the outward collapse of a hydrodynamic impact crater is far more complicated than a dam-break initiated from rest. Contrary, the water displaced by the landslide at no instant reached a state anywhere near a static uplift. The kinetic energy of the landslide imparted on the water body was only partially converted into the potential

energy of the uplift, whereas a significant part prevailed as kinetic energy in the form of the velocity field imposed onto the water body. The initial wave system was related to the upraised hump of the crater. The hump in the free surface quickly becomes detached from the transient impact crater and propagated away from the impact zone as the crater collapsed. The run-up of the base surge on the inclined ramp and the subsequent run-down formed the secondary wave system. The detailed flow fields in the wave generation area will be addressed in [para 4.6].
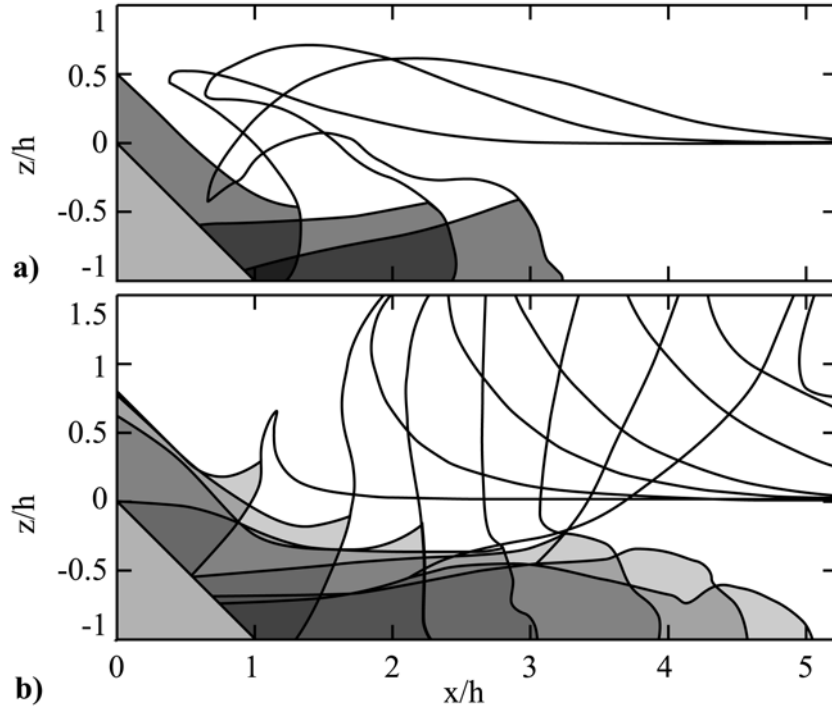
Figure 4.27 **Hydrodynamic impact crater types: a) backward collapsing crater** at $V = 0.79$, **F** $= 2.75$, $S = 0.34$, $h = 0.3\,\mathrm{m}$, first profile at $t\sqrt{g/h} = 0.72$ and time increment $\Delta t\sqrt{g/h} = 0.76$; **a) outward collapsing crater** at $V = 1.57$, **F** $= 4.1$, $S = 0.56$, $h = 0.3\,\mathrm{m}$, first profile at $t\sqrt{g/h} = 0.18$, first 3 trailing profiles with a time increment $\Delta t\sqrt{g/h} = 0.38$ and last 3 profiles with a time increment $\Delta t\sqrt{g/h} = 0.76$.

A sharp criterion to distinguish between the backward and the outward collapsing impact crater could not be found. The impact velocity and the shape of the landslide are critical parameters. Hence the ranges of occurrence of the different crater types were defined in analogy to the flow separation criterion. An outward collapsing water crater was always observed if the slide Froude number **F** $= v_s/\sqrt{gh}$ fulfilled the empirical relationship given by

$$\mathbf{F} > \left(4 - \frac{5}{2}S\right) \tag{4.11}$$

with the relative slide thickness $S = s/h$. The complex transition region in which both collapse types were observed may be determined by

$$\left(\frac{5}{3} + \frac{1}{2}S\right) \leq \mathbf{F} \leq \left(4 - \frac{5}{2}S\right) \tag{4.12}$$

with the occurrence of flow separation given by Eq. 4.10 at the lower end and the range of outward collapsing impact craters given by Eq. 4.11 at the upper end. The observed water crater collapse types and the empirical boundaries given above are shown in Fig. 4.26 together with the criterion for flow separation. The transition from backward to outward collapsing impact craters is highly complex. A deep closure was often observed at the transition resulting in a partial reattachment of the crater boundary on the back of the slide. A deep closure did not cause a significant inclusion of air pockets. The whole upper cavity wall collapsed outward. Therefore cases with a deep closure were also classified as outward collapsing impact craters. Most relevant events of landslide generated impulse waves were observed within the Froude number range $0.5 < \mathbf{F} < 4$. Hence unseparated and separated flows as well as backward and outward collapsing impact craters are expected to occur in real events.

4.5.4 Water displacement

The motion of the water outside the impact crater did not depend on the details of the interior crater motion and may be influenced only by the motion of the crater boundary. The kinetic energy of the mass flow imparted to the fluid was transformed into potential and kinetic energy of the water body. A simple conversion into potential energy represented by a static departure from the stillwater surface was not observed at any instant in time. Therefore a static impact crater with a lip may not be used as initial condition for numerical simulations. A velocity field needs to be superimposed on an initial free surface disturbance (Mader, 2001). The volume and rate of the water displacement determined herein may allow a coupling of the physical model results with numerical models close to the source resulting in hybrid models. Further the water displacement curves may lead to a substitution of the highly complex coupling between the mass flow and the water body by a simplified numerical model.

The water displacement and the displacement rate may be extracted from the PIV recordings. A total of 49 sets of PIV recordings consisting of two juxtaposed areas of view were acquired. The area of view covered in a single recording was not sufficient in most cases. At the largest water depth $h = 0.675\,\text{m}$ investigated the task would require simultaneous recordings of several square meters along the channel, which may be difficult even in the future. The area of the hump in the free surface could not be determined directly because the recordings did not reach far enough downstream in most cases. The water displacement volume V_d as a function of time was extracted from the PIV-recordings specifying that the hump in the free surface has a volume about equal to the volume displaced by the landslide. The total crater volume corresponds to the combined slide and air volume below the stillwater surface. The definition of the water displacement volume V_d is shown in Fig. 4.28. This approach worked well for all cases in the separated flow

regime. In the cases of unseparated flow at low slide impact velocities the task was difficult due to the flow through the granular medium as well as the air detrainment on the back of the slide resulting in a massive phase mixing in the wake of the landslide.
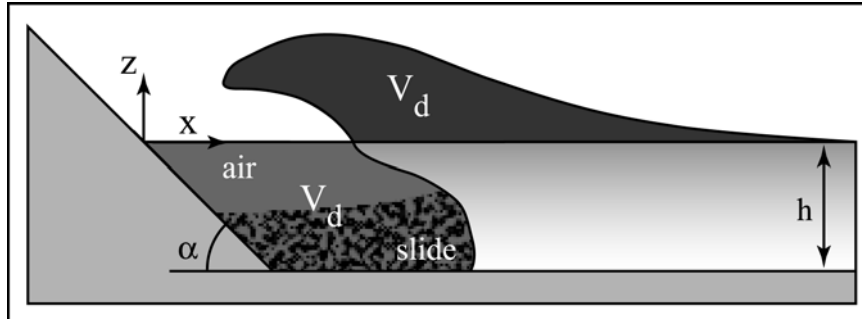
Figure 4.28   **Water displacement volume** V_d corresponding to both the impact crater volume and the water volume under the hump above the stillwater level.

The temporal evolution the water displacement volume V_d was extracted from the PIV recordings of 34 mounted sets with different experimental parameters acquired at $h = 0.30$ and $0.45\,\text{m}$. Only separated flows were considered. In unseparated flows the water displacement volume can also exceed the landslide volume due to the formation of a wave trough in the back of the slide. The water displacement volume in unseparated flows never exceeded the landslide volume by more than a factor of two. In these cases significant errors due to the slide detrainment and the flow through the granulate would lead to spurious results. Hence unseparated flows were not analyzed in this regard. Both backward and outward collapsing impact craters were considered together without the need for distinguishing between them. The temporal evolutions of the normalized water displacement volumes V_d/V_D are shown in Fig. 4.29a). Scaling the time after impact t with the time of the maximum displacement volume t_D and the water displacement volume V_d by the maximum water displacement volume V_D allowed to collapse all displacement volume curves. All curves exhibited a continuos increase of the water displacement volume V_d from the slide impact to the maximum displacement volume V_D. The decay after the maximum was relatively slow at the beginning due to the fact that the landslides penetrated further into the water body as the impact craters were already collapsing. The water displacement estimates became noisier and finally broke down during the collapse of the impact craters because of the massive phase mixing caused either by the surface closure or the inward base surge. The accuracy in the determination of the water displacement volume V_d improved with increasing crater volume. The water displacement volumes were determined to $\pm 5\,\%$.

The water displacement volume as a function of time may be approximated by the empirical relationship

$$\frac{V_d}{V_D} \;=\; \sin\!\left(\frac{\pi}{2}\frac{t}{t_D}\right) \qquad\qquad \textbf{(4.13)}$$

- 90 -

presented by Le Méhauté and Wang (1995) for water waves generated by underwater explosions. Underwater explosions and in particular nuclear blasts always exhibited the largest water displacement rate at $t/t_D = 0$. The water displacement rate caused by a landslide reached the maximum roughly at $t/t_D = 0.3$. The retarding effect may be explained by the strong compaction and deformation of the slide front on impact. Further the landslides did not reach their maximum thickness at the front. Therefore the cross-section in contact with the water increased shortly after the impact. A slight modification of Eq. 4.13 yields

$$\frac{V_d}{V_D} = \sin\left(\frac{\pi}{2}\left(\frac{t}{t_D}\right)^{\frac{3\pi}{8}}\right) \tag{4.14}$$

allowing to account for the initial retarding effect. The impact crater volume expansion was described appropriately by Eq. 4.14, whereas the collapse remained uncertain. The water displacement volume could not be determined during the whole crater collapse. The landslide penetrated further into the water body increasing the water displacement locally at the beginning of the crater collapse. This suggests a slower decay in the water displacement volume than in craters produced by underwater explosions.

The temporal evolution of the water displacement rate was computed by differentiation of the water displacement curve. The temporal evolutions of the normalized water displacement rates Q_d/Q_D are shown in Fig. 4.29b). Scaling the time after impact with the time of the maximum displacement volume t_D and the water displacement rate Q_d by the maximum water displacement rate Q_D allowed to collapse all displacement rate curves. The water displacement rate curves increased to the maximum rapidly and then decayed slower resulting in skewed curves. The uncertainties in the water displacement curves were enhanced by the differentiation. Hence the curves of the water displacement rates were significantly noisier. The accuracy of the water displacement rate estimates may be given to $\pm 20\,\%$.

Differentiation of Eq. 4.13 and rescaling by the maximum displacement rate yields

$$\frac{Q_d}{Q_D} = \cos\left(\frac{\pi}{2}\frac{t}{t_D}\right) \tag{4.15}$$

with the normalized displacement rate Q_d/Q_D and the normalized time after impact t/t_D. Analogously differentiation of Eq. 4.14 and simplification yields

$$\frac{Q_d}{Q_D} = \frac{9}{4\pi}\cos\left(\frac{\pi}{2}\left(\frac{t}{t_D}\right)^{\frac{3\pi}{8}}\right)\frac{3\pi^2}{16}\left(\frac{t}{t_D}\right)^{\frac{3\pi}{8}-1} \tag{4.16}$$

where the first factor on the right side rescales to the maximum displacement rate. The measured water displacement rate curves scattered stronger as compared to those generated by underwater explosions conducted by Le Méhauté and Khangoankar (1992). The curves below Eq. 4.15 in Fig. 4.29b) corresponded to high velocity impacts of thick and

short slides, whereas the curves above Eq. 4.16 represented slow and thin slides. The maximum water displacement rates of underwater explosions at the beginning of the detonation at $t/t_D = 0$ is perfectly represented by Eq. 4.15. The maximum of Eq. 4.16 is located at $t/t_D = 0.3$ matching the averaged time of the peak in the herein measured sets.
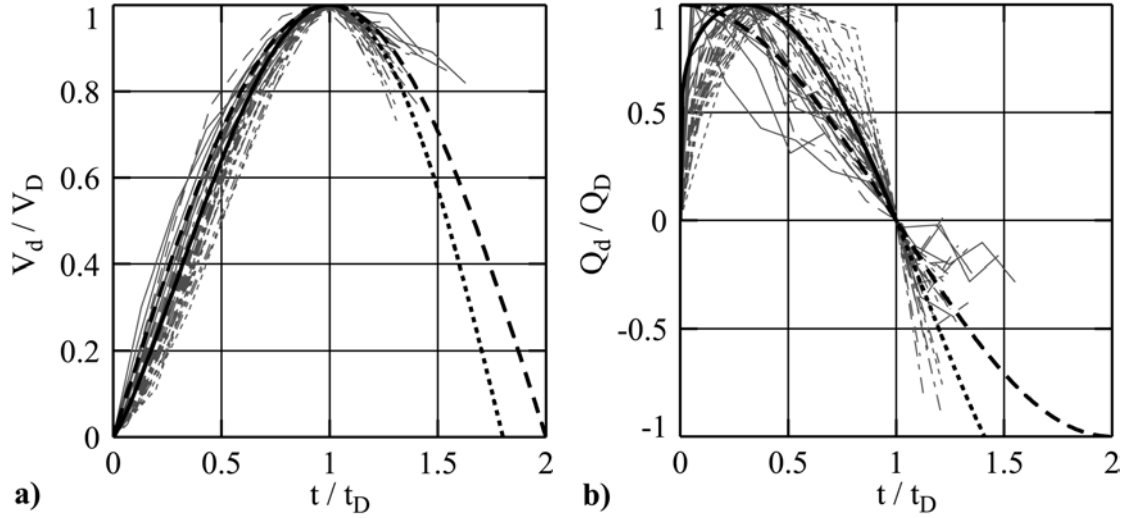
Figure 4.29 **Normalized impact crater formation: a) water displacement** V_d/V_D at (——) $4 < F < 5$, (— —) $3 < F \le 4$, (· — ·) $2.5 < F \le 3$, (----) $2 < F \le 2.5$ with (▬ ▬) Eq. 4.13; (——) Eq. 4.14 at $t/t_D \le 1$, (····) Eq. 4.14 at $t/t_D > 1$; **b) water displacement rate** Q_d/Q_D with (▬ ▬) Eq. 4.15; (——) Eq. 4.16 at $t/t_D \le 1$, (····) Eq. 4.16 at $t/t_D > 1$, symbols as in a).

The empirical relationships Eqs. 4.14 and 4.16 representing the temporal evolutions of the water displacement volume V_d/V_D and the water displacement rates Q_d/Q_D, respectively, require only the determination of the maximum water displacement volume V_D, the maximum water displacement rate Q_D and the time after impact of the maximum displacement volume t_D. These quantities are discussed in the following paragraphs. The water displacement curves may be well suited as input curves for simplified numerical models. The water displacement curves are at the source, whereas the wave profiles are several water depths away from the source and therefore restricted by the two-dimensional model assumption. The water displacement curves may allow to define a source in numerical models without having to cope with the complexity of the subaqueous landslide motion, the flow separation and the impact crater formation.

4.5.5 Maximum water displacement volume

The maximum water displacement volume V_D and the superimposed velocity field are of key importance regarding the whole wave generation process. The maximum water displacement volume was extracted from the water displacement curves shown in Fig. 4.29a). The measured maximum water displacement volumes V_D/V_s and $V_D/(bh^2)$ are shown in Fig. 4.30a). The normalized maximum water displacement volumes were

within $1.8 \leq V_D / V_s \leq 8.1$. Hence the dynamic water displacement volume always significantly exceeded the landslide volume V_s. The largest measured maximum water displacement per unit width was 8.1 times larger than the hydrostatic water displacement due to the added slide mass. The simple hydrostatic water displacement is not of relevance regarding landslide impacts at $\mathsf{F} \geq 1$. Therefore the maximum water displacement volume V_D and not the slide volume V_s needs to be considered as relevant input quantity for initial conditions or uplifts in numerical models. In the presented analysis only cases with flow separation were considered. The maximum water displacement volume of impacts without flow separation is expected within $1 \leq V_D / V_s < 2$. The asymptotic value $V_D / V_s = 1$ may only be obtained by extremely slow landslide impacts at $\mathsf{F} \ll 1$.
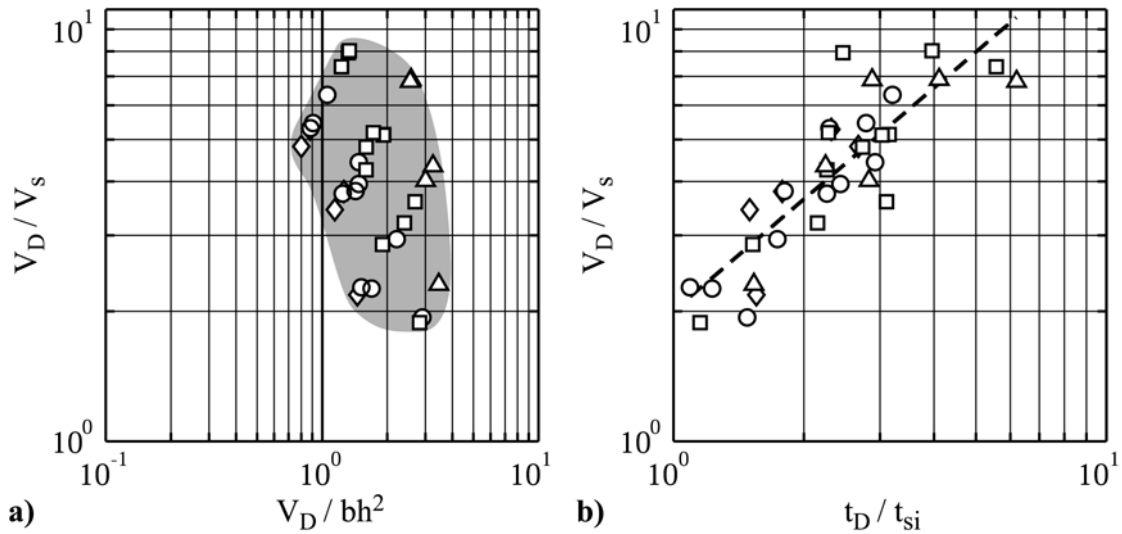
Figure 4.30 **Water displacement volume: a)** V_D / V_s versus $V_D / (bh^2)$ with (▨) range of experiments with flow separation at (◇) $2 < \mathsf{F} \leq 2.5$, (○) $2.5 < \mathsf{F} \leq 3$, (□) $3 < \mathsf{F} \leq 4$, (△) $4 < \mathsf{F} < 5$; **b)** V_D / V_s versus t_D / t_{si} with (– –) Eq. 4.17 and symbols as in a).

The maximum water displacement volume V_D normalized by the landslide volume may be related to the normalized time after impact t_D of the maximum water displacement volume by

$$\frac{V_D}{V_s} = 2 \left(\frac{t_D}{t_{si}} \right)^{0.86} \tag{4.17}$$

with a correlation coefficient $r^2 = 0.59$ and the slide impact duration t_{si}. It is recalled that the slide impact duration t_{si} corresponds to the duration from the slide impact until the rear end of the slide has passed the imaginary still water surface. The normalized maximum water displacement volume V_D / V_s increased with the normalized duration from impact to the maximum displacement volume t_D / t_{si}. Large impact velocities lead to small impact durations t_{si} relative to the time of the maximum water displacement volume t_D. On the other hand small impact velocities resulted in t_D values only slightly larger than

the duration of the slide impact t_{si}. Re-normalizing of Eq. 4.17 with wave related quantities in the denominators yields

$$\frac{V_D}{bh^2} = 0.39\left(t_D\sqrt{\frac{g}{h}}\right)^{2.1}$$

(4.18)

with an improved correlation coefficient $r^2 = 0.85$. The Eqs. 4.17 and 4.18 are shown in Figs. 4.30b) and 4.31a), respectively.

The predictive equation for the maximum water displacement volume $V_D/(bh^2)$ was determined by a multiple regression of the measured values. The multiple regression for the water displacement volume yields

$$\frac{V_D}{bh^2} = 0.8\left(\frac{v_s}{\sqrt{gh}}\right)^1\left(\frac{V_s}{bh^2}\right)^{0.5}$$

(4.19)

with an excellent correlation coefficient $r^2 = 0.93$. The dominant dimensionless quantities are the slide Froude number $\mathbf{F} = v_s/\sqrt{gh}$ and the dimensionless slide volume $V = V_s/(bh^2)$. The dimensionless slide thickness $S = s/h$ only has minor influence on the water displacement volume. The neglection of the slide thickness had almost no effect on the correlation, because the dimensionless slide volume V partially compensated the effect. The slide thickness range covered in the experiments decreased with increasing slide volume. The dimensionless slide thickness and slide volume were therefore not completely independent in this experimental study. The slide thickness increased on average with increasing slide volume. The comparison between the measured values and the predicted ones computed with Eq. 4.19 is shown in Fig. 4.31b). The largest deviations between the measured and the computed values are $< 15\%$.
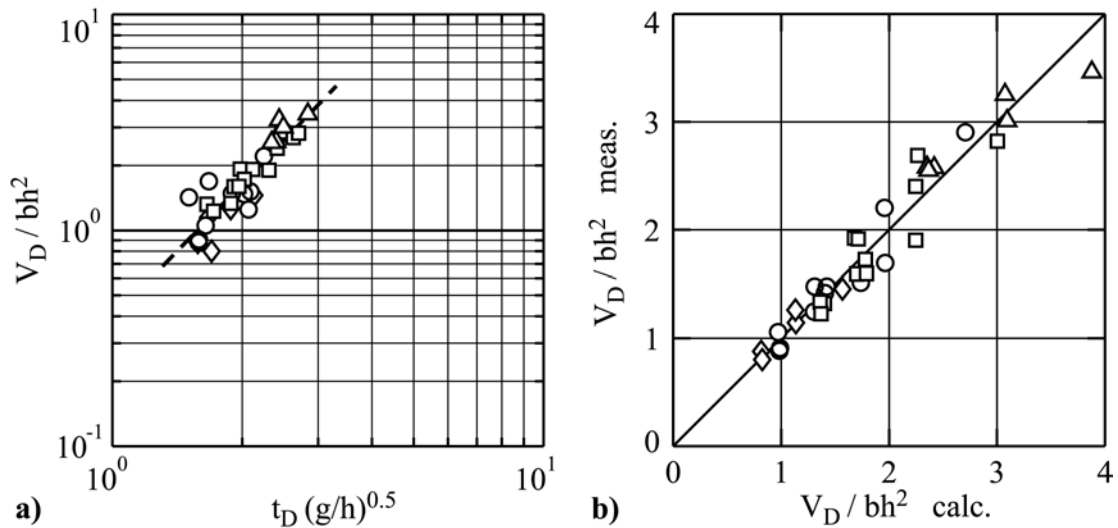
Figure 4.31 **Maximum water displacement volume: a)** $V_D/(bh^2)$ versus $t_D\sqrt{g/h}$ with (— —) Eq. 4.18 and (◇) $2 < \mathbf{F} \leq 2.5$, (○) $2.5 < \mathbf{F} \leq 3$, (□) $3 < \mathbf{F} \leq 4$, (△) $4 < \mathbf{F} < 5$; **b)** $V_D/(bh^2)$ measured versus $V_D/(bh^2)$ computed with Eq. 4.19 and symbols as in a).

The remaining two parameters – the slide Froude number $\mathbf{F} = v_s / \sqrt{gh}$ and the dimensionless slide volume $V = V_s / (bh^2)$ – introduced into the multiple regression may also be considered individually. In both cases the correlation is significantly weaker than in the multiple regression given by Eq. 4.19. None of the single parameter equations described the measured data with sufficient accuracy. Hence the simplified relationship given by Eq. 4.19 is recommended to predict the maximum water displacement volume V_D including the effects of both the slide Froude number and the slide volume.

4.5.6 Maximum water displacement rate

The maximum water displacement rate Q_D was extracted from the water displacement rate curves shown in Fig. 4.29b). The measured maximum water displacement rates $Q_D / \overline{Q}_s$ and $Q_D / (bh\sqrt{gh})$ are shown in Figs. 4.32a) and b), respectively. The maximum water displacement rate always exceeded the mean landslide inflow $\overline{Q}_s = V_s / t_{si}$ and the maximum slide inflow $Q_s = v_s \, s \, b$.
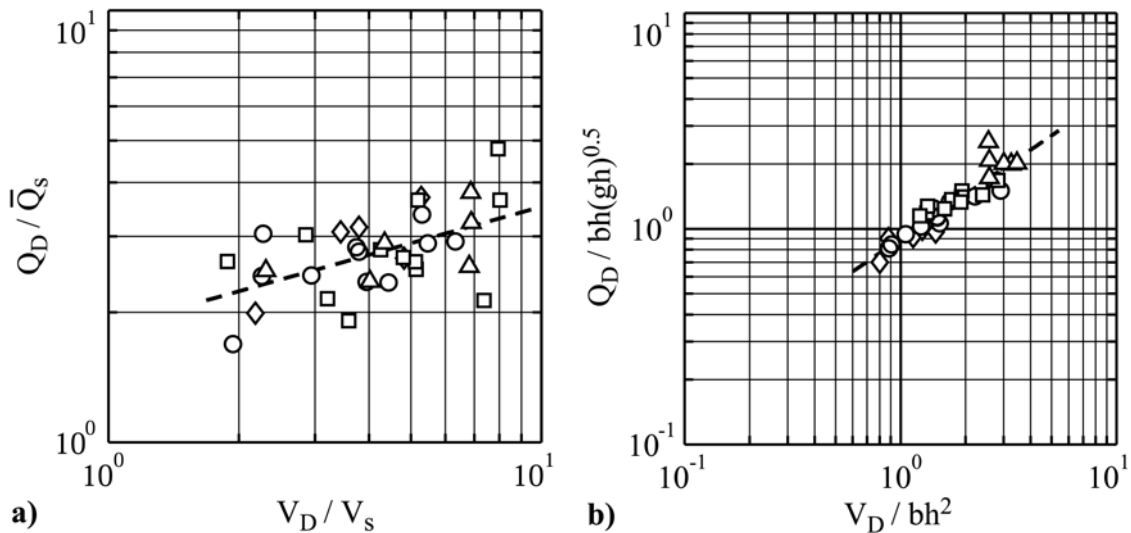
Figure 4.32 **Maximum water displacement rate: a)** $Q_D / \overline{Q}_s$ at ($\Diamond$) $2 < \mathbf{F} \leq 2.5$, ($\bigcirc$) $2.5 < \mathbf{F} \leq 3$, ($\square$) $3 < \mathbf{F} \leq 4$, ($\triangle$) $4 < \mathbf{F} < 5$ with (— —) Eq. 4.20,; **b)** $Q_D / (bh\sqrt{gh})$ with (— —) Eq. 4.21 and symbols as in a).

The maximum water displacement rate normalized by the mean landslide inflow may be related to the normalized maximum water displacement volume by

$$\frac{Q_D}{\overline{Q}_s} = 1.8 \left(\frac{V_D}{V_s} \right)^{0.3}$$

(4.20)

with a poor correlation coefficient $r^2 = 0.3$. An exponential regression with the maximum slide inflow rate Q_s yielded an even poorer correlation of only $r^2 = 0.17$. The normalized maximum water displacement rate $Q_D / \overline{Q}_s$ increased with the normalized maximum

water displacement volume V_D/V_s. Re-normalizing Eq. 4.20 with wave related quantities in the denominators yields

$$\frac{Q_D}{bh\sqrt{gh}} = 0.9\left(\frac{V_D}{bh^2}\right)^{2/3} \tag{4.21}$$

with an improved correlation coefficient $r^2 = 0.79$. The normalized maximum water displacement rates were within $1.7 \leq Q_D/\bar{Q}_s \leq 4.8$ and $1 \leq Q_D/Q_s \leq 2.8$. Hence the dynamic water displacement rate can significantly exceed the landslide inflow. Therefore the maximum water displacement rate Q_D and not the slide inflow Q_s needs to be considered as relevant input quantity for wave maker boundary motions in numerical models. In the presented analysis only cases with flow separation were considered. The maximum water displacement rate of impacts without flow separation may be $Q_D/Q_s \leq 1$. Maximum water displacement values $Q_D/Q_s < 1$ are possible due to flow over the back of the landslide as well as a possible flow through the medium at extremely low slide velocities.

The multiple regression for the maximum water displacement rate $Q_D/(bh\sqrt{gh})$ yields

$$\frac{Q_D}{bh\sqrt{gh}} = 0.6\left(\frac{v_s}{\sqrt{gh}}\right)^1\left(\frac{s}{h}\right)^{0.3} \tag{4.22}$$

with a good correlation coefficient $r^2 = 0.85$. The dominant dimensionless quantity is again the slide Froude number $\mathbf{F} = v_s/\sqrt{gh}$ followed by the dimensionless slide thickness $S = s/h$. The neglection of the slide volume $V = V_s/(bh^2)$ had almost no effect on the correlation. The comparison between the measured values and the predicted ones computed with Eq. 4.22 is shown in Fig. 4.33a).
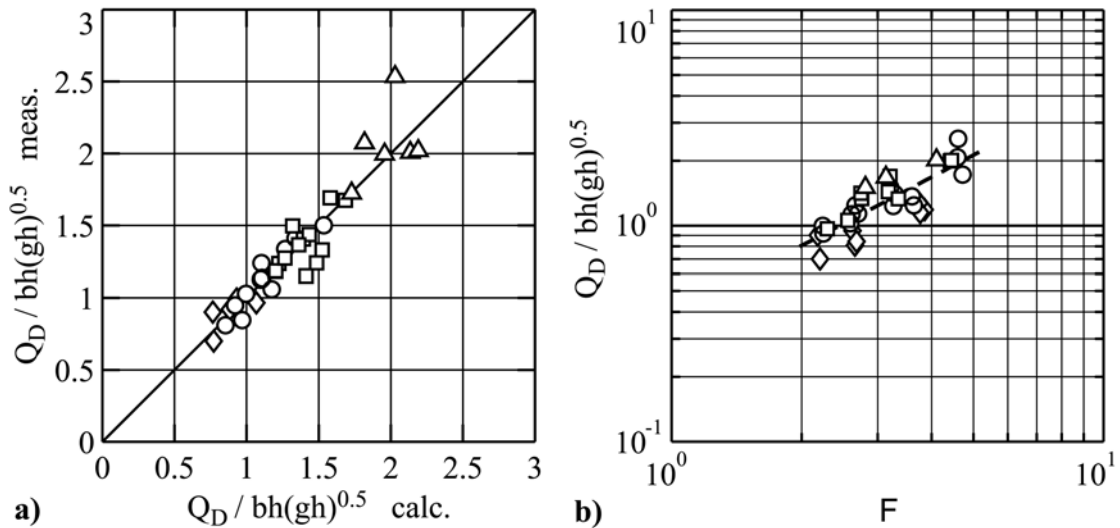
Figure 4.33 **Maximum water displacement rate: a)** $Q_D/(bh\sqrt{gh})$ measured versus $Q_D/(bh\sqrt{gh})$ computed with Eq. 4.22, ($\Diamond$) $2 < \mathbf{F} \leq 2.5$, ($\bigcirc$) $2.5 < \mathbf{F} \leq 3$, ($\square$) $3 < \mathbf{F} \leq 4$, ($\triangle$) $4 < \mathbf{F} < 5$; **b)** $Q_D/(bh\sqrt{gh})$ versus $\mathbf{F} = v_s/\sqrt{gh}$ with (– –) linear regression ($r^2 = 0.67$), ($\Diamond$) $0 < V \leq 0.2$, ($\bigcirc$) $0.2 < V \leq 0.4$, ($\square$) $0.4 < V \leq 0.8$, ($\triangle$) $0.8 < V \leq 2$.

The largest deviations between the measured and the computed values are $< 25\%$. The empirical relationship of Eq. 4.22 indicates a linear increase of the maximum water displacement rate proportional to the slide Froude number. The dependency of the maximum water displacement rate $Q_D/(bh\sqrt{gh})$ on the slide Froude number is shown in Fig. 4.33b). The relationship given by Eq. 4.22 is recommended for the prediction of the maximum water displacement rate.

4.5.7 Duration of impact crater expansion

The duration of the impact crater expansion corresponds to the time of the maximum water displacement volume t_D. The time of the maximum water displacement volume is of fundamental importance regarding the time scale of the whole wave generation process. The duration of the impact crater expansion was extracted from the water displacement curves shown in Fig. 4.29a). The normalized durations of the crater expansions t_D/t_{si} are shown in Figs. 4.34. The duration of the crater expansion t_D may be related to the duration of the subaqueous slide motion t_{sd} by

$$\frac{t_D}{t_{si}} = 0.63\left(\frac{t_{sd}}{t_{si}}\right)^{0.7}$$

(4.23)

with an excellent correlation coefficient $r^2 = 0.9$. The duration of the slide impact t_{si} represents the duration from impact until the rear end of the slide passed the imaginary still water surface. The duration of the subaqueous slide motion t_{sd} corresponds to the timespan from the impact to the deposit. The maximum water displacement volume always occurred after the whole slide mass had penetrated below the imaginary still water surface. The normalized times of the maximum water displacement volumes were within $1.1 \leq t_D/t_{si} \leq 6.2$. The maximum impact crater expansion represented by t_D was always reached well before the subaqueous slide motion was terminated at t_{sd}. Roughly, the maximum water displacement volume occurred at half the duration of the subaqueous slide motion. The average value was $\overline{t_D/t_{sd}} = 0.45$ with a minimum of $t_D/t_{sd} = 0.28$ and a maximum of $t_D/t_{sd} = 0.7$. Hence the slide continued to run-out along the channel bottom while the impact crater was already collapsing. This suggests that the last part of the subaqueous slide motion was of secondary importance regarding the wave generation mechanism. A regression with a wave related time scale in the nominator on the right side of Eq. 4.23 yields

$$\frac{t_D}{t_{si}} = 0.95\left(\frac{\sqrt{h/g}}{t_{si}}\right)^{0.8}$$

(4.24)

with a correlation coefficient $r^2 = 0.87$. The empirical relationship suggests a close to linear dependency of the duration of the impact crater expansion t_D/t_{si} on $(\sqrt{h/g})/t_{si}$.
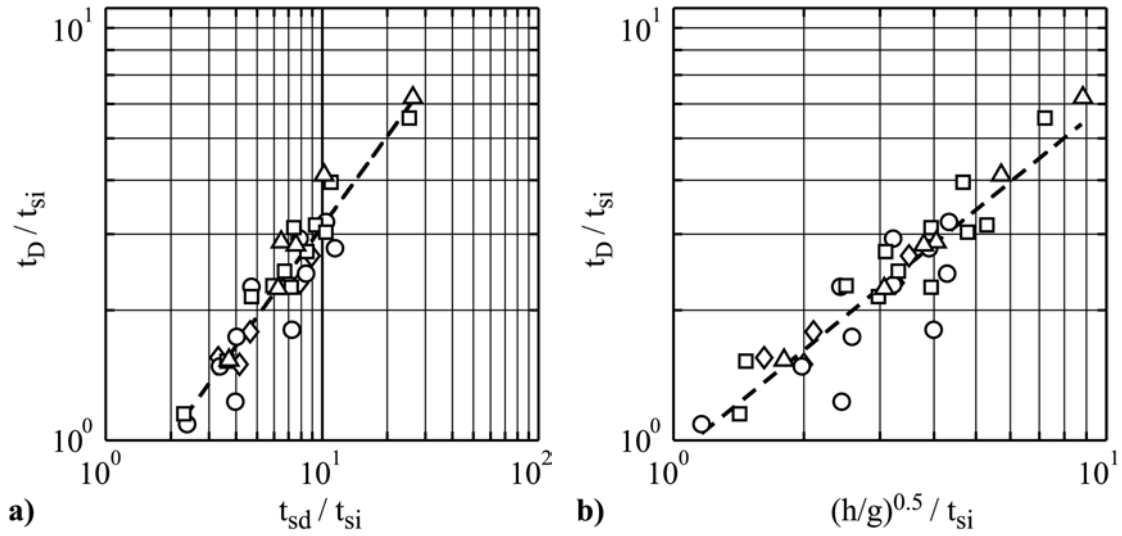
Figure 4.34 **Duration of impact crater expansion:** a) t_D/t_{si} versus t_{sd}/t_{si} at ($\diamondsuit$) $2 < \mathbf{F} \le 2.5$, ($\bigcirc$) $2.5 < \mathbf{F} \le 3$, ($\square$) $3 < \mathbf{F} \le 4$, ($\triangle$) $4 < \mathbf{F} < 5$ with ($\mathbf{-\ -}$) Eq. 4.23; b) t_D/t_{si} versus $\sqrt{h/g}/t_{si}$ with ($\mathbf{-\ -}$) Eq. 4.24 and symbols as in a).

The predictive equation for the duration of the impact crater expansion t_D/t_{si} was determined by a multiple regression of the measured values. The multiple regression yields

$$\frac{t_D}{t_{si}} = 0.95 \left(\frac{v_s}{\sqrt{gh}}\right)^1 \left(\frac{V_s}{bhs}\right)^{-2/3} \tag{4.25}$$

with a correlation coefficient $r^2 = 0.86$. The combined volume to thickness parameter $V/S = V_s/(bhs)$ was introduced because the slide volume $V = V_s/(bh^2)$ and slide thickness $S = s/h$ yielded the same exponents with contrary signs. The parameter V/S may be interpreted as a dimensionless slide length. An increase in slide volume decreases the ratio between the duration of the impact crater expansion and the slide impact duration, whereas an increase in slide thickness increases the duration of the impact crater expansion relative to the slide impact duration. Hence the duration of the impact crater expansion significantly exceeds the slide impact duration for short and thick slides, whereas for thin and elongated slides the duration of the impact crater expansion approaches the slide impact duration. The predominant dimensionless quantity is the slide Froude number $\mathbf{F}$, but the dimensionless slide length V/S may not be neglected. The comparison between the measured values and prediction computed with Eq. 4.25 is shown in Fig. 4.34a). Regarding Eq. 4.25 it needs to be stated that the normalizing impact duration t_{si} on the left hand side basically depends on the impact velocity and the slide length. Hence the slide impact duration t_{si} is not independent of the slide parameters on the right side of Eq. 4.25.

Another approach would be to normalize the duration of the crater expansion by the duration of the subaqueous slide motion t_{sd}. A multiple regression of the dimensionless

parameter t_D/t_{sd} with all three dimensionless quantities **F**, V and S yielded a poor correlation coefficient of only $r^2 = 0.22$. Hence the time of the slide motion t_{sd} from the impact to the deposit is an ill defined time normalization parameter.

A multiple regression with a wave related time scale in the denominator on the right side of Eq. 4.25 yields

$$t_D\sqrt{\frac{g}{h}} = 1.7\left(\frac{v_s}{\sqrt{gh}}\right)^{0.3}\left(\frac{V_s}{bh^2}\right)^{0.2} \qquad (4.26)$$

with a correlation coefficient $r^2 = 0.75$. The dominant dimensionless quantities are the slide Froude number **F** and the dimensionless slide volume V. The neglection of the slide thickness $S = s/h$ had only a minor effect on the correlation coefficient. The comparison between the measured values and prediction computed with Eq. 4.26 is shown in Fig. 4.34b). The exponents in Eq. 4.26 are much smaller than in Eq. 4.25, because $t_D\sqrt{g/h}$ spanned a much smaller range than t_D/t_{si}. The slide impact duration t_{si} is difficult to predict in advance. Hence the relationship given by Eq. 4.26 is recommended for the prediction of the duration of the impact crater expansion.
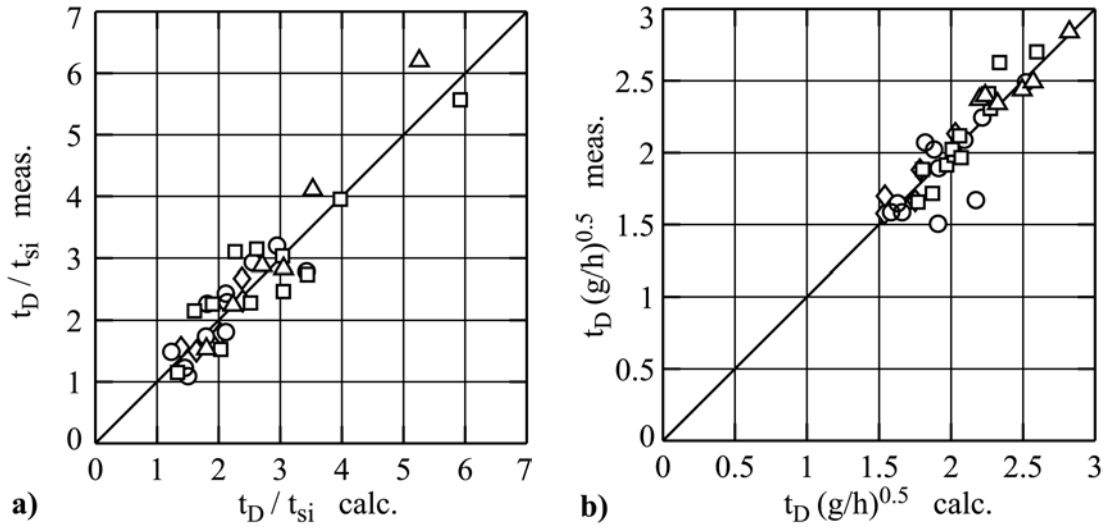
Figure 4.35 **Duration of impact crater expansion: a)** t_D/t_{si} measured versus t_D/t_{si} computed with Eq. 4.25, ($\Diamond$) $2 < $ **F** ≤ 2.5, ($\bigcirc$) $2.5 < $ **F** ≤ 3, ($\square$) $3 < $ **F** ≤ 4, ($\triangle$) $4 < $ **F** < 5; **b)** $t_D\sqrt{g/h}$ measured versus $t_D\sqrt{g/h}$ computed with Eq. 4.26 and symbols as in a).

4.5.8 Time of maximum displacement rate

The time of the maximum water displacement rate t_{qD} characterizes the response characteristics of the impulse transfer from the landslide to the water body. The time of the maximum water displacement rate t_{qD} was extracted from the water displacement curves shown in Fig. 4.29b). The normalized times of the maximum water displacement rates $t_{qD}\sqrt{g/h}$ and t_{qD}/t_D are shown in Figs. 4.36a) and b), respectively. The measurements

of t_{qD} were disturbed by a high noise level resulting in a broad scattering of the data. The maximum water displacement rate had to occur before the collapse of the impact crater initiated. The measurements of the maximum water displacement rates were within $0.05 \leq t_{qD}/t_D \leq 0.6$ and on average at $\overline{t_{qD}/t_D} = 0.3$. Relative to the duration of the slide impact the maximum water displacement rates were recorded at $0.1 \leq t_{qD}/t_{si} \leq 1.25$ with an average at $\overline{t_{qD}/t_{si}} = 0.7$. It is recalled that the duration of the slide impact t_{si} represents the duration from impact until the rear end of the slide passed the imaginary still water surface. Hence the maximum water displacement rate was reached either before the back of the slide penetrated the imaginary still water surface or just thereafter. For comparison underwater explosions always generated the largest water displacement rates at the detonation with $t_{qD} = 0$. The landslides built up their water displacement rate with increasing slide thickness during the slide penetration. Further the strong compaction and deformation of the slide front at impact was responsible for a certain retarding effect. Therefore the water displacements produced by landslide impacts are more difficult to treat analytically than those generated by underwater explosions.

The predictive equation for the time of the maximum water displacement rate $t_{qD}\sqrt{g/h}$ was determined by a multiple regression of the measured values. The multiple regression analysis for the time of the maximum water displacement rate yields

$$t_{qD}\sqrt{\frac{g}{h}} = 2.2\left(\frac{v_s}{\sqrt{gh}}\right)^{-1.6}\left(\frac{V_s}{bh^2}\right)^{0.6}\left(\frac{s}{h}\right)^{-0.8} \tag{4.27}$$

with a weak correlation coefficient $r^2 = 0.38$. For comparison a multiple regression of the dimensionless parameter t_{qD}/t_{si} yielded an even poorer correlation with only $r^2 = 0.15$. The temporal determination of the maximum water displacement rate was unsharp due to the uncertainty in the estimates and the time increment of the recordings. The multiple regression for the time of the maximum water displacement rate t_{qD} normalized by the duration of the crater expansion t_D yields

$$\frac{t_{qD}}{t_D} = 1.4\left(\frac{v_s}{\sqrt{gh}}\right)^{-2}\left(\frac{V_s}{bh^2}\right)^{0.5}\left(\frac{s}{h}\right)^{-0.9} \tag{4.28}$$

with a similar correlation coefficient $r^2 = 0.45$ as Eq. 4.27. The comparisons between the measured values and the predicted ones computed with Eqs. 4.27 and 4.28 are shown in Figs. 4.36a) and b), respectively. The broad scattering was due to the uncertainties involved in the estimates and the limited determination of t_{qD}.
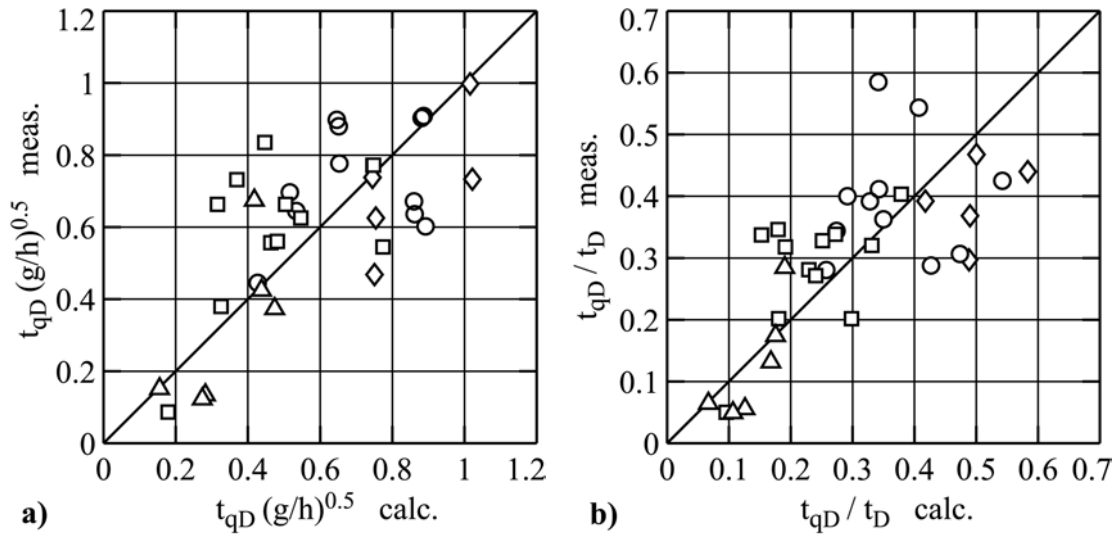
Figure 4.36 **Time of maximum displacement rate: a)** $t_{qD}\sqrt{g/h}$ measured versus $t_{qD}\sqrt{g/h}$ computed with Eq. 4.27, ($\diamond$) $2 < \mathbf{F} \leq 2.5$, ($\bigcirc$) $2.5 < \mathbf{F} \leq 3$, ($\square$) $3 < \mathbf{F} \leq 4$, ($\triangle$) $4 < \mathbf{F} < 5$; **b)** t_{qD}/t_D measured versus t_{qD}/t_D computed with Eq. 4.28, symbols as in a).

The empirical relation of Eq. 4.28 requires the determination of the duration of the crater expansion t_D before hand according to Eq. 4.26. Hence the relationship given by Eq. 4.27 is recommended to predict the time of the maximum water displacement rate t_{qD}.

4.6 Wave generation flow fields

4.6.1 Unseparated flow

Landslide impacts without flow separation on the slide shoulder were observed at relatively low impact velocities. The unseparated and separated flow regimes were defined previously in [para 4.5.2]. A characteristic example of an unseparated flow around a penetrating landslide at $\mathbf{F} = 1.7$ is shown in Figs. 4.37 to 4.46. The set of figures includes the original PIV-images, the velocity vector field, the streamline plot, scalar fields of the velocity components and contour plots of the computed components of the deformation tensor. Regarding the determination of the velocity vector fields and its components it is referred to Appendix E. The deformation tensor and the computation of its components is described in Appendix F. The selected sequence of original PIV recordings is shown in Figs. 4.37. The slide thickness increased during the slide penetration (Fig. 4.37a). The motion of the slide front created a crest above the slide, while the motion of the back of the slide created a trough (Fig. 4.37b). The water displacement was similar to the landslide volume at $\mathbf{F} = 1.7$. Only a minor addition was due to the trough formed on the back and in the wake of the slide. A buckling occurred on the slide shoulder at the beginning of the detrainment of the air included in the pore volume of the granular slide. The buckling may be due to a similar phenomenon as a hydraulic soil break. The air detrainment

indicates the presence of a water flow through the slide, since the pore volume had to be filled with water. A massive phase mixing occurred in the wake of the slide (Fig. 4.37c). The leading wave crest overtook the slide. Large air bubbles rose out of the back of the slide (Fig. 4.37d). The fist size air bubbles at laboratory scale may not be upscaled due to Weber unsimilarity in a Froude model. The amount of air induced into the water body by the slide detrainment increased proportional to the slide volume in unseparated flows. The air concentration decayed and the second wave was formed by a run-up along the inclined ramp in the wake of the slide and subsequent run-down (Figs. 4.37c,d,e,f).

The velocity vector fields and the streamline plots revealed the formation of a full saddle-point in the back of the slide (Figs. 4.38 and 4.39a,b). The full saddle propagated outward behind the leading wave crest and down to the channel bottom forming a half saddle (Figs. 4.38 and 4.39c,d,e). The half saddle marks the back of the leading wave crest where the water surface crosses the stillwater level. Analogously a half-saddle formed at the end of the first trough were the water surface crossed the stillwater level again (Figs. 4.38 and 4.39f,g). The half saddles propagated outward along the channel bottom with the wave pattern. The position of the saddle and half-saddles are characterized by instantaneously zero velocity in the scalar fields of the absolute velocities (Figs. 4.40). The largest absolute water particle velocities were measured locally around the slide front during slide penetration. The largest absolute water particle velocities in the wave field always occurred below the wave crests. The water particle velocity was only fractions of the shallow water wave velocity. The horizontal particle velocities were zero along vertical lines through the half-saddles, whereas the largest values were below the wave crest (Figs. 4.41). The vertical particle velocities were zero along vertical lines through the wave crests (Figs. 4.42). The largest values were encountered at the location of the largest slope of the water surface.

The in-plane divergence was roughly zero in the whole pure water flow area. Hence the fundamental assumption of the two dimensional model is confirmed (Figs. 4.43a,b,c). No out of plane motion was observed except in the massive phase mixing and dissipation area in the wake of the slide. The measurements broke down in the wake of the slide (Figs. 4.43c,d,e). The divergence patterns above the slide deposit were caused by the slide detrainment. The illumination patterns induced by the rising bubble curtain dominated the PIV image recordings. Therefore the correlation analysis looked in on the rising bubbles rather than the seeding particles (Figs. 4.43d,e,f,g). This explains the large vertical velocities above the slide deposit (Figs. 4.42d,e,f,g). The difference in vertical velocity between the air bubbles and the water resulted in negative divergence values above the bubble curtain and positive divergence values below. Further part of the divergence was due to the massive multi-scattering resulting in an ill-defined measurement plane. Three dimensional turbulence was subordinate. Noteworthy are the large negative divergence values along the slide front during the slide penetration (Figs. 4.43a,b,c). These negative values may indicate the presence of a low velocity water flow through the granular slide, which was necessary for the slide detrainment.

The computed out-of-plane vorticity fields are shown in Figs. 4.44. The water flow in the wave generation area and the flow below the outward propagating impulse waves were irrotational. Vorticity was observed on the slide surface due to the shear flow and in the mixing zone above the landslide deposit due to the dissipative turbulence. The PIV-data confirmed the assumption of irrotationality made by all analytical wave theories according to the Laplace equation. Hence a velocity potential exists because the conditions of irrotationality and incompressibility were fulfilled. Further a stream function must exist for all two-dimensional incompressible flow. The stream function determines the velocity vector field. In general, there can be no stream function for three-dimensional flows, with the exception of axis-symmetric flows (Dean and Dalrymple, 1991). The potential flow problem has been determined numerically by the Boundary Integral Equation Method (BIEM) (LeMéhauté and Wang, 1996). The BIEM method provides friction-less solutions whereas the hydrocodes enable dissipative solutions including friction.

The elongational and the shear strain fields are shown in Figs. 4.45 and 4.46, respectively. The elongational strains are zero below wave crests and troughs due to the horizontal velocity vectors. The elongational strains are largest near the free surface at the locations of the largest gradients in the free surface. The zero contour lines of the shear strain mark the transitions from a wave crest to a trough corresponding roughly to the points where the free surface crosses the imaginary still water surface. The maximum shear strain values are always encountered below wave crests and troughs. Both the elongational and the shear strain rates increase with decreasing wavelength and increasing wave height. Larger strain rates result in faster wave attenuations.

The wave profile continuously stretched apart over the short sequence and the waves increased in wavelength L. The first wave crest and trough have completely different characteristics than the second wave crest. The leading wave is an intermediate water depth wave closer to the shallow water wave regime whereas the trailing wave is closer to the deep water regime. The second wave exhibits the classical Stokesian wave profile. The Stokes wave theory performs well if $L/h < 8$. Graphical representations of the classical wave theories and comparisons with experimental data may be found in Wiegel (1964) and LeMéhauté (1976).
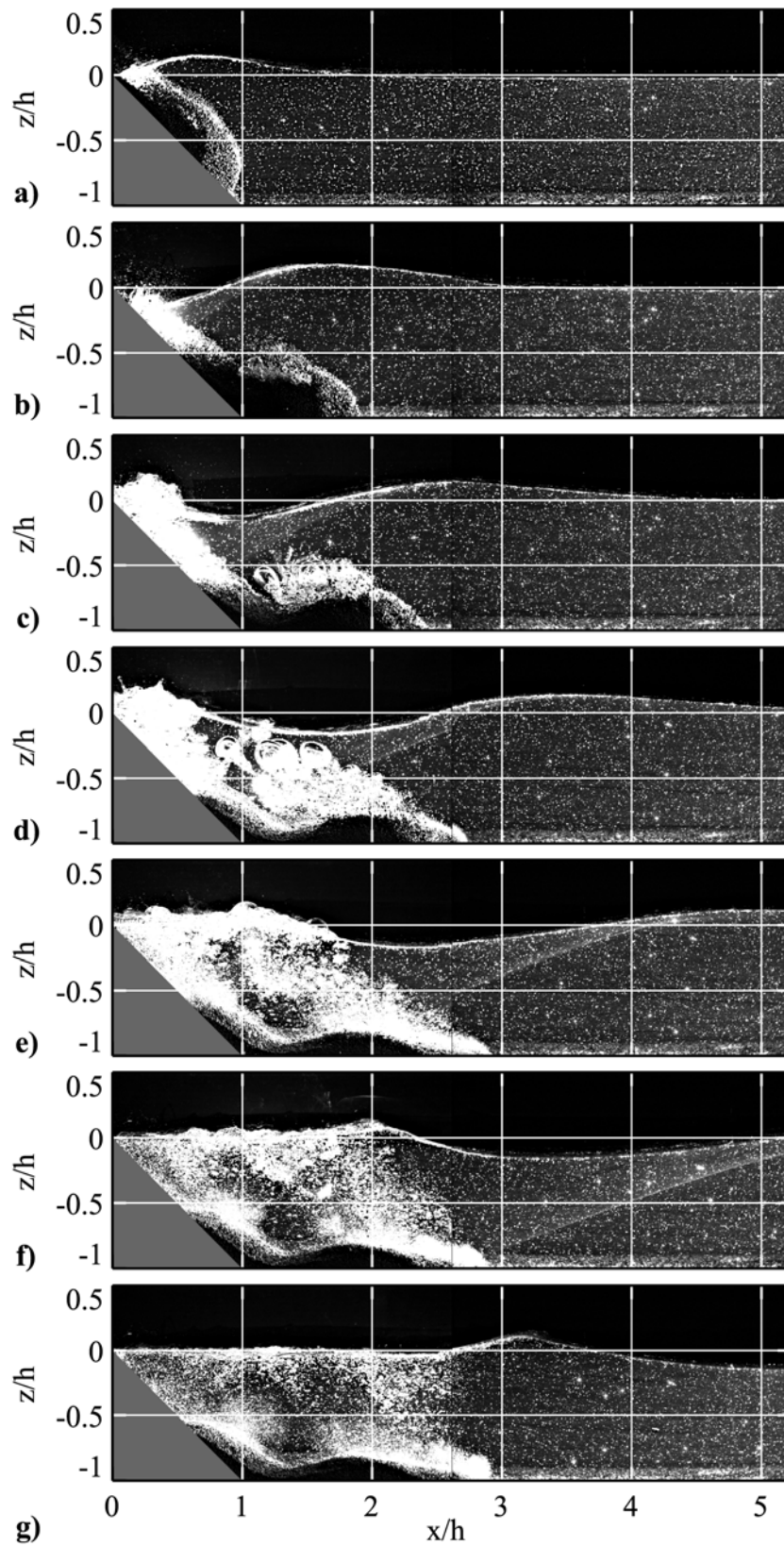
Figure 4.37 **Unseparated flow** PIV-images of two mounted experiments at **F** = 1.7, V = 0.39, S = 0.19, h = 0.3 m and recorded at: **a)** $t\sqrt{g/h}$ = 0.93 , **b)** $t\sqrt{g/h}$ = 2.07 , **c)** $t\sqrt{g/h}$ = 3.22 , **d)** $t\sqrt{g/h}$ = 4.36 , **e)** $t\sqrt{g/h}$ = 5.88 , **f)** $t\sqrt{g/h}$ = 7.41 , **g)** $t\sqrt{g/h}$ = 9.7 .
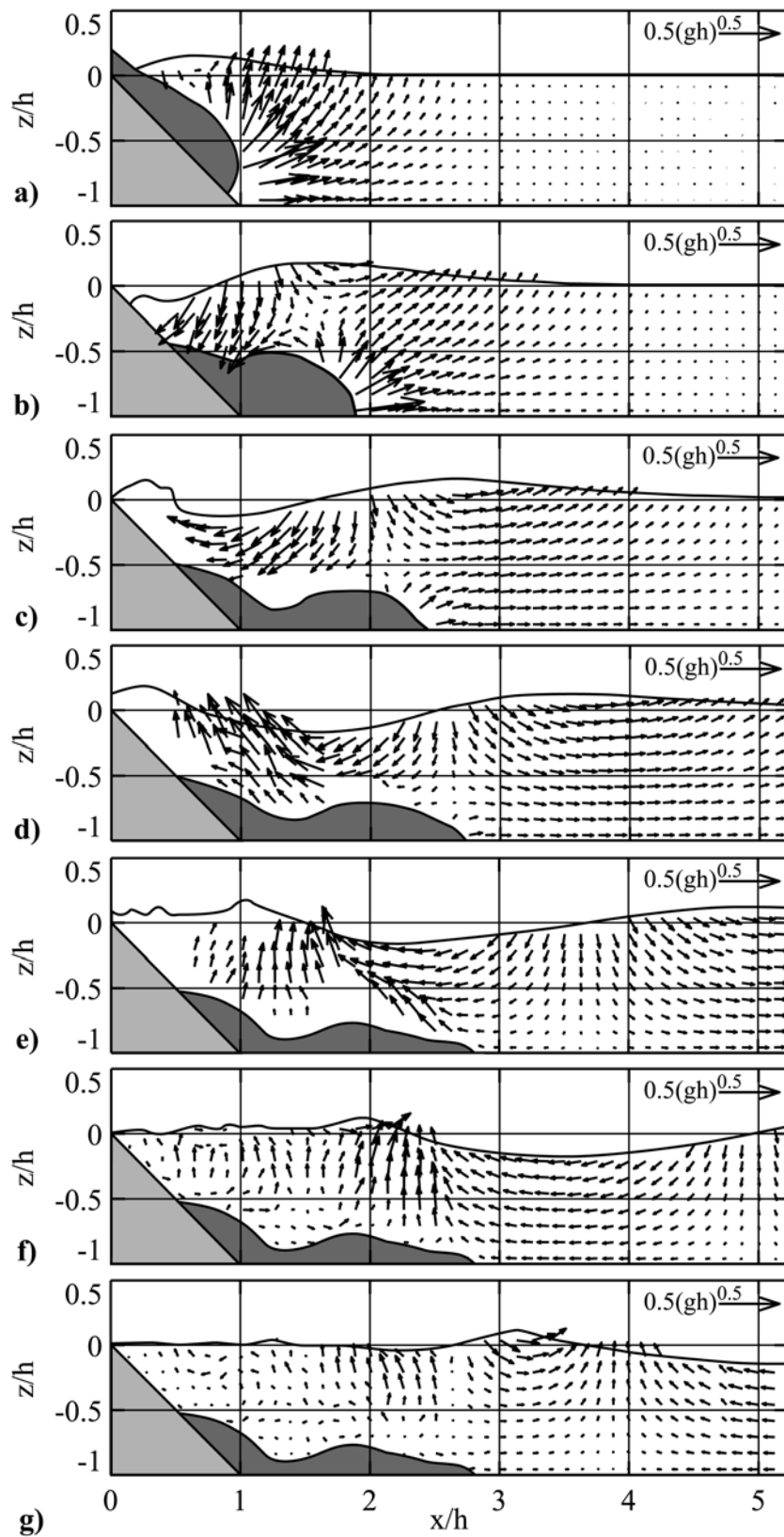
Figure 4.38 **Velocity vector fields** of two mounted unseparated flow experiments at **F** = 1.7, $V = 0.39$, $S = 0.19$, $h = 0.3\,\mathrm{m}$ and recorded at: **a)** $t\sqrt{g/h} = 0.93$, **b)** $t\sqrt{g/h} = 2.07$, **c)** $t\sqrt{g/h} = 3.22$, **d)** $t\sqrt{g/h} = 4.36$, **e)** $t\sqrt{g/h} = 5.88$, **f)** $t\sqrt{g/h} = 7.41$, **g)** $t\sqrt{g/h} = 9.7$.
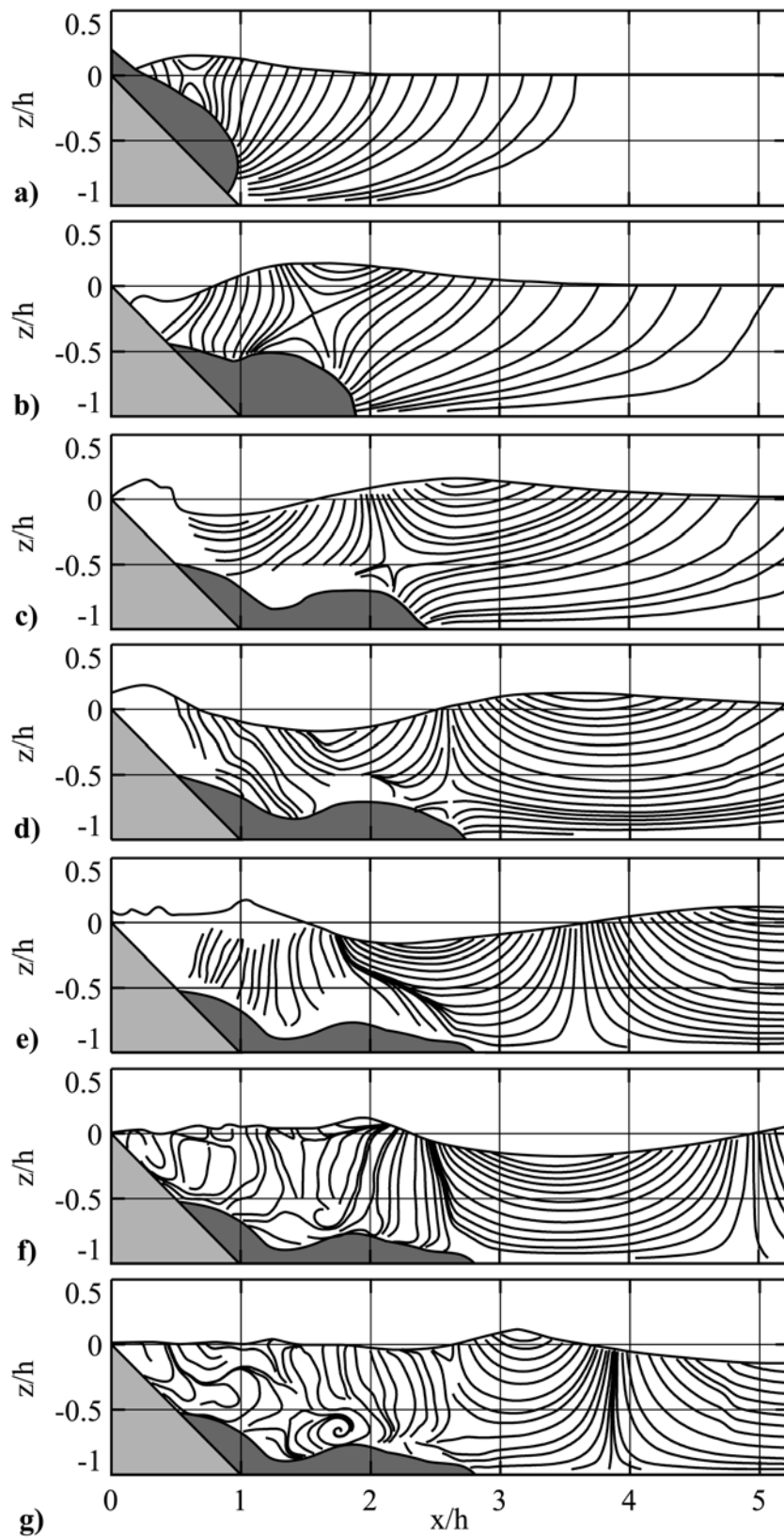
Figure 4.39 **Streamlines** of two mounted unseparated flow experiments at **F** = 1.7, V = 0.39, S = 0.19, h = 0.3 m and recorded at: **a)** $t\sqrt{g/h}$ = 0.93, **b)** $t\sqrt{g/h}$ = 2.07, **c)** $t\sqrt{g/h}$ = 3.22, **d)** $t\sqrt{g/h}$ = 4.36, **e)** $t\sqrt{g/h}$ = 5.88, **f)** $t\sqrt{g/h}$ = 7.41, **g)** $t\sqrt{g/h}$ = 9.7.
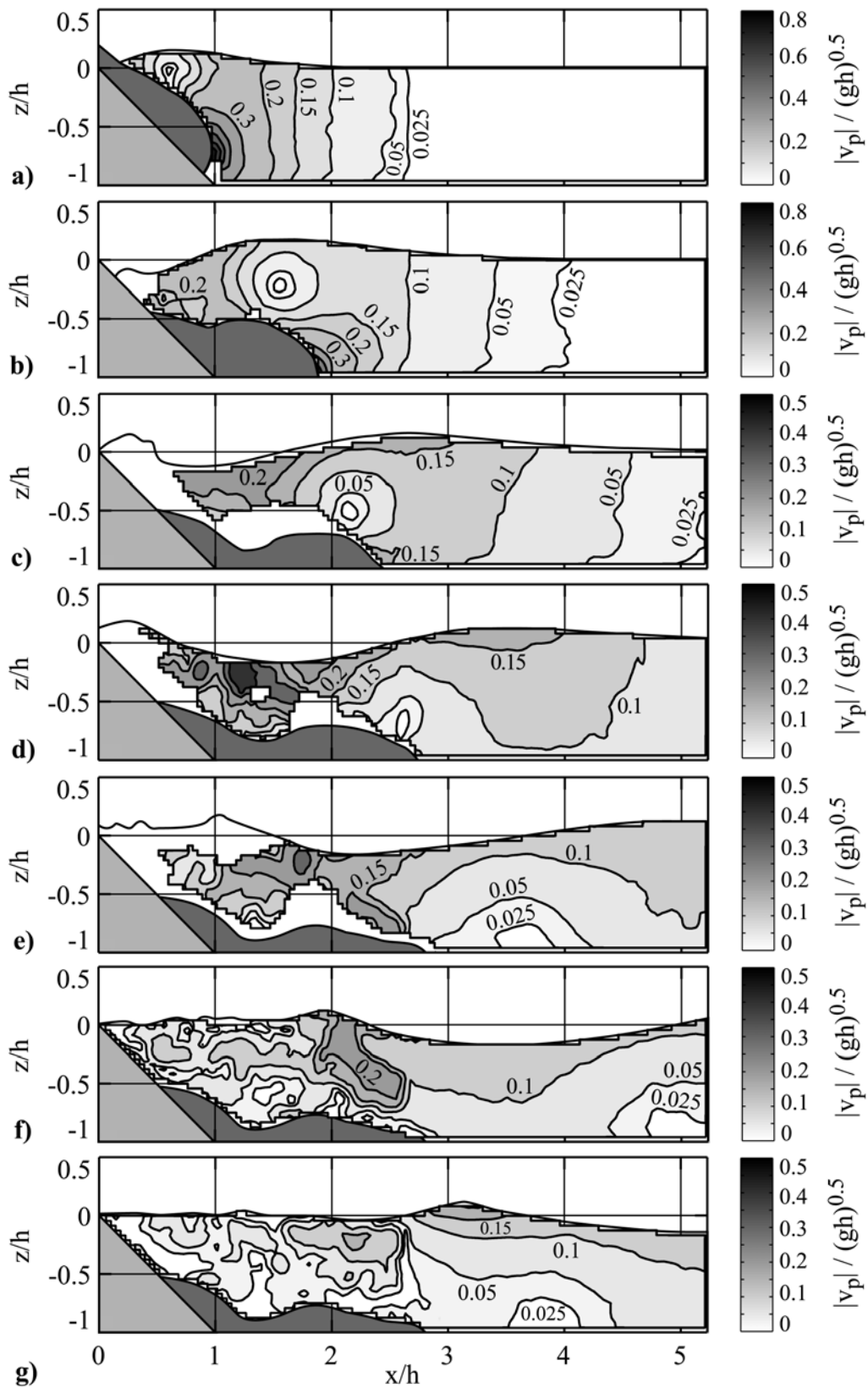
Figure 4.40 **Absolute particle velocity** fields $|v_p|/\sqrt{gh}$ with contour levels at 0.025, 0.05, 0.1, 0.15, 0.2, 0.3, 0.4, 0.5, 0.6, 0.7, 0.8; unseparated flow at **F** = 1.7, *V* = 0.39, *S* = 0.19, *h* = 0.3 m and recorded at $t\sqrt{g/h}$ =: **a)** 0.93, **b)** 2.07, **c)** 3.22, **d)** 4.36, **e)** 5.88, **f)** 7.41, **g)** 9.7.
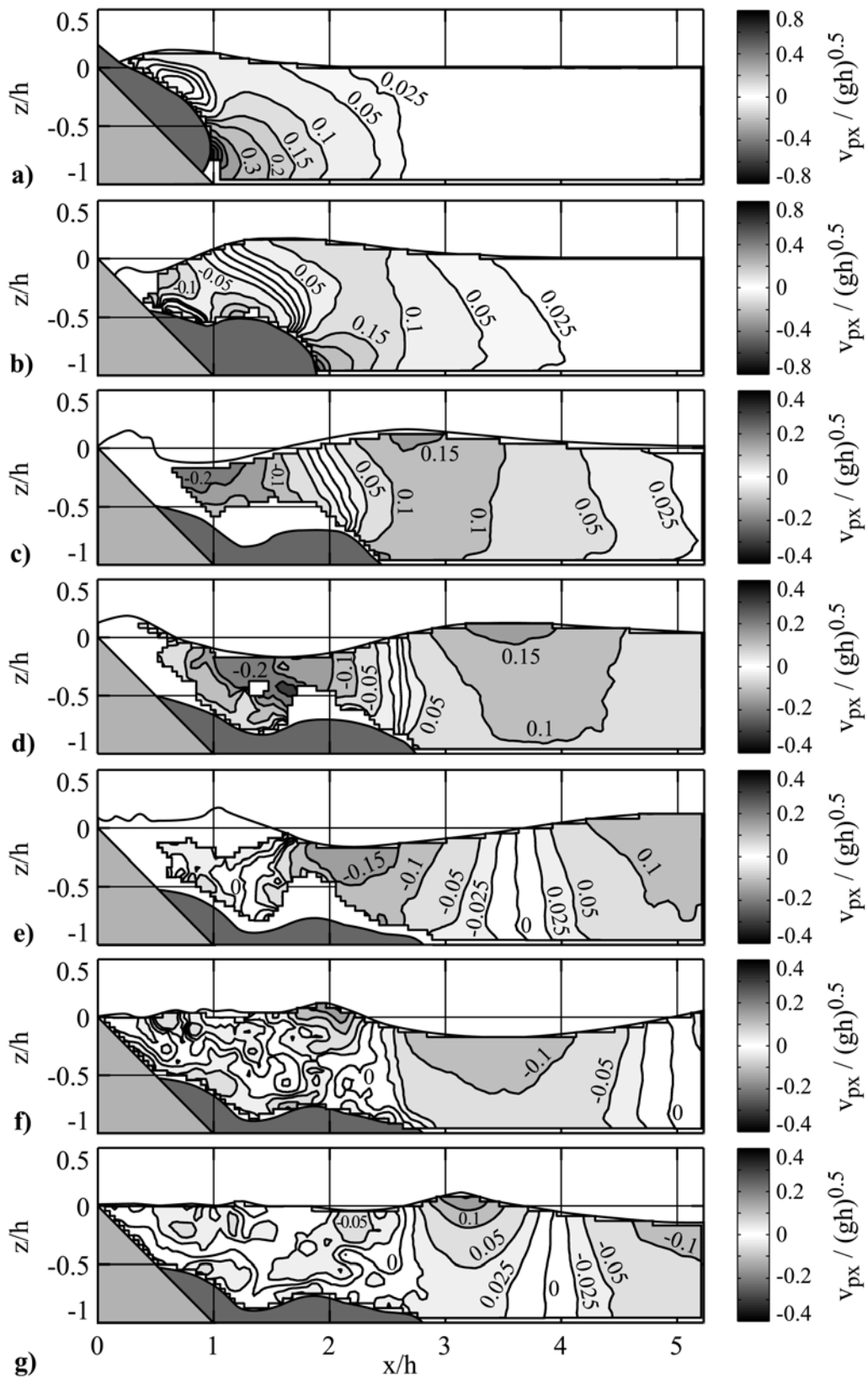
Figure 4.41 **Horizontal particle velocity** fields $v_{px}/\sqrt{gh}$ with contour levels at 0, ± 0.025, ± 0.05, ± 0.1, ± 0.15, ± 0.2, ± 0.3, ± 0.4; unseparated flow at **F** $= 1.7$, $V = 0.39$, $S = 0.19$, $h = 0.3\,\mathrm{m}$ and recorded at $t\sqrt{g/h}$ =: **a)** 0.93, **b)** 2.07, **c)** 3.22, **d)** 4.36, **e)** 5.88, **f)** 7.41, **g)** 9.7.
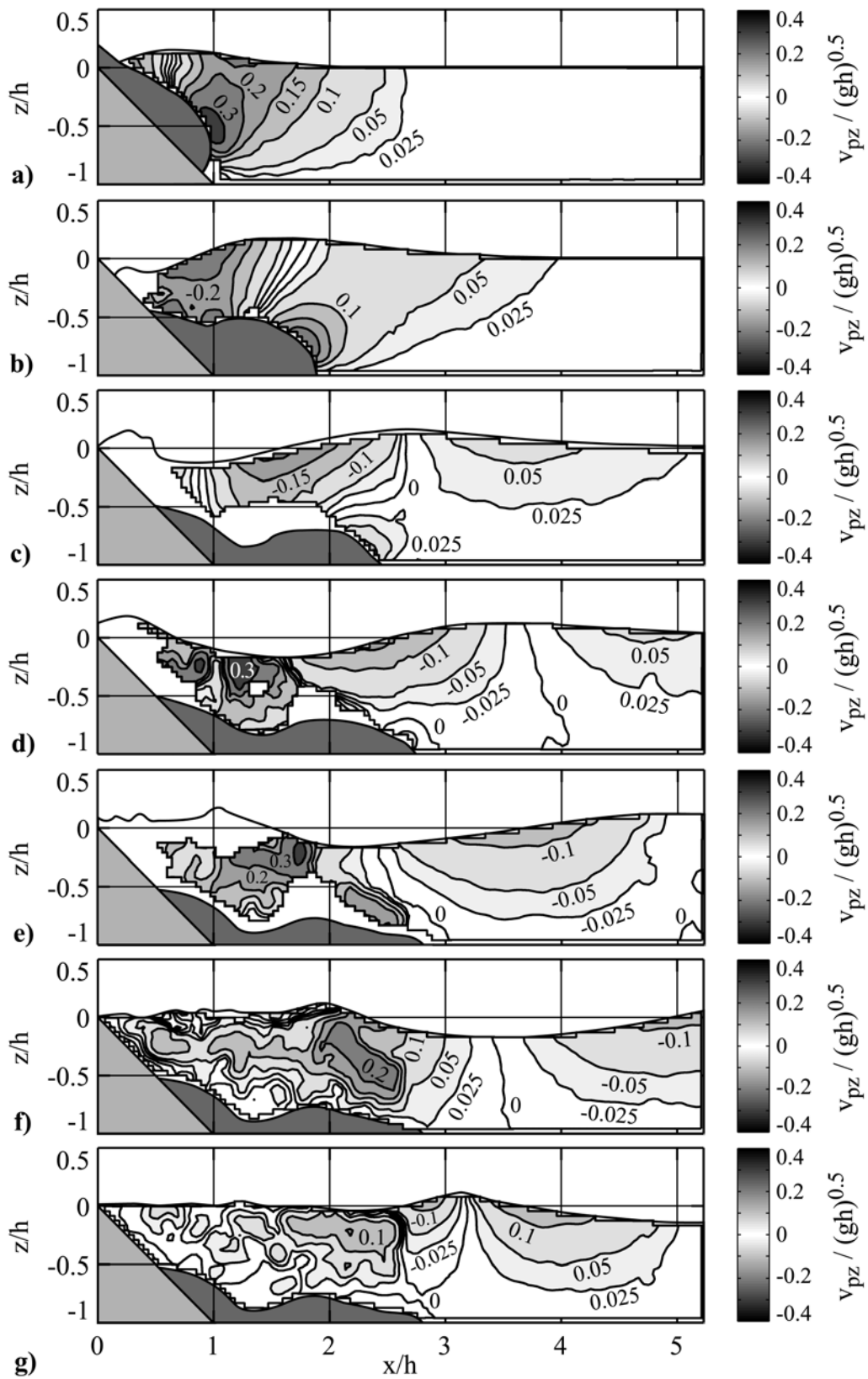
Figure 4.42 **Vertical particle velocity** fields $v_{pz}/\sqrt{gh}$ with contour levels at 0, ±0.025, ±0.05, ±0.1, ±0.15, ±0.2, ±0.3, ±0.4; unseparated flow at $\mathbf{F} = 1.7$, $V = 0.39$, $S = 0.19$, $h = 0.3\,\mathrm{m}$ and recorded at $t\sqrt{g/h}\;=$: **a)** 0.93, **b)** 2.07, **c)** 3.22, **d)** 4.36, **e)** 5.88, **f)** 7.41, **g)** 9.7.
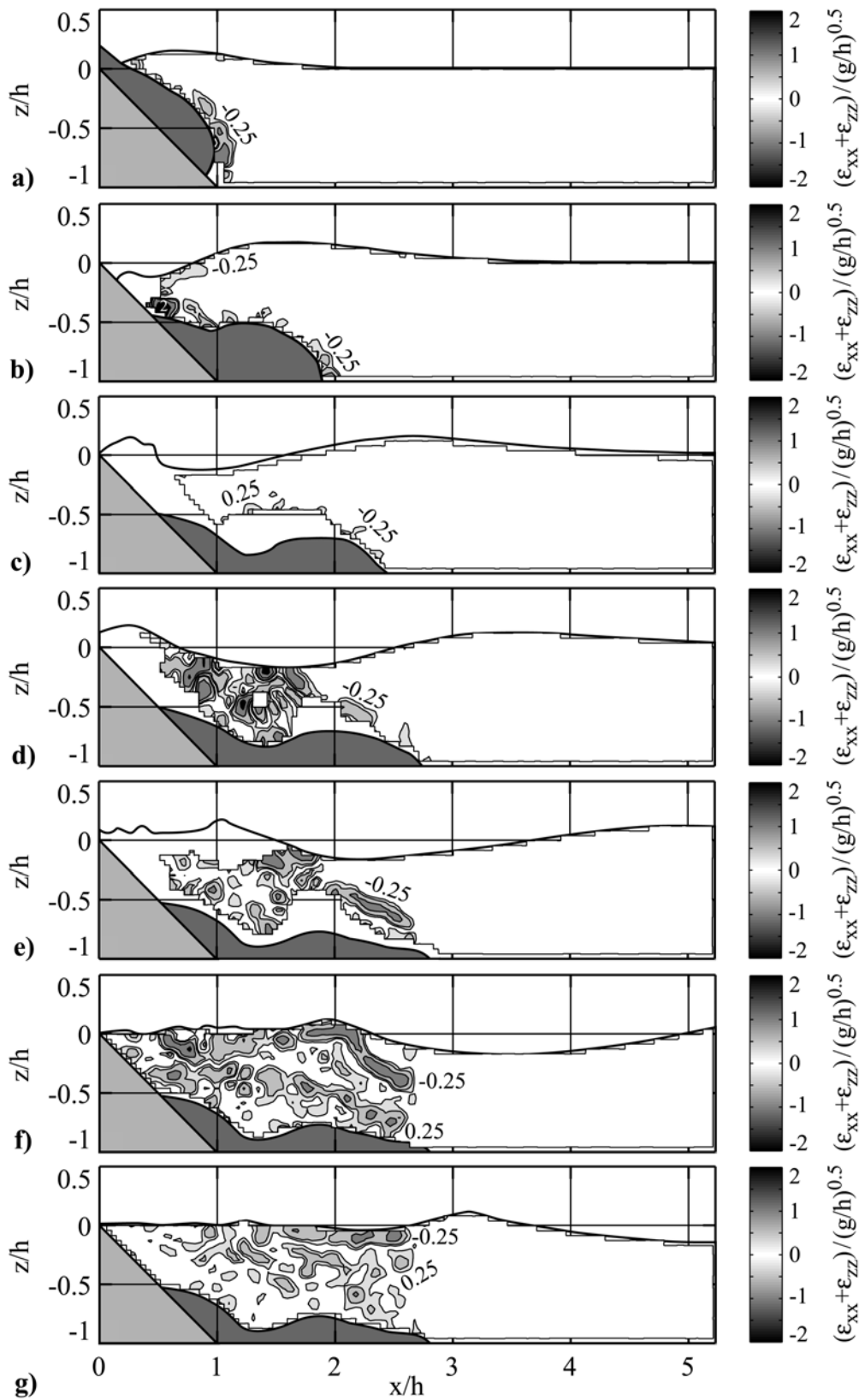
Figure 4.43 **2D-divergence** fields $(\varepsilon_{xx} + \varepsilon_{zz})/\sqrt{g/h}$ with contour levels at ± 0.25, ± 0.5, ± 1, ± 2; unseparated flow at **F** = 1.7, V = 0.39, S = 0.19, h = 0.3 m and recorded at $t\sqrt{g/h}$ =: **a)** 0.93, **b)** 2.07, **c)** 3.22, **d)** 4.36, **e)** 5.88, **f)** 7.41, **g)** 9.7.
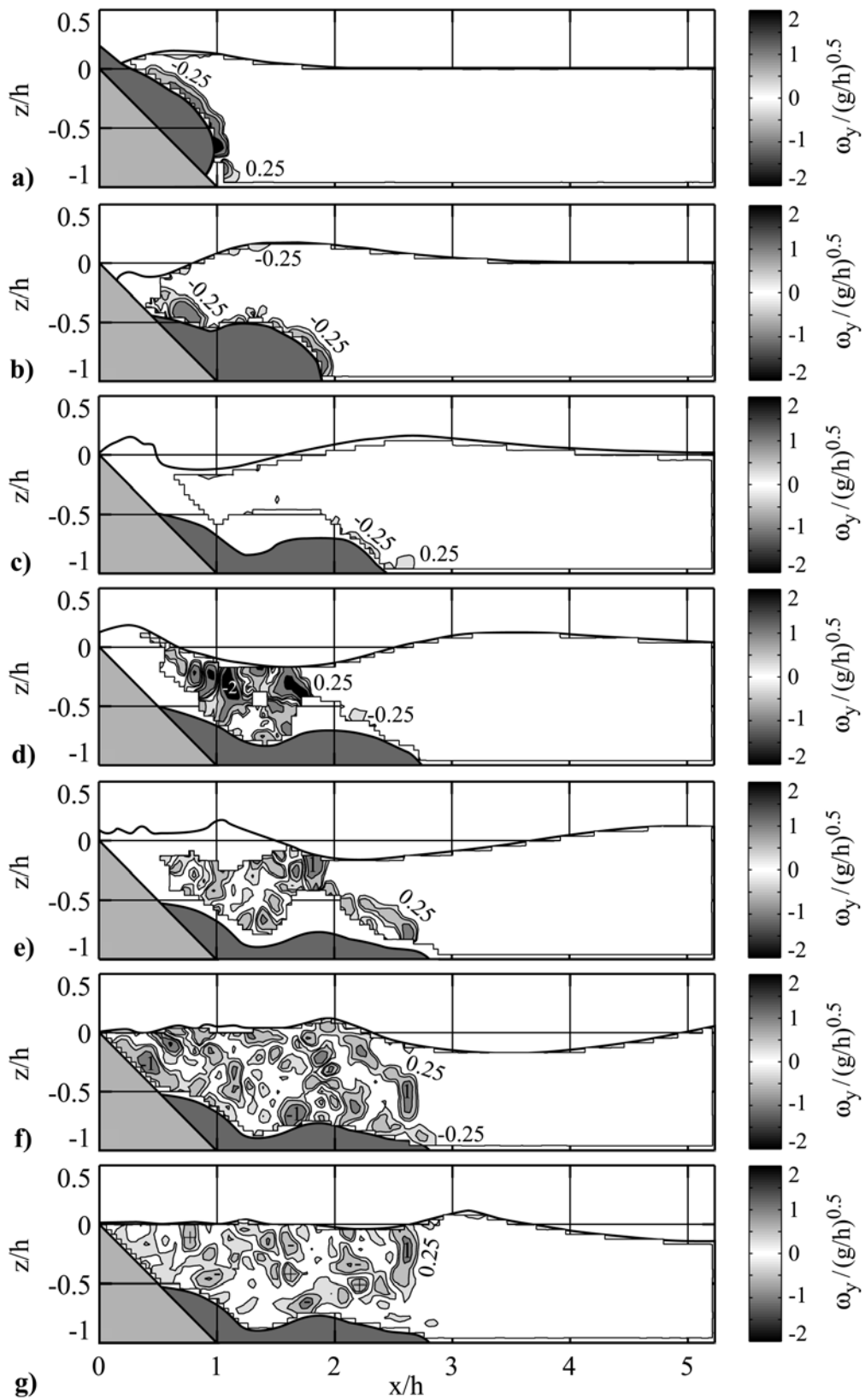
Figure 4.44 **Vorticity** fields $\omega_y/\sqrt{g/h}$ with contour levels at ±0.25, ±0.5, ±1, ±2; unseparated flow at **F** = 1.7, V = 0.39, S = 0.19, h = 0.3m and recorded at $t\sqrt{g/h}$ =: **a)** 0.93, **b)** 2.07, **c)** 3.22, **d)** 4.36, **e)** 5.88, **f)** 7.41, **g)** 9.7.
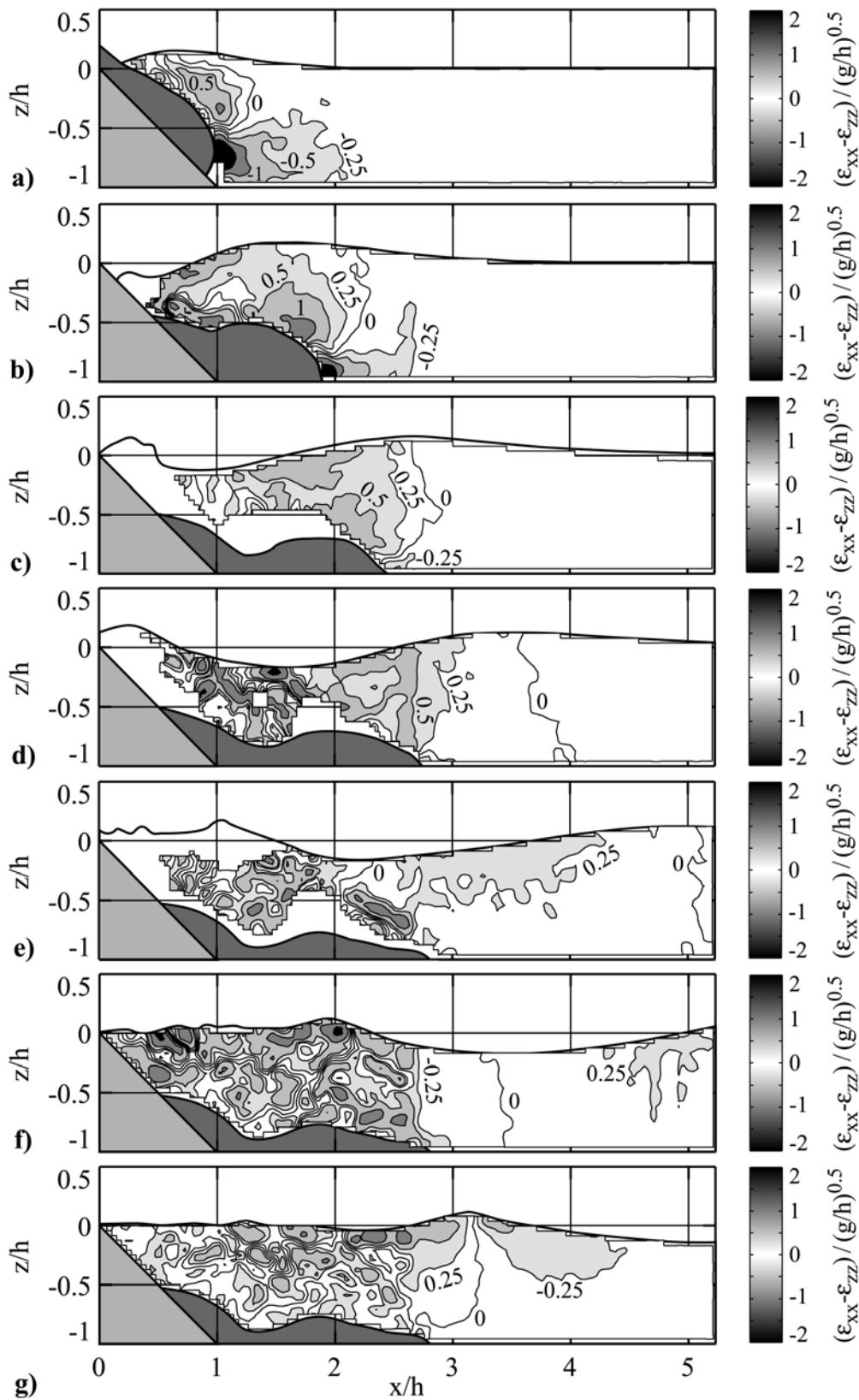
Figure 4.45 **Elongational strain** fields $(\varepsilon_{xx} - \varepsilon_{zz})/\sqrt{g/h}$ with contour levels at 0, ± 0.25, ± 0.5, ± 1, ± 2; unseparated flow at **F** $= 1.7$, $V = 0.39$, $S = 0.19$, $h = 0.3\,\text{m}$ and recorded at $t\sqrt{g/h} =$: **a)** 0.93, **b)** 2.07, **c)** 3.22, **d)** 4.36, **e)** 5.88, **f)** 7.41, **g)** 9.7.
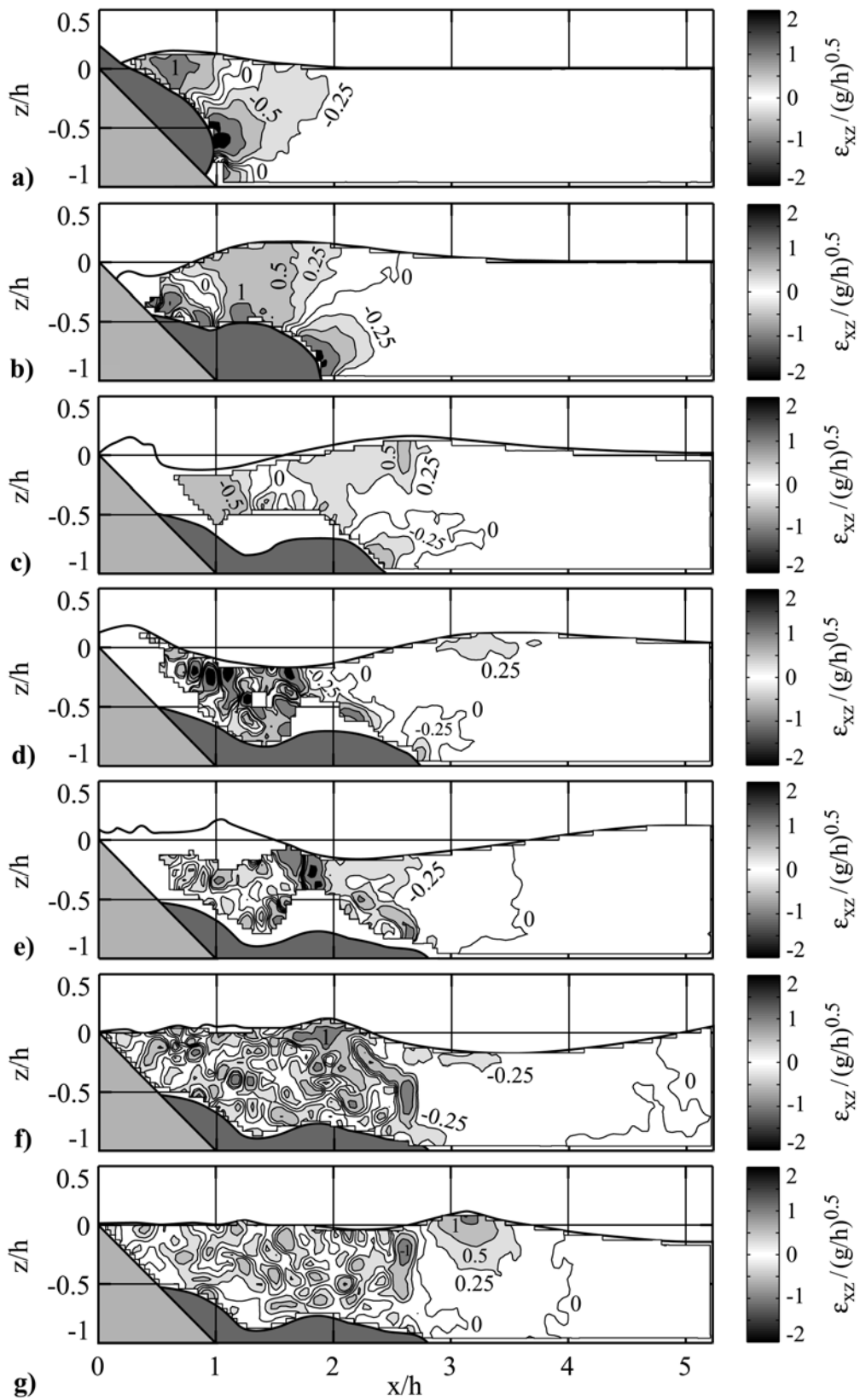
Figure 4.46 **Shear strain** fields $\varepsilon_{xz}/\sqrt{g/h}$ with contour levels at 0, ± 0.25, ± 0.5, ± 1, ± 2; unseparated flow at **F** = 1.7, V = 0.39, S = 0.19, h = 0.3 m and recorded at $t\sqrt{g/h}$ =: **a)** 0.93, **b)** 2.07, **c)** 3.22, **d)** 4.36, **e)** 5.88, **f)** 7.41, **g)** 9.7.

4.6.2 Backward collapsing impact crater

The unseparated and separated flow regimes as well as the backward and outward collapsing impact crater regimes were defined previously in [para 4.5.2] and [para 4.5.3], respectively. The slide Froude number was the primary classification parameter. A characteristic example of a backward collapsing hydrodynamic crater formed by a landslide impact at $\mathbf{F} = 2.8$ is shown in Figs. 4.47 to 4.48. The set of figures includes the original PIV-images, the velocity vector field, the streamline plot, scalar fields of the velocity components and contour plots of the computed components of the deformation tensor. The selected sequence of original PIV recordings is shown in Figs. 4.47. The water flow around the penetrating landslide separated on the slide shoulder (Figs. 4.47a,b). The water was initially expelled upwards and outward by the entry of the landslide forming a water crater. The water crater exposed the ramp and the back of the landslide to the atmosphere. The displaced water volume obviously exceeded the landslide volume significantly. The water displacement volumes and rates were discussed in [para 4.5]. As the process of crater growth has terminated outward bulk motion of water was still present as a residuum. The uplift evolved into a leading wave. The backward collapsing impact crater was governed by a surface closure resulting in the inclusion of air pockets in the form of a cavity (Figs. 4.47c,d). The amount of air inclusion strongly depended on the cavity type. The largest air volume was entrained by backward collapsing impact crater due to the early surface closure. The cavity collapsed and the resulting rebound thereafter issued an almost vertical jet (Figs. 4.47e,f). A considerable portion of the energy imparted to the fluid is lost as a result of turbulent mixing at the impact site and the jet formation. The leading wave had already overtaken the slide front at cavity collapse. Therefore the leading wave crest may be considered unaffected by the surface closure. Possible scale effects due to compressibility and the unscaled atmospheric pressure were addressed previously in [para 3.2.5] and [para 4.5.8], respectively. The detrainment of the landslide occurred during the final stages of the granulate deposition after the cavity collapse (Figs. 4.47e,f).

The velocity vector fields and the streamline plots revealed the formation of a full saddle-point in the water uplift (Figs. 4.48 and 4.49b,c). The full saddle propagated outward behind the leading wave crest and down to the channel bottom forming a half saddle (Figs. 4.48 and 4.49d,e,f). The half saddle marks the back of the leading wave crest where the water surface crosses the stillwater level. The position of the saddle and half-saddles are characterized by instantaneously zero velocity in the scalar fields of the absolute velocities (Figs. 4.50). The largest velocities were measured locally around the slide front during slide penetration. The largest velocities in the wave field always occurred below the wave crests. The water particle velocity was only fractions of the shallow water wave velocity, but increased compared to the unseparated flow example due to the increase in wave height. The horizontal particle velocities were zero along vertical lines through the half-saddles, whereas the largest values were below the wave crest (Figs. 4.51). The vertical particle velocities were zero along vertical lines through the wave crests (Figs. 4.52). The largest values in the wave system were encountered at the location of the largest slope

of the water surface. The vertical velocity in the jet issued by the rebound of the cavity collapse even exceeded the shallow water wave propagation velocity (Fig. 4.52e).

The in-plane divergence was roughly zero in the whole pure water flow area. Hence the fundamental assumption of the two dimensional model is confirmed again (Figs. 4.53). Large divergence values were observed during the cavity collapse and the uprise of the vertical jet (Figs. 4.53e,f). The divergence may have several fluid dynamic and measurement technique related causes. The cavity collapse and vertical jet formation was accompanied by a massive turbulent mixing of the three phases. The dark dots in the stem of the jet are actually granular grains swept along. The massive mixing process was of coarse three dimensional and hence some out of plane motion may not be excluded. Further the illumination patterns during the cavity collapse were dominated by the dark granular grains and the white air bubbles (Figs. 4.47e,f). Hence the correlation analysis likely locked in on the granular grains swept upward in the vertical jet rather than the seeding particles. The large positive divergence values during the formation of the vertical jet may indicate the expansion of the air bubble compressed during the crater collapse (Fig. 4.53e). Noteworthy are the large negative divergence values along the slide front during the slide penetration (Figs. 4.53a,b,c). These negative values may indicate the presence of a low velocity water flow through the granular slide, which was necessary for the slide detrainment.

The computed out-of-plane vorticity fields are shown in Figs. 4.54. The water flow in the wave generation area and the flow below the outward propagating impulse waves were irrotational. Vorticity was observed on the slide surface due to the shear flow and in the mixing zone above the landslide deposit due to the dissipative turbulence. The PIV-data confirmed the assumption of irrotationality made by all analytical wave theories according to the Laplace equation. The largest vorticity values were measured in the vertical jet (Figs. 4.54e,f). These values should be interpreted cautiously due to the large divergence values and the high measurement noise in that area.

The elongational and the shear strain fields are shown in Figs. 4.55 and 4.56, respectively. The elongational strains are zero below wave crests and troughs due to the horizontal velocity vectors. The elongational strains are largest near the free surface at the locations of the largest gradients in the free surface. The largest negative elongational strains were computed in front of the penetrating landslide where the fluid cells are compressed along the horizontal x-axis and expanded vertically (Figs. 4.55a,b,c). Analogously large negative elongational strains were measured in the upward shooting vertical jet (Figs. 4.55e). The maximum shear strain values in the wave field were always encountered below the wave crests. Both the elongational and the shear strain rates increased compared to the previous unseparated flow example due to the larger wave height.
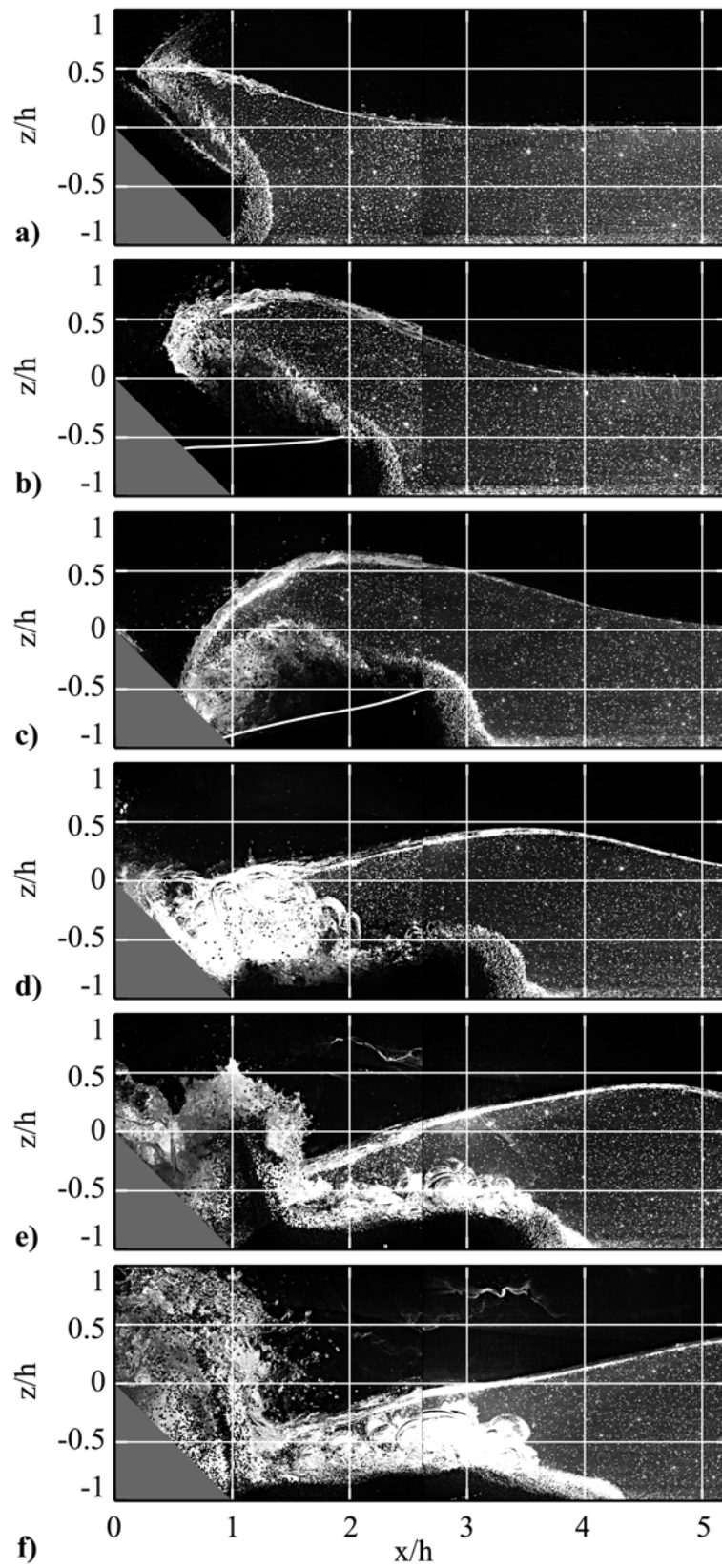
Figure 4.47 **Backward collapsing impact crater** PIV-images of two mounted experiments at **F** = 2.8, V = 0.79, S = 0.34, h = 0.3 m and recorded at: **a)** $t\sqrt{g/h} = 0.72$, **b)** $t\sqrt{g/h} = 1.48$, **c)** $t\sqrt{g/h} = 2.24$, **d)** $t\sqrt{g/h} = 3.01$, **e)** $t\sqrt{g/h} = 3.77$, **f)** $t\sqrt{g/h} = 4.53$.
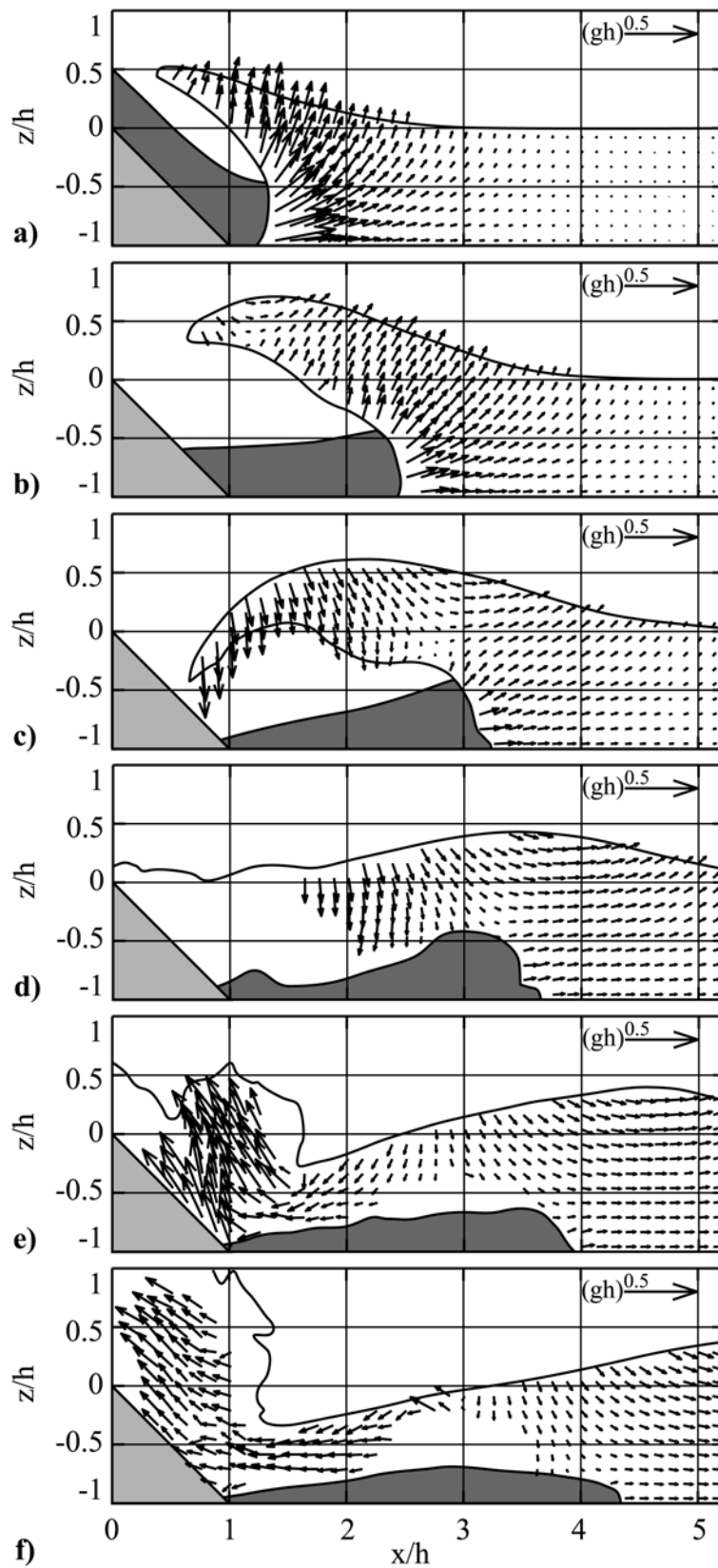
Figure 4.48 **Velocity vector fields** of two mounted backward collapsing impact crater experiments at **F** = 2.8, V = 0.79, S = 0.34, h = 0.3 m and recorded at $t\sqrt{g/h}$ =: **a)** 0.72, **b)** 1.48, **c)** 2.24, **d)** 3.01, **e)** 3.77, **f)** 4.53.
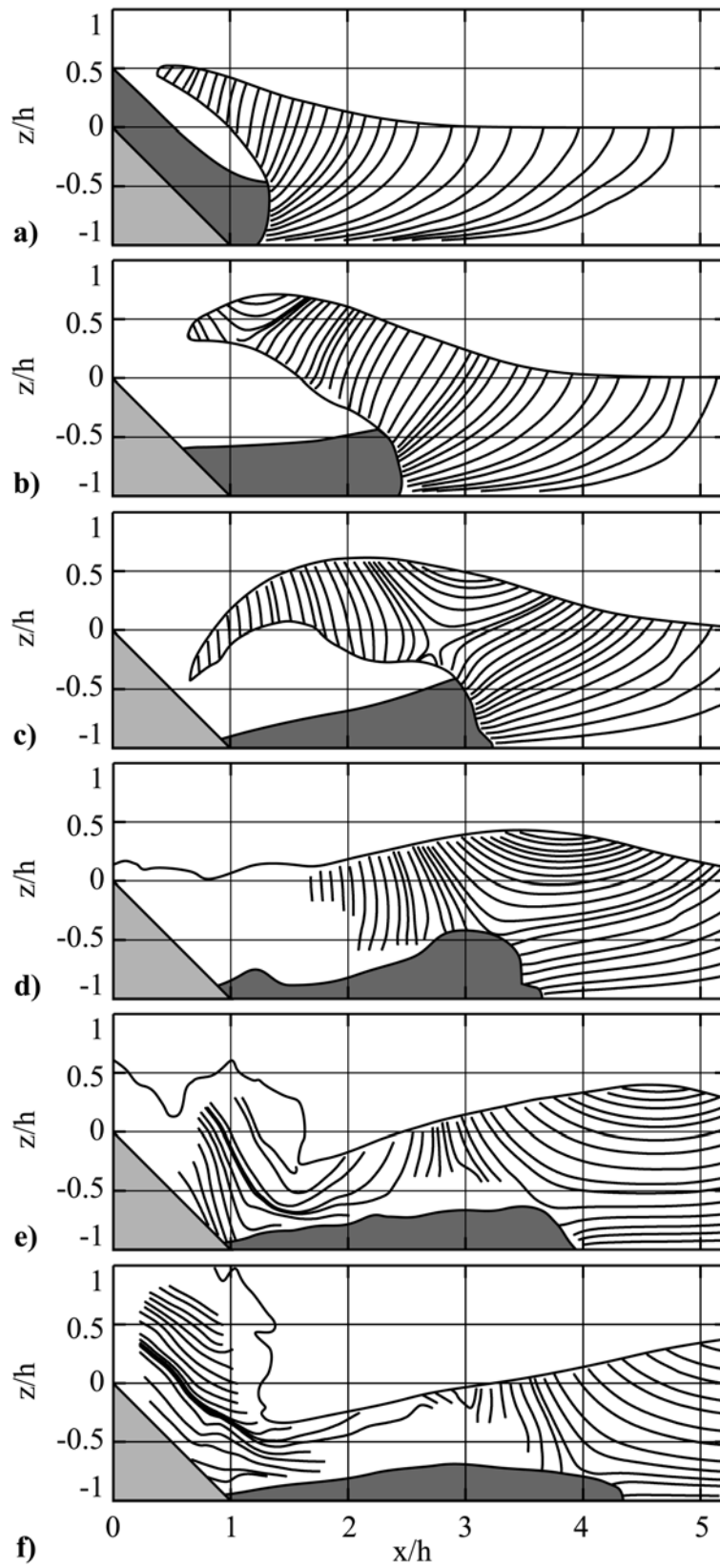
Figure 4.49 **Streamlines** of two mounted backward collapsing impact crater experiments at **F** = 2.8, V = 0.79, S = 0.34, h = 0.3 m and recorded at $t\sqrt{g/h}$ =: **a)** 0.72, **b)** 1.48, **c)** 2.24, **d)** 3.01, **e)** 3.77, **f)** 4.53.
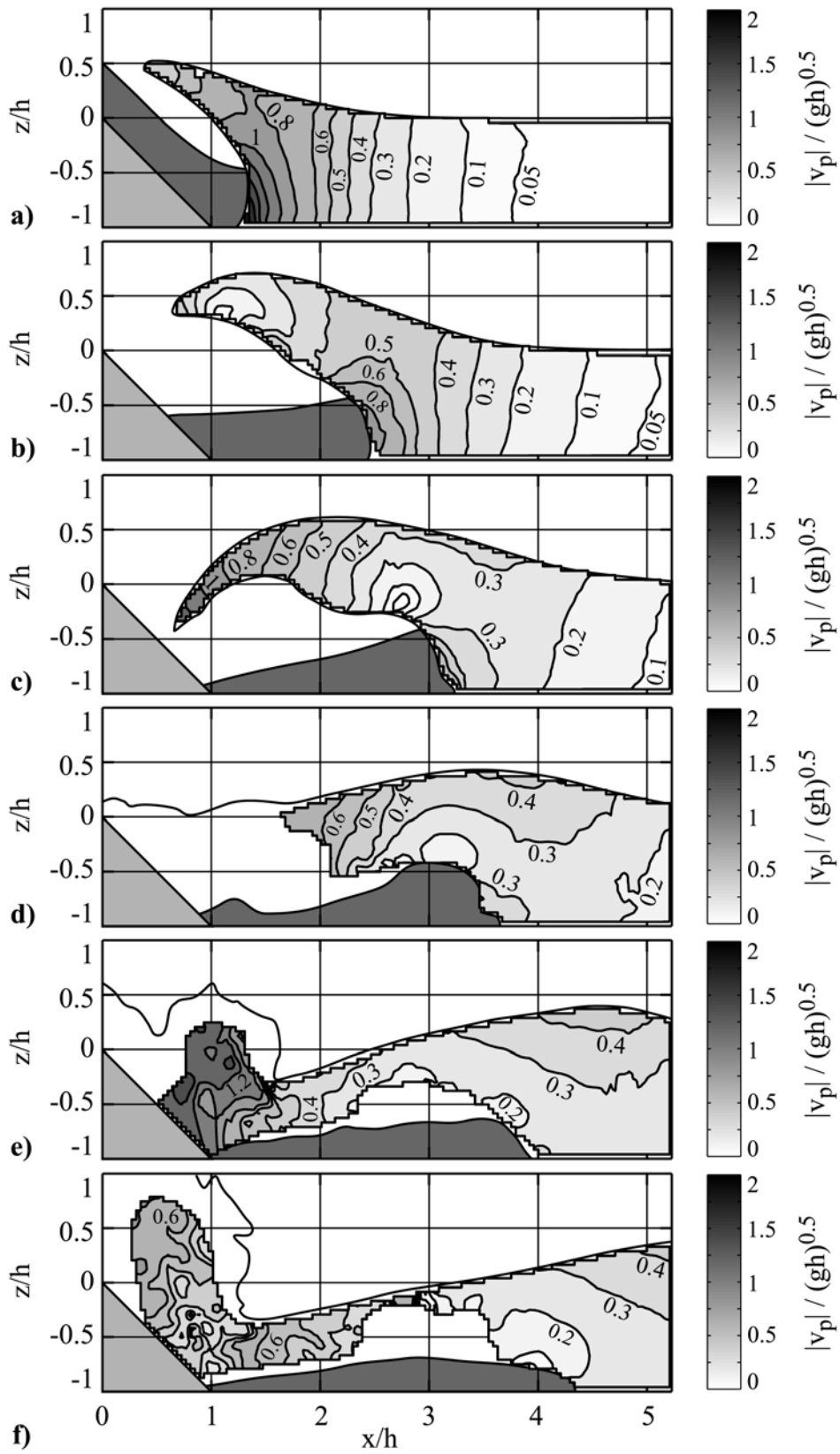
Figure 4.50 **Absolute particle velocity** fields $|v_p|/\sqrt{gh}$ with contour levels at 0.05, 0.1, 0.2, 0.3, 0.4, 0.5, 0.6, 0.8, 1, 1.2, 1.4, 1.6, 1.8, 2; backward collapsing crater at **F** = 2.8, V = 0.79, S = 0.34, h = 0.3 m and recorded at $t\sqrt{g/h}$ =: **a)** 0.72, **b)** 1.48, **c)** 2.24, **d)** 3.01, **e)** 3.77, **f)** 4.53.
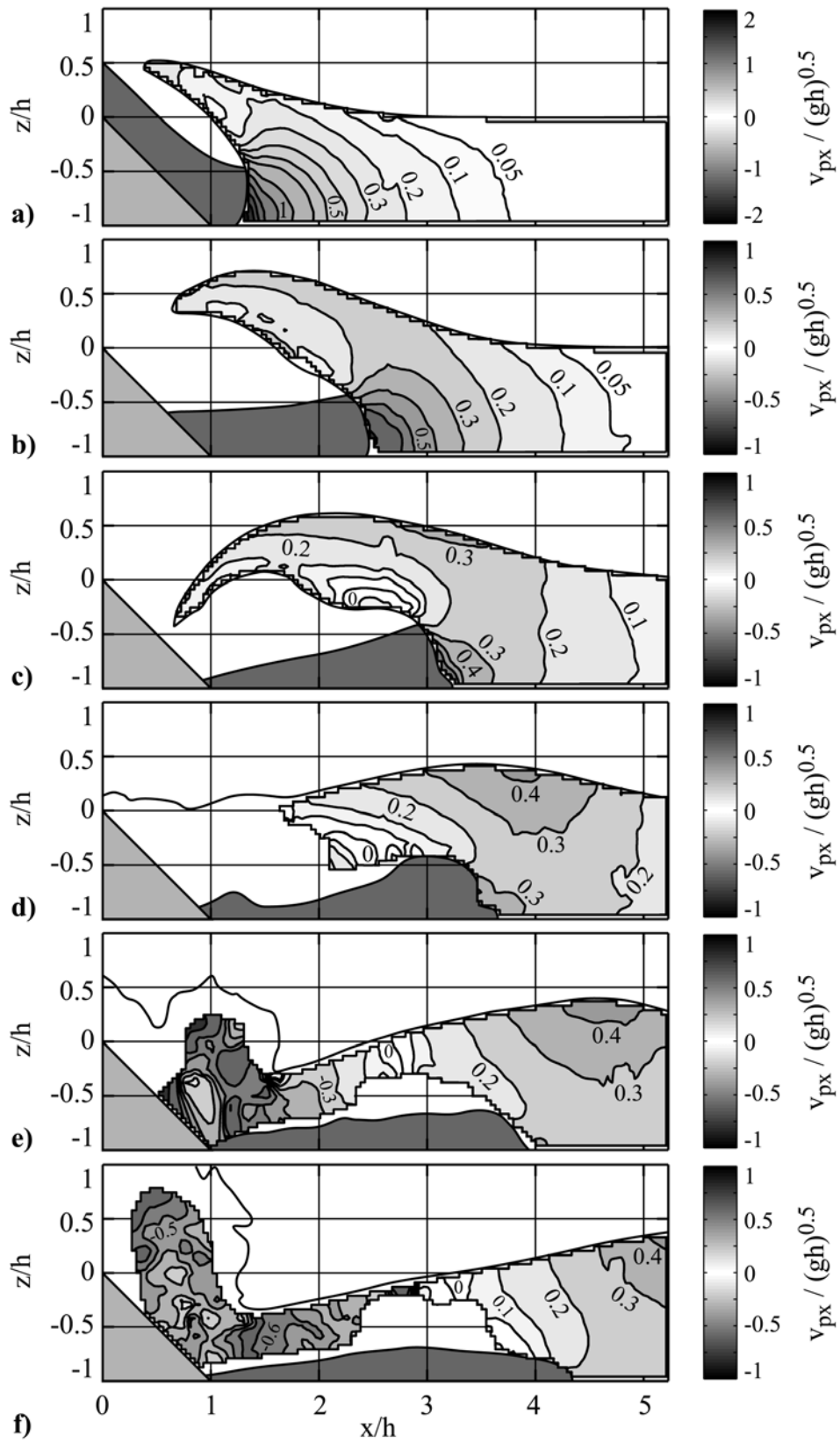
Figure 4.51 **Horizontal particle velocity** fields $v_{px}/\sqrt{gh}$: contours at 0, ± 0.05 , ± 0.1 , ± 0.2 , ± 0.3 , ± 0.4 , ± 0.5 , ± 0.6 , ± 0.8 , ± 1 , ± 1.2 , ± 1.4 , ± 1.6 , ± 1.8 , ± 2 ; experiments at **F** = 2.8, $V = 0.79$, $S = 0.34$, $h = 0.3\,\mathrm{m}$, $t\sqrt{g/h}$ =: **a)** 0.72, **b)** 1.48, **c)** 2.24, **d)** 3.01, **e)** 3.77, **f)** 4.53.
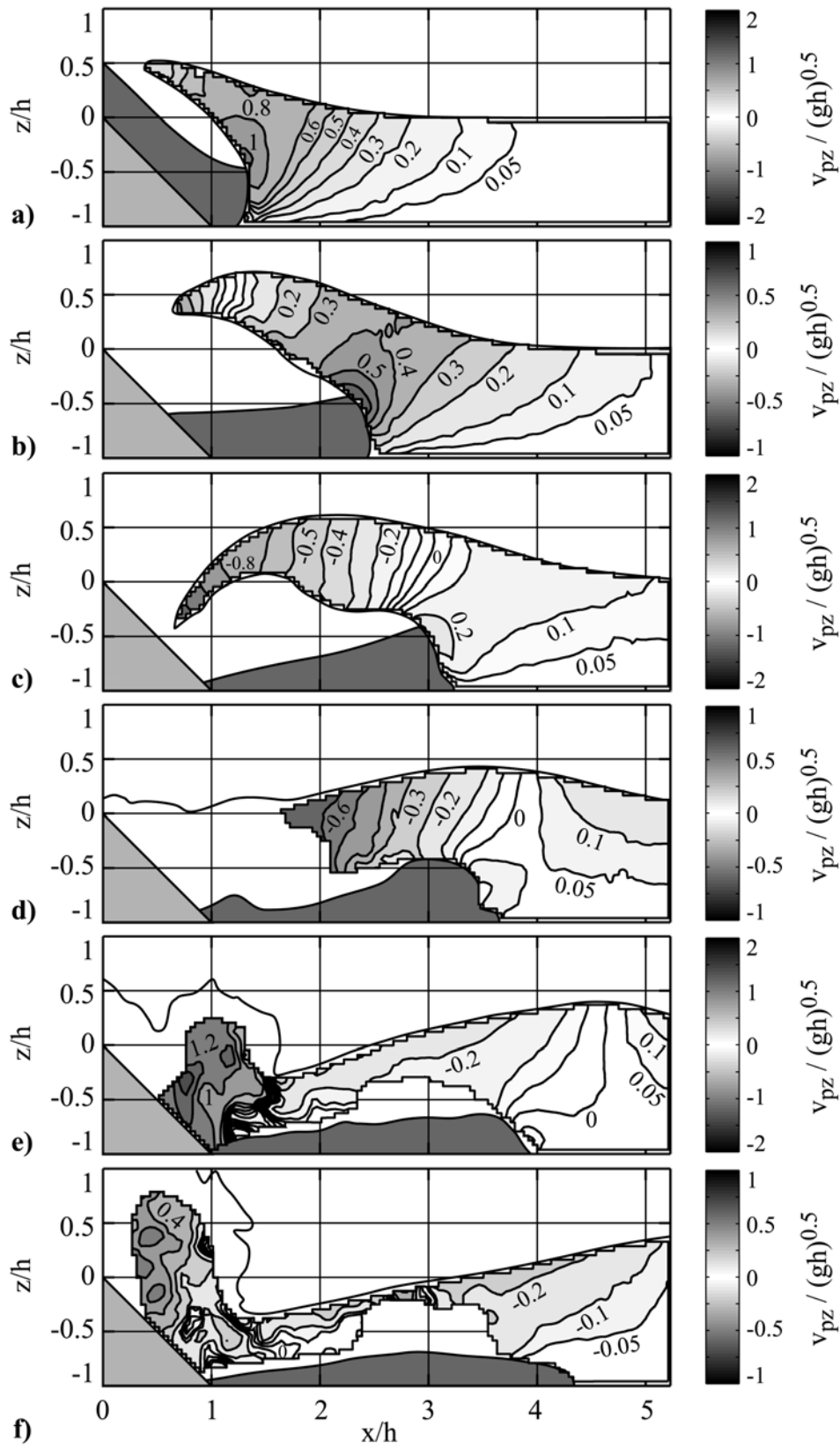
Figure 4.52 **Vertical particle velocity** fields $v_{pz}/\sqrt{gh}$: contours at 0, ± 0.05 , ± 0.1 , ± 0.2 , ± 0.3, ± 0.4, ± 0.5, ± 0.6, ± 0.8, ± 1, ± 1.2, ± 1.4, ± 1.6, ± 1.8, ± 2 ; experiments at **F** = 2.8, $V = 0.79$, $S = 0.34$, $h = 0.3\,\text{m}$, $t\sqrt{g/h} =$: **a)** 0.72, **b)** 1.48, **c)** 2.24, **d)** 3.01, **e)** 3.77, **f)** 4.53.
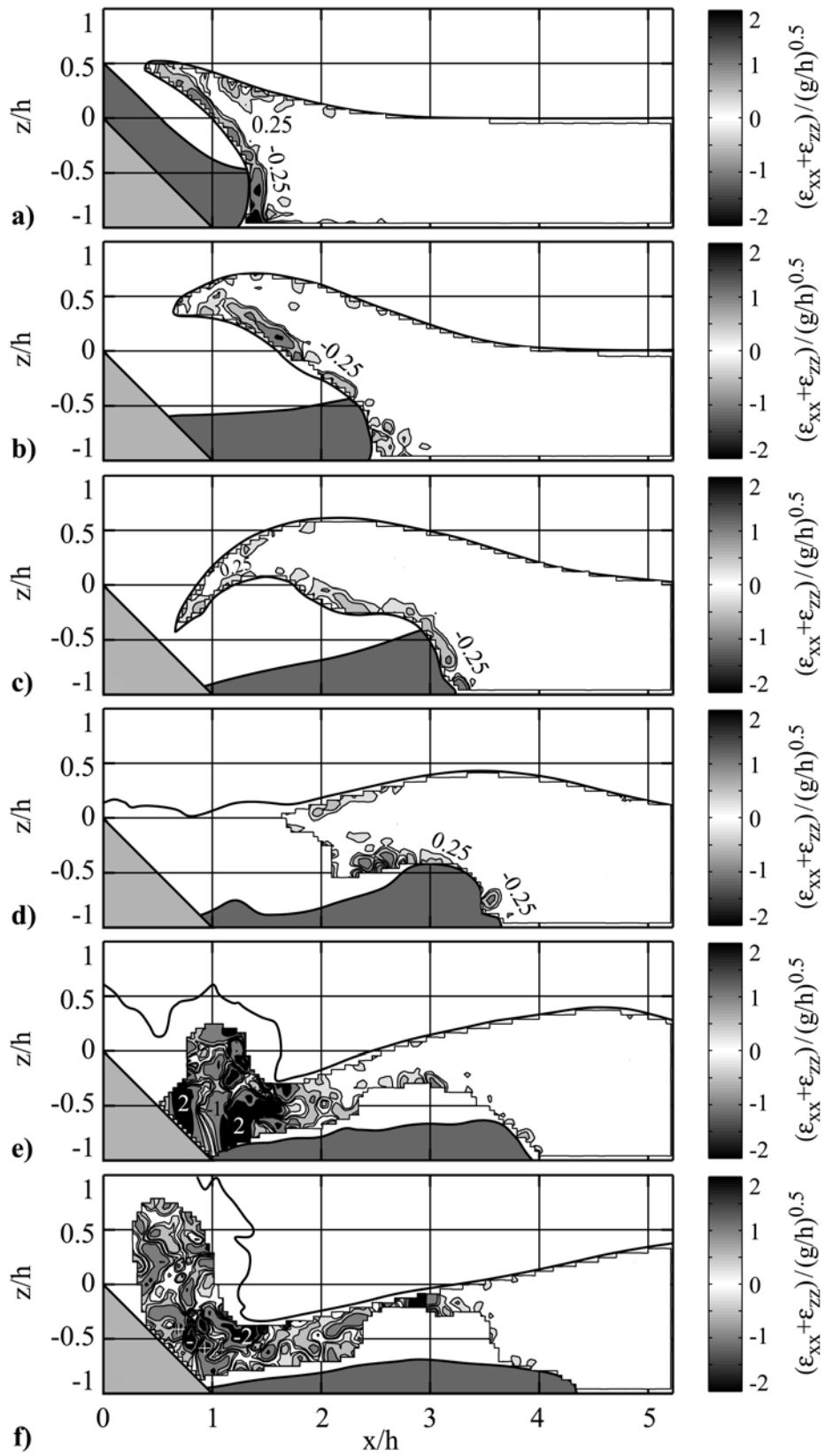
Figure 4.53 **2D-divergence** fields $(\varepsilon_{xx} + \varepsilon_{zz})/\sqrt{g/h}$ with contour levels at ± 0.25, ± 0.5, ± 1, ± 2; backward collapsing impact crater at **F** = 2.8, V = 0.79, S = 0.34, h = 0.3 m and recorded at $t\sqrt{g/h}$ =: **a)** 0.72, **b)** 1.48, **c)** 2.24, **d)** 3.01, **e)** 3.77, **f)** 4.53.
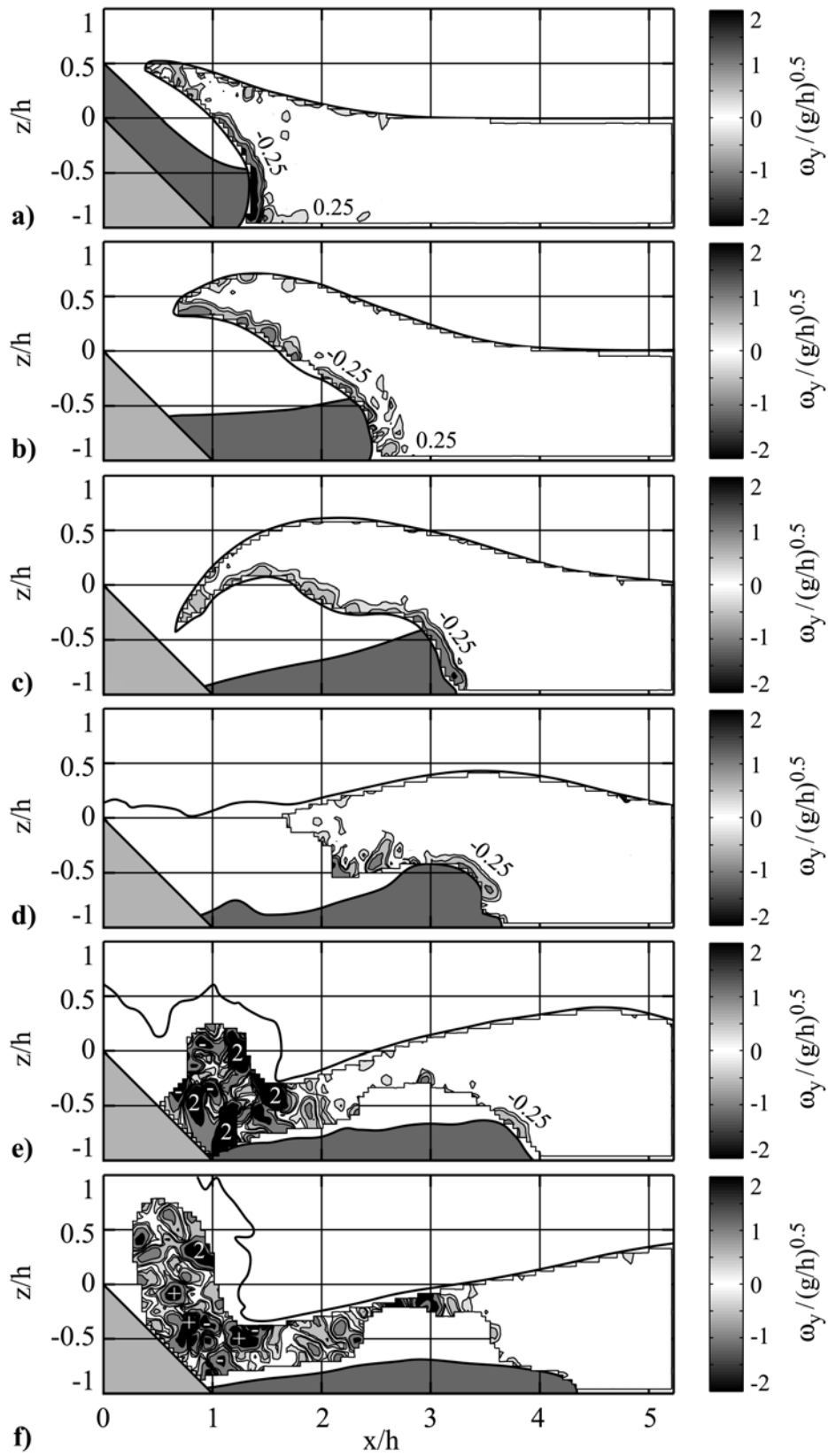
Figure 4.54 **Vorticity** fields $\omega_y/\sqrt{g/h}$ with contour levels at ± 0.25, ± 0.5, ± 1, ± 2; backward collapsing impact crater at **F** = 2.8, $V = 0.79$, $S = 0.34$, $h = 0.3$ m and recorded at $t\sqrt{g/h}$ =: **a)** 0.72, **b)** 1.48, **c)** 2.24, **d)** 3.01, **e)** 3.77, **f)** 4.53.
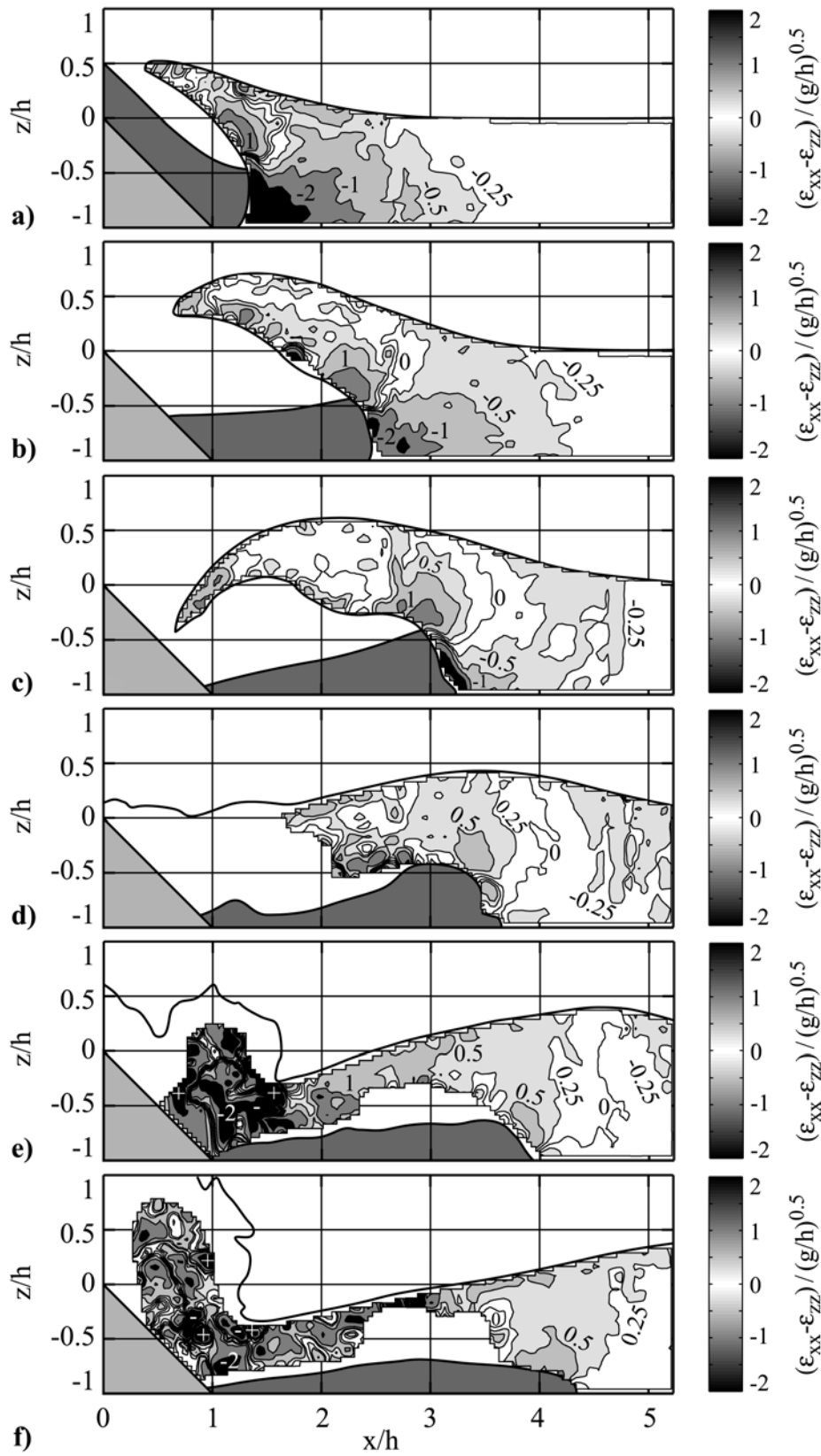
Figure 4.55 **Elongational strain** fields $(\varepsilon_{xx} - \varepsilon_{zz})/\sqrt{g/h}$ with contour levels at 0, ± 0.25, ± 0.5, ± 1, ± 2; backward collapsing impact crater at $\mathbf{F} = 2.8$, $V = 0.79$, $S = 0.34$, $h = 0.3\,\mathrm{m}$ and recorded at $t\sqrt{g/h} =:$ **a)** 0.72, **b)** 1.48, **c)** 2.24, **d)** 3.01, **e)** 3.77, **f)** 4.53.
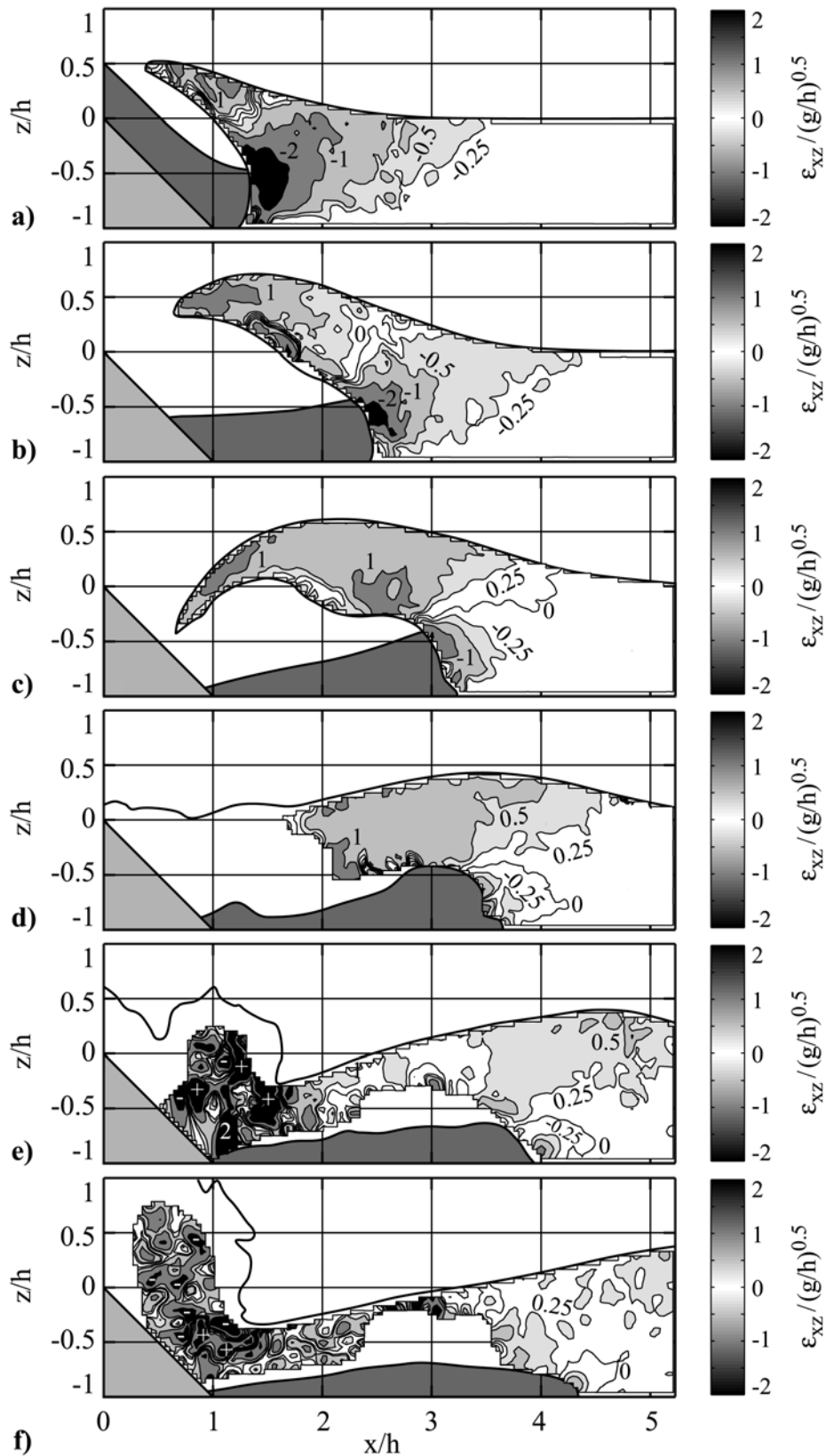
Figure 4.56 **Shear strain** fields $\varepsilon_{xz}/\sqrt{g/h}$ with contour levels at 0, ± 0.25, ± 0.5, ± 1, ± 2; backward collapsing impact crater at **F** $= 2.8$, $V = 0.79$, $S = 0.34$, $h = 0.3\,\mathrm{m}$ and recorded at $t\sqrt{g/h} =:$ **a)** 0.72, **b)** 1.48, **c)** 2.24, **d)** 3.01, **e)** 3.77, **f)** 4.53.

4.6.3 Outward collapsing impact crater

The backward and outward collapsing impact crater regimes were defined previously in [para 4.5.3]. The slide Froude number was the primary classification parameter. A characteristic example at the lower end of the outward collapsing crater regime is shown in Figs. 4.57 to 4.66. The only difference to the previous example of a backward collapsing impact crater was a small increase in Froude number from $\mathbf{F} = 2.8$ to $\mathbf{F} = 3.2$. A second example at the upper end of the outward collapsing crater regime with $\mathbf{F} = 4.1$ is shown in Figs. 4.67 to 4.76. The sets of figures include the original PIV-images, the velocity vector fields, the streamline plots, scalar fields of the velocity components and contour plots of the computed components of the deformation tensor. The selected sequences of original PIV recordings are shown in Figs. 4.57 and 4.67. The water flow around the penetrating landslide separated on the slide shoulder (Figs. 4.57 and 4.67a,b,c). The water was initially expelled upwards and outward by the entry of the landslide forming a water crater. The water crater exposed the ramp and the back of the landslide to the atmosphere. The displaced water volume obviously exceeded the landslide volume significantly. The water displacement volumes and rates were discussed in [para 4.5]. As the process of crater growth has terminated outward bulk motion of water was still present as a residuum. In contrast to the backward collapse no closure occurred in this case. The collapse occurred after the water crater reached its maximum size and the water rushed inwardly under the influence of gravity. The outward collapsing crater resulted in a main positive leading wave and negative base surge (Figs. 4.57 and 4.67d,e). The inrush of water tending to fill the crater from downstream can qualitatively be viewed as an example of the classical dam break problem (Stoker, 1957; Lauber, 1997). The backward motion was initiated at the bottom of the crater wall where the hydrostatic pressure was the largest. The leading wave crest was issued by the crater rim and propagated outward during the crater collapse (Figs. 4.57c,d,e and 4.67e). The run-up of the base surge on the inclined ramp and the subsequent run-down formed the secondary wave system.

The velocity vector fields and the streamline plots revealed the formation of a half saddle in the water uplift (Figs. 4.58, 4.59c,d,e and Figs. 4.68, 4.69d,e). The half saddle separated the outward from the inward flow. The largest velocities were measured locally around the slide front during slide penetration and in the splash (Figs. 4.60, and 4.70). The water particle velocity below the wave crests was only fractions of the shallow water wave velocity, but increased compared to the previous examples due to the increase in wave height. The largest negative values of the horizontal velocity components were observed in the inward rush and run-up along the inclined ramp during the collapse of the impact crater (Figs. 4.61d,e and 4.71e). The negative vertical velocities were observed at the beginning of the crater collapse along the crater walls (Figs. 4.62c,d and 4.72e). Contrary to the classical dam break released from rest, the water displaced by the landslide at no instant reached a state any where near a static uplift. The kinetic energy of the landslide imparted on the water body was only partially converted into the potential energy of the

uplift, whereas a significant part prevailed as kinetic energy in the form of the velocity field imposed onto the water body.

The in-plane divergence was roughly zero in the whole pure water flow area. Hence the fundamental assumption of the two dimensional model is confirmed (Figs. 4.63 and 4.73). Large divergence values were observed during the cavity collapse and the inward rush (Figs. 4.63and 4.73d,e). The divergence may have several fluid dynamic and measurement technique related causes. Slide granulate was sheared off during the penetration of the landslide. This granulate then detached from the crater wall and fell through the water during cavity collapse due to the larger density resulting in band with large negative divergence values (Figs. 4.73e). Noteworthy are the large negative divergence values along the slide front during the slide penetration (Figs. 4.63and 4.73a,b,c). These negative values may indicate the presence of a low velocity water flow through the granular slide, which was necessary for the slide detrainment.

The computed out-of-plane vorticity fields are shown in (Figs. 4.64 and 4.74). The water flow in the wave generation area and the flow below the outward propagating impulse waves were irrotational. Vorticity was observed on the slide surface due to the shear flow and in the mixing zone above the landslide deposit due to the dissipative turbulence. The PIV-data confirmed the assumption of irrotationality made by all analytical wave theories according to the Laplace equation. The largest vorticity values were measured in the inward rush and run-up (Figs. 4.64d,e). These values should be interpreted with caution due to the large divergence values and the high measurement noise induced by the massive phase mixing in that area.

The elongational and the shear strain fields are shown in Figs. 4.65, 4.66 and Figs. 4.75, 4.76, respectively. The largest negative elongational strains were computed in front of the penetrating landslides were the fluid cells are compressed along the horizontal x-axis and expanded vertically (Figs. 4.65 and 4.75a,b). Large positive elongational strains were measured during the crater collapse due to the stretching of the fluid cells along the x-axis (Figs. 4.65d,e and 4.75e). Large positive shear strain values in the wave field were encountered in the crater rim during collapse and below the wave crests (Figs. 4.66c,d,e and 4.76d,e). In front of the slide negative shear strains were observed when the water was uplifted by the slide (Figs. 4.66 and 4.76a,b,c), whereas positive values occurred at the impact of a thick slide (Figs. 4.76a). Both the elongational and the shear strain rates increased compared to the previous examples due to larger wave heights.
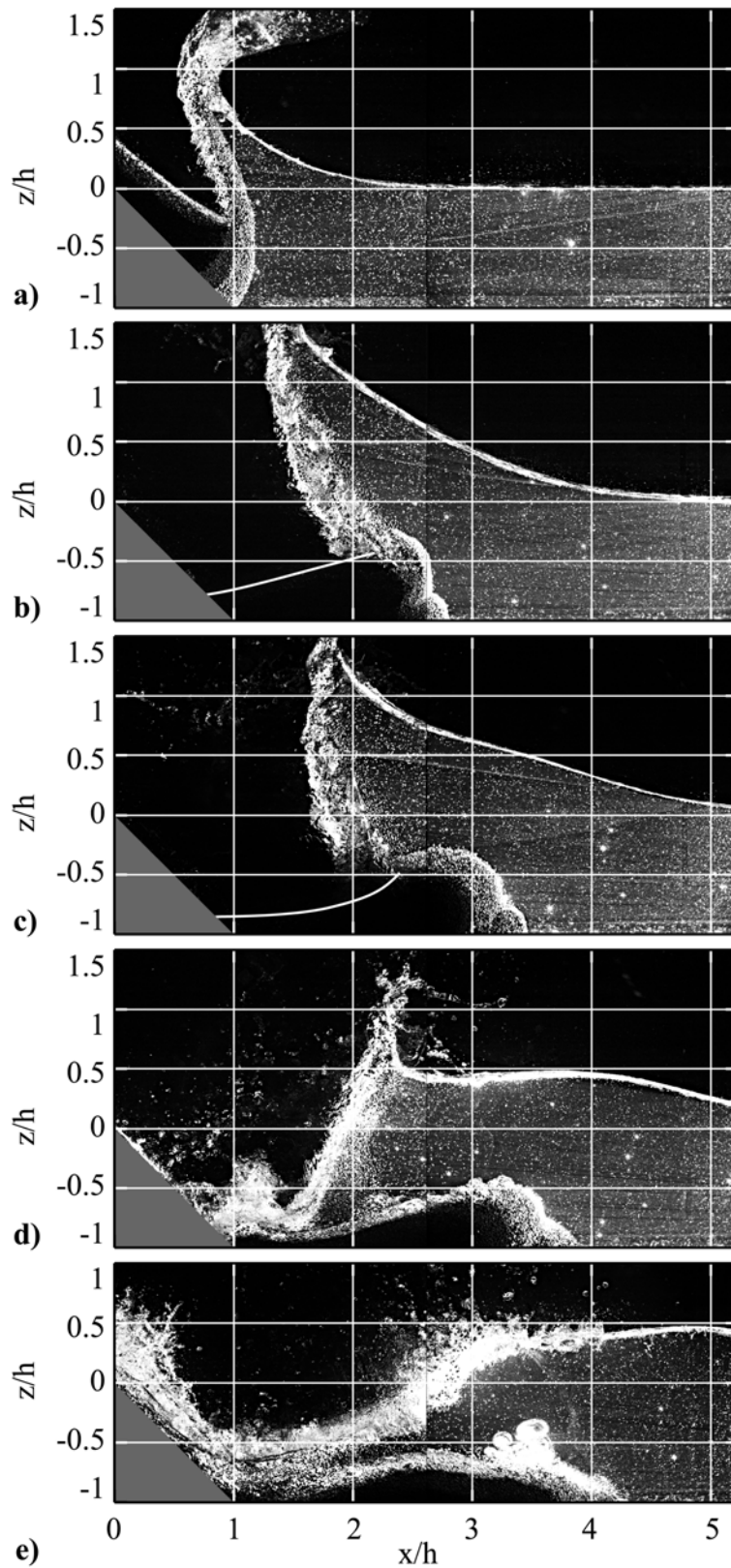
Figure 4.57 **Outward collapsing impact crater** PIV-images of two mounted experiments at
$F = 3.2$, $V = 0.79$, $S = 0.31$, $h = 0.3\,\mathrm{m}$ and recorded at: **a)** $t\sqrt{g/h} = 0.58$, **b)** $t\sqrt{g/h} = 1.73$,
c) $t\sqrt{g/h} = 2.49$, **d)** $t\sqrt{g/h} = 3.25$, **e)** $t\sqrt{g/h} = 4.01$.
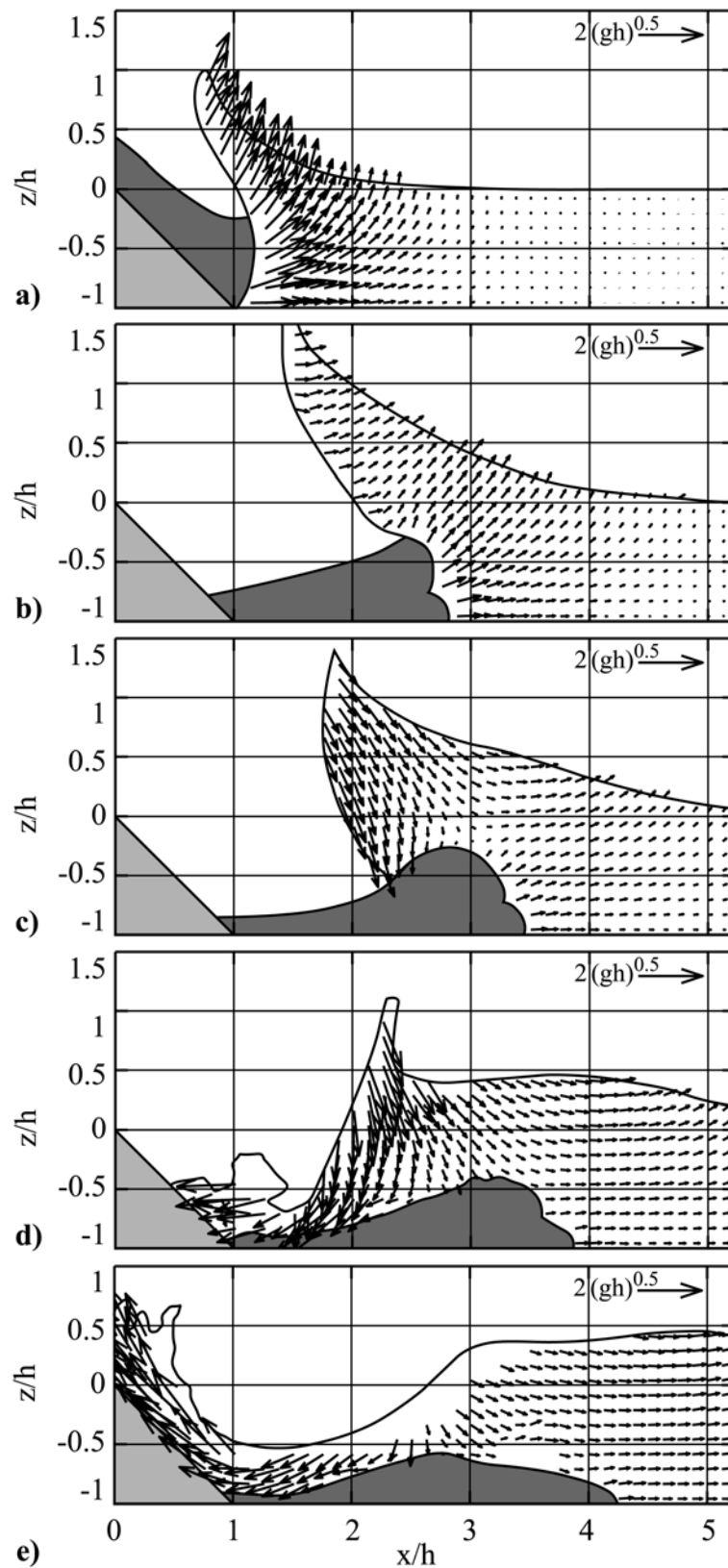
Figure 4.58 **Velocity vector fields** of two mounted outward collapsing impact crater experiments at $\mathbf{F} = 3.2$, $V = 0.79$, $S = 0.31$, $h = 0.3\,\mathrm{m}$ and recorded at: **a)** $t\sqrt{g/h} = 0.58$, **b)** $t\sqrt{g/h} = 1.73$, **c)** $t\sqrt{g/h} = 2.49$, **d)** $t\sqrt{g/h} = 3.25$, **e)** $t\sqrt{g/h} = 4.01$.
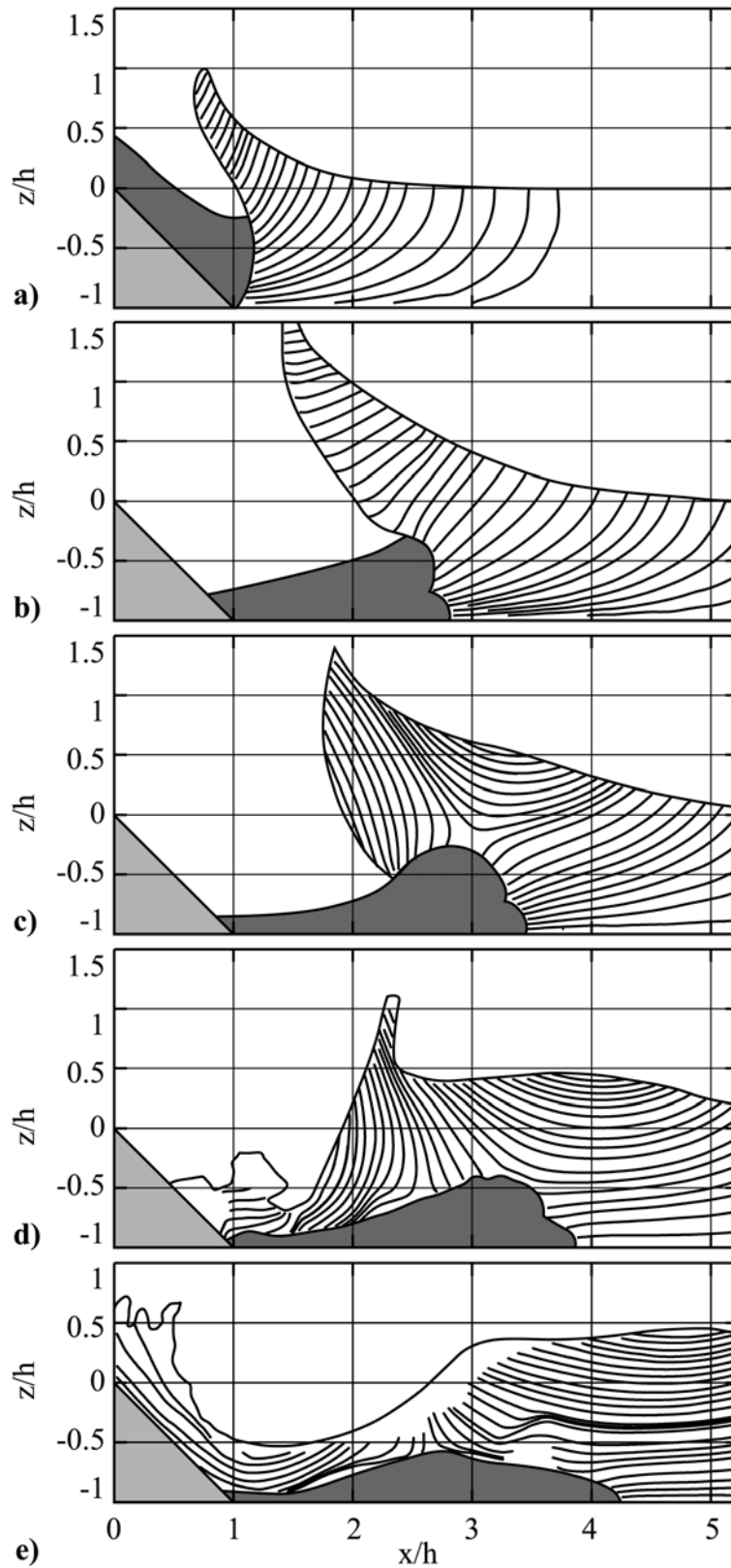
Figure 4.59 **Streamlines** of two mounted outward collapsing impact crater experiments at **F** = 3.2, V = 0.79, S = 0.31, h = 0.3 m and recorded at: **a)** $t\sqrt{g/h}$ = 0.58, **b)** $t\sqrt{g/h}$ = 1.73, **c)** $t\sqrt{g/h}$ = 2.49, **d)** $t\sqrt{g/h}$ = 3.25, **e)** $t\sqrt{g/h}$ = 4.01.
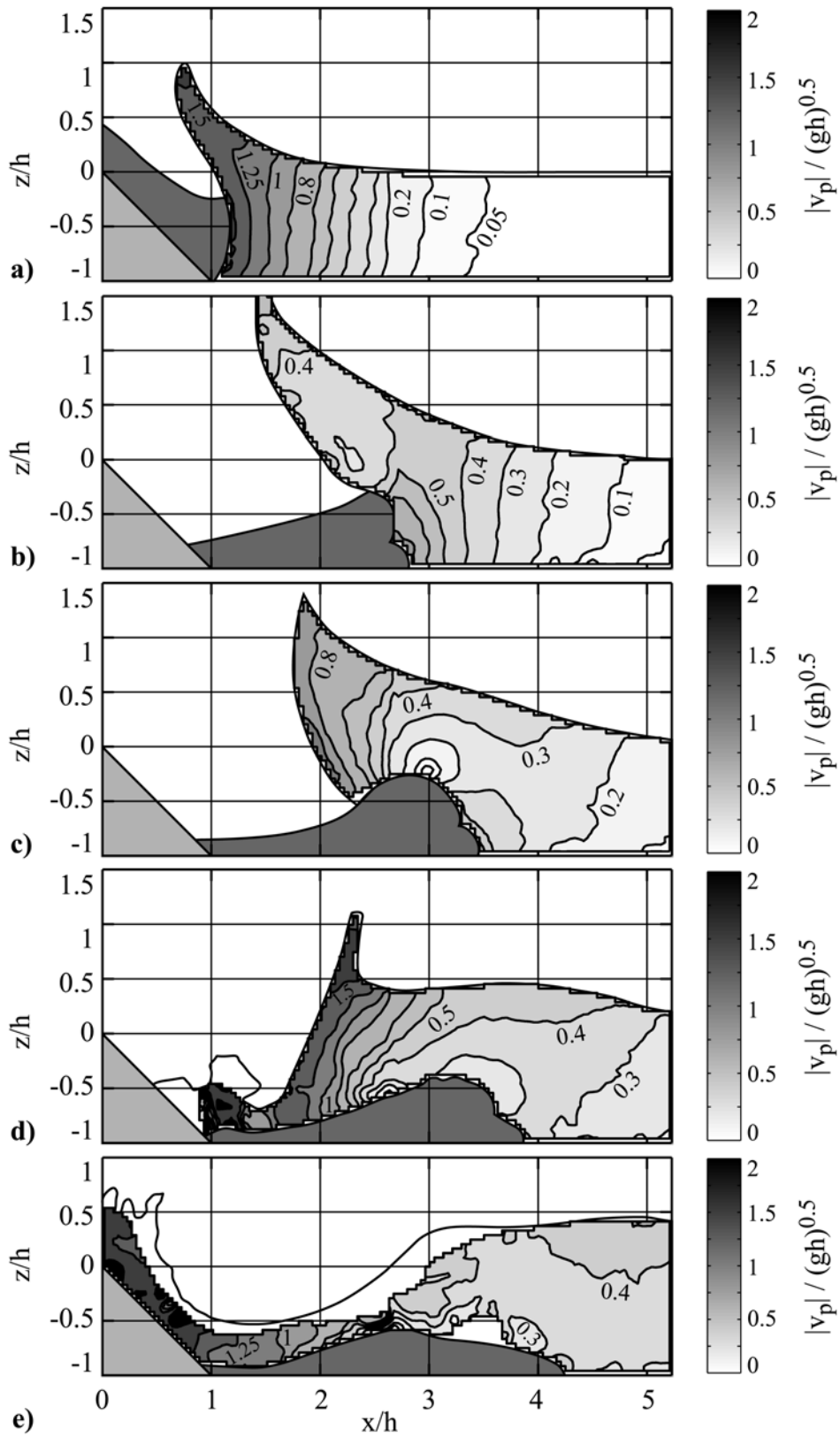
Figure 4.60 **Absolute particle velocity** fields $|v_p|/\sqrt{gh}$ with contour levels at 0.05, 0.1, 0.2, 0.3, 0.4, 0.5, 0.6, 0.8, 1, 1.25, 1.5, 2; outward collapsing crater at **F** = 3.2, V = 0.79, S = 0.31, h = 0.3 m and recorded at $t\sqrt{g/h}$ =: **a)** 0.58, **b)** 1.73, **c)** 2.49, **d)** 3.25, **e)** 4.01.
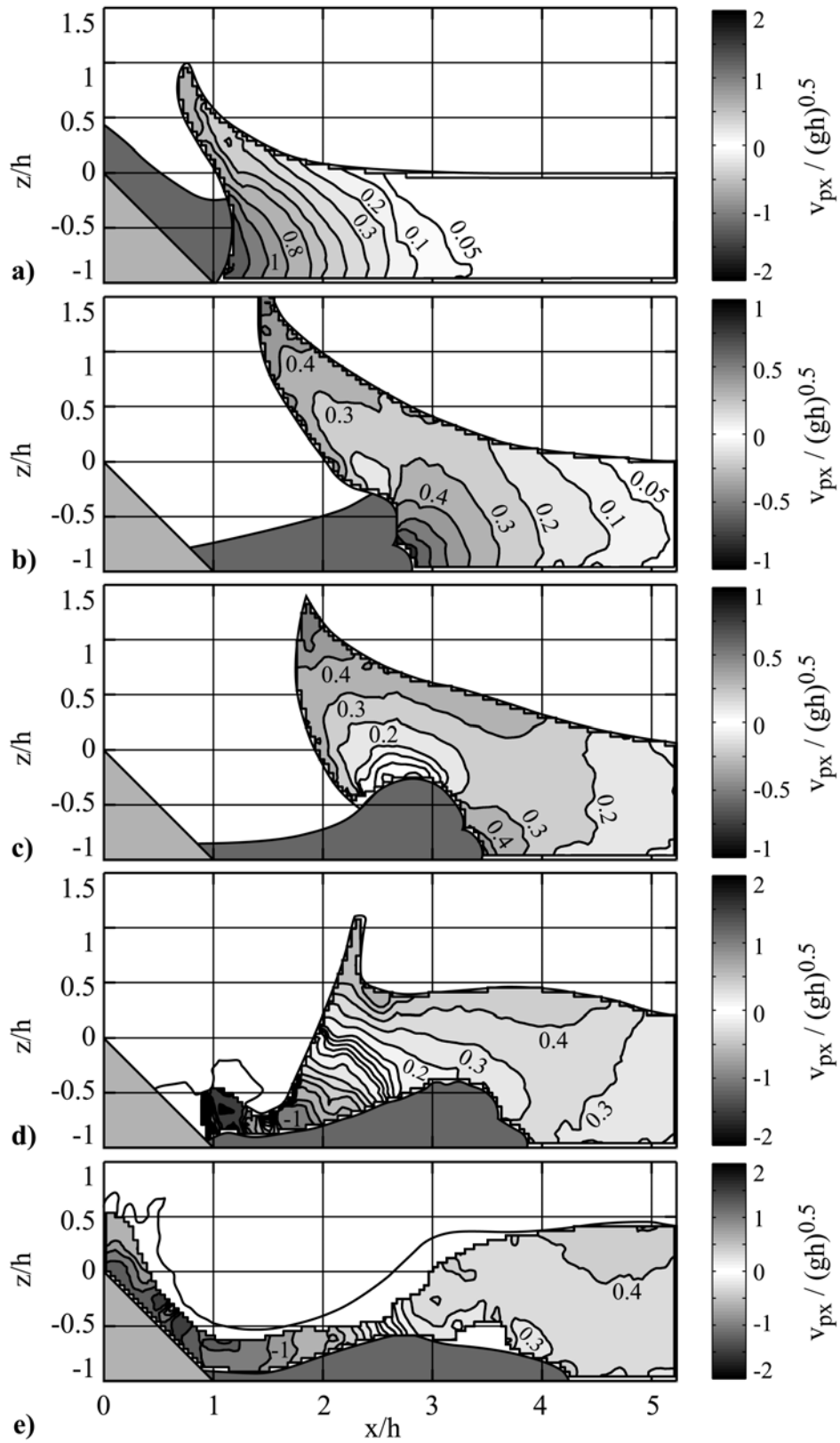
Figure 4.61 **Horizontal particle velocity** fields $v_{px}/\sqrt{gh}$ with contour levels at 0, ± 0.05, ± 0.1, ± 0.2, ± 0.3, ± 0.4, ± 0.5, ± 0.6, ± 0.8, ± 1, ± 1.25, ± 1.5, ± 2; outward collapsing crater at $\mathbf{F} = 3.2$, $V = 0.79$, $S = 0.31$, $h = 0.3\,\text{m}$ and $t\sqrt{g/h} =:$ **a)** 0.58, **b)** 1.73, **c)** 2.49, **d)** 3.25, **e)** 4.01.
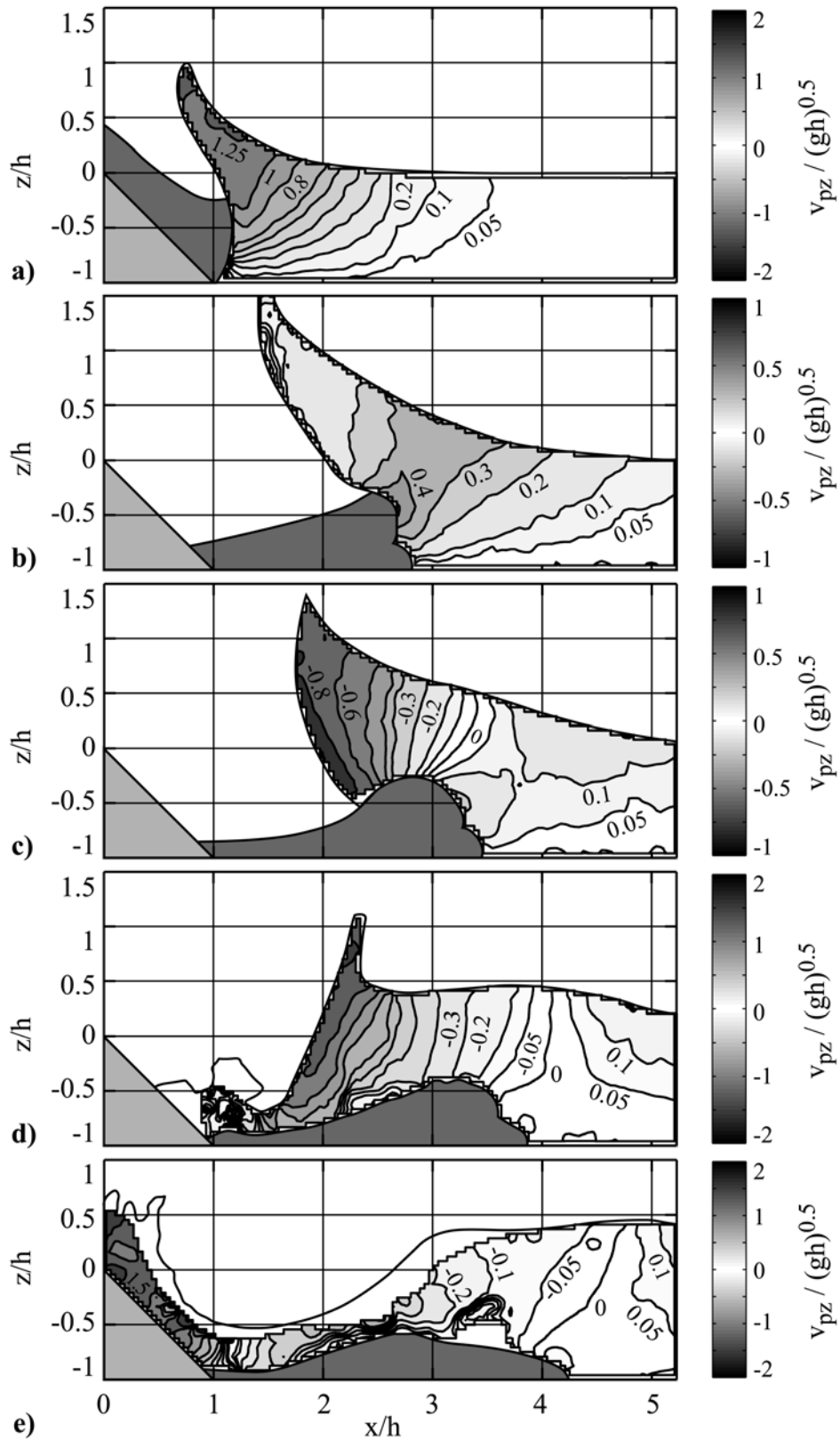
Figure 4.62 **Vertical particle velocity** fields $v_{pz}/\sqrt{gh}$ with contour levels at 0, ±0.05, ±0.1, ±0.2, ±0.3, ±0.4, ±0.5, ±0.6, ±0.8, ±1, ±1.25, ±1.5, ±2; outward collapsing crater at **F** = 3.2, $V = 0.79$, $S = 0.31$, $h = 0.3\,\mathrm{m}$ and $t\sqrt{g/h}$ =: **a)** 0.58, **b)** 1.73, **c)** 2.49, **d)** 3.25, **e)** 4.01.
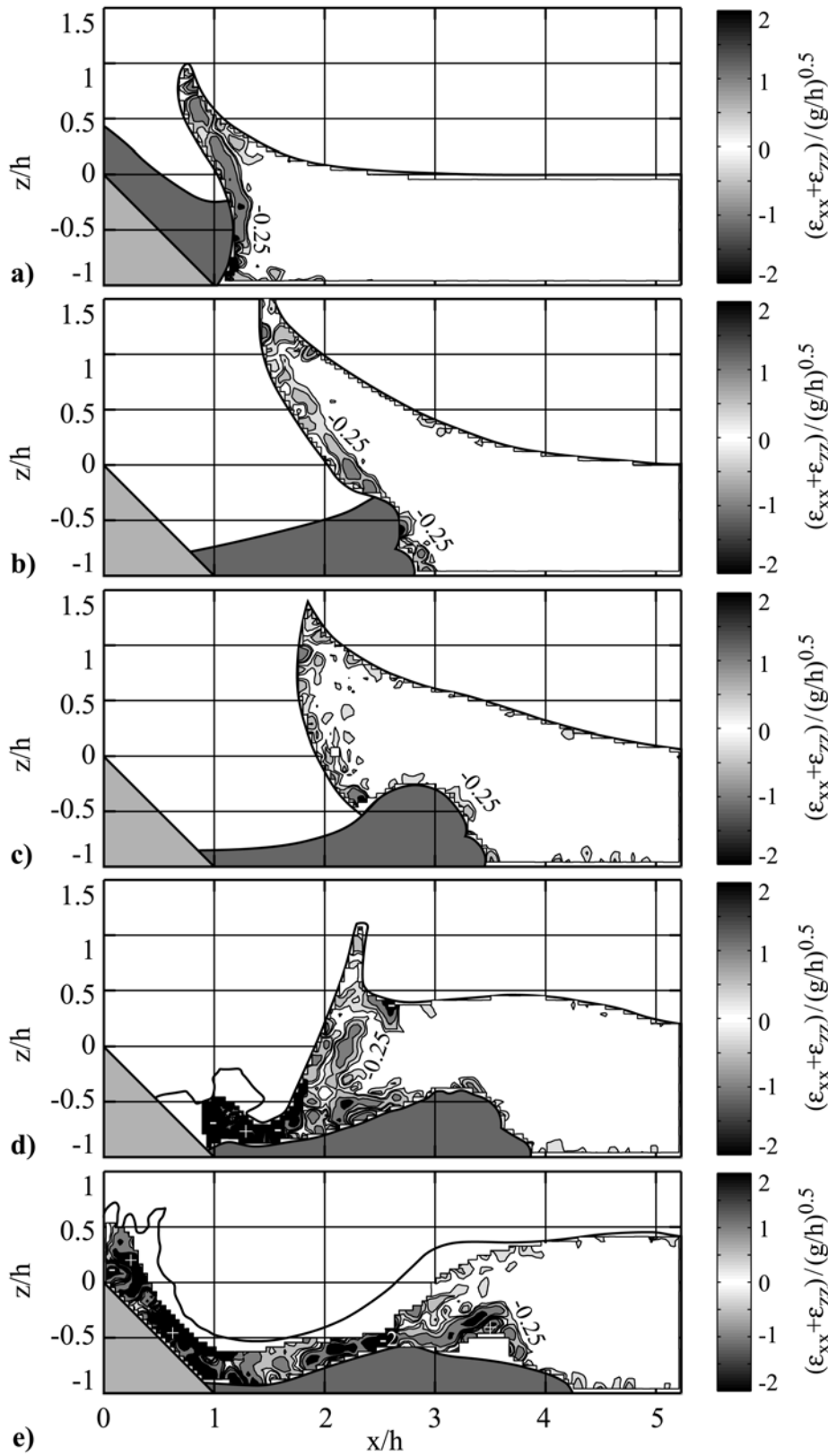
Figure 4.63 **2D-divergence** fields $(\varepsilon_{xx} + \varepsilon_{zz})/\sqrt{g\,h}$ with contour levels at ± 0.25, ± 0.5, ± 1, ± 2; outward collapsing crater at **F** = 3.2, $V = 0.79$, $S = 0.31$, $h = 0.3\,\mathrm{m}$ and recorded at $t\sqrt{g\,/h} =:$ **a)** 0.58, **b)** 1.73, **c)** 2.49, **d)** 3.25, **e)** 4.01.
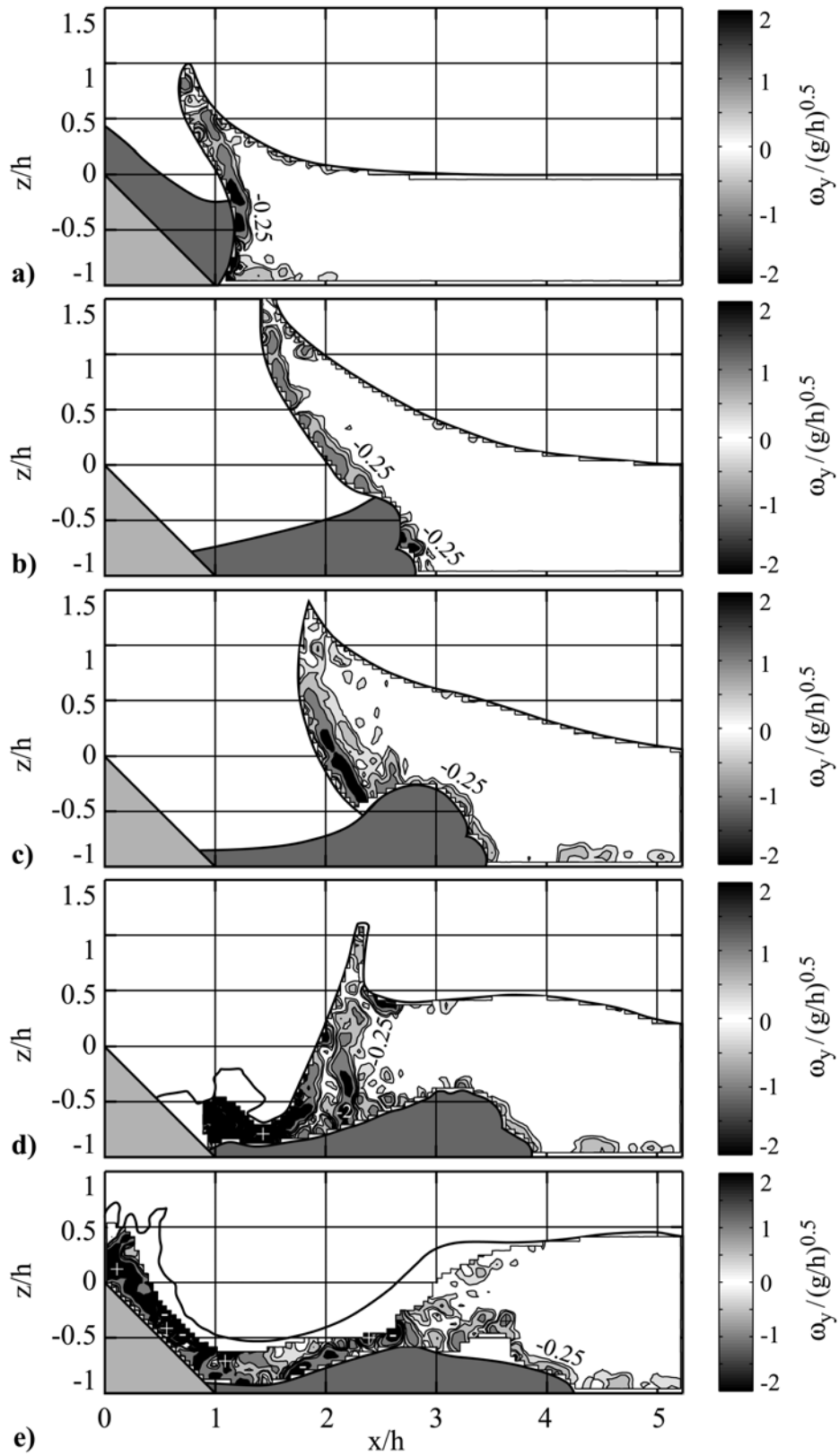
Figure 4.64 **Vorticity** fields $\omega_y/\sqrt{g/h}$ with contour levels at ± 0.25, ± 0.5, ± 1, ± 2; outward collapsing crater at $\mathbf{F} = 3.2$, $V = 0.79$, $S = 0.31$, $h = 0.3\,\mathrm{m}$ and recorded at $t\sqrt{g/h}$ =: **a)** 0.58, **b)** 1.73, **c)** 2.49, **d)** 3.25, **e)** 4.01.
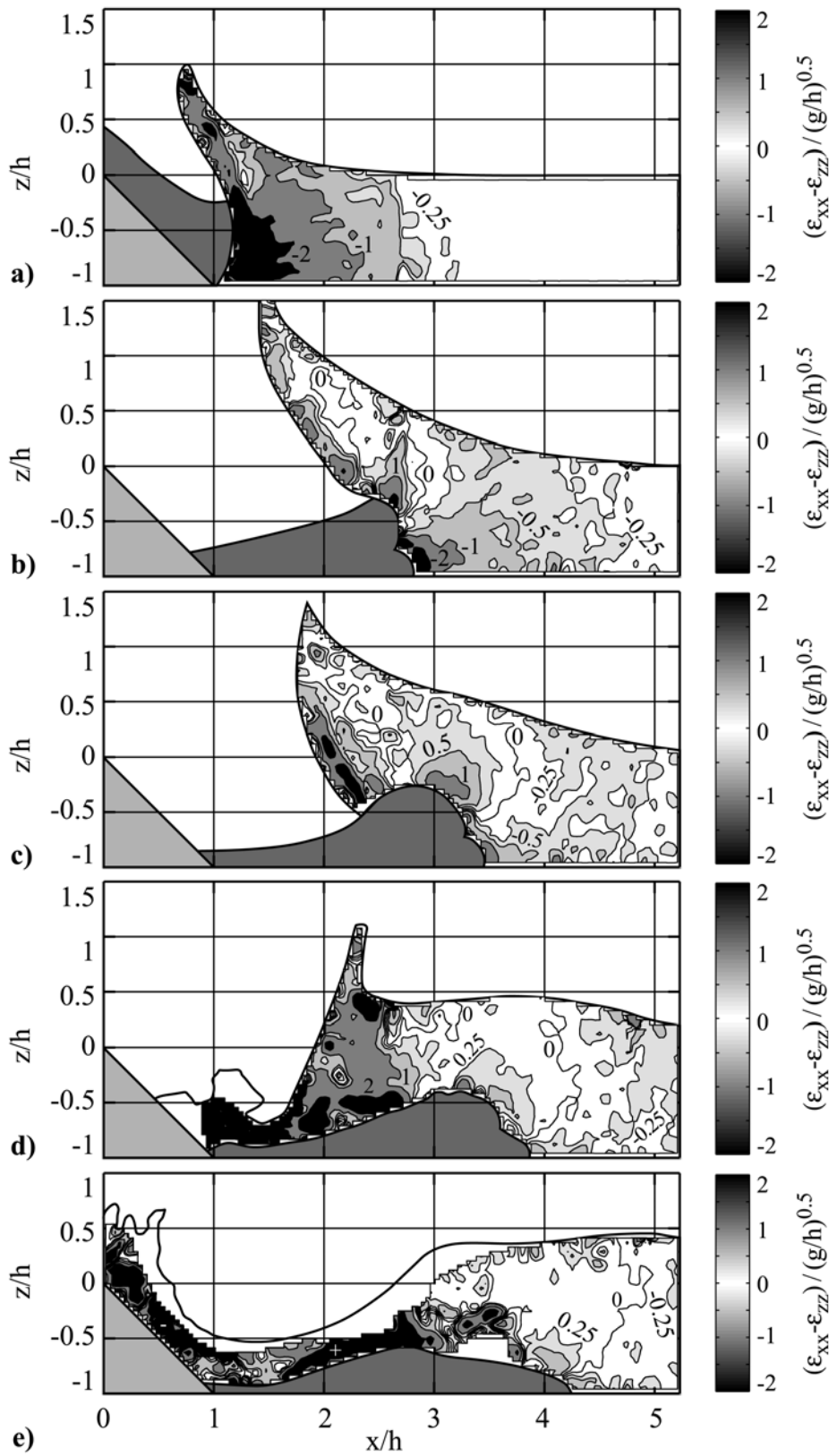
Figure 4.65 **Elongational strain** fields $(\varepsilon_{xx} - \varepsilon_{zz})/\sqrt{g/h}$ with contour levels at 0, ± 0.25, ± 0.5, ± 1, ± 2; outward collapsing crater at **F** = 3.2, $V = 0.79$, $S = 0.31$, $h = 0.3\,\text{m}$ and recorded at $t\sqrt{g/h} =$: **a)** 0.58, **b)** 1.73, **c)** 2.49, **d)** 3.25, **e)** 4.01.
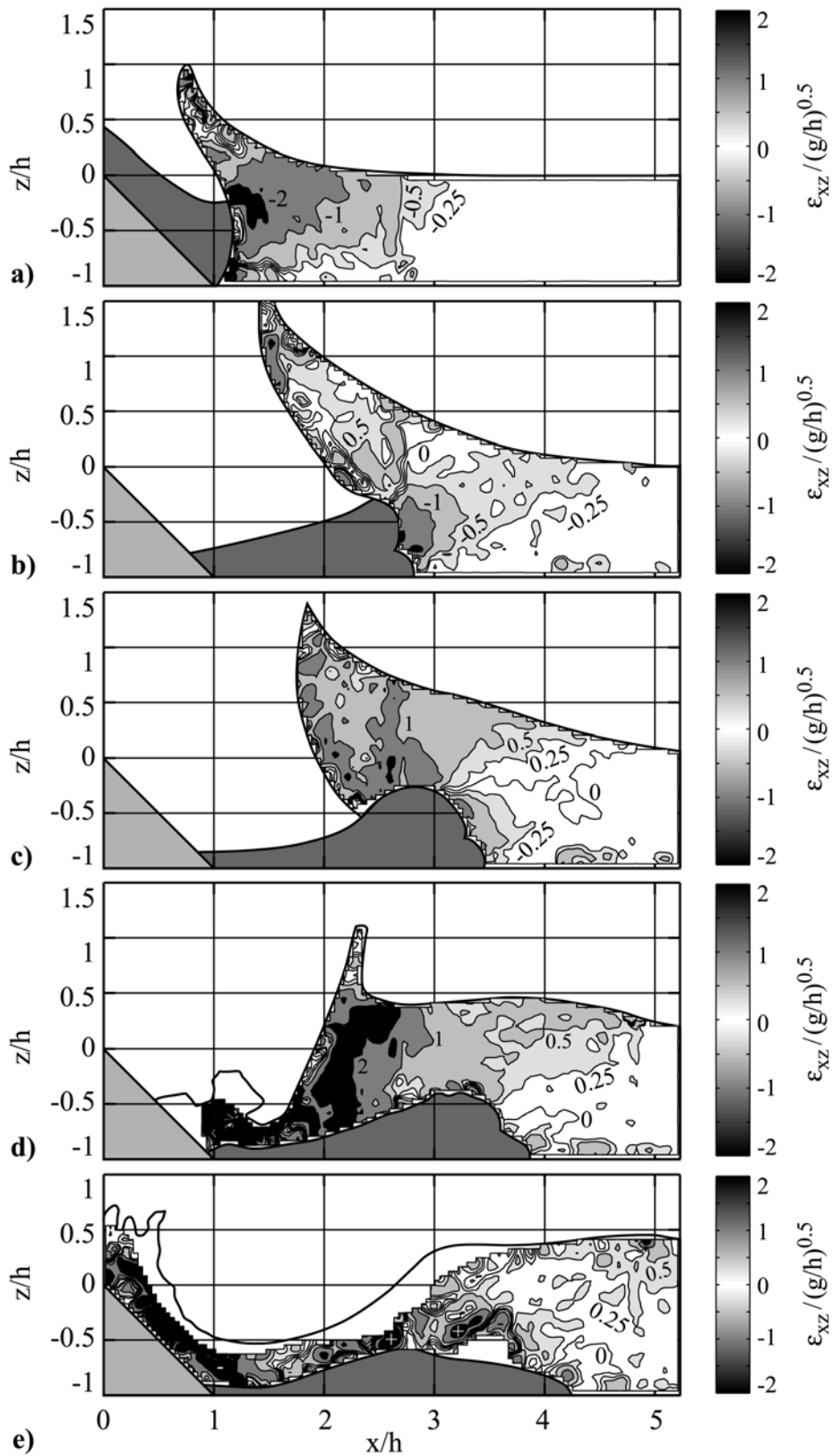
Figure 4.66 **Shear strain** fields $\varepsilon_{xz}/\sqrt{g/h}$ with contour levels at 0, ± 0.25, ± 0.5, ± 1, ± 2; outward collapsing crater at $\mathbf{F} = 3.2$, $V = 0.79$, $S = 0.31$, $h = 0.3\,\mathrm{m}$ and recorded at $t\sqrt{g/h} =:$ **a)** 0.58, **b)** 1.73, **c)** 2.49, **d)** 3.25, **e)** 4.01.
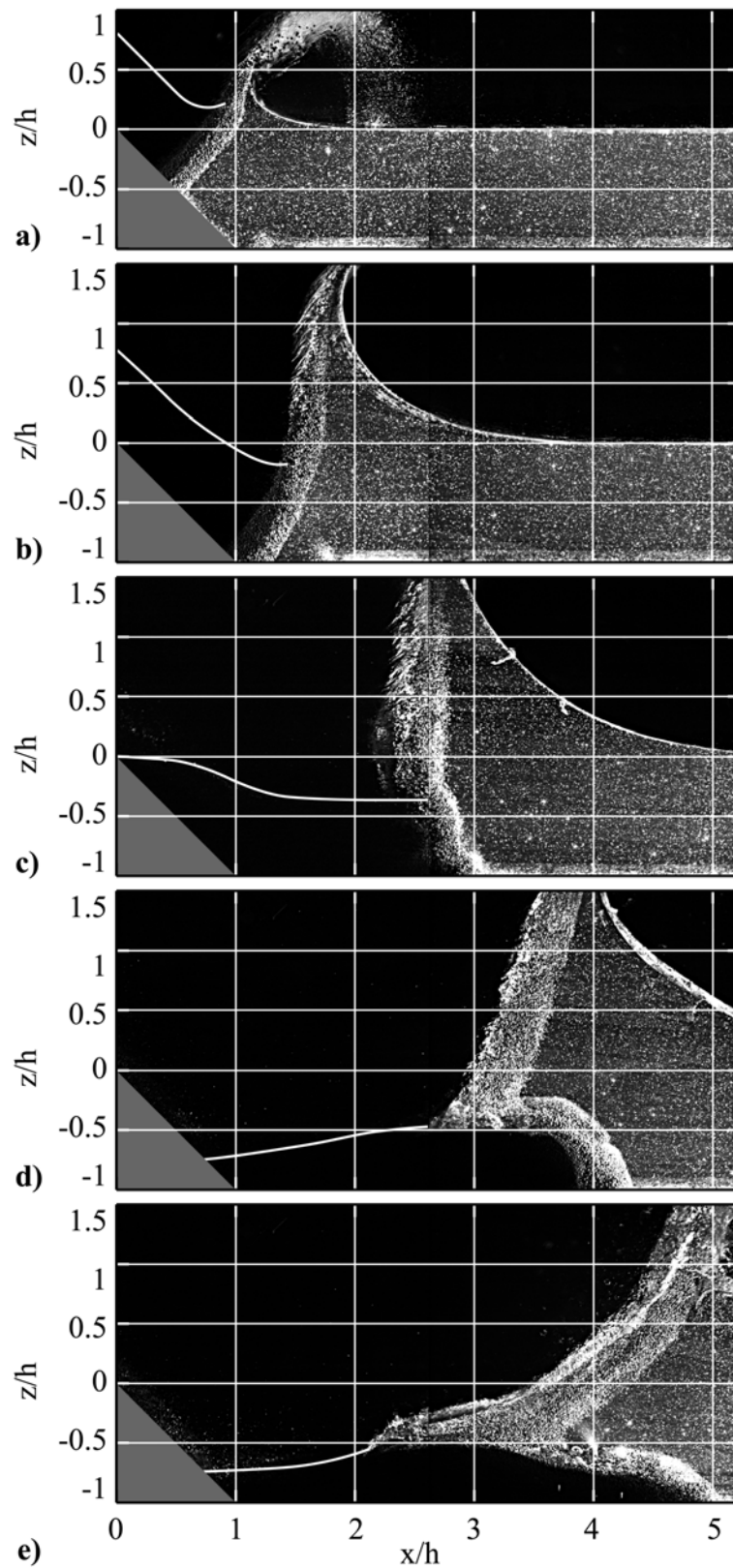
Figure 4.67 **Outward collapsing impact crater** PIV-images of two mounted experiments at $F = 4.1$, $V = 1.57$, $S = 0.56$, $h = 0.3$m and recorded at: **a)** $t\sqrt{g/h} = 0.18$, **b)** $t\sqrt{g/h} = 0.56$, **c)** $t\sqrt{g/h} = 1.33$, **d)** $t\sqrt{g/h} = 2.47$, **e)** $t\sqrt{g/h} = 3.61$.
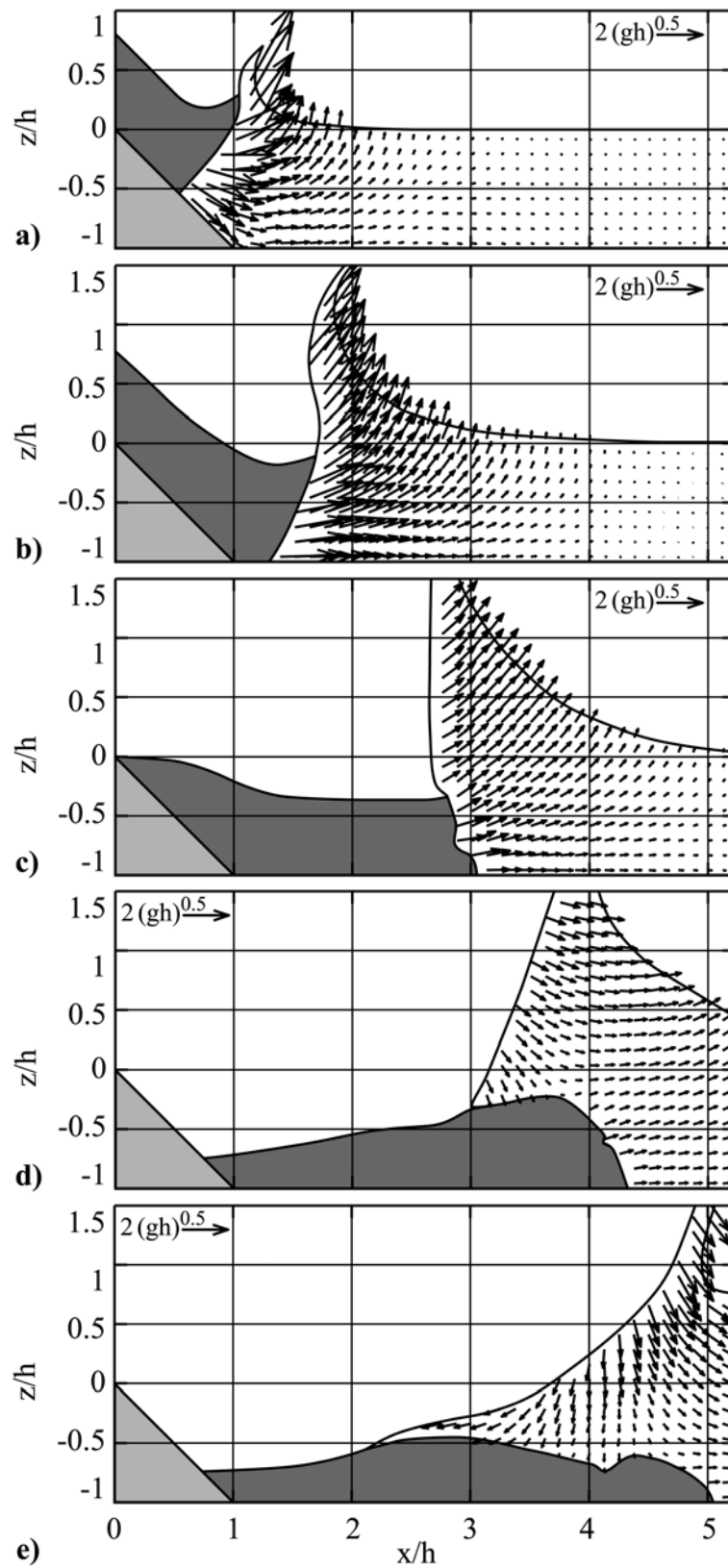
Figure 4.68 **Velocity vector fields** of two mounted outward collapsing impact crater experiments at **F** = 4.1, $V = 1.57$, $S = 0.56$, $h = 0.3\,\text{m}$ and recorded at: **a)** $t\sqrt{g/h} = 0.18$, **b)** $t\sqrt{g/h} = 0.56$, **c)** $t\sqrt{g/h} = 1.33$, **d)** $t\sqrt{g/h} = 2.47$, **e)** $t\sqrt{g/h} = 3.61$.
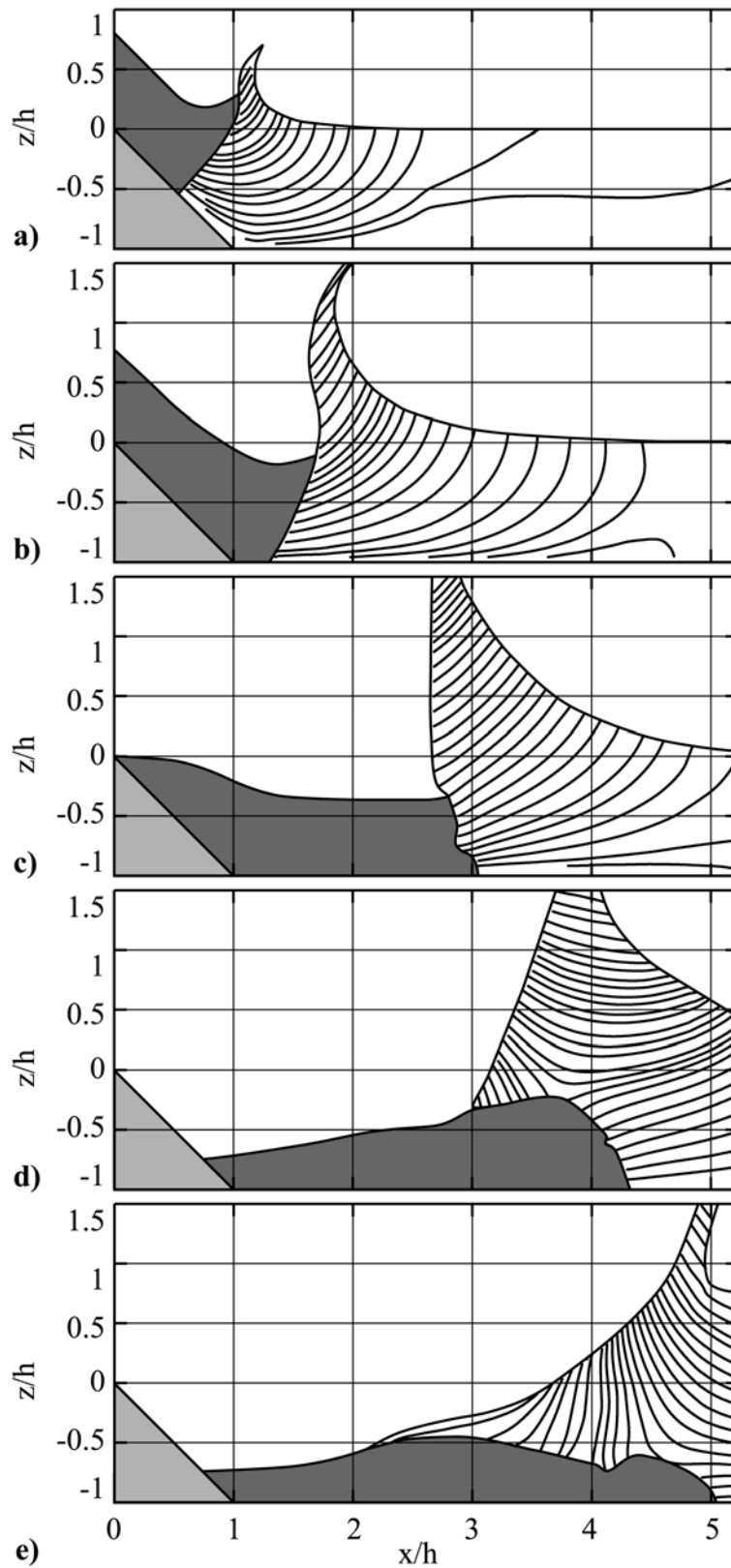
Figure 4.69 **Streamlines** of two mounted outward collapsing impact crater experiments at **F** = 4.1, V = 1.57, S = 0.56, h = 0.3m and recorded at: **a)** $t\sqrt{g/h} = 0.18$, **b)** $t\sqrt{g/h} = 0.56$, **c)** $t\sqrt{g/h} = 1.33$, **d)** $t\sqrt{g/h} = 2.47$, **e)** $t\sqrt{g/h} = 3.61$.
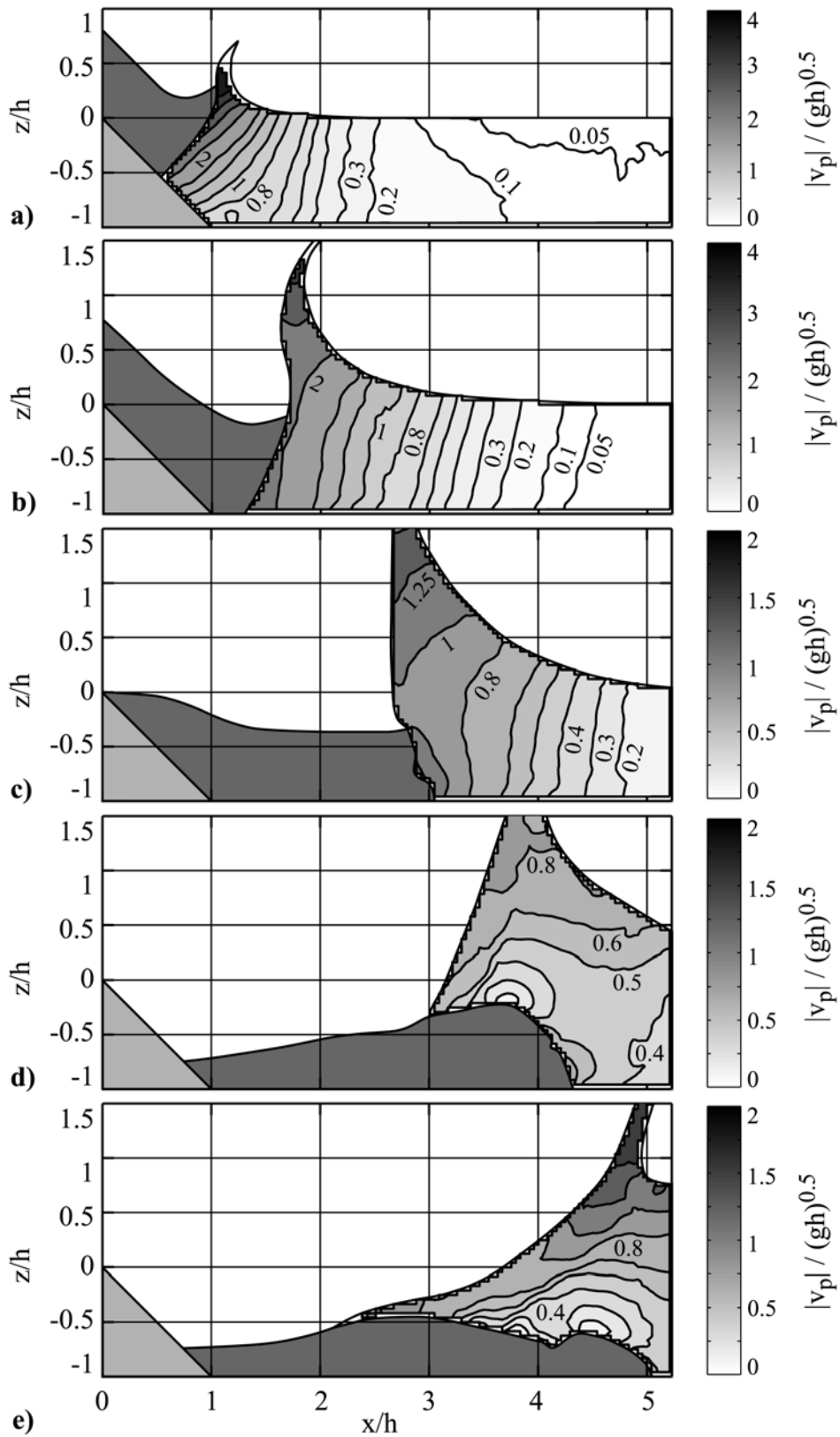
Figure 4.70 **Absolute particle velocity** fields $\left|v_p\right|/\sqrt{gh}$ with contour levels at 0.05, 0.1, 0.2, 0.3, 0.4, 0.5, 0.6, 0.8, 1, 1.25, 1.5, 2, 2.5, 3, 3.5, 4; outward collapsing crater at **F** = 4.1, V = 1.57, S = 0.56, h = 0.3 m and recorded at $t\sqrt{g/h}$ =: **a)** 0.18, **b)** 0.56, **c)** 1.33, **d)** 2.47, **e)** 3.61.
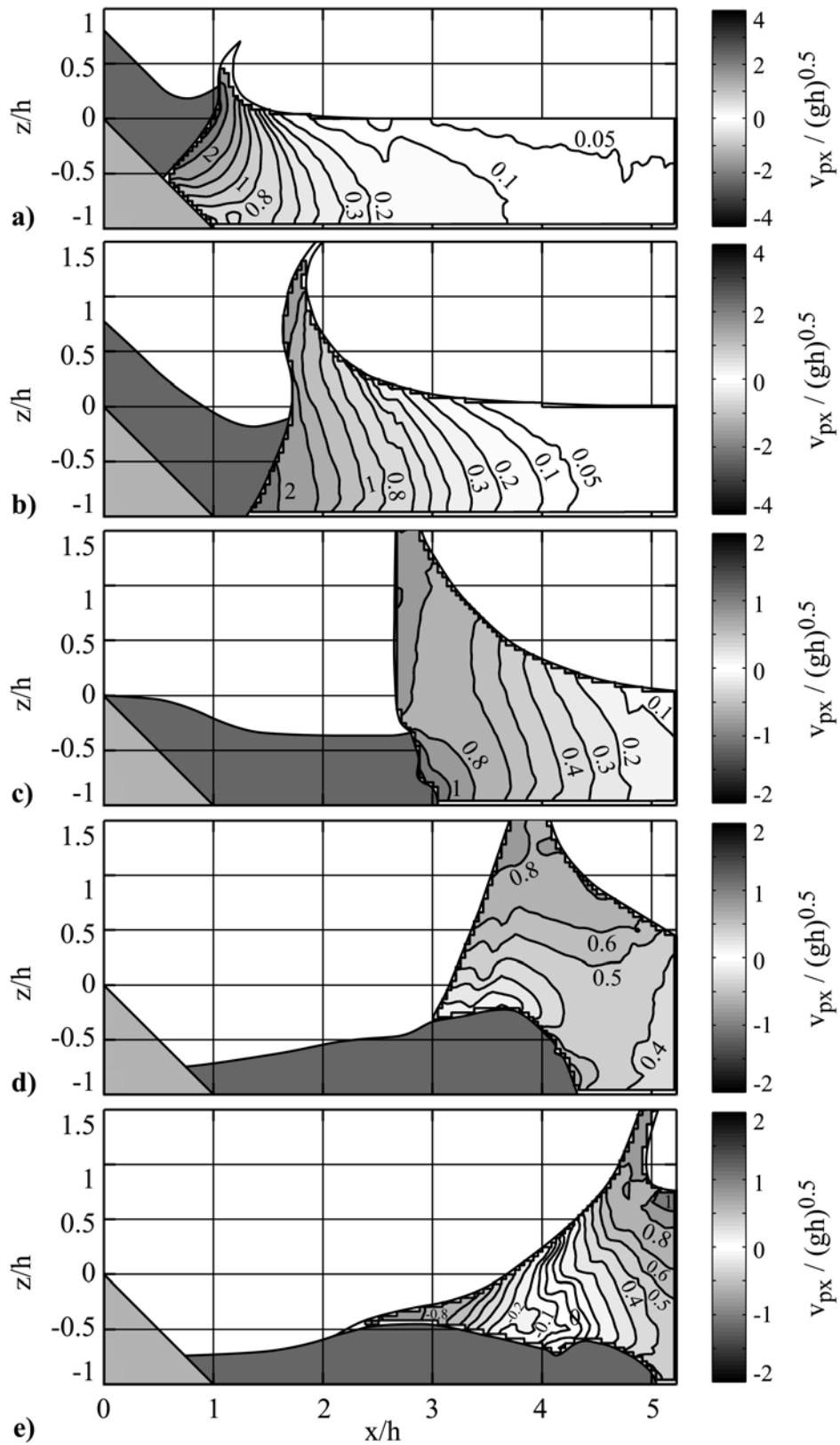
Figure 4.71 **Horizontal particle velocity** fields $v_{px}/\sqrt{gh}$: contours at 0, ±0.05, ±0.1, ±0.2, ±0.3, ±0.4, ±0.5, ±0.6, ±0.8, ±1, ±1.25, ±1.5, ±2, ±2.5, ±3, ±3.5, ±4; experiments at **F** $= 4.1$, $V = 1.57$, $S = 0.56$, $h = 0.3$ m and $t\sqrt{g/h}$ =: **a)** 0.18, **b)** 0.56, **c)** 1.33, **d)** 2.47, **e)** 3.61.
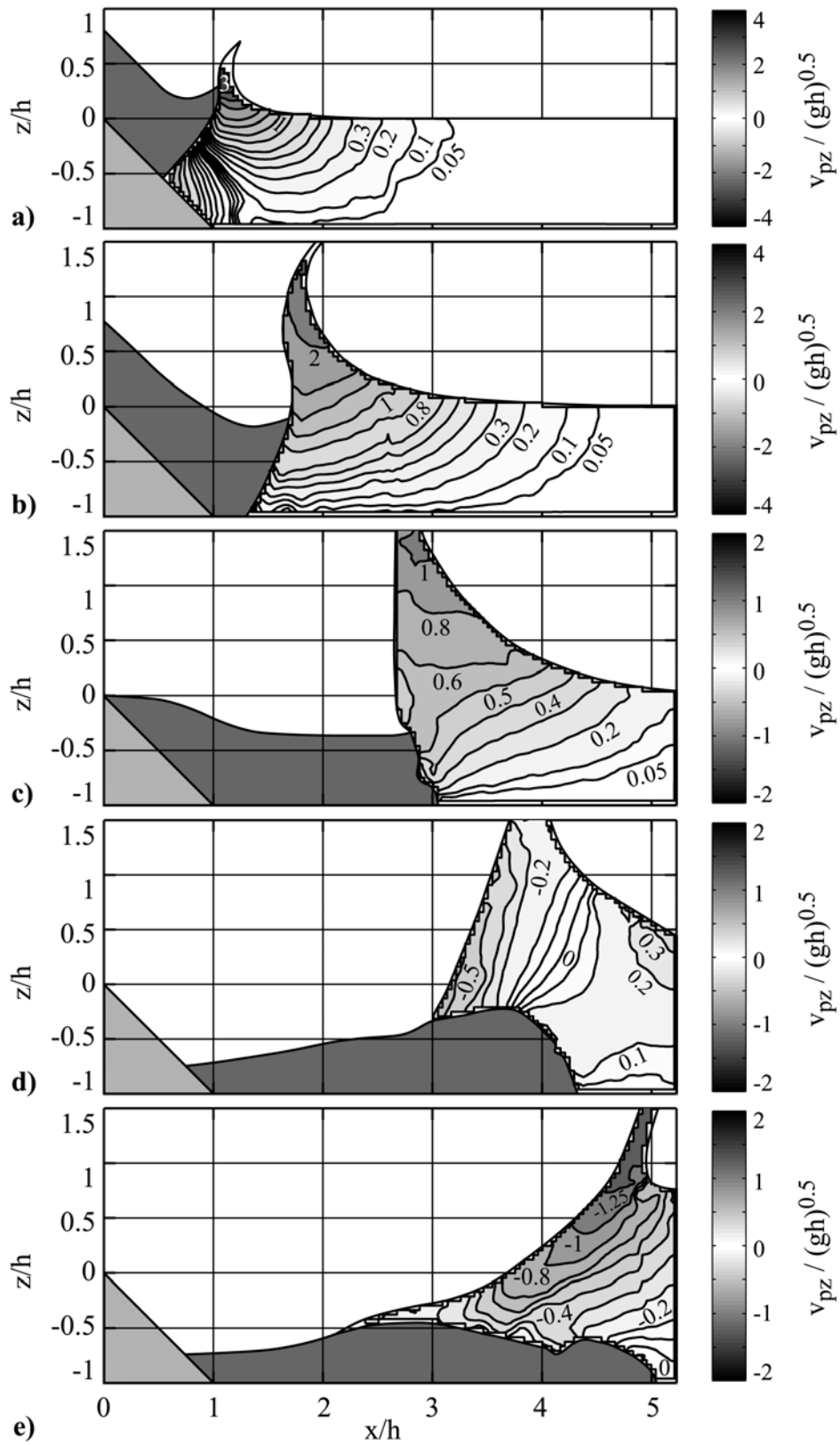
Figure 4.72 **Vertical particle velocity** fields $v_{pz}/\sqrt{gh}$: contours at 0, ± 0.05, ± 0.1, ± 0.2, ± 0.3, ± 0.4, ± 0.5, ± 0.6, ± 0.8, ± 1, ± 1.25, ± 1.5, ± 2, ± 2.5, ± 3, ± 3.5, ± 4; experiments at $\mathbf{F} = 4.1$, $V = 1.57$, $S = 0.56$, $h = 0.3\,\mathrm{m}$ and $t\sqrt{g/h} =$: **a)** 0.18, **b)** 0.56, **c)** 1.33, **d)** 2.47, **e)** 3.61.
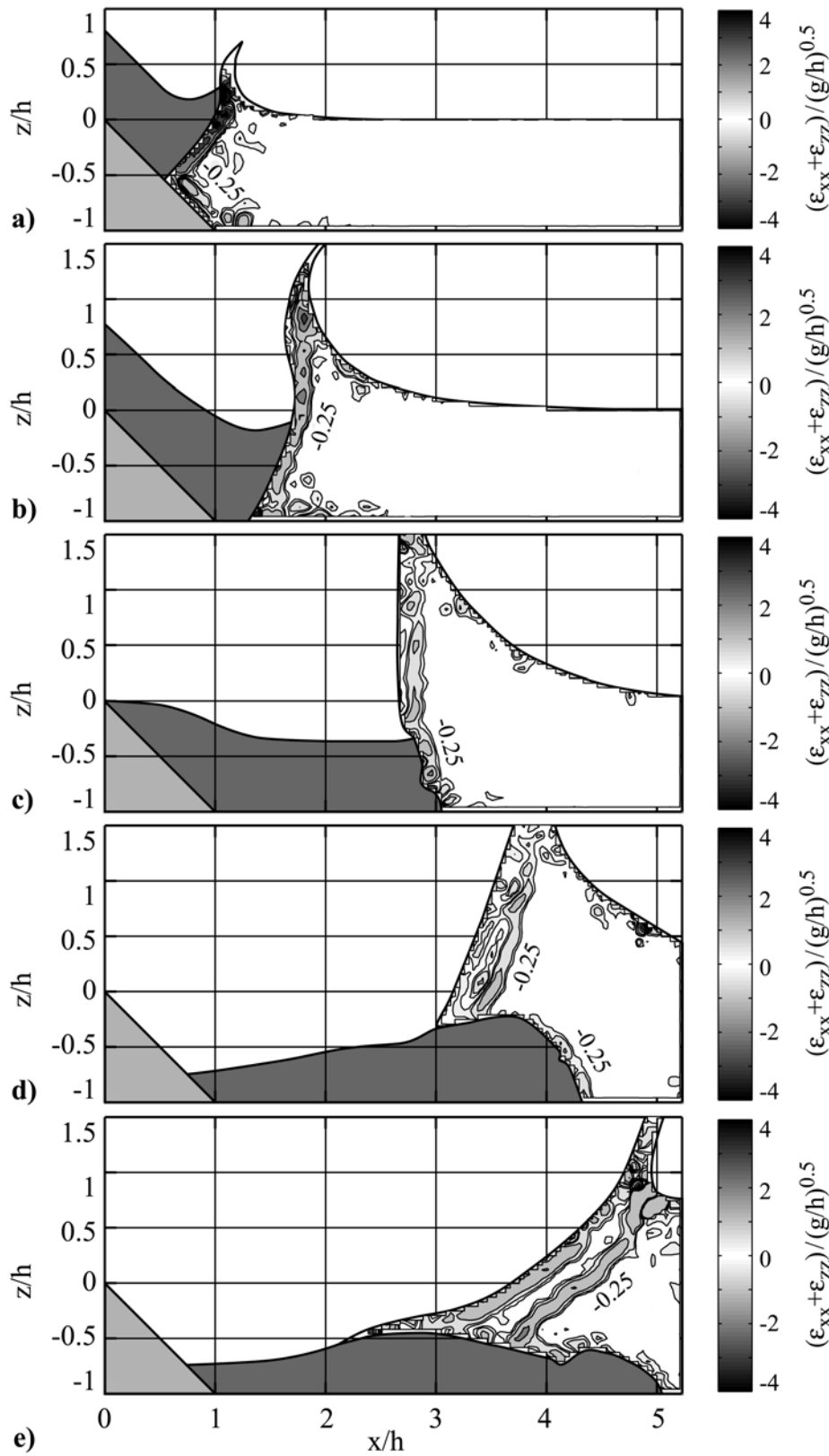
Figure 4.73 **2D-divergence** fields $(\varepsilon_{xx} + \varepsilon_{zz})/\sqrt{g/h}$ with contour levels at ± 0.25, ± 0.5, ± 1, ± 2, ± 3, ± 4; outward collapsing impact crater experiments at **F** $= 4.1$, $V = 1.57$, $S = 0.56$, $h = 0.3\,\mathrm{m}$ and $t\sqrt{g/h} =:$ **a)** 0.18, **b)** 0.56, **c)** 1.33, **d)** 2.47, **e)** 3.61.
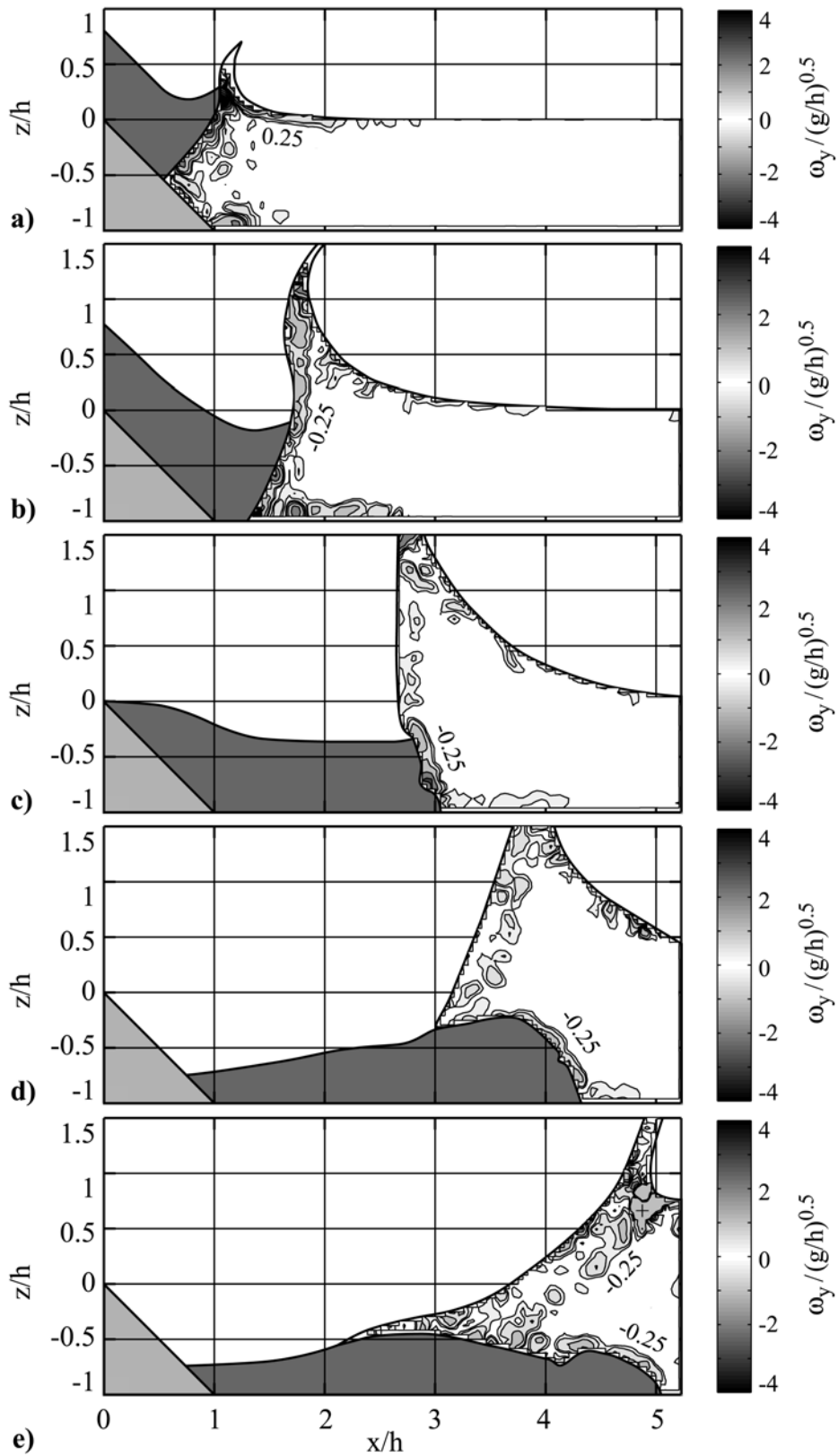
Figure 4.74 **Vorticity** fields $\omega_y/\sqrt{g/h}$ with contour levels at ± 0.25, ± 0.5, ± 1, ± 2, ± 3, ± 4; outward collapsing impact crater experiments at **F** = 4.1, $V = 1.57$, $S = 0.56$, $h = 0.3$ m and $t\sqrt{g/h} =:$ **a)** 0.18, **b)** 0.56, **c)** 1.33, **d)** 2.47, **e)** 3.61.
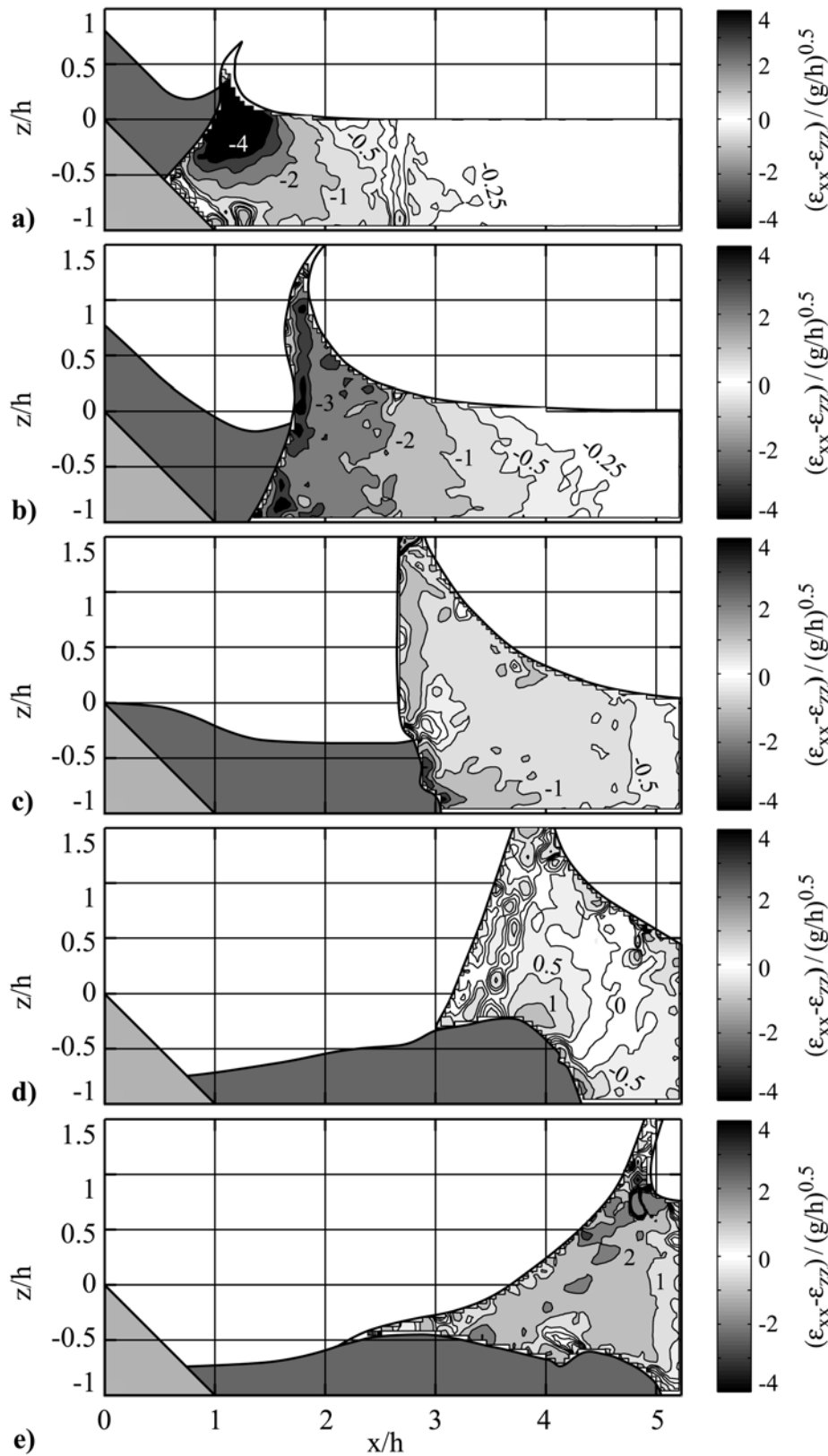
Figure 4.75 **Elongational strain** fields $(\varepsilon_{xx} - \varepsilon_{zz})/\sqrt{g/h}$ with contour levels at 0, ±0.25, ±0.5, ±1, ±2, ±3, ±4; outward collapsing impact crater experiments at **F** = 4.1, V = 1.57, S = 0.56, h = 0.3 m and $t\sqrt{g/h}$ =: **a)** 0.18, **b)** 0.56, **c)** 1.33, **d)** 2.47, **e)** 3.61.
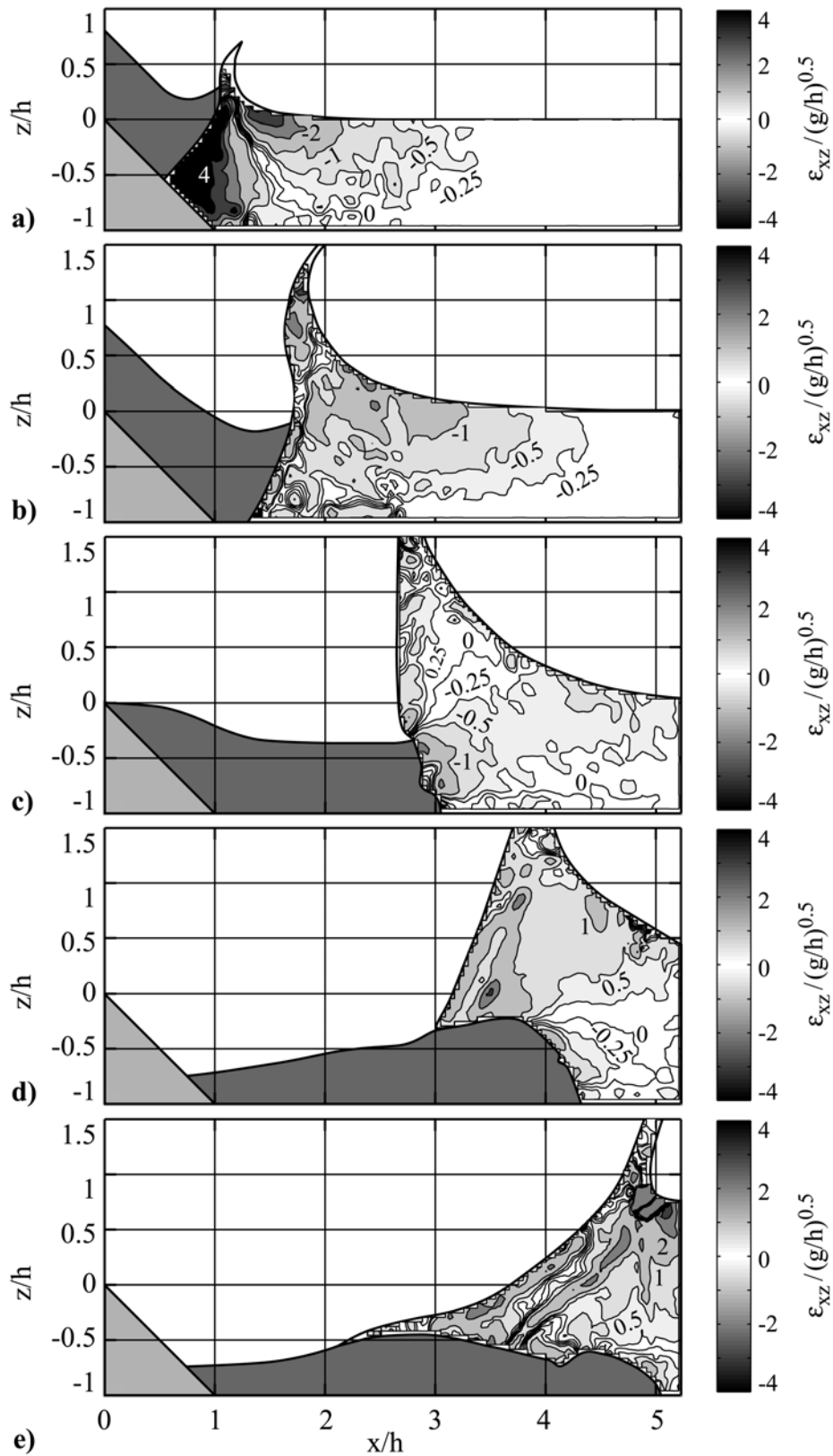
Figure 4.76 **Shear strain** fields $\varepsilon_{xz}/\sqrt{g/h}$ with contour levels at 0, ± 0.25, ± 0.5, ± 1, ± 2, ± 3, ± 4; outward collapsing impact crater experiments at **F** = 4.1, V = 1.57, S = 0.56, h = 0.3 m and $t\sqrt{g/h}$ =: **a)** 0.18, **b)** 0.56, **c)** 1.33, **d)** 2.47, **e)** 3.61.

4.6.4 Bore formation

The second outward propagating wave was a transient bore in most cases except some unseparated flows at the lower end of the investigated Froude number range. A characteristic example of a trailing bore formed as secondary wave is shown in Figs. 4.77 to 4.86. The sets of figures include the original PIV-images, the velocity vector fields, the streamline plots, scalar fields of the velocity components and contour plots of the computed components of the deformation tensor. The selected sequences of original PIV recordings are shown in Figs. 4.77. Previously to the shown image sequence the landslide impact at $F = 4.7$ caused an outward collapsing impact crater analogous to the two preceding examples. The sequence begins with the first wave trough after the leading wave crest had left the area of view and the run-up along the inclined ramp had reached its highest point (Fig. 4.77a). The local reduction in water level following the first wave crest caused by the inrush of water is transmitted outwards as a wave trough. The inward motion along the channel bottom collides with the run-down forming a surge (Fig. 4.77b,c). The surge propagating outward on top of the backward flow is analogous to a transient bore (Fig. 4.77d,e,f,g). A key feature is the dissipation process during its early phase. While the collapse of the crater is not dissipative, a considerable portion of the energy imparted to the fluid is lost as a result of turbulent mixing at the impact site from the rebound of the inward flow. The energy dissipation in a transient bore was computed numerically with the momentum and Bernoulli's theorem. In contrast to the trivial solutions of a hydraulic jump the full form of the equations including the unsteady terms have to be solved numerically. The energy dissipated hydrodynamically remained constant at roughly 40% of the potential and kinetic energies initially transmitted to the fluid by the landslide, independent of the lip shape (LeMéhauté and Khangoankar, 1992). An experimental estimation of the energy dissipated by turbulent mixing would require the extraction of both the potential and kinetic energy of the impact crater rim since part of the energy propagates outward in the form of waves whereas the rest rushes inward. Analytical treatments based on linear wave theory have been presented by Stoker (1957), Kranzer and Keller (1959) and Whitham (1974). The bore propagated outward roughly at $\sqrt{gh}$. As the bore propagates and decays, it is transformed into a non-breaking (non-dissipative) bore and finally a non-linear wave. When the underlying incoming flow reaches sub-critical conditions or the bore height becomes smaller than 60% of the incoming flow depth, the dissipative bore no longer exists (Favre, 1935). It is then transformed into a translatory non-dissipative undular bore which follows the leading wave generated by the lip at a distance.

The velocity vector fields and the streamline plots revealed the internal flow structure during the formation and propagation of a transient bore (Figs. 4.78 and 4.79). The half saddle along the ramp marked the collision between the run-down and the inward rush resulting in a spike a the free surface (Figs. 4.78 and 4.79a,b). The half saddle propagated outward with the bore (Figs. 4.78 and 4.79c,d,e,f,g). The largest velocities were measured locally along the ramp and in the breaking bore (Figs. 4.80). The horizontal water particle velocity in the bore exceeded even the shallow water wave velocity computed with the

still water depth (Figs. 4.81d,e,f). The vertical velocity in the bore was smaller than the horizontal component (Figs. 4.82).

The in-plane divergence field was significantly noisier than the previous examples due to the massive phase mixing and the air entrainment during the bore formation. Nevertheless the flow may be considered essentially two dimensional (Figs. 4.83). The computed out-of-plane vorticity fields are shown in (Figs. 4.84). In contrast to the previous irrotational waves the bore formation involved large positive vorticity values similar to the wave breaking process (Figs. 4.84c,d,e,f,g). The assumption of irrotational flow does not hold for bores.

The elongational and the shear strain fields are shown in Figs. 4.85 and 4.86, respectively. The bore was characterized by positive elongational strains on top of a layer with negative values near the bottom (Figs. 4.85c,d,e). The negative elongational strains marked water cells being compressed along the x-axis and expanded upward due to the collision between the inward flow and the run-down. The shear strain was positive under the bore as also below a wave crest (Figs. 4.86). Large elongational and shear strains in the bore front need to be interpreted carefully due to the massive phase mixing (Figs. 4.85 and 4.86e,f,g).
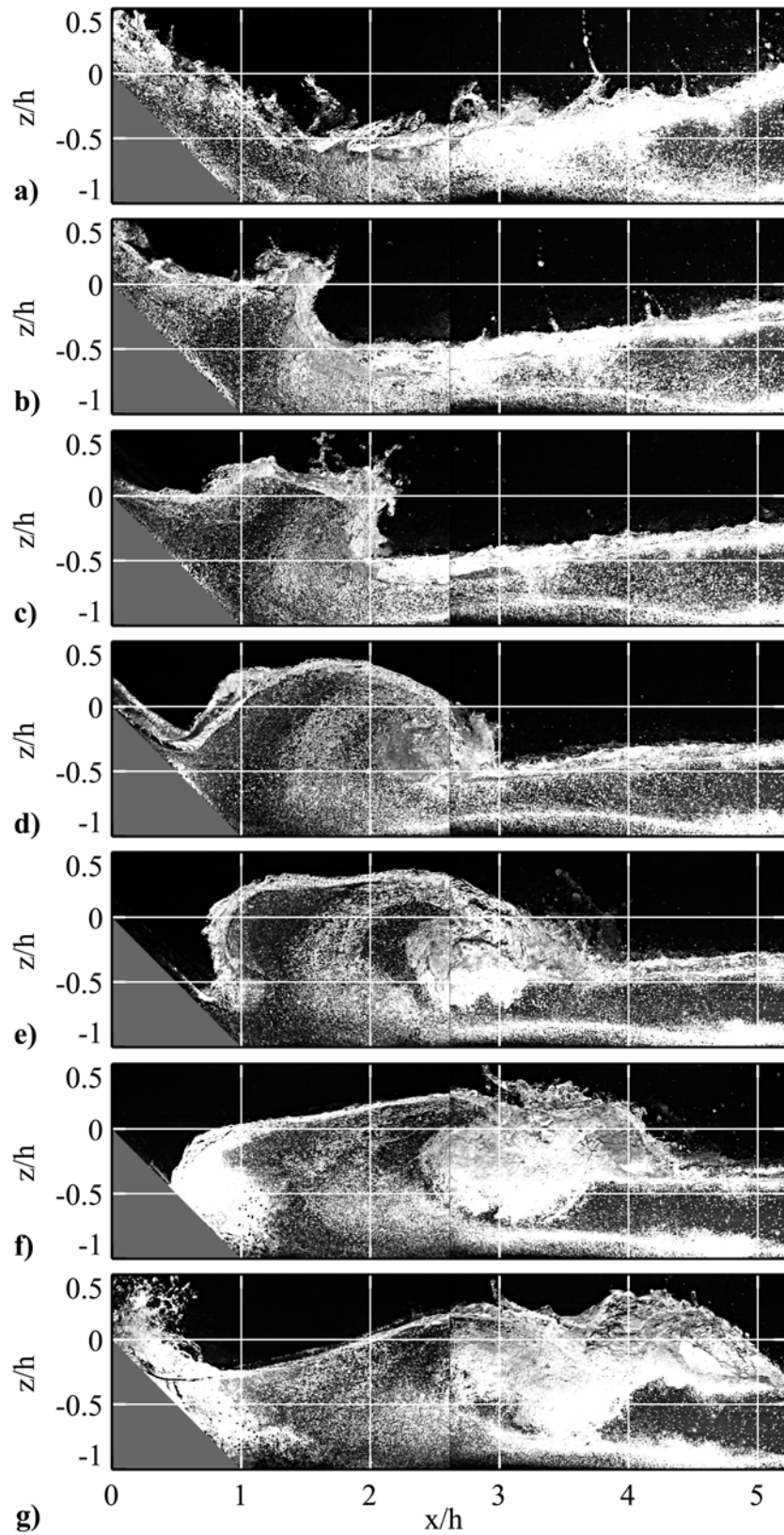
Figure 4.77 **Bore formation** PIV-images of two mounted experiments at **F** = 4.7, V = 0.39, S = 0.17, h = 0.3m and recorded at: **a)** $t\sqrt{g/h}$ = 6.97, **b)** $t\sqrt{g/h}$ = 7.73, **c)** $t\sqrt{g/h}$ = 8.49, **d)** $t\sqrt{g/h}$ = 9.25, **e)** $t\sqrt{g/h}$ = 10.01, **f)** $t\sqrt{g/h}$ = 10.78, **g)** $t\sqrt{g/h}$ = 11.51.
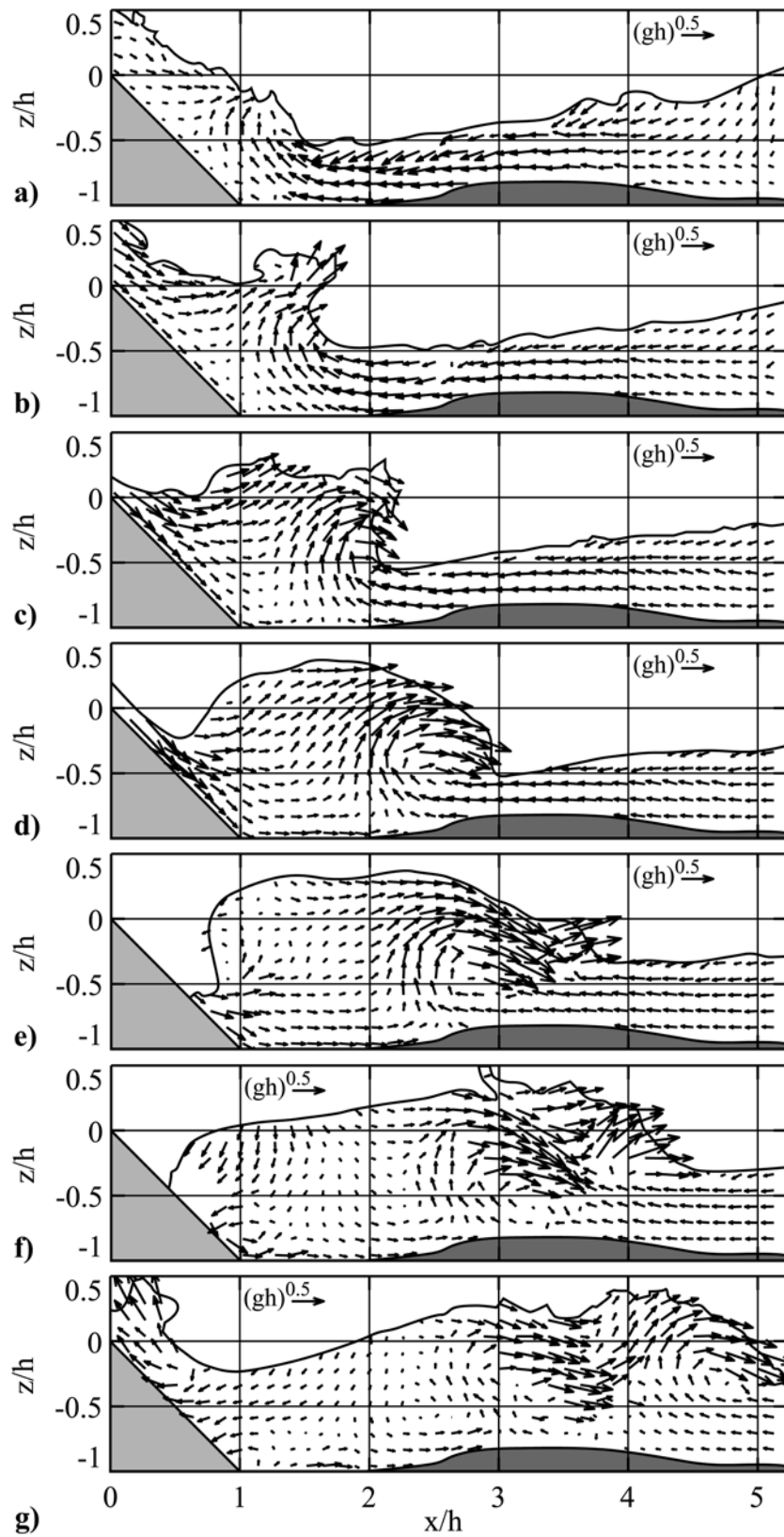
Figure 4.78 **Velocity vector fields** of a bore formation at $\mathbf{F} = 4.7$, $V = 0.39$, $S = 0.17$, $h = 0.3\,\mathrm{m}$ and recorded at: **a)** $t\sqrt{g/h} = 6.97$, **b)** $t\sqrt{g/h} = 7.73$, **c)** $t\sqrt{g/h} = 8.49$, **d)** $t\sqrt{g/h} = 9.25$, **e)** $t\sqrt{g/h} = 10.01$, **f)** $t\sqrt{g/h} = 10.78$, **g)** $t\sqrt{g/h} = 11.51$.
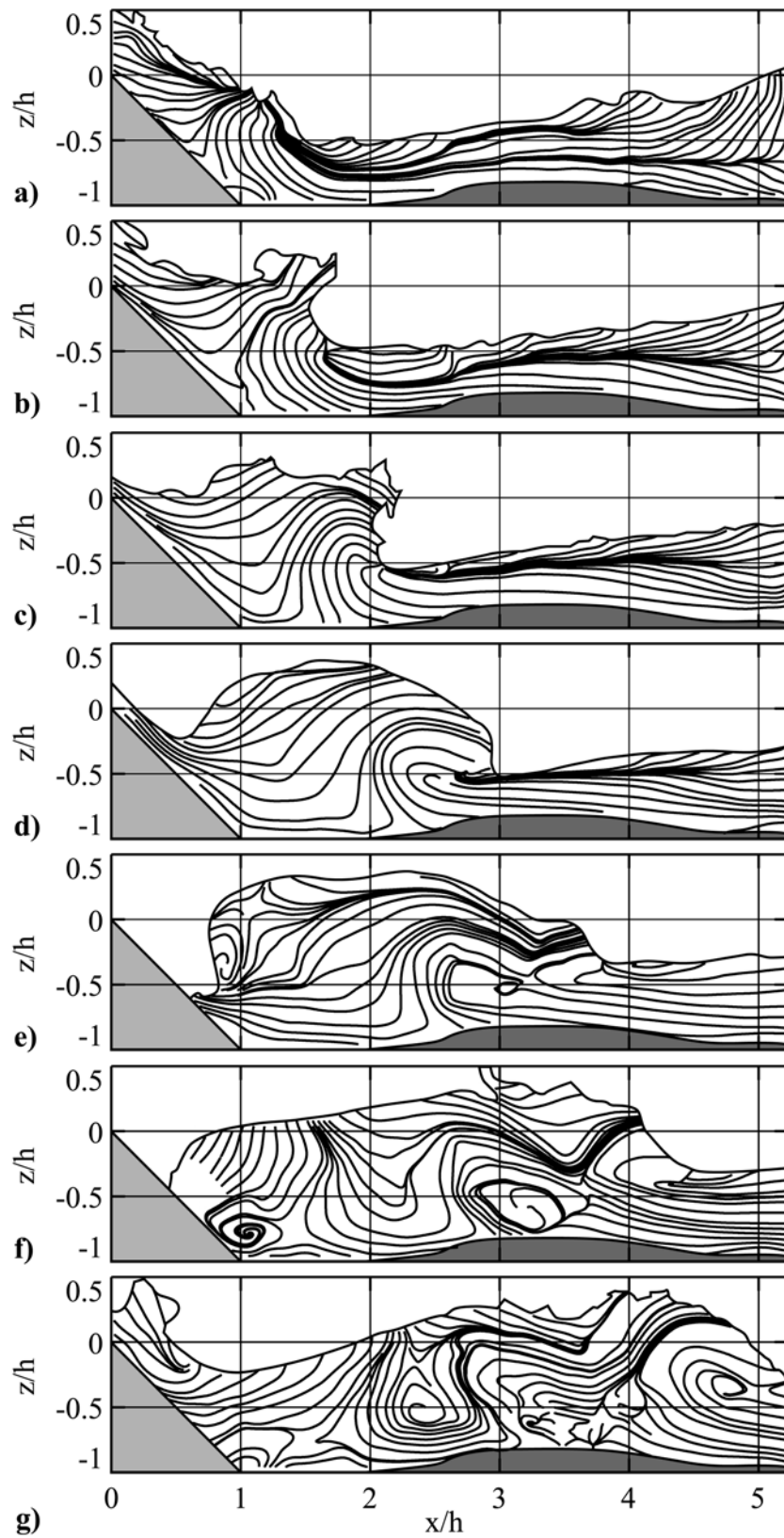
Figure 4.79 **Streamlines** of a bore formation at $\mathbf{F} = 4.7$, $V = 0.39$, $S = 0.17$, $h = 0.3$m and recorded at: **a)** $t\sqrt{g/h} = 6.97$, **b)** $t\sqrt{g/h} = 7.73$, **c)** $t\sqrt{g/h} = 8.49$, **d)** $t\sqrt{g/h} = 9.25$, **e)** $t\sqrt{g/h} = 10.01$, **f)** $t\sqrt{g/h} = 10.78$, **g)** $t\sqrt{g/h} = 11.51$.
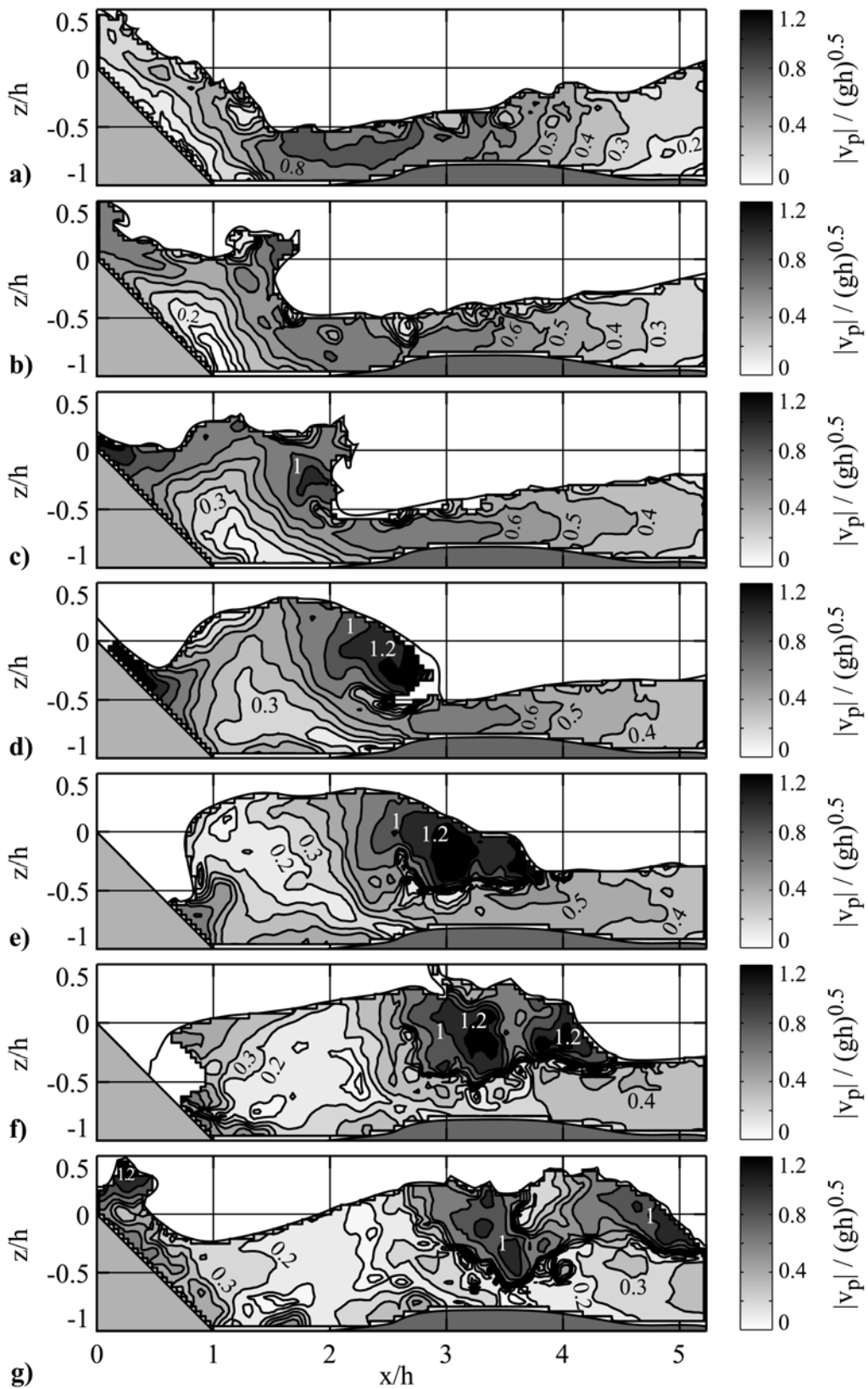
Figure 4.80 **Absolute particle velocity** fields $\left|v_p\right|/\sqrt{gh}$ with contour levels at 0.05, 0.1, 0.2, 0.3, 0.4, 0.5, 0.6, 0.8, 1, 1.2; bore formation at **F** = 4.7, V = 0.39, S = 0.17, h = 0.3 m and recorded at $t\sqrt{g/h}$ =: **a)** 6.97, **b)** 7.73, **c)** 8.49, **d)** 9.25, **e)** 10.01, **f)** 10.78, **g)** 11.54.
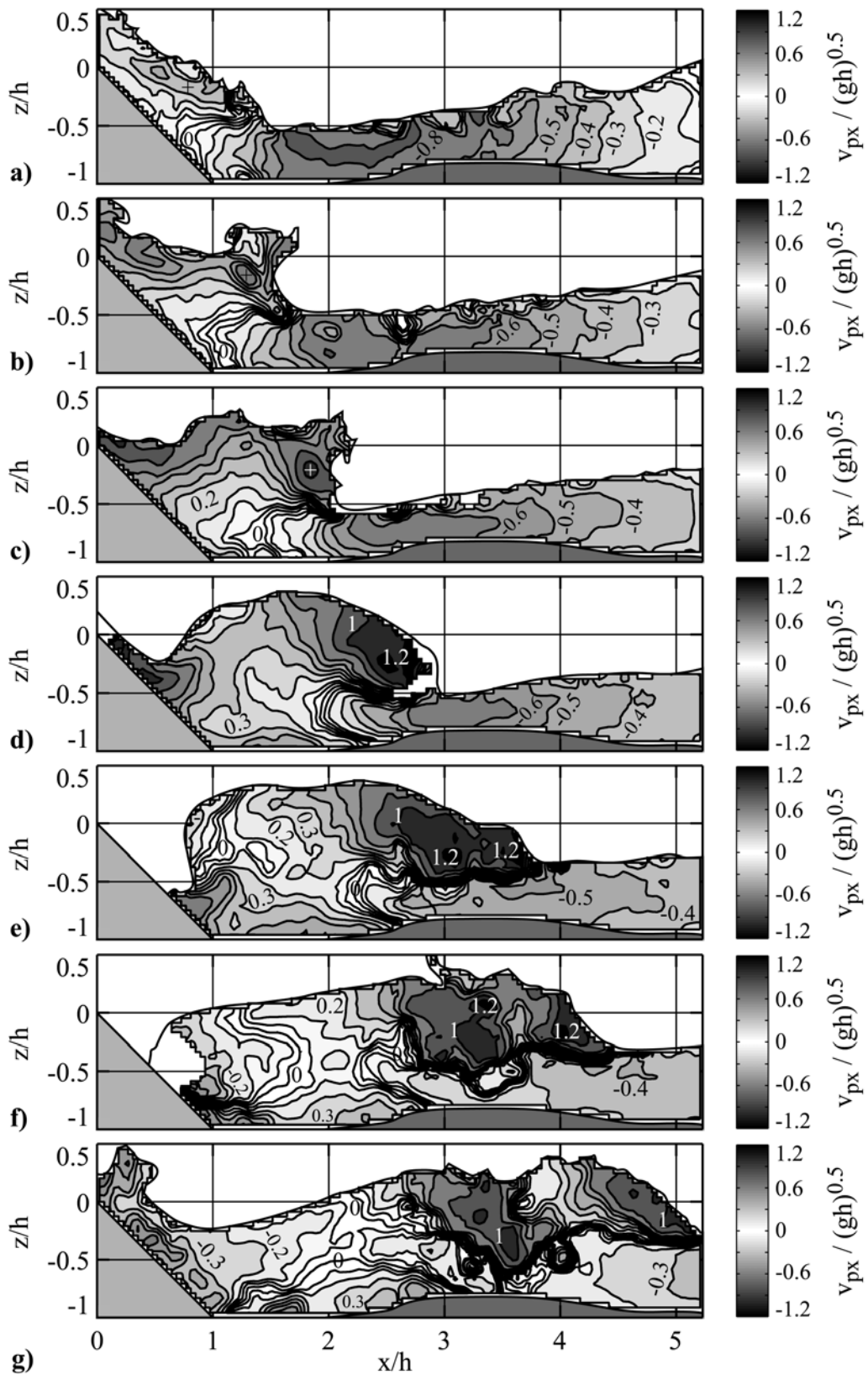
Figure 4.81 **Horizontal particle velocity** fields $v_{px}/\sqrt{gh}$: contours at 0, ±0.05, ±0.1, ±0.2, ±0.3, ±0.4, ±0.5, ±0.6, ±0.8, ±1, ±1.2; bore formation at $\mathbf{F}=4.7$, $V=0.39$, $S=0.17$, $h=0.3\,\text{m}$, recorded at $t\sqrt{g/h}\;=:$ **a)** 6.97, **b)** 7.73, **c)** 8.49, **d)** 9.25, **e)** 10.01, **f)** 10.78, **g)** 11.54.
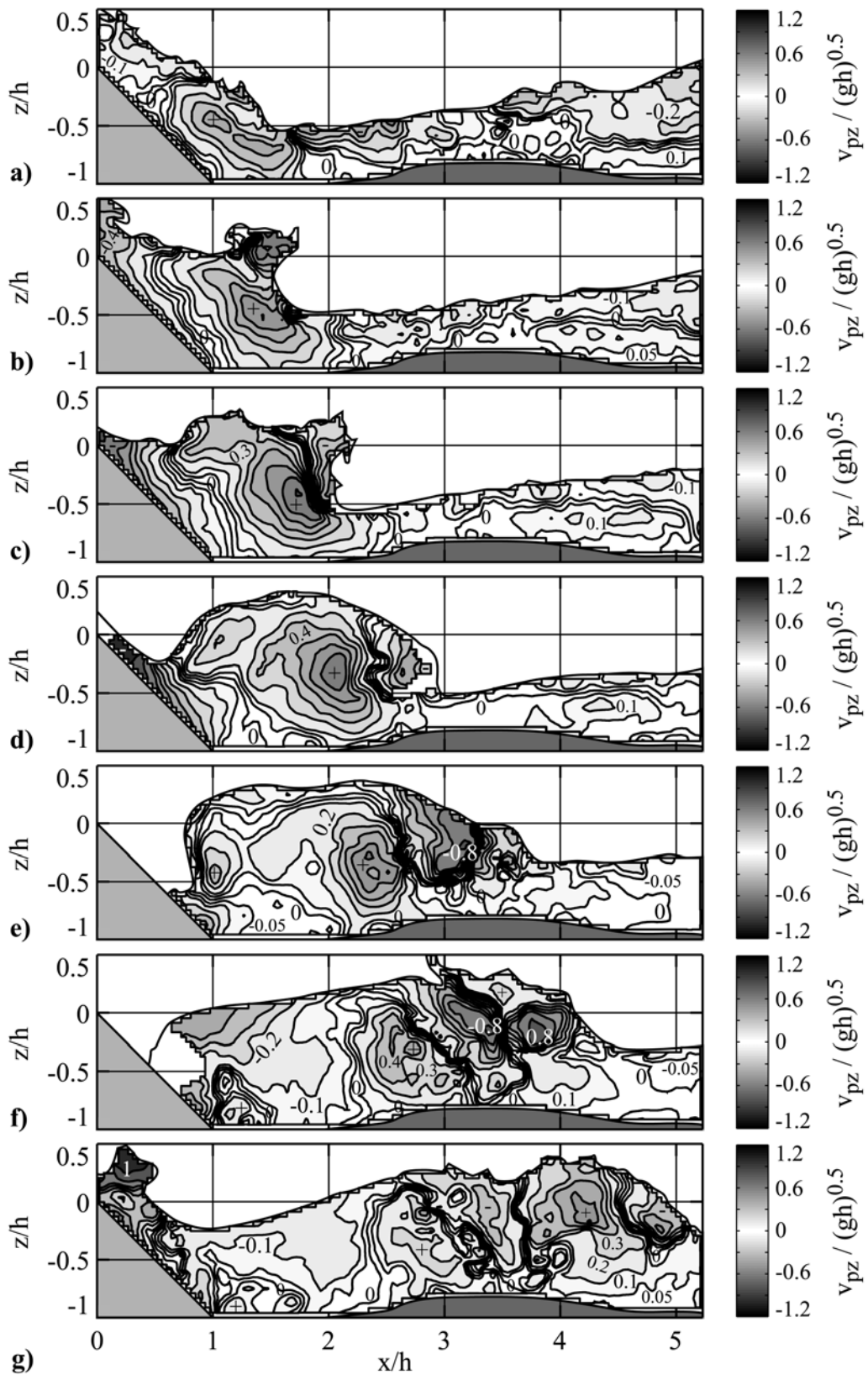
Figure 4.82 **Vertical particle velocity** fields $v_{pz}/\sqrt{gh}$ with contours at 0, ±0.05, ±0.1, ±0.2, ±0.3, ±0.4, ±0.5, ±0.6, ±0.8, ±1, ±1.2; bore formation at **F** = 4.7, $V = 0.39$, $S = 0.17$, $h = 0.3$ m, recorded at $t\sqrt{g/h}$ =: **a)** 6.97, **b)** 7.73, **c)** 8.49, **d)** 9.25, **e)** 10.01, **f)** 10.78, **g)** 11.54.
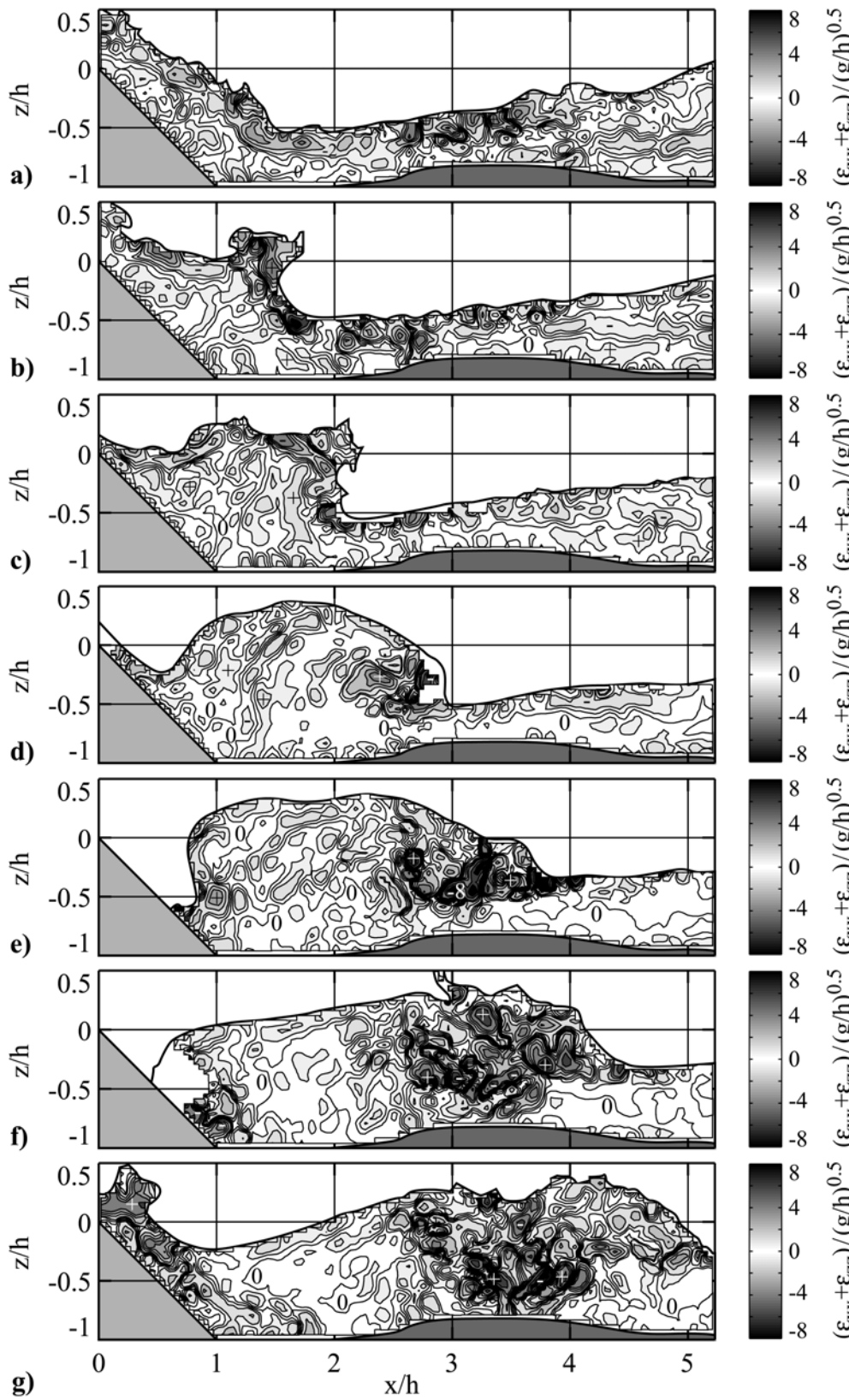
Figure 4.83 **2D-divergence** fields $(\varepsilon_{xx} + \varepsilon_{zz})/\sqrt{g/h}$ with contour levels at 0, ± 0.5, ± 1, ± 2, ± 3, ± 4, ± 6, ± 8; bore formation at **F** = 4.7, $V = 0.39$, $S = 0.17$, $h = 0.3\,\mathrm{m}$ and recorded at $t\sqrt{g/h} =$: **a)** 6.97, **b)** 7.73, **c)** 8.49, **d)** 9.25, **e)** 10.01, **f)** 10.78, **g)** 11.54.
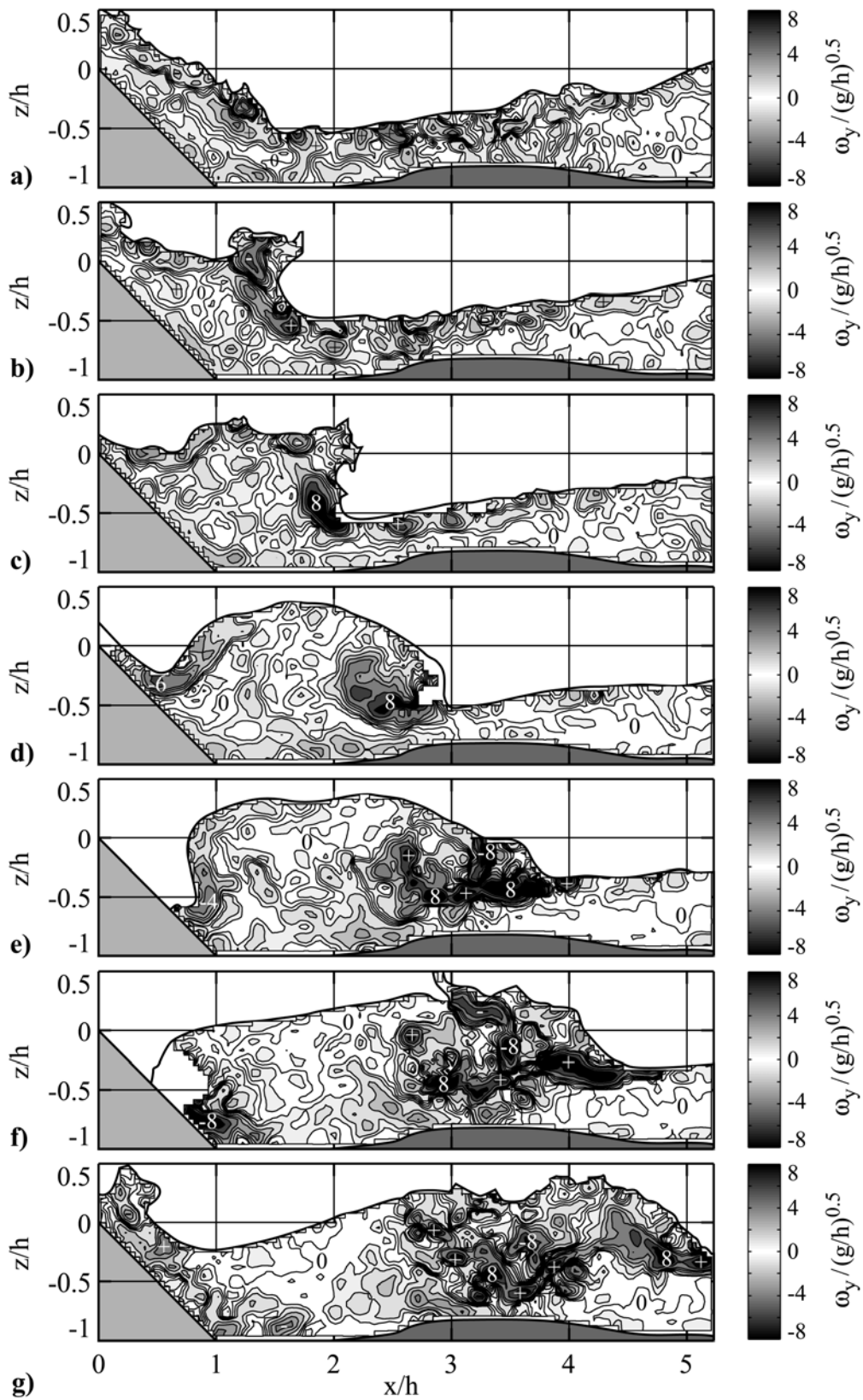
Figure 4.84 **Vorticity** fields $\omega_y/\sqrt{g/h}$ with contour levels at 0, ± 0.5, ± 1, ± 2, ± 3, ± 4, ± 6, ± 8; bore formation at **F** $= 4.7$, $V = 0.39$, $S = 0.17$, $h = 0.3$ m and recorded at $t\sqrt{g/h} =:$ **a)** 6.97, **b)** 7.73, **c)** 8.49, **d)** 9.25, **e)** 10.01, **f)** 10.78, **g)** 11.54.
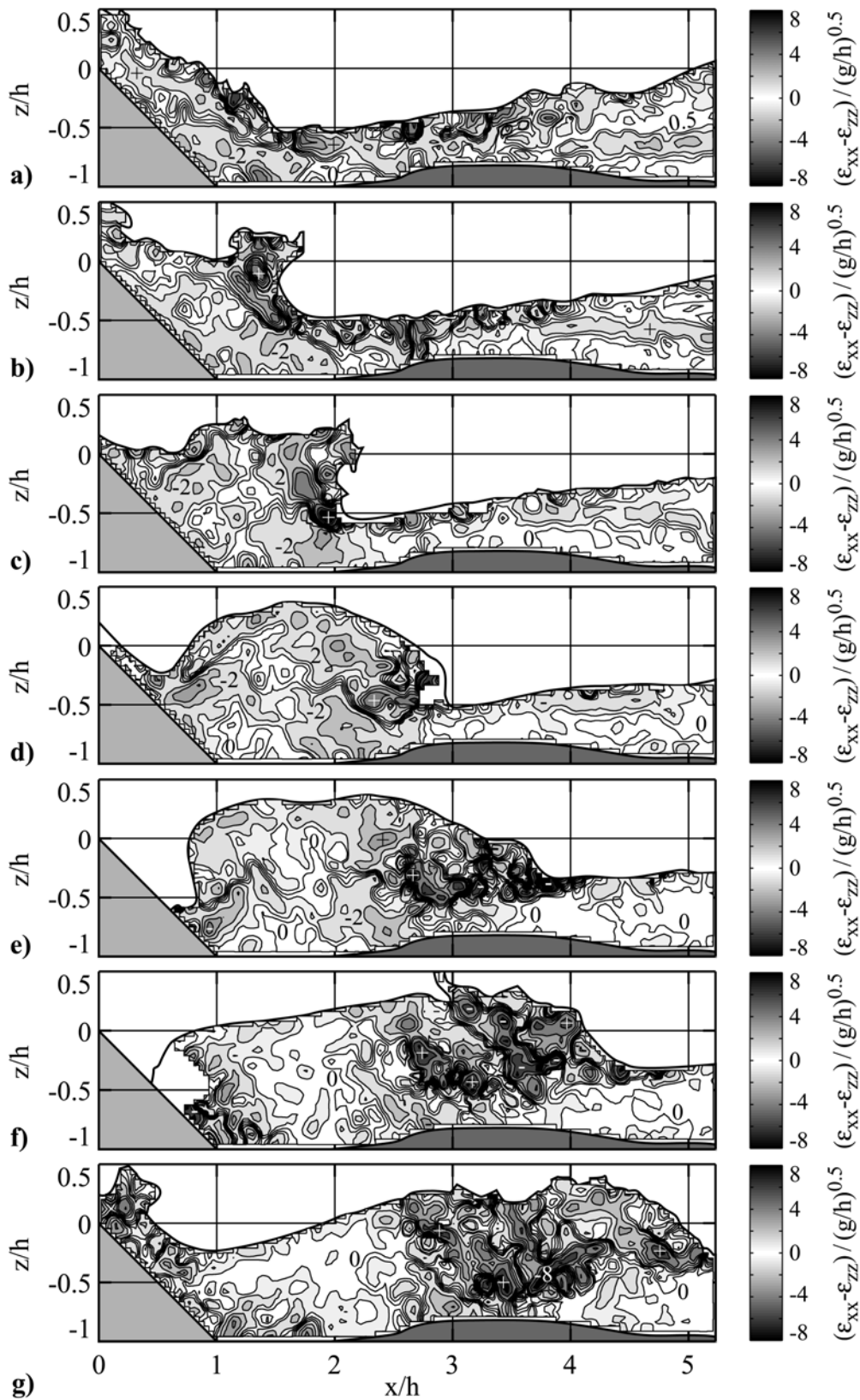
Figure 4.85 **Elongational strain** fields $(\varepsilon_{xx} - \varepsilon_{zz})/\sqrt{g/h}$ with contour levels at 0, ± 0.5, ± 1, ± 2, ± 3, ± 4, ± 6, ± 8; bore formation at **F** = 4.7, V = 0.39, S = 0.17, h = 0.3 m and recorded at $t\sqrt{g/h}$ =: **a)** 6.97, **b)** 7.73, **c)** 8.49, **d)** 9.25, **e)** 10.01, **f)** 10.78, **g)** 11.54.
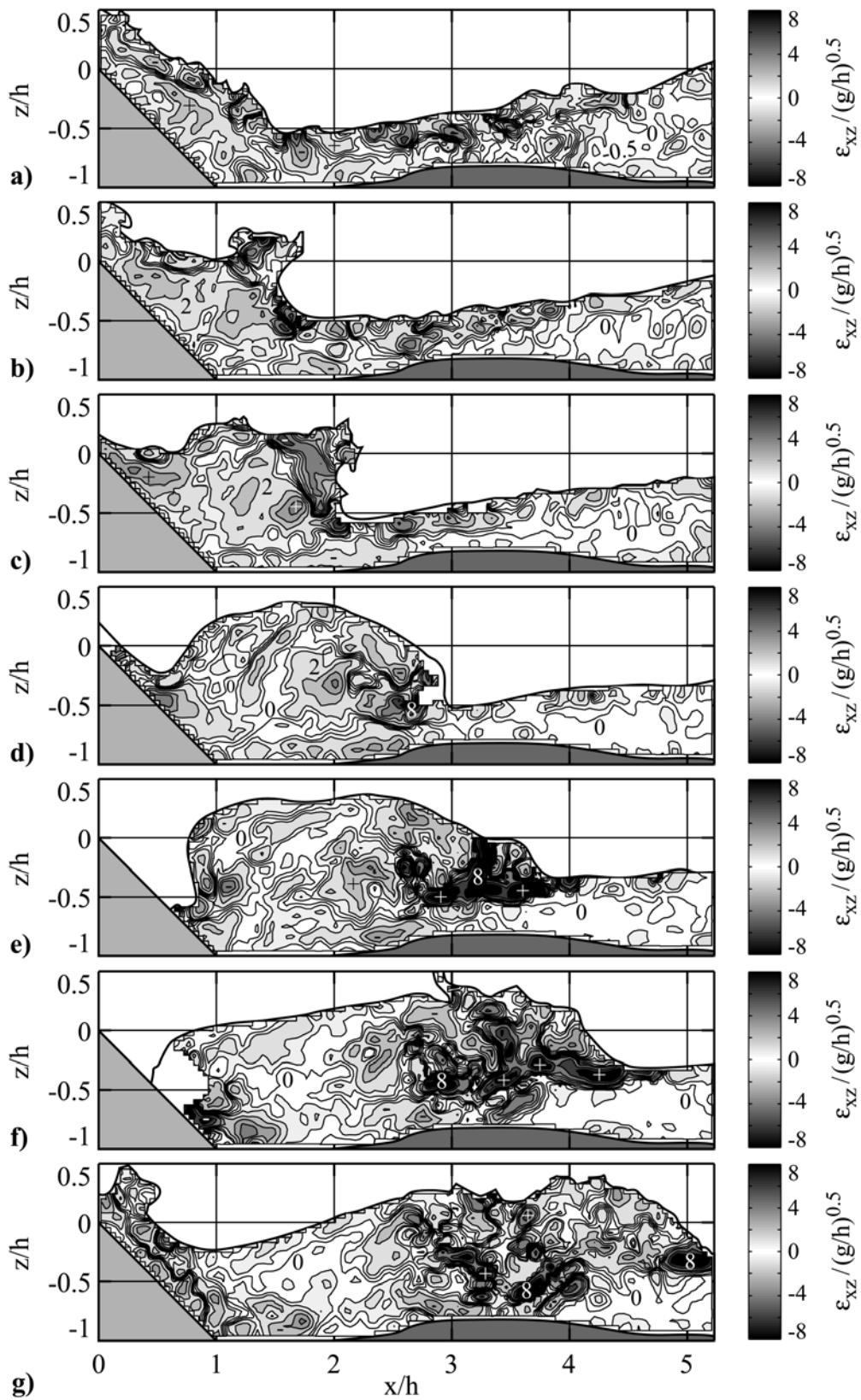
Figure 4.86 **Shear strain** fields $\varepsilon_{xz}/\sqrt{g/h}$ with contour levels at 0, ±0.5, ±1, ±2, ±3, ±4, ±6, ±8; bore formation at **F** $= 4.7$, $V = 0.39$, $S = 0.17$, $h = 0.3\,\mathrm{m}$ and recorded at $t\sqrt{g/h} =:$ **a)** 6.97, **b)** 7.73, **c)** 8.49, **d)** 9.25, **e)** 10.01, **f)** 10.78, **g)** 11.54.

4.7   Wave propagation

4.7.1 Wave profile recordings

The general parameters to describe water waves are shown in Fig. 2.1. The wave profile η (x,t) was recorded at the location of the wave gage as a function of time. The wave features in the propagation area were determined with capacitance wave gages (CWG). Seven CWGs were positioned along the channel axis with a meter spacing as shown in Fig. 3.15. The position of the first wave gage was given by the landslide run-out distance and the slide deposit thickness. The applied capacitance wave gages are described in [para 3.4.3]. The wave gage locations along channel axis were not altered for different still water depths due to the splash sealing – only the vertical positions were adjusted. Hence the relative positions of the wave gages x/h along the channel axis varied with the still water depth h. The wave gage positions x/h along the channel axis for the systematically investigated still water depths h of 0.3, 0.45 and 0.675 m are summarized in Table 4.1. The measurable propagation distance decays with increasing water depth resulting in a relative channel shortening.

Table 4.1   **Wave gage positions** along the channel axis relative to the stillwater depth x/h.

h [m]	CWG1 x/h	CWG2 x/h	CWG3 x/h	CWG4 x/h	CWG5 x/h	CWG6 x/h	CWG7 x/h
0.3	4.77	8.10	11.43	14.77	18.10	21.43	24.77
0.45	3.51	5.73	7.96	10.18	12.40	14.62	16.84
0.675	2.67	4.16	5.64	7.12	8.60	10.08	11.56

Compared to other studies on landslide generated impulse waves the wave channel was relatively short with its length of 11 m, but fully adequate for measuring the near-field wave trains. Kamphuis and Bowering (1970) conducted an experimental study in which a weighted tray was emplaced by a roller ramp – essentially frictionless sliding – into a flume 45 m long, 1 m wide, and of variable water depth h ranging from 0.23 to 0.46 m. Huber (1980) conducted a broad experimental investigation of granular landslide impacts into a channel 30 m long, 0.5 m wide, and with stillwater depths ranging from 0.12 to 0.36 m. These earlier studies allowed the investigation of the wave propagation up to a distance of $x/h \approx 100$. The wave attenuation curves over large propagation distances obtained in extremely small water depths need to be interpreted carefully. For example the viscous damping of the wave amplitudes may be estimated to significant 30 % over a propagation distance of 30 m at $h = 0.12$ m (Keulegan, 1948). Therefore a minimum water depth of $h = 0.30$ m was chosen in this study.

The position of the first wave gage was closer to the impact site than in the experimental studies conducted by Kamphuis and Bowering (1970) or Huber (1980). The present study focused on the wave generation and the near field wave characteristics. The

key contribution here is to clarify the factors that control the impulse wave characteristics in the near field. The near field may be defined as the region just beyond the point were the mass flow stops, but before dispersive effects continuously transform the whole wave train.

4.7.2 Observed wave types

Most water wave systems occurring in nature and many man-made wave systems are transient phenomena. From a practical point of view, while many of these may be regarded as essentially steady state, landslide generated impulse waves are inherently transient. Further unsteady examples are waves generated by explosions, earthquakes and ships. The water waves generated by the model landslides in the present study fall into four main classes of gravity wave types: weakly non-linear oscillatory waves, non-linear transition waves, solitary-like waves and dissipative transient bores. The wave profiles of characteristic examples of weakly non-linear oscillatory waves, strongly non-linear transition waves, a solitary-like wave and a dissipative transient bore are shown in Figs. 4.87a,b,c,d), respectively.
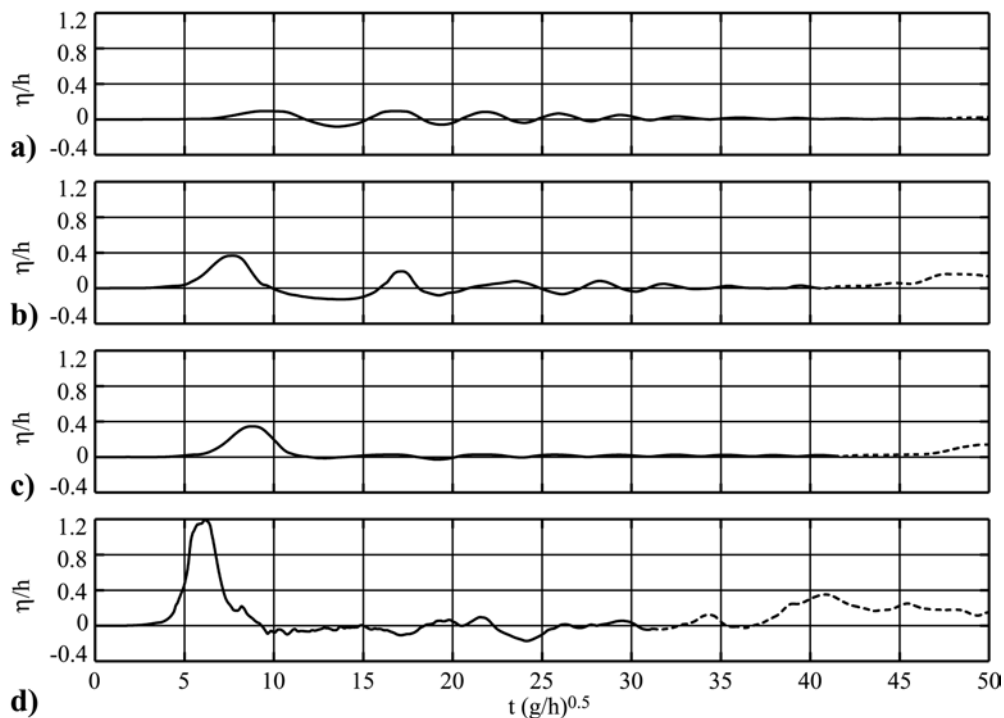
Figure 4.87   **Wave types: a) non-linear oscillatory waves** at $\mathbf{F} = 1.7$, $V = 0.39$, $S = 0.19$, $h = 0.3\,\mathrm{m}$ with (——) valid wave recording and (----) wave recording affected by wave reflection; **b) non-linear transition waves** at $\mathbf{F} = 2.8$, $V = 0.79$, $S = 0.34$, $h = 0.3\,\mathrm{m}$, symbols as in a); **c) solitary-like wave** at $\mathbf{F} = 1.8$, $V = 1.57$, $S = 0.61$, $h = 0.3\,\mathrm{m}$; **b) dissipative transient bore** prior to breaking at $\mathbf{F} = 4.1$, $V = 1.57$, $S = 0.56$, $h = 0.3\,\mathrm{m}$.

This comparison shows the broad spectrum of observed wave types and the significantly different amplitude ranges. The shown wave profiles were recorded at the second wave gage ($x/h = 8.1$). The transient dissipative bore shown in Fig. 4.87d) was recorded prior to breaking. Hence no air is involved.

The propagation behavior of weakly non-linear oscillatory waves, strongly non-linear transition waves, a solitary-like wave and a dissipative transient bore are shown in Figs. 4.88a,b) and 4.89a,b), respectively. All wave profiles were independent of the reflection from the channel back wall at the beginning. The arrival time of the wave reflection was computed for each gage by extrapolating from a 5% rise of water surface relative to the leading wave crest amplitude at the last gage with the measured wave speed to the front of the wave absorber and in negative x-direction to the wave gages.

Linear oscillatory waves defined by $H/h < 0.03$ were not observed. All wave trains without a significantly larger leading wave crest and no long shallow trough were summarized as weakly non-linear oscillatory waves. Oscillatory waves are periodic in the direction of travel and have nearly closed elliptical particle orbitals. Water particles travel both with and against the direction of wave motion. Mass transport is of lesser importance than in other types of waves. Weakly non-linear oscillatory waves were encountered at the lower end of observed wave heights. Weakly non-linear oscillatory wave groups were characterized by a strong frequency dispersion. Dispersion stretched the wave train during propagation and significantly enhanced trailing waves, while the leading wave decayed. The largest wave crest may occur anywhere in the wave train after a certain travel distance. The wave energy in dispersive wave trains travels slower than the individual wave propagation velocity. The wave celerity c is the apparent velocity of a wave crest. The speed at which energy transmission occurs is the group celerity c_G which is related to the wave celerity and has as deep and shallow water asymptotes the values $c/2$ and c, respectively (Appendix C). In the intermediate water depth the group velocity is wave length dependent and lies between the shallow and deep water asymptotes. Dispersive effects were analyzed by Fritz and Liu (2002).

The nonlinear transition wave region is characterized by a main leading wave crest and a long shallow trough followed by a dispersive wave train. The leading wave crest travels significantly faster than the trailing waves resulting in stretching of the wave train. The wave profiles are similar to cnoidal waves, but non steady in a moving reference frame. In contrast cnoidal waves as computed by the Korteweg and de Vries equations are periodic and of permanent form (Wiegel, 1960). The main restriction to the applicability of the KdV equations is the limited frequency bandwidth given by the Ursell number $U \geq 26$ (LeMéhauté and Whang, 1995).

All wave trains characterized by only one primary wave crest were categorized as solitary or solitary-like waves. The wave forms observed in the experiments were not steady in a moving reference frame, in contrast to the solitary wave theory. Pure solitary waves are difficult to obtain in an experiment. The surface displacement of the solitary wave is completely above the still water level and therefore consists only of a crest. The wave period and length are infinite (Wiegel, 1964).
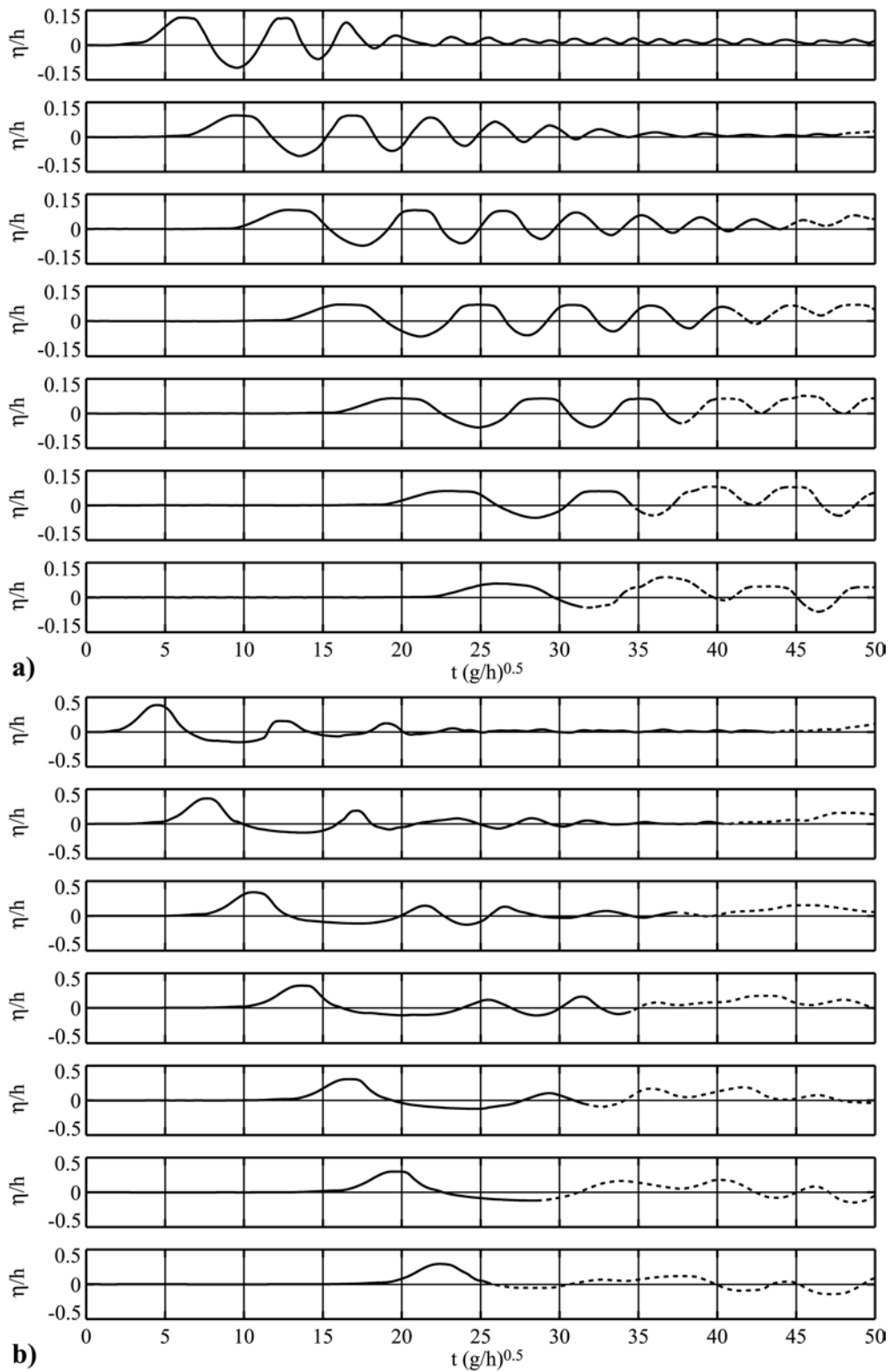
Figure 4.88 **Wave types: a) non-linear oscillatory waves** at **F** = 1.7, *V* = 0.39, *S* = 0.19, *h* = 0.3 m (one of the two mounted runs in Figs. 4.37 to 4.46) with (———) valid wave recording and (----) wave recording affected by wave reflection; **b) non-linear transition waves** at **F** = 2.8, *V* = 0.79, *S* = 0.34, *h* = 0.3 m (one of the two mounted runs in Figs. 4.47 to 4.56) with symbols as in a).
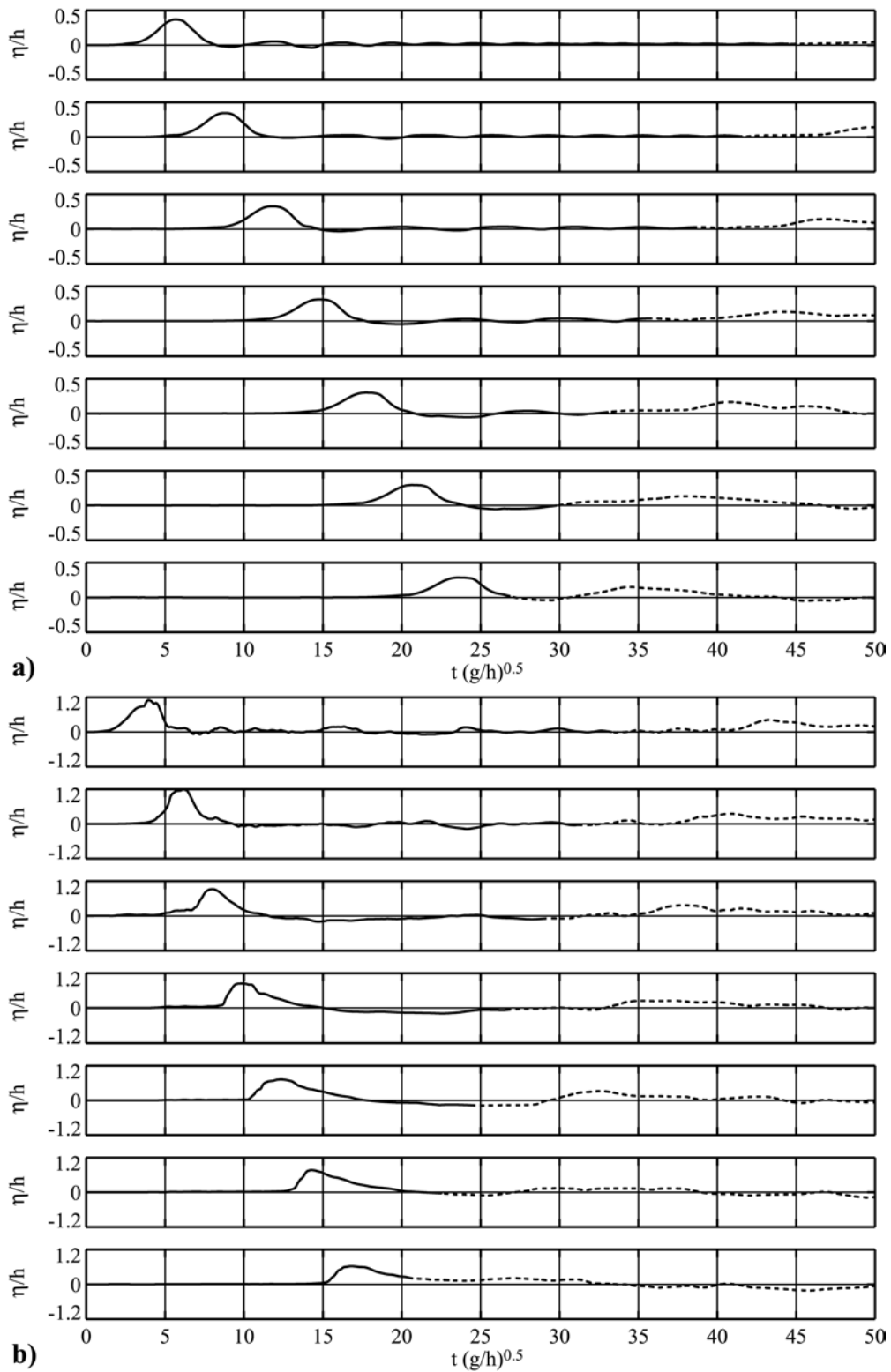
Figure 4.89   **Wave types: a) solitary-like wave** at **F** = 1.8, *V* = 1.57, *S* = 0.61, *h* = 0.3 m with (━━) valid wave recording and (▪▪▪▪) wave recording affected by wave reflection; **b) dissipative transient bore** at **F** = 4.1, *V* = 1.57, *S* = 0.56, *h* = 0.3 m (one of the two mounted runs in Figs. 4.77 to 4.86) with symbols as in a).

The formation of dissipative transient bores as leading wave crest was identified on the analog VHS-recordings, which observed the whole wave tank during the experiments. The bore formation involved wave breaking which is difficult to identify on wave gage profiles without the additional video recordings. Bores were observed when the leading wave crest amplitude exceeded the still water depth $a_{c1} > h$. Only the leading wave crest is of relevance regarding the breaking of the first wave and not the whole wave height since the trough follows the crest. The bore formation and wave breaking was initiated during the outward collapse of an impact crater. Wave breaking was observed before at $1 > a_{c1}/h \geq 0.78$ resulting in short lived local spilling at the wave crest but not in a dissipative transient bore. The bore shown in Figs. 4.89b) decayed and transformed into a non-breaking (non-dissipative) bore and finally a non-linear wave at wave gage 7. The dissipative bore no longer existed at $a_{c1}/h \leq 0.6$ as predicted by Favre (1935). The additional video recordings confirmed that the leading wave crest did not break prior to the third wave gage. Hence almost no air was inside the leading wave crest at the first gage and in most cases also the second wave gage – besides some minor entrainment at the surface due to the splash. The massive decay in wave amplitude from gage 2 to gage 5 was due to the formation of the transient dissipative bore characterized by the rotational motion which only then entrained a large amount of air. The noise in the wave profiles at the fourth and fifth gage may be attributed to the entrained air.

4.7.3 Wave type classification

The regions of wave types produced by a vertical plunger or falling block were previously defined by a synthesis of the theoretical solution (Noda, 1970) and experimental results (Wiegel et al., 1970). The classification was based on the relative block thickness s/h and and the slide Froude number **F**. The same concept is applied herein to granular landslide generated impulse waves. The wave type was determined by the slide Froude number **F** and the relative slide thickness $S = s/h$. The neglection of the dimensionless slide volume $V = V_s/(bh^2)$ will be justified later by the fact that the relative slide volume only had a secondary influence on the amplitude of the leading wave crest. The distinction between the observed wave types may be somewhat arbitrary due to fluent transitions between the different wave types.

A non-linear oscillatory wave pattern was observed if the slide Froude number **F** $= v_s/\sqrt{gh}$ fulfilled the empirical relationship given by

$$\mathbf{F} < (4 - 7.5\,S) \tag{4.29}$$

with the relative slide thickness $S = s/h$. The weakly non-linear oscillatory wave regions encompassed relatively slow and thin slides.

The non-linear transition wave region may be determined by

$$(4 - 7.5\,S) \leq \mathbf{F} < (6.6 - 8\,S) \tag{4.30}$$

with Eq. 4.29 marking the lower end. Non-linear transition waves were produced by slides with a larger impact Froude number or larger slide thickness than those generating an oscillatory wave train.

The solitary or solitary-like wave region may be given by

$$(6.6 - 8S) \leq \mathbf{F} < (8.2 - 8S) \tag{4.31}$$

with Eq. 4.30 marking the lower end. Pure solitary waves may only be generated by slides which are thick and large enough to prohibit the water from flowing over the back of the slide after the slide motion has terminated. At large Froude numbers the cavity collapse always resulted in a minor dissipative wail tail. Solitary-like waves were produced by slides with a larger impact Froude number or larger slide thickness than those generating a non-linear transition wave.

A dissipative transient bore as leading wave was observed if the slide Froude number $\mathbf{F} = v_s / \sqrt{gh}$ fulfilled the empirical relationship given by

$$\mathbf{F} \geq (8.2 - 8S) \tag{4.32}$$

with the relative slide thickness $S = s/h$. Hence bores were formed by thick slides relative to the water depth impacting at a large slide Froude number. The graphical representations of Eqs. 4.29 and 4.32 is shown in Fig. 4.90a).
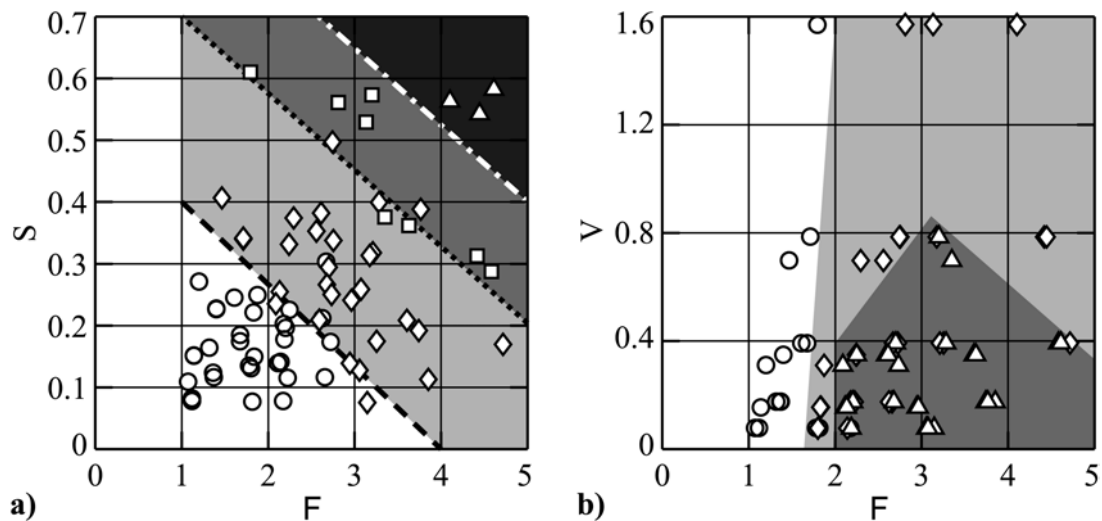
Figure 4.90 **la) Wave type classification** based on the slide Froude number $\mathbf{F} = v_s / \sqrt{gh}$ slide thickness $S = s/h$ with (○) weakly non-linear oscillatory wave, (◇) non-linear transition wave, (□) solitary-like wave, (Δ) dissipative transient bore, (▬ ▬) Eq. 4.29, (••••) Eqs. 4.30 and 4.31, (•▬•) Eq. 4.32, (▨) non-linear transition region, (▨) solitary-like region, (■) bore region; **b) Breaking second wave crest** with (m) non-breaking wave, (◇) spilling breaker, (Δ) dissipative transient bore, (▨) spilling breaker region, (▨) bore region.

The characteristics of the second wave crest or the first trailing wave depended strongly on the wave run-up along the hill slope ramp and the subsequent run-down. The wave run-up on the hillslope ramp on the other hand strongly depended on the size and type of the hydrodynamic impact crater. Again breaking was initiated at the foot of the hillslope ramp

during the generation of the second wave crest making it impossible to apply the classical breaking criterion described in [para C.3]. Nevertheless three main types may be distinguished: non-breaking Stokesian wave, spilling breaker, dissipative transient bore. The wave type was determined by the slide Froude number $\mathbf{F} = v_s \big/ \sqrt{gh}$ and the dimensionless slide volume $V = V_s \big/ (bh^2)$. The neglect of the relative slide thickness $S = s \big/ h$ will be justified later by the fact that the relative slide thickness only had a secondary influence on the amplitude of the second wave crest. The classification is shown in Fig. 4.90b). The wave profile recordings give no indication on wave breaking besides an increased noise in the signal which may also have other causes. The wave breaking was identified on the analog VHS-recordings, which observed the whole wave tank during the experiments. A characteristic example of a dissipative transient bore as first trailing wave formed by the run-down along the hillslope ramp was shown previously in Figs. 4.77 to 4.86.

4.7.4 Wave envelope amplitude attenuation

The wave height and in particular the crest amplitude is of primary interest regarding hazard prevention. The wave amplitude is not half the wave height in the non-linear range. The experiments encompassed only non-linear waves. Hence the wave height concept may lead to serious underestimations of the highest wave crest amplitude. Further regarding the leading wave crest only the crest amplitude is defined. The leading wave will only break when the crest amplitude exceeds a breaker criterion usually defined with the wave height. Therefore the crest and trough amplitudes are considered separately. In most cases the leading wave crest was the highest wave crest. In some cases in the weakly non-linear and the nonlinear transition region the second wave crest exceeded the leading wave crest in height. Further in the weakly non-linear oscillatory region trailing waves were continuously amplified while the leading waves decreased during propagation as shown in Figs. 4.88a). This dispersive effect may result in the tenth wave being the highest after propagating over a large distance (Ward, 2001). Regarding hazard prevention it is of secondary interest which wave is the highest. Therefore the wave envelope concept is introduced (Dean and Dalrymple, 1991). The positive wave envelope amplitude a_c and the negative wave envelope amplitude a_t as a function of the propagation distance $x \big/ h$ are considered independent of their location within the wave train. The definition of the wave envelope and the notation are shown in Fig. 4.91. The maximum positive wave amplitude a_C and the maximum negative wave amplitude a_T with a capital subscript are defined as the maximum measured crest and trough amplitudes independent of their location along the channel axis and their position within the wave group.
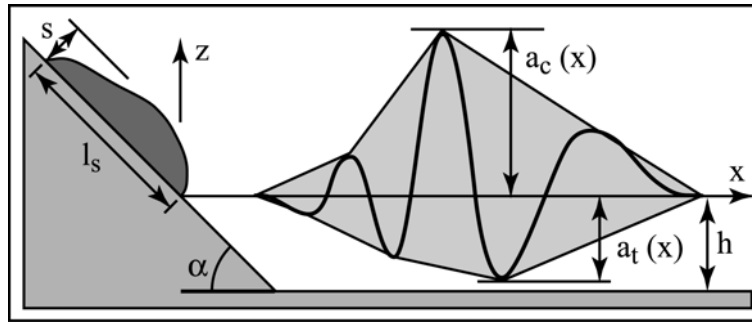
Figure 4.91   **Wave envelope** of the impulse wave train and notation.

The propagation of the envelope amplitudes a_c/h and a_t/h as well as a_c/a_C and a_t/a_C are shown in Figs. 4.92a,b), respectively. The measured crest amplitudes were within $0.05 < a_c/h < 1.25$. The condition for linear wave theory is $a_c/h < 0.03$ (Dean and Dalrymple, 1991). Hence all waves generated by granular landslide impacts in the present study were non-linear. In shallow water the stability of the wave profile depends on the relative wave height. The breaking criterion κ in shallow water was defined from solitary wave theory by McCowan (1894) as

$$\kappa = \frac{H_b}{h_b} = 0.78 \qquad (4.33)$$

a fraction of wave height H to water depth h, where b denotes the value at breaking. In the strongly non-linear range the crest amplitude approaches the wave height $a_c \approx H$ due to the relatively shallow wave trough. The breaking criterion matches the observed breaker heights. The shallow water breaking criterion was exceeded by up to 60% by instantaneous wave heights. All breaking waves or bores were generated by outward collapsing impact craters. Wave breaking or bore formation took some time to develop.

The maximum crest amplitudes were located within $0 < x/h < 12$. In some cases the maximum wave crest amplitude increased initially due to the residual bulk outward motion still present in the water body during the impact crater collapse. Further a strong variation of the decay in wave crest amplitude over propagation distance was observed. Some cases in the weakly non-linear oscillatory wave region decayed rapidly $a_c(x/h = 7)/a_C = 0.5$, whereas others in the non-linear transition wave region or the solitary wave region were almost not attenuated $a_c(x/h = 25)/a_C = 0.9$. The wave attenuation strongly depended upon the wave type and the wave characteristics. Hence a simple draw down curve does not exist. For example Huber and Hager (1997) introduced a wave attenuation according to $(h/x)^{0.25}$. The formula would predict a crest amplitude $a_c(x/h = 25)/a_C = 0.45$. The Huber and Hager formula may grossly underpredict wave amplitudes in certain cases.
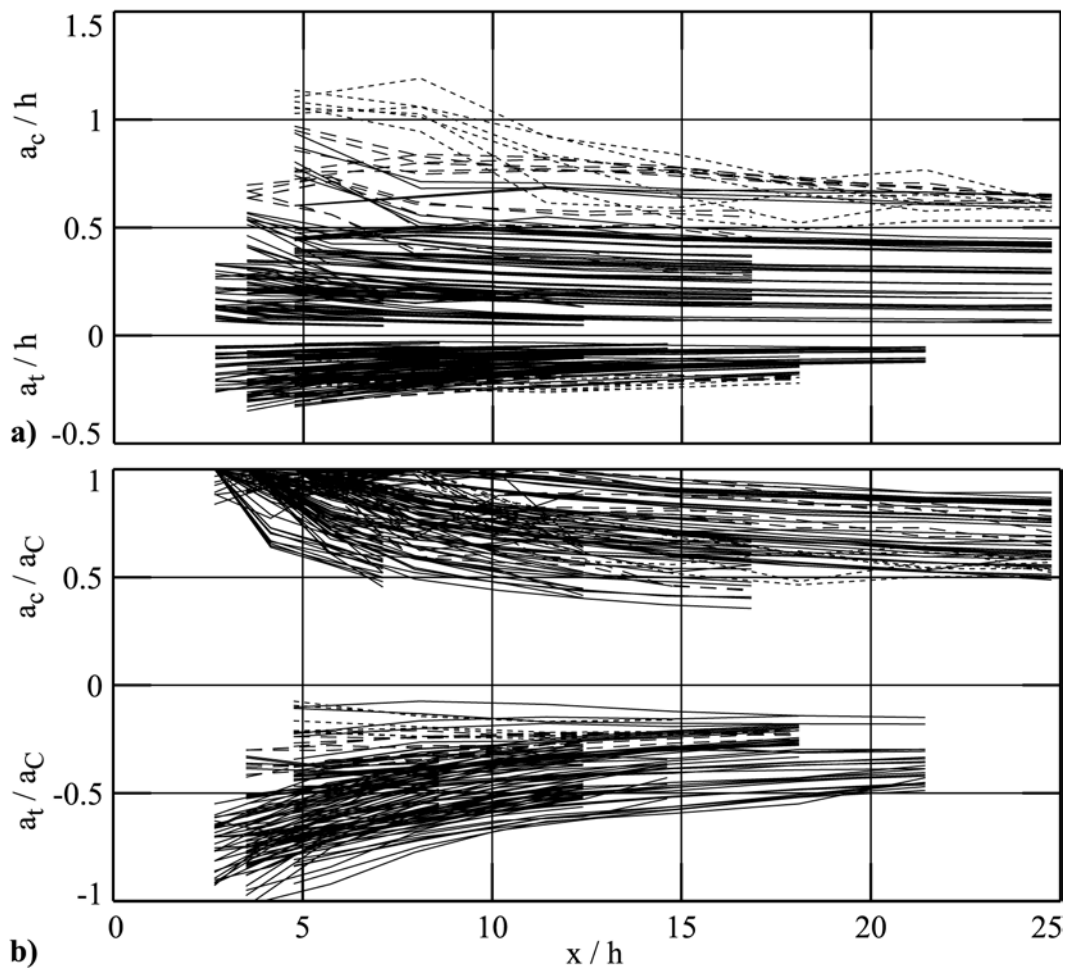
Figure 4.92   **Wave envelope amplitude attenuation: a) maximum amplitudes** a_c/h **and** a_t/h at locations x/h with (—) non-breaking waves, (− −) spilling breakers or white capping, (- - - -) bores; **b) maximum amplitudes** a_c/a_C **and** a_t/a_C **at locations** x/h, symbols as in a).

4.7.5 Wave height partition

The maximum positive wave amplitude a_c and the maximum negative wave amplitude a_t as a function of the propagation distance x/h independent of their location within the wave train were considered in the previous paragraph. The definition of the wave envelope and the notation are shown in Fig. 4.91. The maximum positive wave amplitude a_C and the maximum negative wave amplitude a_T with a capital subscript are defined as the maximum measured crest and trough amplitudes independent of their location along the channel axis and their position within the wave group. Similarly the leading wave crest a_{c1} and trough a_{t1} as well as the second wave crest a_{c2} may be defined as functions of the propagation distance x/h. The maximum leading wave crest amplitude a_{C1}, the maximum leading wave trough amplitude a_{T1} and the maximum second wave crest a_{C2} with a

capital subscript are defined as the maximum measured individual crest and trough amplitudes independent of their location along the channel axis. The definitions of the individual crest and trough amplitudes are shown in Fig. 4.93.
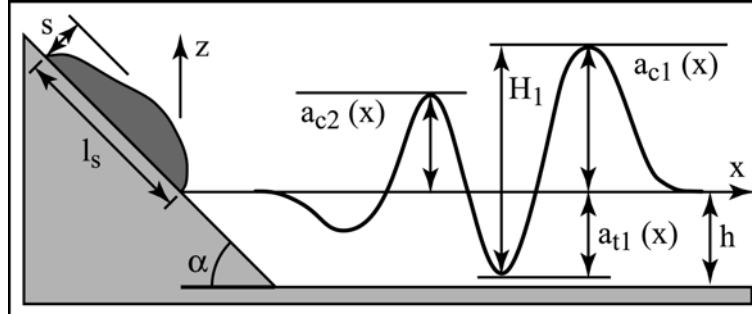
Figure 4.93   **Definitions** of the individual wave crest and trough amplitudes.

The maximum positive wave amplitude a_C and the maximum negative wave amplitude a_T are shown in Fig. 4.94a). All maximum positive wave envelope amplitudes were non-breaking waves or waves prior to breaking. Hence air entrainment is negligible. The maximum crest amplitudes always matched or exceeded the maximum trough amplitudes $a_C \geq a_T$. Un-equipartition between crest and trough amplitudes characterizes the non-linear water waves, whereas in linear wave theory equipartition is assumed. A linear regression between the maximum crest and trough amplitudes yields

$$\frac{a_C}{h} = 2.3 \frac{a_T}{h}$$

(4.34)

with a correlation coefficient $r^2 = 0.45$. The relationship between the maximum crest and trough amplitudes is ill defined. The partition of the total wave height H between the crest and trough amplitudes strongly depended on the wave type. In weakly non-linear oscillatory waves the wave trough increased roughly proportional to the wave crest, whereas in the nonlinear transition wave regime the leading wave trough decreased with increasing nonlinearity or wave crest amplitude. The solitary waves and bores at the upper limit of the possible wave spectrum would theoretically result in $a_T = 0$. In the experiments a small trough was always observed trailing behind solitons and bores. The trailing trough was necessary to compensate for the outward bound mass transport in these non-linear waves.

The maximum leading wave crest amplitude a_{C1} versus the maximum second wave crest amplitude a_{C2} independent of their location along the channel axis is shown in Fig. 4.94b). The relationship between the first and second wave crest amplitudes is ill defined. Dispersion caused the location of the maximum crest amplitude to move backwards within the wave group over large propagation distances. In some cases in the weakly non-linear oscillatory and the transition wave region the second wave crest exceeded the leading wave crest in amplitude $a_{C1} \leq a_{C2}$. These cases were limited to the weakly non-linear range with maximum crest amplitudes $a_C/h \leq 0.3$. In the strongly

non-linear range $a_C/h \geq 0.3$ the largest wave amplitude along the channel axis was always measured in the first wave crest $a_{C1} > a_{C2}$.
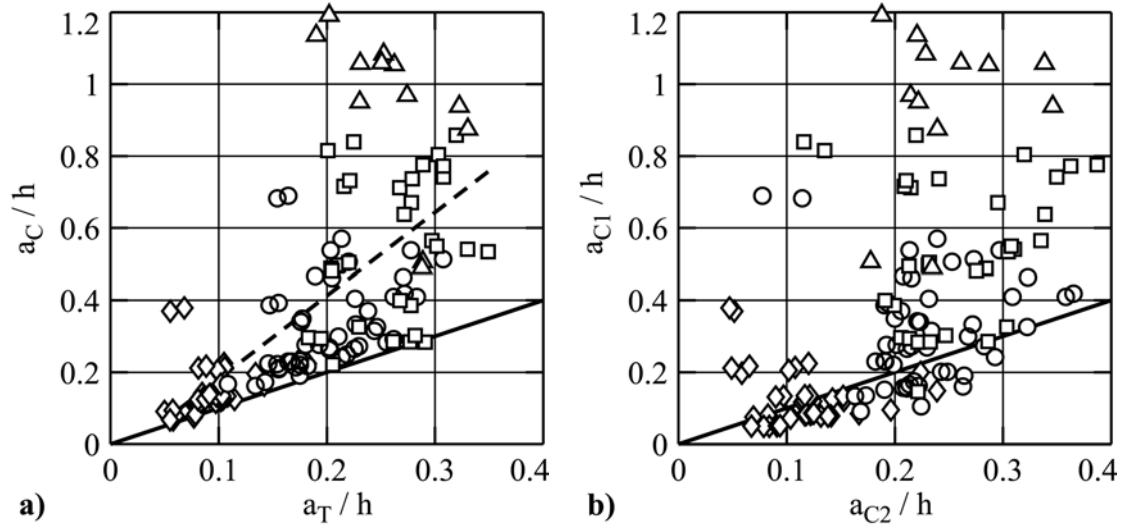
Figure 4.94 **a) Maximum crest amplitude** a_C/h versus maximum trough amplitude a_T/h at ($\Diamond$) $1 < \mathbf{F} < 2$, ($\bigcirc$) $2 \leq \mathbf{F} < 3$, ($\square$) $3 \leq \mathbf{F} < 4$, ($\triangle$) $4 \leq \mathbf{F} < 5$ with (– –) Eq. 4.34 and (—) equipartition $a_C = a_T$; **b) maximum first crest amplitude** a_{C1}/h versus maximum second crest amplitude a_{C2}/h with (—) $a_{C1} = a_{C2}$ and symbols as in a).

4.7.6 Prediction of maximum crest amplitude

The prediction of the maximum wave amplitude is of primary interest regarding hazard prevention. Herein the governing parameters are identified resulting in a predictive equations for the maximum wave crest amplitude. The multiple regressions for the maximum wave crest amplitude a_C/h yields

$$\frac{a_C}{h} = 0.25\left(\frac{v_s}{\sqrt{gh}}\right)^{1.4}\left(\frac{s}{h}\right)^{0.8} \tag{4.35}$$

with excellent correlation coefficient $r^2 = 0.93$. The dominant dimensionless quantity regarding the maximum crest amplitude is the slide Froude number $\mathbf{F} = v_s/\sqrt{gh}$. Further the dimensionless thickness $S = s/h$ had a strong influence on the leading wave crest. The dimensionless slide thickness together with the slide Froude number define the slide inflow rate relative to the outward mass transport under a solitary wave. The comparisons between the measured and the predicted values computed with Eq. 4.35 shown in Fig. 4.95a). The largest deviations between the measured and the computed values are $< 33\%$. The dominant influence of the slide Froude number $\mathbf{F} = v_s/\sqrt{gh}$ on the maximum crest amplitude is shown in Fig. 4.95b).

The neglection of the dimensionless slide volume $V = V_s/(bh^2)$ had almost no effect on the maximum wave crest amplitude. The dimensionless slide thickness and slide

volume were not completely independent in this experimental study. The slide thickness increased on average with increasing slide volume. The dimensionless slide volume may play a role regarding relatively slow and small landslides impacting into relatively deep water. In the limiting case of hydrostatic displacement the landslide volume is the sole parameter. On the other hand at high impact velocities with a dynamic impact crater formation process the dimensionless slide thickness and the slide Froude number are the primary parameters.
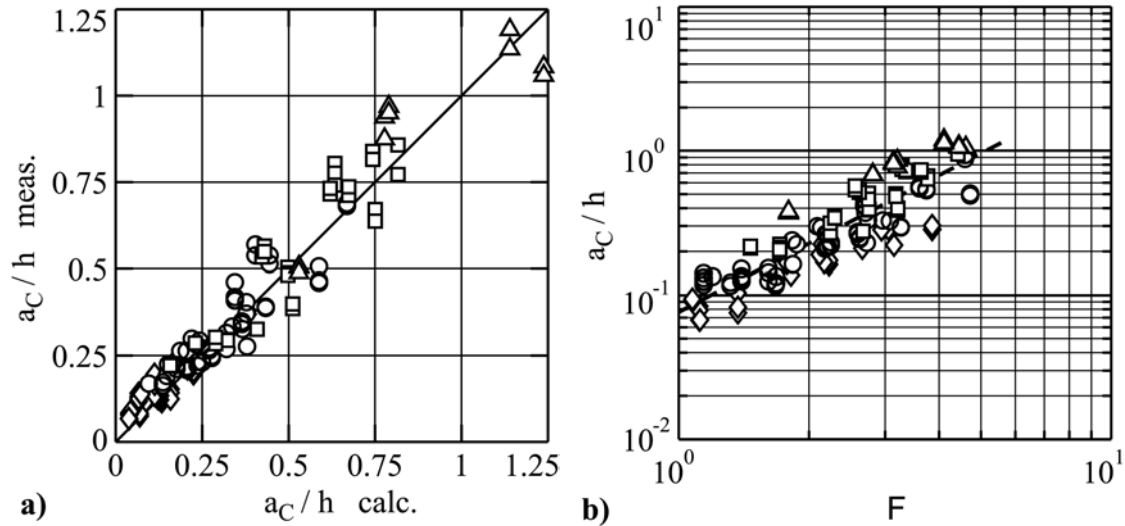
Figure 4.95 **Maximum crest amplitude: a)** a_C/h measured versus a_C/h computed with Eq. 4.35, ($\diamond$) $1 < \mathbf{F} < 2$, ($\bigcirc$) $2 \leq \mathbf{F} < 3$, ($\square$) $3 \leq \mathbf{F} < 4$, ($\triangle$) $4 \leq \mathbf{F} < 5$; **b)** a_C/h versus $\mathbf{F} = v_s/\sqrt{gh}$ with ($\diamond$) $0 < S \leq 0.15$, ($\bigcirc$) $0.15 < S \leq 0.3$, ($\square$) $0.3 < S \leq 0.5$, ($\triangle$) $0.5 < S < 0.7$, (– –) regression ($r^2 = 0.68$).

4.7.7 Prediction of maximum wave trough and second crest amplitudes

The multiple regressions for the maximum wave trough amplitude a_T/h and the maximum second crest amplitude a_{C2}/h yield

$$\frac{a_T}{h} = 0.08\left(\frac{v_s}{\sqrt{gh}}\right)^1 \left(\frac{V_s}{bhs}\right)^{-0.25} \tag{4.36}$$

$$\frac{a_{C2}}{h} = 0.09\left(\frac{v_s}{\sqrt{gh}}\right)^1 \left(\frac{V_s}{bhs}\right)^{-0.4} \tag{4.37}$$

with correlation coefficients $r^2 = 0.73$ and 0.62, respectively. The predominant dimensionless quantity again is the slide Froude number $\mathbf{F}$, but the dimensionless slide length V/S may not be neglected. The multiple regressions yielded the same exponents with altering signs for the slide volume $V = V_s/(bh^2)$ and the slide thickness $S = s/h$, respectively. Hence the parameters were reduced by introducing dimensionless slide

length parameter V/S. The wave trough amplitude a_T/h and the second wave crest amplitude a_{C2}/h are relatively ill defined compared to the largest overall crest amplitude a_C/h, which may be attributed to their generation mechanisms. The leading wave crest is the only wave crest generated directly by the landslide impact, which may explain the excellent correlation coefficient. The following wave trough is formed by the collapse of the hydrodynamic impact crater. The second wave crest was issued by the run-up and subsequent run-down on the hillslope ramp. Therefore the second wave crest strongly depended on the collapse of the hydrodynamic impact crater. An increase in slide volume decreases the maximum wave trough and the second crest amplitudes, whereas an increase in slide thickness increases them. The air volume relative to the slide volume within the impact crater was larger for short and thick slides than for thin and elongated slides. Large air volumes in the impact crater resulted in massive collapses leading to a larger wave trough and subsequent wave run-ups on the hillslope ramp. The comparisons between the measured and the predicted values computed with Eqs. 4.36 and 4.37 are shown in Figs. 4.96a) and b), respectively. Both equations exhibit a similar scattering pattern of the measured values around the predicted ones, because both the wave trough and the second wave crest follow a similar relationship. The accuracy of the predictions decreased towards the back of the wave train. Hence the predictions of the second wave crest amplitude scattered broader than the predictions of the maximum wave trough amplitude, which always corresponded to the first wave trough.
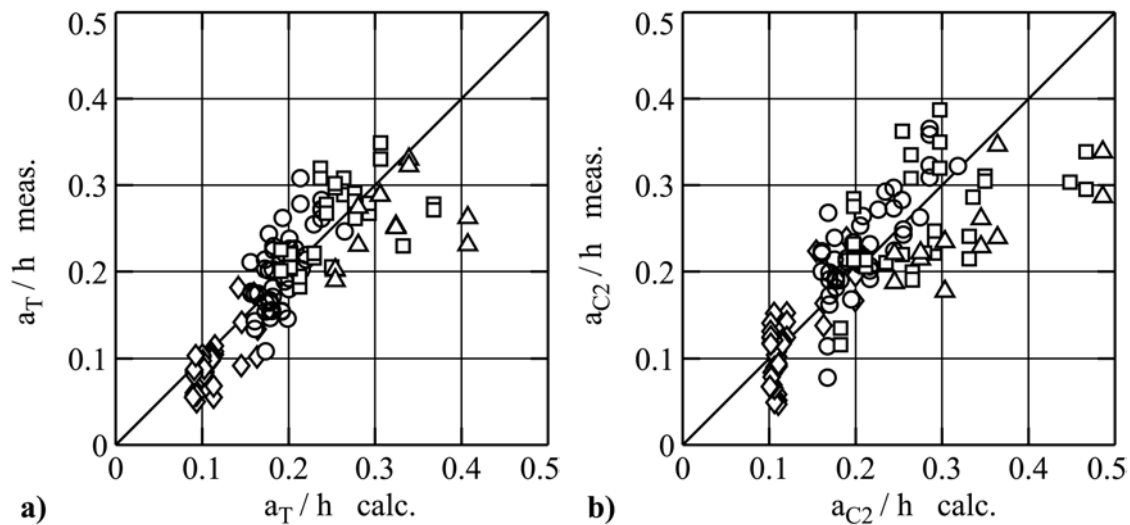
Figure 4.96 **Comparison between measured and computed values: a) Maximum trough amplitude** a_T/h measured versus a_T/h computed with Eq. 4.36, ($\Diamond$) $1 < F < 2$, ($\bigcirc$) $2 \le F < 3$, ($\square$) $3 \le F < 4$, ($\triangle$) $4 \le F < 5$; **b) Maximum second crest amplitude** a_{C2}/h measured versus a_{C2}/h computed with Eq. 4.37 and symbols as in a).

The second wave crest and the maximum wave trough increased with the maximum wave crest in the weakly non-linear region but then decayed towards zero with increasing non-linearity. The solitary waves and the dissipative transient bores are the most non-

linear water waves possible. Both would theoretically have neither a trailing trough nor a second wave crest. In the experiments a minor trough and trailing crest was always observed. This explains the too high predictions for large amplitude troughs and second crests.

4.7.8 Wave amplitudes interdependency

The interdependencies between the maximum wave crest amplitude a_C/h and the maximum wave trough amplitude a_T/h as well as the maximum first crest amplitude a_{C1}/h and the maximum second crest amplitude a_{C2}/h were determined by multiple regressions of the measured values. The multiple regressions for the amplitude ratios a_T/a_C and a_{C2}/a_{C1} yield

$$\frac{a_T}{a_C} = 0.3\left(\frac{v_s}{\sqrt{gh}}\right)^{-0.2}\left(\frac{V_s}{bh^2}\right)^{-0.2}\left(\frac{s}{h}\right)^{-0.4} \tag{4.38}$$

$$\frac{a_{C2}}{a_{C1}} = \frac{3}{8}\left(\frac{v_s}{\sqrt{gh}}\right)^{-0.5}\left(\frac{V_s}{bh^2}\right)^{-0.5}\left(\frac{s}{h}\right)^{-0.3} \tag{4.39}$$

with correlation coefficients $r^2 = 0.41$ and 0.75, respectively. All three dimensionless quantities were of importance. The comparisons between the measured and the predicted values computed with Eqs. 4.38 and 4.39 are shown in Figs. 4.97a) and b), respectively.
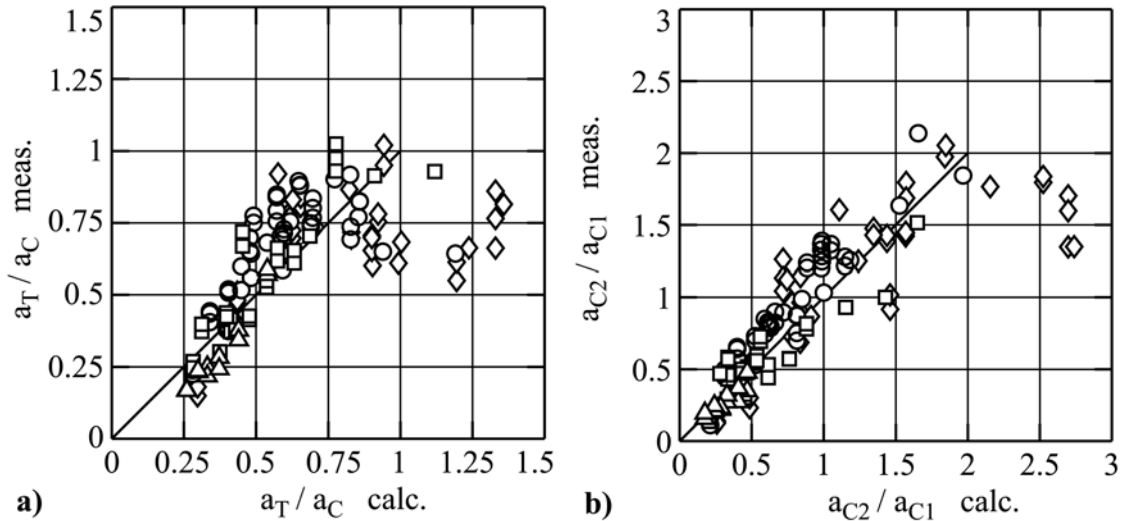
Figure 4.97 **a) Comparison between measured and computed values: a) Maximum trough to crest amplitude ratio** a_T/a_C measured versus a_T/a_C computed with Eq. 4.38, ($\Diamond$) $1 < \mathbf{F} < 2$, ($\bigcirc$) $2 \leq \mathbf{F} < 3$, ($\square$) $3 \leq \mathbf{F} < 4$, (Δ) $4 \leq \mathbf{F} < 5$; **b) Maximum second to first crest amplitude ratio** a_{C2}/a_{C1} measured versus a_{C2}/a_{C1} computed with Eq. 4.39 and symbols as in a).

Both equations exhibit a similar scattering pattern of the measured values around the predicted ones, because both the wave trough and the second wave crest follow a similar relationship. The scattering patterns emphasize the increase in wave trough and second wave crest amplitude with the maximum crest amplitudes in the weakly non-linear region but then decayed towards zero with increasing non-linearity. The solitary waves and the dissipative transient bores would theoretically have neither a trailing trough nor a second wave crest.

4.7.9 Wave period evolution

The wave period of individual waves may be determined in the time domain of the wave gage recordings. The individual waves were determined by performing a zero-crossing analysis. Each wave was defined as the water surface variation between two successive up-crossings of the time series relative to the zero elevation. The upcrossing method was chosen because the wave trains generated by subaerial landslide impacts always start with a rise of the water surface from the zero elevation. Waves defined by the upcrossing method are composed of a wave crest followed by a trough. The leading "upcrossing" is a simple departure of the water surface from the stillwater level. The beginning of the leading wave crest was defined by $\eta = 0.05\, a_{c1}$ corresponding to the point on the time axis where the water surface elevation η reached 5 % of the leading wave crest amplitude a_{c1}. The upcrossing method was commonly applied to the studies of impulse waves. The method chosen for the wave delimitation needs to be considered when comparing the results obtained in different studies. The wave period definitions are shown in Fig. 4.98 with the upcrossing wave period T_1 and the crest to crest wave period T_{c1} of the leading wave.
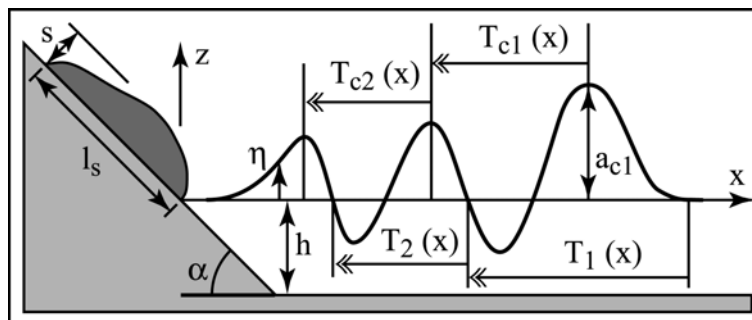
Figure 4.98 **Definitions** of the individual wave periods from rise to rise and crest to crest.

The upcrossing wave period $T_1 \sqrt{g/h}$ and the crest to crest wave period $T_{c1} \sqrt{g/h}$ of the leading wave were determined over the propagation distance range $2 < x/h < 22$ given by the selected water depths and the positions of the first six wave gages (Table 4.1). At the seventh wave gage the wave periods could not be measured because of the falsification due to the wave reflection. The measured wave periods of the leading wave increased with the propagation distance. The upcrossing and crest to crest wave

periods of the leading wave were within $6 < T_1 \sqrt{g/h} < 22$ and $5 < T_{c1} \sqrt{g/h} < 17$, respectively. The upcrossing wave period $T_1 \sqrt{g/h}$ of the leading wave roughly exceeded the first crest to crest wave period $T_{c1} \sqrt{g/h}$ by 20%.

Huber (1980) measured wave periods within $4 < T_{Huber} \sqrt{g/h} < 36$ over the larger propagation distance range $5 \le x/h \le 100$. The upcrossing wave periods are on average 30% above those determined by Huber at the same location x/h. This may be explained by the different wave period definitions. Huber defined the beginning of the leading wave crest by $\eta = 0.5 a_{c1}$ corresponding to the point on the time axis where the water surface elevation η reached half the leading wave crest amplitude a_{c1}.

The upcrossing wave period $T_2 \sqrt{g/h}$ and the crest to crest wave period $T_{c2} \sqrt{g/h}$ of the trailing wave were determined over a propagation distance range $2 < x/h < 19$. At the sixth and seventh wave gages the wave periods could not be measured because of the falsification due to the wave refection. The evolution of the period of the second wave is more complicated than the propagation of the leading wave period due to the effects of dispersion. In general the whole wave train stretched out with the propagation distance. The upcrossing and crest to crest wave periods of the trailing wave were within $3 < T_2 \sqrt{g/h} < 9$ and $3 < T_{c2} \sqrt{g/h} < 9$, respectively. There was almost no difference between the upcrossing period $T_2 \sqrt{g/h}$ and the crest to crest period $T_{c2} \sqrt{g/h}$ of the trailing wave. The lacking difference between the two methods indicates an oscillatory wave form of the trailing waves with minor effects of nonlinearity – such as skewed wave profiles and unequipartition between crest and trough amplitudes. The wave periods of the trailing wave were roughly half the wave period of the leading wave. In general the wave periods decreased towards the back of the wave train.

Rescaling the wave period evolutions of the leading wave with the wave period at $x/h = 5$ allowed to collapse all wave period evolution curves. The arbitrary location was selected due to the availability of wave period estimates at all water depths. Further the bulk of the slide motion was terminated at $x/h = 5$. The relationship defining the wave period at the location of the anchor point will be presented subsequently. The rescaled wave periods $T_1/T_1 (x/h = 5)$ and $T_2/T_2 (x/h = 5)$ are shown in Figs. 4.99a) and b), respectively. The evolution of the leading wave period T_1 may be approximated by the empirical relationship

$$\frac{T_1}{T_1 (x/h = 5)} = 0.6 \left(\frac{x}{h} \right)^{1/3} \tag{4.40}$$

with a good correlation coefficient $r^2 = 0.90$.

Huber (1980) described the wave period increase with propagation distance as

$$T_{Huber} \sqrt{\frac{g}{h}} = 2.85 \left(\frac{x}{h} \right)^{0.45} \tag{4.41}$$

without defining the wave period at an anchor point. Therefore the data scattered by $\pm 50\%$. Rescaling the wave period evolutions of the leading wave with the wave period at $x/h = 5$ yields

$$\frac{T_{Huber}}{T_{Huber}(x/h=5)} = 0.5\left(\frac{x}{h}\right)^{0.45} \tag{4.42}$$

predicting a slightly more rapid increase in wave period than found in the present study.

Kamphuis and Bowering (1970) observed a linear increase of the wave period with propagation distance according to

$$T_1\sqrt{\frac{g}{h}} = 11 + 0.225\left(\frac{x}{h}\right) \tag{4.43}$$

without defining the wave period at an anchor point. Rescaling the wave period of the leading wave with the wave period at $x/h = 5$ yields

$$\frac{T_1}{T_1(x/h=5)} = \frac{1}{12}\left(11 + 0.225\left(\frac{x}{h}\right)\right) \tag{4.44}$$

predicting a slightly slower increase in wave period than found in the present study. The observation distance expanded up to $x/h = 100$ in contrast to the present study with $x/h \leq 25$.
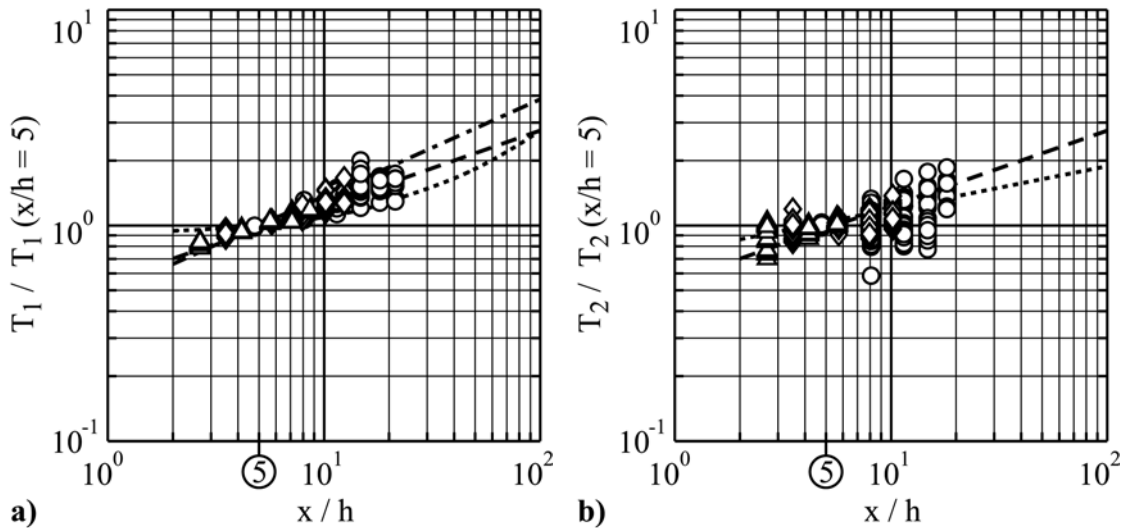
Figure 4.99 **Wave period evolution: a) leading wave upcrossing period** $T_1/T_1(x/h=5)$ versus propagation distance x/h with ($\bigcirc$) $h = 0.3$ m, ($\Diamond$) $h = 0.45$ m, (Δ) $h = 0.675$ m and (— —) Eq. 4.40, (·— ·) Eq. 4.42, (····) Eq. 4.44; **b) second wave upcrossing period** $T_2/T_2(x/h=5)$ versus propagation distance x/h with (— —) Eq. 4.40, (····) regression ($r^2 = 0.1$) and symbols as in a).

The exponential regression for the evolution of the trailing wave period T_2 yielded an extremely poor correlation coefficient $r^2 = 0.1$. The evolution of the trailing wave period is ill defined with some waves increasing and others decreasing in period with the propagation distance. The period of the trailing wave increased slower on average than the period of the leading wave.

4.7.10 Wave period prediction

The attempt to link the wave period of the leading wave T_1 at $x/h = 5$ to the duration of the subaqueous slide motion t_{sd} yielded an extremely poor correlation coefficient $r^2 = 0.02$. Analogous regressions with the slide impact duration t_{si} and the duration of the impact crater expansion t_D instead of the duration of the slide motion t_{sd} resulted in equally poor correlation coefficients $r^2 = 0.04$ and $r^2 = 0.2$, respectively. Hence neither the duration of the subaqueous slide motion t_{sd} nor the slide impact duration t_{si} nor the duration of the impact crater expansion t_D had any significant influence on the wave period. These three time scales only relate to the water displacement but not to the cavity collapse or the run-up and subsequent run-down along the hillslope ramp. The second wave was always generated by the run-down following the run-up along the hillslope ramp. The wave period was governed by the timespan from the initial uplift of the water surface to the run-down along the hillslope ramp. This timespan may not be defined by impact or water displacement related time quantities.

The multiple regression for the normalized wave period of the leading wave T_1 at $x/h = 5$ yields

$$T_1\left[\frac{x}{h} = 5\right]\sqrt{\frac{g}{h}} = 8.9\left(\frac{v_s}{\sqrt{gh}}\right)^{0.2}\left(\frac{V_s}{bh^2}\right)^{0.1} \tag{4.45}$$

with a correlation coefficient $r^2 = 0.75$. The slide Froude number $\mathbf{F} = v_s/\sqrt{gh}$ was identified as the primary parameter governing the period of the leading wave, but the dimensionless slide volume $V = V_s/(bh^2)$ may not be neglected. The dimensionless thickness S had no influence on the wave period. The comparison between the measured and the predicted values computed with Eq. 4.45 is shown in Fig. 4.100a).
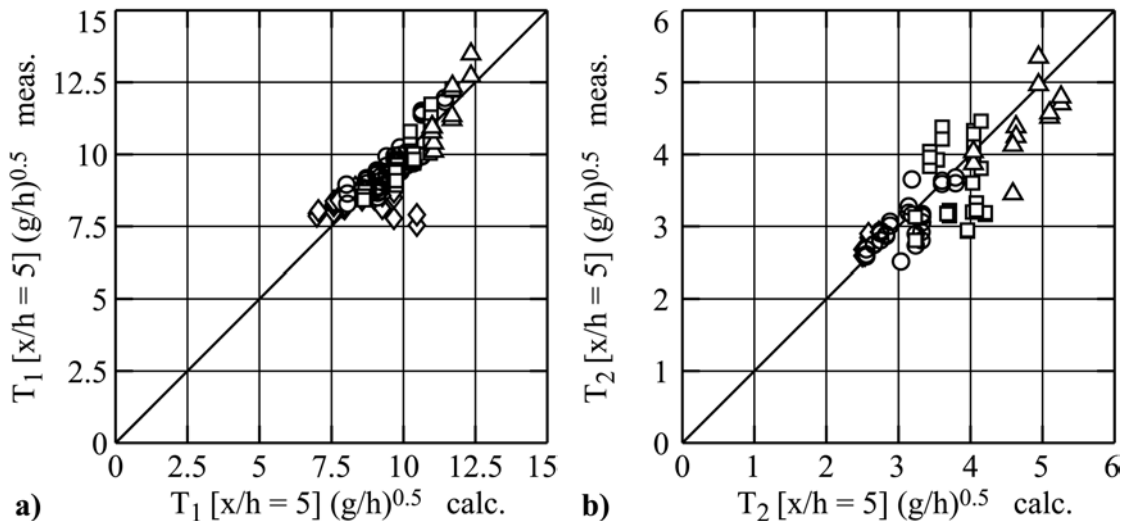
Figure 4.100 **a) Leading wave period** $T_1/T_1(x/h=5)$ measured versus $T_1/T_1(x/h=5)$ computed with Eq. 4.45, ($\Diamond$) $1 < \mathbf{F} < 2$, ($\bigcirc$) $2 \leq \mathbf{F} < 3$, ($\square$) $3 \leq \mathbf{F} < 4$, ($\triangle$) $4 \leq \mathbf{F} < 5$; **b) trailing wave period** $T_2/T_2(x/h=5)$ measured versus $T_2/T_2(x/h=5)$ computed with Eq. 4.46, symbols as in a).

The multiple regression for the normalized wave period of the trailing wave T_2 at $x/h = 5$ yields

$$T_2\left[\frac{x}{h} = 5\right]\sqrt{\frac{g}{h}} = 1.5\left(\frac{v_s}{\sqrt{gh}}\right)^{0.7}\left(\frac{V_s}{bhs}\right)^{0.2} \qquad \textbf{(4.46)}$$

with correlation coefficient $r^2 = 0.63$. The predominant dimensionless quantity again is the slide Froude number **F**, but the dimensionless slide length parameter V/S may not be neglected. The comparison between the measured and the predicted values computed with Eq. 4.46 is shown in Fig. 4.100b).

4.7.11 Wave propagation velocity

The arrival time of an impulse wave which may be determined by the ray path and the wave propagation velocity is of key interest regarding hazard prevention. The wave propagation velocity of linear waves is determined by the wave length L and the stillwater depth h. The measured crest amplitudes were within $0.05 < a_c/h < 1.25$. The condition for linear wave theory is $a_c/h < 0.03$ (Dean and Dalrymple, 1991). Hence all waves generated by granular landslide impacts in the present study were non-linear. In the non-linear range the wave propagation velocity further depends on the relative wave amplitude a/h or wave height H/h. The importance of higher order effects increases with increasing relative wave length L/h. Each single crest and trough had an individual local wave length and travelled with an individual wave propagation velocity. Hence impulse waves are not steady in a reference frame moving at the wave propagation velocity, in contrast to the solitary wave. Therefore each hump in the still water surface may be considered solely.

The wave propagation velocities of individual wave crests and troughs were determined from gage to gage. The wave propagation velocity was defined by the 1 m gage spacing divided by the travel time required for an individual crest or trough to pass the location of the successive gage. The wave period definitions are shown in Fig. 4.98 with the crest velocity c_{c1} and the trough velocity c_{t1} of the leading wave.
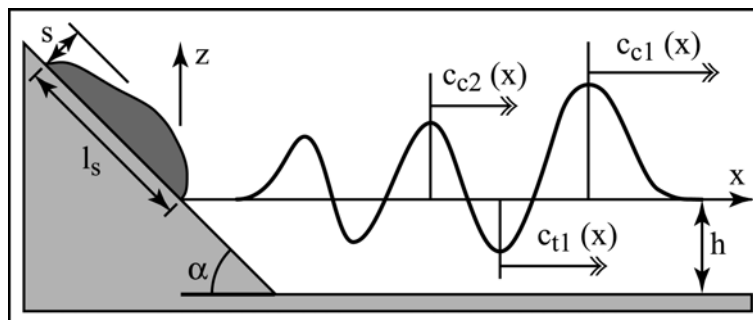
Figure 4.101 **Definitions** of the individual wave crest and trough velocities.

The wave propagation velocity estimates were positioned between successive gages. The selected water depths and the positions of the seven wave gages (Table 4.1) enabled six propagation velocity estimates over a propagation distance range $3 < x/h < 24$ for the leading wave crest. The observation distance decreased to $x/h < 20$ for the first wave trough and the trailing wave crest because of the falsification due to the wave reflection. The propagation velocities of the first wave crest and trough as well as the second wave crest were within $0.8 < c_{c1}/\sqrt{gh} < 1.5$, $0.7 < c_{t1}/\sqrt{gh} < 1$ and $0.6 < c_{c2}/\sqrt{gh} < 1$, respectively, if breaking waves and bores are neglected. The wave propagation velocity decreased from the front to the back of the wave trains due the decreasing wave length of the trailing waves. The second wave crest propagation velocity $c_{c2}/\sqrt{gh}$ was on average 20 to 30% lower than the leading wave crest propagation velocity $c_{c1}/\sqrt{gh}$. In the linear range the wave propagation velocity is limited to $c \leq \sqrt{gh}$. The propagation velocity of the leading wave crest often exceeded the maximum possible linear propagation velocity corresponding the shallow water wave propagation velocity. Hence the wave propagation velocity was strongly affected by the wave non-linearity.

The propagation velocity of the leading wave crest c_{c1} may be compared to the theoretical approximations for a solitary wave. The speed of a solitary wave is given by

$$\frac{c_{c1}}{\sqrt{gh}} \ = \ 1 + \frac{a_{c1}}{2h} \tag{4.47}$$

where $a_{c1} \equiv H$ since the true solitary wave is entirely above the still water level. Eq. 4.47 corresponds to the first approximation of the Laitone theory (1960). Further this theoretical approximation is nearly equal to

$$\frac{c_{c1}}{\sqrt{gh}} \ = \ \sqrt{1 + \frac{a_{c1}}{h}} \tag{4.48}$$

which was determined empirically by Russell (1844), and as a first approximation in the theoretical studies of Boussinesq (1872), Rayleigh (1876), and McCowan (1891). The above equations compared well with experimental investigations on solitary waves (Daily and Stephan, 1953; Naheer, 1978a). The pure solitary wave is difficult to form in the laboratory although it is rather easy to form an approximate solitary wave, one with a tail of dispersive waves. The breaking criterion for a solitary wave was defined by McCowan (1894) as $H_b/h \ = \ 0.78$. Hence the theoretical relationships given by Eqs. 4.47 and 4.48 allow wave celerities c up to 39% and 33%, respectively, beyond the linear shallow water assumption $c \ = \ \sqrt{gh}$ at breaking due to wave non-linearity.

The normalized crest and trough propagation velocity of the leading wave and the normalized crest velocity of the second wave are shown in Figs. 4.102a,b), respectively. The propagation velocity of the leading wave crest c_{c1} follows closely the theoretical approximations for a solitary wave given by Eq. 4.47. The amplitude dispersion characterized by the amplitude to stillwater depth ratio a/h is the primary parameter governing the propagation velocity of the leading wave crest c_{c1}. The noise in the wave propagation velocity estimates was due to local breaking instabilities. Most excess velocity estimates

were determined close to the source. Those are attributed to the velocity vector field imposed by the crater collapse resulting in an augmented propagation velocity. The application of the solitary wave theory close to the impact area delimited by the maximum slide run out x_{sd} is not meaningful, since there the motion was not just unsteady but also forced.
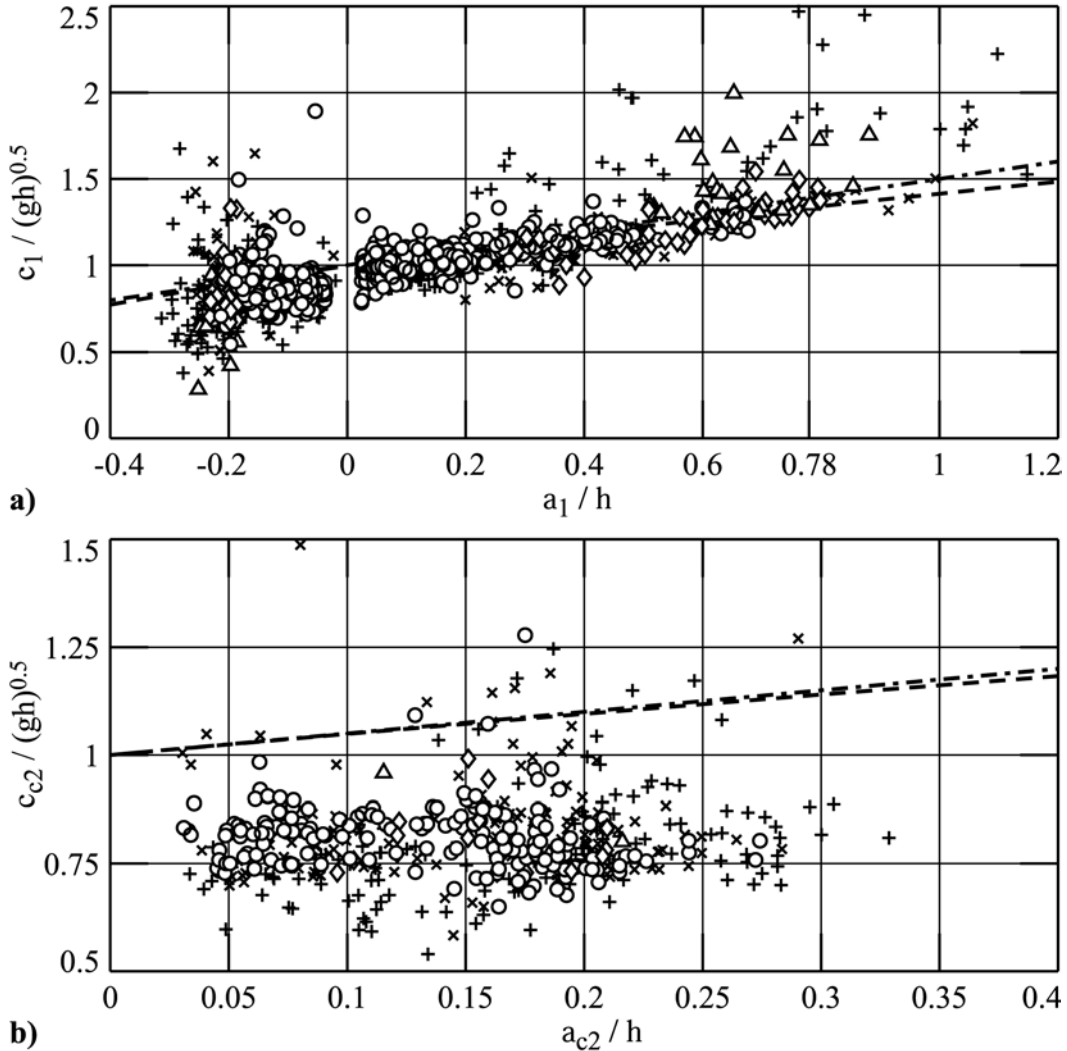
Figure 4.102 **Wave propagation velocity: a) first crest and trough velocities** $c_1/\sqrt{gh}$ versus amplitude a_1/h with (+) first to second gage, ($\times$) second to third gage, ($\bigcirc$) non-breaking wave, ($\diamondsuit$) spilling breaker, ($\triangle$) transient bore, ($-\cdot-$) Eq. 4.47, ($--$) Eq. 4.48; **b) second crest velocity** $c_{c2}/\sqrt{gh}$ versus second crest amplitude a_{c2}/h and symbols as in a).

The solitary wave propagation velocity may be applied to negative amplitude waves corresponding to wave troughs resulting in a reduction of the shallow water wave propagation velocity with increasing trough amplitude. The propagation velocity of the first trough slightly lags the solitary wave propagation velocity defined by the negative trough amplitude and the water depth. The second wave crest propagation velocity concentrated around $c_{c2} \approx 0.8\sqrt{gh}$. The trailing wave propagation velocity even lagged the linear shallow water wave propagation velocity $c = \sqrt{gh}$ by 20% on average. Hence neither the

solitary wave theory nor the linear long wave theory do apply for the trailing waves. The trailing wave propagation velocity reduced by roughly 30% compared to the leading wave crest propagation velocity may be attributed to the shorter wavelength resulting in frequency dispersion. The frequency dispersion was analyzed by Fritz and Liu (2002).

The solitary wave like behavior of the leading wave crest was identified previously by Kamphuis and Bowering (1970) and Huber (1980). Further Le Méhauté and Khangoankar (1992) showed that the propagation velocity of the leading wave crest of an explosion generated impulse wave train matched the solitary wave propagation velocity.

4.7.12 Wave length evolution

The wave length is defined in physical space as the horizontal distance of two successive upcrossings or wave crests. The wave length determined by multiplication of the wave period with the wave propagation velocity corresponds to the wave length in physical space if the wave train is steady from a point of view moving with the wave train. For transient unsteady wave trains such as impulse waves the wave length determined in physical space does not match the pseudo wave length determined in the time domain of the wave gage recordings. A bias may be introduced between them. The wave length defined as the distance between two successive water surface upcrossings or wave crests was determined by

$$\frac{L_1}{h} = \left(T_1\sqrt{\frac{g}{h}}\right)\left(\frac{c_{c1}}{\sqrt{gh}}\right) \tag{4.49}$$

$$\frac{L_{c1}}{h} = \left(T_{c1}\sqrt{\frac{g}{h}}\right)\left(\frac{c_{c1}}{\sqrt{gh}}\right) \tag{4.50}$$

with the first term on the right hand side corresponding to the dimensionless wave period [para 4.7.9] and the second term to the wave crest propagation velocity [para 4.7.11]. The wave length definitions are shown in Fig. 4.103 with the upcrossing wave length L_1 and the crest to crest wave length L_{c1} of the leading wave.
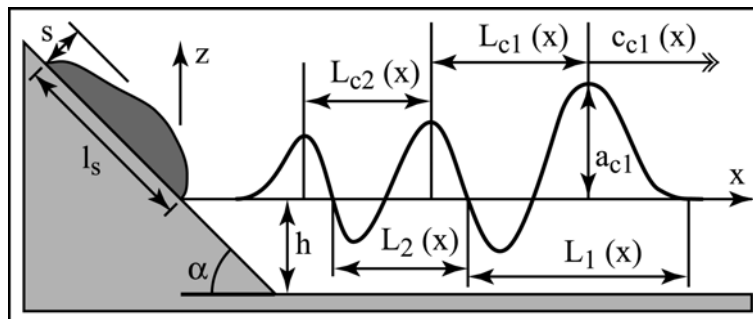
Figure 4.103 **Definitions** of the individual wave lengths from rise to rise and crest to crest.

The evolutions of the upcrossing wave length L_1/h and the crest to crest wave length L_{c1}/h of the leading wave were determined over a propagation distance range $2 < x/h < 22$ given by the selected water depths and the positions of the first six wave gages (Table 4.1). At the seventh wave gage the wave lengths could not be measured because of the falsification due to the wave reflection. The measured wavelengths of the leading wave increased with the propagation distance. The upcrossing and crest to crest wave lengths of the leading wave were within $5 < L_1/h < 25$ and $4 < L_{c1}/h < 20$, respectively. The upcrossing wave length L_1/h of the leading wave roughly exceeded the first crest to crest wave length L_{c1}/h by 20% to 30%. The propagation velocities of the leading wave crest were within $0.8 < c_{c1}/\sqrt{gh} < 1.5$ if breaking waves and bores are neglected. Hence the dimensionless wave length is roughly proportional to the dimensionless wave period determined in [para 4.7.9]. It is recalled that the shallow water wave regime is defined by $L/h \geq 20$. The bulk of the leading impulse waves did not make it into the long wave regime. Hence the leading impulse waves may be classed into the intermediate water depth regime with $2 < L/h < 20$.

Huber (1980) measured wave lengths within $4 < L_{Huber}/h < 40$ over the larger propagation distance range $5 \leq x/h \leq 100$. The upcrossing wave lengths are on average 30% above those determined by Huber at the same location x/h. This may be explained by the different wave length definitions.

The evolutions of the upcrossing wave length L_2/h and the crest to crest wave length L_{c2}/h of the trailing wave were determined over a propagation distance range $2 < x/h < 19$. At the sixth and seventh wave gages the wave lengths could not be measured because of the falsification due to the wave refection. The evolution of the second wave length is more complicated than the propagation of the leading wave length due to the effects of dispersion. In most non-breaking cases the whole wave train stretched out with the propagation distance. The upcrossing and crest to crest wave lengths of the trailing wave were within $2 < L_2/h < 8$ and $2 < L_{c2}/h < 8$, respectively. The trailing impulse waves may be classed into the intermediate water depth regime with $2 < L/h < 20$. The propagation velocities of the trailing wave crest may be approximated by $c_{c2} \approx 0.8\sqrt{gh}$ if breaking waves and bores are neglected. Hence the dimensionless wave length is roughly proportional to the dimensionless wave period determined in [para 4.7.9]. There was almost no difference between the upcrossing wave length L_2/h and the crest to crest wave length L_{c2}/h of the trailing wave. The lacking difference between the two methods indicates an oscillatory wave form of the trailing waves with minor effects of nonlinearity – such as skewed wave profiles and unequipartition between crest and trough amplitudes. The wave lengths of the trailing wave were roughly a third of the leading wave length. In general the wave lengths decreased towards the back of the wave train.

Scaling the wave length evolutions of the leading wave with the wave length at $x/h = 5$ allowed to collapse all leading wave length evolution curves. The arbitrary location $x/h = 5$ was selected due to the availability of wave length estimates at all water depths. Further the bulk of the slide motion was terminated at $x/h = 5$. The rela-

tionship defining the wave period at the location of the anchor point will be presented subsequently. The rescaled wave length $L_1/L_1(x/h = 5)$ is shown in Figs. 4.104a).
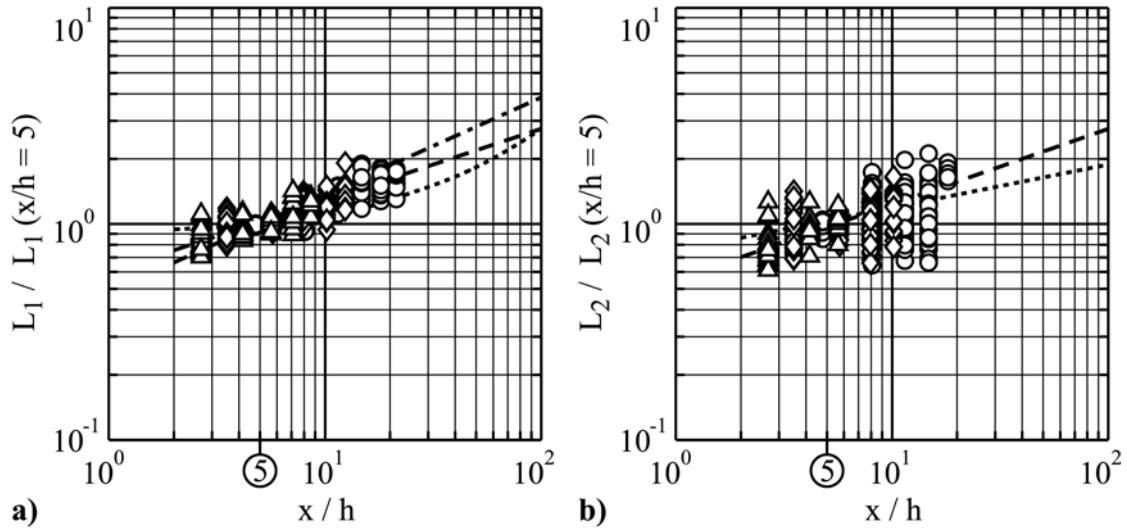
Figure 4.104 **Wave length evolution: a) leading wave length** $L_1/L_1(x/h = 5)$ versus propagation distance x/h with ($\bigcirc$) $h = 0.3$ m, ($\diamondsuit$) $h = 0.45$ m, ($\triangle$) $h = 0.675$ m, (▬ ▬) Eq. 4.51, (▪ ▬ ▪) Eq. 4.53, (▪▪▪▪) Eq. 4.55; **b) trailing wave length** $L_2/L_2(x/h = 5)$ versus propagation distance x/h with (▬ ▬) Eq. 4.51, (▪▪▪▪) regression ($r^2 = 0.15$) and symbols as in a).

The propagation of the leading wave length L_1 may be approximated by the empirical relationship

$$\frac{L_1}{L_1(x/h = 5)} = 0.6\left(\frac{x}{h}\right)^{1/3}$$
(4.51)

with a correlation coefficient $r^2 = 0.81$. The relationship of Eq. 4.51 describing the wave length evolution matches the corresponding wave period related expression of Eq. 4.40.

Huber (1980) described the wave length increase with propagation distance as

$$L_{Huber}/h = 3\left(\frac{x}{h}\right)^{0.45}$$
(4.52)

without defining the wave length at an anchor point. Therefore the data scattered at least by ±50 %. Rescaling the wave length evolutions of the leading wave with the wave length at $x/h = 5$ yields

$$\frac{L_{Huber}}{L_{Huber}(x/h = 5)} = 0.5\left(\frac{x}{h}\right)^{0.45}$$
(4.53)

predicting a slightly more rapid increase in wave length than found in the present study.

Kamphuis and Bowering (1970) observed a linear increase of the wave length with propagation distance according to

$$L_1/h = 11 + 0.225\left(\frac{x}{h}\right)$$
(4.54)

without defining the wave length at an anchor point. Rescaling the wave length of the leading wave with the wave length at $x/h = 5$ yields

$$\frac{L_1}{L_1\,(x/h = 5)} = \frac{1}{12}\left(11 + 0.225\left(\frac{x}{h}\right)\right) \tag{4.55}$$

predicting a slightly slower increase in wave length than found in the present study. The observation distance expanded up to $x/h = 100$ in contrast to the present study with $x/h \leq 25$.

The exponential regression for the evolution of the trailing wave length L_2 yielded an extremely poor correlation coefficient $r^2 = 0.15$. The trailing wave length $L_2/L_2(x/h = 5)$ is shown in Figs. 4.104b). The evolution of the trailing wave length is ill defined with some waves increasing and others decreasing in length with the propagation distance. The length of the trailing wave increased slower on average than the length of the leading wave.

4.7.13 Wave length prediction

Regarding pre-historic and historic events the shape of the subaqueous deposit and the slide run-out $\underset{\sim}{x}_{sd}$ are the only information available of the landslide water interaction. The attempt to link the wave length of the leading wave L_1 at $x/h = 5$ to the subaqueous slide run-out $\underset{\sim}{x}_{sd}$ resulted in

$$L_1\left[\frac{x}{h} = 5\right]\!/h = 4.5\left(\frac{x_{sd}}{h}\right)^{2/3} \tag{4.56}$$

with a correlation coefficient $r^2 = 0.71$. Remarkably the wave length L_1 of the leading wave depends on the subaqueous slide run-out $\underset{\sim}{x}_{sd}$. The normalized wave lengths of the leading wave L_1 at $x/h = 5$ versus the duration of the subaqueous slide run-out $\underset{\sim}{x}_{sd}$ is shown in Figs. 4.105a).

An analogous exponential regression between the subaqueous slide run-out $\underset{\sim}{x}_{sd}$ and the wave length L_2 of the trailing wave at $x/h = 5$ yielded a poor correlation coefficient $r^2 = 0.20$. The correlation between the wave length and the subaqueous slide run-out $\underset{\sim}{x}_{sd}$ is much weaker for the trailing wave than the leading wave. The wave length L_2 of the trailing wave only slightly depends on the subaqueous slide run-out $\underset{\sim}{x}_{sd}$. The normalized wave lengths of the trailing wave L_2 at $x/h = 5$ versus the duration of the subaqueous slide run-out $\underset{\sim}{x}_{sd}$ is shown in Figs. 4.105b).
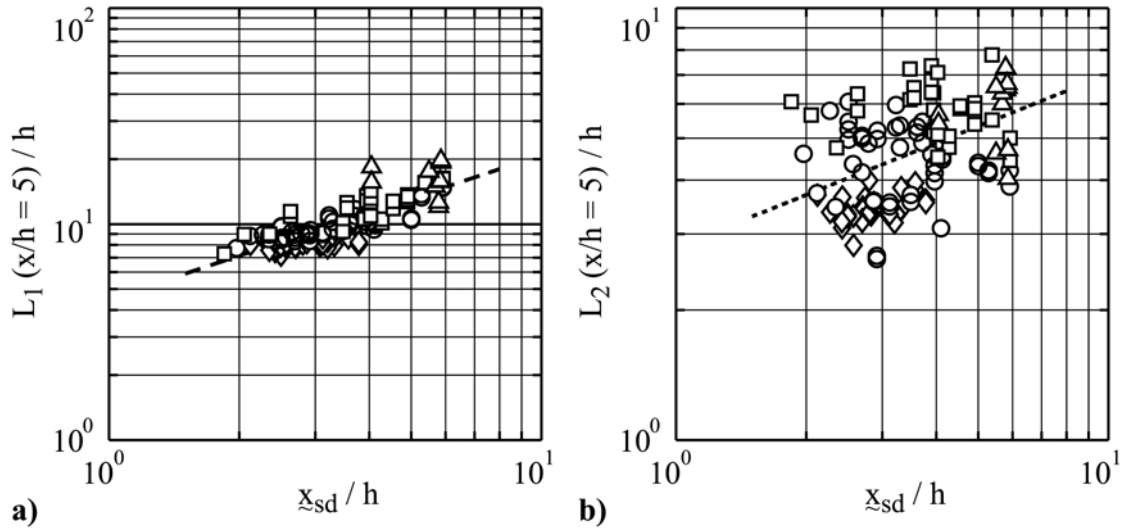
Figure 4.105 **a) Leading upcrossing wave length** $L_1(x/h=5)/h$ versus slide run-out x_{sd}/h with (— —) Eq. 4.56 and (◇) $1 < \mathbf{F} < 2$, (◯) $2 \leq \mathbf{F} < 3$, (☐) $3 \leq \mathbf{F} < 4$, (△) $4 \leq \mathbf{F} < 5$; **b) Trailing upcrossing wave length** $L_2(x/h=5)/h$ versus slide run-out x_{sd}/h with (····) regression ($r^2 = 0.20$) and symbols as in a).

The multiple regression for the normalized wave length of the leading wave L_1 at $x/h = 5$ yields

$$L_1\left[\frac{x}{h} = 5\right]/h = 8.2\left(\frac{v_s}{\sqrt{gh}}\right)^{0.5}\left(\frac{V_s}{bh^2}\right)^{0.2} \tag{4.57}$$

with a correlation coefficient $r^2 = 0.82$. The dominant dimensionless quantities are the slide Froude number $\mathbf{F} = v_s/\sqrt{gh}$ and the dimensionless slide volume $V = V_s/(bh^2)$. The dimensionless thickness $S = s/h$ had no influence on the leading wave length. The dimensionless slide thickness is a parameter regarding vertical length parameters such as the wave amplitudes but not regarding horizontal length parameters such as the wave length. The comparison between the measured and the predicted values computed with Eq. 4.57 is shown in Fig. 4.106a).

The multiple regression for the normalized wave length of the trailing wave L_2 at $x/h = 5$ yields

$$L_2\left[\frac{x}{h} = 5\right]/h = 2.5\left(\frac{v_s}{\sqrt{gh}}\right)^{0.7}\left(\frac{V_s}{bhs}\right)^{-0.1} \tag{4.58}$$

with correlation coefficient $r^2 = 0.66$. The predominant dimensionless quantity again is the slide Froude number $\mathbf{F}$, but the dimensionless slide length parameter V/S may not be neglected. The air volume relative to the slide volume within the impact crater was larger for short and thick slides than for thin and elongated slides. Large air volumes in the impact crater resulted in massive wave run-ups on the hillslope ramp, which affected the wave length of the second wave. The comparison between the measured and the predicted values computed with Eq. 4.58 is shown in Fig. 4.106b).
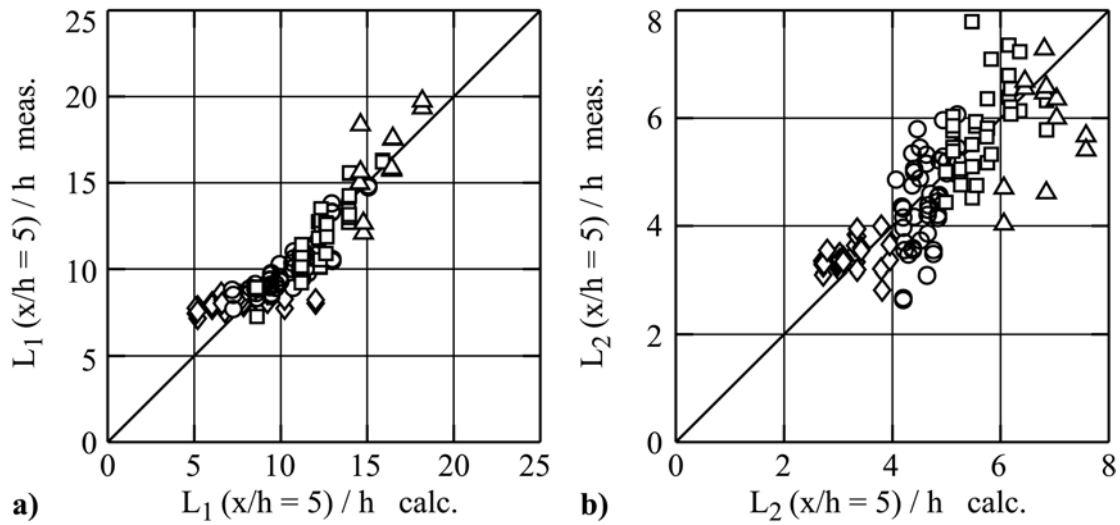
Figure 4.106 **a)** **Leading upcrossing wave length** $L_1(x/h=5)/h$ measured versus $L_1(x/h=5)/h$ computed with Eq. 4.57 and ($\diamondsuit$) $1 < \mathbf{F} < 2$, ($\bigcirc$) $2 \leq \mathbf{F} < 3$, ($\square$) $3 \leq \mathbf{F} < 4$, ($\triangle$) $4 \leq \mathbf{F} < 5$; **b)** **Trailing upcrossing wave length** $L_2(x/h=5)/h$ measured versus $L_2(x/h=5)/h$ computed with Eq. 4.58 and symbols as in a).

Most remarkably the predictive expression of Eq. 4.56, which directly relates the leading wave length L_1 to the subaqueous slide run-out x_{sd}, resulted in a similar correlation coefficient as the multiple regression given by Eq. 4.57. Both may be equally suited to predict the leading wave length L_1 at $x/h = 5$. The direct relationship between the subaqueous slide run-out x_{sd} and the leading wave length L_1 may be of great interest to geologists and geophysicists (pers. com.: Prof. Dr. D. Giardini, Institute of Geophysics, ETH). It may allow to predict the leading wave length L_1 of an impulse wave train directly from the subaqueous slide run-out recorded with sonar or seismic techniques.

4.7.14 Wave non-linearity

In general three criteria may be used to define the wave non-linearity: the relative wave height H/h or amplitude a/h, the wave steepness H/L and the Ursell number $\mathbf{U} = (a_c L^2)/h^3$. In shallow water the most significant parameters regarding nonlinearity are the relative wave height H/h or the relative wave amplitude a/h. In deep water the most relevant parameter is the wave steepness H/L. In intermediate water depth the most significant parameter is the Ursell number, although all three parameters may be considered. The bulk of the measured landslide generated impulse waves may be classified as intermediate water depth waves with $2 < L/h < 20$ [para 4.7.12].

It was shown previously in [para 4.7.4], that the measured crest amplitudes were within $0.05 < a_c/h < 1.25$. The condition for linear wave theory is $a_c/h < 0.03$ (Dean and Dalrymple, 1991). Hence all waves generated by granular landslide impacts in the present study were non-linear. Further it was shown previously in [para 4.7.11], that the

wave propagation velocity strongly depends on the relative wave amplitude a/h confirming the utter importance of higher order terms. Amplitude dispersion is a governing feature of the wave propagation velocity. The full linear wave theory includes frequency dispersion, but does not account for amplitude dispersion.

The wave steepness H_1/L_1 evolution of the leading wave over the propagation distance x/h is shown in Fig. 4.107a). The wave steepness was determined over a propagation distance range $2 < x/h < 22$ given by the selected water depths and the positions of the first six wave gages (Table 4.1). At the seventh wave gage the wave lengths could not be measured because of the falsification due to the wave reflection. The measured steepness of the leading wave decayed with the propagation distance. The wave steepness of the leading wave was within $0.006 \leq H_1/L_1 \leq 0.09$. The condition for linear wave theory is $H/L < 0.006$ (Dean and Dalrymple, 1991). Hence all waves generated by granular landslide impacts in the present study were non-linear.
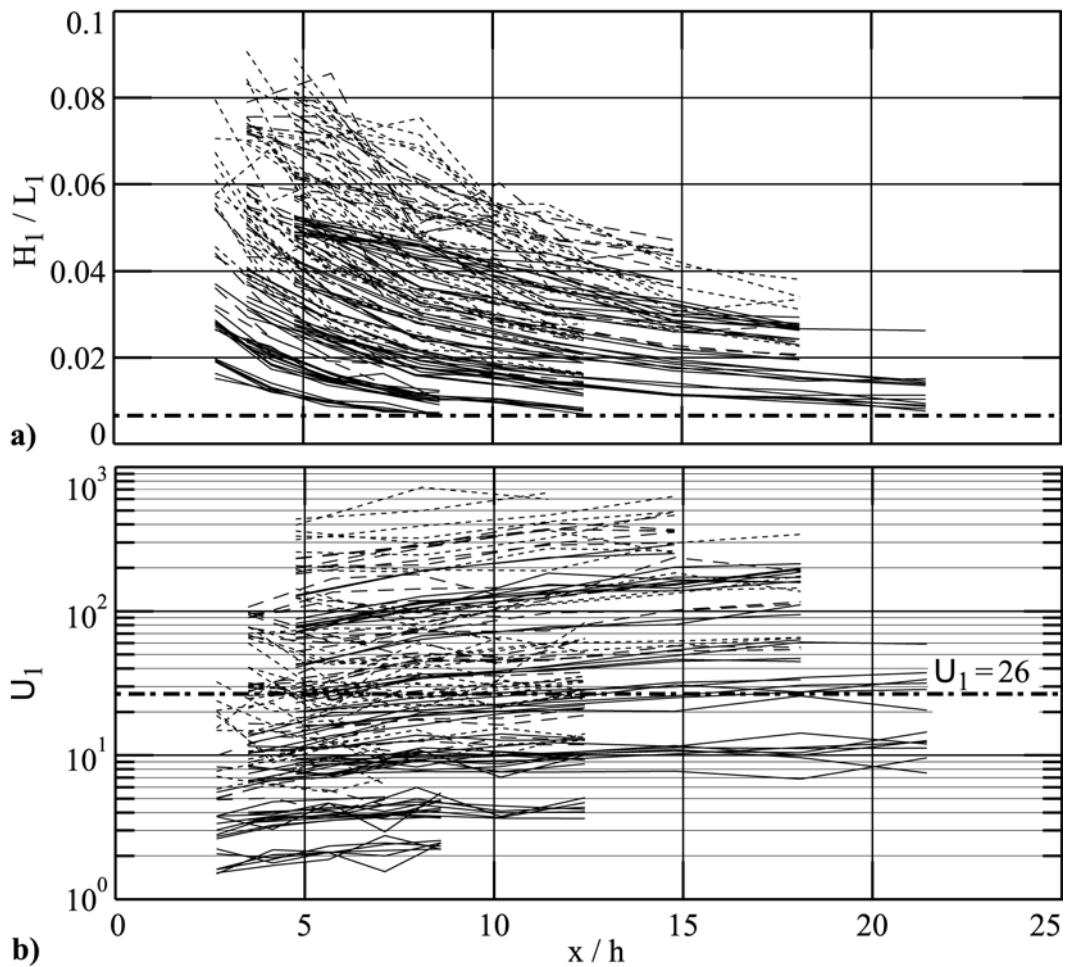
Figure 4.107 **Leading wave: a) wave steepness** H_1/L_1 versus propagation distance x/h of (———) non-breaking waves, (— —) spilling breakers or white capping due to impact crater collapse, (····) transient bores with linear limit (·—·) $H_1/L_1 = 0.06$; **b) Ursell number** $\mathbf{U}_1 = (a_{c1}L_1^2)/h^3$ versus propagation distance x/h with (·—·) $\mathbf{U}_1 = 26$ and symbols as in a).

The limiting wave steepness regarding wave breaking of progressive waves in intermediate water depths was given by Miche (1944) as

$$\frac{H_b}{L_b} = 0.142 \, \tanh\left(\frac{2\pi h_b}{L_b}\right) \tag{4.59}$$

beyond which wave breaking occurs. The subscript b denotes the value at breaking. The steepest possible waves may be observed in deep water. The limiting steepness in deep water was determined by Michell (1893) as

$$\frac{H_b}{L_b} = 0.142 \tag{4.60}$$

beyond which wave breaking occurs. The expression of Eq. 4.60 indicates the largest wave steepness possible for any water wave. The steepness of the leading wave was well below this upper limit, but the leading waves were closer to the shallow water depth wave regime than the deep water depth wave regime. The limiting wave steepness decreases with increasing wave length. For a characteristic wave length $L_1/h \approx 15$ of the leading wave the relationship of Eq. 4.59 yields $H_b/L_b = 0.56$. The theory perfectly matches the experimental measurements. Leading waves with $H_b/L_b \geq 0.56$ always broke at some point along the wave propagation.

The breaking of the leading wave of an impulse wave train may more easily be determined by the relative wave height. The breaking criterion κ in shallow water was defined from solitary wave theory by McCowan (1894) as

$$\kappa = \frac{H_b}{h_b} = 0.78 \tag{4.61}$$

a fraction of wave height H to water depth h. In the strongly non-linear range the crest amplitude approaches the wave height $a_c \approx H$ due to the relatively shallow wave trough. The breaking criterion perfectly matched the observed breaker heights [para 4.7.4]. The shallow water breaking criterion was exceeded by up to 60% by instantaneous wave heights. All breaking waves or bores were generated by outward collapsing impact craters. Wave breaking or bore formation took some time to develop. Therefore a wave exceeding any breaking criterion may remain stable if the run-up on the headland ramp immediately follows the impact. The experimental reproduction of a cross-section of Lituya Bay confirmed that at a wave with $a_c/h = 1.25$ may run-up on the headland prior to breaking (Fritz et al., 2001).

In the intermediate water depth regime the most significant parameter regarding the wave non-linearity is the Ursell number

$$\mathbf{U} = \frac{aL^2}{h^3} \tag{4.62}$$

with the wave amplitude a, the wave length L and the water depth h (Ursell, 1953). The Ursell number gives a ratio of nonlinear to dispersive effects. The Ursell number

$\mathsf{U}_1 = (a_{c1}L_1{}^2)/h^3$ evolution of the leading wave over the propagation distance x/h is shown in Fig. 4.107a). The Ursell number could be determined over a propagation distance range $2 < x/h < 22$ given by the selected water depths and the positions of the first six wave gages (Table 4.1). The Ursell number of the leading wave slightly increased with the propagation distance. The Ursell number of the leading wave was within $1 < \mathsf{U}_1 \le 1000$. The condition for linear wave theory is $\mathsf{U}_1 < 1$ (Lighthill, 1978). Hence all leading waves generated by granular landslide impacts in the present study were non-linear regarding all three non-linearity criteria. Both the wave steepness and the Ursell number estimates roughly correspond to those given by Huber (1980).

The wave steepness H_2/L_2 and the Ursell number $\mathsf{U}_2 = (a_{c2}L_2{}^2)/h^3$ evolutions of the trailing wave over the propagation distance x/h are shown in Figs. 4.108a,b), respectively.
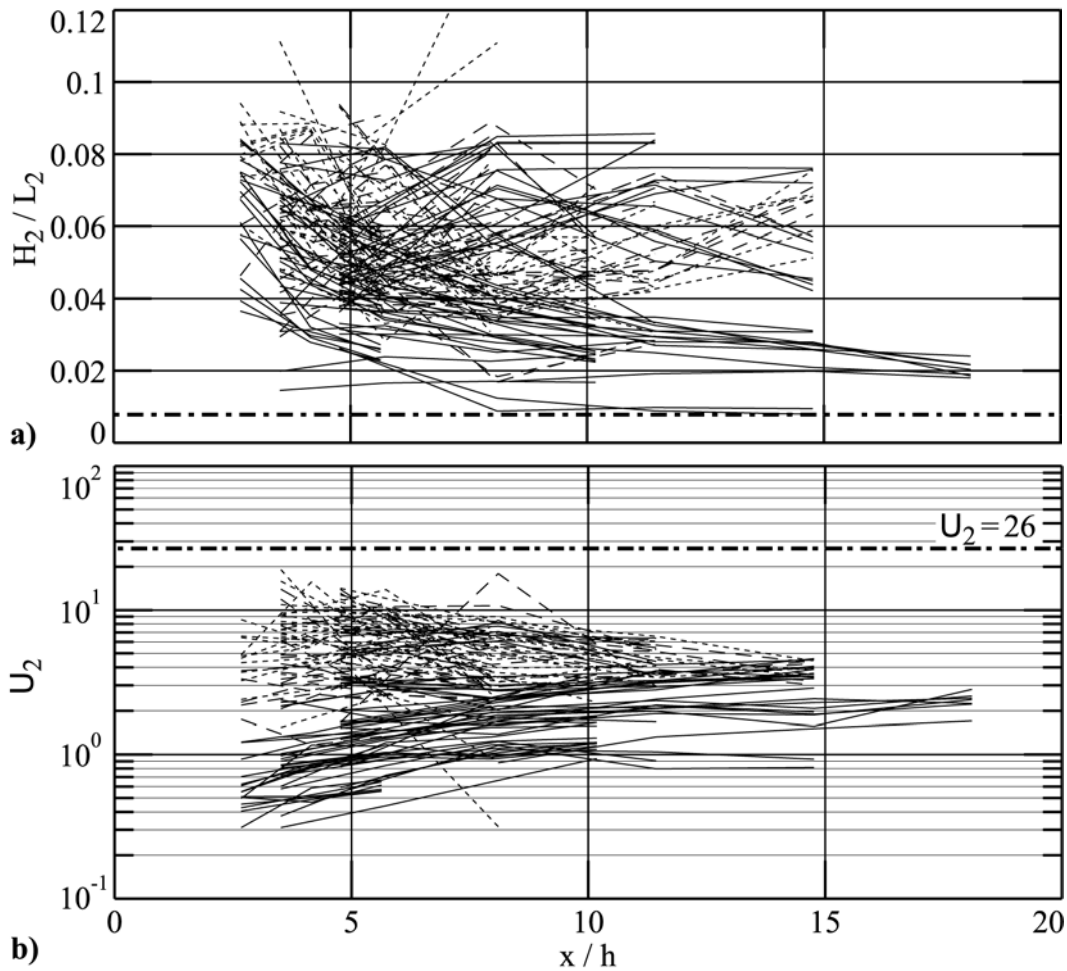
Figure 4.108 **Trailing wave: a) wave steepness** H_2/L_2 versus propagation distance x/h of (——) non-breaking waves, (— —) spilling breakers or white capping due to impact crater collapse, (····) transient bores with linear limit (·—·) $H_2/L_2 = 0.06$; **b) Ursell number** $\mathsf{U}_2 = (a_{c2}L_2{}^2)/h^3$ versus propagation distance x/h with (·—·) $\mathsf{U}_2 = 26$ and symbols as in a).

The wave steepness and the Ursell number could be determined over a propagation distance range $2 < x/h < 19$ given by the selected water depths and the positions of the first six wave gages (Table 4.1). In some cases the wave steepness decayed with the propagation distance in analogy to the leading wave. In other cases the wave steepness increased due to dispersion. Dispersion amplified trailing waves during propagation, while the leading wave decayed. The wave steepness and the Ursell number of the trailing wave were within $0.006 < H_2/L_2 \leq 0.12$ and $0.3 < \mathbf{U}_2 \leq 20$, respectively. The conditions for the linear wave theory are $H/L < 0.006$ and $\mathbf{U}_2 < 1$ (Dean and Dalrymple, 1991). Hence all waves generated by granular landslide impacts in the present study were non-linear.

The limiting wave steepness of progressive waves in intermediate water depths is given by Eq. 4.59 with the deep water asymptote $H_b/L_b = 0.142$ beyond which wave breaking occurs. The steepness of the trailing wave was below this upper limit, but the trailing waves were intermediate water depth waves and not deep water waves – although closer to the deep water than the shallow water wave regime. The limiting wave steepness decreases with increasing wave length. For a characteristic wave length $L_2/h \approx 5$ of the trailing wave the relationship of Eq. 4.59 yields $H_b/L_b = 0.12$. The breaking of the second wave was not directly related to the wave steepness. The second wave was initially a transient bore in most cases, but evolved into a non-breaking progressive wave after a few water depth of propagation distance. The bore was formed by the run-up along the hillslope ramp and the subsequent run-down. The breaking process may therefore be considered as forced.

4.7.15 Leading wave crest volume

The coupling between the mass flow and the water displacement is of crucial importance to numerical modelers (Heinrich, 1992; Jiang and LeBlond, 1992 and 1993; Rzadkiewicz et al., 1997; Mader, 1999; Ward, 2001). The water displacement and the displacement rate extracted from the PIV recordings during the slide impact were presented previously in [para 4.5.4] and [para 4.5.5]. The leading wave crest was directly related to the water displacement induced by the landslide impact, whereas the second wave crest was formed by the run-up along the hillslope ramp and subsequent run-down. Therefore only the volume of the leading wave crest is considered here. Further the volume of the leading wave crest is of fundamental importance regarding the flooding of the shoreline and possible overtopping of dams (Müller, 1995). The volume of the leading wave crest may be determined from the wave gage recordings according to

$$V_{c1} = b \int_{1.crest} \eta \, dx \approx bc_{c1} \int_{1.crest} \eta \, dt \qquad \textbf{(4.63)}$$

by integration of the wave profile recordings from the initial rise of the water surface from the still water level to the first downcrossing and multiplication with the channel width b and the wave crest propagation velocity c_{c1}. The wave crest propagation velocity was

determined previously in [para 4.7.11]. The wave gages only record the wave profile η in the time domain. The assumption $dx = c_{c1}\, dt$ holds for wave trains propagating at constant velocity. The propagation velocities of successive wave crests and troughs commonly varied up to 30 %. Hence integral estimates such as the wave volume, the wave mass or the wave energy extracted from wave profile recordings are of limited accuracy and must be interpreted with care due to the transient and unsteady nature of the impulse waves. Displacement volume estimates measured in a spacial domain such as PIV recordings are of higher accuracy. The definition of the leading wave crest volume V_{c1} is shown in Fig. 4.109 as the area enclosed by the wave profile η from the initial rise to the first downcrossing.
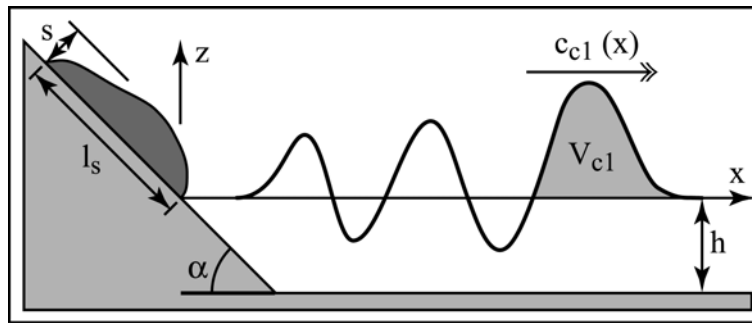
Figure 4.109 **Definition** of the leading wave crest volume V_{c1} as the area enclosed by the wave profile η from the initial rise to the first downcrossing.

The leading wave crest volume V_{c1} altered little over the measured propagation distance range $2 < x/h < 22$ given by the selected water depths, the wave gage positions (Table 4.1) and the arrival times of the front of the wave reflections at the various wave gages. Here only the leading wave crest volumes interpolated at $x/h = 5$ are considered. The arbitrary location was selected due to the availability of unbiased recordings of the whole impulse wave trains at all water depths. Further the bulk of the slide motion was terminated at $x/h = 5$. The leading wave crest volume V_{c1} may be related directly to the maximum water displacement volume V_D by

$$\frac{V_{c1}(x/h = 5)}{bh^2} = 0.6 \left(\frac{V_D}{bh^2}\right)^{1.3} \tag{4.64}$$

with a good correlation coefficient $r^2 = 0.90$. The dependency of the leading wave crest volume V_{c1} on the maximum water displacement volume is shown in Fig. 4.110a). The leading wave crest volume V_{c1} was always smaller or equal to the maximum water displacement volume V_D fulfilling the necessary condition $V_{c1} \leq V_D$. The leading wave crest volume cannot exceed the maximum water displacement volume due to backward water flow induced by the impact crater collapse. The leading wave crest volume can reach the maximum water displacement volume for the special case of soliton-like waves. The smaller the maximum water displacement volume $V_D/(bh^2)$ the smaller was the fraction which went into the leading wave crest volume V_{c1}. This behavior may be

explained by the altering wave generation mechanisms. The smallest water displacement volumes corresponded to unseparated wave generation mechanisms yielding impulse waves closer to the oscillatory wave regime. With increasing relative water displacement volume the wave generation mechanism changed to backward and finally outward collapsing impact craters. Thereby the fraction of the displacement volume, which went into the leading wave crest volume continuously increased.

It is recalled that the maximum water displacement volume V_D always exceeded the landslide volume V_s [para 4.5.5]. The largest measured maximum water displacement per unit width was 8 times larger than the hydrostatic water displacement due to the added slide volume. The simple hydrostatic water displacement is not of relevance regarding the impulse wave generation process at $\mathbf{F} \geq 1$. The leading wave crest volume V_{c1} almost doubled the slide volume V_s on average. Huber (1980) determined a strong decay of the leading wave crest volume V_{c1} relative to the slide volume V_s with increasing slide volume. This observation could not be confirmed by the present study, which indicates only a minor decay of the leading wave crest volume V_{c1} relative to the slide volume V_s with increasing slide volume.
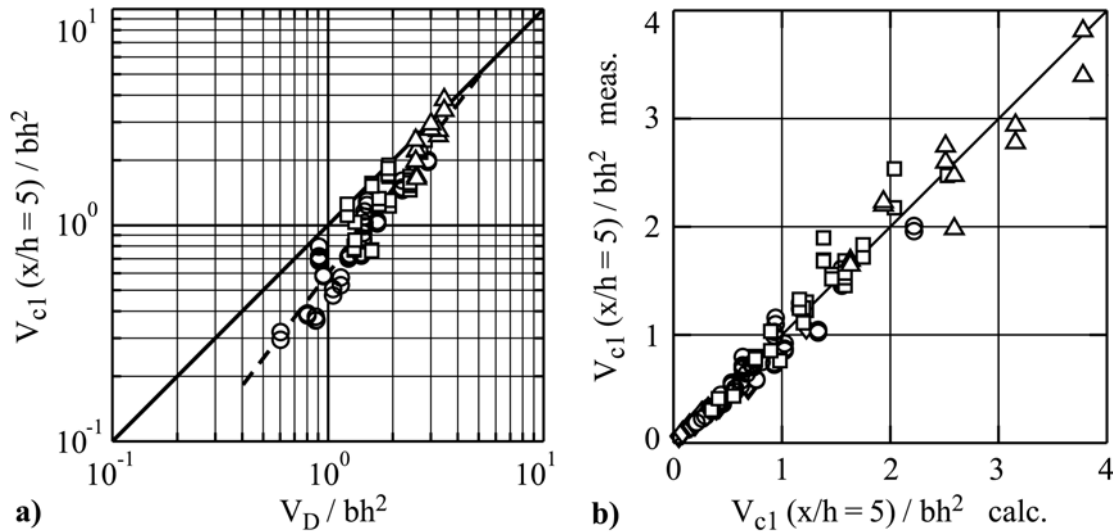
Figure 4.110 **Leading wave crest volume: a)** $V_{c1}(x/h=5)/(bh^2)$ versus the maximum water displacement volume $V_D/(bh^2)$ with ($-\ -$) Eq. 4.64, ($-\!\!-$) $V_{c1} = V_D$ and ($\Diamond$) $1 < \mathbf{F} < 2$, ($\bigcirc$) $2 \leq \mathbf{F} < 3$, ($\square$) $3 \leq \mathbf{F} < 4$, ($\triangle$) $4 \leq \mathbf{F} < 5$; **b)** $V_{c1}(x/h=5)/(bh^2)$ measured versus $V_{c1}(x/h=5)/(bh^2)$ computed with Eq. 4.65 and symbols as in a).

The multiple regression for the leading wave crest volume $V_{c1}(x/h=5)$ yields

$$\frac{V_{c1}(x/h=5)}{bh^2} = 0.55 \left(\frac{v_s}{\sqrt{gh}} \right)^{1.4} \left(\frac{V_s}{bh^2} \right)^{0.4} \left(\frac{s}{h} \right)^{0.4} \tag{4.65}$$

with an outstanding correlation coefficient $r^2 = 0.97$. The correlation even exceeds the indirect determination of the leading wave crest volume by the maximum water displacement volume given by Eq. 4.64. The comparison between the measured values and the

predicted ones computed with Eq. 4.65 is shown in Fig. 4.110b). The dominant dimensionless quantity is again the slide Froude number $\mathbf{F} = v_s / \sqrt{gh}$. The three parameters introduced into the multiple regression may not be reduced. The predicted leading wave crest volume V_{c1} may exceed the maximum water displacement volume V_D for extremely large dimensionless parameters beyond the range covered in the experiments. In such cases the leading wave crest volume V_{c1} has to be assumed equal to the maximum water displacement volume V_D, because it is physically not possible that the leading wave crest volume exceeds the maximum water displacement volume.

4.7.16 Impact energy conversion

In the literature of landslide generated impulse waves two different slide energies were introduced in comparisons with the generated wave energy: the potential slide energy before slide release and the kinetic slide energy upon impact. A simple estimate is the potential energy of a slide, which has been used by Miller (1960) analyzing slides in the field. The potential slide energy was applied to laboratory generated impulse waves by Johnson and Bermel (1949) and Wiegel (1970). The conversion from potential to kinetic energy upon impact may vary significantly among both laboratory studies and observed events due to different friction losses. The potential slide energy before release does not determine the kinetic slide impact energy. Therefore the kinetic slide impact energy was used in the following analysis of the slide to wave energy conversion. The kinetic slide impact energy was also applied by Kamphuis and Bowering (1970) and Huber (1980). The kinetic slide impact energy may be given by

$$E_s = \frac{1}{2} m_s v_s^2 \tag{4.66}$$

with the slide centroid velocity v_s upon impact. The slide impact velocity may be rather difficult to assess in the field. The slide impact velocity may be determined by Eq. 2.2 once a coefficient of friction is known.

The energy inherent to a gravity wave involves two forms: kinetic energy E_{kin}, which is the energy inherent in the orbital motion of the water particles; and potential energy E_{pot} possessed by the particles displaced from their mean position. The surface energy E_σ due to surface tension needs to be considered only for capillary waves and may be neglected for gravity waves under consideration. The wave energy components and the energy partition are described in Appendix G.

The potential wave energy was determined from the wave profiles recorded with the wave gauges according to

$$E_{pot} = \frac{1}{2} b \rho_w \, g \, c \int_0^L \eta^2 \, dt. \tag{4.67}$$

It is recalled that the measured impulse wave trains were transient and non-stationary in a moving reference frame. The variation of the subsequent wave crest and trough propagation velocities by up to 30% was taken into account by computing the potential wave energy for each crest and trough considering the individual wave propagation velocities. The variation of the propagation velocity within a single wave crest is not taken into account.

The total wave energy may be estimated to $E_{tot} \approx 2E_{pot}$ assuming equipartition between the kinetic and the potential wave energy. The total wave energy $E_{tot} = E_{pot} + E_{kin}$ computed numerically may exceed total wave energy estimates based on equipartition between the kinetic and potential wave energy by up to 11% [para G.3]. The accuracy of potential wave energy estimates computed by integration of wave surface profiles recorded with wave gauges in the time domain according to Eq. 4.67 is limited to roughly ±15 % due to the assumption of a constant wave propagation velocity c of individual crests and troughs as well as the noise in the wave gauge recordings induced by the splash. The accuracy of the wave energy estimates may further decay for breaking waves. The total wave energy estimate based on equipartition is fully adequate to the wave surface profiles of transient impulse wave trains recorded with wave gauges in the time domain.

Two different temporal integration ranges were considered. The definition of the integration ranges is shown in Fig. 4.111. The total leading wave crest energy E_{c1} comprises the energy embraced by the initial rise and the first downcrossing of the wave profile η. The total wave train energy E_{wt} comprises the whole energy packet from the initial rise to the end of the wave train.
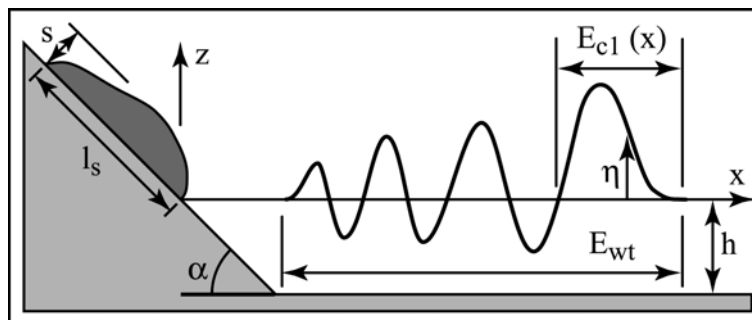
Figure 4.111 **Integration ranges** for the determination of the leading wave crest energy E_{c1} and the wave train energy E_{wt}.

The energy packet of the impulse wave train stretched out during propagation resulting in a decrease of the time localized energy, whereas the total wave energy included in a transient impulse wave train dissipates much slower (Fritz and Liu, 2002). The wave energy disperses with the wave train. The analysis of the dissipation of the total wave energy E_{wt} would require a longer wave tank. In the present study the back of the wave train was often biased by the wave reflection to the third wave gauge.

An analysis of the evolution of the leading wave crest energy E_{c1} over the propagation distance revealed that total wave energy estimates for $x/h < 8$ may be biased due to the impact splashing and the not fully developed wave field. Equipartition may not hold at all too close to the impact area. As the impact crater reached its maximum size the potential energy reached its maximum. Doubling the potential energy to compute the total wave energy may lead to massive overestimates of the total wave energy for $x/h < 8$. Hence the leading wave crest energy E_{c1} at $x/h = 8$ is considered. The arbitrary location was selected due to the availability of leading wave crest energy estimates at all water depths. Further the wave field was fully developed and widely unaffected by the impact splashing at $x/h = 8$.

A strong variation of the decay in the leading wave crest energy over propagation distance was observed. In some cases in the weakly non-linear oscillatory wave region the leading wave crest energy decayed rapidly to $E_{c1}(x/h = 15)/E_{c1}(x/h = 8) = 0.5$, whereas the leading wave crest energy of others in the non-linear transition wave region or the solitary wave region was not dissipated, i.e. $E_{c1}(x/h = 25)/E_{c1}(x/h = 8) = 1$. The decay in the leading wave crest energy E_{c1} does not correspond to the wave energy dissipation except for the transient dissipative bores. The primary cause for the decay of the leading wave crest energy is dispersion for all waves in the intermediate water depth regime. In order to enable the stretching of the energy packed with the propagation distance the leading wave had to travel slightly faster than the centroid of the whole energy packet. The difference between the group velocity and the individual wave propagation velocity increases with decreasing wave length. Part of the energy of the leading wave is passed on to the trailing waves.

The multiple regression for the leading wave crest energy $E_{c1}(x/h = 8)/E_s$ yields

$$\frac{E_{c1}(x/h = 8)}{E_s} = 0.1\left(\frac{v_s}{\sqrt{gh}}\right)^{0.8}\left(\frac{V_s}{bh^2}\right)^{-0.3}\left(\frac{s}{h}\right)^1 \tag{4.68}$$

with a good correlation coefficient $r^2 = 0.81$. The comparison between the measured and the predicted values computed with Eq. 4.68 is shown in Fig. 4.112a). Dumping one of the three dimensionless parameters resulted in significantly weaker correlations. The dominant dimensionless quantities are the slide Froude number $\mathbf{F} = v_s/\sqrt{gh}$ and the slide thickness $S = s/h$. The dominant influence of the slide thickness S on the leading wave crest energy is shown in Fig. 4.112b). Between 2 and 30 % of the kinematic slide impact energy was transferred to the leading wave crest. The wave generation efficiency decreases with increasing dimensionless slide volume V. Similarly the energy conversion decays for explosions with increasing yield in the same water depth (Le Méhauté and Khangoankar, 1992).
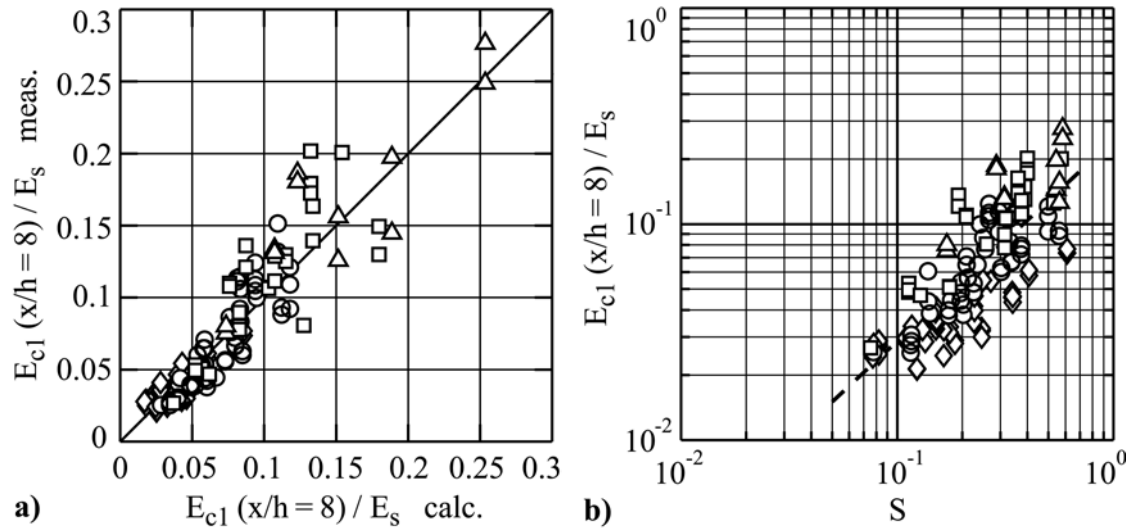
Figure 4.112 **Leading wave crest energy: a)** $E_{c1}(x/h = 8)/E_s$ measured versus $E_{c1}(x/h = 8)/E_s$ computed with Eq. 4.68 and ($\Diamond$) $1 < \mathbf{F} < 2$, ($\bigcirc$) $2 \leq \mathbf{F} < 3$, ($\square$) $3 \leq \mathbf{F} < 4$, ($\triangle$) $4 \leq \mathbf{F} < 5$; **b)** $E_{c1}(x/h = 8)/E_s$ versus $S = s/h$ with (▬ ▬) regression ($r^2 = 0.52$) and symbols as in a).

The propagation velocity of the leading wave crest closely matched the solitary wave propagation velocity [para 4.7.11]. Hence it may be interesting to normalize the leading wave crest energy E_{c1} with the solitary wave energy E_{sol}. The solitary wave energy E_{sol} determined by inserting the measured wave crest amplitude a_{c1} into the relationship given by

$$E_{sol} \approx 2E_{pot} = \frac{8}{3} b \, \rho_w \, g \, h^2 a \sqrt{\frac{a}{3h}} \qquad \textbf{(4.69)}$$

assuming equipartition between the kinetic and the potential wave energy (Boussinesq, 1877 and Munk, 1949). The solitary wave energy is derived in Appendix G. Both estimates assumed equipartition and do not account for the excess kinetic energy in strongly non-linear waves. The wave energy ratio E_{c1}/E_{sol} indicates how close the leading wave crest matches the solitary wave theory. The multiple regression for the leading wave crest energy $E_{c1}(x/h = 8)/E_{sol}(x/h = 8)$ yields

$$\frac{E_{c1}}{E_{sol}}\left[\frac{x}{h} = 8\right] = \frac{2}{3}\left(\frac{v_s}{\sqrt{gh}}\right)^{0.6}\left(\frac{V_s}{bh^2}\right)^{0.2}\left(\frac{s}{h}\right)^{0.2} \qquad \textbf{(4.70)}$$

with a good correlation coefficient $r^2 = 0.94$. The dominant dimensionless quantity is the slide Froude number $\mathbf{F} = v_s/\sqrt{gh}$. The comparison between the measured and the predicted values computed with Eq. 4.70 is shown in Fig. 4.113a). Theoretically, wave energy ratios E_{c1}/E_{sol} beyond unity are not possible. The data with $E_{c1}/E_{sol} \geq 1$ correspond to breaking waves and dissipative transient bores, where air entrainment resulted in too large wave volumes. The wave energy ratio E_{c1}/E_{sol} only indicates how the leading wave crest energy compares to the energy contained in a solitary wave of the same

amplitude. Therefore the different exponents compared to Eq. 4.68 are not surprising. The energy transferred to the leading wave crest E_{c1}/E_s versus the energy ratio E_{c1}/E_{sol} is shown in Fig. 4.113b). The leading wave crest to solitary wave energy ratio increases with the energy conversion from the slide to leading wave crest. Hence leading wave crests with a large energy are similar to a solitary wave in energy content.
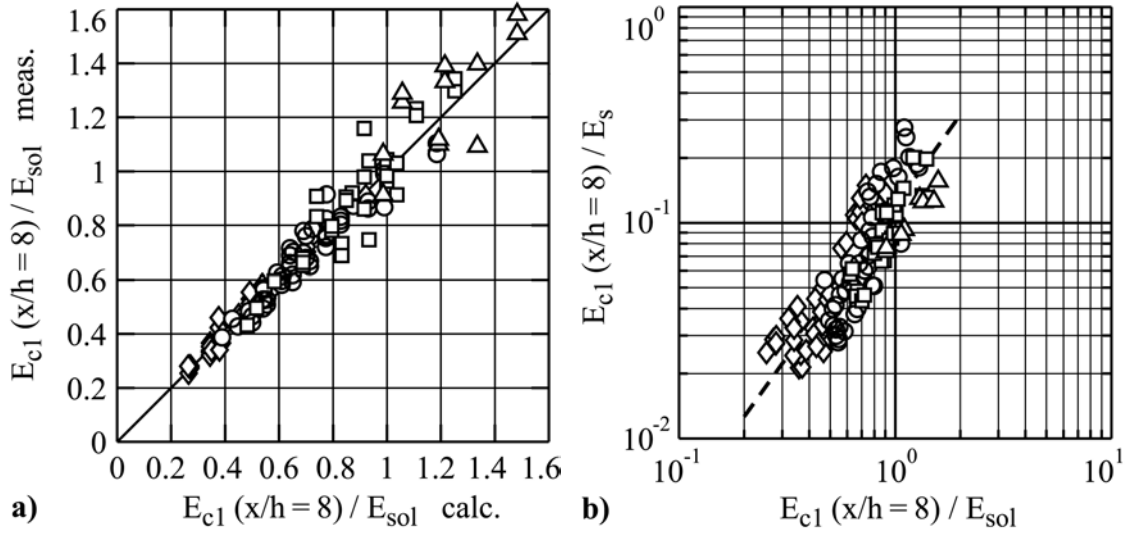
Figure 4.113 **Leading wave crest energy: a)** $E_{c1}(x/h = 8)/E_{sol}(x/h = 8)$ measured versus $E_{c1}(x/h = 8)/E_{sol}(x/h = 8)$ computed with Eq. 4.70 and ($\diamondsuit$) $1 < \mathbf{F} < 2$, ($\bigcirc$) $2 \leq \mathbf{F} < 3$, ($\square$) $3 \leq \mathbf{F} < 4$, ($\triangle$) $4 \leq \mathbf{F} < 5$; **b)** $E_{c1}(x/h = 8)/E_s$ versus $E_{c1}(x/h = 8)/E_{sol}(x/h = 8)$ with (▬ ▬) regression ($r^2 = 0.63$) and symbols as in a).

The wave train energy was determined analogous to the leading wave crest energy. The multiple regression for the wave train energy E_{wt}/E_s yields

$$\frac{E_{wt}}{E_s} = \frac{1}{8}\left(\frac{v_s}{\sqrt{gh}}\right)^{0.5}\left(\frac{V_s}{bhs}\right)^{-1} \tag{4.71}$$

with a good correlation coefficient $r^2 = 0.73$. The comparison between the measured and the predicted values computed with Eq. 4.71 is shown in Fig. 4.114a). The dominant parameters are the slide Froude number $\mathbf{F}$ and the combined volume to thickness parameter V/S. The strong influence of the dimensionless slide length parameter V/S on the wave train energy is shown in Fig. 4.114b). Between 4 and 50% of the kinematic slide impact energy was transferred to the impulse wave train. The wave generation efficiency decreases with increasing dimensionless slide length V/S. An increase in slide volume decreases the slide to wave energy conversion efficiency, whereas an increase in slide thickness increases the slide to wave energy conversion efficiency. Similarly the energy conversion decays for explosions with increasing yield in the same water depth (Le Méhauté and Khangoankar, 1992).
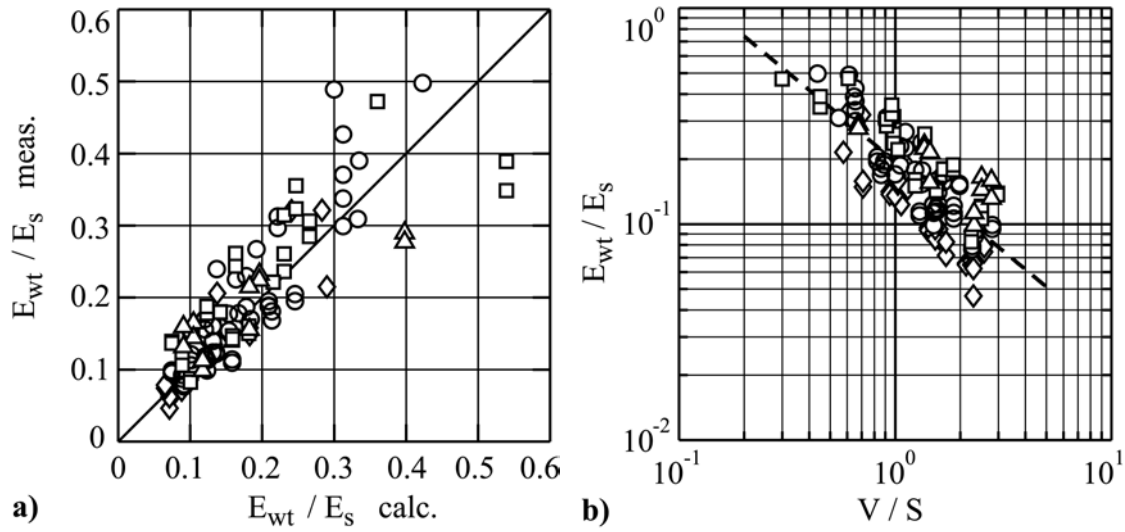
Figure 4.114 **a) Wave train energy** E_{wt}/E_s measured versus E_{wt}/E_s computed with Eq. 4.71 and ($\Diamond$) $1 < \mathbf{F} < 2$, ($\bigcirc$) $2 \le \mathbf{F} < 3$, ($\square$) $3 \le \mathbf{F} < 4$, (Δ) $4 \le \mathbf{F} < 5$; **b)** E_{wt}/E_s versus V/S with (— —) regression ($r^2 = 0.65$) and symbols as in a).

The partition of the wave train energy among the leading wave crest energy and the trailing waves may be analyzed normalizing the leading wave crest energy with the wave train energy. The multiple regression for the leading wave crest to wave train energy ratio E_{c1}/E_{wt} yields

$$\frac{E_{c1}(x/h = 8)}{E_{wt}} = \frac{2}{3}\left(\frac{v_s}{\sqrt{gh}}\right)^{1/3}\left(\frac{V_s}{bh^2}\right)^{2/3} \tag{4.72}$$

with a good correlation coefficient $r^2 = 0.83$. The comparison between the measured values and the predicted ones computed with Eq. 4.72 is shown in Fig. 4.115a). The dominant dimensionless quantity is the dimensionless slide volume $V = V_s/(bh^2)$. An increase in slide Froude number or slide volume increases the amount of the wave train energy included in the leading wave crest. The leading wave crest energy E_{c1}/E_s versus the wave train energy E_{wt}/E_s is shown in Fig. 4.115b). The trend towards an increased leading wave crest energy with increasing wave train energy is weak. Theoretically wave energy ratios E_{c1}/E_{wt} beyond unity are not possible and were not measured. The predicted data with $E_{c1}/E_{wt} > 1$ correspond to breaking waves and dissipative transient bores. Hence the relationship of Eq. 4.72 may be used to predict breaking of the leading wave crest. Between 8 and 100 % of the wave train energy was located in the leading wave crest.
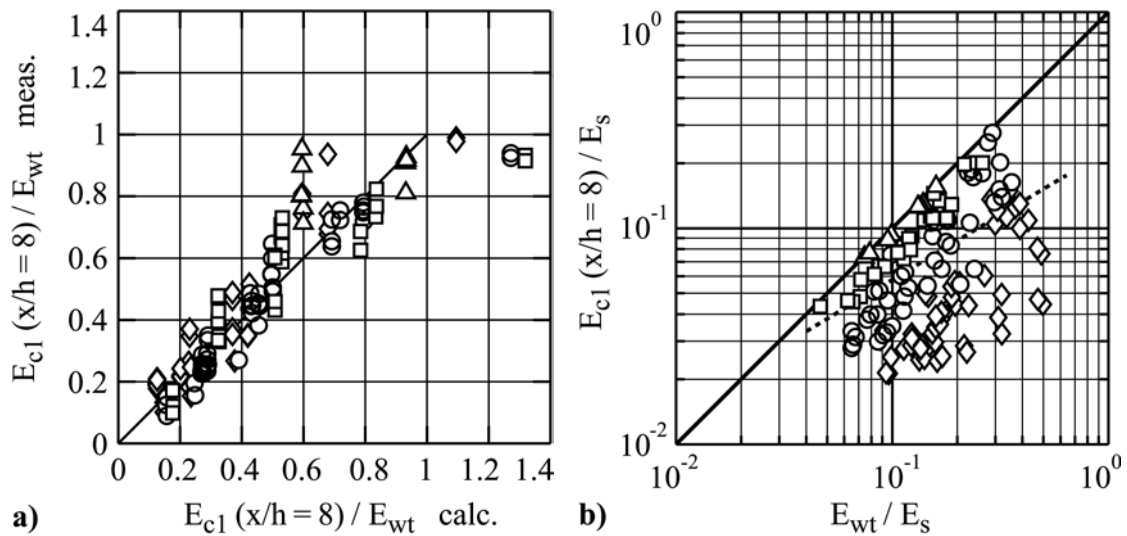
Figure 4.115 **Wave energy partition: a) wave energy ratio** $E_{c1}(x/h = 8)/E_{wt}$ measured versus $E_{c1}(x/h = 8)/E_{wt}$ computed with Eq. 4.72 and ($\Diamond$) $1 < \mathbf{F} < 2$, ($\bigcirc$) $2 \leq \mathbf{F} < 3$, ($\square$) $3 \leq \mathbf{F} < 4$, ($\triangle$) $4 \leq \mathbf{F} < 5$; **b)** leading wave crest energy $E_{c1}(x/h = 8)/E_s$ versus wave train energy E_{wt}/E_s with (••••) regression ($r^2 = 0.20$), (——) $E_{c1} = E_{wt}$ and symbols as in a).

Kamphuis and Bowering (1970) conducted an experimental study in which a weighted tray was emplaced into a flume. The slide impact energy to wave energy conversion ranged from 10 to 50 %. A trend towards a decreasing energy conversion with increasing impact angle was detected. The smallest energy conversion coefficients were determined for slides impacting vertically at $\alpha = 90°$. The granular slide experiments conducted by Huber (1980) yielded slide impact energy to wave energy conversions between 1 and 40 %. Huber did not integrate the square of the wave profile but integrated the square of the analog signal electronically and halved the sum. This approach only yields accurate wave profile integrals for sinusoidal waves. Kamphuis and Bowering (1970) computed the wave energy digitally as in the present study. Gault and Sonett (1982) determined an impact energy to wave energy conversion of 7 % for a projectile impacting at $Ma = 7.5$ into a water body. Watts (2000) determined energy conversions between 2 and 13 % for underwater solid block landslides.

Somewhat controversial estimates of explosion efficiencies may be found in the literature. Jordaan (1969) estimated that in underwater explosions about 40 % of the available energy is used to displace the water around the explosion bubble during its expansion to maximum size. Le Méhauté and Khangoankar (1992) showed that the efficiency of underwater explosions strongly depends on the water depth, the detonation depth and the yield. Explosions in shallow water depth where the explosion bubble vents and reaches ground are extremely inefficient with respect to their wave generation ability. In shallow water depth explosions only 5 % at most of the explosion energy is transferred to the water as potential energy in the form of the hydrodynamic crater and kinetic energy in the form of the outward water motion. The efficiency of underwater explosions rapidly increased with increasing water depth and decreasing yield. In water of identical depth, the lower

yield explosion is more efficient than the higher yield explosion. LeMéhauté and Wang (1995) observed a maximum efficiency of 20% in deep water, which is half the value given by Jordaan (1969). Underwater explosions are inefficient wave generators. Most of the energy released by the explosion is distributed in other effects. The released energy not converted into wave energy is divided, about equally, between shock wave and thermal radiation, both irreversible processes with negligible wave generating effects. A large portion of the potential energy imparted to the water in crater formation is lost to hydrodynamic dissipation during cavity or crater collapse. The energy dissipated hydrodynamically remained approximately constant at 40% (LeMéhauté and Khangoankar, 1992).

The data of the present study, Kamphuis and Bowering (1970) and Huber (1980) yield similar energy conversion ranges. As expected subaqueous slides are less effective wave generators than subaerial slide impacts. Underwater explosions give lower explosion to wave energy ratios than subaerial slide impacts.

5   Discussion of Results

5.1   Introduction

Herein selected results are compared with data obtained previously by others and available observations of real events, whereas short discussions of results were presented together with the experimental results in Chapter 4. The predictive equation for the wave amplitude presented in [para 4.7.6] is compared to previous relationships deduced from other experimental research studies as well as to the Lituya Bay event [para 5.2]. The water particle velocities determined by means of PIV below the impulse waves are compared to the flow fields computed with the analytical solitary wave theory of McCowan (1891) in [para 5.3]. The applicability of the Stokes theory for finite amplitude deep water waves and the cnoidal and solitary wave theories for finite amplitude shallow water waves to the measured non-linear impulse waves classified as intermediate water depth waves is discussed in [para 5.4]. Finally the equivalent coefficients of friction determined in the physical model are compared to observations of real events [para 5.5].

5.2   Comparison of wave amplitude predictions

The validation of any wave amplitude predictive equation must include the comparison with observations of real events. Wave heights of real events near the source were only recorded for minor landslides released by explosions (Müller and Schurter, 1993). Blasting induced landslides may not be representative cases due to possible effects on the landslide consistency and motion. The available information on natural events is mostly limited to landslide scars and deposits, trimlines caused by wave run-ups, and distant tide gage recordings. Therefore the wave heights in the water body must be determined beforehand by means of back calculation from the observed wave run-up. Post-event recordings of the wave run-ups were based either on the trimlines of chopped trees or moved soil. The accuracy of the wave run-up recordings may therefore be limited to several meters. Hence back calculations of wave heights from wave run-up recordings may only yield reliable estimates for events with large wave heights and corresponding large run-ups. Observed run-up heights varied significantly along shorelines due to the effects of the surrounding topography, the bathymetry, multiple reflections, diffraction, spectral superposition and interference. The presented physical model is purely two dimensional in contrast to the natural phenomenon under investigation. Therefore only few events may be well suited for a comparison with two dimensional models.

The Lituya Bay 1958 event may be the best documented subaerial landslide impact into a water body [para B.1.1]. The rockslide impact created a giant gravity wave similar

to a solitary wave with a maximum wave run-up of 524 m in straight prolongation of the slide axis on a spur ridge. The maximum wave run-up is the largest in recorded history and more than doubles any other wave run-up observation. The giant wave run-up reduces observation uncertainties. In a 2D-model radial or lateral wave spreading is neglected. Lateral spreading only occurred in southern direction from the impact site into Gilbert Inlet. In northern direction the impact area was confined to the Lituya Glacier front. In this specific topographic situation wave height reduction due to 3D effects was further limited by the small ratio of 1.6 between propagation distance and slide width. Hence the Lituya Bay 1958 event may be well suited for a direct comparison with two-dimensional models. Further a cross-section of Gilbert Inlet was rebuilt at 1:675 scale in the two-dimensional physical laboratory model (Fritz et al., 2001). The measured wave run-up perfectly matched the trimline of forest destruction on the spur ridge at Gilbert Inlet. The back-calculation of the wave height from the observed trimline of forest destruction using Hall and Watts (1953) run-up formula equaled the measured wave height in Gilbert Inlet. The rock mass with a volume $V_s = 30.6 \times 10^6$ m^3 impacted at a large impact velocity $v_s = 110$ m/s into the water body with a stillwater depth $h = 122$ m. Both the hillslope angle α and the headland angle β were roughly $\alpha = \beta = 45°$. The following assumptions were made regarding the landslide impact shape: mean slide width $b = 823$ m, slide thickness $s = 120$ m, slide length $l_s = 970$ m. The landslides were physically modeled with an artificial granular material (PP-BaSO$_4$), which perfectly matched the assumed rock (amphibole and biotite schist) density $\rho_s = 2.7$ t/m^3. Herewith the dimensionless quantities were determined as follows: the slide Froude number $\mathbf{F} = v_s / \sqrt{gh} = 3.2$, the dimensionless slide volume $V = V_s / (bh^2) = 2.5$, the dimensionless slide thickness $S = s/h = 1$ and dimensionless slide length $l_s / h = 7.9$. The wave profile was recorded at location $x/h = 7.25$ in the physical model. A maximum wave crest amplitude $a_C = a_{C1} = 152$ m was measured followed by a small noisy wave trough $a_T = 10$ m resulting in a total wave height $H = 162$ m.

Characteristic for highly non-linear waves is the large difference between the wave crest and the wave trough amplitudes. Un-equipartition between crest and trough amplitudes characterizes the non-linear water waves, whereas in linear wave theory equipartition is assumed. The assumption of equipartition would result in an underestimation of the wave crest amplitude by roughly a factor of 2 for the Lituya Bay case. The partition of the total wave height H between the crest and trough amplitudes strongly depended on the wave type. The Lituya Bay event demanded a separate investigation of the individual crest and trough amplitudes. The Lituya Bay wave with $a_C / h = 1.25$ fell into the bore regime at the upper limit of the possible wave spectrum. The wave did not break or evolve into a dissipative bore due to the immediate run-up on the headland at the location $x/h = 11$. The small trailing trough $a_T / h = 0.1$ was necessary to compensate for the outward bound mass transport in these non-linear waves. Predicting solely the total wave height H is insufficient and misleading, because the crest amplitude always exceeded or at least matched the trough amplitude $a_C \geq a_T$ in all experiments.

The above assumptions may be introduced into the various predictive equations presented in [para 4.7.6] and [para 2.3], respectively, allowing not only a comparison between them but also with an observed reference case. The comparison between the measured and the predicted wave heights using the equation presented herein and those of the most relevant previous studies is shown in Table 5.1.

Table 5.1 **Comparison of wave amplitude predictions** with the Lituya Bay test case.

Source	Equations and remarks	a_C [m]	a_T [m]	H [m]
Fritz et al., 2001	measured	152	10	162
Eq. 4.35	$\frac{a_C}{h} = 0.25\left(\frac{v_s}{\sqrt{gh}}\right)^{1.4}\left(\frac{s}{h}\right)^{0.8}$	155		
Huber and Hager, 1997	$H = 0.88\sin\alpha\left(\frac{\rho_s}{\rho_w}\right)^{1/4}\left(\frac{V_s}{b}\right)^{1/2}\left(\frac{h}{x}\right)^{1/4}$			94
Kamphuis and Bowering, 1970	$\frac{H}{h} = \left(\frac{v_s}{\sqrt{gh}}\right)^{0.7}\left(0.31 + 0.2\log\left(\frac{l_s s}{h^2}\right)\right) + 0.35e^{-0.08(x/h)}$			159
theoretical solution (Noda, 1970)	$\frac{\eta(x,t)}{s} = f\left\{\frac{v_s}{\sqrt{gh}}, \frac{x}{h}\right\}$	122		
Piston model (Noda, 1970)	$\frac{a_C}{h} = 1.32\frac{v_s}{\sqrt{gh}}$	515		
Slingerland and Voight, 1982	$\log\left(\frac{a_C}{h}\right) = -1.25 + 0.71\log\left(\frac{1}{2}\frac{\rho_s}{\rho_w}\frac{V_s}{h^3}\frac{v_s^2}{gh}\right)$	329		

The herein presented equation for the maximum leading crest amplitude a_C given by Eq. 4.35 perfectly matched the measured crest amplitude $a_{C1} \approx 155$ m.

Kamphuis and Bowering (1970) conducted an experimental study in which a weighted tray was emplaced by a roller ramp into a flume. Their empirical relationship perfectly matched the measured wave height $H \approx 160$ m. The predictive equation consists of a term determining the wave height $H(x/h = 37)$ and a term accounting for the wave attenuation along the wave channel, corresponding to Eqs. 2.2 and 2.4, respectively. The slide Froude number $\mathbf{F} = v_s/\sqrt{gh}$ and the dimensionless slide thickness $S = s/h$ were also identified as primary parameters governing the wave height analogous to the present study. The dimensionless slide length l_s/h was introduced in contrast to the present study with the dimensionless slide volume $V = V_s/(bh^2)$ as third parameter. Remarkable is the excellent agreement between their and the present study. Both studies were conducted at similar laboratory scales, which were larger than the scales of most other studies. Further

the roller based tray of their study and the granular slides of the present study did not result in significantly different results.

Noda (1970) used linear theory to predict the form of the wave motion produced by a body falling vertically into a tank. The solution was represented graphically allowing a rapid determination of the wave amplitude a/s relative to the slide thickness s in dependency of the slide Froude number $\mathbf{F}$ and the propagation distance x/h. The vertically impacting block study with $\alpha = 90°$ did not account for the inclined ramp $\alpha = 45°$. Nevertheless the theoretical solution underestimates the maximum wave amplitude with $a = 122\,\text{m}$ only by 20%. Further accounting for the increase in wave height with decreasing hillslope angle according to Kamphuis and Bowering (1970) may actually result in a close match to the measured wave crest amplitude. The linear solution does not distinguish between the wave crest and trough amplitudes. Hence the trailing wave trough is massively overestimated. Further the wave type was determined by the slide Froude number $\mathbf{F} = v_s/\sqrt{gh}$ and the relative slide thickness $S = s/h$. The classification places the Lituya Bay event in the bore regime in accordance to the present study.

Noda (1970) obtained a theoretical solution for the case of a wall moving horizontally into a body of water. The horizontally penetrating wall model overestimates the measured wave crest amplitude by nothing less than a factor of 3. The forced horizontal motion significantly overestimates even the massive Lituya Bay event with the slide thickness at impact corresponding to the stillwater depth with $s = h$. This model does not account for the water flow over the back of the landslide. Similar overestimations may be produced by depth averaging shallow water equations in the wave generation area (Mader, 1999). Further the forced motion of the landslide and the more effective horizontal penetration direction contribute to the massive overestimation of the measured wave heights.

Slingerland and Voight (1982) presented an empirical regression for the prediction of the dimensionless first wave amplitudes from the dimensionless slide kinetic energy. The predictive relationship given by Eqs. 2.6 and 2.7 overestimates the measured wave height by a factor of 2. The empirical regression was derived from two case studies. Hence the underlying data lacked a systematic parameter variation.

The empirical formula of Huber and Hager (1997) given by Eq. 2.8 for 2D-impulse wave characteristics predicts a wave height of $H = 94\,\text{m}$. This underestimates the measured wave height $H = 162\,\text{m}$ by a factor of 1.8, although $\mathbf{F} = 3.2$ is within the range of experiments conducted by Huber (1980). The wave height partition between the crest and the trough was not determined. The impact shapes of Huber's granular rock avalanches were inherently dependent on impact slide velocity. Rough estimations of slide thickness from photos (Huber, 1980) indicate that Huber's slides at comparable impact Froude numbers were thinner $s < h$. The present study and the sliding block experiments conducted by Noda (1970) and Kamphuis and Bowering (1970) showed a strong dependency of the generated wave heights on the slide impact thickness. The difference in the slide impact thickness may explain why the Huber and Hager formula underestimates the measured wave height. Most disturbing remains that this empirical relationship does not contain any slide impact velocity parameter, whereas all other experimental studies

confirmed the dominant influence of the slide Froude number $\mathbf{F} = v_s / \sqrt{gh}$ on the generated wave height.

Hence the herein presented relationship given by Eq. 4.35 is recommended to predict the maximum leading crest amplitude a_C. Further the empirical relationship presented by Kamphuis and Bowering (1970) is recommended for comparison purposes. Their relationship only allows the prediction of the total wave height H. It is recalled that equipartition between the wave crest and wave trough amplitudes does not hold for landslide generated impulse waves. Halving the total wave height may lead to a serious underestimation of the maximum wave crest amplitude.

5.3 Comparison of water particle velocity fields with solitary wave theory

Comparisons between experimental and analytical flow fields below water waves have rarely been done since whole flow field measurements were previously unavailable. The wave profiles of the different analytical wave theories were compared with experiments by several authors (Wiegel, 1964; Le Méhauté, 1976 among others). Three main solitary wave theories were presented by Boussinesq (1872), McCowan (1891) and Laitone (1960). Laitone's theory predicts too high wave crest velocities resulting in breaking at $H/h = 0.7$ (Wiegel, 1964). Therefore Laitone's theory is not considered here. The notation applied in the solitary wave theory is shown in Fig. 5.1.
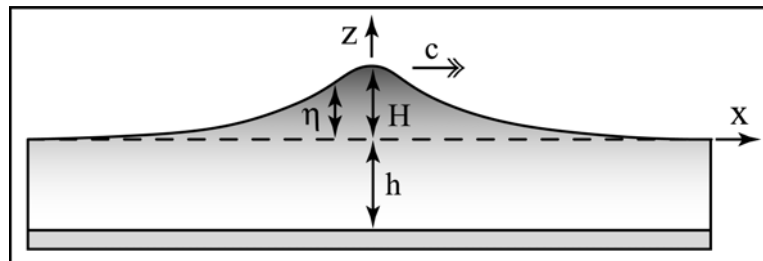
Figure 5.1   **Solitary wave notation** and coordinate system.

The Boussinesq theory was derived from continuity considerations, averaging the velocity over depth. The expressions for the surface profile η, the wave propagation velocity c and the horizontal particle velocity v_{px} yield

$$\eta = H \left(\text{sech} \left(\sqrt{\frac{3H}{4h}} (x - ct) \right) \right)^2 \tag{5.1}$$

$$c = \sqrt{gh \left(1 + \frac{H}{h} \right)} \tag{5.2}$$

$$v_{px} = \frac{c\eta}{(h + \eta)} \tag{5.3}$$

with the wave height *H*. It is recalled that $\mathrm{sech}(\gamma) = \tanh(\gamma)/\sinh(\gamma)$. The vertical particle velocity v_{px} is not included in the theory. In the previous paragraphs selected velocity fields under impulse waves were presented. All examples exhibited a non-uniform velocity distribution over the depth. Further significant vertical velocity components were measured. Hence the Boussinesq theory is of limited use regarding the particle velocities. The success of the Boussinesq theory was due to its simplicity and the reasonable comparison of the surface profile and the wave celerity with experiments (Wiegel, 1964).

The McCowan solitary wave theory is of higher order than the Boussinesq theory and neglects only terms larger than $(H/h)^3$. The McCowan theory satisfies the kinematic free surface boundary condition exactly. Further the vertical distribution of horizontal velocity is non-uniform. The solution of Munk (1949) to the McCowan theory yields:

$$\eta = \frac{hK\sin\left(P\left(1+\frac{\eta}{h}\right)\right)}{P\left(\cos\left(P\left(1+\frac{\eta}{h}\right)\right) + \cosh\left(P\frac{x}{h}\right)\right)} \tag{5.4}$$

$$c = \sqrt{\frac{gh}{P}\tan P} \tag{5.5}$$

$$v_{px} = \frac{cK\left(1 + \cos\left(P\frac{z+h}{h}\right)\cosh\left(P\frac{x}{h}\right)\right)}{\left(\cos\left(P\frac{z+h}{h}\right) + \cosh\left(P\frac{x}{h}\right)\right)^2} \tag{5.6}$$

$$v_{pz} = \frac{cK\sin\left(P\frac{z+h}{h}\right)\sinh\left(P\frac{x}{h}\right)}{\left(\cos\left(P\frac{z+h}{h}\right) + \cosh\left(P\frac{x}{h}\right)\right)^2} \tag{5.7}$$

with the parameters K and P. These parameters were computed numerically from the following relationships

$$K = \frac{2}{3}\left(\sin\left(P\left(1+\frac{2}{3}\frac{H}{h}\right)\right)\right)^2 \tag{5.8}$$

$$\frac{H}{h} = \frac{K}{P}\tan\left(\frac{1}{2}P\left(1+\frac{H}{h}\right)\right). \tag{5.9}$$

according to Munk (1949). The horizontal and vertical water particle velocities were computed according to Eqs. 5.6 and 5.7, respectively. The computed horizontal and vertical velocity fields under solitary waves with $H/h = 0.15$, 0.3, 0.5 and 0.7 are shown in Figs. 5.2 and 5.3.
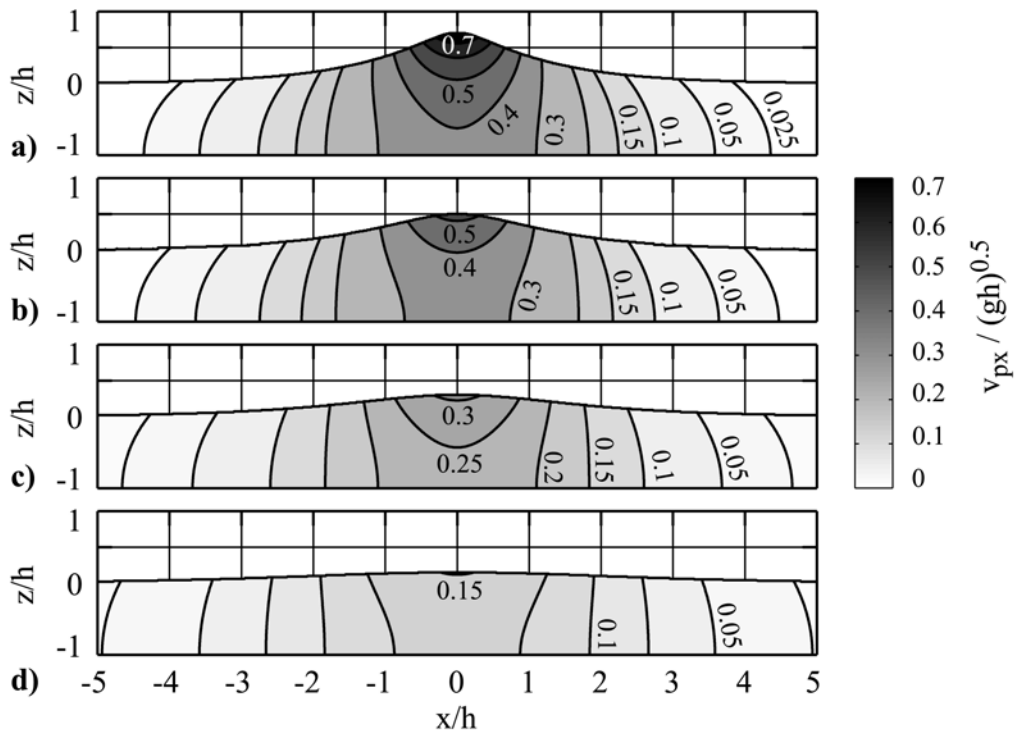
Figure 5.2 **Solitary wave theory** of McCowan: **Horizontal particle velocity** fields $v_{px}/\sqrt{gh}$ computed with Eq. 5.6 at **a)** $H/h = 0.7$, **b)** $H/h = 0.5$, **c)** $H/h = 0.3$, **d)** $H/h = 0.15$.
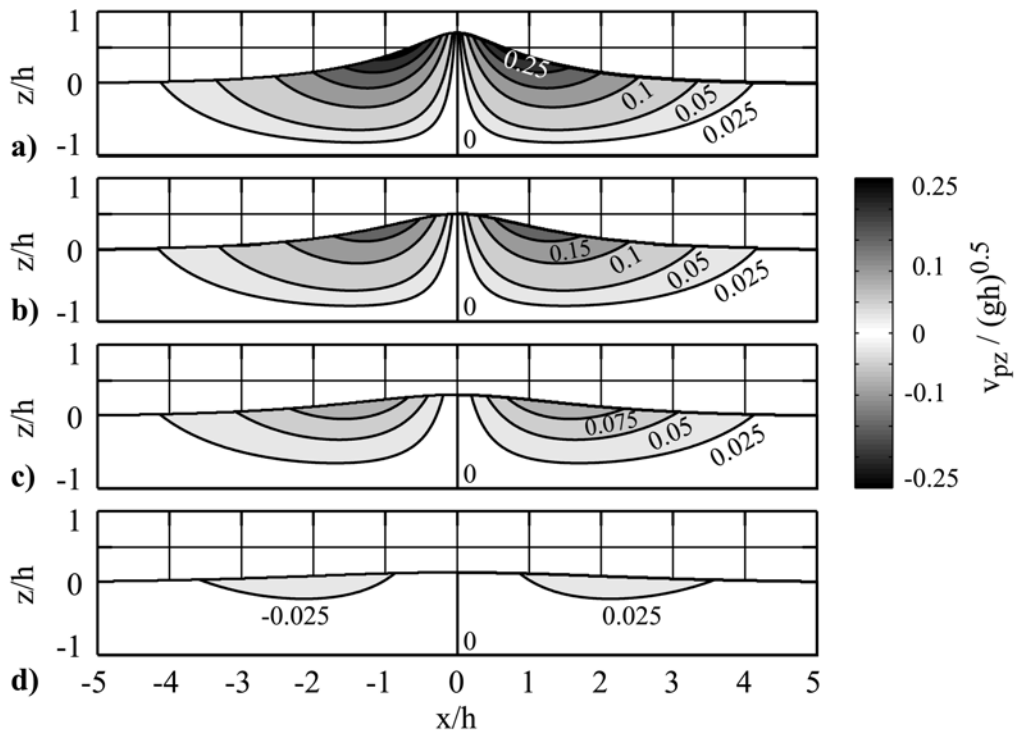
Figure 5.3 **Solitary wave theory** of McCowan: **Vertical particle velocity** fields $v_{pz}/\sqrt{gh}$ computed with Eq. 5.7 at **a)** $H/h = 0.7$, **b)** $H/h = 0.5$, **c)** $H/h = 0.3$, **d)** $H/h = 0.15$.

The horizontal water particle velocities under the solitary wave compared well with the measured distributions under the leading impulse wave crests shown in Figs. 4.41, 4.51, 4.61 and 4.71. Both experiment and theory predict an increase in horizontal water particle velocity towards the wave crest and with increasing wave height. The measured vertical water particle velocities under the leading impulse wave crest are shown in Figs. 4.42, 4.52, 4.62 and 4.72. The highest vertical velocities occurred near the surface at the locations with the steepest slopes. The leading wave crests were shorter in length than the solitary waves. The measured vertical velocity components were larger than those predicted by the solitary wave theory. Hence McCowan's theory may be used to predict the horizontal water particle velocity distributions under the leading impulse wave crests. Laitone's theory outperforms McCowan's solution regarding the wave speed (Wiegel, 1964; Naheer, 1978a,b). The wave fields in the wave generation area are not fully developed and complicated by the penetrating slide and the cavity collapse with higher velocities than below the wave crest. An in depth comparison of the flow fields below impulse waves with the different wave theories may only be possible farther away from the impact area. The measurement of velocity vector fields in the wave propagation area would be required.

The classical nonlinear wave theory – the Korteweg and de Vries (KdV) equations – are two dimensional. The Cnoidal wave theory has rarely been applied to engineering solutions due to the complicated expressions, which may be treated numerically. A synthesis of the Cnoidal wave theory may be found in Wiegel (1964). The front of the leading wave actually behaves nearly like a solitary wave. The problem of wave propagation was solved numerically by the Split-Step Fast Fourier Transform Method, which was initially applied in the field of plasma physics. This numerical method outperformed earlier brute force numerical approaches to resolve the KdV equations. The numerical tools were presented to describe the wave generation mechanism from the existence of a crater with a lip to the wave propagation in the near and far field. However, the trailing waves travelled slower than given by the KdV equation. This is to be expected since they are of higher frequency than the leading wave and therefore enter the realm of Stokesian waves instead of the KdV equations. Therefore an extended versions of the KdV equations was presented and solved numerically (Le Méhauté and Khangoankar, 1992).

5.4 Applicability of classical wave theories

All measured impulse waves were non-linear [para 5.4]. Contrary to the linear wave theory a nonlinear wave theory which is accurate over the whole range from shallow to deep water waves does not exist [para C.2]. Of practical relevance are mainly the Stokes theory for finite amplitude deep water waves and the cnoidal and solitary wave theories for finite amplitude shallow water waves. In all these nonlinear wave theories there is mass transport as a result of irrotationality and nonlinearity.

Stokes (1847) developed a second-order theory for finite amplitude waves using a power series based on H/L which requires that H/h be small and thus is applicable for deep water and much of the intermediate depth. The results diminish in accuracy as the wave steepness increases. For large wave steepness up to the breaking limit fifth-order theory is commonly used. Skjelbreia and Hendrickson (1961) and Fenton (1985) presented the fifth-order Stokes theory. Fenton (1985) tabulated the necessary formulas for wave calculations.

Korteweg and de Vries (1895) developed a finite amplitude wave theory applicable in shallow water, commonly know as cnoidal wave theory or KdV equations. Cnoidal theory involves Jacobian elliptical functions in contrast to the series of trigonometric functions in Stokes theory. Cnoidal waves are periodic and of permanent form. Cnoidal wave theories were presented by Keulegan and Patterson (1940), Keller (1948), Laitone (1960), Wehausen and Laitone (1960), and Chappelear (1962). In all cases the results are extremely difficult to apply. A synthesis was presented by Wiegel (1960). The most commonly used cnoidal wave theory is to the first order of approximation, but it is capable of describing waves of finite height in shallow water. Higher orders of approximation diverge significantly from experimental results, which confirms that higher-order theories are not necessarily better than their lower-order counterparts (Le Méhauté, 1976).

The transition between the validity ranges of the fifth order Stokes and the first order cnoidal wave theories occurs in the intermediate water depth regime. The Ursell number may be used to separate the validity ranges. The transition occurs roughly at $\mathbf{U} = 26$ (Le Méhauté, 1976). The transition line is shown in Figs. 4.107b) and 4.108b). The cnoidal and Stokes theories may be applicable for $\mathbf{U} \geq 26$ and $\mathbf{U} < 26$, respectively (Sorensen, 1993). The transition line cuts through the Ursell number spectrum $1 < \mathbf{U}_1 \leq 1000$ of the leading wave. It was shown with an instantaneous wave frequency analysis that the wave frequency continuously increased towards the back of an impulse wave train (Fritz and Liu, 2002). Hence the actual Ursell number of the leading wave crest may be slightly higher than determined with the upcrossing wave length. Most of the leading wave crests closely followed the propagation velocity given by the solitary wave theory [para 4.7.11]. Hence the cnoidal wave theory may be applicable to most leading waves, whereas some at the lower end of the spectrum may fall into the Stokesian regime. All trailing waves with $\mathbf{U} < 26$ may not be described by the cnoidal wave theory. The trailing waves from the second wave crest backwards fall into the Stokesian regime. The validity ranges of the various wave theories together with range of measured impulse waves is shown in Figs. 5.4.
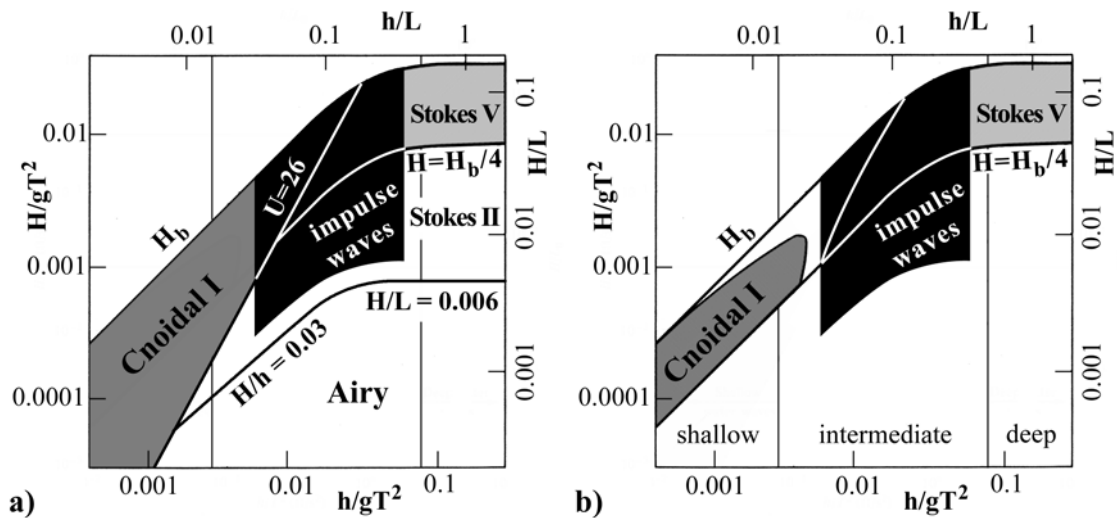
Figure 5.4   **Applicability of analytical wave theories: a) recommended ranges** after LeMéhauté (1976) with (■) measured impulse waves range; **b) validities** defined by the best fit to the dynamic free surface boundary condition (Dean, 1970) with symbols as in a).

The impulse wave range roughly corresponds to those given by Kamphuis and Bowering (1970) and Huber (1980). Further the impulse wave range matches the spectrum of explosion generated waves determined by LeMéhauté and Khangoankar (1992). The propagation velocity of the leading wave crest of an impulse wave train matched the solitary wave propagation velocity. The solitary wave like behavior of the leading wave crest was identified previously by Kamphuis and Bowering (1970) and Huber (1980). However, the trailing waves tend to travel slower than given by the Korteweg - de Vries (KdV) equations describing the cnoidal wave theory. The solitary wave theory is a limiting case of the KdV equations. The trailing waves exceed the limiting wave frequency of the cnoidal wave theory. The trailing waves are of higher frequency than the leading wave and therefore approach the realm of Stokesian waves instead of the KdV equations in analogy to explosion generated impulse waves (LeMéhauté and Khangoankar, 1992). The narrow frequency bandwidth of the KdV equations limits their applicability to impulse waves. The frequency range may be broadened by extending the classical KdV equations. The numerical tools were presented to describe the wave generation mechanism from the existence of a crater with a lip to the wave propagation in the near and far field (LeMéhauté and Khangoankar, 1992).

5.5 Comparison of the equivalent coefficient of friction with observations

Through a series of empirical observations, Heim (1932) concluded that the travel distance of a landslide depends on the height of the fall, the regularity of the pathway, and the size of the fallen rock mass. Heim found that the slope of the energy line for smaller

landslides is about the same as the coefficient of friction of sliding blocks. The equivalent coefficient of friction was defined as the maximum drop height divided by the maximum run-out length (Fig. 4.24).

Unlike the coefficient of friction, which is a material constant and whose value is independent of the size of a sliding block, the equivalent coefficient of friction is a function of the total landslide volume. Most natural rock types have coefficients of friction of 0.6 or higher (Jaeger and Cook, 1979), with movement expected only over terrains with an average slope angle of at least 30°. This expectation was confirmed for relatively small volume landslides and flows of dry granular materials in the laboratory (Savage, 1984). The present physical model study perfectly matches the conclusions drawn by Savage. All measured equivalent coefficients of friction were within the range $0.6 < f < 1$ given in [para 4.4.6]. The only difference between the present physical model study and the experiments of Savage is the combined subaerial and subaqueous landslide run-out. Noteworthy is that the partially submerged landslide run-out did not lead to a significant decrease of the equivalent coefficient of friction. However, as the slide volume increases beyond 100'000 m³ in subaerial mass movements, the equivalent coefficient of friction decreases to values as low as 0.1 or less. All cases with relevant impulse waves reviewed in Appendix B were caused by landslide impacts with volumes V_s of at least 100'000 m³. Therefore friction reduction for large landslides needs to be considered in some cases.

A double logarithmic plot of the equivalent coefficient of friction as a function of landslide volume is shown in Fig. 5.5 for subaerial dry-rock avalanches of non-volcanic origin (Scheidegger, 1973), submarine landslides (Hampton, et al., 1996), Martian landslides (McEwen, 1989) and the physical model data of the present experimental study on landslide generated impulse waves. The effective coefficient of friction is the parameter best suited to a comparison between the physical model results and the observations of real events due to the available data sets. All three data sets of observations indicate a significant decay of the equivalent coefficient of friction with increasing volume. In particular the subaerial and Martian data sets show a strong linear correlation. The correlation for subaerial landslides between the landslide volume V_s in m³ and the equivalent coefficient of friction f is

$$\log f = -0.15666 \cdot \log V_s + 0.62419 \qquad \textbf{(5.10)}$$

with a correlation coefficient of 0.82. The observed equivalent coefficients of friction for large landslides are much smaller than explainable by either sliding or dispersive grain-flow mechanisms. Various models have been proposed to explain the mobility of large landslides, including fluidization by air (Kent, 1966); frictionless support on a layer of trapped and compressed air (Shreve, 1966, 1968); movement over a molten basal layer, melted by friction and high pressure (Erismann, 1979); grain flow with friction reduced by the presence of dust (Hsü, 1975); inertial grain flow or mechanical fluidization (Davis, 1982); grain separation by acoustic energy (Melosh, 1979, 1987); vaporization of few percent of water in largely unsaturated materials (Habib, 1975; Goguel, 1978); and segregation of the water into a saturated basal layer (Johnson, 1978). These models have various

strengths and weaknesses, but no consensus has been reached. The data compiled by Scheidegger (1973) consists mostly of Alpine landslides. The relationship also depends on the type of material involved in the mass movement. Quick clays for example have friction coefficients at the lower end of friction coefficients observed for submarine landslides (Edgers and Karlsrud, 1982). The presented relationship may therefore not be applied to some slide materials and quick clays in particular.

In most cases the subaqueous slide motion occurred unobserved or in prehistoric times. The only evidence often are the subaqueous landslide deposits. The subaqueous deposits, being covered by water, are discovered and surveyed with remote-sensing instruments such as acoustic-reflection profilers, swath-bathymetry systems, or side-scan sonar imagers. Direct observation via submersibles or bottom photography sometimes is done as a follow-up to discovery by remote sensing (Greene et al., 1991). Some landslides are deduced strictly on the basis of deformed sediment in cores (Gutmacher and Normark, 1993). A significant difference between the physical model and real events is the excavation. In the physical model the slide mass remains constant from the impact to the deposit, whereas in real events excavation along the sliding surface continuously increases the slide mass. Further subaqueous deposits are often moved with the landslide or pushed away. In some cases the impact on the sediments may even cause a break-up of whole sediment layers on the lake or sea floor (Hampton, 1996). In both the Tafjord [para B.1.3] and the Lake Loen events [para B.1.4] the volume of sediments moved at the bottom of the slope exceeded the original slide volume. In the physical model the steel plate at the channel bottom interdicted any interaction between the landslide and sediment layers on the bottom. Therefore caution should prevail in the interpretation of a comparison between physical model slide deposits and surveyed subaqueous landslide deposits.

Submarine landslides reached volumes more than two orders of magnitude larger than the largest known subaerial landslide. The equivalent coefficient of friction can be orders of magnitude smaller for submarine landslides. Therefore submarine landslides can originate on nearly flat surfaces. The submarine data in Fig. 5.5 shows considerable scatter which indicates the limitations of a simple slide dynamic model. Subaqueous landslides are not only affected by friction and gravity, but also drag forces exerted by the surrounding seawater, both at the front and on top of the moving mass are an important feature.

Mars may be the only planetary body other than Earth known unequivocally to have long run-out lengths for dry landslides (Lucchitta, 1979). The least-squares fit to the landslide data from Valles Marineris shown in Fig. 5.5 has a correlation coefficient of 0.90. Although the slopes of the terrestrial and Valles Marineris trends in Fig. 5.5 are nearly identical, there is an offset between the trends. At a given equivalent friction coefficient, the Martian landslides are typically about 50 to 100 times more voluminous than the terrestrial counterparts, or at a given volume, the friction coefficient is about two times larger on Mars. Gravity on Mars is 2.6 times smaller than on Earth with $g = 3.72$ m/s^2 and $g = 9.81$ m/s^2, respectively. Frictional models do not predict any effect from reducing g, because both the driving and resistance forces are reduced proportionally. The offset might be explained by the effect of a lower g on flows with high yield strengths (McEven,

1989). For example a Bingham material would have a thicker flow deposit on a planet with reduced g.

In the physical model the length scale was only altered by a factor of two and hence the volume per unit width by a factor of 4. Therefore all the data of the physical model collapse roughly on a point in the double logarithmic diagram shown in Fig. 5.5.
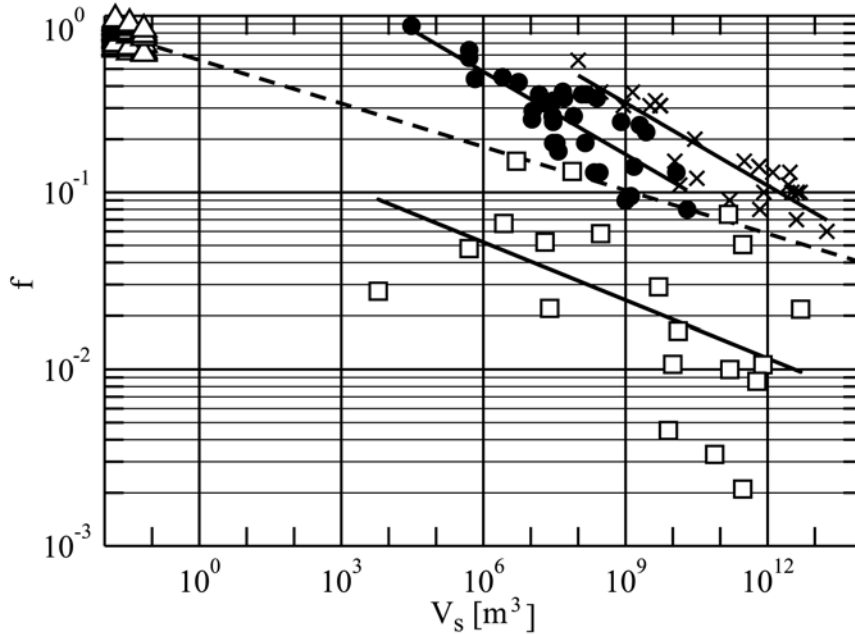
Figure 5.5 **Equivalent coefficient of friction** f vs. landslide volume V_s [m^3] for (●) subaerial landslides (Scheidegger, 1973), (□) submarine landslides (Hampton et al., 1996), (✕) Martian landslides (McEwen, 1989), (——) corresponding linear least-squares correlations, (Δ) physical model data with (– –) extrapolation by Eq. 5.11.

A linear regression of the physical model data including the dimensional slide volume V_s as sole parameter resulted in

$$f = 0.58\, V_s^{-0.077} \tag{5.11}$$

with an extremely poor correlation coefficient $r^2 = 0.11$. The relationship described in Eq. 5.11 is not dimensionless but the equivalent coefficient of friction f is dimensionless. This approach was only selected in order to compare with the available data from observations, where other parameters are mostly unknown. The physical model data confirmed the decay of the equivalent coefficient of friction with increasing slide volume indicated by the observations of real events. The slope of the decay of the equivalent coefficient of friction with increasing slide volume in the physical model is about half the slope of the decay in the observations of subaerial slides. A significant laboratory scale series would require at least an order of magnitude in scale difference to enable extrapolations by up to 15 orders of magnitude in slide volume or 5 to 6 orders of magnitude in length scale. Further not all physical processes involved may be included in a physical model at laboratory scale. In particular the friction reduction processes discussed previously are difficult to

produce in a small scale physical model. Therefore the conclusions drawn from laboratory experiments alone need to be considered with care.

The comparison between the physical model data and the equivalent coefficient of friction of both the subaerial and submarine landslide observations revealed increasing differences with augmenting scale ratios. The largest submarine landslide run-out distances were therefore up to 10 times larger than granular model run-outs up-scaled by factors of 10'000 to 100'000. The run-outs of slides modeled as blocks remain up to a factor of 100 short due to the stopping at the channel bottom. During most of the run-out distance the landslide velocity lags the wave propagation velocity and therefore primarily affects the trailing waves. In narrow Alpine lakes or reservoirs the landslide run-out distance is strongly affected by the lake bathymetry and the slide usually rams into the opposite flank after a short travel distance. In super critical landslide impacts the initial impulse transfer forming the first wave crest is most important and trailing waves generated during landslide run-out are usually much smaller near the impact and may be augmented during wave propagation due to dispersion. At which scale or scale difference and under which conditions effects of the unscalable landslide run-out distance become relevant is unclear and it remains the main source of concern regarding scale effects.

The force exerted by the landslide on the water may consist of three components, one due to the displacement of the water, the pressure drag and the viscous drag. The viscous drag or the skin friction drag is not scaled in a Froude model and therefore orders of magnitude to large in the present physical model study. Similar to the friction problem in unsaturated granular flows discussed in Appendix A.2, the slide run-out distance may be determined by comparison with real event slide deposits. This is commonly done by numerical modelers to calibrate landslide motion, deformation and run-out distance (Ward, 2001). Efforts to map submarine landslide deposits globally are currently undertaken (Keating and McGuire, 2000). Subaqueous landslide deposits in Swiss lakes are currently investigated using sonar and seismic techniques (pers. com.: Prof. Dr. D. Giardini, ETH Zürich).

6 Conclusions

6.1 Summary of results

The initial phase of landslide generated impulse waves in reservoirs, lakes, bays or oceans was investigated in a two-dimensional physical laboratory model based on the generalized Froude similarity. The main results of the experimental study focusing on the slide impact and wave generation as well as the wave propagation in the near field may be summarized as follows:

- Landslides were successfully modeled with an artificial granular material consisting of barium-sulfate and polypropylene (PP-BaSO$_4$) with grain density $\rho_g = 2.64$ t/m^3, grain diameter $d_g = 4$ mm, porosity $n = 39\%$, internal friction angle $\phi = 43°$ and bed friction angle $\delta = 24°$. The granulate density matches common natural rock formations such as granite, limestone, sandstone and basalt.

- A novel pneumatic landslide generator was developed. The pneumatic landslide generator allowed to control the slide impact characteristics, thus allowing exact reproduction and independent variation of single dynamic slide parameters: slide release velocity $v_B = 0$ and 3 to 7.5 m/s with $\pm 5\%$, slide thickness $s = 0.05$ to 0.2 m with $\pm 5\%$, slide mass $m_s = 27$, 54 and 108 kg. In particular different slide impact shapes were produced for the same slide velocity and mass. Starting the experiments with controlled initial conditions just before impact allowed to minimize effects of the larger slide friction in physical models compared to real events. Further lateral boundary effects were limited to the reduced granular flow distance after slide release.

- Laser distance sensors (LDS) successfully scanned the profiles of the granular slides before impact allowing the determination of the relevant slide thickness s at impact.

- Capacitance wave gauges (CWG) consisting of standard industrial electronics and in-house-made probes determined the wave features in the wave propagation area, whereas several other sensors were not capable to cope with the high wave dynamics, the splashing and the air entrainment due to wave breaking.

- Particle image velocimetry (PIV) was successfully applied to large areas of view up to 0.8×0.8 m in the impact and wave generation zone characterized by large velocity gradients near the interface between the water and the slide as well as massive mixing of the three phases: water, slide granulate and entrained air. Digital masking techniques were applied to distinguish between phases thereafter allowing phase separated image processing. PIV is ideally suited to the analysis of instantaneous flow fields in extremely unsteady flows.

- The following dimensionless quantities for a 2D model were obtained: slide Froude number $\mathbf{F} = v_s / \sqrt{gh}$, dimensionless slide thickness $S = s/h$, dimensionless slide volume $V = V_s/(bh^2)$, dimensionless wave propagation distance x/h, dimensionless slide density ρ_s/ρ_w, slide impact angle α.

- The Froude number $\mathbf{F}$, the dimensionless slide volume V and the dimensionless slide thickness S were altered systematically within $1 < \mathbf{F} < 4.8$, $0.07 < V < 1.6$ and $0.07 < S < 0.6$, respectively. The wave characteristics were determined over a propagation distance $2.5 < x/h < 25$ depending on the water depth. The slide impact angle and the slide density were not altered and remain to be explored.

- The subaqueous slide motion including the slide displacement and the slide velocity were fully described in terms of the slide impact velocity, the duration of the subaqueous slide motion and the slide run-out. The slide run-out and the duration of the subaqueous slide motion were determined by multiple regressions with the Froude number $\mathbf{F}$, the dimensionless slide volume V and the dimensionless slide thickness S as parameters.

- The equivalent coefficient of slide friction f was determined by a multiple regression with the Froude number $\mathbf{F}$ and the dimensionless slide volume V. The equivalent coefficient of friction decays in the model with increasing slide volume analogous to field observations of subaerial, submarine and Martian landslides. The comparison between the physical model data and the field data revealed increasing differences with augmenting scale ratios.

- A flow separation criteria based on the slide Froude number $\mathbf{F}$ and the dimensionless slide thickness S allowed to distinguish between separated and unseparated flow regimes in the impact and wave generation area. In the separated flow regime an impact crater formed.

- In the separated flow regime two types of impact craters were defined based on the slide Froude number $\mathbf{F}$ and the dimensionless slide thickness S. The backward collapsing impact crater was characterized by a surface closure during crater collapse forming an air cavity, whereas in the outward collapsing impact crater no cavity was formed.

- The temporal evolution of the water displacement and the water displacement rate were fully described in terms of the time of the maximum water displacement, the maximum water displacement and the maximum water displacement rate in analogy to water waves generated by under water explosions.

- The time of the maximum water displacement, the maximum water displacement and the maximum water displacement rate were determined by multiple regressions. The slide Froude number $\mathbf{F}$ was identified as the dominant parameter.

- The maximum water displacement volume always exceeded the landslide volume. The largest measured maximum water displacement per unit width was 8 times larger than the hydrostatic water displacement due to the added slide mass. The simple hydrostatic water displacement is not of relevance regarding landslide impacts for $\mathbf{F} \geq 1$.

- The macro-structure of the flow in the impact and wave generation area was determined with particle image velocimetry (PIV). Mounted areas of view resulted in 49 flow map sequences covering 1.6×0.8 m. The following flow maps were computed: velocity vector, streamline, absolute velocity, horizontal and vertical particle velocity, in-plane divergence, out-of-plane rotation, elongational and shear strain rate.

- The horizontal particle velocities under the leading impulse wave crest compared well to the solitary wave theory after McCowan (1891), whereas the vertical particle velocities significantly exceeded those given by the solitary wave theory. The water particle velocities increased with increasing non-linearity or wave height. The water particle velocities in the wave propagation zone were always smaller than the wave propagation velocity except for breaking waves and bores. Hence McCowan's theory may be used to predict the horizontal water particle velocity distributions under the leading impulse wave crests.

- The in-plane divergence was roughly zero in the whole pure water flow area confirming the two dimensional model assumption.

- The out-of-plane vorticity was roughly zero in the wave generation area and below the outward propagating water waves. The non-breaking landslide generated impulse waves are irrotational. Hence a velocity potential exists because the conditions of irrotationality and incompressibility were fulfilled. Further a stream function must exist for all two-dimensional incompressible flows. The assumption of irrotationality does not hold for breaking waves and bores, which involved large positive vorticity.

- Elongational and shear strains governed the flow fields in both the impulse wave generation and propagation zones. The elongational strains are zero below wave crests and troughs due to the horizontal velocity vectors and largest near the free surface at the locations of the largest gradients in the free surface. The zero contour lines of the shear strain mark the transitions from a wave crest to a trough corresponding roughly to the points where the free surface crosses the imaginary still water surface. The maximum shear strain values are always encountered below wave crests and troughs. Both the elongational and the shear strain rates increased with decreasing wavelength and increasing wave height. Larger strain rates result in faster wave attenuations.

- Four different wave types were observed: weakly non-linear oscillatory wave, non-linear transition wave, solitary-like wave, and dissipative transient bore. The wave type classification was based on the slide Froude number **F** and the dimensionless slide thickness S.

- The wave attenuation strongly depended upon the wave type and the wave characteristics. Hence a simple draw down curve does not exist. The practical engineer may be on the safe side assuming no wave attenuation in the case of two-dimensional wave propagation. Regarding the three-dimensional wave attenuation it is referred to Huber (1980) and Huber and Hager (1997).

- The leading wave crest amplitude as well as the wave envelope crest and trough amplitudes were determined by multiple regressions. The slide Froude number **F** was identified as the dominant parameter.

- The partition of the total wave height H between the crest and trough amplitudes strongly depended on the wave type. Unequipartition between crest and trough amplitudes characterizes these non-linear water waves. The maximum crest amplitudes at least matched and mostly exceeded the maximum trough amplitudes $a_C \geq a_T$. In weakly non-linear oscillatory waves the wave trough increased roughly proportional to the wave crest, whereas in the nonlinear transition wave regime the leading wave trough decreased with increasing wave crest amplitude reaching result in $a_T \approx 0$ for solitary-like waves and bores at the upper limit of the possible wave spectrum.

- The first wave crest was always the highest exceeding the second wave crest $a_{C1} > a_{C2}$ in the strongly non-linear range with maximum crest amplitudes $a_C / h \geq 0.3$. The second wave crest exceeded the leading wave crest $a_{C1} \leq a_{C2}$ in the weakly non-linear range $a_C / h \leq 0.3$ in some cases. In the far field any wave in the wave group may be the highest due to dispersion.

- The novel relationships for the prediction of the wave amplitude were compared to the wave amplitudes determined in the 1:675 scale model of the Lituya bay cross section, which matched the maximum wave run-up caused by the rockslide impact in 1958 (Fritz et al., 2001). The amplitude predictions matched the measured wave amplitudes of the largest impulse wave in recorded history.

- The period and wave length of the leading and the second wave at $x/h = 5$ were determined by multiple regressions. The slide Froude number **F** was identified as the dominant parameter.

- The wave length of the leading wave strongly depends on the subaqueous slide run-out. In contrast the wave period could neither be linked to the duration of subaqueous slide motion nor the time of the maximum water displacement volume. Both wave generator time scales yielded poor correlations.

- The propagations of the leading and the second wave periods and wave lengths were determined as a function of the propagation distance x/h. The wave period and the wave length increased with the propagation distance.

- Most impulse waves were in the intermediate water depth regime with wave periods $6 < T_1 \sqrt{g/h} < 22$ and $3 < T_2 \sqrt{g/h} < 9$ as well as wave lengths $5 < L_1 / h < 30$ and $2 < L_2 / h < 8$, respectively. The wave period and wave length of the second wave were roughly 2 to 3 times shorter than wave period and wave length of the leading wave. In general the wave period and wave length decreased towards the back of the wave train.

- The propagation velocity of the leading wave crest follows closely the theoretical approximations for a solitary wave. The amplitude dispersion characterized by the amplitude to stillwater depth ratio a/h is the primary parameter governing the propagation velocity of the leading wave crest c_{c1}. Further the solitary wave propagation velocity may be applied to negative amplitude waves corresponding to wave troughs resulting in a reduction of the shallow water wave propagation velocity with increasing trough amplitude. The propagation velocity of the first trough slightly lags the solitary wave propagation velocity.

- The second wave crest propagation velocity concentrated around $c_{c2} \approx 0.8 \sqrt{gh}$. The trailing wave propagation velocity even lagged the linear shallow water wave propagation velocity by 20% on average. Hence neither the solitary wave theory nor the linear long wave theory do apply for the trailing waves. The trailing wave propagation velocity reduction by roughly 30% compared to the leading wave crest propagation velocity may be attributed to the shorter wavelength resulting in frequency dispersion.

- The wave steepness of the leading wave was within $0.006 \leq H_1 / L_1 \leq 0.09$. The measured steepness of the leading wave decayed with the propagation distance. The Ursell number of the leading wave was within $1 < U_1 \leq 1000$. The Ursell number of the leading wave slightly increased with the propagation distance. The wave steepness

and the Ursell number of the trailing wave were within $0.006 < H_2/L_2 \leq 0.12$ and $0.3 < \mathbf{U}_2 \leq 20$, respectively. Hence all waves generated by granular landslide impacts in the present study were non-linear.

- The breaking of the leading wave of an impulse wave train may be determined by the relative wave height $H_b/h_b = 0.78$ defined from solitary wave theory by McCowan (1894). The limiting wave steepness of the trailing waves may be determined by the breaking criterion given by Miche (1944) for progressive intermediate water depth waves.

- The measured impulse waves may be classified with the Ursell number. The cnoidal and Stokes theories may be applicable for $\mathbf{U} \geq 26$ and $\mathbf{U} < 26$, respectively (Sorensen, 1993). The transition line cuts through the Ursell number spectrum $1 < \mathbf{U}_1 \leq 1000$ of the leading wave. Hence the cnoidal wave theory may be applicable to most leading waves, whereas some at the lower end of the spectrum may fall into the Stokesian regime. All trailing waves from the second wave crest backwards fall into the Stokesian regime with $\mathbf{U} < 26$. The trailing waves exceed the limiting wave frequency of the cnoidal wave theory. The trailing waves are of higher frequency than the leading wave and therefore approach the realm of Stokesian waves instead of the KdV equations.

- The volume of the leading wave crest was determined by a multiple regression. The slide Froude number $\mathbf{F}$ was identified as the dominant parameter. The leading wave crest volume was smaller than the maximum water displacement volume for non-breaking waves. The smaller the maximum water displacement volume the smaller was the fraction which went into the leading wave crest volume.

- The energy packet of the impulse wave train stretched out during propagation resulting in a decrease of the time localized energy, whereas the total wave energy included in a transient impulse wave train dissipates much slower (Fritz and Liu, 2002). The wave energy disperses with the wave train during propagation.

- A strong variation of the decay in the leading wave crest energy over propagation distance was observed. In some cases the leading wave crest energy decayed rapidly, whereas others were almost not dissipated or dispersed depending on the wave type.

- The energy contained in the leading wave crest was determined by a multiple regression. The slide Froude number $\mathbf{F}$ and the dimensionless slide thickness S are the dominant parameters. The wave generation efficiency decreases with increasing dimensionless slide volume. Between 2 and 30% of the kinematic slide impact energy was transferred to the leading wave crest.

- The energy contained in the whole wave train was determined by a multiple regression with the Froude number $\mathbf{F}$, the dimensionless slide volume V and the dimensionless slide thickness S as parameters. An increase in slide volume decreases the slide to wave energy conversion, whereas an increase in slide thickness increases the wave generation efficiency. Between 4 and 50% of the kinematic slide impact energy propagated outward in the impulse wave train.

- The partition of the wave energy among the leading wave and the trailing waves was determined by a multiple regression. The dominant parameters were the slide Froude number $\mathbf{F}$ and the dimensionless slide volume V. An increase in slide volume

decreases the slide to wave energy conversion, whereas an increase in slide thickness increases the wave generation efficiency. An increase in slide Froude number or slide volume increases the amount of the wave train energy included in the leading wave crest. Between 8 and 100% of the wave train energy was located in the leading wave crest.

6.2 Outlook

Several important parameters were not altered in the present study – in particular the slide impact angle α, the granulate density ρ_g and the grain size distribution. The hillslope ramp and the pneumatic landslide generator were designed to enable the investigation of the slide impact angle from 30° to 90°. Hence the presented experimental setup has the capability to enable the investigation of all remaining parameters besides the inherent simplification of the two dimensional model. The slide impact angle was investigated previously but the different studies yield controversial results. Huber (1980) detected an increase in both wave amplitude and energy conversion with increasing impact angle, whereas all others determined a contrary trend. Granulate densities of relevance are those corresponding to avalanches and glacier falls as well as asteroids besides the most important density of natural rock formations analyzed herein. Possible scale effects were only investigated in the comparison with the field observations from the Lituya Bay event. The lack of different artificial grain size diameters prohibited a rigorous scale series. Once different grain size diameters of the artificial granulate are available this gap may be filled. Nevertheless scale series may only give an indication of possible scale effects close to the laboratory scales. An extrapolation in the other direction towards the prototype may be dangerous due to other effects not included at laboratory scale and the extraordinary huge scale differences of up to 4 orders of magnitude. The too high viscosity of the liquid in the model could be reduced or altered in the right direction by a factor of 4 with an increased water temperature. Compressibility and shock wave effects are not included in the laboratory model because the regime changes at higher impact velocities and may therefore only be assessed with numerical simulations. Finally the present and future experimental studies will remain leafless trees if they are not combined with numerical simulations. The local topography and bathymetry of natural water bodies may only be included in numerical models or site specific physical models. The complex wave patterns due to multiple reflections and interference may only be treated numerically. Site specific physical model studies are truncated after the first run-up due to the too strong damping of the incident wave during the wave refection. Promising progress has been made in the numerical simulation of impulse waves.

Notation

a	[L]	= wave amplitude
a_c	[L]	= positive wave envelope amplitude
a_{c1}	[L]	= first wave crest amplitude
a_{c2}	[L]	= second wave crest amplitude
a_C	[L]	= maximum positive wave envelope amplitude
a_{C1}	[L]	= maximum first wave crest amplitude
a_{C2}	[L]	= maximum second wave crest amplitude
a_t	[L]	= negative wave envelope amplitude
a_{t1}	[L]	= first wave trough amplitude
a_T	[L]	= maximum negative wave envelope amplitude
a_{T1}	[L]	= maximum first wave trough amplitude
b	[L]	= slide width
c	[LT^{-1}]	= wave celerity
c_{c1}	[LT^{-1}]	= first wave crest propagation velocity
c_{c2}	[LT^{-1}]	= second wave crest propagation velocity
c_G	[LT^{-1}]	= wave group velocity
c_{t1}	[LT^{-1}]	= first wave trough propagation velocity
Ca	[-]	= Cauchy number
d	[L]	= grain diameter
E	[-]	= dimensionless energy
E_{c1}	[ML^{2}T^{-2}]	= total energy of the leading wave crest
E_{kin}	[ML^{2}T^{-2}]	= kinetic wave energy
E_{pot}	[ML^{2}T^{-2}]	= potential wave energy
E_s	[ML^{2}T^{-2}]	= slide impact energy
E_{sk}	[ML^{2}T^{-2}]	= dimensionless slide kinetic energy
E_{sol}	[ML^{2}T^{-2}]	= total solitary wave energy
E_{tot}	[ML^{2}T^{-2}]	= total wave energy
E_{wt}	[ML^{2}T^{-2}]	= total energy of the whole wave train
E_σ	[ML^{2}T^{-2}]	= water surface energy due to surface tension
f	[-]	= equivalent coefficient of friction
$\mathbf{F}$	[-]	= slide Froude number $\mathbf{F} = v_s / \sqrt{gh}$
$\mathbf{F}_*$	[-]	= densimetric Froude number
g	[LT^{-2}]	= gravitational acceleration

h	[L]	= stillwater depth
H	[L]	= wave height
H_1	[L]	= first wave height
H_2	[L]	= second wave height
H_b	[L]	= breaker wave height
Ha	[-]	= Hammack number
k	[L^{-1}]	= wave number
l_s	[L]	= slide length
L	[L]	= wave length
L_1	[T]	= wave length: first to second upcrossing
L_2	[T]	= wave length: second to third upcrossing
L_{c1}	[T]	= wave length: first to second crest
L_{c2}	[T]	= wave length: second to third crest
m	[M]	= mass
m_s	[M]	= slide mass
m_{wd}	[M]	= wave drift mass discharged in one period
Ma	[-]	= Mach number
n	[-]	= slide porosity
N	[-]	= prototype to model scale ratio of subscript variable
q	[-]	= dimensionless slide volume per unit width
p_{atm}	[ML^{-1}T^{-2}]	= atmospheric pressure
Q_d	[L^3]	= water displacement rate
Q_D	[L^3]	= maximum water displacement rate
$\overline{Q}_s$	[-]	= mean slide displacement rate $\overline{Q}_s = V_s/t_{si}$
r	[L]	= radial propagation distance
R	[L]	= wave run-up height
$\mathbf{R}_*$	[L]	= grain size Reynolds number
s	[L]	= slide thickness
s_{sc}	[L]	= normal distance from slide centroid to ramp
s_{box}	[L]	= slide thickness in box
S	[-]	= relative slide thickness $S = s/h$
Sk	[-]	= Stokes number
t	[T]	= time after impact
t_{si}	[T]	= slide impact duration
t_{sd}	[T]	= duration of subaqueous slide motion
t_D	[L^3]	= time of maximum water displacement volume
t_{qD}	[L^3]	= time of maximum water displacement rate

T	[T]	= wave period
T_1	[T]	= wave period: first to second upcrossing
T_2	[T]	= wave period: second to third upcrossing
T_{c1}	[T]	= wave period: first to second crest
T_{c2}	[T]	= wave period: second to third crest
U	[-]	= Ursell number
U$_1$	[-]	= Ursell number of first wave
U$_2$	[-]	= Ursell number of second wave
v	[LT^{-1}]	= velocity
v_p	[LT^{-1}]	= particle velocity
v_{px}	[LT^{-1}]	= streamwise horizontal component of particle velocity
v_{py}	[LT^{-1}]	= crosswise horizontal component of particle velocity
v_{pz}	[LT^{-1}]	= vertical component of particle velocity
v_s	[LT^{-1}]	= slide centroid velocity at impact
v_{sc}	[LT^{-1}]	= slide centroid velocity
v_{sf}	[LT^{-1}]	= slide front velocity
V	[-]	= dimensionless slide volume $V = V_s / (bh^2)$
V_{c1}	[L^3]	= water volume of leading wave crest
V_d	[L^3]	= water displacement volume
V_D	[L^3]	= maximum water displacement volume
V_s	[L^3]	= slide volume
W	[-]	= Weber number
x	[L]	= streamwise coordinate
x_{ramp}	[L]	= streamwise coordinate along the ramp
$\underset{\sim}{x}$	[L]	= streamwise coordinate parallel to ramp and slide bottom
$\underset{\sim}{x}_{sd}$	[L]	= subaqueous slide run-out measured along slide path
$\underset{\sim}{x}_{sf}(t)$	[L]	= subaqueous slide front travel distance
z	[L]	= vertical coordinate
α	[°]	= slide impact angle
α_{sc}	[°]	= centroid path angle
β	[°]	= wave run-up angle
γ	[°]	= wave propagation direction
δ	[°]	= bed friction angle
ϕ	[°]	= granulate internal friction angle
Δx_{0B}	[L]	= horizontal slide travel distance cut short by pneumatics
Δz_{0B}	[L]	= slide drop height cut short by pneumatic landslide generator
Δz_{sc}	[L]	= slide centroid drop height

ϑ	[radians]	= phase angle
η	[L]	= water surface displacement
κ	[-]	= breaking criterion
ξ	[L]	= slide thickness $\xi(t)$
μ	$[ML^{-1}T^{-1}]$	= dynamic viscosity
ν	$[L^2T^{-1}]$	= kinematic viscosity
Π_i	[-]	= ith dimensionless Π-term
ρ	$[ML^{-3}]$	= density
ρ_{air}	$[ML^{-3}]$	= air density
ρ_g	$[ML^{-3}]$	= granulate density
ρ_p	$[ML^{-3}]$	= particle density
ρ_s	$[ML^{-3}]$	= mean slide density
ρ_w	$[ML^{-3}]$	= water density
σ	$[MT^{-2}]$	= surface tension
τ	$[ML^{-1}T^{-2}]$	= shearing stress
ω	$[T^{-1}]$	= circular wave frequency
ζ	[°]	= slide centroid angle

Subscripts

b	= at breaking
B	= maximum of slide box related value in an experiment
box	= slide box of the pneumatic landslide generator
$flap$	= flap of the slide box opening mechanism
g	= granulate
G	= wave group
min	= statistical minimum
max	= statistical maximum
p	= particle
R	= run-up
s	= slide
sc	= slide centroid
sf	= slide front
w	= water
$*$	= shear

Superscripts

$'$	= per unit width
$\bar{\ }$	= mean value

Statistical symbols

n	[-]	= sample number
r	[-]	= correlation coefficient
σ	[-]	= standard deviation
ε	[ ]	= absolute error

Triax shear tests related symbols in [3.3.2.2]

h_{triax}	[L]	= initial height of a soil probe in a triax shear cell
V_{triax}	[L^3]	= initial volume of a soil probe in a triax shear cell
ΔV	[L^3]	= change in soil probe volume during a triax shear test
Δz	[L]	= change in soil probe height during a triax shear test
ϕ'	[-]	= effective internal friction angle
ϕ'_{max}	[-]	= maximum effective internal friction angle
ϕ'_{ult}	[-]	= ultimate effective internal friction angle
σ'	[-]	= effective normal tension
σ'_1	[-]	= effective axial normal tension
σ'_3	[-]	= effective lateral normal tension
τ	[-]	= shear tension
$\tau_{failure}$	[-]	= shear resistance

Optical and PIV related symbols in [3.4]

a	[L^{-1}]	= absorption coefficient
C_p	[L^{-3}]	= number of seeding particles per unit volume
d_{diff}	[L]	= diffraction limited minimum particle image diameter
d_e	[L]	= diffracted particle image diameter
d_τ	[L]	= recorded particle image diameter
D_a	[L]	= diaphragm aperture
E_{laser}	[L]	= laser pulse energy
Ex	[L]	= optical exposure
$\overline{Ex}$	[L]	= mean optical exposure
f	[L]	= focal length
$f_\#$	[-]	= f-number
I	[-]	= matrix intensity function of interrogation window
$\hat{I}$	[-]	= Fourier transform of windowed matrix intensity function
$\hat{I}^*$	[-]	= complex conjugate of $\hat{I}$
M	[-]	= magnification
n	[-]	= refractive index

N_{iw}	[-]	= number of seeding particles in an interrogation window
N_{pair}	[-]	= number of detected particle image pairs in window
p	[L]	= interrogation window size $p \times p$ pixel; 1 pixel = 9 μm
P	[-]	= probability
P_{il}	[-]	= probability of in-plane loss of particle
P_{ol}	[-]	= probability of out-of-plane loss of particle
R_{II}	[-]	= cross-correlation function
v'	[LT^{-1}]	= velocity fluctuation
V_{iw}	[L^3]	= interrogation volume
x_{ip}	[L]	= area of view x-dimension in image plane
x_{op}	[L]	= area of view x-dimension in object plane
y_{ip}	[L]	= image distance
y_{op}	[L]	= object distance
z_{ip}	[L]	= area of view z-dimension in image plane
z_{op}	[L]	= area of view z-dimension in object plane
δy	[L]	= depth of field
$\varepsilon_{\Delta x}$	[L]	= random displacement Δx error
ε_{v_x}	[LT^{-1}]	= random velocity component v_x error
ε_v	[LT^{-1}]	= random velocity v error
ε_{tot}	[LT^{-1}]	= total velocity v error
ε_{bias}	[LT^{-1}]	= velocity v error due to biased correlation analysis
ε_{optics}	[LT^{-1}]	= velocity v error due to optical imaging errors
ε_{track}	[LT^{-1}]	= velocity v error due to particle flow tracking error
Δt	[T]	= laser pulse separation
Δx	[L]	= mean particle image displacement in interrogation window
Δy_{op}	[L]	= light-sheet thickness
Δz	[L]	= mean particle image displacement in interrogation window
λ	[L]	= wave length

Deformation tensor related symbols in [4.6]

δv_p	[1/T]	= deformation tensor
ε_{xx}	[1/T]	= streamwise horizontal elongational strain component
ε_{xy}	[1/T]	= shear strain component
ε_{xz}	[1/T]	= shear strain component
ε_{yx}	[1/T]	= shear strain component
ε_{yy}	[1/T]	= crosswise horizontal elongational strain component
ε_{yz}	[1/T]	= shear strain component

ε_{zx}	[1/T]	= shear strain component
ε_{zy}	[1/T]	= shear strain component
ε_{zz}	[1/T]	= vertical elongational strain component
ω_x	[1/T]	= vorticity vector component (in-plane)
ω_y	[1/T]	= vorticity vector component (out-of-plane)
ω_z	[1/T]	= vorticity vector component (in-plane)

Abbreviations

CCD	= charge coupled device
CWG	= capacitance wave gage
DNS	= direct numerical simulations
DSR	= dynamic spatial range
DVR	= dynamic velocity range
FFT	= fast Fourier transform
FWHM	= full width at half maximum
LDA	= laser doppler anemometry
LDS	= laser distance sensor
KdV	= Korteweg - de Vries
Nd.YAG	= neodymium yttrium aluminum garnet (crystal for laser rod)
PIV	= particle image velocimetry
PTU	= programmable timing unit
RAM	= random access memory
SPH	= smoothed particle hydrodynamics
TTL	= hardware trigger

References

Abelson, H.I. (1970). Pressure measurements in the water-entry cavity. *J. Fluid Mech.* **44**(1):129-144.

Adrian, R.J. (1984). Scattering particle characteristics and their effect on pulsed laser measurements of fluid flow: speckle velocimetry vs particle image velocimetry. *Applied Optics* **23**(11):1690-1691.

Adrian, R.J., Yao, C.-S. (1985). Pulsed laser technique application to liquid and gaseous flows and the scattering power of seed materials. *Applied Optics* **24**(1):44-52.

Adrian, R.J. (1988). Statistical properties of particle image velocimetry measurements in turbulent flow. *Laser Anemometry in Fluid Mechanics* **3**:115-129, Eds. Adrian, R.J. et al., Ladoan, Lisbon.

Adrian, R.J. (1991). Particle-imaging techniques for experimental fluid mechanics. *Ann. Rev. Fluid Mech.* **23**:261-304.

Adrian, R.J. (1995). Limiting resolution of particle image velocimetry for turbulent flow. *Proc. 2nd Turbulence Research Assoc. Conf.* **2**(1):1-19. Pohang Inst. Tech., Korea.

Adrian, R.J. (1996). Bibliography of particle velocimetry using imaging methods: 1917-1995. TAM *report* 817, UILU-ENG-96-6004. University of Illinois, Urbana.

Adrian, R.J. (1997). Dynamic ranges of velocity and spatial resolution of particle image velocimetry. *Meas. Sci. Technol.* **8**(12):1393-1398.

Aida, I. (1975). Numerical experiments of the tsunamis associated with the collapse of Mt. Mayuyama in 1792. *J. Seismol. Soc. Japan* (Zisin) **28**(4):449-460. (In Japanese with English abstract).

Airy, G.B. (1845). Tides and waves. *Encyclopaedia Metropolitana* **5**:241-392, London.

Asano, S. (1979). Light scattering properties of spheroidal particles. *Applied Optics* **18**(5):712-723.

Asano, S., Sato, M. (1980). Light scattering by randomly oriented spheroidal particles. *Applied Optics* **19**(6):962-974.

Bachmann, G., Narici, L., Beckenstein, E. (2000). *Fourier and wavelet analysis.* Springer, New York.

Bachus, E. (1955). Pressluftschleier als Bauhilfsmassnahme. *Der Bauingenieur* **30**(7):267-268. (in German)

Bagnold, R.A. (1954). Experiments in a gravity-free dispersion of large solid spheres in a Newtonian fluid under shear. *Proc. Royal Soc. London* **225**(A):49-63.

Ball, J.W. (1970). Hydraulic model studies, wave action generated by slides into Mica reservoir. *Report.* Western Canada Hydraulic Laboratories, Vancouver, Canada.

Banner, M.L., Peregrine, D.H. (1993). Wave breaking in deep water. *Ann. Rev. Fluid Mech.* **25**:373-397.

Basset, A.B. (1888). *A treatise on hydrodynamics.* Deighton, Bell and Co., Cambridge.

Benjamin, T.B. (1995). Verification of the Benjamin-Lighthill conjecture about steady water waves. *J. Fluid Mech*. **295**:337-356.

Biesel, F. (1949). Calcul de l'amortissement d'une houle dans un liquide visqueux de profondeur finie. *La Houille Blanche* **4**(5):630-634.

Birkhoff, G. (1950). *Hydrodynamics: a study in logic, fact and similitude*. Dover Press, New York.

Birkoff, T., Zarantonello, F.H. (1957). *Jets, wakes and cavities*. Academic Press, New York.

Bjerrum, L., Jørstad, F. (1968). Stability of rock slopes in Norway. *Norwegian Geotechnical Institute Publication* **79**:1-11. Norwegian Geotechnical Institute, Oslo.

Blevins, R.D. (1979). *Applied fluid dynamics handbook*. Van Nostrand Reinhold, New York.

Bohren, C.F., Huffman, D.R. (1998). *Absorption and scattering of light by small particles*, 3rd ed., John Wiley, New York.

Boillot, A., Prasad, A.K. (1996). Optimization procedure for pulse separation in cross-correlation PIV. *Exp. Fluids* **21**:87-93.

Bollrich, G (1989). *Technische Hydromechanik* II. VEB Verlag für Bauwesen, Berlin. (in German)

Boussinesq, J. (1871). Théorie de l'intumescence liquid appelée onde solitaire ou de translation, se propagent dans un canal rectangulaire. *Comptes Rendus Acad. Sci.* **72**:755-759.

Boussinesq, J. (1872). Théorie des ondes et des remous que se propagent le long d'un canal rectangulaire horizontal, en communiquant au liquide contenu dans ce canal des vitesses sensiblement pareilles de la surface au fond. *J. Math. Pures Appl.* **17**:55-108.

Boussinesq, J. (1877). Essai sur la théorie des eaux courantes. Institute de France, Académie des Sciences. *Mémoires présentés par divers savants* **23**.

Brevik, I. (1976). Partial wave damping in pneumatic breakwaters. *J. Hydr. Div.*, ASCE, **102**(HY9):1167-1176.

Broili, L. (1967). New knowledge on the geomorphology of the Vajont slide slip surface. *Rock Mech. Engrg. Geol.* **5**(1):38-88.

Brücker, C. (1997). 3D scanning PIV applied to an air flow in a motored engine using digital high-speed video. *Meas. Sci. Technol.* **8**(12):1480-1492.

Brücker, C. (2000). 3-D measurements of bubble motion and wake structure in two-phase flow using 3-D scanning particle-image velocimetry (3D-SPIV) and stereo-imaging. *Laser techniques applied to fluid mechanics*, selected papers from the 9th International Symposium: Lisbon 1998, Portugal. Eds. Adrian, R.J. et al., Springer, New York.

Buckingham, E. (1914). On physically similar systems. *Physical Rev.* **4**:354-376.

Camus, G., Vincent, P.M. (1983). Discussion of a new hypothesis for the Krakatau volcanic eruption in 1883. *J. Volcanol. and Geotherm. Res.* **19**:167-173.

Campbell, C.S. (1990). Rapid granular flows. *Annu. Rev. Fluid Mech.* **22**:57-92.

Chang, K.-A., Liu, P.L.-F. (1998). Velocity, acceleration and vorticity under a breaking wave. *Physics of Fluids* **10**(1):327-329.

Chang, K.-A., Liu, P.L.-F. (1999). Experimental investigation of turbulence generated by breaking waves in water of intermediate depth. *Physics of Fluids* **11**(11):3390-3400.

Chappelear, J.E. (1962). Shallow water waves. *J. Geophys. Res.* **67**:4693-4704.

Chaudhry, H., Mercer, A.G., Cass, D. (1983). Modelling of slide-generated waves in a reservoir. *J. Hydr. Engrg.*, ASCE, **109**(11):1505-1520.

Chen, B., Saffman, P.G. (1980). Numerical evidence for the existence of new types of gravity waves of permanent form on deep water. *Stud. Appl. Maths* **62**:1-21.

Chiang, W.L., Divorky, D., Parnicky, P., Wier, W. (1981). Numerical model of landslide-generated waves. *Tetra Tech. Report* T-3472, U.S. Dept. of Commerce, Pasadena, California.

Coleman, H.W., Steele, W.G., Jr. (1999). *Experimentation and uncertainty analysis for engineers*, 2nd ed., John Wiley, New York.

Cooke, R.J.S. (1981). Eruptive history of the volcano at Ritter Island. Cooke-Ravian Volume of Volcanological Papers, Ed. Johnson, R.W. *Geol. Surv. Papua New Guinea Mem.* **10**:115-123.

Costa, J.E., Schuster, R.L. (1991). Documented historical landslide dams from around the world. *U.S. Geological Survey Open-File Report* 91-239.

Cox, D.T., Kobayashi, N., Okayasu, A. (1996). Bottom shear stress in the surface zone. *J. Geophys. Res.* **101**(C6):14'337-14'348.

Cox, D.T., Kobayashi, N. (2000). Identification of intense, intermittent coherent motions under shoaling and breaking waves. *J. Geophys. Res.* **105**(C6):14'223-14'236.

Crawford, D.A., Boslough, M.B., Trucano, T.G., Robinson, A.C. (1994). The impact of comet Shoemaker-Levy 9 on Jupiter. *Shock Waves* **4**:47-50.

Crawford, D.A., Mader, C.L. (1998). Modeling asteroid impact and tsunami. *Science of Tsunami Hazards* **16**(1):21-30.

Dailey, J.W., Stephan, S.C., Jr. (1953). Characteristics of the solitary wave. *Trans. ASCE* **118**:575-587.

Dalrymple, R.A. (1985). *Physical modelling in coastal engineering*. Balkema, Rotterdam.

Darwin, C. (1953). Note on hydrodynamics. *Proc. Cambridge Phil. Soc.* **49**:342-354.

Das, M.M., Wiegel, R.L. (1972). Waves generated by the horizontal motion of a wall. *J. Waterw. Harbors Coastal Engrg. Div.*, ASCE, **98**(WW1):49-65.

Davidson, D.D., Whalin, R.W. (1974). Potential landslide-generated water waves, Libby Dam and Lake Koocanusa, Montana. *Technical Report* H-74-15, Waterways Experiment Station, U.S. Army Corps of Engineers, Vicksburg, Miss.

Davidson, D.D., McCartney, B.L. (1975). Water waves generated by landslides in reservoirs. *J. Hydraulics Div.* ASCE, **101**(HY12):1489-1501.

Davis, T.R.H. (1982). Spreading of rock avalanche debris by mechanical fluidization. *Rock Mechanics* **15**(1):9-24.

Daubechies, I. (1992). *Ten lectures on wavelets*. CBMS-NSF Regional Conference Series in Applied Mathematics, SIAM, Philadelphia.

Day, S.J., Carracedo, J.C., Guillou, H., Gravestock, P. (1999). Recent structural evolution of the Cumbre Vieja volcano, LaPalma, Canary Islands: volcanic rift zone reconfiguration as a precursor to volcano flank instability?. *J. Volcan. Geotherm. Res.* **94**:135-167.

Dean, R.G. (1965). Stream function representation of nonlinear ocean waves. *J. Geophys. Res.* **70**:4561-4572.

Dean, R.G. (1970). Relative validities of water wave theories. *J. Waterw. Harbors Coastal Engrg. Div.*, ASCE, **96**(WW1):105-119.

Dean, R.G. (1974). Evaluation and development of water wave theories for engineering application. *Special Report 1*, U.S. Army Coastal Engineering Research Center, Ft. Belvoir, VA.

Dean, R.G., Perlin, M. (1986). Intercomparison of near bottom kinematics by several wave theories and field and laboratory data. *Coastal Engrg.* **9**:399-437.

Dean, R.G., Dalrymple, R.A. (1991). Water wave mechanics for engineers and scientists. *Advanced series on ocean engineering* **2**. World Scientific, Singapore.

Debnath, L. (1994). *Nonlinear water waves*. Academic Press, London.

Denny, M.W. (1993). *Air and water: the biology and physics of life's media*. Princeton University Press.

De Quervain, F. (1980). *Tabellen zum Mineral- und Gesteinsbestimmen*, 3rd ed., Verlag der Fachvereine VdI, Zürich. (in German)

Dion, N.P., Embrey, S.S. (1981). Effects of Mount St. Helens eruption on selected lakes in Washington. *USGS Circular* 850-G.

Dracos, T. (1990). *Hydraulik*, 3rd ed., Verlag der Fachvereine, Zürich.

Dysthe, K.B. (1979). Note on a modification to the nonlinear Schrödinger equation for application to deep water waves. *Proc. R. Soc. Lond.* **369**(A):105-114.

Eames, I., Belcher, S.E., Hunt, J. C. R. (1994). Drift, partial drift, and Darwin's proposition. *J. Fluid Mech.* **275**:201-223.

Edgers, L., Karlsrud, K. (1982). Soil flows generated by submarine slides – case studies and consequences. *Proc. 3rd Int. Conf. on the Behavior of Offshore Structures*, Cambridge, **2**:425-437.

Embrey, S.S., Dion, N.P. (1988). Effects of the 1980 eruption of Mount St. Helens on the limnological characteristics of selected lakes in western Washington. *USGS Water-Resources Investigations Report* 87-4263.

Emrich, R.J. (1981). Fluid dynamics. *Methods of experimental physics* **18**(A). Academic Press, New York.

Erismann, T.H. (1979). Mechanisms of large landslides. *Rock Mechanics* **12**(1):15-46.

Favre, H. (1935). *Étude théorique et expérimentale des ondes de translation dans les canaux découverts*. Dunod, Paris.

Fenton, J.D. (1985). A fifth-order Stokes theory for steady waves. *J. Waterway, Port, Coastal, and Ocean Engrg.*, ASCE, **111**(2):216-234.

Fincham, A.M., Spedding, G.R. (1997). Low cost, high resolution DPIV for measurements of turbulent fluid flow. *Exp. Fluids* **23**(6):449-462.

Fincham, A.M., Delerce, G. (2000). Advanced optimization of correlation imaging velocimetry algorithms. *Exp. Fluids* **29**(7):S13-S22.

Fomin, N.A. (1998). *Speckle photography for fluid mechanics measurements*. Springer, Berlin.

Fouras, A., Soria, J. (1998). Accuracy of the out-of-plane vorticity measurements derived from in-plane velocity field data. *Exp. Fluids* **25**(5):74-84.

Francis, P.W. (1985). The origin of the 1883 Krakatau tsunamis. *J. Volcanol. and Geotherm. Res.* **25**:349-363.

Freds∅e, J., Deigaard, R. (1992). Mechanics of coastal sediment transport. *Advanced series on ocean engineering* 3. World Scientific, Singapore.

Fritz, H.M., Hager, W.H., Minor, H.-E. (2001). Lituya Bay case: rockslide impact and wave run-up. *Science of Tsunami Hazards* **19**(1):3-22.

Fritz, H.M. (2002). PIV applied to landslide generated impulse waves. *Laser techniques for fluid mechanics*, 305-320, selected papers from the 10th International Symposium: Lisbon 2000, Portugal. Eds. Adrian, R. J. et al., Springer, New York.

Fritz, H.M., Moser, P. (2002). Pneumatic landslide generator. *Int. J. Fluid Power*. submitted.

Fritz, H.M., Liu, P.C. (2002). An application of wavelet transform analysis to landslide generated impulse waves. *Proc. 4th International Symposium on Ocean Wave*

Measurement and Analysis, San Francisco 2001, Eds. Edge, B.L. et al., ASCE, **2**:1477-1486.

Fugazza, M., Natale, L. (1992). Hydraulic design of perforated breakwaters. *J. Waterway, Port, Coastal, and Ocean Engrg.*, ASCE, **118**(1):1-14.

Galvin, C.J., Jr. (1964). Wave-height prediction for wave generators in shallow water. *Tech. Memo* **4**, U.S. Army, Coastal Engineering Research Center.

Galvin, C.J., Jr. (1968). Breaker type classification on three laboratory beaches. *J. Geophys. Res.* **73**(12):3651-3659.

Galvin, C.J., Jr. (1969). Breaker travel and choice of design wave height. *J. Waterw. Harbors Coastal Engrg. Div.*, ASCE, **95**(WW2):175-200.

Gault, D.E., Sonett, C.P. (1982). Laboratory simulation of pelagic asteroidal impact: Atmospheric injection, benthic topography, and the surface wave radiation field. Geological implications of impacts of large asteroids and comets on the earth, Eds. Silver, L.T., Schultz, P.H., *Geological Society of America Special Paper* **190**:69-92.

Gharib, M., Rambod, E., Shariff, K. (1998). A universal time scale for vortex ring formation. *J. Fluid Mech.* **360**:121-140.

Gillon, M.D., Saul, G.J. (1996). Stabilization of Cairnmuir landslide. *Landslides*, 1693-1698, Ed. Senneset, Balkema, Rotterdam.

Glicken, H. (1996). Rockslide-debris avalanche of May, 18, 1980, Mount St. Helens Volcano, Washington. *U.S. Geological Survey Open-File Report* 96-677.

Goguel, J. (1978). Scale-dependent rockslide mechanisms, with emphasis on the role of pore fluid vaporization. Rockslides and avalanches **1**:693-705, Ed. Voight, B. *Developments in geotechnical engineering* **14A**. Elsevier, Amsterdam.

Goodman, J.W. (1996). *An introduction to Fourier optics*. McGraw-Hill, San Francisco.

Gozali, S., Hunt, B. (1989). Water waves generated by close landslides. *J. Hydr. Res.* **27**(1):49-60.

Grant, I., Owens, E.H. (1990). Confidence interval estimates in PIV measurements of turbulent flows. *Applied optics* **29**(10):1400-1402.

Grant, I., ed. (1994). *Selected papers on particle image velocimetry.* SPIE Milestone Series MS99. SPIE Optical Engineering Press, Bellingham, Washington.

Grant, I., Smith, G.H., Infield, D., Wang, X., Zhao, Y., Fu, S. (1994). Measurements of the flow around wind turbine rotors by particle image velocimetry. *Proc. 7th Int. Symp. on Applications of Laser Techniques to Fluid Mechanics*, Lisbon, paper 10.5.

Grant, I., Fu, S., Pan, X., Wang, X. (1995). The application of an in-line, stereoscopic, PIV system to 3-component velocity measurements. *Exp. Fluids* **19**:214-221.

Grant, I. (1997). Particle image velocimetry: a review. *Proc. Instn. Mech. Engrs.* **211**(C):55-76.

Grant, I., Pan, X. (1997). The use of neural techniques in PIV and PTV. *Meas. Sci. Technol.* **8**(12):1399-1405.

Grant, I., Pan, X., Romano, F., Wang, X. (1998). Neural network method applied to the stereo image correspondence problem in three-component, particle image velocimetry. *Applied Optics* **37**(17):3656-3663.

Gray, C., Greated, C.A. (1988). The application of particle image velocimetry to the study of water waves. *Optics and Lasers in Engrg.* **9**:265-276.

Gray, C., Greated, C.A., McCluskey, D.R., Easson, W.J. (1991). An analysis of the scanning beam PIV illumination system. *Meas. Sci. Technol.* **2**:717-724.

Greene, H.G., Gardner-Taggart, J., Ledbetter, M.T., Barminiski, R., Chase, T.E., Hicks, K.R., Baxter, C. (1991). Offshore and onshore liquefaction at Moss Landing spit, central California – result of the October 17, 1989, Loma Prieta earthquake. *Geology* **19**:945-949.

Grimstad, E., Nesdal, S. (1991). The Loen rockslides – a historical review. *Norwegian Geotechnical Institute Publication* **182**:1-6. Norwegian Geotechnical Institute, Oslo.

Günther, A., Rudolf von Rohr, Ph. (2002). Influence of the optical configuration on temperature measurements with fluid-dispersed TLCs. *Exp. Fluids* **32**(5):533-541.

Gutmacher, C.E., Normark, W.R. (1993). Sur submarine slide, a deep-water sediment failure. in submarine landslides: selected studies in the U.S. exclusive economic zone, eds. Schwab, W.C., Lee, H.J., Twichell, D.C., *U.S. Geol. Surv. Bull.* **2002**:123-134.

Habib, P. (1975). Production of gaseous pore pressure during rockslides. *Rock Mechanics* **7**(3):193-197.

Hall, J.V., Jr., Watts, G.M. (1953). Laboratory investigation of the vertical rise of solitary waves on impermeable slopes. *Tech. Memo.* **33**, U.S. Army Corps of Engineers, Beach Erosion Board.

Hammack, J.L. (1973). A note on tsunamis: Their generation and propagation in an ocean of uniform depth. *J. Fluid Mech.* **60**:769-799.

Hampton, M.A., Lee, H.J., Locat, J. (1996). Submarine landslides. *Reviews of Geophysics* **34**(1):33-59.

Harbitz, C.B. (1992). Model simulations of tsunamis generated by the Storegga slides. *Mar. Geol.* **105**:1-21.

Harbitz, C.B., Pedersen, G., Gjevik, B. (1992). Numerical simulations of large water waves due to landslides. *J. Hydr. Engrg.*, ASCE **118**(10):1325-1342.

Harkrider, D.G., Press, F. (1967). The Krakatoa air-sea waves: an example of pulse propagation in coupled systems. *Geophys. J. R. Astron. Soc.* **13**:149-159.

Hart, D.P. (1998). Super-resolution PIV by recursive local correlation. *Proc.* VSJ-SPIE98, AB149:1-10.

Hart, D.P. (2000). PIV error correction. *Laser techniques applied to fluid mechanics*, selected papers from the 9th International Symposium: Lisbon 1998, Portugal. Eds. Adrian, R.J. et al., Springer, New York.

Hattori, M. (1986). Experimental study on the validity range of various wave theories. *Proc. 20th Int. Conf. on Coastal Engineering* **1**:232-246, ASCE, Taipei.

Hecht, E. (1998). *Optics*, 3rd ed.; Addison-Wesley, Reading, Mass.

Hecht, J. (1992). *The laser guidebook*, 2nd ed.; McGraw-Hill, New York.

Heezen, B.C., Ewing, M. (1952). Turbidity currents and submarine slumps, and the Grand Banks earthquake. *American Journal of Science* **250**:849-873.

Heim, A. (1932). *Bergsturz und Menschenleben*. Fretz und Wasmuth, Zürich. (in German)

Heinrich, P. (1992). Nonlinear water waves generated by submarine and aerial landslides. *J. Waterway, Port, Coastal, and Ocean Engrg.*, ASCE, **118**(3):249-266.

Herbich, J.B. (1990). *Handbook of coastal and ocean engineering* 1. Gulf Publishing, Houston.

Hering, F., Leue, C., Wierzimok, D., Jähne, B. (1997). Particle tracking velocimetry beneath water waves. Part 1: visualization and tracking algorithms. *Exp. Fluids* **23**(6):472-482.

Hering, F., Leue, C., Wierzimok, D., Jähne, B. (1998). Particle tracking velocimetry beneath water waves. Part 2: Water waves. *Exp. Fluids* **24**(1):10-16.

Hesselink, L. (1988). Digital image processing in flow visualization. *Ann. Rev. Fluid Mech.* **20**:421-485.

Hills, J.G., Goda, M.P. (2001). The asteroid tsunami project at Los Alamos. *Science of Tsunami Hazards* **19**(1):55-65.

Hinze, J.O. (1975). *Turbulence*, 2nd ed., McGraw-Hill, New York.

Hitz, B.C., Ewing, J.J., Hecht, J. (2001). *Understanding laser technology*, 3rd ed.; IEEE Press and John Wiley, New York.

Hjelmfelt, A.T., jr., Mockros, L.F. (1966). Motion of discrete particles in a turbulent fluid. *Appl. Sci. Res.* **16**:149-161.

Holst, G.C. (1998). *CCD arrays, cameras and displays*. SPIE Optical Engineering Press, Bellingham, Wa.

Holst, M. (1977). Underwater explosions. *Annu. Rev. Fluid Mech.* **9**:187-214.

Horikawa, K. (1978). *Coastal engineering: an introduction to ocean engineering*. University of Tokyo Press.

Horikawa, K. (1988). *Nearshore dynamics and coastal processes: theory, measurement, and predictive models*. University of Tokyo Press.

Housen, K.R., Schmidt, R.M. (1983). Crater ejecta scaling laws: fundamental forms based on dimensional analysis. *J. Geophys. Res.* **88**(B3):2485-2499.

Hrubes, J.D. (2001). High-speed imaging of supercavitating underwater projectiles. *Experiments in Fluids* **30**(1):57-64.

Hsü, K.J. (1975). Catastrophic debris streams (sturzstroms) generated by rockfalls. *Geol. Soc. Am. Bull.* **86**(1):128-140.

Hsü, K.J. (1989). *Physical principles of sedimentology*. Springer, Berlin.

Huang, H.T., Fielder, H.F., Wang, J.J. (1993a). Limitation and improvement of PIV, part I: limitation of conventional techniques due to deformation of particle image patterns. *Exp. Fluids* **15**:168-174.

Huang, H.T., Fielder, H.F., Wang, J.J. (1993b). Limitation and improvement of PIV, part II: particle image distortion, a novel technique. *Exp. Fluids* **15**:263-273.

Huang, H.T., Dabiri, D., Gharib, M. (1997). On errors of digital particle image velocimetry. *Meas. Sci. Technol.* **8**(12):1427-1440.

Huang, L.H., Chao, H.I. (1992). Reflection and transmission of water wave by porous breakwater. *J. Waterway, Port, Coastal, and Ocean Engrg.*, ASCE, **118**(5):437-452.

Huber, A. (1976). Grenzen der Froude'schen Ähnlichkeit bei der Nachbildung flacher Wasserwellen im hydraulischen Modell. *VAW-Mitteilung* 21, Ed. Vischer, D., Versuchsanstalt für Wasserbau, Hydrologie und Glaziologie, ETH Zürich. (in German)

Huber, A. (1980). Schwallwellen in Seen als Folge von Bergstürzen. *VAW-Mitteilung* 47, Ed. Vischer, D., Versuchsanstalt für Wasserbau, Hydrologie und Glaziologie, ETH Zürich. (in German)

Huber, A., Hager, W.H. (1997). Forecasting impulse waves in reservoirs. *Dix-neuvième Congrès des Grands Barrages* C**31**:993-1005. Florence, Italy. Commission International des Grands Barrages: Paris.

Hudson, J.D., Dykhno, L., Hanratty, T.J. (1995). Turbulence production in flow over a wavy wall. *Exp. Fluids* **20**:257-265.

Hughes, S. (1993). Physical models and laboratory techniques in coastal engineering. *Advanced series on ocean engineering* 7. World Scientific, Singapore.

Hungr, O., Morgenstern, N.R. (1984a). Experiments on the flow behaviour of granular materials at high velocity in an open channel flow. *Geotéchnique* **34**:405-413.

Hungr, O., Morgenstern, N.R. (1984b). High velocity ring shear tests on sand. *Geotéchnique* **34**:415-421.

Hunt, B. (1988). Water waves generated by distant landslides. *J. Hydr. Res.* **26**(3):307-322.

Hunt, B. (1994). Newtonian fluid mechanics treatment of debris flow and avalanches. *J. Hydr. Engrg.*, ASCE, **120**(12):1350-1363.

Hunt, J.C.R., Abell, C.J., Peterka, J.A., Woo, H. (1997). Kinematical studies of the flows around free or surface mounted obstacles; applying topology to flow visualization. *J. Fluid Mech.* **86**(1):179-200.

Hutter, K., Svendsen, B., Rickenmann, D. (1996). Debris flow modeling: a review. *Continuum Mech. Thermodyn.* **8**:1-35.

Imaichi, K., Ohmi, K. (1983). Numerical processing of flow-visualization pictures – measurement of two-dimensional vortex flow. *J. Fluid Mech.* **129**:283-311.

Imamura, F., Gica, E.C. (1996). Numerical model for tsunami generation due to subaqueous landslide along a coast. *Science of Tsunami Hazards* **14**(1):13-28.

Infeld, E., Rowlands, G. (2000). *Nonlinear waves, solitons and chaos*, 2nd ed.; Cambridge University Press.

Ippen, A.T., Kulin, G, Raza, M.A. (1955). Damping characteristics of the solitary waves. *Hydraulic Lab. Tech. Rep.* 16, MIT, Cambridge, Mass.

Ippen, A.T., Kulin, G. (1957). The effects of boundary resistance on the solitary wave. *La Houille Blanche* **12**(3):390-407.

Ippen, A.T. (1966). *Estuary and coastline hydrodynamics*. McGraw-Hill, New York.

Iversen, H.W. (1952). Waves and breakers in shoaling water. Gravity waves, *Circular* **521**:1-12, National Bureau of Standards, Washington, D.C.

Iverson, R.M. (1997). The physics of debris flows. *Rev. Geophys.* **35**(3):245-296.

Jaeger, J.C., Cook, N.G.W. (1979). *Fundamentals of rock mechanics*. Chapman and Hall, London.

Jähne, B. (1997). *Digital image processing – concepts, algorithms, and scientific applications*, 4th ed.; Springer, Berlin.

Jamieson, W.W., Mansard, P.D. (1987). An efficient upright wave absorber. *Proc. Coastal Hydrodynamics* 1987, Ed. Dalrymple, R.A., Newark, Delaware, ASCE, **1**:124-139.

Jennings, D.N., Newton, C.J., Beetham, R.D., Smith, G. (1991). Stabilization of the Nine Mile Creek schist landslide complex. *Landslides*, 759-764, Ed. Bell, Balkema, Rotterdam.

Jensen, A., Sveen, J.K., Grue, J., Richon, J.-B., Gray, C. (2001). Accelerations in water waves by extended particle image velocimetry. *Exp. Fluids* **30**(5):500-510.

Jiang, L., LeBlond, P.H. (1992). The coupling of a submarine slide and the surface waves which it generates. *J. Geophys. Res.* **97**(C8):12'731-12'744.

Jiang, L., LeBlond, P.H. (1993). Numerical modelling of an underwater Bingham plastic mudslide and the waves which it generates. *J. Geophys. Res.* **98**(C6):10'303-10'317.

Jiang, L., LeBlond, P.H. (1994). Three-dimensional modeling of tsunami generation due to a submarine mudslide. *J. Phys. Ocean.* **24**:559-573.

Johnson, C., Mader, C.L. (1994). Modelling the 105 ka Lanai tsunami. *Science of Tsunami Hazards* **12**(1):33-38.

Johnson, R.S. (1997). *A modern introduction to the mathematical theory of water waves*. Cambridge University Press.

Johnson, R.W. (1978). Blackhawk landslide, California, USA. Rockslides and avalanches **1**:481-504, Ed. Voight, B. *Developments in geotechnical engineering* **14A**. Elsevier, Amsterdam.

Johnson, R.W. (1987). Large scale volcanic cone collapse: the 1888 slope failure of Ritter volcano, and other examples from Papua New Guinea. *Bull. Volcanology* **49**:667-679.

Johnson, W.L., Bermel, K.J. (1949). Impulsive waves in shallow water as generated by falling weights. *Trans. Am. Geophys. Union* **30**(2):223-230.

Jordaan, J.M. (1969). Simulation of waves by an underwater explosion. *J. Waterw. Harbors Coastal Engrg. Div.*, ASCE, **95**(WW3):355-377.

Jørstad, F. (1968). Waves generated by landslides in Norwegian fjords and lakes. *Norwegian Geotechnical Institute Publication* **79**:13-32. Norwegian Geotechnical Institute, Oslo.

Kajiura, K. (1990). Tsunamis. *Ocean Engineering Science* 9A, Eds. LeMéhauté, B., Hanes, D.M.; John Wiley, New York.

Kamphuis, J.W., Bowering, R.J. (1970). Impulse waves generated by landslides. *Proc. 12th Coastal Engineering Conf.* ASCE **1**:575-588.

Kamphuis, J.W. (1975). Friction factor under oscillatory waves. *J. Waterw. Harbors Coastal Engrg. Div.*, ASCE, **101**(WW2):135-144.

Katayama, N. (1974). Old records of natural phenomena concerning the Shimabara catastrophe. *Sci. Rpt. Shimabara Volcano Observ., Fac. Sci. Kyushu Univ.* **9**.

Keane, R.D., Adrian, R.J. (1990). Optimization of particle image velocimeters. Part 1: Double pulsed systems. *Meas. Sci. Technol.* **1**:1202-1215.

Keane, R.D., Adrian, R.J. (1991). Optimization of particle image velocimeters. Part 2: Multiple pulsed systems. *Meas. Sci. Technol.* **2**:963-974.

Keane, R.D., Adrian, R.J. (1992). Theory of cross-correlation analysis of PIV images. *Appl. Sci. Res.* **49**:191-215.

Keane, R.D., Adrian, R.J. (1993). Theory of cross-correlation analysis of PIV images. *Flow visualization and image analysis*, ed. Nieuwstadt, F.T.M., Kluwer Academic Publishing, Dordrecht.

Keane, R.D., Adrian, R.J., Zhang, Y. (1995). Super-resolution particle image velocimetry. *Meas. Sci. Technol.* **6**:754-768.

Keating, B.H., McGuire, W.J. (2000). Island edifice failures and associated tsunami hazards. *Pure Appl. Geophys.* **157**:899-955.

Keller, J.B. (1948). The solitary wave and periodic waves in shallow water. *Commun. Pure Appl. Math.* **1**:323-339.

Kent, P.E. (1966). The transport mechanism in catastrophic rock falls. *Journal of Geology* **74**:79-83.

Kerker, M. (1969). *The scattering of light*. Academic Press, New York.

Keulegan, G.H., Patterson, G.W. (1940). Mathematical theory of irrotational translation waves. *J. Res.,* Nat. Bur. Stand.*,* **24**:47-101.

Keulegan, G.H., (1948). Gradual damping of solitary waves. *J. Res.,* Nat. Bur. Stand.*,* **40**:487-498.

Keulegan, G.H. (1950). Wave motion. *Engineering Hydraulics*, Ed. Rouse, H.; John Wiley, New York.

Kieffer, J.C. (1981). Fluid dynamics of the May 18 blast at Mount St. Helens. The 1980 eruptions of Mount St. Helens, Washington, Eds. Lipman, P.W., Mullineaux, D.R. *U.S. Geological Survey Professional Paper* **1250**:379-400.

Kiersch, G.A. (1964). Vajont reservoir disaster. *Civil Engineering* ASCE **34**(3):32-39.

Kit, E., Shemer, L. (1989). On dissipation coefficients in a rectangular wave tank. *Acta Mechanica* **77**:171-180.

Kit, E., Shemer, L., Pelinovsky, E., Talipova, T., Eitan, O., Jiao, H.-Y. (2000). Nonlinear wave group evolution in shallow water. *J. Waterway, Port, Coastal, and Ocean Engrg.*, ASCE, **126**(5):221-228.

Kneubühl, F.K. (1997). *Oscillations and waves*. Springer, Berlin.

Korsunsky, S. (1997). Nonlinear waves in dispersive and dissipative systems with coupled fields. *Pitman Monographs and Surveys in Pure and Applied Mathematics* **83**. Addison Wesley Longman, Harlow, England.

Korteweg, D.J., de Vries, G. (1895). On the change of form of long waves advancing in a rectangular canal, and on a new type of long stationary waves. *Phil. Mag.* **5**(39):422-443.

Körner, H.J. (1976). Reichweite und Geschwindigkeit von Bergstürzen und Fliessschneelawinen (in German). *Rock Mechanics* **8**(3):225-256.

Körner, H.J. (1983). Zur Mechanik der Bergsturzströme von Huascarán, Peru (in German). *Hochgebirgsforschung* **6**:71-110.

Kranzer, H.C., Keller, J.B. (1955). Water waves produced by explosions. *Publication Institute of Mathematical Sciences,* New York University, IMM-NYU **222**.

Kranzer, H.C., Keller, J.B. (1959). Water waves produced by explosions. *J. Appl. Phys.* **30**:398-407.

Kündig, R., Mumenthaler, T., Eckardt, P., Keusen, H.R., Schindler, C., Hofmann, F., Vogler, R., Guntli, P. (1997). *Die mineralischen Rohstoffe der Schweiz.* Schweizerische Geotechnische Kommission, Zürich. (in German)

Laitone, E.V. (1960). The second approximation to cnoidal and solitary waves. *J. Fluid Mech.* **9**:430-444.

Lamb, H. (1932). *Hydrodynamics*, 6th ed., Dover Publications, New York.

Landreth, C.C., Adrian, R.J. (1990). Impingement of a low Reynolds number turbulent circular jet onto a flat plate at normal incidence. *Exp. Fluids* **9**(1):74-84.

Lang, H.-J., Huder, J. (1990). Bodenmechanik und Grundbau – das Verhalten von Böden und die wichtigsten grundbaulichen Konzepte , 4th ed., Springer, Berlin.

Langhaar, H.L. (1957). *Dimensional analysis and theory of models*. John Wiley, New York.

Latter, J.H., (1981). Tsunamis of volcanic origin: summary of causes, with particular reference to Krakatau, 1883. *Bull. Volcanol.* **44**(3):467-490.

Lauber, G. (1997). Experimente zur Talsperrenbruchwelle im glatten geneigten Rechteckkanal. *VAW-Mitteilung* 152, Ed. Vischer, D., Versuchsanstalt für Wasserbau, Hydrologie und Glaziologie, ETH Zürich (in German).

Law, L., Brebner, A. (1968). On water waves generated by landslides. *3rd Australas. Conf. on Hydraulics and Fluid Mechanics*, Sydney, Paper 2561:155-159.

Lawson, N.J., Rudman, M., Guerra, A., Liow, J.-L. (1999). Experimental and numerical comparisons of the break-up of a large bubble. *Exp. Fluids* **26**(6):524-534.

Lean, G.H. (1967). A simplified theory of permeable wave absorbers. *J. Hydr. Res.* **5**(1):15-30.

LeBlond, P.H., Mysak, L.A. (1978). *Waves in the ocean*. Elsevier Scientific, New York.

Lee, M., Longoria, R.G., Wilson, D.E. (1997). Cavity dynamics in high-speed water entry. *Physics of Fluids* **9**(3):540-550.

Lee, M.M., Chwang, A.T. (2000). Scattering and radiation of water waves by permeable barriers. *Physics of Fluids* **12**(1):54-65.

LeMéhauté, B., Divoky, D., Lin, A. (1968). Shallow water waves a comparison of theories and experiments. *Proc. 11th Conf. on Coastal Engineering* **1**:86-107, ASCE, London.

LeMéhauté, B. (1972). Progressive wave absorber. *J. Hydr. Res.* **10**(2):153-169.

LeMéhauté, B. (1976). *An introduction to hydrodynamics and water waves*. Springer, New York.

LeMéhauté, B., Wang, S., Lu, C.-C. (1987). Cavities, domes and spikes. *J. Hydr. Res.*, IAHR, **25**(5):583-602.

LeMéhauté, B. (1990). Similitude. The Sea, Eds. LeMéhauté, B., Hanes, D.M., *Ocean Engineering Science* **9B**:955-980. John Wiley, New York.

LeMéhauté, B., Khangoankar, T. (1992). Generation and propagation of explosion generated waves in shallow water. *Technical Report* DNA-TR-92-40, Defense Nuclear Agency, Washington D.C. (unclassified, limited distribution).

LeMéhauté, B., Wang, S. (1995). Water wave generated by underwater explosions. *Advanced series on ocean engineering* **10**. World Scientific, Singapore.

Levi-Civita, T. (1912). Sulle onde di canale. *Atti Accad. Lincei, Rend. Cl. Sci. Fis. Mat. Nat.* **21**(5):3-14.

Levi-Civita, T. (1921). Qüestions de mecànica clàssica i relativista. *Conferències donades el Gener de 1921*. Barcelona: Institut d'Estudis Catalans.

Liggett, J.A. (1994). *Fluid mechanics*. McGraw-Hill, New York.

Lighthill, J. (1978). *Waves in fluids*. Cambridge University Press.

Lin, P., Chang, K.-A., Liu, P.L.-F. (1999). Runup and rundown of solitary waves on sloping beaches. *J. Waterway, Port, Coastal, and Ocean Engrg.*, ASCE, **125**(5):247-255.

Lindken, R., Gui, L., Merzkirch, W. (1999). Velocity measurements in multiphase flow by means of particle image velocimetry. *Chem. Eng. Technol.* **22**(3):202-206.

Lindken, R., Merzkirch, W. (2000). Velocity measurements of liquid and gaseous phase for a system of bubbles rising in water. *Exp. Fluids* **29**(7):S194-S201.

Liu, A., Shen, X., Smith, G.H., Grant, I. (1992). Particle image velocimetry measurements of wave-current interaction in a laboratory flume. *Optics and Lasers in Engrg.* **16**:239-264.

Liu, Z.C., Landreth, C.C., Adrian, R.J., Hanratty, T.J. (1991). High resolution measurement of turbulent structure in a channel with particle image velocimetry. *Exp. Fluids* **10**(4):301-312.

Longuet-Higgins, M.S. (1953). Mass transport in water waves. *Phil. Trans. R. Soc. London* **A 245**:535-581.

Longuet-Higgins, M.S. (1974). On the mass, momentum, energy and circulation of a solitary wave. *Proc. R. Soc. London* **A 337**:1-13.

Longuet-Higgins, M.S. (1975). Integral properties of periodic gravity waves of finite amplitude. *Proc. R. Soc. London* **A 342**:157-174.

Longuet-Higgins, M.S. (1986). Eulerian and Lagrangian aspects of surface waves. *J. Fluid Mech.* **173**:683-707.

Longuet-Higgins, M.S. (1987). Lagrangian moments and mass transport in Stokes waves. *J. Fluid Mech.* **179**:547-555.

Longuet-Higgins, M.S. (1988). Lagrangian moments and mass transport in Stokes waves, Part 2, water of finite depth. *J. Fluid Mech.* **186**:321-336.

Longuet-Higgins, M.S., Cleaver, R.P. (1994). Crest instabilities of gravity waves, Part 1, the almost highest wave. *J. Fluid Mech.* **158**:115-129.

Longuet-Higgins, M.S., Cleaver, R.P., Fox, M.J.H. (1994). Crest instabilities of gravity waves, Part 2, matching and asymptotic analysis. *J. Fluid Mech.* **259**:333-344.

Longuet-Higgins, M.S., Dommermuth, D.G. (1997). Crest instabilities of gravity waves, Part 3, nonlinear development and breaking. *J. Fluid Mech.* **336**:33-50.

Longuet-Higgins, M.S., Tanaka, M. (1997). On the crest instabilities of steep surface waves. *J. Fluid Mech.* **336**:51-68.

Lucchitta, B.K. (1979). Landslides in Valles Marineris, Mars. *J. Geophys. Res.* **84**:8097-8113.

Luff, J.D., Drouillard, T., Rompage, A.M., Linne, M.A., Hertzberg, J.R. (1999). Experimental uncertainties associated with particle image velocimetry (PIV) based vorticity algorithms. *Exp. Fluids* **26**(1):36-54.

Macfarlane, D.F., Gillon, M.D. (1996). The performance of landslide stabilization measures, Clyde power project, New Zealand. *Landslides*, 1747-1757, Ed. Senneset, Balkema, Rotterdam.

Macfarlane, D.F., Jenks, D.G. (1996). Stabilization and performance of No. 5 Creek slide, Clyde power project, New Zealand. *Landslides*, 1739-1746, Ed. Senneset, Balkema, Rotterdam.

Mader, C.L. (1988). *Numerical modeling of water waves*. University of California press, Berkeley.

Mader, C.L. (1997). *Numerical modeling of explosives and propellants*, 2nd ed., CRC Press, Boca Raton, Fl.

Mader, C.L. (1999). Modeling the 1958 Lituya Bay mega-tsunami. *Science of Tsunami Hazards* **17**(2):57-67.

Mader, C.L. (2001). Modeling the La Palma landslide tsunami. *Science of Tsunami Hazards* **19**(3):160-182.

Madsen, O.S. (1971). On the generation of long waves. *J. Geophys. Res.* **76**(36):8672-8683.

Madsen, P.A. (1983). Wave reflection from a vertical permeable wave absorber. *Coastal Engrg.* **7**(5):381-396.

Mangeney, A., Heinrich, P., Roche, R. (2000). Analytical solution for testing debris avalanche numerical models. *Pure Appl. Geophys.* **157**:1081-1096.

McCowan, J. (1891). On the solitary wave. *Phil. Mag. J. Sci.* **32**(5):45-58.

McCowan, J. (1894). On the highest wave of permanent type. *Phil. Mag. J. Sci.* **38**:351.

McEven, A.S. (1989). Mobility of large rock avalanches: Evidence from Valles Marineris, Mars. *Geology* **17**(12):1111-1114.

McGlaun, J.M., Thompson, S.L., Elrick, M.G. (1990). CTH: a three-dimensional shock wave physics code. *Int. J. Impact Engrg.* **10**:351-360.

Mei, C.C. (1989). The applied dynamics of ocean surface waves. *Advanced series on ocean engineering* 1. World Scientific, Singapore.

Mei, R. (1996). Velocity fidelity of flow tracer particles. *Exp. Fluids* **22**(1):1-13.

Melling, A. (1997). Tracer particles and seeding for particle image velocimetry. *Meas. Sci. Technol.* **8**(12):1406-1416.

Melosh, H.J. (1979). Acoustic fluidization: a new geologic process?. *J. Geophys. Res.* **84**:7513-7520.

Melosh, H.J. (1987). The mechanics of large rock avalanches. Debris flows/avalanches: processes, recognition, and mitigation, Eds. Costa, J.E., Wieczorek, G.F., *Geological Society of America Reviews in Engineering Geology* **7**:41-49.

Melville, W.K. (1982). The instability and breaking of deep water waves. *J. Fluid Mech.* **115**:165-185.

Melville, W.K., Veron F., White, C.J. (2002). The velocity field under breaking waves: coherent structures and turbulence. *J. Fluid Mech.* **454**:203-233.

Meyer, R.E. (1971). *Introduction to mathematical fluid dynamics*. John Wiley, New York.

Meyer, W., Carpenter, P.J. (1982). Filling of Spirit Lake, Washington, May 18, 1980, to July 31, 1982. *U.S. Geological Survey Open-File Report* 82-771.

Meyer, W., Sabol, M.A., Schuster, R.L. (1986). Landslide dammed lakes at Mount St. Helens, Washington. Landslide dams: processes, risk and mitigation, Ed. Schuster, R.L. *Geotechnical Special Publication*, ASCE, **3**:21-41.

Miche, R. (1944). Movement ondulatoires de la mer en profondeur constante ou decroissante. *Ann. des Ponts et Chaussées*.

Michell, J.H. (1893). On the highest waves in water. *Phil. Mag. J. Sci.* **36**:430-437.

Mie, G. (1908). Beiträge zur Optik trüber Medien, speziell kolloidaler Metallösungen. *Ann. Physik* 25(4):377-445. (in German)

Miles, J.W. (1980). Solitary waves. *Ann. Rev. Fluid Mech.* **12**:11-43.

Miller, D.J. (1960). Giant waves in Lituya Bay, Alaska. *Geological Survey Professional Paper* 354-C. U.S. Government Printing Office, Washington D.C.

Miller, R.L., White, R.V. (1966). A single-impulse system for generating solitary, undulating surge, and gravity shock waves in the laboratory. *Fluid Dynamics and Sediment Transport Laboratory Report* **5**, Dept. Geophys. Sci., Univ. Chicago, Ill.

Miller, R.L. (1970). Prediction curves for waves near the source of an impulse. *Proc. 12th Coastal Engrg. Conf.*, ASCE, **1**:609-624, Washington, D.C.

Miller, R.L. (1972). The role of surface tension in breaking waves. *Proc. 13th Coastal Engrg. Conf.*, ASCE, **1**:433-449, Vancouver, B.C.

Monaghan, J.J. (1992). Smoothed particle hydrodynamics. *Ann. Rev. Astron. Astrophys.* **30**:543-574.

Monaghan, J.J., Cas, R.A.F., Kos, A.M., Hallworth, M. (1999). Gravity currents descending a ramp in a stratified tank. *J. Fluid Mech.* **379**:39-69.

Monaghan, J.J., Kos, A.M. (1999). Solitary waves on a cretan beach. *J. Waterway, Port, Coastal, and Ocean Engrg.*, ASCE, **125**(3):145-154.

Monaghan, J.J., Kos, A.M. (2000). Scott Russell's wave generator. *Physics of Fluids* **12**(3):622-630.

Monnier, J.C., Croisier, G., Stanislas, M. (2000). Analysis of the synthetic image 9 from the Europiv database. *Particle image velocimetry – progress towards industrial application*, eds. Stanislas, M. et al., Springer, New York.

Moore, G.W., Moore, J.G. (1988). Large-scale bedforms in boulder gravel produced by giant waves in Hawaii. *Geol. Soc. Am. Spec. Pap.* **229**:101-110.

Moore, J.G., Moore, G.W. (1984). Deposit from a giant wave on the island of Lanai. *Science* **264**:1312-1315.

Moore, J.G., Clague, D.A., Holcomb, R.T., Lipman, P.W., Normark, W.R., Torresan, M.E. (1989). Prodigious submarine landslides on the Hawaiian Ridge. *J. Geophys. Res.* **94**(B12):17'465-17'484.

Moore, J.G., Normark, W.R. (1994). Giant Hawaiian landslides. *Annu. Rev. Earth Planet. Sci.* **22**:119-144.

Moore, J.G., Normark, W.R., Holcomb, R.T. (1994). Giant Hawaiian underwater landslides. *Science* **264**(5155):46-47.

Mudge, M.R. (1965). Rockfall-avalanche and rockslide-avalanche deposits at Sawtooth Ridge, Montana. *Bull. Geol. Soc. Am.* **76**:1003-1014.

Müller, D. (1992). Felssturz Ölberg an der Axenstrasse – Untersuchung der Schwallwellengefahr im Urnersee. *VAW-Report* **4059** (unpublished), Versuchsanstalt für Wasserbau, Hydrologie und Glaziologie, ETH Zürich. (in German)

Müller, D., Schurter, M. (1993). Impulse waves generated by an artificially induced rockfall in a Swiss lake. *Proc. 25th IAHR Congress*, Tokyo, Japan, **4**:209-216.

Müller, D. (1994). Physical modelling and field measurements of impulse waves. *Proc. Int. Symp. Waves-Physical and Numerical Modelling*, Eds. M. Isaacson & M. Quick, University of British Columbia, Vancouver, Canada, **1**:307-315.

Müller, D. (1995). Auflaufen und Überschwappen von Impulswellen an Talsperren. *VAW-Mitteilung* 137, Ed. Vischer, D., Versuchsanstalt für Wasserbau, Hydrologie und Glaziologie, ETH Zürich. (in German)

Müller, L. (1964). The rock slide in the Vajont Valley. *Rock Mech. Engrg. Geol.* **2**(3-4):148-212.

Müller, L. (1968). New considerations on the Vajont slide. *Rock Mech. Engrg. Geol.* **6**(1-2):1-91.

Munk, W.H. (1949). The solitary wave theory and its applications to surf problems. *Ann. N.Y. Acad. Sci.* **51**:376-424.

Naheer, E. (1978a). Laboratory experiments with solitary wave. *J. Waterw. Harbors Coastal Engrg. Div.*, ASCE, **104**(WW4):421-436.

Naheer, E. (1978b). The damping of solitary waves. *J. Hydr. Res*, IAHR, **16**(3):235-249.

Nettel, S. (1995). *Wave physics: oscillations – solitons – chaos*, 2nd ed.; Springer, Berlin.

Nielsen, P. (1992). Coastal bottom boundary layers and sediment transport. *Advanced series on ocean engineering* 4. World Scientific, Singapore.

Noda, E. (1970). Water waves generated by landslides. *J. Waterw. Harbors Coastal Engrg. Div.*, ASCE, **96**(WW4):835-855.

Noda, E. (1971). Fourier analysis of transient wave systems. *J. Waterw. Harbors Coastal Engrg. Div.*, ASCE, **97**(WW4):663-670.

Nogueira, J., Lecuona, A., Rodríguez, P.A. (1997). Data validation, false vectors correction and derived magnitudes calculation on PIV data. *Meas. Sci. Technol.* **8**(12):1493-1501.

Normark, W.R., Moore, J.G., Torresan, M.E. (1993). Giant volcano-related landslides and the development of the Hawaiian Islands. Submarine landslides: selected studies in the US exclusive economic zone, Eds. Schwab, W.C. et al. *US Geol. Surv. Bull.* **2002**:184-196.

Ogawa, T., (1924). Notes on the volcanic and seismic phenomena in the volcanic district of Shimabara, with a report on the earthquake of December 8, 1922. *Mem. Coll. Sci., Kyoto Imp. Univ., Ser. B*, **1**(2).

Ouellet, Y., Datta, I. (1986). A survey of wave absorbers. *J. Hydr. Res.* **24**(4):265-280.

Pararas-Carayannis, G. (1999). Analysis of mechanism of tsunami generation in Lituya Bay. *Science of Tsunami Hazards* **17**(3):193-206.

Plafker, G., Eyzaguirre, V.R. (1979). Rock avalanche and wave at Chungar, Peru. Rockslides and avalanches **2**:269-279, Ed. Voight, B. *Developments in geotechnical engineering* **14B**. Elsevier, Amsterdam.

Pouliquen, O. (1999a). Scaling laws in granular flows down rough inclined planes. *Physics of Fluids* **11**(3):542-548.

Pouliquen, O. (1999b). On the shape of granular fronts down rough inclined planes. *Physics of Fluids* **11**(7):1956-1958.

Prasad, A.K., Adrian, R.J., Landreth, C.C., Offutt, P.W. (1992). Effect of resolution on the speed and accuracy of particle image velocimetry interrogation. *Exp. Fluids* **13**:105-116.

Prins, J.E. (1958). Characteristics of waves generated by a local disturbance. *Trans. Am. Geophys. Union* **39**(5):865-874.

Proakis, J.G., Manolakis, D.G. (1996). *Digital signal processing: principles, algorithms, and applications*. Prentice Hall, Upper Saddle River, NJ.

Pugh, F.J., Wilson, K.C. (1999). Velocity and concentration distributions in sheet flow above plane beds. *J. Hydr. Engrg.*, ASCE, **125**(2):117-125.

Raffel, M., Willert, C.E., Kompenhans, J. (1998). *Particle image velocimetry – a practical guide*. Springer, Berlin.

Rahman, M. (1995). *Water waves: relating modern theory to advanced engineering applications*. Clarendon Press, Oxford.

Raney, D.C., Butler, H.L. (1975). A numerical model for predicting the effects of landslide generated water waves. *U.S. Army Corps of Engineers Waterways Experiment Station Report* H-75-1, U.S. Dept. of Commerce, Springfield, Va.

Ratkowsky, D.A. (1990). Handbook of nonlinear regression models. *Statistics: textbooks and monographs* **107**. Dekker, New York.

Raudkivi, A.J. (1990). *Loose boundary hydraulics*, 3rd ed.; Pergamon Press, Oxford.

Rayleigh, L. (1876). On waves. *London, Edinburgh, Dublin Phil. Mag. J. Sci.* **1**(4):257-279.

Rayleigh, L. (1877). On progressive waves. *Proc. London Math. Soc.* **9**:21-26.

Remoissenet, M. (1999). *Waves called solitons*, 3rd ed.; Springer, Berlin.

Ronneberger, O., Raffel, M., Kompenhans, J. (1998). Advanced evaluation algorithms for standard and dual plane particle image velocimetry. *Proc. 9th Int. Symp. on Applications of Laser Techniques to Fluid Mechanics*, Lisbon, paper 10.1.

Rooij de, F., Dalziel, S.B., Linden, P.F. (1999). Electrical measurement of sediment layer thickness under suspension flows. *Exp. Fluids* **26**(8):470-474.

Rösgen, T., Wozniak G., Wozniak K. (1990). Image processing for laser speckle velocimetry using the 2-D fast Fourier transform. *Applied Optics* 29(35):5298-5302.

Roth, G.I., Mascenik, D.T., Katz, J. (1999). Measurements of the flow structure and turbulence within a ship bow wave. *Physics of Fluids* **11**(11):3512-3523.

Royer, H. (1997). Holography and particle image velocimetry. *Meas. Sci. Technol.* **8**(12):1562-1572.

Russell, J.S. (1837). Report of the Committee on Waves. *Report of the 7th Meeting of the British Association for the Advancement of Science*, Liverpool, **7**:417-496.

Russell, J.S. (1844). Report on waves. *Report of the 14th Meeting of the British Association for the Advancement of Science*, York, **14**:311-390.

Rzadkiewicz, S.A., Mariotti, C., Heinrich, P. (1997). Numerical simulations of submarine landslides and their hydraulic effects. *J. Waterway, Port, Coastal, and Ocean Engrg.*, ASCE, **123**(4):149-157.

Sager, J.W., Chambers, D.R. (1986). Design and construction of the Spirit Lake outlet tunnel, Mount St. Helens, Washington. Landslide dams: processes, risk and mitigation, Ed. Schuster, R.L. *Geotechnical Special Publication*, ASCE, **3**:42-58.

Sander, D. (1990). Weakly nonlinear unidirectional shallow water waves generated by a moving boundary. *VAW-Mitteilung* 105, Ed. Vischer, D., Versuchsanstalt für Wasserbau, Hydrologie und Glaziologie, ETH Zürich.

Sarpkaya, T., Isaacson, M. (1981). *Mechanics of wave forces on offshore structures*. Van Nostrand Reinhold, New York.

Savage, S.B. (1979). Gravity flow of cohesionless granular materials in chutes and channels. *J. Fluid Mech.* **92**:53-96.

Savage, S.B. (1984). The mechanics of rapid granular flows. *Advances in Applied Mechanics* **24**:289-366.

Savage, S.B., Hutter, K. (1989). The motion of a finite mass of granular material down a rough incline. *J. Fluid Mech.* **199**:177-215.

Savas, Ö. (1985). On flow visualization using reflective flakes. *J. Fluid Mech.* **152**:235-248.

Scarano, F., Riethmuller, M.L. (1999). Iterative multigrid approach in PIV image processing with discrete window offset. *Exp. Fluids* **26**(6):513-523.

Scarano, F., Riethmuller, M.L. (2000). Advances in iterative multigrid PIV image processing. *Exp. Fluids* **29**(7):S51-S60.

Scheidegger, A.E. (1973). On the prediction of the reach and velocity of catastrophic landslides. *Rock Mechanics* **5**(3):231-236.

Schmidt, R.M., Holsapple, K.A. (1980). Theory and experiments on centrifuge cratering. *J. Geophys. Res.* **85**(B1):235-252.

Schmit, C.E., Cartmel, D.B., Eldridge, R.B. (2001). The experimental applications of X-ray tomography to a vapor-liquid contactor. *Chem. Eng. Sci.* **56**:3431-3441.

Schmitt, F., Ruck, B. (1986). Laserlichtschnittverfahren zur qualitativen Strömungsanalyse. *Laser und Optoelektronik* **18**(2):107-131. (in German)

Schuster, R.L., Costa, J.E. (1986). A perspective on landslide dams. Landslide dams: processes, risk and mitigation, Ed. Schuster, R.L. *Geotechnical Special Publication*, ASCE, **3**:1-20.

Schuster, R.L. (1996). The 25 most catastrophic landslides of the 20th century. *Landslides*, Eds. Chacón et al., Balkema, Rotterdam.

Schwartz, L.W. (1974). Computer extension and analytical continuation of Stokes' expansion for gravity waves. *J. Fluid Mech.* **62**:552-578.

Sedov, L.I. (1959). *Similarity and dimensional methods in mechanics*. Academic Press, New York.

Seeger, A., Affeld, K., Goubergrits, L., Kertzscher, U., Wellnhofer, E. (2001). X-ray-based assessment of the three-dimensional velocity of the liquid phase in a bubble column. *Exp. Fluids* **31**(2):193-201.

Self, S., Rampino, M.R. (1981). The eruption of Krakatau. *Nature* **294**:699-704.

Sharpe, C.F.S., 1938. *Landslides and related phenomena*. Columbia Univ. Press, New York.

Shemer, L., Kit, E., Jiao, H.-Y., Eitan, O. (1998). Experiments on nonlinear wave groups in intermediate water depth. *J. Waterway, Port, Coastal, and Ocean Engrg.*, ASCE, **124**(6):320-327.

Shemer, L., Jiao, H.-Y., Kit, E., Agnon, Y. (2001). Evolution of a nonlinear wave field along a tank: experiments and numerical simulations based on the spatial Zakharov equation. *J. Fluid Mech.* **427**:107-129.

Shepard, F. (1967). *Submarine geology*, 2nd ed., Harper, New York.

Shi, A., Teng, M.H., Wu, T.Y. (1998). Propagation of solitary waves through significantly curved shallow water channels. *J. Fluid Mech.* **362**:157-176.

Shi, H.-H., Takami, T. (2001). Some progress in the study of the water entry phenomenon. *Experiments in Fluids* **30**(4):475-477.

Shields, A. (1936). Anwendung der Ähnlichkeits-Mechanik und der Turbulenzforschung auf die Geschiebebewegung. *Mitteilung* 26. Preussische Versuchsanstalt für Wasserbau und Schiffbau, Berlin. (in German)

Shifrin, K.S. (1988). *Physical optics of ocean water*. AIP translation series. American Institute of Physics, New York.

Shreve, R.L. (1966). Sherman landslide, Alaska. *Science* **154**:1639-1643.

Shreve, R.L. (1968). The Blackhawk landslide. *Geological Society of America, Special Paper* **108**.

Shusser, M., Gharib, M. (2000). Energy and velocity of a forming vortex ring. *Physics of Fluids* **12**(3):618-621.

Siebert, L., Glicken, H., Tadahide, U. (1987). Volcanic hazards from Bezymianny- and Bandai-type eruptions, *Bull. Volcanol.* **45**:435-459

Silvester, R. (1974). Coastal engineering, **1**. *Developments in geotechnical engineering* **4A**. Elsevier, Amsterdam.

Simkin, T., Fiske, R.S. (1983). *Krakatau 1883 – the volcanic eruption and its effects*. Smithonian Institution Press, Washington, D.C.

Simpson, J.E. (1997). *Gravity currents in the environment and the laboratory*, 2nd ed., Cambridge University Press.

Simpson, R.L. (1989). Turbulent boundary-layer separation. *Ann. Rev. Fluid Mech.* **21**:205-234.

Skaldnev, M.F., Popov, I.Y. (1969). Studies of wave loads on concrete slope protections of earth dams. *Symposium on Wave Action*, paper 7, Delft, March 24-28.

Skerrett, R.G. (1921). Smashing angry seas with bubbles of compressed air. *Compressed Air Mag.* **26**(1):9921-9927.

Skjelbreia, L., Hendrickson, J.A. (1961). Fifth order gravity wave theory. *Proc. 7th Conf. on Coastal Engineering* **1**:184-196. Engineering Foundation Council on Wave Research. University of California, Berkeley.

Skyner, D. (1996). A comparison of numerical predictions and experimental measurements of the internal kinematics of a deep-water plunging wave. *J. Fluid Mech.* **315**:51-64.

Slingerland, R.L., Voight, B. (1979). Occurrences, properties and predictive models of landslide-generated impulse waves. Rockslides and avalanches **2**:317-397, Ed. Voight, B. *Developments in geotechnical engineering* **14B**. Elsevier, Amsterdam.

Slingerland, R.L., Voight, B. (1982). Evaluating hazard of landslide-induced water waves. *J. Waterw. Port Coastal and Ocean Div.*, ASCE, **108**(WW4):504-512.

Soloff, S.M., Adrian, R.J., Liu, Z.-C. (1997). Distortion compensation for generalized stereoscopic particle image velocimetry. *Meas. Sci. Technol.* **8**(12):1441-1454.

Son, S.Y., Kihm, K.D. (2001). Evaluation of transient turbulent flow fields using digital cinematographic particle image velocimetry. *Exp. Fluids* **30**(5):537-550.

Sorensen, R.M. (1993). *Basic wave mechanics: for coastal and ocean engineers*. John Wiley, New York.

Spurk, J.H. (1992). *Dimensionsanalyse in der Strömungslehre*. Springer, Berlin. (in German)

Stanislas, M., Kompenhans, J., Westerweel, J., eds. (2000). *Particle image velocimetry – progress towards industrial application*. Kluwer Academic Publishers, Dordrecht.

Stive, M.J.F. (1985). A scale comparison of waves breaking on a beach. *Coastal Engineering* **9**:151-158.

Stoker, J.J. (1957). *Water waves*. Interscience, New York.

Stokes, G.G. (1847). On the theory of oscillatory waves. *Trans. Cambridge Philos. Soc.* **8**:441-455.

Storr, G.J., Behina, M. (1999). Experiments with large diameter gravity driven impacting liquid jets. *Experiments in Fluids* **27**(1):60-69.

Strang, G., Nguyen, T. (1997). *Wavelets and filter banks*, revised ed., Wellesley-Cambridge Press, Wellesley, Mass.

Struik, D. J. (1926). Détermination rigoureuse des ondes irrotationelles permanentes dans un canal à profondeur finie. *Math. Ann.* **95**:595-634.

Suzuki, H., Furuya, T. (1999). Hazard mapping at the Unzen volcano and the 1792 Mayuyama landslide. *Landslides of the world*, Ed. Sassa, K., Japan Landslide Society. Kyoto University Press.

Symons, G.L. (1888). The eruption of Krakatau, and subsequent phenomena. *The report of the Krakatoa Committee of the Royal Society*, London.

Synolakis, C.E. (1987). The run-up of solitary waves. *J. Fluid Mech.* **185**:523-545.

Synolakis, C.E. (1991). Generation of long waves in laboratory. *J. Waterway, Port, Coastal, and Ocean Engrg.*, ASCE, **116**(2):252-266.

Takahashi, T. (1991). *Debris flow*. IAHR Monograph Series. Balkema, Rotterdam.

Takehara, K., Adrian, R.J., Etoh, G.T., Christensen, K.T. (2000). A Kalman tracker for super-resolution PIV. *Exp. Fluids* **29**(7):S34-S41.

Talipova, T., Pelinovsky, E., Kit, E. (1995). Wind wave simulation in coastal zone. *Proc. Coast. Dyn.*, ASCE, **95**:105-115.

Tao, B., Katz, J., Meneveau, C. (2000). Geometry and scale relationships in high Reynolds number turbulence determined from three-dimensional holographic velocimetry. *Physics of Fluids* **12**(5):941-944.

Tappin, D.R., Matsumoto, T., Watts, P., Satake, K., McMurty, G.M., Matsuyama, M., Lafoy, Y., Tsuji, Y., Kanamatsu, T., Lus, W., Iwabuchi, Y., Yeh, H., Matsumoto, Y., Nakamura, M., Mahoi, M., Hill, P., Crook, K., Anton, L., Walsh, J.P. (1999). Sediment slump likely caused 1998 Papua New Guinea tsunami. *Trans. Amer. Geophys. Union, EOS* **80**:329-340.

Teng, H.M., Wu, T.Y. (1992). Nonlinear water waves in channels of arbitrary shape. *J. Fluid Mech.* **242**:211-233.

Teng, H.M., Wu, T.Y. (1994). Evolution of long waves in variable channels. *J. Fluid Mech.* **266**:303-317.

Teng, M.H. (1997). Solitary wave solution to Boussinesq equations. *J. Waterway, Port, Coastal, and Ocean Engrg.*, ASCE, **123**(3):138-141.

Thoroddsen, S.T., Bauer, J.M. (1999). Qualitative flow visualization using colored lights and reflective flakes. *Physics of Fluids* **11**(7):1702-1704.

Tinti, S., Bortolucci, E. (2000). Energy of water waves induced by submarine landslides. *Pure Appl. Geophys.* **157**:281-318.

Tocher, D., Miller, D.J. (1959). Field observations on effects of Alaskan earthquake of 10 July, 1958. *Science* **129**:394-395.

Tognacca, C. (1999). Beitrag zur Untersuchung der Entstehungsmechanismen von Murgängen. *VAW-Mitteilung* 164, Ed. Minor, H.-E., Versuchsanstalt für Wasserbau, Hydrologie und Glaziologie, ETH Zürich. (in German)

Townson, J.M., Kaya, Y. (1988). Simulations of the waves in Lake Botnen created by the Rissa landslide. *Proc. Inst. Civ. Eng.* **85**(2):145-160.

Tritton, D.J. (1988). *Physical fluid dynamics*, 2nd ed., Oxford University Press.

Tucker, M.J. (1991). *Waves in ocean engineering – measurement, analysis, interpretation*. Ellis Horwood, New York.

Tulin, M.P., Waseda, T. (1999). Laboratory observations of wave group evolution, including breaking effects. *J. Fluid Mech.* **378**:197-232.

Unoki, S., Nakano, M. (1953). On the Cauchy-Poisson waves caused by the eruption of a submarine volcano. *Oceanogr. Mag.* **4**:199-141.

Urgeles, R., Masson, D.G., Canals, M., Watts, A.B., Le Bas, T. (1999). Recurrent large-scale landsliding on the west flank of La Palma, Canary Islands. *J. Geophys. Res.* **104**(B11):25'331-25'348.

Ursell, F. (1953a). Mass transport in gravity waves. *Proc. Cambridge Phil. Soc.* **49**:145-150.

Ursell, F. (1953b). The long wave paradox in the theory of gravity waves. *Proc. Cambridge Phil. Soc.* **49**:685-694.

Ursell, F., Dean, R.G., Yu, Y.S. (1960). Forced small-amplitude water waves: a comparison of theory and experiment. *J. Fluid Mech.* **7**:3-52.

van de Hulst, H.C. (1957). *Light scattering by small particles*. John Wiley, New York.

Van Dorn, W.G. (1961). Some characteristics of surface waves in the sea produced by nuclear explosions. *J. Geophys. Res.* **66**:3845-3862.

Varnes, D.J. (1958). Landslide types and processes. *Highw. Res. Board Spec. Rep.* **29**. *Natl. Acad. Sci.-Natl. Res. Counc. Publ.* **544**:22-47.

Varnes, D.J. (1978). Slope movements types and processes. Landslides analysis and control, Eds. Shuster, R.L., Krizek, R.J. *Transportation Res. Board Spec. Rep.* **176**:11-33.

Verbeek, R.D.M. (1884). The Krakatau eruption. *Nature* **30**:10-15.

Villeneuve, M., Savage, S.B. (1993). Nonlinear, dispersive, shallow-water waves developed by a moving bed. *J. Hydraulic Res.* **31**(2):249-266.

Vischer, D.L., Hager, W.H. (1998). *Dam hydraulics*. John Wiley, Chichester.

Voight, B. (1981). Time scale for the first movements of the May 18 eruption. The 1980 eruptions of Mount St. Helens, Washington, Eds. Lipman, P.W., Mullineaux, D.R. *U.S. Geological Survey Professional Paper* **1250**:69-86.

Voight, B., Glicken, H., Janda, R.J., Douglass, P.M. (1981). Catastrophic rockslide-avalanche of May 18. The 1980 eruptions of Mount St. Helens, Washington, Eds. Lipman, P.W., Mullineaux, D.R. *U.S. Geological Survey Professional Paper* **1250**:347-377.

Voight, B., Faust, C. (1982). Frictional heat and strength loss in some rapid landslides. *Géotechnique* **32**:43-54.

Voight, B., Janda, R.J., Glicken, H., Douglass, P.M. (1983). Nature and mechanics of the Mount St. Helens rockslide-avalanche of 18 May 1980. *Géotechnique* **33**:243-273.

von Huerte, R., Bourgois, J., Miller, J., Pautot, G. (1989). A large tsunamogenic landslide and debris flow along the Peru Trench. *J. Geophys. Res.* **94**:1703-1714.

Wagner, W., Kruse, A. (1998). Properties of water and steam. *Industrial Standard IAPWS-IF97*. Springer, Berlin.

Walder, J.S., Sorensen, O.E., Watts, P. (2002). Water waves generated by subaerial mass flows. *J. Geophys. Res.* **107**(B...):..... (accepted).

Walkden, M., Muller, G., Bruce, T. (1998). Low-cost particle image velocimetry: system and application. *Proc. 8th Int. Offshore and Polar Engrg. Conf.*, Montréal, Canada. ISOPE, **8**(3):679-685.

Ward, S.N. (2001). Landslide tsunami. *J. Geophys. Res.* **106**(B6):11'201-11'215.

Ward, S.N., Day, S.J. (2001). Cumbre Vieja volcano - potential collapse and tsunami at LaPalma, Canary Islands. *Geophys. Res. Lett.* **28**(17):3397-3401.

Watts, P. (1997). Water waves generated by underwater landslides. *Ph.D.-Thesis*, California Inst. of Technol., Pasadena.

Watts, P. (1998). Wavemaker curves for tsunamis generated by underwater landslides. *J. Waterway, Port, Coastal, and Ocean Engrg.*, ASCE, **124**(3):127-137.

Watts, P. (2000). Tsunami features of solid block underwater landslides. *J. Waterway, Port, Coastal, and Ocean Engrg.*, ASCE, **126**(3):144-152.

Watts, P., Imamura, F., Grilli, S. (2000). Comparing model simulations of three benchmark tsunami generation cases. *Science of Tsunami Hazards* **18**(2):107-123.

Weggel, J.R. (1972). Maximum breaker height. *J. Waterw. Harbors Coastal Engrg. Div.*, ASCE, **98**(WW4):529-548.

Wehausen, J.V., Laitone, E.V. (1960). *Surface waves*. Handbuch der Physik, Ed. Flügge, S., vol. 9, Strömungsmechanik III. Springer, Berlin.

Wernet, M., Pline, A. (1993). Particle displacement tracking technique and Cramer-Rao lower bound error in centroid estimates from CCD imagery. *Exp. Fluids* **15**:295-307.

Westerweel, J. (1993). *Digital particle image velocimetry: theory and application*. Delft University Press.

Westerweel, J. (1994). Efficient detection of spurious vectors in particle image velocimetry data. *Exp. Fluids* **16**(3):236-247.

Westerweel, J. (1997). Fundamentals of digital particle image velocimetry. *Meas. Sci. Technol.* **8**(12):1379-1392.

Westerweel, J., Dabiri, D., Gharib, M. (1997). The effect of a discrete window offset on the accuracy of cross-correlation analysis of digital PIV recordings. *Exp. Fluids* **23**(1):20-28.

Westerweel, J. (2000). Theoretical analysis of the measurement precision in particle image velocimetry. *Exp. Fluids* **29**(7):S3-S12.

Westerweel, J., Van Oord, J. (2000). Stereoscopic PIV measurements in a turbulent boundary layer. *Particle image velocimetry – progress towards industrial application*, eds. Stanislas, M. et al., Springer, New York.

Wharton, W.J.L. (1888). On the seismic sea waves caused by the eruption of Krakatau August 26th and 27th, 1883. The eruption of Krakatau, and subsequent phenomena, Ed. Symons, G.L. *The report of the Krakatoa Committee of the Royal Society*, 89-151, London.

Whitham, G.B. (1974). *Linear and nonlinear waves*. John Wiley, New York.

Wiegel, R.L. (1955). Laboratory studies of gravity waves generated by the movement of a submerged body. *Trans. Am. Geophys. Union* **36**(5):759-774.

Wiegel, R.L. (1960). A presentation of cnoidal wave theory for practical application. *J. Fluid Mech.* **7**:273-286.

Wiegel, R.L. (1964). *Oceanographical engineering*. Prentice-Hall, Englewood Cliffs, N.J.

Wiegel, R.L., Noda, E.K., Kuba, E.M., Gee, D.M., Tornberg, G.F. (1970). Water waves generated by landslide in reservoirs. *J. Waterw. Harbors Coastal Engrg. Div.*, ASCE, **96**(WW2):307-333.

Wieland, M., Gray, J.M.N.T., Hutter, K. (1999). Channelized free-surface flow of cohesionless granular avalanches in a chute with shallow lateral curvature. *J. Fluid Mech.* **392**:73-100.

Willert, C.E., Gharib, M. (1991). Digital particle image velocimetry. *Exp. Fluids* **10**:181-193.

Willert, C.E. (1997). Stereoscopic digital particle image velocimetry for application in wind tunnel flows. *Meas. Sci. Technol.* **8**(12):1465-1479.

Williams, J.M. (1985). *Tables of progressive gravity waves*. Pitman, Boston.

Wu, T.Y. (1981). Long waves in ocean and coastal waters. *J. Engrg. Mech. Div.* ASCE **107**:401-522.

Yalin, M.S. (1971). *Theory of hydraulic models*. MacMillan, London.

Yih, C.-S. (1985). New derivations of Darwin's Theorem. *J. Fluid Mech.* **152**:163-172.

Yih, C.-S. (1995). Kinetic-energy mass, momentum mass, and drift mass in steady irrotational subsonic flows. *J. Fluid Mech.* **297**:29-36.

Yih, C.-S. (1997). The roll of drift mass in the kinetic energy and momentum of periodic water waves and sound waves. *J. Fluid Mech.* **331**:429-438.

Yokoyama, I. (1981). A geophysical interpretation of the 1883 Krakatau eruption. *J. Volcanol. and Geotherm. Res.* **9**:359-378.

Zakharov, V.E. (1968). Stability of periodic waves of finite amplitude on the surface of a deep fluid. *J. Appl. Mech. Tech. Phys.* **9**:190-194.

Zakharov, V.E., Kuznetsov, E.A. (1997). Hamiltonian formalism for nonlinear waves. *Physics – Uspekhi*, Russian Academy of Sciences, **40**(11):1087-1116.

Zhang, J., Tao, B., Katz, J. (1997). Turbulent flow measurement in a square duct with hybrid holographic PIV. *Exp. Fluids* **23**(5):373-381.

Zierep, J. (1991). *Ähnlichkeitsgesetze und Modellregeln der Strömungslehre*, 3rd ed. Braun, Karlsruhe. (in German)

Appendix A: Landslides

A.1 Landslide classification

The term landslide is widely used as an all inclusive term for almost all varieties of slope movements, including some that involve little or no true sliding. Slope movements have been classified in many ways. In the English literature the classification by Varnes (1978) shown in its abbreviated form in Table A.1 is probably the most widely used. The first level criteria used in this classification are the type of movement primarily and the type of material secondarily. The types of movement are divided into five main groups: falls, topples, slides, spreads, and flows. The materials are divided into two classes: rock and engineering soils; soils are further divided into debris and earth. For graphic illustrations and examples of the various combinations of movements and materials refer to Varnes (1978).

Table A.1   **Classification of slope movements** after Varnes (1978).

TYPE OF MOVEMENT		TYPE OF MATERIAL		
		Bedrock	Engineering soils	
			coarse	fine
Falls		Rock fall	Debris fall	Earth fall
Topples		Rock topple	Debris topple	Earth topple
Slides	rotational	Rock slump	Debris slump	Earth slump
	translational	Rock block slide	Debris block slide	Earth block slide
		Rock slide	Debris slide	Earth slide
Lateral spreads		Rock spread	Debris spread	Earth spread
Flows		Rock flow	Debris flow	Earth flow
Complex		Combination of two or more types of movement		

There is a complete gradation from debris slides to debris flows, depending on water content, mobility, and character of the movement. Important regarding impulse waves is the transition from debris slide to debris avalanche as the movement becomes much more rapid. The term debris avalanche is included in the more general term debris flow. The term debris avalanche is commonly used for very rapid to extremely rapid debris flows of dry or largely unsaturated granulates.

A.2 Landslide dynamics

Heim (1932) found that the slope of the energy line for smaller landslides is about the same as the coefficient of friction of sliding blocks and referred to this slope as the equivalent coefficient of friction. The equivalent coefficient of friction was defined as the maximum drop height divided by the maximum run-out length. Unlike the coefficient of friction, which is a material constant and whose value is independent of the size of a sliding block, the value of the equivalent coefficient of friction is a function of the total landslide volume. Most natural rock types have coefficients of friction of 0.6 or higher (Jaeger and Cook, 1979), so movement is expected only over terrain with an average slope of at least 30°. This expectation is confirmed for relatively small volume landslides and flows of dry granular materials in the laboratory (Savage, 1984). However, as the volume increases beyond 100'000 m^3 in subaerial mass movements, the equivalent coefficient of friction decreases to values as low as 0.1 or less. All cases with relevant impulse waves reviewed in Appendix B were caused by landslide impacts with volumes V_s of at least 100'000 m^3. Therefore friction reduction for large landslides needs to be considered. A double logarithmic plot of the equivalent coefficient of friction in function of landslide volume is shown in Fig. A.1 for subaerial dry-rock avalanches of non-volcanic origin (Scheidegger, 1973), submarine landslides (Hampton, et al., 1996) and Martian landslides (McEwen, 1989). All three data sets indicate a massive decay of the equivalent coefficient of friction with increasing volume. In particular the subaerial and Martian data sets show a strong linear correlation.
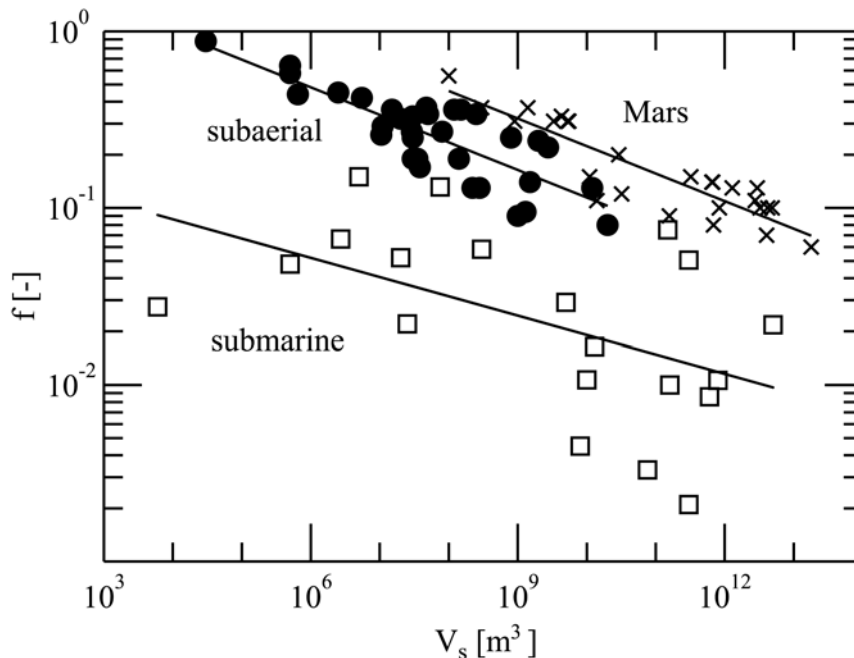
Figure A.1 **Equivalent coefficient of friction *f*** vs. landslide volume V_s for (●) subaerial landslides (Scheidegger, 1973), (□) submarine landslides (Hampton et al., 1996), (✕) Martian landslides (McEwen, 1989), (—) corresponding linear least-squares correlations.

The equivalent coefficient of friction f was defined as the maximum drop height divided by the maximum run-out length (Heim, 1932 and Hsü, 1975). The correlation for subaerial landslides between the landslide volume V_s in m³ and the equivalent coefficient of friction f is

$$\log f = -0.15666 \log V_s + 0.62419 \qquad \textbf{(A.1)}$$

with a correlation coefficient of 0.82. The observed equivalent coefficients of friction for large landslides are much smaller than explainable by either sliding or dispersive grain-flow mechanisms. Various models have been proposed to explain the mobility of large landslides, including fluidization by air (Kent, 1966); frictionless support on a layer of trapped and compressed air (Shreve, 1966, 1968); movement over a molten basal layer, melted by friction and high pressure (Erismann, 1979); grain flow with friction reduced by the presence of dust (Hsü, 1975); inertial grain flow or mechanical fluidization (Davis, 1982); grain separation by acoustic energy (Melosh, 1979, 1987); vaporization of few percent of water in largely unsaturated materials (Habib, 1975; Goguel, 1978); and segregation of the water into a saturated basal layer (Johnson, 1978). These models have various strengths and weaknesses, but no consensus has yet been reached. The data compiled by Scheidegger (1973) consist mostly of Alpine landslides. The relationship also depends on the type of material involved in the mass movement. Quick clays for example have friction coefficients at the lower end of friction coefficients observed for submarine landslides (Edgers and Karlsrud, 1982). The presented relationship may therefore not be applied to some slide materials and quick clays in particular.

The impact velocity of an imminent landslide may be predicted using the friction coefficient computed with Eq. A.1 if the landslide volume can be estimated beforehand. The slide impact velocity v_s according to the Newtonian laws of motion is

$$v_s = \sqrt{2g\Delta z(1 - f \cot \alpha)} \qquad \textbf{(A.2)}$$

with the gravity g, the hill slope angle α and the drop height Δz. For engineering purposes it is recommended to compare the slide velocity estimate given by Eq. A.1 with an upper limit calculation neglecting frictional losses. Landslide velocities up to 150 m/s have been observed in recorded history (Körner, 1976).

Submarine landslides reached volumes more than two orders of magnitude larger than the largest known subaerial landslide. The equivalent coefficient of friction can be orders of magnitude smaller for submarine landslides. Therefore submarine landslides can originate on nearly flat surfaces. The submarine data in Fig. A.1 show considerable scatter which indicates the limitations of a simple slide dynamic model. Subaqueous landslides are not only affected by friction and gravity, but also drag forces exerted by the surrounding seawater, both at the front and on top of the moving mass being an important feature.

Mars may be the only planetary body other than Earth known unequivocally to have long run-out lengths for dry landslides (Lucchitta, 1979). The least-squares fit to the landslide data from Valles Marineris shown in Fig. A.1 has a correlation coefficient of 0.90. Although the slopes of the terrestrial and Valles Marineris trends in Fig. A.1 are nearly

identical, there is an offset between the trend lines. At a given equivalent friction coefficient, the Martian landslides are typically about 50 to 100 times more voluminous than the terrestrial counterparts, or at a given volume, the friction coefficient is about two times larger on Mars. Gravity on Mars is 2.6 times smaller than on Earth with $g = 3.72$ m/s^2 and $g = 9.81$ m/s^2, respectively. Frictional models do not predict any effect from reducing g, because both the driving and resistance forces are reduced proportionally. The offset might be explained by the effect of a lower g on flows with high yield strengths (McEven, 1989). For example a Bingham material would have a thicker flow deposit on a planet with reduced g.

Appendix B: Observed cases

B.1 Subaerial landslide impact generated waves

B.1.1 Lituya Bay, Alaska

Lituya Bay is a T-shaped tidal inlet that cuts through the coastal lowlands and the foothills flanking the Fairweather Range of the St. Elias Mountains on the south coast of Alaska, Figs. B.1 and B.2. The stem corresponding to the main part of the T-shaped bay is 12 km long and extends northeastward from the bay entrance. The width of the stem ranges from 1.2 to 3.3 km except at the entrance, which is only 300 m wide. The bay fills and slightly overflows a depression carved by a valley glacier of which Lituya, North Crillon and Cascade glaciers are remnants. Submarine contours show a pronounced U-shaped trench with steep walls and a broad flat floor sloping gently downward from the head of the bay to a maximum depth of 220 m. Minimum depth at the entrance of the bay is 10 m.
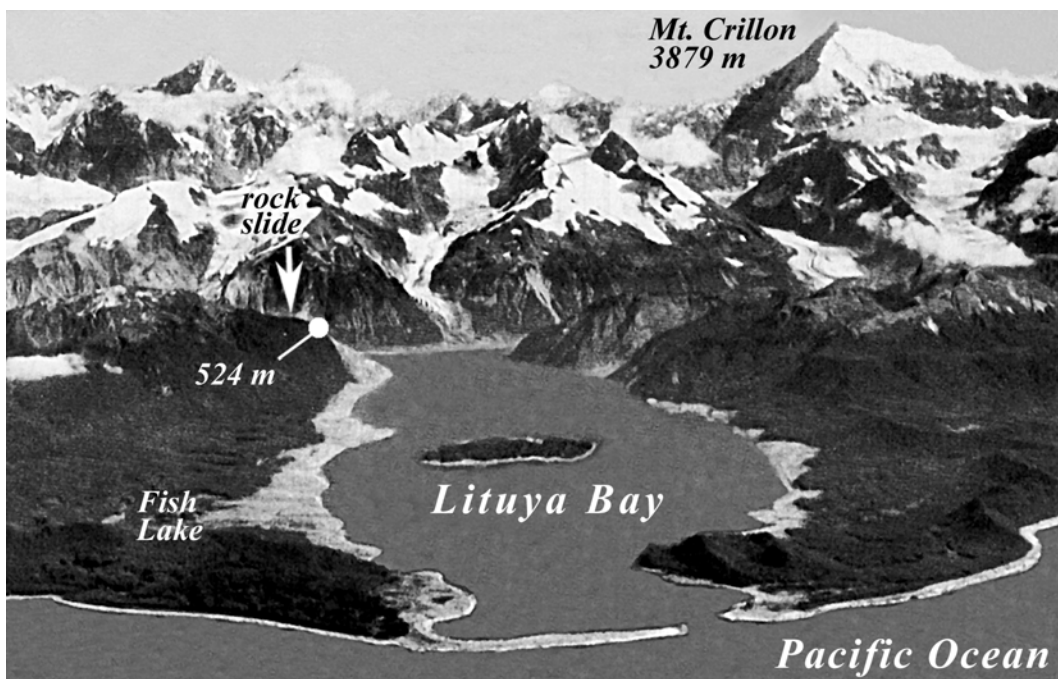

Figure B.1 **Lituya Bay** overview in August 1958 (Miller, 1960). Forest destroyed to a maximum elevation of 524 m and a maximum distance of 1100 m from high-tide shoreline at Fish Lake due to a giant wave generated on July 9, 1958 by a rockslide at the head of the bay.

At the head of the bay the walls are fjord-like glacially over-steeped. The walls have been buttressed by glaciers until recently. Radiocarbon dates on high moraines suggest retreat of glaciers only in the last millennium (Slingerland and Voight, 1979). The two arms at the head of the bay are part of a great trench that extends tens of kilometers to the

northwest and southeast as a topographic expression of a major transform fault, named Fairweather fault, as shown in Fig. B.2.

Giant waves have occurred in Lituya Bay at least four and probably five times during the last two centuries emphasizing the unique geologic and tectonic setting of the bay. Frequent occurrence of giant waves in Lituya Bay, as compared to other similar bays, is attributed to the combined effect of recently glaciated steep slopes, highly fractured rocks and deep water in an active fault zone, heavy rainfall, frequent freezing and thawing (Miller, 1960). Three extreme wave run-ups in 1853 or 1854, 1936 and 1958 carved sharp trimlines of chopped trees to elevations beyond 100m on to the slopes of Lituya Bay (Miller, 1960; Fritz et al., 2001). In 1958 the largest wave run-up of 524m in recorded history was observed on a spur ridge on the southwest wall of Gilbert Inlet. Only the 1958 event is further considered here since the causes of the earlier events remain unconfirmed.
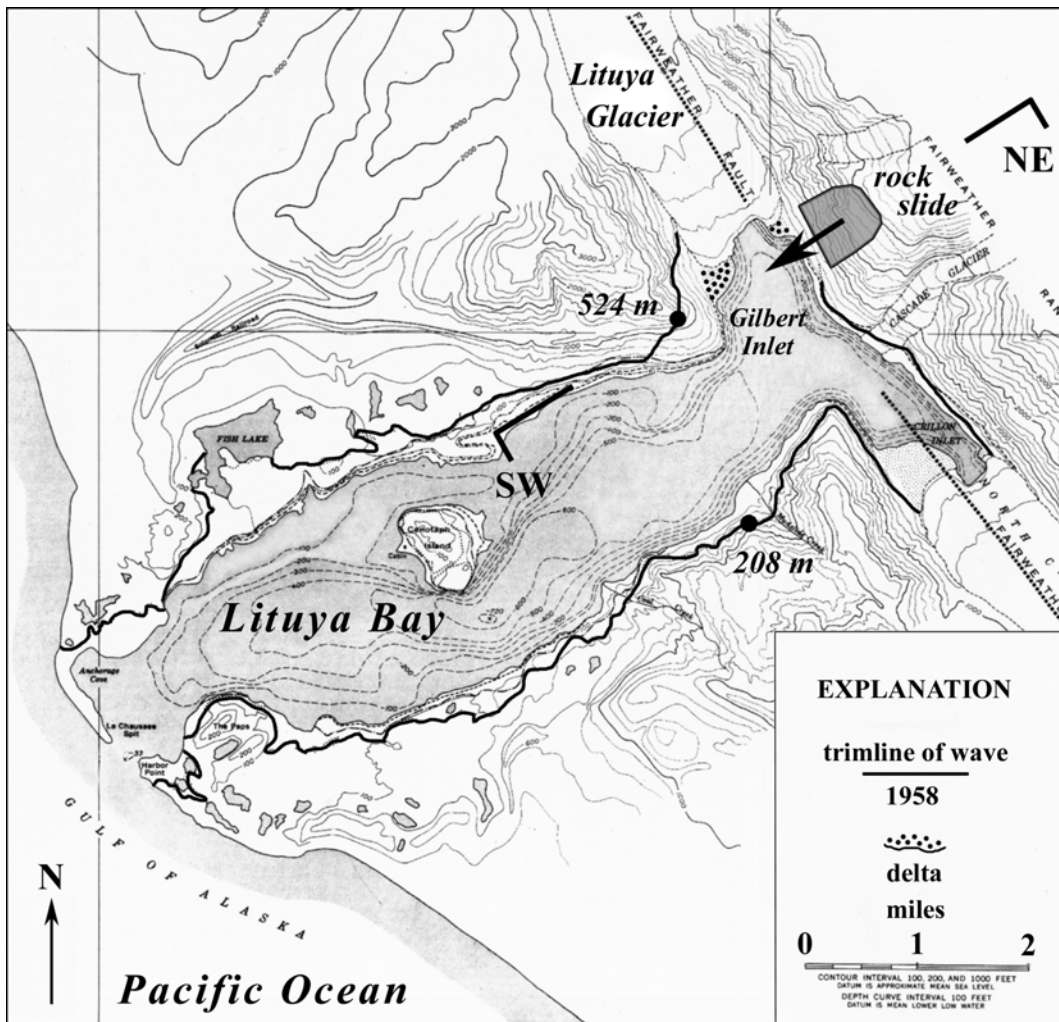
Figure B.2 **Lituya Bay map** showing topographic and bathymetric contours, trace of Fairweather fault, 1958 rockslide and trimline of giant wave run-up (Miller, 1960). Forests destroyed to maximum elevations of 524m and 208m on north and south shores, respectively.

Beginning 10:16 p.m. local time, July 9, 1958, the southwest sides and bottoms of Gilbert and Crillon Inlets moved northwestward and up relative to the northeast shore at the head of the bay, on the opposite side of the Fairweather fault. Total movement as much as 6.4 m horizontally and 1 m vertically was noted (Tocher and Miller, 1959). Intense shaking in Lituya Bay continued for 1 to 4 minutes, the range of estimates of two eyewitnesses that anchored in the bay. The earthquake had a magnitude of 8.3 on Richter scale. No less than 1 minute and no more than 2½ minutes after the earthquake was first felt a large mass of rock slid from the northeast wall of Gilbert Inlet (Figs. B.2 and B.3).
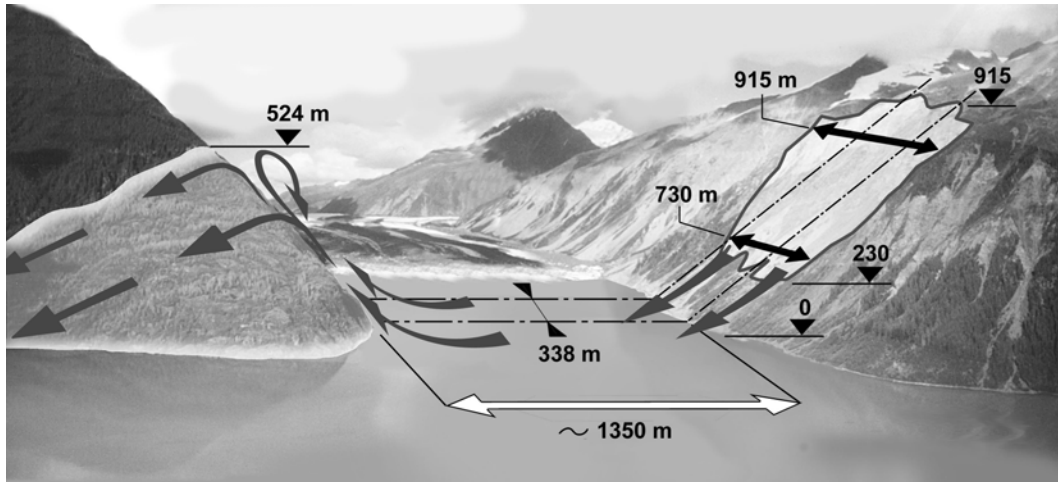
Figure B.3   **Gilbert Inlet illustration** showing rockslide dimensions, impact site and wave run-up to 524 m on spur ridge directly opposite to rockslide impact. Direction of view is North and the front of Lituya Glacier is set to 1958 post slide position. Illustration background is synthesized from two oblique images taken in 1997 (Photos: courtesy of Charles L. Mader).

The rockslide was triggered impulsively by fault movement and intense earthquake vibrations giving a sharp localization on time axis. It is highly probable that the entire mass plunged into Gilbert Inlet as a unit at the time of the earthquake. Pararas-Carayannis (1999) classified the mass movement as subaerial rockfall to distinguish from gradual processes of ordinary landslides whereas Miller (1960) judged it to be near the borderline between rockslide and rockfall as defined by Sharpe (1938) and Varnes (1958). The rockslide occurred in an area of previously active sliding to an altitude of 915 m on a slope averaging 40°. The rocks are mainly amphibole and biotite schists with an assumed density of 2.7 t/m^3. The dimensions of the slide on the slope as mapped by Miller (1960) are accurate, but the thickness of slide mass normal to the slope could be estimated only roughly (Miller, 1960). The main mass of the slide presumably involved a prism of rock roughly triangular in cross-section, with width dimensions from 732 m to 915 m (Miller, 1960 and Slingerland and Voight, 1979), length measured down the slope of 970 m (Slingerland and Voight, 1979), maximum thickness of about 92 m normal to the slope, and a center of gravity at about 610 m altitude (Miller, 1960). Dimensions are illustrated in Fig. B.3. Miller estimated the volume from these as 30.6×10^6 m^3.

Prior to the rockslide low deltas of gravel had built out into Gilbert Inlet at the south-east and northwest margins of the Lituya Glacier front. Part of the slide must have hit the Lituya Glacier and glacial gravel deltas due to the pre-slide situation of slide mass, deltas and glacier front as illustrated in Fig. B.2. A detailed pre and post slide situation of Gilbert Inlet was indicated in Miller (1960). The Lituya Glacier front was a nearly straight vertical wall almost normal to the axis of Gilbert Inlet after the rockslide, shown in Fig. B.4. During the event as much as 400 m of ice had been sheared off on parts of the glacier front and the gravel deltas were pushed or washed away. The rockslide impact created a giant gravity wave similar to a solitary wave with a maximum wave run-up of 524 m in straight prolongation of the slide axis on a spur ridge on the southwest shore of Gilbert Inlet (Figs. B.4 to B.5a). The run-up of 524 m is seven times higher than the highest wave run-up observed 1936 in Loen Lake [para B.1.4] and roughly doubles wave run-ups in Vajont reservoir [para B.2.1] and Spirit Lake [para B.1.7].
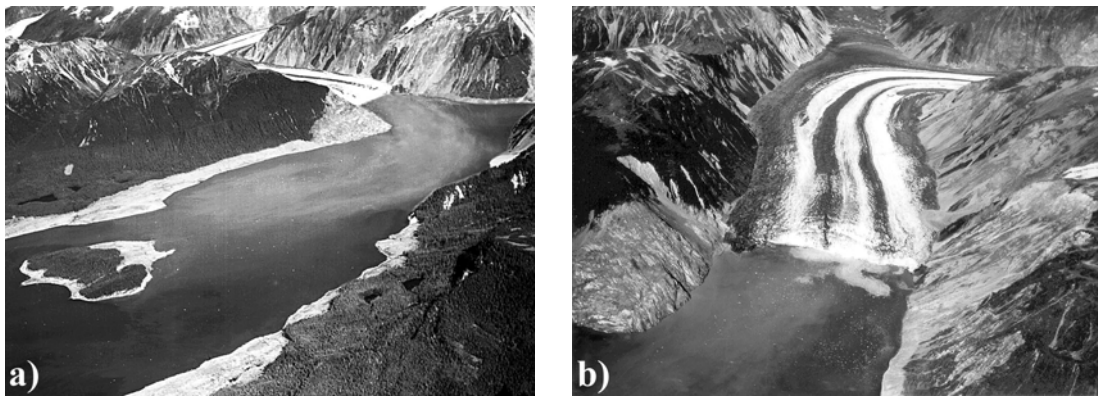
Figure B.4   **Trimlines** carved by giant wave in 1958: **a) NE-view of Lituya Bay** from Cenotaph Island to Gilbert Inlet with rockslide scar at the head of the bay, trimlines of destructed forest with spur ridge where the wave ran up 524 m and partially overtopped; **b) NW-view of Gilbert Inlet** with landslide scar, new front of Lituya Glacier and effect of wave run-up to 524 m on the spur ridge wiping out all trees and eroding the soil down to the bedrock (Photo: courtesy of USGS).

A simplified 3D physical model of Lituya Bay at a 1:1'000 scale was constructed at the University of California, Berkeley (R.L. Wiegel in Miller, 1960). Wiegel concluded from physical model observations, that a sheet of water washed up the slope opposite to the landslide to an elevation of at least three times the water depth for a slide impacting Gilbert Inlet as a unit and very rapidly. At the same time a large wave, several hundred feet high, moved in the southerly direction, causing a peak rise to occur in the vicinity of Mudslide Creek. The highest mark of chopped trees at an altitude of 208 m on the south shore trimline is shown in Fig. B.5b). Wiegel (1964) estimated the hydrodynamic forces exerted on the trees by the wave as roughly ten times greater than the force necessary to snap or uproot trees. The wave then swung around into the main portion of Lituya Bay, due to refraction and diffraction. The movements of the main wave and the tail were complicated within the bay by reflections and bathymetric effects, but scale modeling apparently pro-

duced a good approximation to the Lituya Bay event. Unfortunately no measured data are available from these 3D experiments. Fritz et al. (2001) accurately reproduced the 524m run-up in a 2D physical model of the rockslide impact into Gilbert Inlet including the run-up on the headland spur ridge.
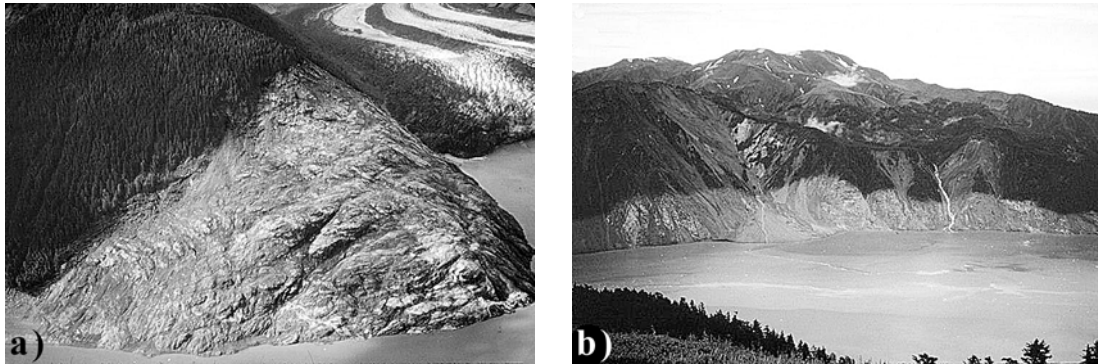
Figure B.5 **Highest marks** on trimlines carved by giant wave in 1958: a) N-view of spur ridge cleared from trees and soil down to bare rock up to a maximum altitude of 524m; b) S-view of trimline in the Mudslide Creek area on the south shore of Lituya Bay with wiped out trees to an altitude of 208m. (Photos: courtesy of USGS).

B.1.2 Yanahuin Lake, Peru

Yanahuin Lake is a small glacial lake at about 4400m altitude near the International Divide in the Province of Pasco, Peru. Yanahuin Lake is in the headwaters of the Rio Chancay which flows roughly 120km southwest-ward through a precipitous valley to the Pacific Ocean. Yanahuin Lake occupies a glacier-scoured rock basin in an area of typical alpine glacial topography which is characterized by broad, U-shaped valleys separated by steep ridges. The lake is about 870m long and 360m wide, covers a surface area of roughly 100'000 m^2 and has a volume of about 3.8×10^6 m^3. A camp and a mine of the Chungar Mining Company (Cia. Minería Chungar, S.A.) were constructed on the north shore of Yanahuin Lake in an area of moderate but irregular slope. Most of the camp was situated on a narrow, glaciated rock bench up to 35m above the lake level. The south side of the lake is characterized by a steep slope which extends from the lake up to a ridge crest at an altitude of about 4900m. An aerial photo of Yanahuin Lake is shown in Fig. B.6.
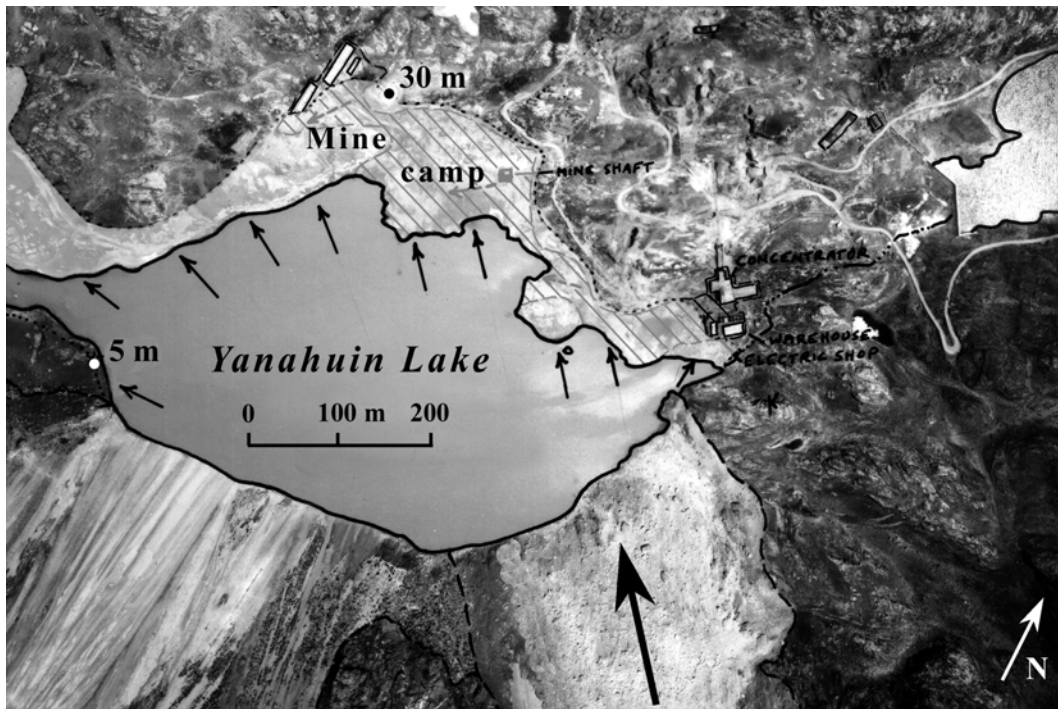
Figure B.6   **Yanahuin Lake** vertical aerial photo with rock slide, direction of wave movement, destroyed mine camp and maximum wave run-up heights (Photo: courtesy of Servicio Aero-Fotográfico Nacional, Lima, Peru).

On March 18, 1971 a rock avalanche fell from an outcrop of closely jointed limestone located approximately 400 m above the southeastern shore of Yanahuin Lake. The exact location of the released rock mass, with an estimated volume of 100'000 m^3, is shown in Fig. B.7a). The density of the limestone was assumed to 2.6 t/m^3. The debris avalanche roared down a talus slope averaging 45° before it splashed into the head of the lake, which it partially filled. The avalanche debris consisted mainly of boulders and blocks of lime-stone, some of which measured up to 4 m in diameter. The water displaced by the debris avalanche formed an impulse wave that ran up the opposite shore to a maximum elevation of 30 m above lake level, devastating virtually all of the mining camp. The location of the maximum wave run-up and the two remaining houses of the mining camp are shown in Fig. B.7b). A bizarre aspect of the Yanahuin Lake event was that water from the wave run-up flowed into a mine shaft killing several miners in the underground workings. The death toll in the mining camp and the mine itself summed up to 600 casualties.

Figure B.7   **Yanahuin Lake: a) SW-view** from the north shore across the lake to the rock avalanche source and the talus debris; **b) E-view** of the wave run-up area with the maximum run-up height, the destroyed mining camp and the two remaining houses in the background (Photos: courtesy of George Plafker, USGS).

The glacially oversteeped ridge on the south shore of Yanahuin Lake showed signs of instability prior to the catastrophic event on March 18, 1971. A small rockfall occurred in February 1970 from the lower part of the 1971 avalanche source. This rockfall generated an impulse wave about 1.5 m high that washed inland to a distance of 25 m along the opposite shore. Although the wave did not cause any damage, residents were sufficiently alarmed to request an investigation. After the investigation the camp was moved to higher grounds, but only a year later it was tragically confirmed that the camp was not dislocated high enough.

B.1.3 Tafjord, Norway

Tafjord forms the innermost branch of Norddalsfjord which is an arm of the Storfjord in west Norway. Tafjord is about 9 km long and 1 to 1.5 km wide as shown in Fig. B.8. Tafjord is flat bottomed with depth variation between 200 and 220 m. The surrounding mountains reach up to heights of 1700 m. On April 7, 1934 a large portion of rock named Langflåhammaren fell off the northeast flank of Tafjord on Sunnmøre. The rockslide with a volume of 1.5×10^6 m^3 was released from a maximum altitude of 730 m (Bjerrum and Jørstad, 1968). The rockslide was 230 m wide and consisted of hard gneiss with an assumed density of 2.7 t/m^3 (Slingerland and Voight, 1979). The fault plane in the rip-off area had a slope angle of 65° whereas the impact angle by the fjord was estimated to 45° (Harbitz et al., 1992). A scree deposit called Heggura situated below Langflåhammaren

was activated by the slide. The released scree deposit had a volume of at least 1.5×10^6 m^3 (Harbitz et al., 1992).
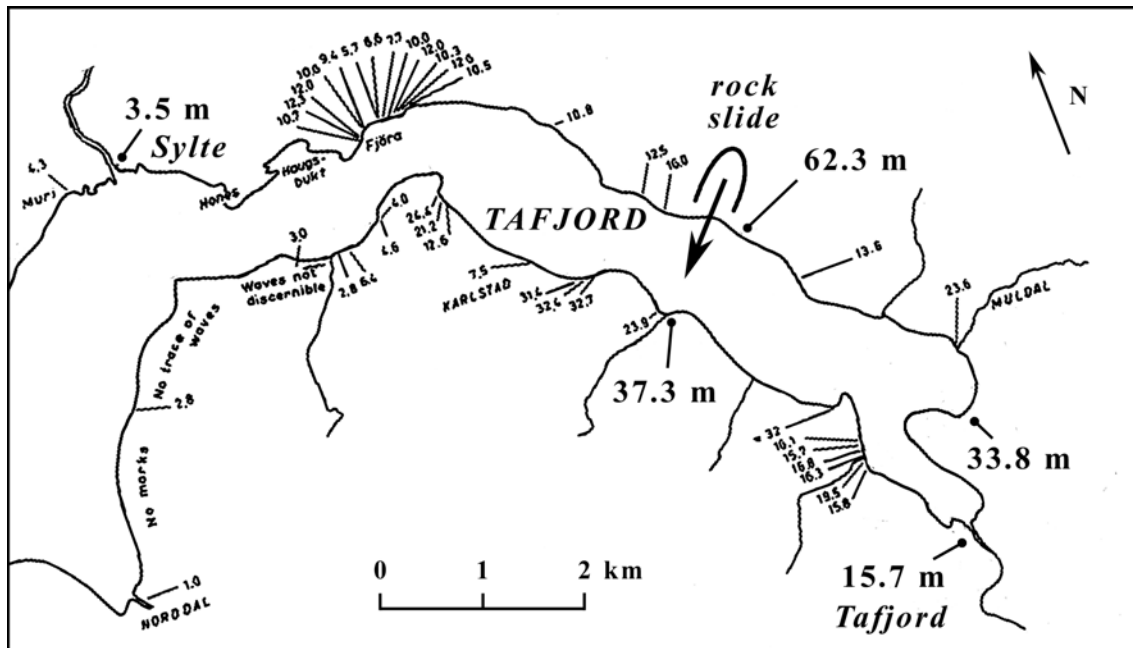
Figure B.8 **Tafjord map** with the location of the 1934 rockslide at Langflåhammaren and wave run-up heights observed along the shore in meters (after Jørstad, 1968).

The impact of possibly 3×10^6 m^3 of rock into Tafjord generated large waves. The waves spread in both directions and caused great destruction, 41 persons perished and a large number of buildings, quays and boats were swept away. The altitude of the trimline caused by the wave run-up was measured at several locations. The wave run-up heights varied considerably within short distances along the shoreline. The maximum wave run-up height of 62.3 m was found 200 m to the south-east of the slide impact site but on the same shore as the slide. The second highest wave run-up of 37.3 m was measured across the fjord in direct prolongation of the slide axis at a distance of 1 km from the impact site. At Sødalsvik, about 3 km from the impact site, a wave run-up of 33.8 m was observed. The increase in wave run-up heights towards the head of the fjord was due to the decrease in water depth. At Tafjord, about 4 km from the slide, the wave reached 300 m inland and ran up to a height of 15.7 m. According to eye witnesses from Tafjord the village was hit by 3 different huge waves, at 3 to 5 minute intervals. The last wave was attributed the largest (Jørstad, 1968). The sea remained extremely rough for more than half an hour, and did not calm down before 8 hours after slide occurrence. The view from the boat houses of Tafjord village towards the slide scar is shown in Fig. B.9a). Tafjord partially hides behind a fjord bend.

Figure B.9 **Tafjord: a) Slide scar** from the 1934 Langflåhammaren rockslide viewed from the boat houses of Tafjord village (Photo: courtesy of Carl B. Harbitz, NGI). **b) Fjord bend** from Sylte in a SE-view into Tafjord with the slide scar from the 1934 Langflåhammaren rockslide in the background and the port of Sylte in the foreground (Photo: courtesy of Normans Kunsforlag A-S Oslo, Norway).

The view from Sylte, about 6 km from the slide, towards the rockslide scar is shown in Fig. B.9b). Direct wave propagation from the impact site is inhibited by a S-shaped double bend in the fjord topography. Harbitz (1992) demonstrated with numerical simulations that most of the energy transferred to water waves is on cross fjord propagating components and found that the energy leakage for these wave components through the S-shaped double bend into the outer part of the fjord was small. Nevertheless the wave reached 100 m inland and ran up to 3.5 m in Sylte. A telephone call from Tafjord warned the population living along Storfjord. More than an hour later waves were observed in towns at distances between 50 and 90 km from the impact site (Jørstad, 1968).

Harbitz (1992) simulated the Tafjord event with a numerical model based on the hydrodynamic shallow water equations. Harbitz admits that shallow water wave equation assumptions such as hydrostatic pressure distribution, small variation in velocity with depth and small wave amplitudes relative to water depth are violated in the nearfield of the rockslide impact during a short period of time and in run-up areas with gentle slopes. For the given Tafjord topography and bathymetry the numerical simulations by Harbitz (1992) show the dependency of the generated wave heights on slide impact velocity and shape. Between 7 and 13 % of the mechanical energy content in the slide, at the instant of penetration into the water body, was converted to wave energy. Predicted run-up heights were in good agreement with measured run-up heights on steep slopes for the following parameters: slide impact velocity = 50 m/s, slide length = 400 m, slide width = 260 m and maximum slide thickness = 75 m. Post-event estimation of slide impact velocity and shape is extremely difficult. The rockslide probably broke up into a debris slide as the rock mass hit and moved a large volume of scree and glacial deposits before actually impacting into Tafjord (Slingerland and Voight, 1979). In areas with gentle beach slopes the numerical model undershot observed wave heights severely. The primary wave had reached the opposite side of the fjord 30 s after slide impact as shown in Fig. B.10a). Once the leading

wave was reflected from the shore Harbitz (1992) computed complex wave patterns 2 minutes after slide impact as shown in Fig. B.10b).
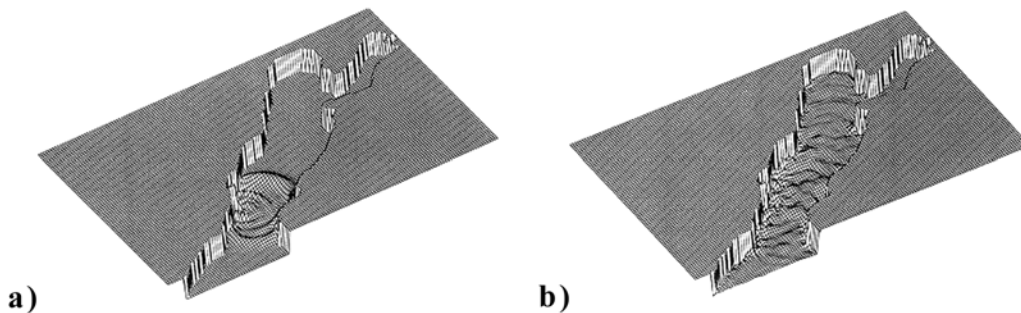

Figure B.10 **Wave patterns** of the 1934 Tafjord event in a perspective view towards the fjord head computed by Harbitz (1992) at **a)** t = 30 s and **b)** t = 120 s after rockslide impact.

These numerical simulations highlight interfering crosswise and lengthwise oscillations due to multiple reflections along the shore and reflections from the fjord bends. Harbitz (1992) further demonstrated that the three waves observed by eyewitnesses in Tafjord were not caused by the slide characteristics but due to multiple wave reflections and interference. This is consistent with the long time intervals of several minutes observed by the eyewitnesses.

B.1.4 Loen Lake, Norway

Loen Lake is situated in the inner part of Nordfjord in west Norway just south of the 62° northern lattitude. Loen Lake lies 48 m above mean sea level, is 11 km long and 1.5 km wide. The maximum depth is 132 m and the water volume 0.69 km^3. At the south-western part of the lake Ravnefjell rears steeply up 2000 m above Loen Lake. From the same location shown in Fig. B.11 at Ravnefjell seven major rockslides occurred during the period 1905 to 1950, two of which generated huge waves causing 134 fatalities – roughly half the population living along the lake shore at the time. In total about 3×10^6 m^3 of rock mass were released. The rock was a hard gneiss with an assumed density of 2.7 t/m^3 (Grimstad and Nesdal, 1991).
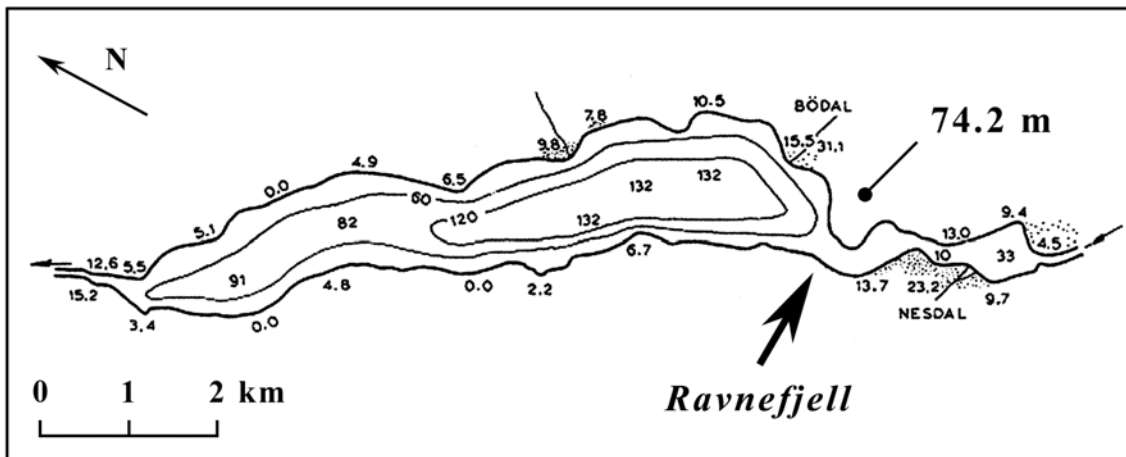
Figure B.11 **Loen Lake map** showing bathymetric contours, location of the 1936 Ravnefjell rockslide and maximum wave run-up height of 74.2m in direct prolongation of slide axis (after Bjerrum and Jørstad, 1968).

On January 15, 1905 a block about 100m high, 50m wide and 10m thick fell from a height of about 500m on the almost vertical wall. At the foot of the wall the rock with a volume of 50'000m^3 hit a moraine, in part covered by scree, and thereby released about 300'000m^3 of moraine which resulted in a massive slide comprising about 350'000m^3. This produced a maximum wave run-up of 40.5m in direct prolongation of slide axis. The lateral spreading of the wave and multiple reflections destroyed two villages causing 61 fatalities (Bjerrum and Jørstad, 1968).

On September 13, 1936 another slide occurred from the same slide area at Ravnefjell. The slide masses were released from an altitude between 400 and 800m as shown in Fig. B.12. The slide volume comprised about 1×10^6 m^3. The generated wave was considerably larger and more destructive than in 1905. Although after the slide in 1905 houses were rebuilt at a higher level than before, almost all were lost and 73 persons perished. After the slide detailed wave run-up heights were measured. The maximum wave run-up of 74.2m was again observed in direct prolongation of the slide axis (Fig. B.11). The observed run-up heights decreased rapidly but in discontinuous manner with increasing distance from the slide. At the lake exit where the basin narrows wave run-up heights increased again to 15m at a lateral distance of more than 8km from the impact site washing away the bridge at Vassenden (Jørstad, 1968). This multiplication in wave run-up height was attributed to wave energy convergence due to the narrowing topography and decreasing water depth (Slingerland and Voight, 1979). The strong variation in run-up heights along the shore demonstrates the great importance of multiple reflections, interference, refraction, diffraction and shadowing effects behind promontories.
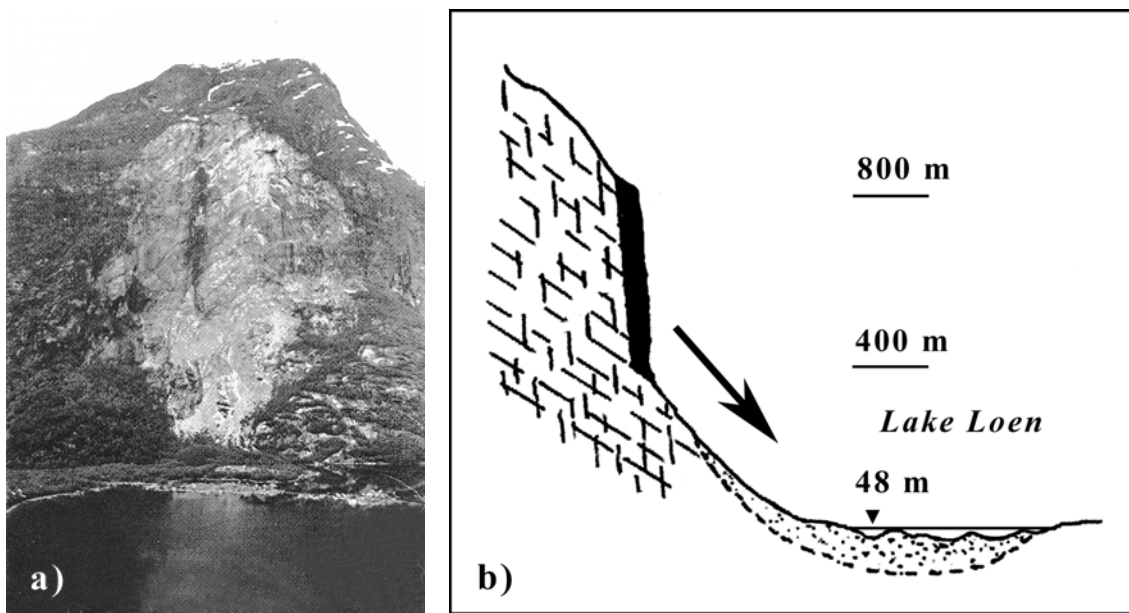
Figure B.12 **Ravnefjell and Loen Lake: a) Slide scar** of 1936 rockslide (Photo: courtesy of NGI). **b) Cross-sectional sketch** along slide axis showing main rock joints, pre-slide location of released slide mass and post-slide bathymetry of Loen Lake (after Grimstad and Nesdal, 1991).

Three slides followed at the same location between 1936 and 1950. The release of the slide masses was caused by hydraulic jacking and splitting along rock joints parallel to the almost vertical mountain side shown in Fig. B.12b) due to frequent freezing and thawing. The slope angle at the bottom of the wall decreased from 65° to 40° during the slide series. The debris from the slide series progressively filled the lake to a large extend at the impact site reducing subsequent wave heights generated from the Ravnefjell slide source (Grimstad and Nesdal, 1991). Post-event estimation of slide impact velocities and shapes is extremely difficult. All the Ravnefjell slides involved collapsed exfoliation sheets of rock which hit and released large volumes of scree before impacting into an irregular bay of variable depth (Slingerland and Voight, 1979). The impact on the scree must have led to a massive break-up of the rock mass and transformation into a debris slide or avalanche.

## B.1.5 Lake Uri, Switzerland

The Lake Uri, a branch of the Lake of Four Cantons, is situated in the Alpes of central Switzerland (Fig. B.13a). The Lake of Uri is 11 km long, 1.1 to 2.5 km wide and about 200 m deep. On April 10, 1992 some 16'000 m^3 of limestone with an estimated density of 2.7 t/m^3 were blasted off an almost vertical cliff called Ölberg situated above a main road named Axenstrasse on the east shore of Lake Uri (Müller and Schurter, 1993). The location of the rockfall is shown on the map in Fig. B.13a). A cross-section with the endangered road gallery and the toppling rock situated between 60 and 130 m above the lake

level prior to the blasting is shown in Fig. B.13b). The slope angle averages roughly 80° from the cliff straight down to the lake bed.
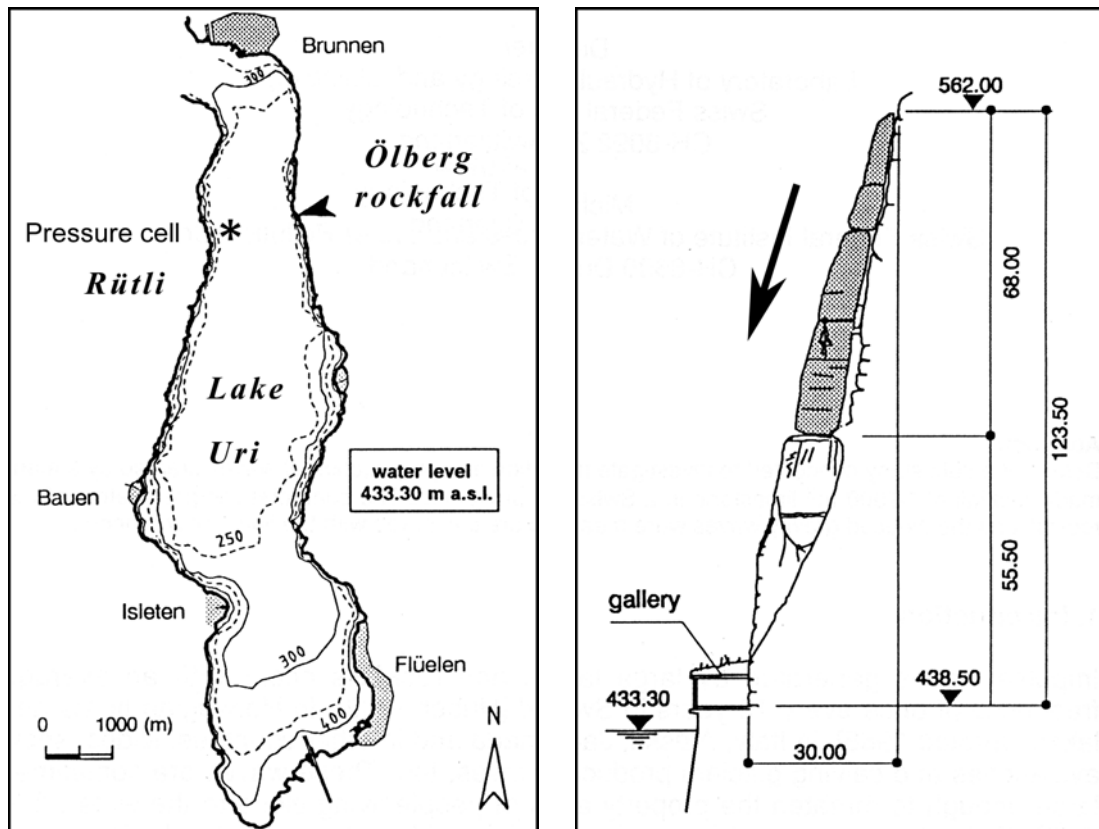

Figure B.13 **a) Lake Uri map** with bathymetry, location of rockfall and pressure cell for wave recording at a distance of 1330m from the impact site and 190m off the shore near Rütli. **b) Cross-section** of Ölberg with the endangered road gallery and the toppling rock before blasting on the almost vertical cliff – the slope angle averages roughly 80° from the cliff straight down to the lake bed (after Müller and Schurter, 1993).

The explosion with 4.75 t of TNT blasted the rock mass of the cliff and simultaneously disintegrated it in blocks smaller than 1.5 m in diameter. Roughly 4 s after ignition the first rock debris hit the water surface as shown in Fig. B.14a). The debris fall impacted the water with a front velocity of about 20 m/s over a core impact area 60 to 80m wide along the shore and about 60m perpendicular to the shore. Small debris and dust covered an area within a 200m radius from the blasting. Prior to blasting hydraulic model test at a 1:400 scale were conducted at the VAW-laboratory to predict the resulting wave heights at various locations. A comparison of the debris fall created by the blasting in nature and model is shown in Fig. B.14.
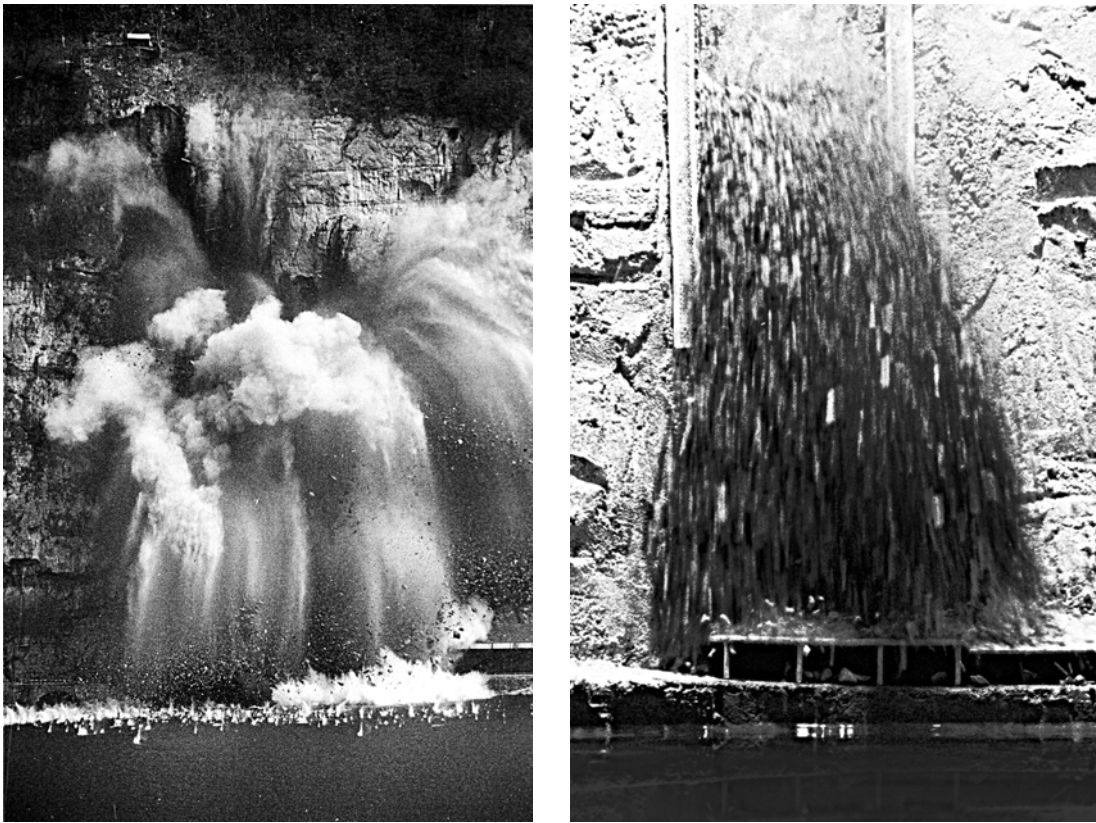
Figure B.14 **Rockfall** into Lake of Uri, roughly 4 s after ignition: **a) Blasting** off 16'000 m^3 of limestone on April 10, 1992 and **b)** its debris fall counterpart in the physical Froude similarity **model** at a 1:400 scale in the VAW-laboratory (after Müller, 1992).

During the field measurement campaign a large set of data was collected, including off shore wave heights, wave run-up heights and water particle velocities 4 m above the lake bottom (Müller and Schurter, 1993). The wave record obtained with the pressure cell 190 m off the shore near Rütli and 1350 m from the impact site is shown in Fig. B.15 (Müller, 1994). The location of the pressure cell is shown in Fig. B.13.
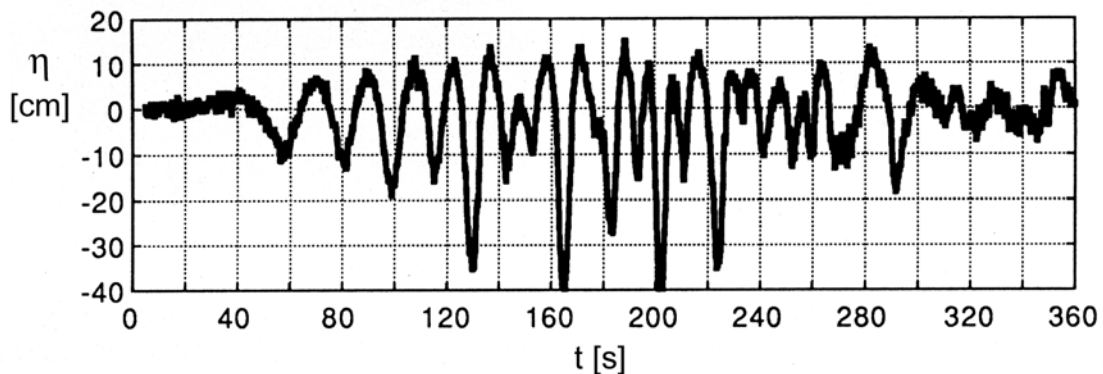

Figure B.15 **Wave record** with water surface elevation η as a function of time t after ignition recorded with a pressure cell located at a distance of 1330 m from the impact site and 190 m off the shore near Rütli (Fig. B.13).

The wave record shown in Fig. B.15 was affected by wave reflections due to the location just 200 m offshore. Only the first small wave crest at t = 40 s after blasting was unaffected by wave reflections. A separation of incident and reflected waves from the record is not possible. The first wave was 0.18 m high, 1000 m long and travelled at a propagation velocity of 37 m/s. The first wave was in the intermediate depth regime (Dean and Dalrymple, 1991). Müller (1994) compared the field data with measurements obtained in the 1:400 scale model at the VAW-laboratory prior to blasting. Wave run-ups and reflections were significantly damped by scale effects in the laboratory due to extremely small wave amplitudes of only a few millimeters. Wave run-ups and reflections were factors too small in the laboratory in comparison to values predicted by theory and run-up factors obtained from the field data.

B.1.6 Unzen volcano, Japan

Several disastrous tsunamis caused by landslides have been documented in Japan. The worst catastrophe occurred on May 21, 1792 at the Unzen volcanic complex on the island of Kyushu. A simple gravitational collapse of the Mayuyama lava dome resulted in a debris avalanche that swept into the Ariake Sea (Ogawa, 1924). A synthetic topography of the Unzen volcano on the Shimabara peninsula and the Ariake Sea is shown in Fig. B.16a). Katayama (1974) showed that no explosive eruptions accompanied the collapse of cold rock at Mayuyama. The lava dome had formed due to volcanic activity some 4000 years before the collapse. Another vent of the Unzen volcano at a distance 4 km from Mayuyama lava dome was active in 1792. A series of major earthquakes started on April 21, 1792. Deformation and small slope movements preceded the Mayuyama collapse. Fear of landslides prompted evacuation of virtually all residents of Shimabara one month before the collapse. Concern waned as seismicity dropped and towns-people had returned to their homes before the catastrophe. On May 21, 1792 the lava dome collapsed to an altitude of about 700 m. The amphitheater shaped slide scar shown in Fig. B.16b) spans about 1.3 km. The height and the distance from the top of landslide to the toe of deposition were 760 m and about 6.5 km, respectively (Suzuki and Furuya, 1999). The debris avalanche had a volume of 0.34 km^3 (Siebert et al., 1987). About 80% of the slide volume entered into Ariake Sea. The submarine deposition covers an area of about 15 km^2 and extended the shoreline by almost 1 km. The debris avalanche overrode the southern part of Shimabara causing few thousand casualties. The Ariake Sea has a maximum depth of 64 m near the impact site (Slingerland and Voight, 1979). Large parts of the Ariake Sea are very shallow with water depths between 10 to 20 m (Aida, 1975).
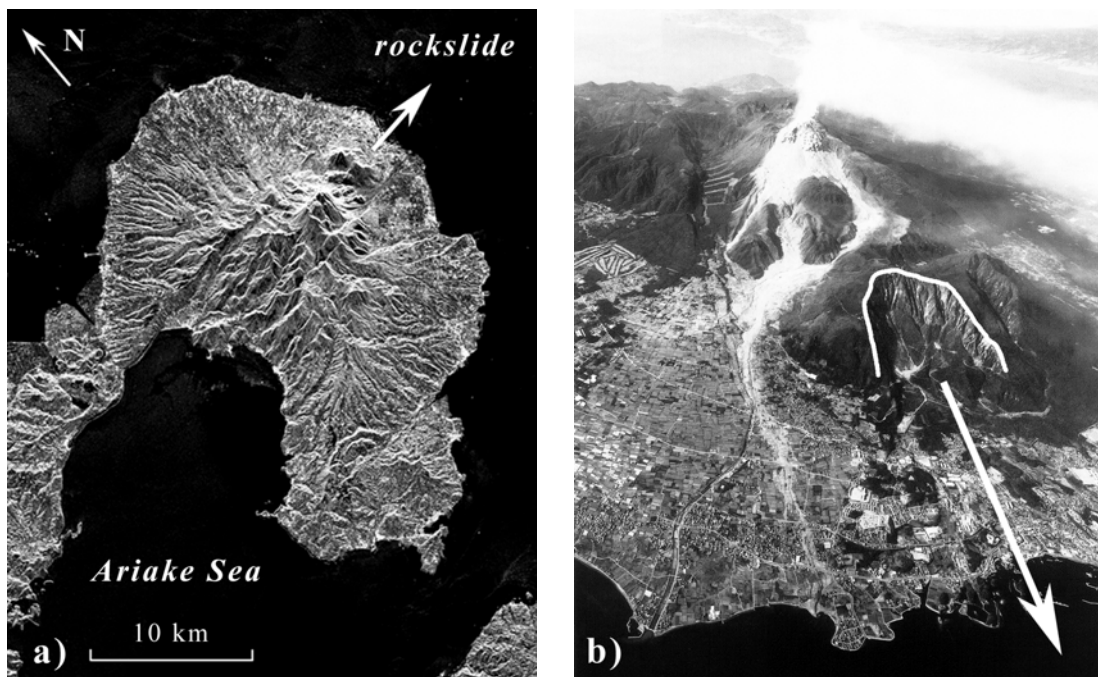
Figure B.16 **Unzen volcano: a) Topography** acquired by Spaceborn Imaging Radar-C/ X-Band Synthetic Aperture Radar (SIR-C/X-SAR) aboard the space shuttle Endeavour in 1994 (Photo: courtesy of NASA, Jet Propulsion Laboratory, P-45150). **b) Eastern view** of Unzen volcano on the Shimabara Peninsula in 1992 with the amphitheater shaped slide scar formed by the partial collapse of the Mayuyama lava dome in 1792 (Photo: courtesy of Asia Air Survey Co. Ltd.).

The debris avalanche impacted into the Ariake Sea at an impact angle $\alpha \leq 10°$ (Slingerland and Voight, 1979). The slide impact created a series of three main waves in short succession. The second wave was the highest. Reported wave heights range from 10 to 30m (Ogawa, 1924). Most of the 9720 fatalities at Shimabara resulted from lateral spreading and back-washing of the impulse waves. The tsunami affected low lying areas of the city to the north of the impact site and swept 77km of the peninsula coastline reaching up to 1km inland (Ogawa, 1924). The tsunami travelled 20km across the Ariake Sea, resulting in an additional 4996 fatalities in Kumamoto province. The total number of casualties was estimated to 14'500. Damage occurred along more than 120km of coastline on both sides of the Ariake Sea. About 6000 houses were washed away. Agricultural fields covering an area of about $25\,\text{km}^2$ were flooded and more than 1600 ships lost (Ogawa, 1924). Numerical simulations by Aida (1975) agreed fairly well with the observed tsunami behavior, if an influx of 18'000m^3/min per unit length of shore during 2 to 4 minutes was assumed. This suggests a slide impact velocity of about 20 m/s. The estimated tsunami energy was 5×10^{12} J – two to three orders of magnitude smaller than the available potential energy of the debris avalanche. Aida (1975) modelled tsunami propagation velocities around 40 km/h. Only 30 minutes warning would have been available for communities across the Ariake Sea and even less for towns along Shimabara peninsula.

B.1.7 Spirit Lake, Mount St. Helens

The bulging sector of the north slope of Mount St. Helens collapsed on May 18, 1980, thereby creating probably the largest mass movement in recorded history. A series of moderate to severe earthquakes preceded the collapse which involved a total rock volume of 2.5 km^3. The mass movement was classified by Voigth et al. (1981) as a rockslide-avalanche after Mudge (1965). The initial movement of the rockslide was interpreted as a series of retrogressive slope failures based on examination of eyewitness photographs (Voight, 1981). The event may be subdivided into three separate stages (Voight et. al, 1983). The first failure of the series, called slide A, began to slide northward from the summit of the mountain about 10s after a 5.2 magnitude earthquake (Voight, 1981). The slide A had a volume of 0.8 km^3. The detachment surface dipped from 2800m northwards at about 50° to 60°, but flattened with depth. The paths of slide A are shown in Fig. B.17.
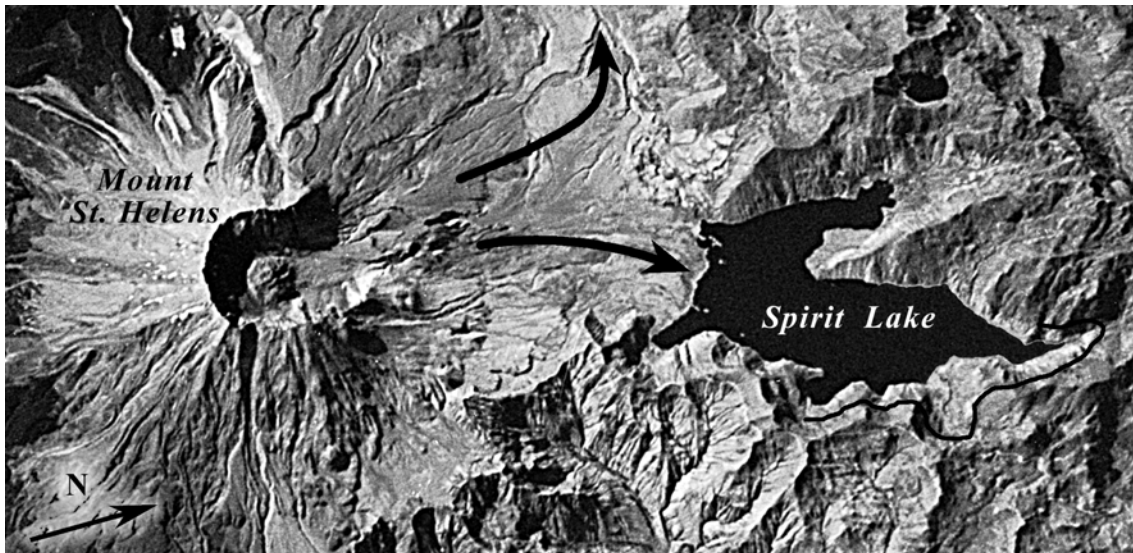
Figure B.17   **Spirit Lake** and Mount St. Helens volcano (2548 m after May 18, 1980) with the rockslide-avalanche deposits extending outward from the volcano caldera to the northwest and northeast into Spirit Lake on a near vertical space born image shot in 1994. The volcano caldera spans 2km in east-west direction. The trimline along several kilometers of the Spirit Lake east shore with wave run-ups larger than 200m is indicated (Photo: courtesy of NASA, # STS064-051-025).

Details concerning the slide evolution were ascertained from eyewitness photograph sequences (Voight, 1981; Voight et al., 1981). Within about 40s from the moment of detachment the slide A reached a maximum velocity of about 80 m/s. The failure of the north face of Mount St. Helens began as a slide – displacements occurring along one or several surfaces or relatively narrow zones (Varnes, 1978). It was apparent from the deposits, however, that the material soon disintegrated into particles of various size and took on the characteristics of a flowing debris-avalanche as particles interacted with each other and interstitial fluids. A lobe from the slide A rammed into Spirit Lake at an assumed velocity of 80 m/s. The impact caused a wave run-up beyond 200m above orig-

inal lake level along several kilometers of the Spirit Lake east shore as shown in Fig. B.17. The debris deposited in Spirit Lake had a total volume of 0.43 km^3 and most of it was from slide A (Meyer and Carpenter, 1982). The large mass impact most likely moved the whole water body of Spirit Lake creating a seiche or standing wave oscillation. The lake was dammed immediately by the debris-avalanche and the mean lake level raised by 60 m. Other parts from slide A made a 90° left turn and travelled down from the North Fork Toutle River valley.

The cryptodome an its surrounding hydrothermal system were unroofed by the slide A. The rapid depressurization resulted in the initial explosion of the lateral blast (Kieffer, 1981). Meanwhile, retrogressive failure continued with slides B and C. These trailing slides scarcely interacted with the water of Spirit Lake and therefore it is referred to Voight et. al (1983) or Glicken (1996) for further description. The potential energy released during the whole slide sequence was estimated to 7×10^{16} J (Voight et al., 1983).

The debris-avalanche deposits were analyzed in great detail after the event (Glicken, 1996). The mean specific gravity of the solids was estimated to 2.7 t/m^3 and the mean dry bulk density of disturbed material to 1.68 t/m^3. The mean pre-slide density of the part of Mount St. Helens that became the debris avalanche was calculated to 2.31 t/m^3. This decay in mean bulk density during the debris-avalanche was due to the dilatation caused by massive block shattering, disaggregation, particle interaction and mixing during transport. The mean porosity of the disturbed material was estimated to 38 %. The deposited material was heterogeneous in grain size and varied from clay-size particles to blocks over 100 m in diameter (Voight et al., 1983). Debris avalanche samples contained mean values of 46 weight percent gravel and 45 weight percent sand. The average friction angle was estimated to 41° and the in-situ permeability to 9×10^{-6} m/s.

A comparison of aerial photographs taken before and after the debris avalanche impacted into Spirit Lake showed that the lake increased in size and rose in altitude. The mean lake level increased from 975 m (before May 18, 1980) to 1049 m in 1981 and the lake surface area from 5.3 km^2 to 8.9 km^2 (Dion and Embrey, 1981), whereas the maximum water depth decreased from 58 m to 34 m (Embrey and Dion, 1988). The deposited debris volume of 0.43 km^3 roughly doubled the pre-event lake volume of 0.2 km^3. The water volume contained in Spirit Lake rose continuously because of the outlet blockage by the debris avalanche deposits. By March 1983, Spirit Lake contained 0.45 km^3 of water and the risk of catastrophic flooding due to dam failure or overtopping increased (Meyer et al., 1986). The U.S. Army Corps of Engineers began to control the lake level by an interim plan of barge-based pumping and discharge into outlet channels. In April 1985, these temporary measures were replaced by a permanent 2.4 km long diversionary tunnel with a diameter of 3.4 m (Sager and Chambers, 1986). For a worldwide overview on landslide dammed lakes and related processes it is referred to Schuster and Costa (1986), and Costa and Schuster (1991).

B.2 Partially submerged landslide generated waves

B.2.1 Vajont reservoir, Italy

The Vajont river is an affluent of the Piave River located in the Dolomite Alps of the Veneto Region, about 100 km north of Venice. Whilst proposals to site a dam at this location were made in the 1920's, excavation of the site began in 1956 and the dam was completed in September 1960. The double curved arch dam is 265.5 m high and still ranks among the worlds highest thin arch dams. The dam was build across a deep, narrow, V-shaped gorge and the crest length measures only 160 m. An aerial view of the Vajont valley is shown in Fig. B.18.
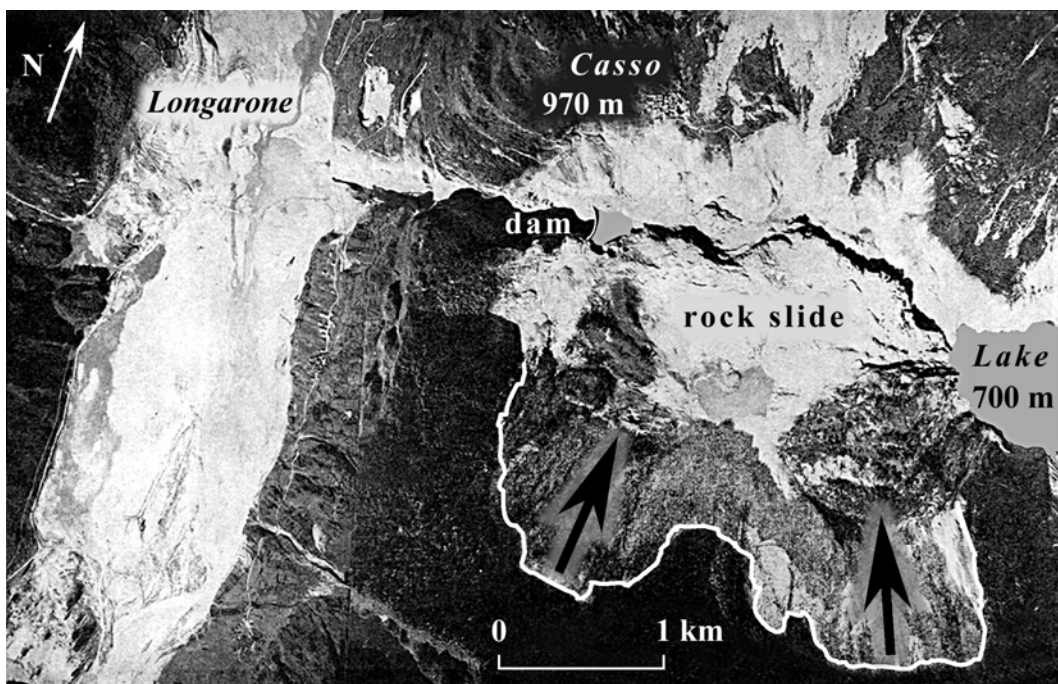

Figure B.18 **Aerial view of Vajont valley** after the event with reservoir and arch dam, rock slide deposit and slide scar, trimlines of impulse wave run-up and flood wave in the Piave Valley (Photo: courtesy of ENEL).

The maximum storage capacity of the reservoir was 169×10^6 m^3. Filling was initiated in February 1960, before final completion of the dam. On November 4, 1960, when the reservoir depth had reached 180 m, a first large slope failure occurred on the south flank. 700'000 m^3 of limestone slid into the lake in about ten minutes. At the same time a huge joint of 2 km length opened up, suggesting that a very large landslide had been mobilized. As a result the water depth of the reservoir was gently dropped back to 135 m and the creeping of the large rock mass reduced to 1 mm per day. From October 1961 to November 1962 the water depth was raised to 240 m and the creeping velocity reached 12 mm per day. In November 1962 a second lowering was slowly undertaken. In April 1963 the water depth was reduced to 185 m and the deformation rate was effectively zero.

The third filling of the reservoir was intended in April 1963 and by early September 1963 a water depth of 250 m was reached. The creeping had increased to 35 mm per day and the third reservoir draw down was initiated. By October 9, 1963 the water depth was lowered to 240 m but creeping rates up to 200 mm per day were recorded. On October 9, 1963 the southern flank of Vajont reservoir collapsed on a length of more than 2 km as shown in Fig. B.18.

Collapse occurred during reservoir drawdown in a final attempt to reduce flank creeping and the reservoir was only about two-thirds full with 115×10^6 m^3 of water. The partially submerged rockslide with a volume of 0.24 km^3 penetrated like a piston almost horizontally into the reservoir at velocities up to 30 m/s. The density of the limestone was estimated to 2.7 t/m^3. The entire mass slid northward and the centroid dropped about 200 m in altitude. The energy release was estimated to 1.3×10^{15} J (Erismann, 1979). The wave run-up in direct prolongation of slide axis reached the lowest houses of Casso 270 m above reservoir level before impact corresponding to 245 m above dam crest (Müller, 1964). The slide scar, the slide deposit, the reservoir remnants and the trimline of wave run-up are shown in Fig. B.18. A geological cross-section of Vajont gorge with outlined rock layers, pre and post event position of slide mass is shown in Fig. B.19. The back of the slide scar had a hill slope angle of 40° whereas the bottom was almost horizontal.
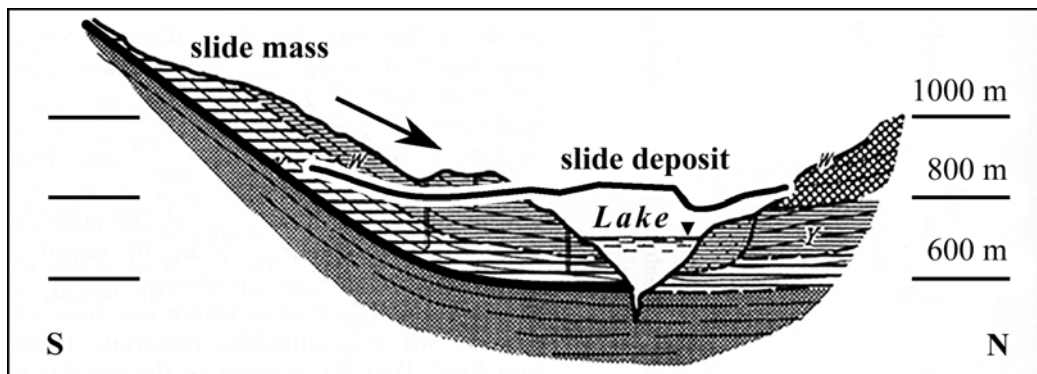
Figure B.19 **Geological S-N-cross-section** of Vajont Valley along slide axis with outlines of rock layers and lake level prior to the slide, and surface of rockslide deposit (after Müller, 1964).

The rock mass moved as an entire block and deformed only due to the inclination change in the sliding surface from 40° to 0°. The mean travel distance of 500 m was relatively small compared to the dimensions of the slide mass and therefore no disintegration of the slide into a debris slide or even debris avalanche occurred. The upright trees on the surface of the slide deposit shown in Fig. B.20a) confirm the block motion. The thin arch dam in the narrow, V-shaped gorge and the rockslide deposit are shown in Fig. B.20a). The rockslide deposit came within 50 m of the left abutment and towers up to 140 m above the dam crest. The lateral spreading of the surge overtopped the dam crest by more than 100 m. The thin arch dam withstood the overtopping and sustained no damage to the structural shell and the abutments. Only the roadway was damaged on the dam crest. The water volume which overtopped the dam crest was estimated to 30×10^6 m^3. The flood wave

dropped more than 500m down the Vajont gorge and into the Piave Valley causing utter destruction to the villages of Longarone, Pirago, Villanova, Rivalta and Fae. The village of Longarone before and after the event is shown in Figs. B.20b) and c), respectively. More than 2000 persons perished. The damage was estimated to 200 Million US-Dollars – 2001 equivalent: roughly 1 Billion US-Dollars (Schuster, 1996). A by-pass tunnel was used to control the water level behind the slide dam (Kiersch, 1964).
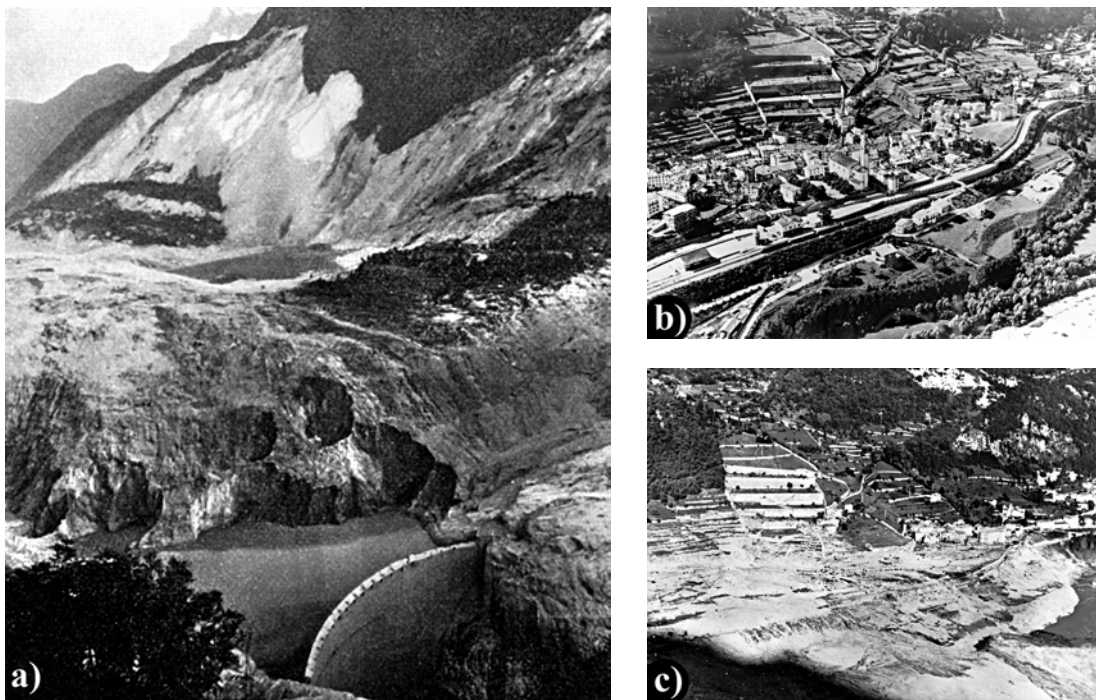

Figure B.20 **a) Vajont arch dam** and the remnants of the reservoir which was almost completely filled by the rockslide over a distance of 2km dam-upstream. Note the slide scar in the background. **b) Longarone village before** the catastrophe and **c) Longarone village after** being erased by the flood wave (Photos: courtesy of ENEL).

After the catastrophic event detailed investigations on the failure causes were undertaken. A creeping movement of the slide was observed over years before the event but a sudden slope failure was not predicted. The sliding surface was localized in 50 to 150mm thin clay layers within the limestone (Broili, 1967). It remains likely that increasing the reservoir level raised pore pressures in the clay layers, reducing the effective normal strength and hence the shear resistance. The reservoir drawdown induced hydraulic pressures that increased the shear stresses as water in the jointed limestone tried to drain (Müller, 1968). Frictional heating of the pore water in the slip surface due to the slide movement probably caused a further reduction in friction coefficient (Voight and Faust, 1982).

B.2.2 Ritter Island, Papua New Guinea

Ritter Island is located in the Bismarck Sea northeast of Papua New Guinea. Ritter volcano is one of several active volcanoes in the 1000 km long Bismarck volcanic arch. The Island almost completely disappeared under the sea on March 13, 1888. The event seems to have been simply a cone collapse accompanied by little, if any, eruptive activity. The disappearance by subsidence of Ritter Island gave rise to a tsunami which was observed at distances up to 500 km. The brunt of the tsunami must have been felt to the west in the direction of the slope failure, but the only run-up record available was from New Britain located to the east of Ritter Island. On New Britain a maximum wave run-up of 15 m was recorded (Cooke, 1981). Only a small part of the previously 780 m high volcano remained above sea level. Ritter island today is a 1.9 km long arcuate island whose western side is a cuspidal, crater-wall escarpment facing to the west-northwest. The escarpment is highest in the middle of the island at about 140 m above sea level, and it diminishes in height towards the northwest and southwest. Bathymetric survey revealed a large westward-facing avalanche amphitheater on Ritter Island (Johnson, 1987). The amphitheater spans up to 4.4 km in width and encloses an area of about 13 km^2. The volume of rock displaced in 1888 was estimated to as much as 4 to 5 km^3 assuming an asymmetric Ritter Island prior to the collapse as shown in Fig. B.21. The rocks forming Ritter Island are of basaltic and low-silica andesitic composition. The westside dipped at about 20° to 25° whereas the eastern flank represents the flank of the volcano prior to the event with a maximum angle of roughly 45°. The 1888 Ritter event was only one, possibly the latest, of several likely examples of large scale slope failures on Papua New Guinea volcanic islands.
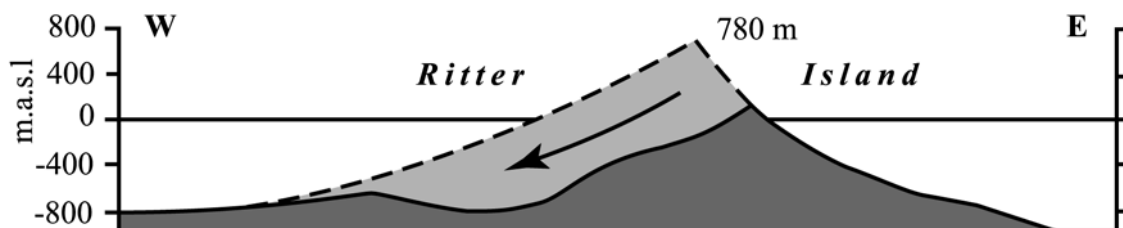

Figure B.21 **Ritter Island W-E-profile** in slide axis with superposition of rock mass released in the 1888 large scale slope failure assuming a gradual, moderate slope for the entire western flank of the volcano (after Johnson, 1987).

B.2.3 Nuuanu, Hawaii

The extensive area covered by major submarine mass wasting deposits along a 2200 km stretch of the Hawaiian Ridge from 200 km northwest of Midway to the island of Hawaii was mapped systematically using the digital side-looking sonar system GLORIA (Moore and Normark, 1994). A sonograph of the sea floor northeast of the Oahu is shown in Fig. B.22a). An astonishing result of the survey was the discovery of many giant land-

slides on the submarine flanks of the Hawaiian Ridge. At least 68 major landslide deposits more than 20km long were delimited along the mapped 1.3×10^6 km^2 of the Hawaiian Ridge. These surveys demonstrated that both the size and number of prehistoric submarine landslides on the flanks of the Hawaiian Ridge were much greater than previously assumed. Medium-sized landslide deposits with volumes of tens of km^3, which are common in shallow waters, were not mapped due to difficulties with side-scan sonar in shallow waters near the coast – note the unmapped area around the islands of Oahu and Molokai in Fig. B.22a). A detailed assessment of smaller but more frequent landslides is necessary to estimate hazards posed by submarine landslides (Normark et al., 1993). The deposits of 17 well defined major landslides along the Hawaiian Ridge are shown in Fig. B.22b). These 17 slump and debris avalanche deposits are exposed over about 100'000 km^2 of the ridge and adjacent sea floor from Kauai to Hawaii, covering an area more than 5 times the land area of the islands.
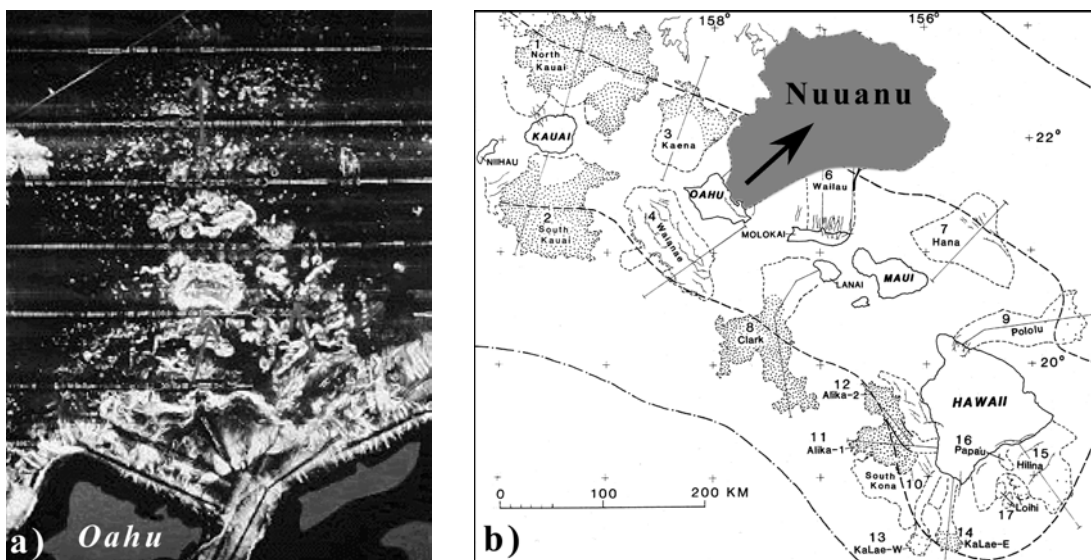

Figure B.22   **Nuuanu landslide: a) GLORIA digital side-scan sonar image** of the sea-floor in the landslide run-out area N-E of the island Oahu (Sonograph: courtesy of USGS), **b) landslide run-out area map** (Moore et al., 1989).

The debris avalanches commonly have an amphitheater shaped slide scar at their head and hummocky surfaces with little or no internal structure in the lower part. Most of the deposits from these large slope failures lie in water deeper than 2000m. The debris avalanche deposits are 0.05–2km thick and possess an overall gradient of only 3°. Some of the individual debris avalanche deposits are up to 230km long and about 5000km^3 in volume, ranking them among the largest mapped on Earth. These large landslides on oceanic volcanoes are exceeded in volume only by mass failures on Mars. The largest known landslide in the Valles Marineris on Mars reached a volume of 17'880km^3 (McEven, 1989). Fast moving debris-avalanche deposits are long compared to width, and thinner than deposits from slow moving slumps. Rapid movement during single events was indicated by the thinness and great length of the avalanches, by movement uphill in their distal

reaches, and by their hummocky, fragmented surfaces that resemble the hummocky terrain of subaerial rapidly emplaced landslides, such as the 1980 Mount St. Helens debris avalanche (Moore et al., 1994). This similarity further suggests that submarine debris avalanches can move rapidly like the Mount St. Helens avalanche, and therefore pose the secondary hazard of tsunami production (Moore and Moore, 1988). Oceanic disturbances caused by rapid emplacements of debris avalanches may have produced high-level wave deposits found on several islands, such as the 365 m elevation Hulopoe Gravel on Lanai. This coral bearing marine conglomerate has been dated at about 100'000 years ago. Similar tsunami deposits on Molokai are about 200'000 years old (Moore and Moore, 1988).

The largest mapped landslide deposit on Earth is the Nuuanu debris avalanche off the northeast flank of Koolau volcano on the island of Oahu. The mosaic of sonographs in Fig. B.22a) and the corresponding map in Fig. B.22b) show the run-out area located northeast of Oahu. The deposit covers an area of 23'000 km^3 and is about 230 km long as measured from its headwall at Nuuanu Pali on Oahu to its toe half way up the southwest flank of the Hawaiian Arch. The average deposit thickness was estimated to 200 m using conservative assumptions, which yields a slide volume of about 5000 km^3. The debris avalanche slid down to the depth of at least 4600 m, crossed the Hawaiian Deep and moved uphill a distance of about 140 km to its 4300 m deep terminus. Hence the vertical upslope transport was 300 m without considering the thickness of the slide in the deep which will increase the upslope distance at least by 30 %. The momentum necessary for the slide to ride up such a slope requires that it reached a speed of at least 80 m/s at the base of the canyon (Ward, 2001). Nevertheless the estimated slide velocity of 80 m/s substantially lags the shallow water wave propagation velocities of 140 m/s and 200 m/s in water depths of 2000 m and 4000 m, respectively. Ward (2001) numerically computed the impulse waves generated by the Nuuanu landslide using linear wave theory. Nonlinear effects were neglected, which allowed spectral waveform decomposition, independent propagation and reconstruction by superposition. No long wave or shallow water assumption was made, since even for the largest known landslide on Earth not all generated waves make it into the shallow water wave regime. The computed wave patterns are shown in Fig. B.23a) and Fig. B.23b) at time after initiation of slope failure $t = 1$ h and $t = 4.5$ h, respectively (Ward, 2001).
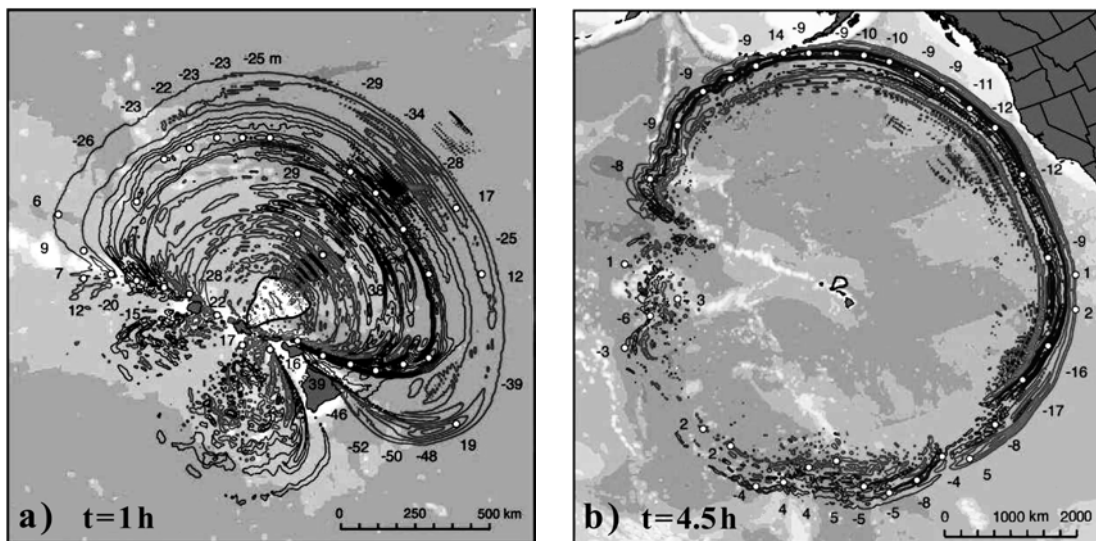
Figure B.23 **Wave patterns** at **a)** *t* = **1 h** and **b)** *t* = **4.5 h** computed by Ward (2001) for the Nuuanu landslide assuming linear wave theory.

At *t* = 1 h the mass movement had been completed for 20 minutes. The wave pattern was characterized by the directionality of the radial wave propagation. The largest waves travelled parallel to the slide axis toward the northeast. The Hawaiian Islands and the varying water depth caused wave diffraction and refraction. At *t* = 4.5 h vanguards of the tsunami reached the Aleutian Islands and the west coast of North America. After crossing half of the Pacific Ocean, waves 200 km offshore managed to retain 10 m of amplitude. At the same time the wave heights in the southwest quadrant were an order of magnitude smaller due to the disruption caused by the Hawaiian Islands.

B.2.4 Krakatau volcano, Indonesia

Krakatau volcano is located in the Sunda Straits of Indonesia approximately 40 km west of Java and south of Sumatra. The eruption of Krakatau in 1883 was responsible for one of the worst natural disasters in recorded history. The most intense eruptive activity occurred on August 27, 1883 when the northern part of the 832 m high Krakatau cone collapsed into the sea. After the collapse only a small part of Krakatau was left. From the Krakatau area of 33 km^2 before the event, some 23 km^2 collapsed and 5 km^2 were newly added during the eruption. During the collapse the volcano was cut through almost perpendicularly, so that the internal structure of the basalt volcano became eminently visible. The remaining island with its remarkable 832 m high natural cross-section is shown in Fig. B.24b). The rocks of Krakatau consisted of two petrographic groups: pyroxene andesit and basalt. Their density was assumed to 2.6 t/m^3. Where the engulfed island had been prior to the event, the sea was up to 300 m deep thereafter. The generated tsunami swept the coasts of Sumatra and Java in the Sunda Straits and caused 36'000 fatalities.
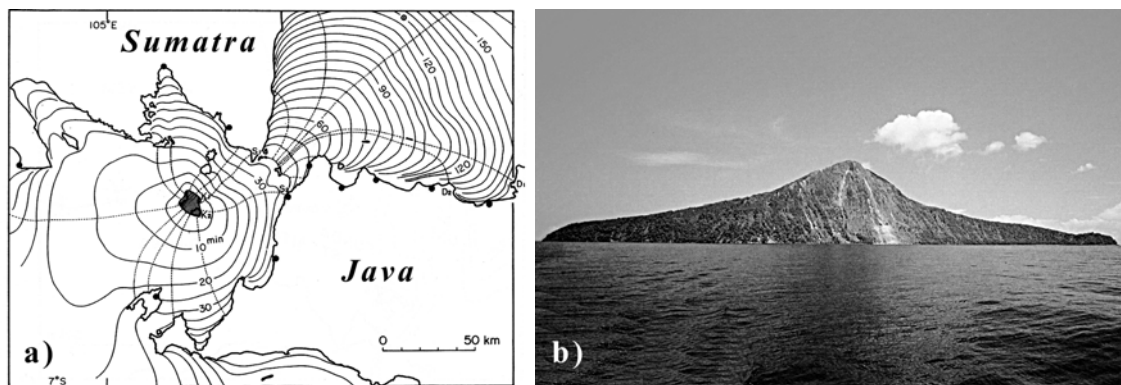
Figure B.24　**a) Refraction diagram** of the tsunami caused by the 1883 Krakatau event in the Sunda Straits (Yokoyama, 1981). **b) Krakatau** with north-facing scarp formed by the collapse and engulfment of the volcano during the eruption of August 27, 1883. The collapse cut near the former summit, and this remarkable 832 m high natural cross-section reveals the volcano's internal structure (photo: courtesy of M. Krafft).

The tsunamis were among the largest ever recorded, and were detectable on tide gages in Mauritius and the Arabian Peninsula, at a distance of more than 7000 km away from Krakatau. An excellent compilation of all the available records was given by Simkin and Fiske (1983). There was one exceptionally large sea wave (tsunami) on August 27, 1883 and several smaller ones. The recordings of the sea waves in most ports near Krakatau began with rises of the sea level (Symons, 1888). The largest wave was caused by the cave-in of Krakatau, the sudden submergence of a tremendous rock mass into the sea (Verbeek, 1884; Self and Rampino, 1981; Camus and Vincent, 1983; Francis, 1985). Most of the smaller waves were air/sea coupled waves (Francis, 1985). Wharton (1888) maintained that some waves were produced by the fall of ejecta into the water and Latter (1981) argued that some of the waves were caused by the emplacement of massive pyroclastic flows. Harkrider and Press (1967) applied the theory of pulse propagation to the atmosphere and ocean coupling. Resonant coupling led to an earlier arrival of the sea waves – than deducable from water wave propagation paths – at most far away stations such as Hawaii. The rise of the largest wave in the ocean must have been about 15 m (Verbeek, 1884). On the west coast of Java in the Sunda Straits near Anjer, 54 km from Krakatau, the wave ran up to a height of 36 m and in Merak, 64 km from Krakatau, to a height of 35 m (Verbeek, 1884). The wave run-up heights differed strongly from place to place and depended on the steepness and shape of the coastline, depth of the sea along the coastline, distance from Krakatau, and degree of protection of the coastline by islands. The refraction diagram of the Krakatau tsunami computed by Yokoyama (1981) using shallow water wave equations is shown in Fig. B.24a). The refraction diagram shows the circular spreading of the tsunami from the point source and the wave refraction due to changes in bathymetry. In the Sunda Straits to the northeast of Krakatau, with a mean water depth of 40 m, the wave propagation time lines are narrow spaced – indicating a slow propagation velocity. Towards the southwest of Krakatau the spacing of the wave propagation time lines and the wave propagation speed increase due to the water depth of more than 1000 m.

Appendix C: Gravity water wave theory

C.1 Linear water wave theory

The parameters to describe water waves are shown in Fig. C.1. The important parameters are the wave length L and the wave height H or the amplitude a. All other parameters, such as wave propagation velocity c and wave period T can be determined theoretically from these quantities. In the special case of the linear wave theory the wave height equals twice the wave amplitude. The wave length may be defined from crest to crest, trough to trough, surface upcrossing to upcrossing or downcrossing to downcrossing – they are all the same in the special case of the linear wave theory.
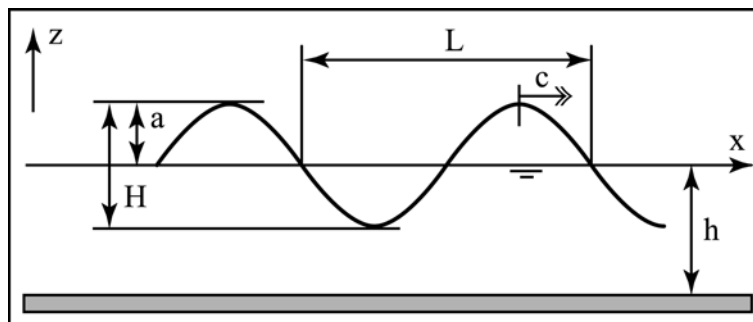
Figure C.1   **Definition** of the main wave parameters for the linear wave theory.

The simplest and most fundamental approach to the solution of the Laplace equation with the kinematic and dynamic boundary conditions is to assume the wave height H to be small compared with both the wavelength L and stillwater depth h. Nonlinear terms of the order $(H/L)^2$ are neglected (Airy, 1845). The resulting equations are known as the Airy theory, linear wave theory, small-amplitude wave theory and sinusoidal wave theory. Linear wave theory is extensively used in engineering practice. It is the only water wave theory applicable to the full range of shallow, intermediate, and deep water depths. The general range of validity is defined as

$$\frac{H}{h} < 0.03, \quad \text{and} \quad \frac{H}{L} < 0.006 \tag{C.1}$$

according to Dean and Dalrymple (1991). Its predictions are often in good agreement with experiments even when the wave height departs from small amplitude wave assumptions. Of particular interest regarding rough estimates of impulse wave propagation velocities is the wave celerity c defined as

$$c = \sqrt{\frac{g}{k}\tanh(kh)} = \frac{g}{\omega}\tanh(kh) \tag{C.2}$$

with the wave number k and the circular wave frequency $\omega = 2\pi/T$. The wave number k is related to wave celerity c and period T by the identities

$$k = \frac{\omega}{c} = \frac{2\pi}{L} = \frac{2\pi}{cT}, \quad \text{and} \quad c = \frac{L}{T} = \frac{\omega}{k} = \frac{2\pi}{kT} \tag{C.3}$$

The hyperbolic functions have convenient shallow and deep water asymptotes. In shallow water with $L/h > 20$ the wave speed is determined by

$$c = \sqrt{gh} \tag{C.4}$$

and solely depends on the water depth h. Small amplitude waves in shallow water are non-dispersive and therefore all waves travel with the same propagation velocity. In deep water with $L/h < 2$ the wave celerity is determined by

$$c = \frac{gT}{2\pi} = \sqrt{\frac{gL}{2\pi}} \tag{C.5}$$

which resolves to $1.56T$ for SI-units. In deep water the wave celerity solely depends on the wave period T. In intermediate depth water the wave celerity depends both on water depth and wave period. In deep and intermediate depth waters frequency dispersion causes a stretching of the wave group due to the wave period dependent propagation velocity. The wave celerity equation and its asymptotes are shown in Fig. C.2.
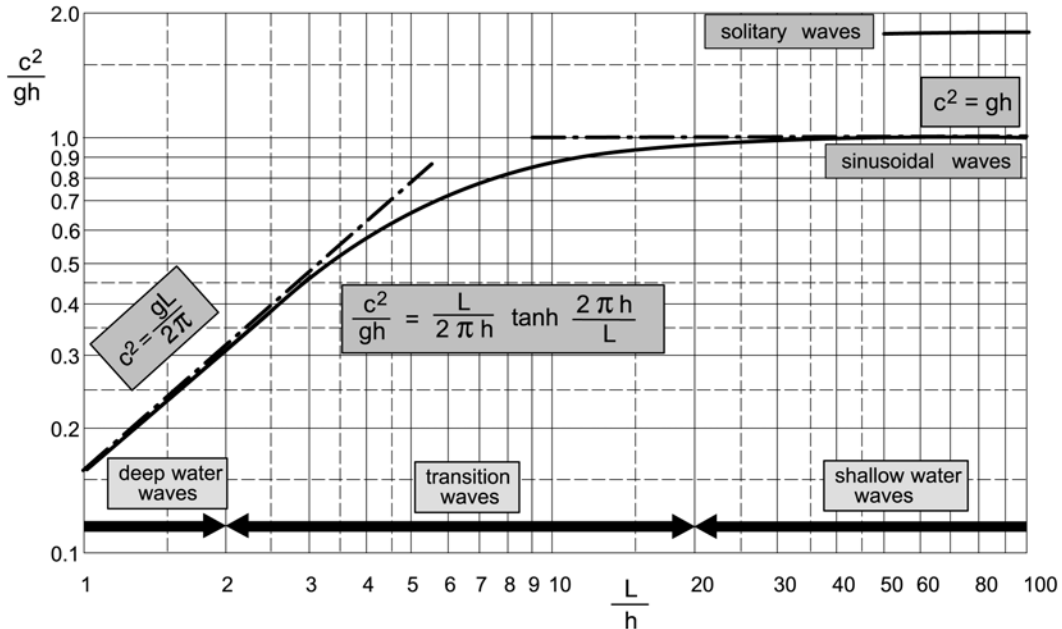
Figure C.2 **Dimensionless wave celerity** $c^2/(gh)$ versus relative wave length L/h for the linear wave theory and the upper band formed by the solitary wave theory, after Dean and Dalrymple (1991).

The wave celerity c is the apparent velocity of a wave crest. Small-amplitude water waves do not transmit mass but energy. The speed at which energy transmission occurs is the group celerity c_G which is related to the wave celerity by

$$c_G = \frac{c}{2}\left(1 + \frac{2kh}{\sinh 2kh}\right)$$ (C.6)

and has as deep and shallow water asymptotes the values $c/2$ and c, respectively. Therefore, in deep water, the energy is transmitted at only half the speed of the wave profile, and in shallow water, the wave profile and energy travel at the same speed.

C.2 Nonlinear water wave theories

As the height of a wave increases relative to water depth and wavelength, nonlinear terms in the free surface boundary conditions cause the wave profile to become non-sinusoidal. As the crests become more peaked the troughs become flatter. Nonlinear waves are governed by nonlinear partial differential equations. In general, neither the superposition principle of Huygens nor the principle of unperturbed propagation can be applied to nonlinear waves. The amplitudes of linear waves as solutions of the basic linear partial differential equations can be chosen arbitrarily. On the contrary, the amplitudes of the nonlinear waves are determined by their basic differential equations. As a consequence periods, wavelengths and wave celerities depend on their amplitudes. Second and higher order effects are much stronger in shallow than in deep water. With relatively increasing water depth dispersion becomes stronger which weakens nonlinear effects and shortens their persistence during wave propagation.

Contrary to the linear wave theory a nonlinear wave theory which is accurate over the whole range from shallow to deep water waves does not exist. In shallow water the most significant parameters regarding nonlinearity are the relative wave height H/h and the relative wave amplitude a/h. In deep water the most relevant parameter is the wave steepness H/L. In intermediate water depth the most significant parameter is the Ursell number

$$\mathbf{U} = \frac{aL^2}{h^3}$$ (C.7)

with wave amplitude a, wave length L and water depth h (Ursell, 1953). The Ursell number gives a ratio of nonlinear to dispersive effects. There are two general types of finite amplitude wave theories in use: analytical theories with power series truncation at a certain order and numerical theories where a power series solution to the Laplace equation is iteratively optimized. Of practical relevance are mainly the Stokes theory for finite amplitude deep water waves, the cnoidal and solitary wave theories for finite amplitude shallow water waves, and the Dean stream function numerical theory which is applicable throughout the entire range. In all these nonlinear wave theories there is mass transport as a result of irrotationality and nonlinearity.

Stokes (1847) developed a second-order theory for finite amplitude waves using a power series based on H/L which requires that H/h be small and thus is applicable for deep water and much of the intermediate water depth. The results diminish in accuracy as the wave steepness increases. For large wave steepnesses up to the breaking limit fifth-order theory is commonly used. Skjelbreia and Hendrickson (1961) and Fenton (1985) presented the fifth-order Stokes theory. Fenton (1985) tabulated the necessary formulas for wave calculations.

Korteweg and de Vries (1895) developed a finite amplitude wave theory applicable in shallow water, commonly know as cnoidal wave theory based on the KdV equations. Cnoidal theory involves Jacobian elliptical functions in contrast to the series of trigonometric functions in Stokes theory. Cnoidal waves are periodic and of permanent form. Cnoidal wave theories were presented by Keulegan and Patterson (1940), Keller (1948), Laitone (1960) and Chappelear (1962). In all cases the results are extremely difficult to apply. A synthesis was presented by Wiegel (1960). The most commonly used cnoidal wave theory is to the first order of approximation, but it is capable of describing waves of finite height in shallow water. Higher orders of approximation diverge significantly from experimental results, which confirms that higher-order theories are not necessarily better than their lower-order counterparts (LeMéhauté, 1976). Cnoidal theory may be applicable for $\mathbf{U} \geq 26$ (Sorensen, 1993). Kit et al. (2000) and Talipova et al. (1995), among others, applied the generalized KdV equation to the study of wave group evolution in shallow water. Kit et. al (2000) obtained a good agreement between experimental and numerical results for weakly nonlinear waves with $a/h \leq 0.19$. Wave group demodulation leads to a spectrum broadening accompanied by a spreading of the wave energy along the group in the time domain.

Boussinesq (1871, 1872) presented the translatory solitary wave theory. The surface displacement of the solitary wave is completely above the still water level and therefore consists only of a wave crest. The wave period and length are infinite. The vertical distribution of horizontal velocity was assumed to be uniform. The terms in $(H/h)^2$ were neglected. The solitary wave moves at a constant celerity c, where

$$c = \sqrt{g(h + a)} \qquad \textbf{(C.8)}$$

with stillwater depth h and wave amplitude a. The positive amplitude a is equal to the wave height H for the solitary wave. Characteristic for nonlinear waves is the increase in wave celerity with increasing amplitude. For applications of the solitary wave theory it is referred to Munk (1949) and Wiegel (1964). McCowan (1894) and Laitone (1960) presented second-order solutions, where terms in $(H/h)^3$ were neglected. These higher order solutions have a nonuniform vertical distribution of the horizontal velocity in contrast to the Boussinesq theory. Naheer (1978a) compared the theories of Boussinesq, McCowan and Laitone to experimental results. The major criteria of comparison were the surface profile, the wave celerity, and the fluid particle velocity. Differences were small for $H/h < 0.2$. None of the theories accurately described the three comparison criteria. The theory of Boussinesq was recommended for practical engineering purposes due to the

simpler expressions and a fair overall representation of all three features. A synthesis of higher order solutions is given by Miles (1980) and numerical solutions were presented by Monaghan and Kos (2000), Shi et al. (1998), Teng (1997), Teng and Wu (1992, 1994), among others.

Zakharov (1968) presented the most general nonlinear wave model, which describes temporal evolution of nonlinear waves in Fourier space. Zakharov's derivation is based on the Hamiltonian formalism (Zakharov and Kuznetsov, 1997). The Zakharov equation has no restrictions on spectral width in contrast to the cubic Schrödinger equation. Both the cubic Schrödinger and Dysthe equations can be derived from Zakharov equation (Dysthe, 1979). Shemer et al. (2001) conducted experimental and numerical studies on the evolution of nonlinear wave fields in intermediate water depth. Much better agreement with the experiments was obtained for the simulations based on the spatial Zakharov equations than the cubic Schrödinger model (Shemer et al., 1998). In particular, impressive agreement was obtained regarding the characteristic skewed shapes of the wave groups. Shemer proposed the application of the Zakharov model to some weakly nonlinear experiments on landslide generated impulse waves during a visit to VAW-laboratory (personal communication: Lev Shemer, 2000).

C.3 Wave breaking

In simplest terms, for a given water depth and wave period a wave will break when the wave grows to reach a certain limiting height or steepness. As the wave height and horizontal asymmetry increase so does the crest particle velocity, which approaches and becomes equal to the wave phase speed at breaking (Iverson, 1952). Commonly, breaking waves have been classified into four different types based on the physical changes of the surface profile during the breaking process. These are spilling, plunging, collapsing, and surging breakers (Wiegel, 1964; Galvin, 1968).

In shallow water the stability of the wave profile depends on the relative wave height. The breaking criterion κ in shallow water, for beaches of mild slope, was defined from solitary wave theory by McCowan (1894) as

$$\kappa = \frac{H_b}{h_b} = 0.78 \tag{C.9}$$

a fraction of wave height H to water depth h, where subscript b denotes the value at breaking. For the solitary wave with the breaking criterion $\kappa = 0.78$ and the wave celerity c described in Eq. C.8 an increase in wave celerity c of about 33 % compared to the linear shallow water assumption shown in Fig. C.2 is possible. On slopes the breaking criterion strongly depends on the slope angle β (Galvin, 1968 and 1969; Iversen, 1952). Breaker wave heights H_b rapidly increase with increasing slope angle β. The maximum value of the breaking criterion was estimated to $\kappa = 1.56$ for the special case of a vertical slope and doubles McCowan's breaking criterion (Weggel, 1972).

In deep water the wave stability depends critically on the wave steepness *H/L*. The limiting steepness was determined by Michell (1893) as
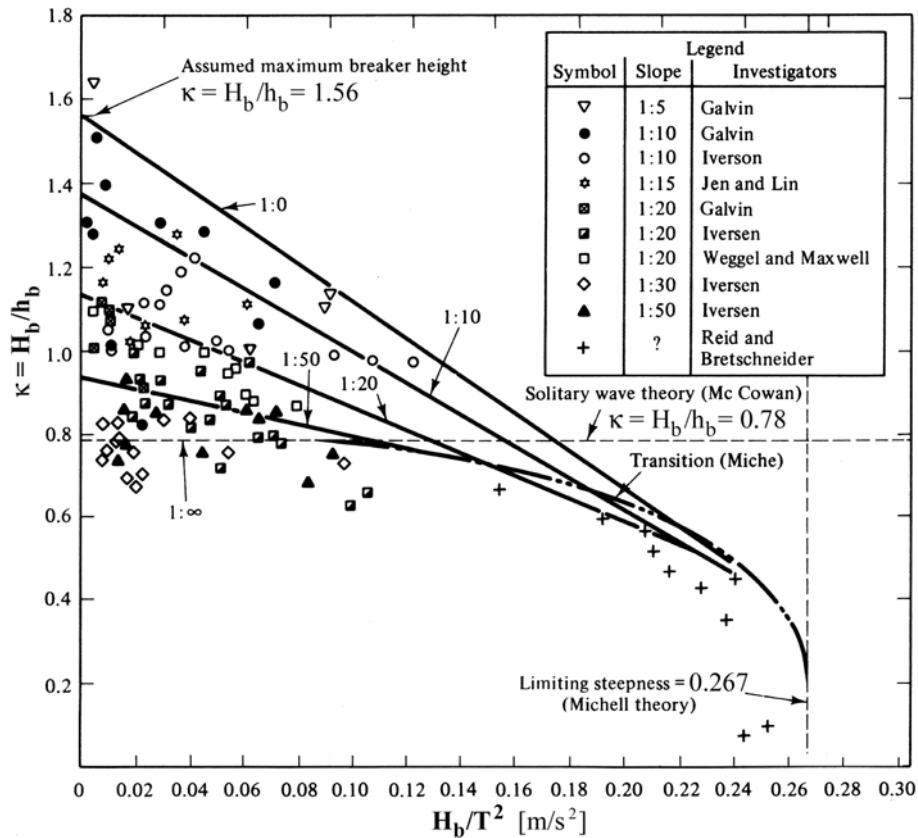
$$\frac{H_b}{L_b} = 0.142 \quad \text{and} \quad \frac{H_b}{gT_b^2} = 0.027 \qquad \textbf{(C.10)}$$

beyond which wave breaking occurs.

The limiting steepness of progressive waves in intermediate water depths was given by Miche (1944) as

$$\frac{H_b}{L_b} = 0.142 \tanh\left(\frac{2\pi h_b}{L_b}\right). \qquad \textbf{(C.11)}$$

A synthesis of experimental data and theoretical breaking limits is shown in Fig. C.3.

Figure C.3   **Breaking criterion** κ versus breaker steepness H_b/T^2, synthesis of experimental observations and theoretical solutions (Weggel, 1972).

The fine details of the breaking mechanism are complex, involving such matters as the interaction with sub-harmonic instability waves and rotationality at the vicinity of the wave crest as well as the rate of the surface profile asymmetry growth (Melville, 1982; Banner and Peregrine, 1993; Longuet-Higgins and Cleaver, 1994; Longuet-Higgins et al., 1994; Longuet-Higgins and Tanaka, 1997; Longuet-Higgins and Dommermuth, 1997; Chang and Liu, 1998 and 1999; Tulin and Waseda, 1999).

C.4 Validity of different wave theories

Unfortunately the range of validities of the various wave theories is not well defined. It is not possible to specify definite ranges for which a specific wave theory should be used, because different criteria such as water particle velocities, surface profiles and wave celerities or mathematical validities yield different ranges (Sorensen, 1993). Some efforts to verify the various wave theories are discussed herein.

Wiegel (1964) summarized some of the early wave flume investigations and comparisons with wave theories. The measurements in fairly shallow water were inconclusive in comparing the cnoidal and small amplitude theories.

Le Méhauté (1968, 1976) compared measured horizontal water particle velocity distributions to 12 wave theories. No theory was uniformly exceptionally valid. The validity ranges of the various theories are shown in Fig. C.4a). Le Méhauté remarked that such a graph is somewhat arbitrary and merely qualitative, since comprehensive investigation of the errors which are made regarding several criteria by using various theories in various domains had not been done.

Dean (1970, 1974) extended the comparison of Le Méhauté to include the numerical stream function theory (Dean, 1965). Dean (1970) compared the wave theories regarding their mathematical validity on the basis of rms-errors in the kinematic and dynamic surface boundary conditions. The ranges of best fit for analytical theories are shown in Fig. C.4b). Dean (1974) compared the theories on the basis of horizontal water particle velocity distributions. In both the mathematical (Dean, 1970) and physical validity study (Dean, 1974) the analytical theories were outperformed in all criteria by the numerical stream function theory (Dean, 1965) regarding the whole range of water waves from shallow to deep water and up to the breaking limits. The complete superiority of the relatively simple numerical method was further confirmed in comparison with precise Laser Doppler Anemometer LDA-measurements (Hattori, 1986). A synthesis of the stream function theory regarding practical applications is given by Herbich (1990).
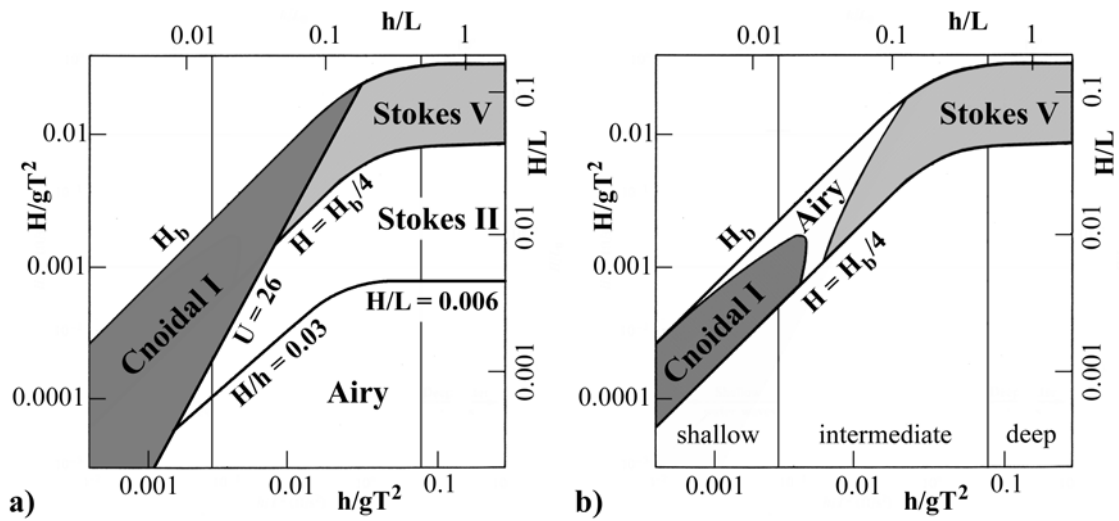
Figure C.4   **Analytical wave theories: a) recommended ranges** after Le Méhauté (1976); **b) validities** defined by the best fit to the dynamic free surface boundary condition (Dean, 1970).

Dean and Perlin (1986) compared the wave theories with laboratory and field data. The comparison revealed the utter difficulties in applying analytic monochromatic wave theories to an irregular sea.

As a practical matter, linear small-amplitude wave theory yields a valid first approximation to nonlinear theory. The solitary wave theory as a maximum limiting shallow water wave may be used to estimate the range of possible nonlinear effects. Approximate analytical solutions exist for certain steady state profiles such as the solitary and cnoidal waves, whereas transient wave profiles need to be treated numerically. The Stokes, cnoidal and solitary wave theories are somewhat deficient in accurately describing wave characteristics for larger wave steepnesses up to near breaking. Use of higher order does not result in solutions that converge when extreme wave steepnesses are considered (Schwartz, 1974). Extreme difficulties were encountered in attempting to develop these theories to higher than a few orders. Consequently numerical methods are common to the coastal engineering practice since more than two decades.

Appendix D: Triax shear tests

The triaxial shear tests were conducted by Dr. Tom Ramholt at IGT-ETH (courtesy: chair of Prof. Dr. S. Springman). A total of four triax shear tests were conducted on the PP-BaSO$_4$ granulate: three tests on the dry probes with lateral tensions σ'_3 of 50, 100 and 300 kN/m^2 plus one on a water saturated probe with $\sigma'_3 = 100$ kN/m^2. The notation regarding triax shear tests is shown in Fig. D.1a) according to Lang and Huder (1990).
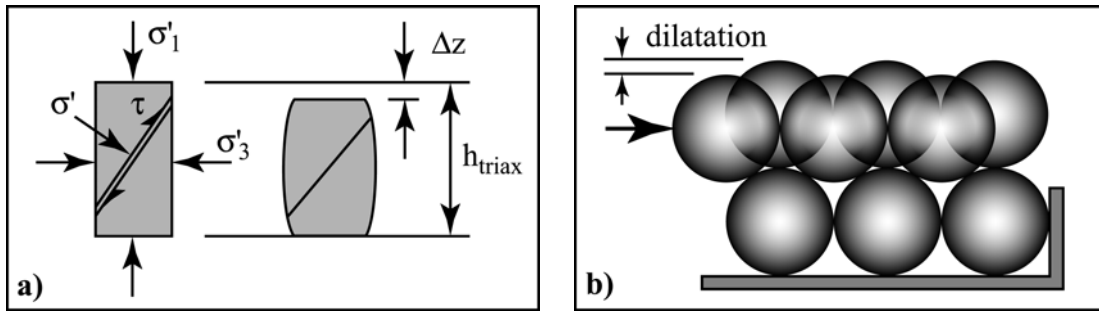

Figure D.1   **a) Notation** for triax shear tests; **b) dilatation** of densely packed spheres during failure in a plain strain shear test.

Quasi-static shear devices such as triax shear tests can only characterize the failure and yield behavior of granular materials in the quasi-static flow regime and the relevance of their results to rapid granular flows may be difficult to assess (Savage, 1984). Nevertheless triax shear tests allow to determine the type of failure, the effective internal friction angle and the volume increase during failure due to dilatation. A densely packed granulate has to dilatate in order to deform as shown in Fig. D.1b). The porosity and the mean density of the granular mass are thereby altered. A mass of densely packed spheres has a porosity $n = 26$ %, which may be increased to 49% in its loosest packing. Thereby the mean density of the bulk mass is reduced by a third. Effects of grain interaction and saltation characterizing the grain-inertia regime of rapid granular flows may further increase porosity and decrease mean slide density up to continuum break-down. In the present study a multiple quasi-static failure had to occur within the granulate at the start of an experiment to enable slide deformation whereas the sliding was induced by a failure along the bed. The slide rapidly deformed after the granulate was released from the slide box as it slid down the ramp. Grain-inertia effects such as saltation which may have been present at the slide front were nought by the slide compaction at impact on the water surface. Hence the slide deformation under forced multi-axial tensions during slide penetration into the water body may be described by granular characteristics obtained with triax shear tests.

Two dry PP-BaSO$_4$ granulate probes after failure in triax shear tests are shown in Figs. D.2a) and b), respectively. In all tests failure occurred after dilatation and no grain

failures were observed. A brittle failure is shown in Fig. D.2a) at a low lateral tension $\sigma_3' = 50 \, \text{kN}/\text{m}^2$. The probe exhibits a single failure plane. Experiments at low side tensions may correspond best to the initial slide deformation at release from the slide box, although no dominant failure plane was observed within the granular mass during sliding. The failure type transforms from a brittle failure to a plastic failure as the lateral tension increases. A plastic failure is shown in Fig. D.2b) at a high lateral tension $\sigma_3' = 300 \, \text{kN}/\text{m}^2$. Plastic failures are complex with no dominant failure plane. At slide impact on the water surface a normal pressure forcing was exerted on the slide front and only the top and back sides of the slide were free to deform whereas the bottom and lateral boundaries were given by the ramp and the wave tank walls. This complex multi-axial tension state may therefore be represented to some extent by a triax shear test with a high lateral tension.
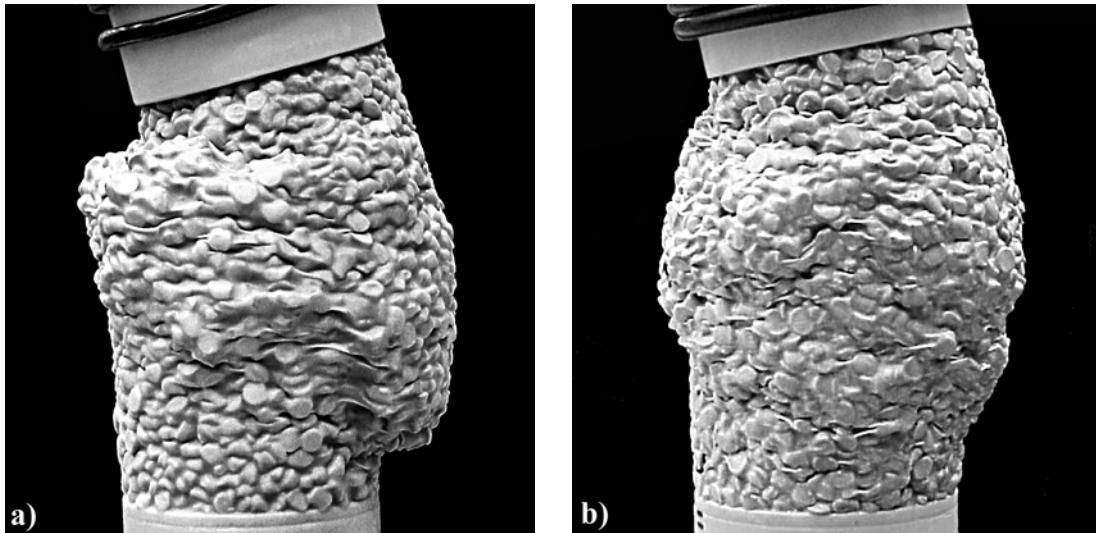
Figure D.2 **Effect of lateral tension** on failure mechanism of dry PP-BaS0$_4$ probes in triax shear tests: **a)** lateral tension $\sigma_3' = 50 \, \text{kN}/\text{m}^2$; **b)** lateral tension $\sigma_3' = 300 \, \text{kN}/\text{m}^2$ (photos: courtesy of Dr. Tom Ramholt, IGT-ETH).

The slide granulate may not be considered dry anymore after slide penetration into the water body. The initially air filled pore volume of the slide was continuously filled with ambient water as slide detrainment occurred during slide run-out. At some instance during slide run-out along the channel bottom a complete water saturation of the granulate was reached. A dry and a wet PP-BaSO$_4$ granulate probe were analyzed in triax shear tests in order to assess possible effects of pore water on the failure mechanism and the effective internal friction angle ϕ'. A dry and a wet probe are shown in Figs. D.3a) and b), respectively, after failure in experiments at a lateral tension of $\sigma_3' = 100 \, \text{kN}/\text{m}^2$. Both probes exhibited a dominant failure plane. No significant difference in failure mechanism was revealed. This may be explained by the fact that the resistance of coarse granulates is primarily due to grain interlocking. Dynamic effects such as the drag exerted by the water

on the granular slide surface during slide run-out or the flow of water through the granu-
late are not assessable with triax shear tests.
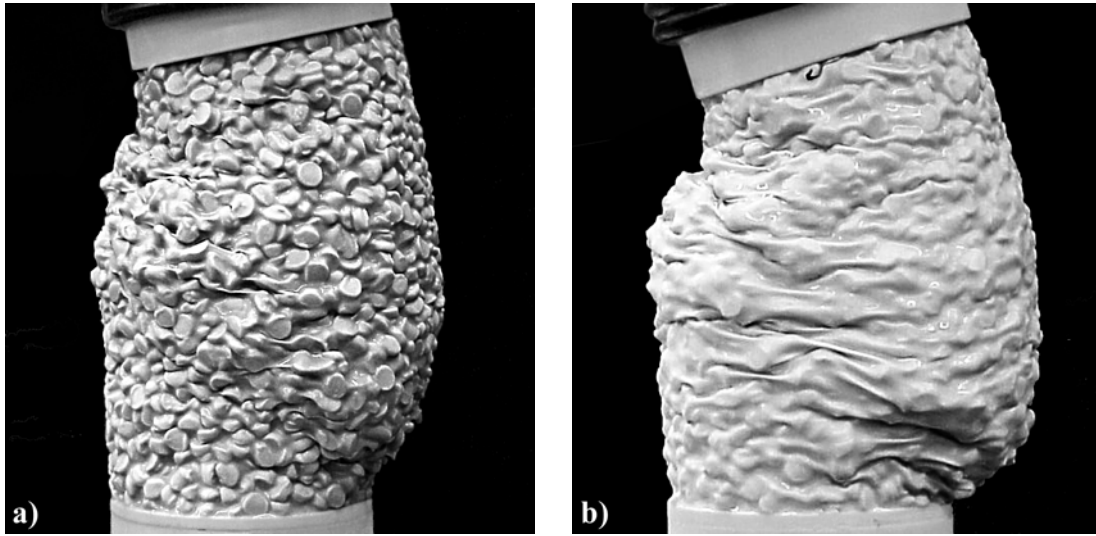
Figure D.3   **Effect of pore water** on failure mechanism of PP-BaS0$_4$ probes in triax shear
tests with $\sigma_3' = 100 \, \text{kN/m}^2$: **a)** dry granulate; **b)** water saturated granulate (photos: courtesy of
Dr. Tom Ramholt, IGT-ETH).

The triax shear test data recorded by Dr. Tom Ramholt at IGT-ETH was analyzed
according to Lang and Huder (1990). The deviator $(\sigma_1' - \sigma_3')$ and the dilatation $\Delta V/V_{triax}$
are shown in Figs. D.4a) and b), respectively.
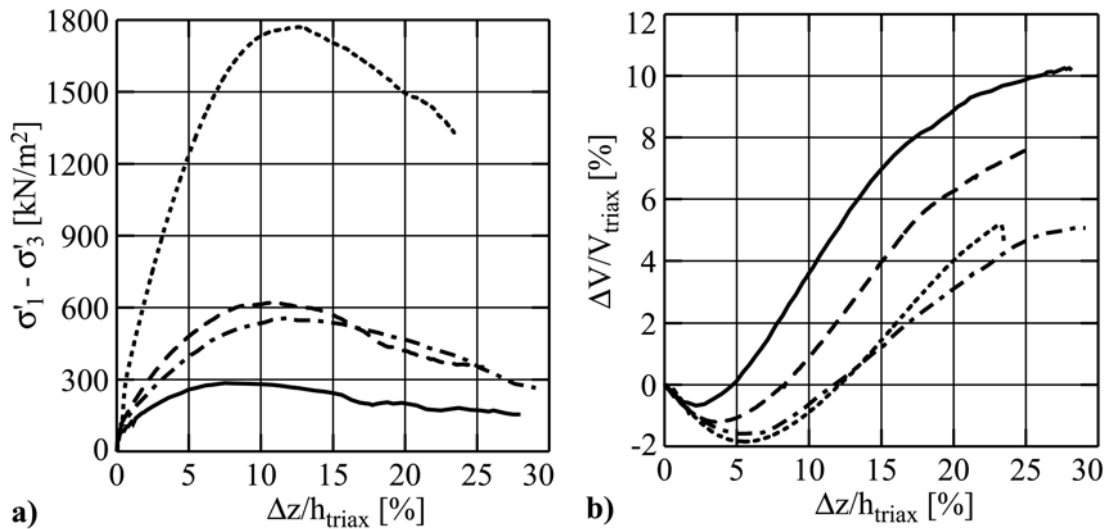
Figure D.4   **Triax shear tests** on the PP-BaS0$_4$ granulate: **a) deviator** of dry probes with
lateral tensions of (——) $\sigma_3' = 50 \, \text{kN/m}^2$, (— —) $\sigma_3' = 100 \, \text{kN/m}^2$, (----) $\sigma_3' = 300 \, \text{kN/m}^2$
and (· — ·) wet probe with $\sigma_3' = 100 \, \text{kN/m}^2$; **b) dilatation** with symbols as in a).

The deviator gives the difference between the axial tension σ_1' and the lateral tension σ_3'.
The dilatation relates the change in probe volume ΔV during deformation to the initial

probe volume V_{triax}. The deformation is described as the decrease in probe height Δz relative to the initial probe height h_{triax}. The notation is shown in Fig. D.1a). The deviator curves exhibit a characteristic behavior of granular probes with a rise to the maximum resistance at failure and a decay to the remaining ultimate resistance thereafter. The corresponding dilatation increases continuously during deformation after a minor initial compaction. Most relevant regarding the deformation of a granular mass sliding down the ramp is the experiment with the lowest lateral pressure $\sigma'_3 = 50 \, kN/m^2$. The experiment with the lowest side tension shows an increase in probe volume of 10 % during deformation.

Several failure criteria have been proposed but only the simple Mohr-Coulomb criterion prevailed. The Mohr-Coulomb failure law for a cohesion less soil yields

$$\sin \phi' \ = \ \frac{\sigma'_1 - \sigma'_3}{\sigma'_1 + \sigma'_3} \tag{D.1}$$

with effective friction angle ϕ' expressed in effective tensions σ'. The maximum resistance and the ultimate resistance were used to compute the maximum effective friction angle ϕ'_{max} and the ultimate effective friction angle ϕ'_{ult}, respectively. The shear resistance of a cohesion less soil was determined by

$$\tau_{failure} \ = \ \sigma' \tan \phi'_{max} \tag{D.2}$$

with the maximum effective friction angle ϕ'_{max}. The Mohr-Coulomb failure law is shown graphically in Fig. D.5. Mohr's tension circles are shown for both the maximum and the ultimate resistance values obtained for the PP-BaSO$_4$ granulate.
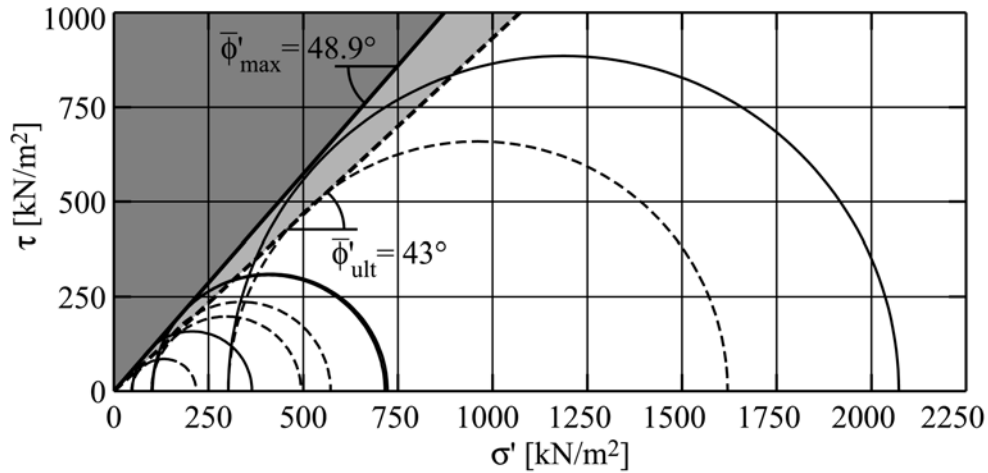
Figure D.5 **Mohr-Coulomb failure law**: Mohr's tension circles of (——) maximum and (— —) ultimate resistance values obtained with triax shear tests conducted on the PP-BaS0$_4$ granulate; (■) failure, (■) post failure deformation.

The results of the triax shear tests on the PP-BaSO$_4$ granulate are summarized in Table D.1. The mean values of the maximum effective friction angle $\bar{\phi}'_{max}$ and the ulti-

mate effective friction angle $\bar{\phi}'_{ult}$ were computed to 48.9° and 43°, respectively. More relevant regarding the deformation of the granular slide mass during granular flow down the ramp is the smaller ultimate effective friction angle ϕ'_{ult}.

***Table D.1***   **Effective internal friction angles** of the PP-BaS0$_4$ granulate obtained from triax shear tests.

Granulate	σ'_3	ϕ'_{max}	ϕ'_{ult}
dry	50 kN/m^2	49.8°	42.7°
dry	100 kN/m^2	48.8°	41.7°
wet	100 kN/m^2	48.8°	44.6°
dry	300 kN/m^2	48.2°	43.3°
		$\bar{\phi}'_{max} = 48.9°$	$\phi'_{ult} = 43°$

The triax shear tests on the artificial granulate exhibited an exemplary behavior of a coarse granulate. Hence the artificial material ideally substituted natural granulates such as gravel often used in laboratory studies of landslides. The results obtained with the artificial granulate are therefore unconditionally comparable to results obtained in experiments with natural gravels.

Appendix E: Particle image velocimetry (PIV)

E.1 Introduction

Particle image velocimetry (PIV) is a measurement technique which uses multiple images of flow tracing particles in a light sheet to measure the two in-plane velocity components of the host fluid simultaneously throughout the area of interest. The planar particle-image velocimeter optical system is shown schematically in Fig. E.1.
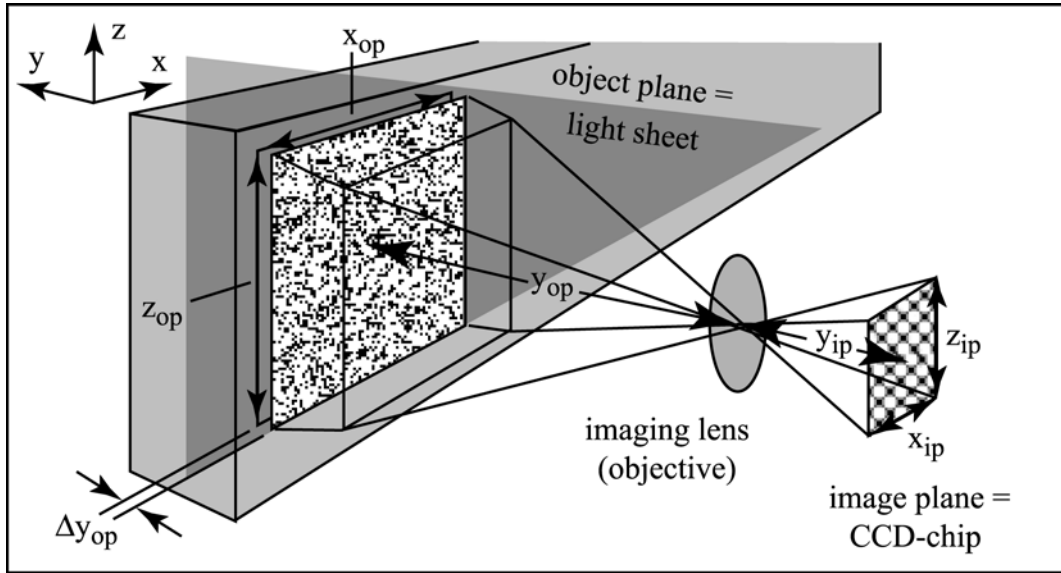
Figure E.1   **Schematic representation of the geometric imaging set-up** with all planes orthogonal to the y-axis and perspective image distortion caused by the difference in refractive index between the water in the wave tank with $n = 1.33$ and the air outside with $n = 1$.

The tracer particles in the fluid are illuminated by a pulsed laser light sheet defining the object plane. The particles scatter light into an objective lens located perpendicular to the light sheet, so that its in-focus plane coincides with the illuminated slice of fluid. The images are formed in the image plane on the chip of the digital CCD-camera. Double images of the particles are acquired at a flow velocity dependent time interval Δt and a camera magnification factor M defined as

$$M = x_{ip}/x_{op} = z_{ip}/z_{op} \qquad \text{(E.1)}$$

with coordinates denoted *ip* and *op* in the image and object planes, respectively. The factor $M \neq y_{ip}/y_{op}$ due to perspective image distortion caused by the difference in refractive index between the water in the wave tank with $n = 1.33$ and the air outside with $n = 1$.

The images are stored on a computer and the velocity vector fields are computed by means of cross-correlation analysis.

PIV had originally evolved from laser speckle velocimetry and speckle interferometry common to solid mechanics (Rösgen et al., 1990, Fomin, 1998). The initial groundwork for a PIV theory was laid down by Adrian (1988) describing the expectation value of the auto-correlation function. This description provided the framework for experimental design rules (Keane and Adrian, 1990). Then the theory was generalized to include multiple-exposure recordings (Keane and Adrian, 1991), cross-correlation analysis (Keane and Adrian, 1993) and super-resolution (Keane et al., 1995). The use of digital CCD-cameras for direct recording of the particle images on a computer became common (Willert and Gharib, 1991). As the resolution and image format of electronic cameras is still orders of magnitude lower than that of a photographic medium, digitalization cannot be ignored. The theory was extended by Westerweel (1993) to include digital PIV images and the estimation of the displacement at sub-pixel level. Reviews on the PIV method have been written by Adrian (1991), Grant (1997) and Westerweel (1997). For a collection of selected milestone papers it is referred to Grant (1994). A bibliography on PIV with nearly 1200 references was compiled by Adrian (1996). Books covering most aspects of PIV were presented by Raffel et al. (1998) and Stanislas (2000). Recent developments expanded the PIV-method to measure the three components of the velocity vector either in a plane by means of stereoscopic PIV (Grant et al., 1995; Willert, 1997; Westerweel and Van Oord, 2000) or in a volume with holographic PIV (Royer, 1997; Zhang et al., 1997; Tao et al., 2000) and scanning PIV (Brücker, 1997). Further advanced concepts for the analysis of the recordings by neural networks were also presented (Grant and Pan, 1997; Grant et al., 1998).

PIV yields spatial velocity information about instantaneous flow fields. Therefore PIV is well suited for the analysis of extremely unsteady flows such as landslide generated impulse waves or water waves in general. PIV was successfully applied to water waves since the early days of the method in numerous studies (Gray and Greated, 1988; Gray et al., 1991; Liu et al., 1992; Skyner, 1996; Hering et al., 1997, 1998; Lin et al, 1999; Roth et al., 1999; Jensen et. al, 2001; Son and Kim, 2001; among others). Only system specific aspects of the application of PIV to landslide generated impulse waves are covered here. Large scale digital particle image velocimetry (PIV) was applied to the decisive initial phase with slide impact, impulse transfer, flow separation, cavity formation, energy conversion and wave generation. The extremely unsteady three phase flow consisting of granular matter, water and air posed formidable challenges to the non-intrusive, instantaneous whole field PIV-measurement technique.
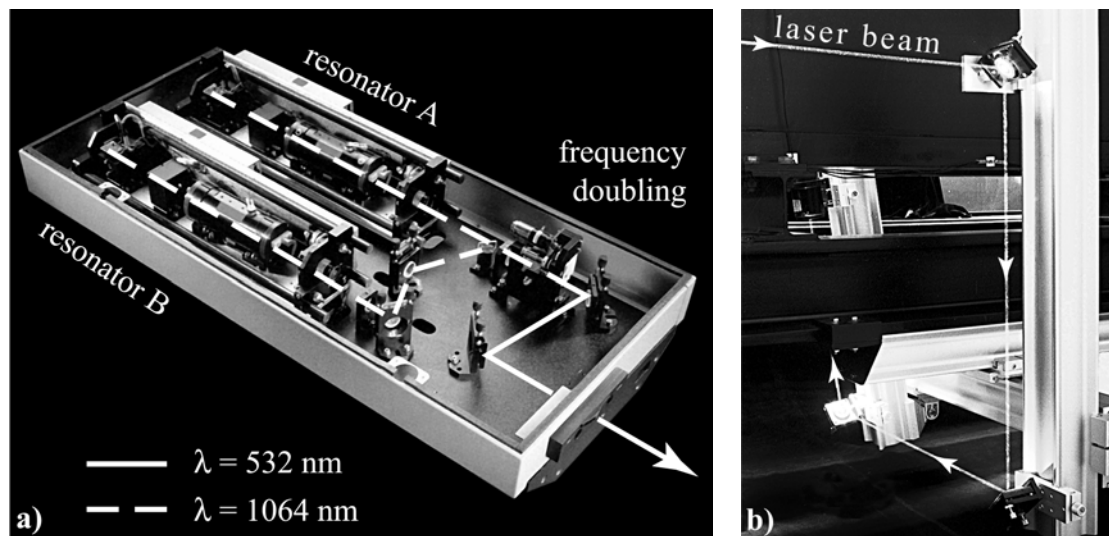
E.2 Laser light-sheet

In most applications of PIV to water waves the laser light sheet simply penetrated either vertically through the channel bottom without any disturbing optical components inside

the channel (Gray and Greated, 1988; Gray et al., 1991; Liu et al., 1992; Skyner, 1996; Jensen et. al, 2001; among others) or through the water surface (Lin et al, 1999). In this application the splash formed during impact and the slide penetration along the channel bottom denied optical access vertically through the water surface and the channel bottom in the impact area, respectively. Hence the light sheet had to be deflected from downstream into the wave generation area. Under these circumstances only a laser light-sheet could keep the measurement plain slim. Laserless PIV systems may introduce significant errors due to the depth of the measurement volume and perspective imaging. Even in a two dimensional wave flow field additional errors of up to ±10 % were reported (Walkden et al., 1998).

A twin cavity Nd.YAG-laser was used as the light source emitting frequency doubled pulses at 532nm with a repetition rate of 2×15 Hz and pulse energies of 2×225 mJ at 532 nm (Surelite-PIV, Continuum Inc., Santa Clara, Ca.). The laser had a Gaussian beam profile, a beam diameter of 5 mm and a pulse width of 5 ns at 532 nm. The peak light power during a laser pulse was equivalent to 45 MW. The solid state laser and the open beam guidance outside the wave channel are shown in Figs. E.2a) and b), respectively. The operation principle of frequency doubled Nd.YAG-lasers is described by Hecht (1992) and Hitz et al. (2001).

Figure E.2   **a) Nd.YAG-laser** with twin cavities and frequency doubling; **b) Laser beam guidance** outside and under the wave tank.

The light sheet was generated right below the partially glassed bottom of the wave channel using a three lens configuration (Hecht, 1998). The Galilean telescope was originally provided by the manufacturer (LaVision GmbH, Göttingen, D), but the optical layout was redesigned by the author and all lenses were altered (Eksma Inc., Vilnius, Lithuania). The laser light sheet and its adjustment principle are shown in Figs. E.3a) and b), respectively. First, the laser beam was sent through a plano-concave cylindrical lens (focal length $f = -90$ mm), followed by a bi-convex spherical lens ($f = +105$ mm) and

finally a plano-concave cylindrical lens ($f = -10$ mm). Altering the distance between the first two lenses allowed light-sheet thickness adjustments whereas changing the distance between the latter lenses adjusted the divergence of the light-sheet.
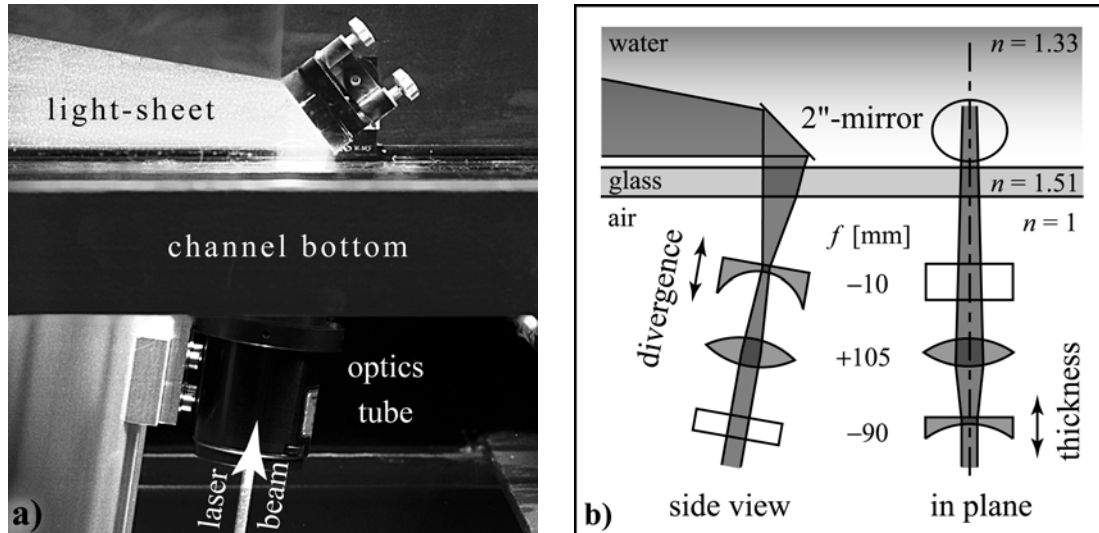
Figure E.3 **a) Laser light-sheet** and under water mirror on channel bottom; **b) Optical components** and laser light-sheet adjustment principle.

The laser beam axis penetrated the glassed channel bottom under an angle of roughly 80° to avoid aligned back reflections from the glass surface which did not have an anti-reflective coating. An under water mirror deflected the light-sheet from 2.5 to 4 m downstream axially into the wave generation zone creating a large vertical light-sheet. The large vertical light-sheet is shown in Fig. E.4 during a high speed slide impact experiment. The 2"-mirror is shown in Fig. E.3a). The axial positions along the channel of both the under water mirror and the light-sheet optics were adjusted according to still water depth, area of view and expected wave heights. The light-sheet in pure tab water had a thickness 3 mm in the area of interest. The lightsheet thickness roughly tripled to $\Delta y_{op} \approx 9$ mm in the area of interest with added seeding particles due to multiple scattering. Only the area of interest was seeded and the focus in the light-sheet thickness was set behind the area of interest to ensure a homogenic scattering intensity distribution within the whole measurement area. The light-sheet calibration plate is shown in Fig. E.6a). The exact position of the light-sheet was determined with thermo-sensitive paper (Kodak Linagraph; Galmag AG, Untersiggenthal, CH). The light absorption loss under water may be estimated to 16 % using an absorption coefficient $a = 0.042$ m^{-1} for radiation at 532 nm according to Shifrin (1988)
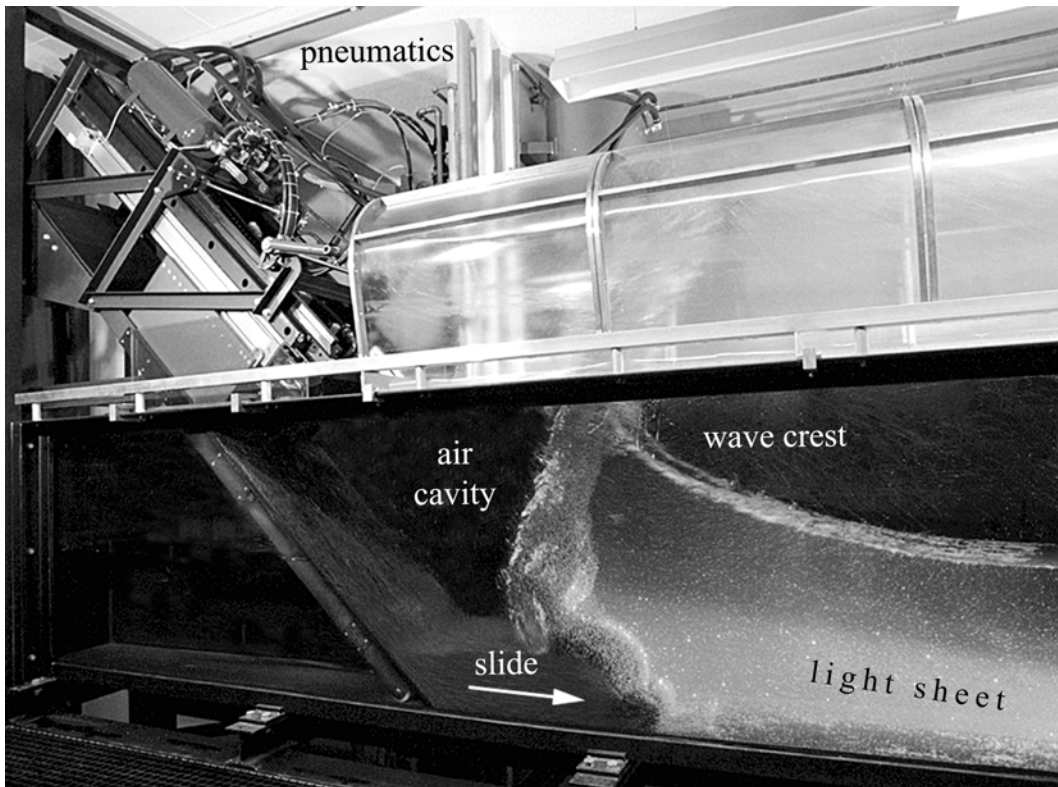
Figure E.4 **Laser light sheet** with a $f = -20$ mm plano-concave cylindrical lens (third lens) during a slide impact experiment at **F** = 3.3, $m = 108$ kg, $h = 0.45$ m and $\alpha = 45°$.

E.3 Digital image acquisition

PIV recording was conducted with a mega-resolution progressive scan CCD-camera (Holst, 1998). The full-frame interline transfer CCD-camera (Kodak-ES1.0DC) is shown in Fig. E.5a). Image areas as large as 784(H) mm $\times$ 765(V) mm were captured reading out 1008(H) $\times$ 984(V) pixels of the CCD-sensor. Images were acquired into the RAM of the PC during a maximum of 5 s at a data rate of roughly 30 MB/s – given by the 30 Hz frame rate and the 8 bit pixel-depth. The data acquisition was controlled from the analysis-software (LaVision DaVis PIV-package). Image exposure occurred in the back-to-back mode (Raffel et al., 1998). The frame straddling is shown in Fig. E.5b). The first laser pulse was placed just before the interline transfer, while the second pulse was placed thereafter. The pulse separation Δt was altered within 1 and 17 ms depending on slide impact velocity and area of view. Each pair of back-to-back single exposure images allowed velocity field calculation by means of cross-correlation. With the camera frame rate of 30 Hz the time resolution of the PIV-system was 2D-2C velocity vector field estimation at 15 Hz.

A precision measurement objective (Schneider-Kreuznach: Xenon) with a focal length $f = 25.6$ mm and a f-number $f_\# = 1.4$ (max. $f_\# = 0.95$) was used. The f-number is related to the diaphragm aperture D_a by $f_\# = f / D_a$. The objective had an excellent light

transmission of 89 % at $\lambda = 532$ nm, a relative illumination of 84 % in the corner of the images at $f_\# = 1.4$ and a geometric barrel distortion < 0.7 %. A 532 nm linepass filter (FWHM = 10 nm; Andover Corp., Salem, NH) avoided interference with the laser distance sensors at 675 nm and reduced the noise on the second image when working with room light. The reduction of light intensity due to the filter was 30 %.
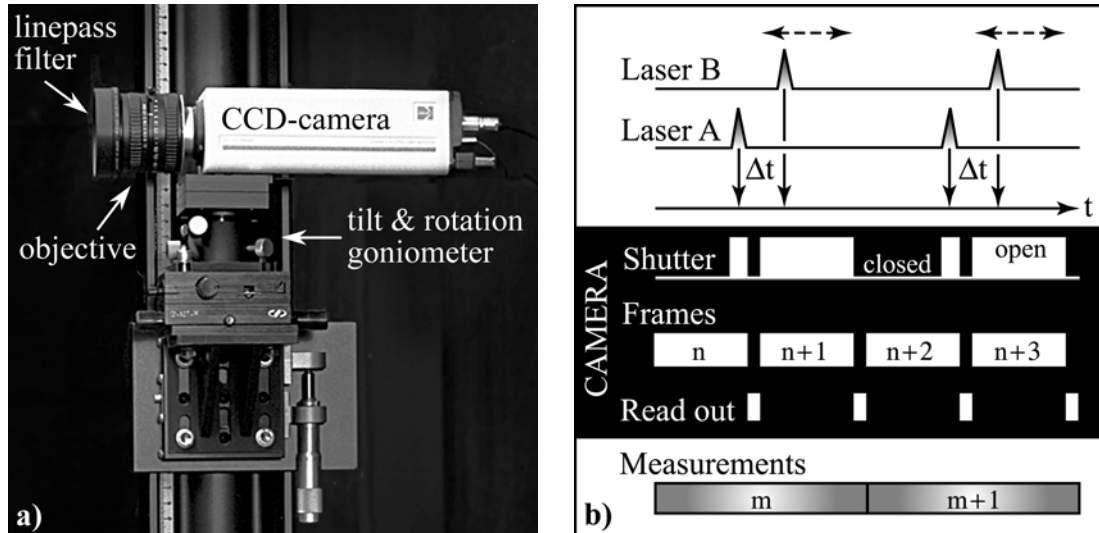

Figure E.5   **a) CCD-camera** with optics and adjustable support; **b) Frame straddling** camera operation mode with double frame single exposure measurements and adjustable laser pulse separation.

The camera was calibrated with a calibration plate positioned in the light-sheet plane. The large calibration plate with dimensions of 1.4×0.7 m and engraved crosses on a 40 mm grid is shown in Fig. E.6a).
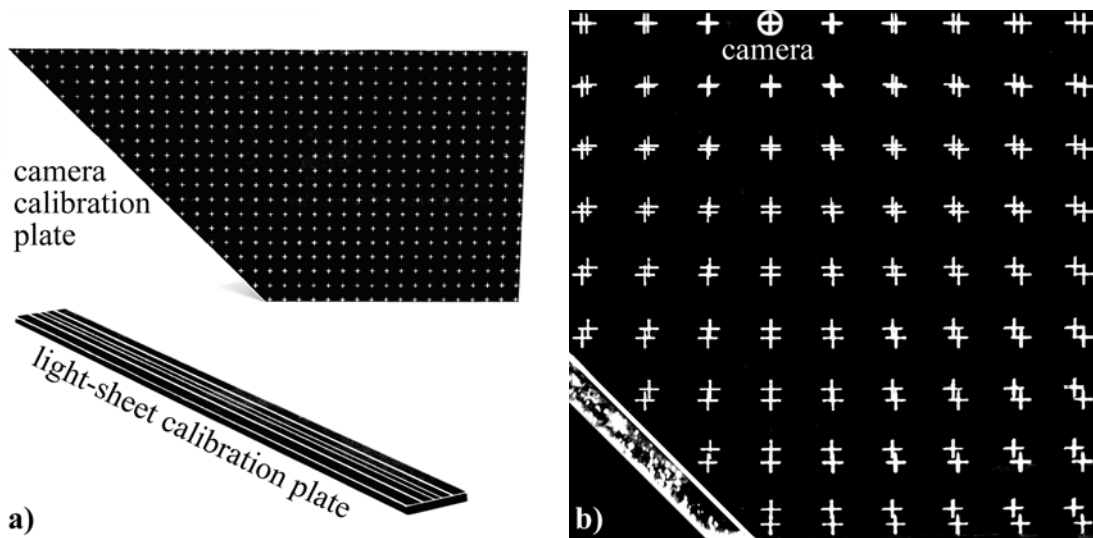
Figure E.6   **a) Calibration plates** for camera area of view and laser light-sheet positioning; **b) Overlaid calibration image parts** of an in-situ double calibration in air and under water.

Parts of overlaid calibration images acquired with an empty and water filled wave tank are shown in Fig. E.6b). The corresponding geometric imaging is shown in Fig. E.7. The observation distance was roughly 2.3 m with 2.03 m in air ($n = 1$) and 0.25 m under water ($n = 1.33$) separated by 25 mm float glass ($n = 1.51$). The difference in refractive index between air ($n = 1$) and water ($n = 1.33$) bent the ray paths at channel penetration towards the objective axis reducing effects of perspective imaging. The reduction of the under water area of view due to refraction in calibration images is shown in Fig. E.6b). The millimeter per pixel scale of an object located in the measurement plane and in the channel filled with water was 3 % smaller than in the empty channel. The recordings corresponded to images acquired with the virtual camera shown in Fig. E.16. The angular view in the measurement object roughly corresponded to objectives with a focal length $f \approx 35$ mm for the CCD-chip and $f \approx 140$ mm for standard photographic film.
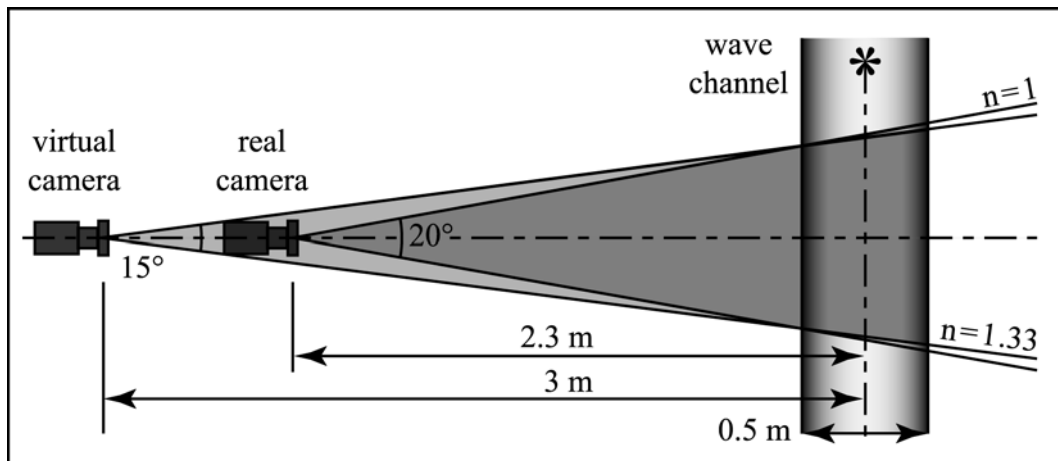
Figure E.7 **Geometric imaging** with camera angle of view and refraction in a top view of the experimental setup.

In a laser-less PIV system the perspective imaging would significantly affect the measurement accuracy. The x- and z-scales of an object in the wave channel depended on the position along the camera axis. The scales of objects located at the front and back sidewalls of the channel varied by ± 8 % relative to the channel axis in a channel filled with water and by ± 11 % in an empty channel, respectively. In the present setup errors due to perspective imaging were minimized by strictly confining the measurement volume with the laser light-sheet and the objective depth of field. Other solutions to reduce effects of perspective imaging would be to significantly increase the object distance or the use of a telecentric objective (Günther and Rudolf von Rohr, 2002). Both alternatives are difficult to use in large scale applications. Even an objective with a much larger focal length positioned at an object distance of 10 m would induce perspective errors of ± 2 % for the same area of view. Telecentric objectives for large scale applications would exceed any academic research funding.

The magnification factor was $M = 0.0115$ according to Eq. E.1. The depth of field δy was determined to

$$\delta y = 4(1 + M^{-1})^2 f_\#^2 \lambda \approx 33\,\text{mm} \qquad \textbf{(E.2)}$$

with $\lambda = 532$ nm and $f_\# = 1.4$ (Adrian, 1991). The camera position was adjusted to an accuracy of ± 1 mm. The geometric barrel distortion was corrected to an accuracy of $\pm 0.1\,\%$ with the image correction tool implemented in the analysis software (LaVision DaVis® PIV-package). The general mapping functions are the same as for stereoscopic PIV (Soloff et al., 1997). Any uncorrected distortions would directly affect the accuracy of the velocity vector field.

E.4 Seeding particles

Even with a 1k by 1k CCD-camera spatial resolution was limited for large scale applications. Large tracer particles were required to avoid peak locking problems during correlation analysis or even particle detection problems since only 60 % of the pixel areas were light sensitive. Seeding particles with a mono disperse diameter of $d_p = 1.6$ mm, a density of $\rho_p = 1.006$ g/cm^3 and a refractive index of $n = 1.52$ were used. The seeding particles are shown in Fig. E.8a).
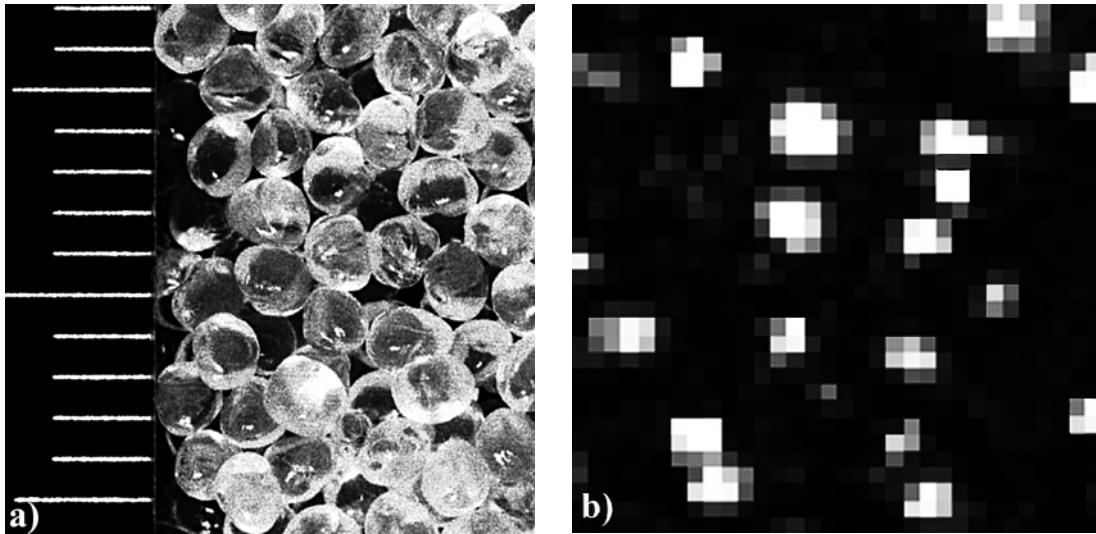
Figure E.8   **a) Seeding particles**: Grilamid, $d_p = 1.6$ mm, $\rho_p = 1.006$ g/cm^3; **b) Particle image pattern** in a 32×32 pixel interrogation window created by laser light scattering in water.

Particles of this size had to be transparent (absorption coefficient $a = 0.2$ mm^{-1}) and spherical to give round particle images as experienced during preliminary testing. Opaque particles produced shadow stripes in the light-sheet, whereas the images of ground particles were dependent on particle orientation (Bohren and Huffman, 1998; Thoroddsen and Bauer, 1999; Savas, 1985; Asano and Sato, 1980; Asano, 1979). No commercial seeding particles meeting the requirements regarding density matching, transparency, shape and size were available on the market. Grilamid (L20/L16 natur) – the lightest available

polyamide (PA12) – was kindly provided by Ems-Chemie AG (Domat/Ems, CH). Spherical particles were kindly produced by means of underwater pelletizing in a test facility (GALA Kunststoff- und Kautschukmaschinen GmbH, D).

Of key importance for the performance of the PIV flow analysis method [para E.8] are a high particle image density and a homogenous distribution of the seeding particles in the continuum. First, the amplitude of the correlation peak and the probability of a valid detection increase with increasing particle image pairs. Hence the particle image density also limits the obtainable spatial resolution corresponding to the minimal interrogation window size. Second, the particle image density has a direct influence on the measurement uncertainty (Raffel et al., 1998). The number of seeding particles N_{iw} per interrogation volume V_{iw} defined by a $p \times p$ pixel interrogation window and the laser light sheet thickness Δy_{op} is

$$N_{iw} = C_p V_{iw} = C_p \Delta y_{op} \frac{p^2}{M} \tag{E.3}$$

with the mean number of particles per unit volume C_p and magnification M (Adrian, 1984). The sample 32×32 pixels interrogation window shown in Fig. E.8b) contains $N_{iw} = 18$ particles, which results in $C_p \approx 0.3\%$ with $\Delta y_{op} \approx 9\,\text{mm}$. The probability of finding N_{iw} particles in an interrogation volume V_{iw} obeys a Poisson distribution

$$P\,(N_{iw}\ \text{in}\ V_{iw}) = \frac{(C_p V_{iw})^{N_{iw}}}{N_{iw}} e^{-C_p V_{iw}} \tag{E.4}$$

if the particles are modeled as randomly distributed points (Adrian, 1991). The number of detectable particle image pairs N_{pair} is defined as

$$N_{pair} = N_{iw}(1 - P_{il})(1 - P_{ol}) \tag{E.5}$$

with the probabilities of in-plane loss of particles P_{il} and out-of-plane loss of particles P_{ol}, respectively (Keane and Adrian, 1992). The in-plane loss of particles approaches $P_{il} \to 0$ for the applied iterative multigrid interrogation technique (Scarano and Riethmuller, 2000). The P_{ol} is assumed to be of the order of a few percent. The macro-scale flow field is well confined to 2D by the physical model and micro-scale turbulent structures are filtered out by the use of large tracer particles. In this application it is assumed that the out-of-plane velocity and accompanying effects such as out-of-plane loss of particles within Δt are negligible. This is confirmed later by the computed divergence fields with zero values [para 4.6]. The valid detection probability in a first cross-correlation pass exceeds 95% for $N_{pair} > 7$ (Keane and Adrian, 1992) or $N_{pair} > 5$ (Raffel et al., 1998). These criteria are easily fulfilled for interrogation window sizes of 64×64 and 32×32 pixel. The criteria for valid detection in a final iteration pass is $N_{pair} \geq 3$ (Raffel et al., 1998). Hence the minimal final interrogation window size is limited to 16×16 pixel.

E.5 Particle dynamics

The accuracy of the velocity determination is ultimately limited by the ability of the tracer particles to follow the instantaneous motion of the continuous medium. The flow fidelity of the seeding particles is crucial for large particles in liquids and any particles in gas flows. Most challenging are large particles in air (Grant et al., 1994). Most treatments of the behavior of seeding particles use the argument of Stokes for low Reynolds number flow around a sphere. Assuming spherical particles and neglecting the interaction between individual particles, the terminal settling velocity v_p can be derived from Stokes' drag law

$$v_p = \frac{(\rho_p - \rho_w)\, d_p^2}{18\,\mu}\, g = 8\,\text{mm/s} \tag{E.6}$$

with $d_p = 1.6$ mm and $\rho_p = 1.006$ g/cm^3. The vertical drift was two to three orders of magnitude smaller than the observed peak flow velocities. This estimation is somewhat theoretical since the particles had a certain variation in particle density due to the production process and a maximum water absorption of 1.5 %. Therefore part of the particles drifted to the water surface while others settled down. After an hour without stirring some particles were still suspended in the channel with a still water depth of $h = 0.675$ m. The simple Stokes drag model is not always a sufficient criteria (Grant, 1997; Melling, 1997). There is no need to consider the behavior of particle swarms for the present application.

Estimates of the frequency response and the behavior of tracer particles in an unsteady flow may be based on the Basset equation (Basset, 1888; Hinze, 1975; Emrich, 1981; Schmitt and Ruck, 1986; Mei, 1996). The Basset equation was applied to analyze the flow fidelity of seeding particles beneath water waves (Hering et al., 1997). The Basset equation for particles in an unsteady flow is given according to Hinze (1975) by

$$\frac{\pi d_p^3}{6}\rho_p \frac{dv_p}{dt} = 3\pi\mu d_p (v_p - v_w) + \frac{\pi d_p^3}{6}\rho_w \frac{dv_w}{dt} + \frac{1}{2}\frac{\pi}{6}d_p^3 \rho_w \left(\frac{dv_w}{dt} - \frac{dv_p}{dt}\right) \tag{E.7}$$

$$+ \frac{3d_p^2}{2}\sqrt{\pi\rho_w \mu} \int_{t_0}^{t}d\underset{\sim}{t}\left(\frac{dv_w}{d\underset{\sim}{t}} - \frac{dv_p}{d\underset{\sim}{t}}\right)/\sqrt{t - \underset{\sim}{t}}$$

with the dynamic viscosity μ, the starting time t_0 and the integration time $\underset{\sim}{t}$; the index w refers to the water and the index p to the tracer particle. The term on the left-hand side is the force required to accelerate the particle. On the right-hand side the first term is the viscous resistance force according to Stokes' law. The second term is due to the pressure gradient in the fluid around the particle imposed by fluid acceleration. The third term is the force to accelerate the "added" mass of the particle relative to the ambient fluid. The fourth or Basset term accounts for effects of the deviation in flow pattern from steady state. Hjelmfelt and Mockros (1966) presented a solution to the Basset equation for the motion of particles in an oscillatory turbulent flow. The fluid velocity v_w and the particle velocity v_p were expressed as Fourier integrals

$$v_w = \int_0^\infty [\Re \cos(\omega t) + \aleph \sin(\omega t)] d\omega \qquad \textbf{(E.8)}$$

$$v_p = \int_0^\infty \left| \frac{v_p'}{v_w'} \right| [\Re \cos(\omega t + \vartheta) + \aleph \sin(\omega t + \vartheta)] d\omega \qquad \textbf{(E.9)}$$

with the angular frequency ω of turbulent motion, the amplitude ratio $\left| v_p' / v_w' \right|$ of the particle and water velocity fluctuations v_p' and v_w', the phase lag ϑ of the particle motion and parameters $\Re$ and $\aleph$. The amplitude ratios and phase angles were computed for various density ratios ρ_p / ρ_w as function of the Stokes number Sk defined as

$$Sk = \sqrt{\frac{\nu}{\omega d_p^2}} \qquad \textbf{(E.10)}$$

which is a characteristic non-dimensional frequency of the particle response. The results are shown in Figs. E.9.
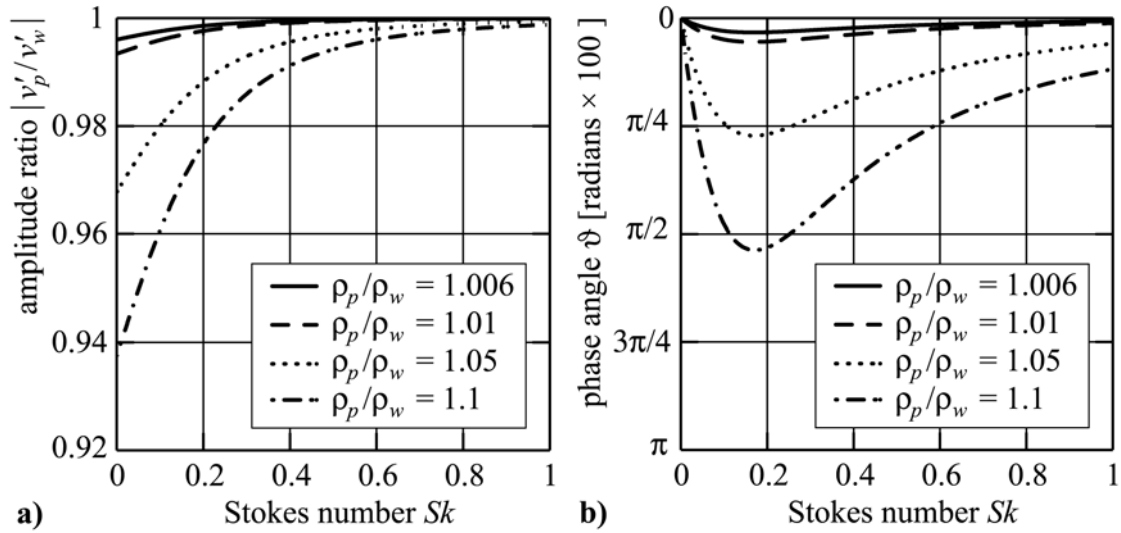
Figure E.9 **Motion of discrete particles in a turbulent fluid** according to the Hjelmfelt-Mockros solution to the Basset equation: **a) velocity fluctuation amplitude ratios**; **b) phase angles**.

In determining the response of seeding particles to an unsteady fluid velocity field, the high frequency part of the spectrum is of interest. If a particle can follow a high frequency fluctuation, it will better track the low frequency fluctuations of the large scale turbulent motion. The usual range of frequencies in turbulent flows reaches up to 10 kHz (Hinze, 1975). Assuming a maximum oscillation frequency $\omega/(2\pi) = 10$ kHz gives a Stokes number $Sk = 0.0025$ for the seeding particles with $d_p = 1.6$ mm. The curve for the seeding particles with a density ratio $\rho_p / \rho_w = 1.006$ in Fig. E.9a) gives a velocity fluctuation amplitude ratio of 0.996 or an error of only 0.4 %. This minor slip between particle and ambient fluid is negligible. The assumed oscillation frequency is more than an order of

magnitude higher than typical illumination frequencies $1/\Delta t$ between the first and the second laser pulses. For lower frequencies corresponding to higher Stokes numbers Sk the slip between particle and ambient fluid is smaller as shown in Fig. E.9a). Hence the inherent assumption in PIV, that the particles follow the fluid, is practically fulfilled.

E.6 Particle imaging

The optimum configuration of the PIV-system was determined according to Adrian (1995, 1997). The error in PIV velocity measurements strongly depends on the particle image diameter. The most important consideration in this large scale PIV application was to avoid under-sampled particle images according to Nyquist's criterion. Under-sampling would lead to both mean bias errors in locating the particle and random errors (Prasad et al., 1992; Wernet and Pline, 1993; Westerweel, 1993). The uncertainty in velocity detection would increase roughly by a factor of 10 for too small particle images (Raffel et al., 1998). The recorded particle image diameter d_τ is given approximately by

$$d_\tau = \sqrt{d_e^2 + d_r^2} = 20.6\ \mu m \tag{E.11}$$

where d_e is the optical particle image diameter prior to being recorded and $d_r = 9\ \mu m$ given by the pixel spacing represents the resolution of the CCD-sensor. The recorded particle image diameter d_τ corresponded to 2.3 pixels with the CCD-pixel diameter of 9 μm (CCD-size 9 mm^2). This ensured minimum peak detection uncertainty of 0.03 pixel according to Raffel et al. (1998). The diffracted particle image diameter d_e was estimated to

$$d_e = \sqrt{d_{diff}^2 + M^2 d_p^2} = 18.5\ \mu m \tag{E.12}$$

with the magnification factor $M = 0.0115$ and the seeding particle diameter $d_p = 1.6$ mm (Goodman, 1996). Diffraction limited imaging and a Gaussian intensity distribution of the geometric particle image were assumed (Adrian and Yao, 1985). The diffraction limited minimum image diameter d_{diff} was determined to

$$d_{diff} = 2.44(1 + M)f_\# \lambda = 2\ \mu m \tag{E.13}$$

with the laser wave length $\lambda = 532$ nm and the diaphragm aperture $f_\# = 1.4$. The diffraction limited minimum image diameter d_{diff} was only about 10 % of the recorded particle image diameter d_τ. Diffraction contributed less than 1 % to the recorded particle image diameter d_τ. Hence the tracer particles with $d_p/\lambda = 3008$ were outside the Mie scattering range and in the geometric optics light scattering range (Mie, 1908; Kerker, 1969).

In the geometric optics light scattering range with $d_p \gg \lambda$ the average energy of the scattered light increases with $(d_p/\lambda)^2$ and the particle image intensity is independent of the particle diameter, as both the scattered light and the image area increase with d_p^2 (van de Hulst, 1957; Bohren, 1998). Hence the average particle image intensity was independent of the particle image diameter. The electrical output of a photo detector array pro-

duced by the light scattered from seeding particles is proportional to the optical exposure Ex, defined as the energy per unit area (Adrian, 1991). The mean exposure $\overline{Ex}$ averaged over the area of a particle image in the geometric scattering regime is given by

$$\overline{Ex} \propto \frac{E_{laser}D_a^2}{y_{op}^2 M^2 z_{op} \Delta y_{op}} \approx 15 \text{ Jm}^{-2} \tag{E.14}$$

with a laser pulse energy $E_{laser} = 0.225$ J, a diaphragm aperture $D_a = 18.3$ mm, an object distance $y_{op} = 2.3$ m, a magnification factor $M = 0.0115$, an area of view height $z_{op} = 0.765$ m and a light sheet thickness $\Delta y_{op} = 9$ mm. This equation allows to determine the PIV system parameters within the geometric scattering regime.

E.7 Image enhancement

The extremely unsteady three phase flow consisting of granular matter, water and air complicated the image analysis and vector-field calculation. Typical raw and unprocessed PIV-images are shown in Figs. E.10. Large scale digital particle image velocimetry (PIV) was applied to the decisive initial phase. The impact area is shown in Fig. E.10a) during the first stage with slide impact, impulse transfer, flow separation, cavity formation, energy conversion and wave generation. The three phases – granular material, water and air – are separated along distinct interfaces. The granular slide is deformed due to impact and deflection at the channel bottom. The slide has reached maximum thickness and minimum length due to compaction. The characteristic "B" shape at the slide front forms due to deflection at the channel bottom. In water, laser light is scattered by transparent spherical seeding particles and a speckle pattern is formed on the slide surface in channel axis due to direct illumination from the laser light-sheet.Subsequently the cavity collapse accompanied by air inclusion and the granulate detrainment during slide run-out along the channel bottom caused the massive phase mixing shown in Fig. E.10b). The flow fields, interfuses, void fraction as well as the light scattering properties in the impact area changed completely within fractions of a second. Massive additional multi-scattering of the laser light due to the air bubbles significantly increased the background noise – note the higher background intensity level in Fig. E.10b) compared to Fig. E.10a). The light-sheet thickness broadened in large parts of the area of interest.
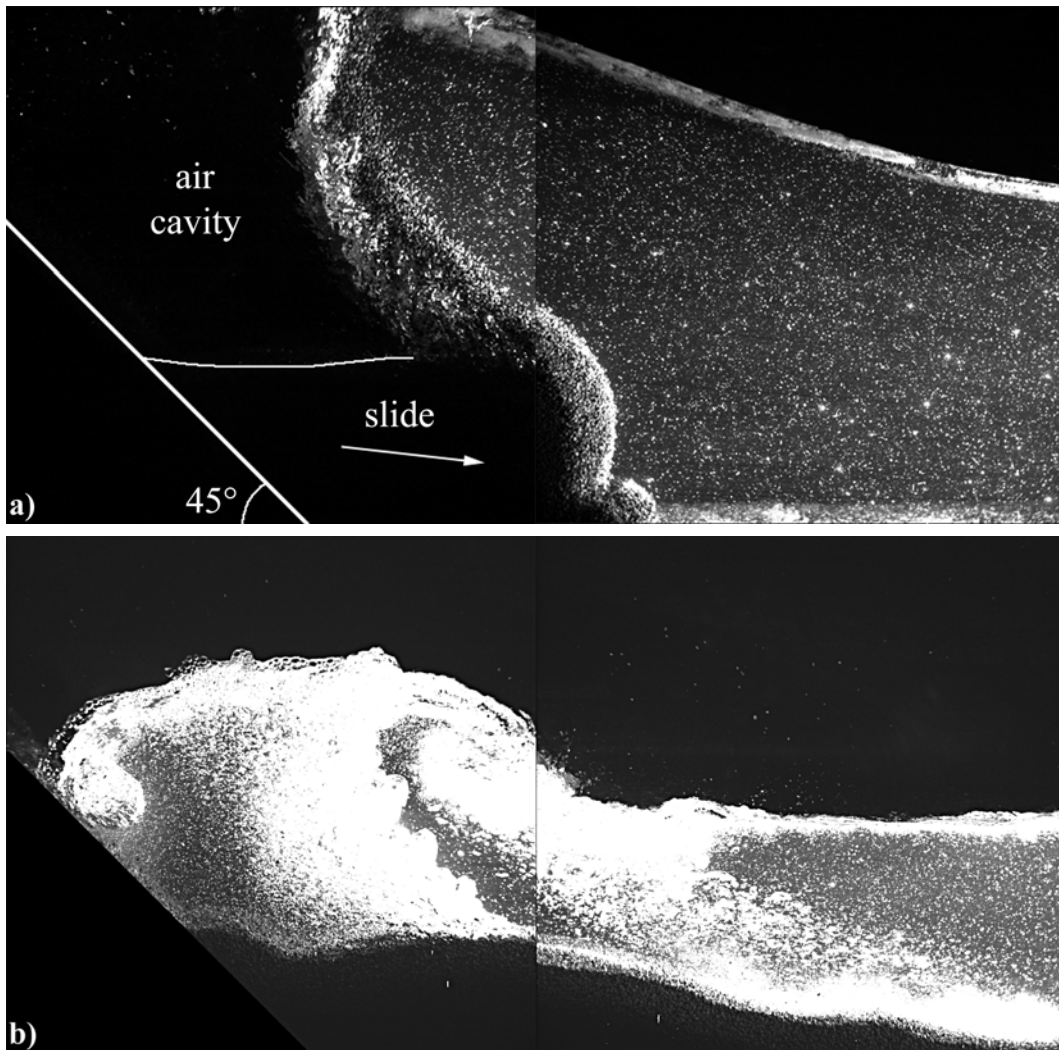
Figure E.10   **PIV-images:** two adjacent PIV-images without pre-processing from two different runs juxtaposed, total area captured 1568 mm $\times$ 765 mm; **F** = 2.0, m = 108 kg, h = 0.45 m, α = 45°, time after impact: **a)** t = **0.41 s** and **b)** t = **1.68 s**.

A velocity vector-field calculation directly from raw images by means of a correlation analysis would be biased due to the significantly varying illumination intensity levels within both time and space. Inherent assumptions in PIV are homogeneously distributed tracer particles and illumination intensity levels within corresponding interrogation windows. Further the flow fields were limited to varying parts of the images. These artefacts were accounted for during image pre-processing. Pre-processing is strongly application specific and in this case even impact stage dependent. The pre-processing steps applied to an example are shown in Fig. E.11. First the illumination intensity fluctuations in the background were removed with a sliding background subtraction (Jähne, 1997). Similar to a high pass filter the large fluctuations were filtered out whereas the small fluctuations corresponding to the tracer particle signals could pass through. Thereafter the flow field was isolated from the rest of the image with digital masks (Roth et al., 1999; Lindken et al., 1999; Brücker, 2000; Lindken and Merzkirch, 2000). The ramp and the water surface

were masked to avoid biased correlation signals due to total reflections and light scattering of floating seeding particles. The masks were further applied to distinguish between phases thereafter allowing phase separated image processing. A combined analysis method for PIV in water flow and laser speckle velocimetry (LSV) on the corona of the landslide surface was applied (Fritz, 2002). The mask shown in Fig. E.11c) isolates the water flow from the rest of the image to evaluate the velocity vector field in the water flow with PIV.
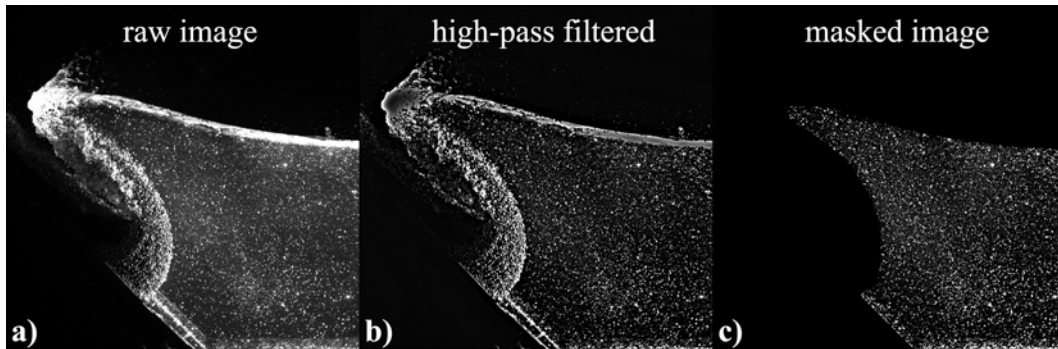
Figure E.11 **Pre-processing** on the example of a PIV-image with first laser pulse illumination – corresponding second frame is not shown: **a) raw PIV-image**; **b) high-pass filtered image**; **c) masked image**.

In order to calculate velocity vectors on the slide surface with LSV part of the slide surface were unmasked. Most of the tongue-shaped granular slide surface is both out of the light-sheet plane and camera depth of field (Eq. E.2). To avoid systematic errors because of perspective imaging of out-of-plane objects only the corona of the slide in channel axis within the depth of field and directly illuminated by the laser was left uncovered. The air bubble speckle patterns in Fig. E.10b) created by interference of the light scattered from dense air bubbles were also isolated with the same masking technique. White-out image areas in Fig. E.10b) were caused by over-illumination due to the significantly higher light scattering intensity in flow fields with large void fractions. Over-illuminated image areas where removed with masks, because it is simply impossible to retrieve even a reduced accuracy velocity vector from a white image area (Lawson et al., 1999).

E.8 Adaptive multipass cross-correlation analysis

The cross-correlation analysis was conducted using a commercial analysis software (LaVision DaVis PIV-package). A large variety of numerical interrogation techniques with numerous options were developed over the last decade – most of them being implemented in the analysis software. The software further allowed the implementation and combination with user C-code for application specific solutions. The optimum configuration of the interacting image acquisition and processing had to be determined specifically

for this large scale PIV application. An advanced interrogation technique was required to cope with the locally large velocity gradients due to the presence of a strong shock. Only the applied interrogation scheme is described herein. For an overview on the various implementations and analysis methods in PIV it is referred to Grant (1994, 1997), Westerweel (1997), Raffel et al. (1998) and Stanislas et al. (2000).

By means of cross-correlation analysis instantaneous 2D-2C velocity vector fields were computed. Although speckle patterns on the slide corona and PIV patterns in water differed strongly (Fritz, 2002), they were analyzed using the same software algorithm. For laser speckle velocimetry (LSV) conducted on the slide surface and PIV in water an adaptive multipass algorithm (Scarano and Riethmuller, 2000) was applied. The advanced digital interrogation method successfully combines several techniques: digital PIV (Willert and Gharib, 1991), cross-correlation analysis (Keane and Adrian, 1992, 1993), discrete window offset (Westerweel et al., 1997), fractional window offset (Scarano and Riethmuller, 2000), iterative multigrid processing with window refinement (Hart, 1998; Scarano and Riethmuller, 1999), window distortion (Huang et al., 1993a,b; Fincham and Spedding, 1997; Fincham and Delerce, 2000). A schematic overview on the iterative cross-correlation analysis procedure is shown in Fig. E.12.

The adaptive multipass algorithm for high-resolution analysis by using recursive local correlations builds around a basic spacial cross-correlation function R_{II} in its discrete form

$$R_{II}(\Delta x, \Delta z) = \frac{1}{p^2} \sum_{i=0}^{p-1} \sum_{j=0}^{p-1} I_1(i,j)\, I_2(i+\Delta x,\, j+\Delta z) \tag{E.15}$$

for $p \times p$ pixel interrogation windows, where I_1 and I_2 are matrix intensity functions from corresponding interrogation windows. The correlation plane for displacements Δx and Δz within $\pm p/2$ is not computed directly but via a much faster standard cyclic FFT-based algorithm (Westerweel, 1993; Raffel et al., 1998). The cross-correlation function R_{II} of the two intensity functions I_1 and I_2 is equivalent to a complex conjugate multiplication of their Fourier transforms (Bachman et al., 2000)

$$R_{II} \Leftrightarrow \hat{I}_1 \cdot \hat{I}_2^{\,*} \tag{E.16}$$

where $\hat{I}_1$ and $\hat{I}_2$ are the Fourier transforms of the matrix intensity functions I_1 and I_2, respectively, and $\hat{I}_2^{\,*}$ is the complex conjugate of $\hat{I}_2$. The fractional part of the displacement is determined by interpolation of the correlation peak. In this application the so-called three-point Gaussian interpolation method was applied (Willert and Gharib, 1991; Ronneberger et al., 1998). The velocity vector components v_x and v_z are computed by

$$v_x = \frac{\Delta x / M}{\Delta t}, \quad v_z = \frac{\Delta z / M}{\Delta t} \tag{E.17}$$

with the window displacements Δx and Δz determined from the correlation plane and the image acquisition settings given by the magnification M and the laser pulse separation Δt.
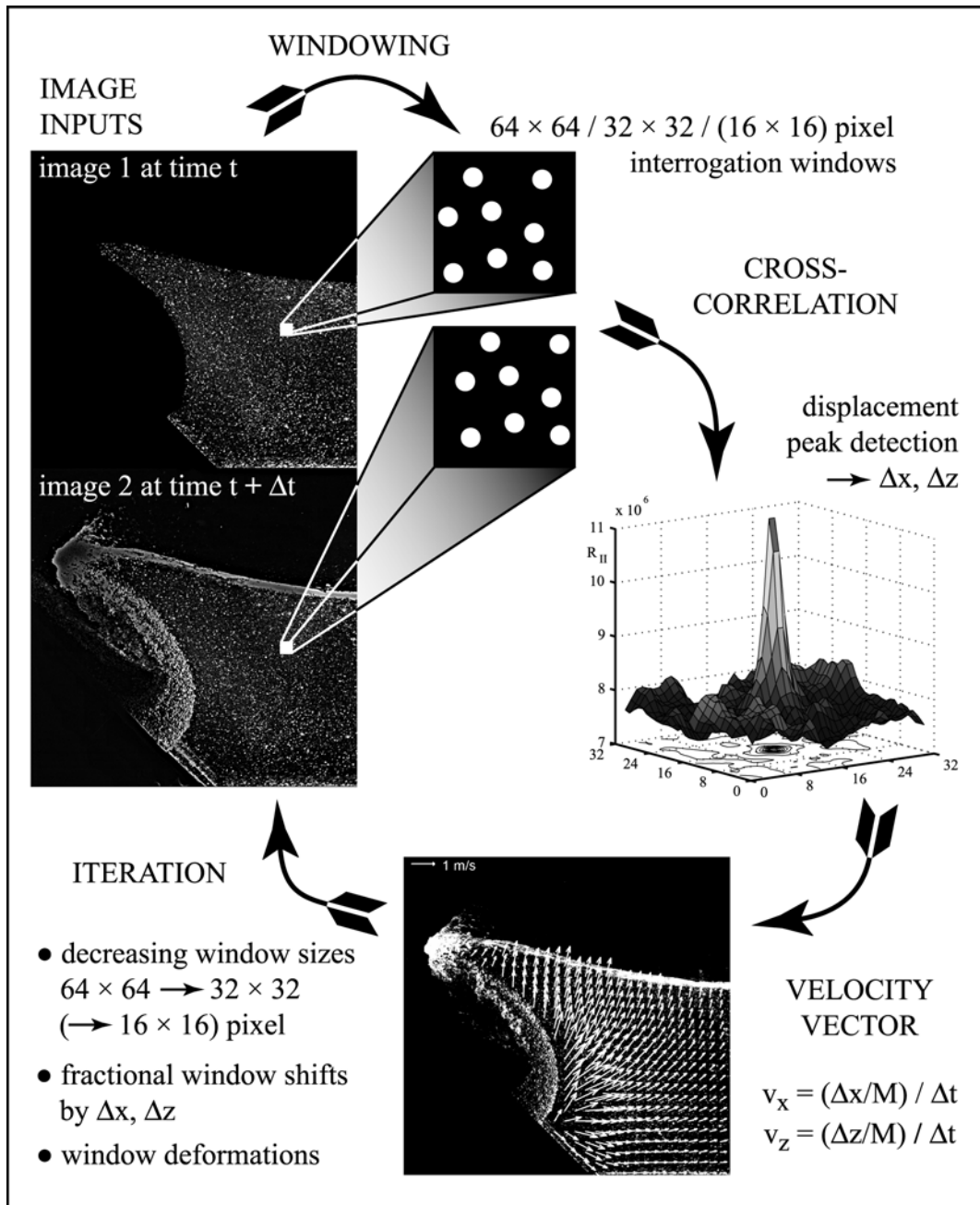
Figure E.12 **Adaptive multipass algorithm** analysis procedure based on recursive cross-correlation analysis of corresponding interrogation windows combined with iterative window refinement, window shifts and deformations.

The adaptive multi-pass algorithm first calculated a reference vector field from the double image input. A standard cross-correlation interrogation was performed with a relatively large interrogation window size (64×64 pixels) and a mean initial window shift. The calculated vector field was used as reference vector field for the next higher resolution level. The previous interrogation window size was refined after each iteration. The displacement data of the previous pass was used as a best-choice window shift to offset the interrogation windows with respect to each other. The iteration was repeated until the

final window size (32×32 or 16×16 pixels) was reached. In this manner the window shift was adaptively improved to compute the vectors with iteratively refined interrogation windows thereby increasing both spatial resolution and dynamic range. First iterations were conducted with square windows, discrete window offsets and discrete cross-correlation. Last iterations with the final window size were conducted with fractional window offsets, window deformations and continuous images computed by interpolation. The iterative analysis of the velocity vector field allowed the estimation of not only the displacement field but also the gradient spatial distribution. Similar to the grid refinement the particle separation from the penultimate pass was used for the deformation of the interrogation window in the last pass. The software calculated an imaginary vector for each corner of an interrogation window, which determined a deformation tensor for each interrogation window. The window deformation accounted for continuum deformation in terms of rotation, shearing and dilatation. A better particle matching was achieved in regions with large velocity gradients near the slide surface. The window deformation technique offers the capability to measure with displacement gradients up to 50 % (Scarano and Riethmuller, 2000). Nevertheless, the success of the method relied on a reasonable estimate of the velocity field at the first interrogation with square windows and a mean window shift. Therefore the deviation of the particle separations within an interrogation window over Δt should not exceed the mean particle diameter (Keane and Adrian, 1990). From this restriction follows the recommended upper limit of 5 % for the displacement differences within a 32×32 interrogation window with respect to the mean displacement (Keane and Adrian, 1992). Raffel et al. (1998) report simulations with displacement gradients up to 15%.

During the iteration process questionable vectors were detected and rigorously removed to avoid loss of correlation in the following iteration with a refined grid. Spurious vectors in general originate from undersampled interrogation spots. In this application the amount of spurious vectors in the water flow field was relatively low (about 1 %). Spurious vectors were determined with a local median filter and a peak ratio or so-called Q-factor (Westerweel, 1994; Nogueira et al., 1997; Hart, 2000).

In practice velocity vectors could be calculated from maximum window displacements up to 20 pixels. Large velocity vectors near the slide front could still be computed from particle image displacements which are larger than the final window sizes using the adaptive multi-pass algorithm since the window shifts were locally adapted to the mean local flow. For comparison in a single-pass standard cross-correlation analysis without local velocity vector predictors as initial window shifts and an interrogation window size of 16×16 pixels velocity vectors could be calculated from up to 8 pixel window displacements at best – in practice only 4 pixels. In general window displacements after subtracting the initial window shift should not exceed a quarter of the interrogation window size (Keane and Adrian, 1990).

Super-resolution PIV consisting in a further reduction of the final window size (Hart, 1998) or a final combination with a particle tracking velocimetry (PTV) algorithm (Keane et al., 1995; Takehara et al., 2000) for particle pairing was useless in this application. Test

interrogations with final window sizes of 8×8 pixels resulted in a significant increase in measurement noise as had to be expected (Keane et al., 1995). Undersampling inevitably leads to a decay in measurement accuracy for such small interrogation windows.

E.9 Dynamic velocity range and spatial resolution

The key image acquisition parameters together with the interrogation algorithm determined the performance of the PIV system. An optimum configuration of the interacting image acquisition and processing parameters was determined for this application. After selection of the area of view and with the given CCD-sensor the magnification M and the tracer particle diameter d_p were determined by Eq. E.1 and by solving Eq. E.12 for d_p, respectively. Then the task reduced to an optimization of the laser pulse separation Δt depending on the maximum flow field velocity, the magnification and the interrogation technique (Boillot and Prasad, 1996). A PIV system is described by the dynamic velocity range (DVR), the dynamic spatial resolution (DSR) and the accuracy according to Adrian (1997). The dynamic velocity range in the x-axis was defined as

$$DVR = \frac{v_{x_{max}}}{\varepsilon_{v_x}} = \frac{\Delta x_{max}}{\varepsilon_{\Delta x}} = 160 \qquad \text{(E.18)}$$

with the maximum displacement in the image plane Δx_{max} and the random displacement error $\varepsilon_{\Delta x}$. Analogous definition holds for the z-axis. The maximum displacement $\Delta x_{max} = 16$ pixel in the image plane corresponded to a quarter of the initial interrogation window size 64×64 pixel, which should not be exceeded after initial window shift subtraction (Keane and Adrian, 1990). A conservative assumption was made for the random displacement error $\varepsilon_{\Delta x} = 0.1$ pixel defining the minimum resolvable displacement fluctuation [para E.10]. The laser pulse separation Δt was determined for each experiment from Eq. E.17 with the allowed maximum displacement $\Delta x_{max} = 16$ pixel, the given CCD-Pixel dimension of 9 µm and the expected maximum flow field velocity. The random displacement error $\varepsilon_{\Delta x} = 0.1$ pixel corresponds to $\varepsilon_{v_x} = 0.035$ m/s at a slide impact velocity $v_s = 8$ m/s. The random velocity error ε_{v_x} varied proportionally with $v_{x_{max}}$, because the laser pulse separation Δt was adapted to the maximum flow field velocity of an experiment.

The dynamic spatial range (DSR) was defined as the area of view divided by the smallest resolvable spatial variation. Essentially, this ratio is the same as the number of independent (i.e. non-overlapping) vector measurements that can be made across the linear dimension of the area of view. The dynamic spatial range (DSR) was defined as

$$DSR = \frac{x_{ip}}{p} = 63 \qquad \text{(E.19)}$$

for an interrogation window size with $p = 16$ pixels and the image plane dimension $x_{ip} = 1008$ pixels. The DSR = 31 for an interrogation window size with $p = 32$ pixels. The

DSR would be limited by the maximum displacement $\Delta x_{max} = 16$ pixel if interrogation window sizes with $p < 16$ were applied and given by $DSR = x_{ip}/\Delta x_{max} = 63$. Hence a further decrease in interrogation window size during image analysis would not increase spatial resolution. The interrogation window sizes $p = 16$ and 32 pixels correspond to 12.4 and 24.8 mm, respectively, in the object plane with $M = 0.0115$.

E.10 Measurement accuracy

In depth investigations of the different errors involved in PIV with a combination of numerical simulations with synthetic images and experimental benchmark cases were conducted by Huang et al. (1997), Raffel et al. (1998) and Westerweel (2000). The measurement accuracy in PIV depends on the experimental setup and an optimum configuration of the interacting image acquisition and processing. The measurement error is a function of the particle image displacement, the particle image diameter, the velocity gradient within the interrogation window and the image density represented by the particle image pairs in the interrogation window. Further the numerical interrogation technique has a strong influence on the accuracy (Fincham and Delerce, 2000). The absolute measurement error of a single displacement vector ε_{tot} may be expressed as

$$\varepsilon_{tot} = \underbrace{\varepsilon_{bias} + \varepsilon_{v}}_{analysis} + \underbrace{\varepsilon_{optics} + \varepsilon_{track}}_{recording} \tag{E.20}$$

with a bias error ε_{bias}, a random error ε_{v}, an optical imaging error ε_{v} and a particle flow tracking error ε_{track}. The first two errors arise from the interrogation technique and the latter two from the recording process. The absolute measurement error of a single displacement vector ε_{tot} was determined to $\varepsilon_{tot} \leq 0.07$ m/s .

The interrogation window deformation minimized errors due to velocity gradients within interrogation windows. The adaptive multipass algorithm allowed to nought the bias error $\varepsilon_{bias} \rightarrow 0$ (Scarano and Riethmuller, 2000). The optical imaging error was determined to $\varepsilon_{optics} \leq 0.008$ m/s at a slide impact velocity $v_s = 8$ m/s from uncorrected optical distortions of ± 0.1 % [para E.6]. The particle flow tracking error was computed to $\varepsilon_{track} = 0.008$ m/s with Eq. E.6.

The random error was computed to $\varepsilon_{v} \leq 0.05$ m/s from the random displacement error. A conservative assumption was made for the random displacement error $\varepsilon_{\Delta x} = 0.1$ pixel defining the minimum resolvable displacement fluctuation (Raffel et al., 1998; Scarano and Riethmuller, 2000). The random displacement error $\varepsilon_{\Delta x} = 0.1$ pixel corresponds to $\varepsilon_{v_x} = 0.035$ m/s or $\varepsilon_{v} = 0.05$ m/s at a slide impact velocity $v_s = 8$ m/s. The random velocity error ε_{v_x} varied proportionally with $v_{x_{max}}$, because the laser pulse separation Δt was adapted to the maximum flow field velocity of an experiment. Hence the random velocity error decayed to $\varepsilon_{v} = 0.015$ m/s at a slide impact velocity $v_s = 2.5$ m/s . For comparison Son and Kihm reported a random displacement error of

$\varepsilon_{\Delta x} = 0.04$ pixel in a similar application of PIV to surface wave breaking and with the same analysis software (LaVision DaVis® PIV-package). The accuracy of PIV measurements evolved together with the advances in PIV. An interrogation uncertainty of 0.001 pixels for the algorithm used in this application was determined from numerical simulations with synthetic images (Scarano and Riethmuller, 2000). Synthetic images were used to compare the performance of various analysis algorithms (Monnier et al., 2000). Interrogation uncertainty levels of 0.1 pixels were confirmed for PIV measurements interrogated with standard cross-correlation analysis and sub-pixel interpolation (Willert and Gharib, 1991), whereas without sub-pixel interpolation the interrogation uncertainty was limited to 0.5 pixels (Hesselink, 1988). For the interrogation analysis with discrete window offset and sub-pixel interpolation random errors of 0.04 pixel were confirmed in a grid-turbulence experiment (Westerweel et al., 1997).

Comparisons of PIV measurements with single point sensors are usually based on time averaging over many samples (Grant and Owens, 1990). Various authors ensured the accuracy and reliability of PIV by comparison with laser doppler anemometry (LDA). Difference errors between the two techniques were normally less than 2 % (Liu et al., 1992). An other comparison of analog PIV measurements with LDA measurements and direct numerical simulations (DNS) confirmed a measurement accuracy of about 1 % of the full-scale velocity (Liu et al., 1991). A PIV-system error of 4 mm/s was given by Lin et al. (1999) for an application of PIV to the run-up of solitary waves with roughly half the camera area of view compared to this application. In an application of PIV to Stokes' waves a relative standard deviation of 0.6 % for PIV velocity measurements was achieved and further the velocity measurements matched the Stokes wave theory with deviations of a few percent (Jensen et al., 2001).

Appendix F: Flow field quantities

F.1 Critical points

A convenient way to describe the processes that take place in a flow is through its topology. Complex flow patterns may be described by the critical point concept, which provides a framework and methodology. At critical points (or singular points) in the flow field the streamline slope becomes indeterminate and the velocity is instantaneously zero relative to an appropriate observer. Singular points are the salient features of a flow pattern – given their type and distribution, most of the remaining flow field may be deduced (Hunt et al., 1997). The generic flow patterns are shown in Fig. F.1. The flow fields in the slide impact and impulse wave generation area were extremely unsteady. In an unsteady flow the streamlines, the particle paths and the streaklines are different, whereas in a steady flow their all identical. In the unsteady flow PIV provided an instantaneous velocity vector field, which allowed the extraction of instantaneous streamlines being tangent to the velocity vector field in every point. The streamline patterns evolved with time and the singular points propagated outward with the impulse waves.
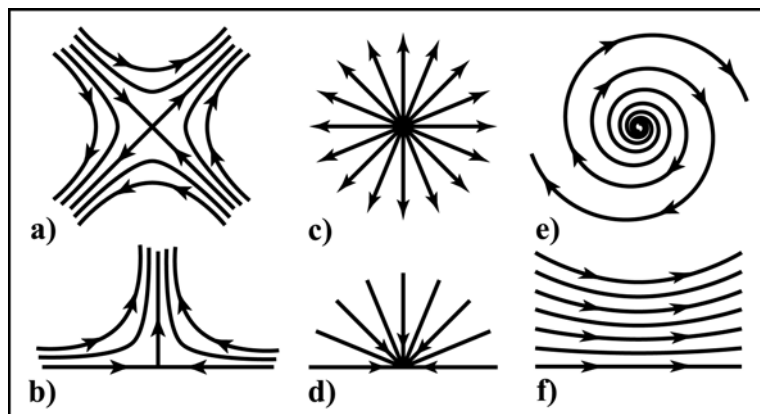
Figure F.1   **Generic flow types: a)** saddle point, **b)** half-saddle, **c)** nodal point, **d)** half-node, **e)** foci or eddie, **f)** streaming zone.

The macro structure of the flow was two-dimensional as confirmed by the by the in-plane divergence fields. The only exception was the turbulent dissipation after the impact crater collapse. Therefore no nodal points were observed. Further the whole landslide impact and wave generation process did not contain eddies, except in the phase mixing in the wake of the slide. Hence the dominant parts of the flow fields were rotationless, which is confirmed later. Rotation only played a fundamental role in the breaking of waves and the formation of bores.

F.2 Deformation tensor

In general the pressure, density and velocity fields would be required to completely recover all terms in the Navier-Stokes equation. Clearly, the task of obtaining all these field quantities simultaneously is unrealistic at present. However, the velocity fields obtained by PIV can be used to estimate other fluid mechanical quantities by means of differentiation or integration.

First it is determined which terms can actually be calculated from the planar velocity fields. The standard PIV only provides a two-dimensional projection of the three-dimensional velocity vector, while more advanced PIV methods such as stereoscopic PIV provide three-component velocity data. Unless several light sheet planes are recorded simultaneously the PIV method can only provide a single plane of velocity data, thereby excluding any possibility of calculating gradients normal to the light sheet. In order to show which differential terms can actually be computed, the full velocity gradient tensor or deformation tensor δv_p may be given first

$$\delta v_p = \begin{bmatrix} \dfrac{\partial v_{px}}{\partial x} & \dfrac{\partial v_{py}}{\partial x} & \dfrac{\partial v_{pz}}{\partial x} \\[2mm] \dfrac{\partial v_{px}}{\partial y} & \dfrac{\partial v_{py}}{\partial y} & \dfrac{\partial v_{pz}}{\partial y} \\[2mm] \dfrac{\partial v_{px}}{\partial z} & \dfrac{\partial v_{py}}{\partial z} & \dfrac{\partial v_{pz}}{\partial z} \end{bmatrix} \tag{F.1}$$

with the particle velocity vector v_p and its components v_{px}, v_{py} and v_{pz}. The terms which may be determined with standard planar PIV are written bold. The decomposition of the deformation tensor into a symmetric part and an anti symmetric part yields

$$\delta v_p = \begin{bmatrix} \dfrac{\partial v_{px}}{\partial x} & \dfrac{1}{2}\left(\dfrac{\partial v_{py}}{\partial x}+\dfrac{\partial v_{px}}{\partial y}\right) & \dfrac{1}{2}\left(\dfrac{\partial v_{pz}}{\partial x}+\dfrac{\partial v_{px}}{\partial z}\right) \\[2mm] \dfrac{1}{2}\left(\dfrac{\partial v_{px}}{\partial y}+\dfrac{\partial v_{py}}{\partial x}\right) & \dfrac{\partial v_{py}}{\partial y} & \dfrac{1}{2}\left(\dfrac{\partial v_{pz}}{\partial y}+\dfrac{\partial v_{py}}{\partial z}\right) \\[2mm] \dfrac{1}{2}\left(\dfrac{\partial v_{px}}{\partial z}+\dfrac{\partial v_{pz}}{\partial x}\right) & \dfrac{1}{2}\left(\dfrac{\partial v_{py}}{\partial z}+\dfrac{\partial v_{pz}}{\partial y}\right) & \dfrac{\partial v_{pz}}{\partial z} \end{bmatrix} \tag{F.2}$$

$$+ \begin{bmatrix} 0 & \dfrac{1}{2}\left(\dfrac{\partial v_{py}}{\partial x}-\dfrac{\partial v_{px}}{\partial y}\right) & \dfrac{1}{2}\left(\dfrac{\partial v_{pz}}{\partial x}-\dfrac{\partial v_{px}}{\partial z}\right) \\[2mm] \dfrac{1}{2}\left(\dfrac{\partial v_{px}}{\partial y}-\dfrac{\partial v_{py}}{\partial x}\right) & 0 & \dfrac{1}{2}\left(\dfrac{\partial v_{pz}}{\partial y}-\dfrac{\partial v_{py}}{\partial z}\right) \\[2mm] \dfrac{1}{2}\left(\dfrac{\partial v_{px}}{\partial z}-\dfrac{\partial v_{pz}}{\partial x}\right) & \dfrac{1}{2}\left(\dfrac{\partial v_{py}}{\partial z}-\dfrac{\partial v_{pz}}{\partial y}\right) & 0 \end{bmatrix} \tag{F.3}$$

and the substitution of the strain and vorticity components results in

$$
\delta v_p = \begin{bmatrix} \varepsilon_{xx} & \frac{1}{2}\varepsilon_{xy} & \frac{1}{2}\varepsilon_{xz} \\[2mm] \frac{1}{2}\varepsilon_{yx} & \varepsilon_{yy} & \frac{1}{2}\varepsilon_{yz} \\[2mm] \frac{1}{2}\varepsilon_{zx} & \frac{1}{2}\varepsilon_{zy} & \varepsilon_{zz} \end{bmatrix} + \begin{bmatrix} 0 & \frac{1}{2}\omega_z & -\frac{1}{2}\omega_y \\[2mm] -\frac{1}{2}\omega_z & 0 & \frac{1}{2}\omega_x \\[2mm] \frac{1}{2}\omega_y & -\frac{1}{2}\omega_x & 0 \end{bmatrix}
\tag{F.4}
$$

with the elongational strains ε_{xx}, ε_{yy} and ε_{zz}, the shearing strains $\varepsilon_{xy} = \varepsilon_{yx}$, $\varepsilon_{xz} = \varepsilon_{zx}$ and $\varepsilon_{yz} = \varepsilon_{zy}$. The curl of the velocity vector yields the vorticity vector

$$
\omega = \operatorname{curl} v_p = \nabla \times v_p
\tag{F.5}
$$

with the components ω_x, ω_y and ω_z. Thus the symmetric tensor represents the strain tensor with the elongational strains on the diagonal and the shearing strains on the off-diagonal, whereas the anti symmetric part contains only the vorticity components of the vorticity vector.

F.3 Differential quantities

The applied standard planar PIV provided only the v_{px} and v_{pz} components of the particle velocity vector v_p. Further only a single plain was measured simultaneously and therefore the data could only be differentiated in the x and z directions. Hence only a few terms of the deformation tensor δv_p could be extracted from the planar velocity vector fields determined by PIV. The following terms were computed

$$
\varepsilon_{xx} + \varepsilon_{zz} = \frac{\partial v_{px}}{\partial x} + \frac{\partial v_{pz}}{\partial z}
\tag{F.6}
$$

$$
\omega_y = \frac{\partial v_{px}}{\partial z} - \frac{\partial v_{pz}}{\partial x}
\tag{F.7}
$$

$$
\varepsilon_{xx} - \varepsilon_{zz} = \frac{\partial v_{px}}{\partial x} - \frac{\partial v_{pz}}{\partial z}
\tag{F.8}
$$

$$
\varepsilon_{xz} = \frac{\partial v_{pz}}{\partial x} + \frac{\partial v_{px}}{\partial z}
\tag{F.9}
$$

corresponding to the in plane divergence $\varepsilon_{xx} + \varepsilon_{zz}$, the out of plane vorticity component ω_y, the elongational strain rate $\varepsilon_{xx} - \varepsilon_{zz}$ and the shear strain rate ε_{xz}. Local velocity vector fields resulting in positive estimates of the vorticity, the shear strain and the elongational strain as well as the deformations of the fluid element are shown in Figs. F.2a,b), respectively. The vorticity component ω_y is positive if $\partial v_{px}/\partial z > 0$ and $\partial v_{pz}/\partial x < 0$ which corresponds to a driving rotation regarding the breaking of a wave propagating in positive x-

direction. The shear strain ε_{xz} is positive if $\partial v_{px}/\partial z > 0$ and $\partial v_{pz}/\partial x > 0$. In an irrotational distortion the principal axes of deformation do not change their orientation in contrast to a rotational motion. In this context it may be worthwhile recalling that a simple shear flow along a boundary is not at all irrotational but causes high vorticity values over a narrow linear region (Tritton, 1988). The elongational strain $\varepsilon_{xx} - \varepsilon_{zz}$ is positive if $\partial v_{px}/\partial x > 0$ and $\partial v_{pz}/\partial z < 0$ which corresponds to an elongation of the fluid element along the x-axis.
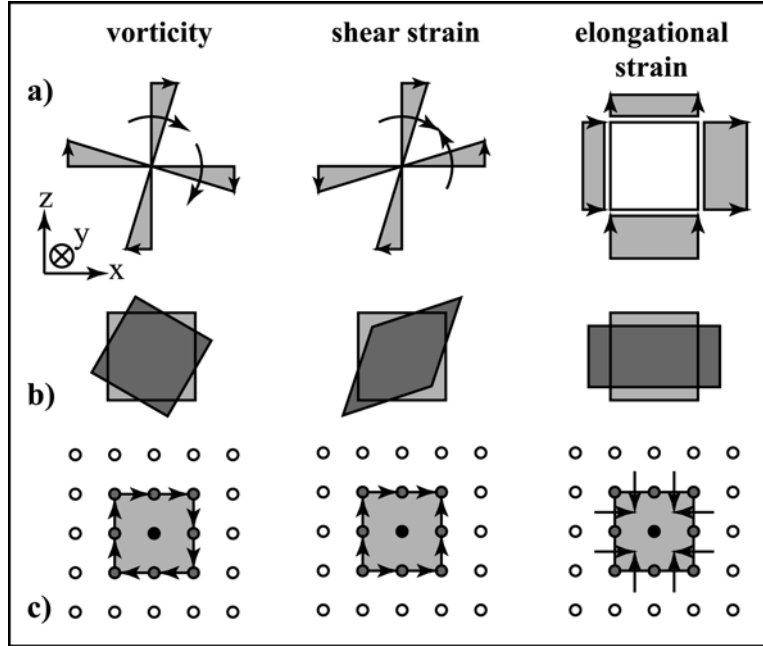
Figure F.2   **Differential quantities** obtainable with planar PIV data: vorticity, shear strain and elongational strain; **a) velocity vector fields** resulting in positive differential quantities; **b) deformation** of the fluid element; **c) implementation** of the differential estimators.

The conservation of mass equation for an incompressible fluid, where ρ is constant, reduces to the simple form

$$\text{div } v_p = \nabla v_p = \varepsilon_{xx} + \varepsilon_{yy} + \varepsilon_{zz} = \frac{\partial v_{px}}{\partial x} + \frac{\partial v_{py}}{\partial y} + \frac{\partial v_{pz}}{\partial z} = 0 \qquad \textbf{(F.10)}$$

which must be true at every location in the fluid (Meyer, 1971). This equation is also referred to as the continuity equation. The flow field satisfying Eq. F.10 is termed a non-divergent flow. The sum of the in-plane extensional strains $\varepsilon_{xx} + \varepsilon_{zz}$ corresponds to the two dimensional divergence. The out-of-plane strain ε_{yy} may be determined by

$$\varepsilon_{yy} = \frac{\partial v_{py}}{\partial y} = -(\varepsilon_{xx} + \varepsilon_{zz}) = -\left(\frac{\partial v_{px}}{\partial x} + \frac{\partial v_{pz}}{\partial z}\right) \qquad \textbf{(F.11)}$$

if the condition for an incompressible flow Eq. F.10 is fulfilled. The flow may be considered two dimensional if $\varepsilon_{xx} + \varepsilon_{zz} = 0$ prevails. However it should be kept in mind that $\varepsilon_{xx} + \varepsilon_{zz} \neq 0$ would only indicate the presence of an out-of-plane flow, whereas the out-

of-plane velocity may only be measured with stereoscopic PIV (Grant et al., 1995; Willert, 1997; Westerweel and Van Oord, 2000). In this regard it is interesting to note that the additional availability of the third velocity component in a single plane would not lead to any additional strains or vorticity components. The full deformation tensor may only be determined with instantaneous three velocity component measurements in a whole volume. All three velocity components may be measured instantaneously in a volume by means of holographic PIV at present resulting in up to 1 million simultaneous velocity vectors (Royer, 1997; Zhang et al., 1997; Tao et al., 2000).

F.4 Differential estimators

Since PIV provides the velocity vector field sampled on a two-dimensional, evenly spaced grid, finite differencing or standard path integration schemes have to be employed in the estimation of the spatial derivatives of the velocity gradient tensor δv_p. Moreover, each velocity vector is disturbed by a measurement uncertainty called noise. Further the recovered velocity estimates are not completely independent because the neighboring interrogation areas partly sample the same particles. It is a common practice to oversample a PIV recording twice – corresponding to a 50% overlap of the interrogation windows – to fulfill the Nyquist sampling theorem as well as to extract the maximum spatial resolution. The effect of the 50% oversampling on the estimation of the differential quantities is small, whereas a 75% overlap would lead to significantly noisier differential estimates (Raffel et al., 1998).

By definition the vorticity is related to the circulation by the Stokes theorem. The vorticity was determined based on the application of the Stokes theorem on a small surface

$$\omega_y = \lim_{S \to 0} \oint \frac{v_p \, dl}{S} \qquad \text{(F.12)}$$

where l denotes the path of integration around the surface S (Landreth and Adrian, 1990). The vorticity at a sampling point was estimated by a circulation around the neighboring eight samples as shown in Fig. F.2c). The vorticity estimator based on circulation out performed simple finite difference schemes in a comparison (Westerweel, 1993). This performance testing confirmed that the noise is amplified by the differentiation of the PIV data. A differential estimator uncertainty of 20% would require a velocity measurement with an accuracy of roughly 2%. Such a high accuracy was only accomplished for the peak velocities in a measurement with an optimal adaption of the pulse separation (Appendix E). The accuracy of the differential quantities may be considered roughly one order of magnitude lower than the measurement accuracy of the velocity vector fields. In depth investigations of the differential estimators and their uncertainties were conducted by several authors (Westerweel, 1993; Fouras and Soria, 1998; Raffel et al., 1998; Luff et al., 1999). Similar approaches as to the vorticity estimation were used in the estimation of the shear strain and the out-of-plane strain shown in Figs. F.2b,c), respectively. The elon-

gational strain and the divergence were estimated by calculating the net flow across the boundaries of the contours.

F.5 Integral quantities

The velocity fields obtained by PIV may be used to estimate other fluid mechanical quantities by means of integration (Imaichi and Ohmi, 1983). If the flow field under investigation is nearly two dimensional, steady as well as incompressible the pressure field could be estimated through the numerical integration of the steady Navier-Stokes equations in two-dimensional form (Hudson et al., 1995). Further pass integrals would allow to determine the mass flows across a control surface or line as well as the stream function in certain cases. In the present application of PIV to landslide generated impulse waves the task is complicated by the unsteadiness of the flow, the continuously altering interfaces and the phase mixing. The unsteady flow prohibits the calculation of the pressure field, which would be of interest at the interface between the slide and the water. An accurate estimation of both the potential and kinetic energies of the flow field in the wave generation area, immediately after impact during slide penetration would be of interest to numerical modelers (pers. com.: Dr. Steven Ward, UCSC). Basically, PIV could provide all the necessary data with the water and slide surfaces as well as the velocity vector fields, but the task would require extremely large measurement areas. Even two adjacent areas of view mounted together in 49 sets of the present study are not sufficient in most cases, although covering an instantaneous measurement area of $0.8 \times 1.6 \, \text{m}$.

Appendix G: Wave energy

G.1 Potential wave energy

The potential energy E_{pot} of any wave, or system of waves, due to the elevation or depression of the fluid above or below the mean water level is

$$E_{pot} = \frac{1}{2} b \rho_w g \int_0^L \eta^2 \, dx \tag{G.1}$$

with the water surface elevation η from the stillwater level (Rayleigh, 1877; Lamb, 1932). The general relationship of Eq. G.1 for the potential wave energy may be transformed to

$$E_{pot} = \frac{1}{2} b \rho_w g c \int_0^L \eta^2 \, dt \tag{G.2}$$

by assuming a constant wave propagation velocity c. It is recalled that the measured impulse wave trains were transient and non-stationary in a moving reference frame. Subsequent wave crests and troughs had different wave propagation velocities varying by up to 30% [para 4.7.11]. Even the up- and down-crossings of the surface profile embracing individual wave crest or troughs did not travel at the same propagation velocity. Hence potential wave energy computations based on Eq. G.2 are less accurate than direct estimates according to Eq. G.1. Direct estimates require the measurement of the water surface in space, which is only possible with imaging techniques. The wave gauges only recorded the water surface profile in time.

G.2 Kinetic wave energy

The general expression for the kinetic energy of any gravity water wave is

$$E_{kin} = \frac{1}{2} b \rho_w \int_0^L \int_{-h}^{\eta} (v_{px}^2 + v_{pz}^2) \, dz \, dx \tag{G.3}$$

with the local horizontal and vertical water particle velocities v_{px} and v_{pz}, respectively (Rayleigh, 1877; Lamb, 1932). The direct determination of the kinetic energy of a water wave requires the instantaneous measurement of the water particle velocity vector field covering the area from the bottom to the free surface and over the whole wave length. Basically, PIV could provide all the necessary data with the water surface as well as the velocity vector fields, but the task would require extremely large measurement areas. Even two adjacent areas of view mounted together in 49 sets of the present study are not

sufficient in most cases, although an instantaneous measurement area of $0.8 \times 1.6\,\text{m}$ was covered. The mean and the turbulent kinetic energy of small areas under breaking waves was extracted from PIV-data by Melville et al. (2002). The general relationship of Eq. G.3 for the kinetic wave energy may be transformed to

$$E_{kin} = \frac{1}{2}b\rho_w c^2 \int_0^T \int_{-h}^{\eta} v_{px}^2 \, dz \, dt \qquad \textbf{(G.4)}$$

by assuming strict periodicity and a constant wave propagation velocity c. The relationship of Eq. G.4 requires only a continuous measurement of the horizontal velocity profile at an arbitrary cross-section. The wave gauges provide continuous surface profiles whereas the velocity profiles are only available at 15Hz. The available PIV data sets do not cover the area from the impact to the first wave gauge – except for the smallest still-water depth $h = 0.3\,\text{m}$. Further the slide front reached slightly beyond the first wave gauge and the collapsing impact crater reached out to the first wave gauge in some cases. Hence an accurate estimation of the kinetic wave energy would require PIV measurements further away from the slide impact area in the wave propagation zone. Finally it is recalled that the measured impulse wave trains were transient and non-stationary in a moving reference frame. Subsequent wave crests and troughs had different wave propagation velocities varying by up to 30% [para 4.7.11]. Even the up- and down-crossings of the surface profile embracing individual wave crest or troughs did not travel at the same propagation velocity. Hence kinetic wave energy computations based on Eq. G.4 are less accurate than direct estimates according to Eq. G.3.

The relationship for the kinetic wave energy Eq. G.4 may be simplified by introducing the wave drift mass m_{wd}

$$m_{wd} = b\rho_w \int_0^T \int_{-h}^{\eta} v_{px}^2 \, dz \, dt \qquad \textbf{(G.5)}$$

which corresponds to the water mass discharged in one period at an arbitrary cross-section. The definition of the drift mass per period is valid for both water waves and sound waves. The wave drift mass is simply related to the momentum per wavelength and the kinetic wave energy. Introducing the drift mass given by Eq. G.5 in the relationship for the kinetic wave energy Eq. G.4 yields

$$E_{kin} = \frac{1}{2}m_{wd} c^2 \qquad \textbf{(G.6)}$$

according to Yih (1997). The simple relationships of Eq. G.6 holds for two-dimensional periodic water waves and sound waves. This kinetic energy definition is rigorous and not restricted to linear waves. It is valid not only for symmetric waves such as those treated by Stokes (1847) and Struik (1926), but also for unsymmetrical waves such as discovered by Chen and Saffman (1980) and Benjamin (1995). Further the waves may be of finite amplitude. Nevertheless strict periodicity is required besides the general assumption of

irrotationality. The wave crests and troughs of a transient impulse wave train travel at individual wave propagation velocities and strict periodicity is not fulfilled. Analogously the momentum per wavelength is $m_{wd}c$. These simple relationships are also applicable to three-dimensional periodic waves if the kinetic energy, momentum, and drift mass are considered for one wave cell, the area of which is the product of the wavelengths in two perpendicular directions.

Early in this century Levi-Civita (1912, 1921) showed that, for periodic water waves, twice the kinetic energy per wavelength is equal to the momentum per wavelength times the wave velocity c. But he did not relate either quantity to the drift mass, although drift in water waves was not unknown in his time. Midway through this century and in the same year, Ursell (1953) and Longuet-Higgins (1953, 1975) studied mass transport in periodic water waves, and Darwin (1953) studied fluid drift caused by a body moving (along the x-axis) with constant velocity from $x = -\infty$ to $+\infty$ in an inviscid fluid of constant density and infinite extent. But neither Ursell nor Longuet-Higgins conceived the notion of drift mass per period (in time) of the waves, and Darwin already knew that his drift mass is ill defined, since the defining integral is not uniformly convergent, but dependent on how infinity is approached. Further studies of Darwin's problem can be found in Yih (1985, 1995) and Eames et al. (1994).

G.3 Energy partition

In the special case of linear water waves the kinetic wave energy E_{kin} equals the sum of the potential wave energy E_{pot} and the surface energy E_σ due to surface tension, resulting in

$$E_{kin} = E_{pot} + E_\sigma \tag{G.7}$$

according to Lighthill (1978). The relationship of Eq. G.7 does not hold for non-linear waves of finite amplitude and the difference between the two sides may become significant depending on the application. The surface energy E_σ due to surface tension needs to be considered only for capillary waves and may be neglected for the gravity waves under consideration. The total wave energy E_{tot} thus becomes

$$E_{tot} = m_{wd}c^2 \tag{G.8}$$

which resembles a famous formula in physics. Except in the shallow water depth regime the wave drift mass may not be determined accurately from wave gauge recordings in the time domain. In deep and intermediate water depth waves travel in groups. Individual waves die out at the front and are formed at the back of a group. Energy transmission is maximal where the waves in the group reach maximal size. It follows that the energy is contained within the wave group, and is propagated at the group speed. The energy flux is defined as the product of wave energy times wave group velocity c_G. In shallow water the wave group velocity equals the wave propagation velocity $c_G = c$. In intermediate

water depth the group velocity decreases relative to the wave propagation velocity with decreasing wave length. In deep water the group velocity equals half the wave propagation velocity $c_G = 0.5c$ (Dean and Dalrymple, 1991).

For solitary waves the horizontal water particle velocities v_{px} always point in the direction of wave propagation. Hence the wave drift mass m_{wd} corresponds to the whole water mass above the stillwater surface $z = 0$ (Longuet-Higgins, 1974). The solitary wave is the sole water wave where the drift mass is simple to measure. The potential energy of a solitary wave is according to Boussinesq (1877) and Munk (1949)

$$E_{pot} = \frac{4}{3} b \rho_w g h^2 a \sqrt{\frac{a}{3h}} \qquad \text{(G.9)}$$

It is recalled that the amplitude of a solitary wave corresponds to the total wave height $H = a$. The total energy of a solitary wave E_{sol} may be approximated by

$$E_{sol} \approx 2E_{pot} = \frac{8}{3} b \rho_w g h^2 a \sqrt{\frac{a}{3h}} \qquad \text{(G.10)}$$

assuming equipartition between the kinetic and the potential wave energy. The relationship of Eq. G.10 was used by Huber (1980) to compute the energy of soliton like waves.

The potential and the kinetic energies of sinusoidal waves are

$$E_{pot} = E_{kin} = \frac{1}{4} b \rho_w g a^2 L \qquad \text{(G.11)}$$

assuming equipartition (Lamb, 1932). The wave energy of sinusoidal waves is proportional to the square of the wave height.

Since the kinetic energy is difficult to measure in most cases the assumption of the wave energy equipartition between the kinetic and the potential energy was made by all previous authors analyzing landslide generated impulse waves – often without even remarking that other partitions between kinetic and potential wave energies are also possible. Numerical values of wave energy partitions for different water waves may rarely be found in the literature before digital computers became available. The kinetic and the potential energies for solitary waves up to the breaking limit $H_b/h = 0.78$ were computed with the full relationships given by Eqs. G.1 and G.3, respectively. The necessary expressions for the water surface profile, the wave propagation velocity and the vertical and horizontal water particle velocities were presented previously in [para 5.3] according to McCowan (1891). Further full numerical solutions for almost all types of waves spanning the whole range from the deep to the shallow water depth regime and from small amplitudes up to breaking heights were computed and tabulated by Williams (1985). Synthesis of the computed kinetic to potential wave energy ratios E_{kin}/E_{pot} versus the wave height to water depth ratio H/h and the wave height to breaking height ratio H/H_b are shown in Figs. 0.1a,b), respectively. As mentioned previously the breaking limit increases with the wavelength reaching a maximum for solitary waves at $H_b/h = 0.78$. The kinetic wave energy exceeds the potential wave energy in finite amplitude or non-linear gravity waves. Equipartition between the kinetic and the potential energy prevails only in small

amplitude or linear waves. The kinetic to potential wave energy ratio E_{kin}/E_{pot} increases with increasing wave height and wave length. The largest wave energy ratio is reached with $E_{kin}/E_{pot} = 1.22$ in solitary waves prior to breaking at $H_b/h = 0.78$.
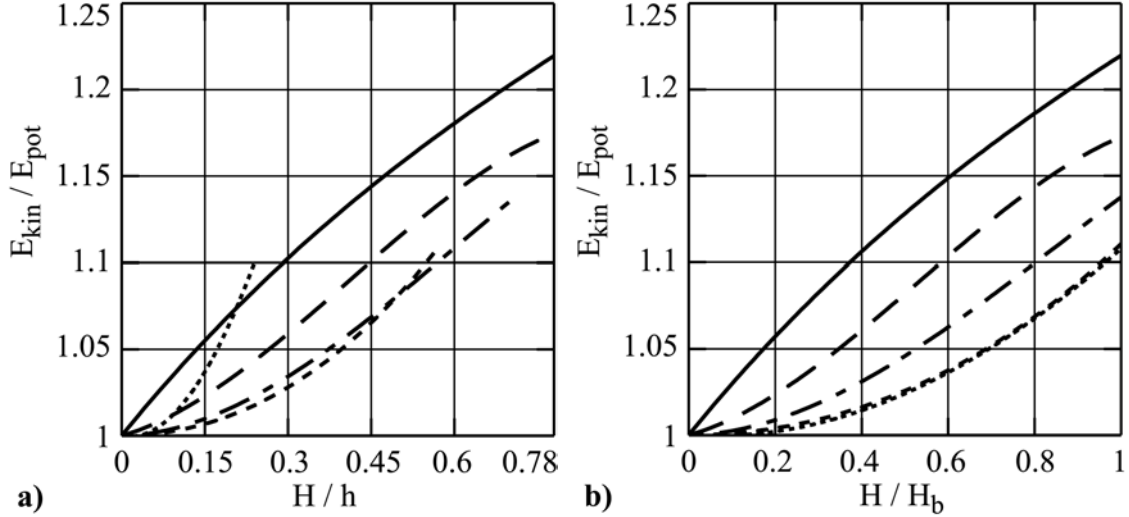
Figure 0.1 **Wave energy partition**: **a)** E_{kin}/E_{pot} versus H/h for (──) solitary wave and periodic waves with (— —) $L/h = 20$, (·—·) $L/h = 10$, (---) $L/h = 5$, (····) $L/h = 2$; **b)** E_{kin}/E_{pot} versus H/H_b with symbols as in a).

Hence the total wave energy $E_{tot} = E_{pot} + E_{kin}$ computed numerically may exceed total wave energy estimates based on equipartition between the kinetic and potential wave energy by up to 11%. The accuracy of potential wave energy estimates computed by integration of wave surface profiles recorded with wave gauges in the time domain according to Eq. G.2 is limited to roughly ±15 % due to the assumption of a constant wave propagation velocity c of individual crests and troughs as well as the noise in the wave gauge recordings induced by the splash. The accuracy of the wave energy estimates may further decay for breaking waves. The variation of the subsequent wave crest and trough propagation velocities by up to 30% was taken into account by computing the potential wave energy for each crest and trough considering the individual wave propagation velocities. The variation of the propagation velocity within a single wave crest is not taken into account. The up- and down-crossings of the surface profile embracing individual wave crests or troughs did not travel at the same propagation velocity. The total wave energy estimate $E_{tot} \approx 2E_{pot}$ based on equipartition is fully adequate to the wave surface profiles of transient impulse wave trains recorded with wave gauges in the time domain.

The time localized wave energy may be computed from the wavelet spectrum of the wave gauge recordings according to Fritz and Liu (2002). The energy packet of the impulse wave train stretched out during propagation resulting in a decrease of the time localized energy, whereas the total wave energy included in a transient impulse wave train dissipates much slower. The wave energy disperses with the wave train. The analysis of the wave energy dissipation within the whole impulse wave train would require a longer

wave tank. In the present study the back of the wave train was often biased by wave reflection to the third wave gauge.

Regarding comparisons of experimental data and field data it is worthwhile recalling that a basic problem in fluid dynamics is the relationship between the Eulerian and the Lagrangian representations of the fluid motion. Surface waves can be recorded in two kinds, either with a fixed (Eulerian) probe or with a free-floating (Lagrangian) buoy. For steep waves, the differences between corresponding properties can be very marked according to Longuet-Higgins (1986, 1987 and 1988).

Acknowledgments

I would like to thank all persons and organizations that contributed to the work described in this thesis. In particular I would like to acknowledge the following individuals:

Curriculum Vitae

Hermann M. Fritz
born on May 20, 1972 in Zürich, Switzerland
citizen of Switzerland (CH)

10/1997 - 10/2002	Ph.D. studies at the Laboratory of Hydraulics, Hydrology and Glaciology (VAW) of the Swiss Federal Institute of Technology (ETH), Zürich, Switzerland Ph.D.-thesis: "Initial phase of landslide generated impulse waves"
07/1997 - 09/1997	project engineer in the river hydraulics section at the Laboratory of Hydraulics, Hydrology and Glaciology (VAW) of the Swiss Federal Institute of Technology (ETH)
10/1991 - 01/1997	diploma studies in Civil Engineering at the Swiss Federal Institute of Technology (ETH), Zürich, Switzerland diploma thesis: "Strömungsverhältnisse bei Dammüberfällen"
06/1994 - 11/1995 01/1997 - 05/1997	military service
04/1985 - 09/1991 04/1979 - 04/1985	Secondary school, KS Hohe Promenade Zürich, Switzerland primary school in Zürich, Switzerland elementary school in Burtonsville, Md, USA